
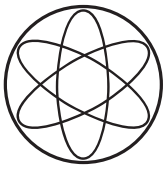

Searches for new resonances decaying to a Higgs and a vector boson with the ATLAS detector at the LHC

ANDREAS HÖNLE

Dissertation

München 2021

TECHNISCHE UNIVERSITÄT MÜNCHEN
Fakultät für Physik

Max-Planck-Institut für Physik
(Werner-Heisenberg-Institut)

Searches for new resonances decaying to a Higgs and a vector boson with the ATLAS detector at the LHC

Andreas Hönle

Vollständiger Abdruck der von der Fakultät für Physik der Technischen Universität München zur Erlangung des akademischen Grades eines

Doktors der Naturwissenschaften (Dr. rer. nat.)

genehmigten Dissertation.

Vorsitzender:

apl. Prof. Dr. Norbert Kaiser

Prüfer der Dissertation:

1. apl. Prof. Dr. Hubert Kroha
2. Prof. Dr. Lothar Oberauer

Die Dissertation wurde am 29.06.2021 bei der Technischen Universität München eingereicht und durch die Fakultät für Physik am 08.07.2021 angenommen.

Searches for new resonances decaying to a Higgs and a vector boson with the ATLAS detector at the LHC

Andreas Hönle

Abstract

Several physics phenomena cannot be explained by the otherwise experimentally thoroughly tested Standard Model of particle physics, implying that it is not a complete theory. This advocates the existence of new elementary particles with masses at the TeV scale, that are contained in a more fundamental theory. Many extensions of the Standard Model predict the existence of additional Higgs bosons or heavy neutral and charged vector bosons. This thesis presents general searches for such particles with the ATLAS detector at the Large Hadron Collider at CERN, based on minimal theoretical assumptions. This allows for the re-interpretation of search results in the framework of many theories beyond the Standard Model, with the focus on the predictions of benchmark scenarios within the Two-Higgs Doublet Model (2HDM) and the Heavy Vector Triplet (HVT) Model. The new particles are searched for in the Vh diboson decay channels with a Standard Model vector boson $V = W^{\pm}, Z$, and the Higgs boson h, focusing on the semileptonic $\nu\bar{\nu}b\bar{b}$, $\ell^{\pm}\overset{(-)}{\nu}_{\ell}b\bar{b}$, and $\ell^{\pm}\ell^{\mp}b\bar{b}$ ($\ell = e, \mu$) final states with Higgs decays into a pair of b-quarks. Results using pp collision data at $\sqrt{s} = 13$ TeV, recorded with the ATLAS detector between 2015 and 2018, are presented. No significant excess of events over the background-only expectation is observed and upper limits on the resonance production cross section times branching ratio are set at 95 % confidence level.

Results are presented for the search in the $\ell^{\pm}\overset{(-)}{\nu}_{\ell}b\bar{b}$ final state using 36.1 fb^{-1} of proton-proton collision data. Cross section times branching ratio values for a HVT W' resonance, $\sigma_{pp\to W'\to Zh}\times\mathcal{B}(h \to b\bar{b}, c\bar{c})$, between 0.22 pb and 1.1 fb are excluded at 95 % confidence level for W' resonance masses between 500 GeV and 5 TeV. The limits correspond to the exclusion of HVT W' resonance masses below 2.82 TeV in the HVT benchmark models.

Limits are also set on the cross section times branching ratio values for a HVT Z' vector boson and a 2HDM A pseudoscalar, using 139 fb^{-1} of data in the $\nu\bar{\nu}b\bar{b}$ final state and in the combination of $\nu\bar{\nu}b\bar{b}$ and $\ell^{\pm}\ell^{\mp}b\bar{b}$ final states. 95 % confidence level upper limits on cross sections times branching ratios are set between 0.30 fb and 31 pb, depending on final state, signal model, and production mode, for resonance masses between 300 GeV and 5 TeV. In the HVT benchmark models, Z' resonances with masses below 3.0 TeV are excluded at 95 % confidence level.

Acknowledgements
I want to thank Sandra Kortner for supervising my PhD and for her tireless and continuous support throughout my time at the Max-Planck-Institute for Physics. I am thankful to Hubert Kroha who—as a second supervisor of my master's thesis—originally introduced me to the spectacular ATLAS experiment and ultimately offered me a PhD position in his research group. I am deeply grateful for the countless excellent learning opportunities and the positive atmosphere that the MPP ATLAS research group provides, including my participation in national and international summer schools, and supporting my 8-month-long research stay at CERN, Geneva.

Thank you to Lothar Oberauer and Norbert Kaiser for being on my dissertation committee.

After joining the MPP ATLAS group, Felix Müller was there as my first day-to-day supervisor, and he did a fantastic job. He introduced me to the new, fascinating, and slightly scary world of cutting-edge high energy physics, including its very own (very special) way of developing analysis software. I learned to like and respect Felix as a mentor, supervisor, and individual.

The gap left behind after Felix' departure was filled by the incredibly skilled, hard-working Dominik Duda, without whom most of the results presented in this thesis would have never been achieved. I am impressed by the profound understanding of collider physics and the huge experience he brought to the table, and enjoyed every minute of our collaboration.

I am grateful for the brilliant minds I had the pleasure to collaborate with as part of my analysis work. Most notably Spyridon Argyropoulos, Garabed Halladjian, Stephen Jiggins, Hannah Arnold, Wade Fisher, Kalliopi Iordanidou, Nora Pettersson, Makayla Vessella, Ulla Fischer, Tong Qiu, and Tong Li.

Further I want to thank my colleagues at the Max-Planck-Institute who made my time there unforgettable. My office mates Korbinian Schmidt-Sommerfeld, and, after I moved to Katharina Ecker's former desk, Philipp Gadow, and Verena Walbrecht. My table tennis rivals Stefan Maschek and Christian Graf. My Schafkopf buddies Miroslav Gabriel, Mathias Hüther, Lorenz Emberger, and Martin Schuster. And of course the people responsible for phenomenal Ringberg meetings and DPGs, Nicolas Köhler, Rainer Röhrig, and Johannes Junggeburth.

Most importantly I want to say thank you to my ever-supporting family, who always allowed me to make my own choices and to follow my passion. Their contribution to where I am today cannot be overstated. Lastly, I want to mention my partner Lena, who unconditionally supported me throughout the entire time of my PhD, and who raised my spirits in all the frustrating times. Thank you!

Table of contents

INTRODUCTION

With the advent of modern particle accelerators in the 1950s, a fascinating quest to understand the fundamental building blocks of our universe began. The new machines produced a plethora of previously unobserved particles (*e.g.* [1]). Today, these particles are identified as composite, built from the elementary particle content of the Standard Model of Particle Physics. The Standard Model (SM) is a relativistic quantum field theory that combines three of the four fundamental forces in nature: the strong interaction, the weak interaction, and the electromagnetic interaction. The fourth interaction, gravity, is many orders of magnitude weaker and is not contained in the Standard Model. Efforts to combine all four interactions in a unified theory continue to this day.

The success of the Standard Model as a theory of the fundamental physical processes is unprecedented. Not only was it able to bring order to the vast number of newly observed particles, it also correctly predicted the existence of previously unobserved particles, such as the neutral and charged weak gauge bosons [2–5], the top quark [6, 7], or the most recently discovered Higgs boson [8, 9]. However, there are conflicts between the Standard Model predictions and astrophysical observations. The particles of the Standard Model only account for about 5 % of the energy in the observable universe. The remaining 95 % are attributed to Dark Energy and Dark Matter whose nature is still not understood. Furthermore, there are many theoretical shortcomings of the Standard Model. The observed mass of the Higgs boson, for example, would require unnaturally large fine-tuning [10] in the Standard Model—an issue addressed by many extensions of the Standard Model.

The Standard Model is based on a rich theoretical framework of quantum fields and symmetry principles, of which it is one of the simpler possible realisations. More complex realisations are explored in theoretical extensions of the Standard Model. For instance, the Higgs sector in the Standard Model needs not be limited to a single SU(2) Higgs doublet, but can be extended by a second Higgs doublet [11], which predicts—amongst others—a new pseudoscalar A boson. Such models address questions unsolved by the Standard Model, like the abundance of matter over anti-matter in

the observable universe. Common to many extensions of the Standard Model is the prediction of additional heavy vector bosons, $W'^{\pm}$ and Z'. These new particles are the result of an extra SU(2) symmetry group in the extended theory, similar to the weak gauge symmetry in SU(2) in the Standard Model. The similar properties of these particles in a wide range of models in combination with the clear experimental signature makes them the perfect probes for a segue into an era of physics beyond the Standard Model. Heavy vector bosons can be described by an effective Lagrangian in the so-called Heavy Vector Triplet models [12].

If they exist, the new heavy Higgs and vector bosons with masses at the TeV scale can be produced in proton-proton collisions at the Large Hadron Collider (LHC) at CERN, Geneva. The general-purpose ATLAS detector at the LHC is desgined for the search for such new particles in different decay modes. After the discovery of the Higgs boson at the LHC in 2012, the ATLAS experiment now pursues detailed measurements of Higgs boson properties, its interactions with Standard Model particles, and with possible new particles beyond the Standard Model. Hence, studying the Higgs boson provides a powerful probe for the exploration of new models. In many cases, the new A, $W'^{\pm}$, and Z' bosons are predicted to decay into a Higgs boson and a SM vector boson ($W^{\pm}$ and Z). Searches for new bosons in these decay channels are the subject of this thesis. All presented searches have been performed in semi-leptonic final states with a leptonic weak gauge boson decay and the Higgs boson decay in the dominant mode into a pair of b-quarks. Leptonic weak gauge boson decays are chosen to provide an efficient trigger and to allow for a strong suppression of the multijet background processes.

In this thesis, searches with the ATLAS detector for new heavy resonance decaying into a SM vector boson and a Higgs boson in three different final states are discussed. The final states are associated to the vector boson decay modes comprising in addition to b-quarks: neutrino pairs from Z boson decay; a neutrino and a charged lepton (electron or muon) from W boson decay; and two charged leptons from Z boson decay. In order to maximise the sensitivity of the search for the new particles (A, $W'^{\pm}$, Z'), different decay final states are combined.

The thesis is structured as follows. In Chapter 1, a short introduction to the Standard Model of Particle Physics is given. Extensions of the Standard Model predicting the existence of additional heavy resonances decaying into a Higgs boson and a vector boson are discussed in Chapter 2. The LHC and the ATLAS detector are described in Chapter 3. The search for new heavy charged Wh resonances in the final state with a neutrino, a charged lepton, and a b-quark pair is presented in Chapter 4. Chapter 5 details the search for neutral Zh resonances in the final state with a neutrino pair and a b-quark pair. The latter search is combined with the search in the final state with two oppositely charged leptons and a b-quark pair, as described in Chapter 6. Finally, a summary of the results and an outlook for future developments is given in Chapter 7. Throughout the thesis, figures with neither an ATLAS label nor a reference have been produced by the author of this thesis as an internal contribution to the results presented in Refs. [13–16] or as an optimisation with respect to these publications.

CHAPTER ONE

THE STANDARD MODEL OF PARTICLE PHYSICS

The Standard Model of Particle Physics (SM) is a relativistic quantum field theory. Its symmetry principles were used to predict the existence of new particles, like the weak gauge bosons [2–5], the top quark [6, 7], and—most recently—the Higgs boson [8, 9]. The existence of the Higgs boson is a result of spontaneous electroweak symmetry breaking—a concept that allows for the preservation of the electroweak gauge symmetry of the Lagrangian for massive fields. The SM with its local gauge interactions is a renormalizable theory. It enables accurate calculations of cross sections and branching fractions in perturbation theory. The predictions of the SM have been tested in countless experiments and—to date—are in excellent agreement with the measurements. A recent summary of tests of SM predictions performed by the ATLAS collaboration is shown in Figure 1.1. The SM impressively describes the measured cross sections over more than ten orders of magnitude.

This chapter provides a brief introduction to the basic concepts of the SM. It relies on the summary provided in Ref. [18]. A more complete introduction to the physics of the SM is given in Refs. [19–21].

1.1 Particle content of the Standard Model

The SM describes the interactions of quarks, leptons, and gauge bosons and the Higgs boson. It is a Yang-Mills theory [22, 23] based on the gauge group

$$\mathrm{SU}(3)_C \times \mathrm{SU}(2)_L \times \mathrm{U}(1)_Y . \tag{1.1}$$

As a gauge theory, the SM is based on the principle of local symmetry. According to Noether's theorem [24], these symmetries give rise to conserved charge quantum numbers associated with the particle fields.

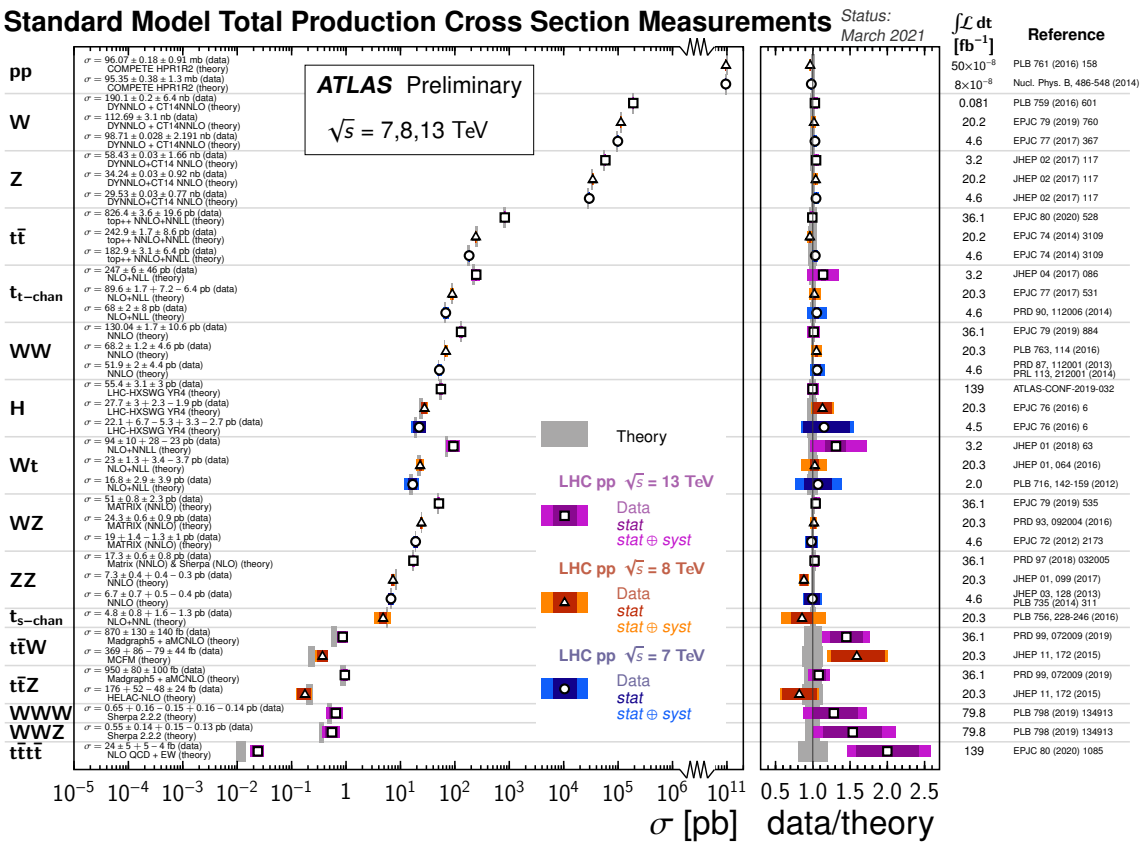

Figure 1.1: Summary of total Standard Model particle production cross section measurements by the ATLAS experiment, corrected for decay branching fractions, compared to the theoretical expectations and their ratio. Originally published in Ref. [17].

The strong interaction is described by $\mathrm{SU}(3)_C$, leading to the conservation of the associated colour charges in the theory of quantum chromodynamics (QCD) [25–28]. The mediating particles of the strong interaction are the eight massless gluon fields G^a_μ, $a = 1, \ldots, 8$. The free parameter of the strong interaction is the strong gauge coupling constant g_s, often expressed in terms of the strong finestructure constant $\alpha_s = g^2/(4\pi)$.

The electroweak interaction is based on the local gauge symmetry group $\mathrm{SU}(2)_L \times \mathrm{U}(1)_Y$ [29–31], corresponding to the conservation of the weak isospin quantum numbers I, I_3 and of the weak hypercharge Y. The gauge fields of the electroweak theory are the isotriplet W^i_μ, $i = 1, 2, 3$, and the isosinglet B_μ with the coupling constants g and g', respectively. Explicit mass terms are not allowed for the gauge fields as they would violate gauge invariance. In order to obtain the observed massive $W^\pm$ and Z bosons, the $\mathrm{SU}(2)_L \times \mathrm{U}(1)_Y$ symmetry is spontaneously broken to the residual electromagnetic gauge group $\mathrm{U}(1)_Q$ with conserved electric charge Q [32–37]. The charge quantum numbers of the

unified electroweak gauge theory are related via the Gell-Mann-Nishijima relation [38, 39]

$$Q = I_3 + Y/2. \tag{1.2}$$

The three families of quarks and leptons, fermions with spin $1/2$, appear in the fundamental representation of the group $\mathrm{SU}(2)_L \times \mathrm{U}(1)_Y$ as left-handed components of Dirac spinor fields $\psi_f(x)$,

$$\psi_f(x)_L = \frac{1-\gamma_5}{2}\psi_f(x). \tag{1.3}$$

The left-handed fermion fields from isospin doublets with $I = 1/2$ and participate in interactions with the charged $W^{\pm}$ bosons, while the right-handed fields

$$\psi(x)_R = \frac{1+\gamma_5}{2}\psi(x), \tag{1.4}$$

are $\mathrm{SU}(2)_L$ singlets with $I = 0$. Since the right-handed singlets do not couple to the charged weak gauge bosons, the weak interaction is maximally parity violating.

The SM classifies the fermions in three families of leptons and quarks. Quarks carry colour charge, while leptons do not. The three families of left-handed isospin doublets and right-handed isospin singlets of leptons (electron, muon, and tau lepton, and their respective neutrino partner) are

$$\begin{pmatrix}\nu_e\\ e^-\end{pmatrix}_L, \quad \begin{pmatrix}\nu_\mu\\ \mu^-\end{pmatrix}_L, \quad \begin{pmatrix}\nu_\tau\\ \tau^-\end{pmatrix}_L, \quad {e^-}_R, \quad {\mu^-}_R, \quad {\tau^-}_R. \tag{1.5}$$

Right-handed neutrinos and left-handed anti-neutrinos do not couple to the SM interactions.

The $\mathrm{SU}(2)_L$ quark doublets contain up- and down-type quarks with electric charge quantum numbers of $2/3$ and $-1/3$, respectively. The three families up-type quarks are the up (u), charm (c), and top (t) quarks. The corresponding down-type quarks are the down (d), strange (s), and bottom (b) quarks. They form colour triplets under $\mathrm{SU}(3)_C$,

$$q = \begin{pmatrix}q^r\\ q^g\\ q^b\end{pmatrix}, \tag{1.6}$$

and carry colour charges $C = r, g, b$. The quark eigenstates of the strong and the electromagnetic interaction are identical with their mass eigenstates. The weak quark eigenstates in the $\mathrm{SU}(2)_L$ doublets, however, differ from the mass eigenstates according to experimental observation. The weak and mass eigenstates of the quarks are connected by unitary transformations. In the charged weak interaction,

the up-type quarks interact with the down-type states transformed by the Cabibbo-Kobayashi-Maskawa (CKM) mixing matrix [40, 41],

$$\begin{pmatrix} u \\ c \\ t \end{pmatrix} \overset{W^{\pm}}{\longleftrightarrow} \begin{pmatrix} d' \\ s' \\ b' \end{pmatrix} = \begin{pmatrix} V_{ud} & V_{us} & V_{ub} \\ V_{cd} & V_{cs} & V_{cb} \\ V_{td} & V_{ts} & V_{tb} \end{pmatrix} \begin{pmatrix} d \\ s \\ b \end{pmatrix}. \tag{1.7}$$

The latest absolute values of the CKM matrix are [42]

$$|V| = \begin{pmatrix} 0.97370 \pm 0.00014 & 0.2245 \pm 0.0008 & 0.00382 \pm 0.00024 \\ 0.221 \pm 0.004 & 0.987 \pm 0.011 & 0.00410 \pm 0.00140 \\ 0.0080 \pm 0.0003 & 0.0388 \pm 0.0011 & 1.013 \pm 0.030 \end{pmatrix} \tag{1.8}$$

which shows a hierarchy of coupling strengths of charged weak transitions between the quark families, decreasing with distance between the families. Neutral flavour changing weak interactions are strongly suppressed in the SM.

The right-handed quarks have weak isospin $I = 0$ and transform as $\mathrm{SU}(2)_L$ singlets,

$$u_R, d_R, c_R, s_R, t_R, b_R. \tag{1.9}$$

1.2 Lagrangian formalism of the Standard Model

As a quantum field theory, the SM is described by a Lagrangian density. For a field $\phi(x)$, the action $S[\phi] = \int \mathrm{d}^4x \mathcal{L}(\phi(x))$ is used in combination with Hamilton's principle of least action to obtain the equations of motion

$$\partial_\mu \frac{\partial \mathcal{L}(\phi)}{\partial(\partial_\mu \phi)} - \frac{\partial \mathcal{L}(\phi)}{\partial \phi} = 0. \tag{1.10}$$

The spin-0 Higgs boson is described by a scalar field $\phi(x)$. Fermions with spin $1/2$ are described by spinor fields $\psi(x)$. Finally, the spin-1 gauge bosons are described by vector fields A_μ.

The SM Lagrangian density consists of the terms

$$\mathcal{L} = \mathcal{L}_{\text{Gauge}} + \mathcal{L}_{\text{Fermion}} + \mathcal{L}_{\text{Higgs}} + \mathcal{L}_{\text{Yukawa}}, \tag{1.11}$$

corresponding to the pure gauge field kinematic terms, the fermion kinematic and gauge coupling terms, the Higgs sector field terms, and Yukawa interactions between fermions and the Higgs field. The terms will be explained in more detail in the following.

The presence of the SM fields is a direct consequence of requiring the observed local gauge symmetries of the Lagrangian density. A global U(1) symmetry, for instance, corresponds to the invariance under phase transformations $\phi(x) \rightarrow \phi'(x) = e^{i\alpha}\phi(x)$ with constant phase α. Promoting the phase to a space-time-dependent function, $\alpha \rightarrow \alpha(x)$, the symmetry transformation becomes a local phase transformation, $\phi(x) \rightarrow \phi'(x) = e^{i\alpha(x)}\phi(x)$. In order to establish symmetry of the Lagrangian under the local phase transformation, a vector field A_μ is introduced with minimal gauge invariant coupling to the fermion fields via replacement of the derivative by the covariant derivative,

$$\partial_\mu \rightarrow D_\mu = \partial_\mu - ieA_\mu. \tag{1.12}$$

The Abelian gauge group U(1) describes the electromagnetic interaction. The vector field A_μ thus corresponds to the electromagnetic field potential with coupling strength to the fermion fields given by the electric charge e. The concept can be generalised to non-Abelian gauge symmetries. For the electroweak $\mathrm{SU}(2)_L \times \mathrm{U}(1)_Y$ symmetry of the SM, the gauge vector fields W^i_μ ($i = 1, 2, 3$) with the coupling constant g and the singlet gauge field B_μ with the coupling constant g' are introduced. The $\mathrm{SU}(3)_C$ symmetry gives rise to the eight gluon gauge fields G^a_μ ($a = 1, \ldots, 8$) with the coupling constant g_s. The covariant derivatives for $\mathrm{SU}(2)_L \times \mathrm{U}(1)_Y$ are different for left- and right-handed fields,

$$D^{L,R,\,\mathrm{ew}}_\mu = \partial_\mu - igI^{L,R}_i W^i_\mu - ig'\frac{Y}{2}B_\mu, \tag{1.13}$$

where $I^R_i = 0$, and $I^L_i = \frac{1}{2}\sigma_i$ ($i = 1, 2, 3$) are the three weak isospin components given by the Pauli matrices σ_i. The corresponding covariant derivates for $\mathrm{SU}(3)_C$ are

$$D^{\mathrm{strong}}_\mu = \partial_\mu - ig_s\frac{\lambda_a}{2}G^a_\mu, \tag{1.14}$$

with the eight $\mathrm{SU}(3)_C$ colour charge operators expressed in terms of the 3×3 Gell-Mann matrices λ_a ($a = 1, \ldots, 8$) in the fundamental representation. Combined, the covariant derivative of the $\mathrm{SU}(3)_C \times \mathrm{SU}(2)_L \times \mathrm{SU}(1)_Y$ gauge symmetry of the SM becomes

$$D^{L,R}_\mu = \partial_\mu - i\frac{\lambda_a}{2}G^a_\mu - igI^{L,R}_i W^i_\mu - ig'\frac{Y}{2}B_\mu. \tag{1.15}$$

1.2.1 Gauge field term

The pure gauge field term $\mathcal{L}_{\text{Gauge}}$ consists of the kinematic energy density terms of the SM vector boson fields with their field strength tensors

$$\mathcal{L}_{\text{Gauge}} = -\frac{1}{4} G^a_{\mu\nu} G^{\mu\nu,a} - \frac{1}{4} W^i_{\mu\nu} W^{\mu\nu,i} - \frac{1}{4} B_{\mu\nu} B^{\mu\nu}, \tag{1.16}$$

The field strength tensors for the electroweak fields are

$$\begin{aligned} B_{\mu\nu} &= \partial_\mu B_\nu - \partial_\nu B_\mu, \\ \text{and} \quad W^i_{\mu\nu} &= \partial_\mu W^i_\nu - \partial_\nu W^i_\mu + g \varepsilon_{ijk} W^j_\mu W^k_\nu, \end{aligned} \tag{1.17}$$

with the totally antisymmetric tensor ε_{ijk} comprising the structure constants of the $\text{SU}(2)_L$ group. For the strong interaction, the field strength tensors are

$$G^a_{\mu\nu} = \partial_\mu G^a_\nu - \partial_\nu G^a_\mu + g_s f_{abc} G^b_\mu G^c_\nu, \tag{1.18}$$

with the $\text{SU}(3)_C$ structure constants f_{abc}. The terms including the structure constants arise from the non-Abelian nature of the gauge groups and are responsible for the fundamental three- and four-point interactions between the weak gauge bosons and between the gluons. No explicit mass terms are allowed for the gauge fields, as they would violate the local electroweak gauge symmetry. The masses are rather generated by means of the spontaneous electroweak symmetry breaking.

1.2.2 Fermion term

The fermion term comprises the kinetic fermion energy density and the interactions with the gauge bosons

$$\mathcal{L}_{\text{Fermion}} = \sum_j \overline{\psi}^j_L i\gamma^\mu D^L_\mu \psi^j_L + \sum_{j,\sigma} \overline{\psi}^j_{R\sigma} i\gamma^\mu D^R_\mu \psi^j_{R\sigma}, \tag{1.19}$$

where the index $j = 1, 2, 3$ indicates the lepton and quark generation. The fields are the left-handed SU(2) doublets $\psi^j_L = (\psi^j_{L+}, \psi^j_{L-})^T$ and the right-handed singlets $\psi^j_{R\sigma}$. The index $\sigma = \pm$ denotes the up-type (+) and down-type (−) of the fermions. The covariant derivative $D^{L,R}_\mu$ (*cf.* Equation (1.18)) gives rise to the interactions between fermions and gauge bosons. No mass terms are present, as they would violate the (global) electroweak gauge invariance by mixing left- and right-handed states. The fermions obtain their masses as a result of the Yukawa interactions with the Higgs field.

1.2.3 Higgs sector

The term $\mathcal{L}_{\text{Higgs}}$ consists of the Higgs field kinematic term and the Higgs potential,

$$\mathcal{L}_{\text{Higgs}} = (D_\mu \Phi)^\dagger (D^\mu \Phi) - V(\Phi), \tag{1.20}$$

with the scalar complex Higgs doublet $\Phi(x) = (\phi^+(x), \phi^0(x))^T$ with isospin $I = \frac{1}{2}$ and hypercharge $Y = 1$. The covariant derivative corresponds to D^L_μ given by Equation (1.13) and provides the interaction with the W^i_μ and B_μ fields. The Higgs self-interaction is due to the quadratic and quartic terms in the Higgs potential,

$$V(\phi) = -\mu^2 \Phi^\dagger \Phi + \frac{\lambda}{4} (\Phi^\dagger \Phi)^2, \tag{1.21}$$

with the free parameters μ^2 and $\lambda > 0$. The physically interesting case is $\mu^2 < 0$, where the potential is minimised by the non-zero vacuum field configurations $(\Phi^\dagger \Phi)_0 = 2\mu^2/\lambda$. Choosing one specific (*e.g.* the real and electrically neutral configuration one), results in the non-zero ground state

$$\phi_0 = \langle 0|\Phi|0\rangle = \frac{1}{\sqrt{2}} \begin{pmatrix} 0 \\ v \end{pmatrix}, \tag{1.22}$$

with the vacuum expectation value (VEV) $v = |\phi_0| = 2\mu/\sqrt{\lambda}$. This choice of a ground state with non-zero VEV breaks the $\text{SU}(2)_L \times \text{SU}(1)_Y$ symmetry spontaneously, resulting in the residual $\text{U}(1)_Q$ symmetry of the electromagnetic interaction with conserved electric charge.

The Higgs doublet can be expanded around the chosen minimum, yielding in unitary gauge

$$\Phi(x) = \frac{1}{\sqrt{2}} \begin{pmatrix} 0 \\ v + h(x) \end{pmatrix}, \tag{1.23}$$

where $h(x)$ is the massive Higgs scalar field with $m_h = \mu\sqrt{2}$. By choosing the unitary gauge, the massless Goldstone boson excitations of the ground state are absorbed in the longitudinal-polarisation degrees of freedom of the weak gauge bosons, awarding them with their masses.

In order to obtain the mass eigenstates of the physical photon and Z boson fields, A_μ and Z_μ, a rotation of the weak eigenstates by the Weinberg angle θ_W is performed,

$$\begin{pmatrix} Z_\mu \\ A_\mu \end{pmatrix} = \begin{pmatrix} \cos\theta_W & \sin\theta_W \\ -\sin\theta_W & \cos\theta_W \end{pmatrix} \cdot \begin{pmatrix} W^3_\mu \\ B_\mu \end{pmatrix}. \tag{1.24}$$

The charged gauge bosons are given by the linear combinations

$$W_\mu^\pm = \frac{1}{\sqrt{2}}(W_\mu^1 \mp W_\mu^2). \tag{1.25}$$

The Weinberg angle relates the vector boson masses $M_{W,Z}$ and the electroweak coupling constants,

$$\cos\theta_W \equiv \frac{g}{\sqrt{g^2 + g'^2}} = \frac{M_W}{M_Z}. \tag{1.26}$$

1.2.4 Higgs Yukawa couplings

The Yukawa term in the SM Lagrangian introduces the fermion masses after spontaneous electroweak symmetry breaking. In unitary gauge it is then given by

$$\mathcal{L}_{\text{Yukawa}} = -\sum_f m_f \overline{\psi}_f \psi_f - \sum_f \frac{G_f}{\sqrt{2}} \overline{\psi}_f \psi_f h, \tag{1.27}$$

where the index f runs over all charged fermions. The fermions masses are proportional to the Yukawa coupling constants G_f and are given by

$$m_f = G_f \frac{v}{\sqrt{2}}. \tag{1.28}$$

In general, the Yukawa couplings for the quark sector have to be considered as complex matrices in generation space, $G_u = (G_{ij}^u)$, and $G_d = (G_{ij}^d)$. This leads to the mixing of the mass eigenstates of the quark flavours. Leptons do not mix in the minimal model, as the lepton number is conserved.

1.3 Limitations of the Standard Model

Despite the excellent agreement of SM predictions and measurements performed in countless experiments over the timespan of several decades, essential problems are not solved by the SM. A few outstanding problems are listed below.

- Neutrinos in the SM are massless. However, the observation of neutrino oscillations requires that they have non-vanishing mass [43]. The Pontecorvo-Maki-Nakagawa-Sakata [44, 45] mixing matrix describes the mixing of the neutrino mass eigenstates similarly to the CKM matrix. The direct measurement of neutrino masses and fixing the mass hierarchy is the subject of ongoing and planned experiments [46].

- The SM completely neglects gravity, which is instead described by Einstein's theory of General Relativity. The two theories are incompatible.
- Theories conserving the charge-parity (CP) symmetry cannot explain the observed asymmetry between matter and anti-matter. The only source of CP violation in the SM is the complex phase in the CKM matrix which is too small to explain the abundance of matter compared to anti-matter in the observable universe [47, 48].
- Even though CP violation is *a priori* allowed to occur in the strong interaction, tight experimental constraints require it to be very small [49]. This asks for a mechanism preventing strong CP violation that does not exist in the SM. This observation is referred to as the *strong CP problem* [50]. Amongst others, axion models [51]—which in some cases also predict the existence of new heavy resonances—address the strong CP problem.
- The Higgs pole mass would receive quadratic radiative loop corrections Δm_h^2,

$$m_h^2 = (m_h^{\text{pole}})^2 + \Delta m_h^2 = (m_h^{\text{pole}})^2 + \text{const.} \times \Lambda^2, \tag{1.29}$$

  where all particles with masses up to the cut-off scale Λ [52] contribute. If the SM were the correct theory up to the largest energy scale, given by the Planck mass $m_{\text{Planck}} \sim 10^{18}$ GeV, either no additional fundamental particles with masses between the scale of electroweak symmetry breaking (~ 100 GeV) and the Planck scale would exist, or mass corrections on the order of the Planck scale would occur. These corrections would have to be cancelled by the fine-tuning of the pole mass with extremely high precision in order to result in the measured Higgs boson mass of $m_h = 125$ GeV. This problem is also referred to as the *fine-tuning* or the *hierarchy* problem of the SM. The observation of new heavy particles at the TeV scale would establish a cut-off scale far below m_{Planck}, thereby strongly limiting the precision of the Higgs mass fine-tuning.

CHAPTER TWO

BEYOND THE STANDARD MODEL: DIBOSON RESONANCES

The incompleteness of the Standard Model (SM) asks for extensions that answer the open questions. Theories beyond the Standard Model (BSM) are introduced to account for at least a part of these questions. Such theories often predict the existence of new particles—particles that can potentially be produced in pp collisions at the LHC.

If the four-momenta of the decay products of such particles can be fully reconstructed in the experiment, resonances in the invariant mass distribution of the final state particles provide a powerful signature in the search for new phenomena. In view of the newly discovered Higgs boson, it is of particular interest to search for new particles to which it might couple. There are several models predicting new particles decaying into a weak vector boson ($V = W, Z$) and the Higgs boson. Two representative models will be considered for this thesis.

The first is the Heavy Vector Triplet (HVT) model [12]. In Section 2.1 the additional particles added to the SM due to a second SU(2) gauge boson triplet are introduced. Three new heavy vector bosons $W'^{\pm}$and Z', are described. Another extension is the Two-Higgs Doublet Model (2HDM) [11] that contains two Higgs doublet fields. This is one of the most straight-forward extensions of the Higgs sector of the SM and addresses several open questions, such as the baryon asymmetry, the existence of axions, or dark matter. It is required in the Minimal Supersymmetric extension of the standard model (MSSM). The 2HDM is described in more detail in Section 2.2.

2.1 Heavy Vector Triplet Model

The Heavy Vector Triplet (HVT) model is a generic, simplified theory framework introducing new electroweak spin-one resonances, which are common to many new physics scenarios. The precise structure of interactions with the SM particles differs between the models, ranging from weakly coupled models with new heavy Z' [53–63] and W' [64–72] vector bosons to strongly coupled models like the Composite Higgs [73–79] and even some Technicolor [80–88] models. Common to all these

models is that they contain new resonances with a reasonably narrow decay width ($\Gamma/M \lesssim 0.1$). The new particles therefore would manifest themselves in the analysis as narrow resonances in the invariant mass distributions of their decay products on top of a smoothly falling background mass spectrum. While specific models are theoretically consistent, they often involve numerous free parameters of which not all can be simultaneously explored. In practice, many of these parameters have to be fixed to certain benchmark values, limiting the parameter space to be explored. Simplified models overcome these limitations. Sacrificing the full theoretical consistency, the HVT simplified model describes the properties of a new resonance from a phenomenological point-of-view, ignoring the precise mechanism from which the additional gauge boson triplet arises. In the approach of Ref. [12], which is used as one of the models for the interpretation of the data in this thesis, the new particles are real vector states V_μ^a ($a = 1, 2, 3$) in the adjoint representation of $\mathrm{SU}(2)_L$ with zero hypercharge. They describe two charged and one neutral spin-one particle with the mass eigenstates

$$V_\mu^\pm = \frac{V_\mu^1 \mp \mathrm{i} V_\mu^2}{\sqrt{2}} \quad \text{and} \quad V_\mu^0 = V_\mu^3. \tag{2.1}$$

The dynamics of the new vector bosons is described by a phenomenological Lagrangian

$$\begin{aligned}\mathcal{L} = &-\frac{1}{4} D_{[\mu} V_{\nu]}^a + \frac{m_V^2}{2} V_\mu^a V^{\mu\, a} \\ &+ \mathrm{i} g_V c_H V_\mu^a H^\dagger \tau^a \overset{\leftrightarrow}{D}{}^\mu H + \frac{g^2}{g_V} c_F V_\mu^a J_F^{\mu\, a} \\ &+ \frac{g_V}{2} c_{VVV} \varepsilon_{abc} V_\mu^a V_\nu^b D^{[\mu} V^{\nu]\, c} + g_V^2 c_{VVHH} V_\mu^a V^{\mu\, a} H^\dagger H - \frac{g}{2} c_{VVW} \varepsilon_{abc} W^{\mu\nu\, a} V_\mu^b V_\nu^c,\end{aligned} \tag{2.2}$$

where ε_{abc} is the Levi-Civita symbol. The coupling strengths are the $\mathrm{SU}(2)_L$ gauge coupling g and a new coupling strength g_V describing the typical magnitude of the new heavy vector triplet interactions. In the given parametrisation, the combination $c_H g_V$ (with a dimensionless constant c_H) describes the interaction with the Higgs boson field and the SM vector boson fields, and $c_F g^2 / g_V$ (with the dimensionless constant c_F) the interaction with the SM fermion fields. The first line of Equation (2.2) contains the V kinetic and mass terms with the mass parameter m_V and the trilinear and quadrilinear interactions with the SM vector bosons, which are described by the covariant derivatives

$$D_{[\mu} V_{\nu]} = D_\mu V_\nu - D_\nu V_\mu, \qquad D_\mu V_\nu^a = \partial_\mu V_\nu^a + g \varepsilon^{abc} W_\mu^b W_\nu^c, \tag{2.3}$$

The second line of Equation (2.2) is the most relevant one for physics at the LHC, as it describes the interactions of the new particles with the Higgs weak isospin currents

$$\mathrm{i} H^\dagger \overset{\leftrightarrow}{D}{}^\mu \tau^a H = \mathrm{i} H^\dagger \tau^a D^\mu H - \mathrm{i} D^\mu H^\dagger \tau^a H, \tag{2.4}$$

and with the left-handed SM fermion currents

$$J_F^{\mu\, a} = \sum_f \bar{f}_L \gamma^\mu \tau^a f_L. \tag{2.5}$$

In this notation, $\tau^a = \sigma^a/2$ with the Pauli matrices σ^a ($a = 1, 2, 3$). The parameter c_H modifies the coupling of V to the Higgs and the SM vector bosons and is expected to be close to unity. This interaction includes in particular the V decay into a pair of bosons, *e.g.* a SM vector and a SM Higgs boson. The parameter c_F modifies the strength of the direct interactions of V with fermions, and—in the context of searches for diboson decays—the Drell-Yan production of the V resonance.

The third line of Equation (2.2) contains three new interactions with free parameters. To a first approximation these interactions are irrelevant for the interactions at the LHC [12] and are thus disregarded. Consequently, the HVT model is entirely described by three parameters: c_H, c_F, and m_V.[1]

Since the vector fields V_μ^a are not mass eigenstates, the mass parameter m_V is not the physically observed mass and the SM and HVT fields can mix. From diagonalisation of the mass matrices for the neutral and the charged vector bosons [12], a relation between vector boson mass parameters in the HVT model is obtained

$$m_W^2 M_\pm^2 = \cos^2\theta_W m_Z^2 M_0^2. \tag{2.6}$$

Here $M_\pm$ and M_0 are the masses of the new heavy charged and the neutral vector bosons, m_W and m_Z the masses of the SM weak vector bosons, and θ_W is the Weinberg angle. Compared to the masses $m_W \simeq 80.4\,\text{GeV}$ and $m_Z \simeq 91.2\,\text{GeV}$ of the SM vector bosons [42], the new vector bosons assume masses at the TeV scale, since the lower mass range is already excluded by the current data. This implies a mass hierarchy between SM vector bosons and HVT vector bosons, and for such a scenario the measurement of the value of $\cos^2\theta_W = 1 - 0.23$ is only restored when the charged and neutral HVT masses are degenerate at the per-cent level,

$$M_\pm^2 = M_0^2(1 + O(1\,\%)). \tag{2.7}$$

Therefore, most experimental searches only assume a single mass value for both the charged $W'^\pm$and the neutral Z' resonances.

The modifications of the couplings to the SM particles, c_H and c_F, in Equation (2.2) are free parameters. The coupling strength is $c_H g_V$ for SM Higgs and weak vector bosons and $c_F g^2/g_V$ for

[1] The authors of Ref. [12] consider splitting c_F into more components: $c_F V \cdot J_F \to c_l V \cdot J_l + c_q V \cdot J_q + c_3 V \cdot J_3$, allowing for different couplings to leptons, light quarks, and third-generation quarks. In a diboson search with no sensitivity to the quark flavour in the $q\bar{q}$ production, however, no distinction has to be made and one can assume $c_l = c_q = c_3 = c_F$.

SM fermions. In order to cover large parts of the phenomenological possibilities, two benchmark scenarios with fixed values for c_H and c_F—*Model A* and *Model B*—are suggested by Ref. [12]. Both models contain the additional heavy vector triplet and have $c_F \simeq 1$, but they differ in their coupling strength to the SM Higgs and weak vector bosons. Model A is based on an extended gauge symmetry in which the heavy vector triplet arises from spontaneous symmetry breaking. In this model, c_H is suppressed such that [12]

$$g_V c_H \simeq g^2 c_F / g_V . \tag{2.8}$$

Consequently, similar decay branching ratios to bosons and fermions are predicted. The coupling to the SM particles is overall suppressed by the factor g^2/g_V. In contrast, Model B has $|c_H| = 1$, and therefore

$$g_V c_H \simeq -g_V , \qquad g^2 c_F / g_V \simeq g^2 / g_V , \tag{2.9}$$

meaning unsuppressed coupling to the SM Higgs and weak vector bosons, while the coupling to fermions remains suppressed by g^2/g_V. In Model B, values $1 \leq g_V \leq 5$ are considered. For these values, the model strongly favours decays of new vector bosons into diboson states, while the decays into fermions are strongly suppressed. In contrast, Model A is inspired by weakly coupled scenarios, *i.e.* values $1 \leq g_V \leq 3$. Theory predictions in this thesis are produced with $g_V = 1$ ($g_V = 3$) for HVT Model A (Model B).

To illustrate the differences between the two models, the decay branching fractions of a new neutral resonance for Models A and B are shown in Figure 2.1. In Model A, all branching fractions are of the same order of magnitude and no decay mode is favoured. In Model B, however, the decay into two bosons is strongly favoured, providing strong motivation for diboson resonance searches. It is worth mentioning that for large values of g_V, Model B predicts broad resonances ($\Gamma/M \gg 0.1$), such that the narrow width approximation (NWA) no longer holds true. For this reason, experimental searches are interpreted in Model B only for g_V values smaller than five.

The dominant production modes of the new particles are the Drell-Yan-like (DY) quark annihilation process and vector boson fusion (VBF). Leading-order Feynman diagrams for both processes are shown in Figure 2.2. The VBF production is suppressed due to the electroweak coupling $\alpha_{\mathrm{EW}} = g^2/(4\pi)$ to W and Z bosons, making the DY production by far dominant in most scenarios. However, the VBF production becomes dominant in scenarios in which the coupling to fermions is suppressed, *i.e.* $c_F \to 0$. The feasibility studies in Ref. [12] predict that the LHC data with an integrated luminosity of $100\,\mathrm{fb}^{-1}$ at $\sqrt{s} = 14\,\mathrm{TeV}$ provide sensitivity to VBF-produced resonances with masses of up to 2.5 TeV. Therefore, besides the DY production mode, the VBF production is relevant for searches with Run 2 LHC data.

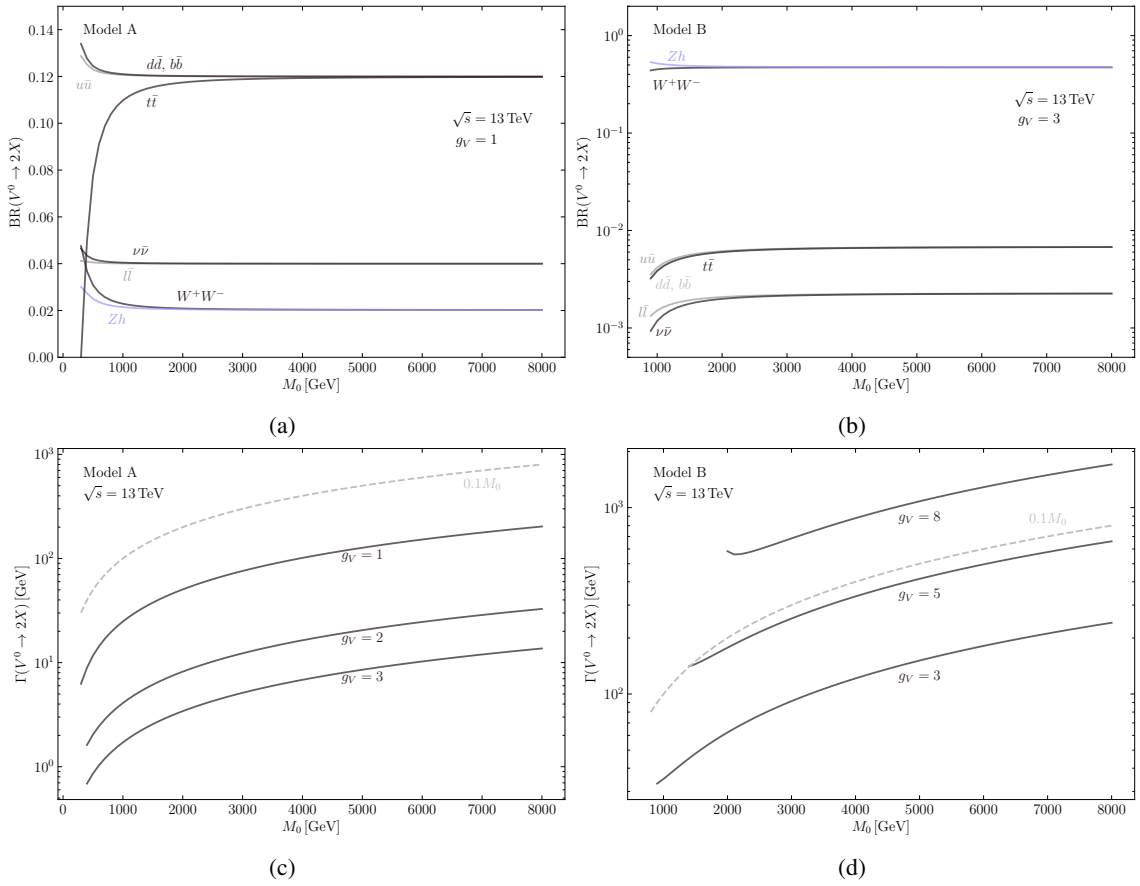

Figure 2.1: The HVT model predictions. The top row shows the branching fractions for different decays of the neutral heavy vector boson resonance as a function of its mass *(a)* in Model A and *(b)* in Model B. The bottom row shows the decay width of the neutral heavy vector boson resonance for different g_V values *(c)* in Model A and *(d)* in Model B. The dashed line indicates the threshold above which the resonance is considered broad because $\Gamma/M > 0.1$. Theoretically excluded points (*e.g.* because of complex decay width) are not shown. The data were generated with the HVT calculator [12].

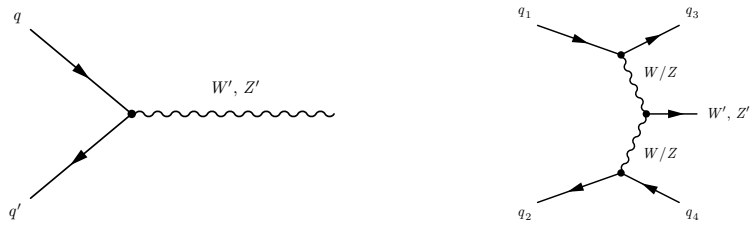

Figure 2.2: Leading-order Feynman diagrams for *(a)* the DY and *(b)* the VBF production modes of the heavy vector bosons W' and Z'.

Leading-order Feynman diagrams for the DY production of new resonances decaying into Vh or VV pairs ($V = W, Z$) are shown in Figure 2.3 for the semileptonic final states, where one SM boson decays into leptons, while the other (h or V) decays hadronically. The ATLAS collaboration has

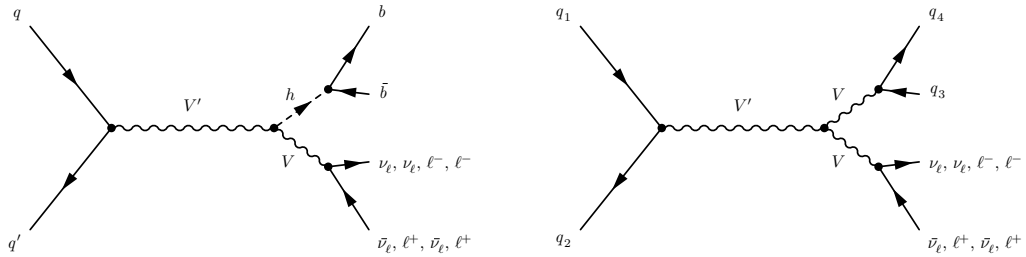

Figure 2.3: Semileptonic decays of *(a)* Vh and *(b)* VV heavy vector boson resonance $V' = W', Z'$ in DY production.

conducted searches for diboson resonances in these and other final states. Searches for the $W' \to VV$ and $V' \to Vh$ resonances (where $V' = W', Z'$) were performed using Run 1 LHC data at $\sqrt{s} = 8$ TeV. VV decay final states of $\ell\nu qq$ [89, 90], $\ell\ell qq$ [91], $\ell\nu\ell\ell$ [92], and $qq\,qq$ with two reconstructed jets [93] have been considered. These searches have been interpreted in terms of an extended gauge model (EGM) W' [94] which is closely related to the HVT benchmark Model A with $g_V = 1$.

The exclusion limits on the cross section times branching ratio $\sigma(pp \to X) \times B(X \to WZ)$ for heavy vector boson production in the fully leptonic final state are shown in Figure 2.4(a). The predictions of the EGM W' model and the HVT model are also shown. In a wide mass range, the EGM W' model predictions are very similar to those of the HVT Model A with $g_V = 1$, underlining the similarity of the two models. Resonance masses of above 1.52 TeV, 1.49 TeV, 0.76 TeV, and 1.56 TeV are excluded in the EGM W', HVT A ($g_V = 1$), HVT A ($g_V = 3$), and HVT B ($g_V = 3$) models, respectively [92]. In addition to the two HVT benchmark models, the HVT parameter combinations $(g^2/g_V)c_F$ and $g_V c_H$ were scanned resulting in the observed exclusion contours shown in Figure 2.4(b). Strong constraints on the scanned parameter space are obtained for relatively small resonance masses of 1 TeV or below. For heavier resonances with masses above 2 TeV, a large part of the parameter space is still allowed [92].

The exclusion limits on $\sigma(pp \to W') \times \mathrm{BR}(W' \to WZ)$ from the analysis of $\ell\nu qq$ and $\ell\ell qq$ final states are shown in Figure 2.5 together with the EGM W' prediction. Here, W' masses above 1.49 TeV and 1.59 TeV, respectively, are excluded at the 95 % C.L. [89, 91]. For fully hadronic final state, the exclusion limit on $\sigma(pp \to W') \times \mathrm{BR}(W' \to WZ)$ is shown in Figure 2.6(a). EGM W' masses between 1.3 and 1.5 TeV are excluded at the 95 % C.L. In this search, a slight excess of events is observed with respect to the background-only hypothesis for resonance masses around 2 TeV. The excess has a local significance of 3.4 and a global significance of 2.5 standard deviations. The

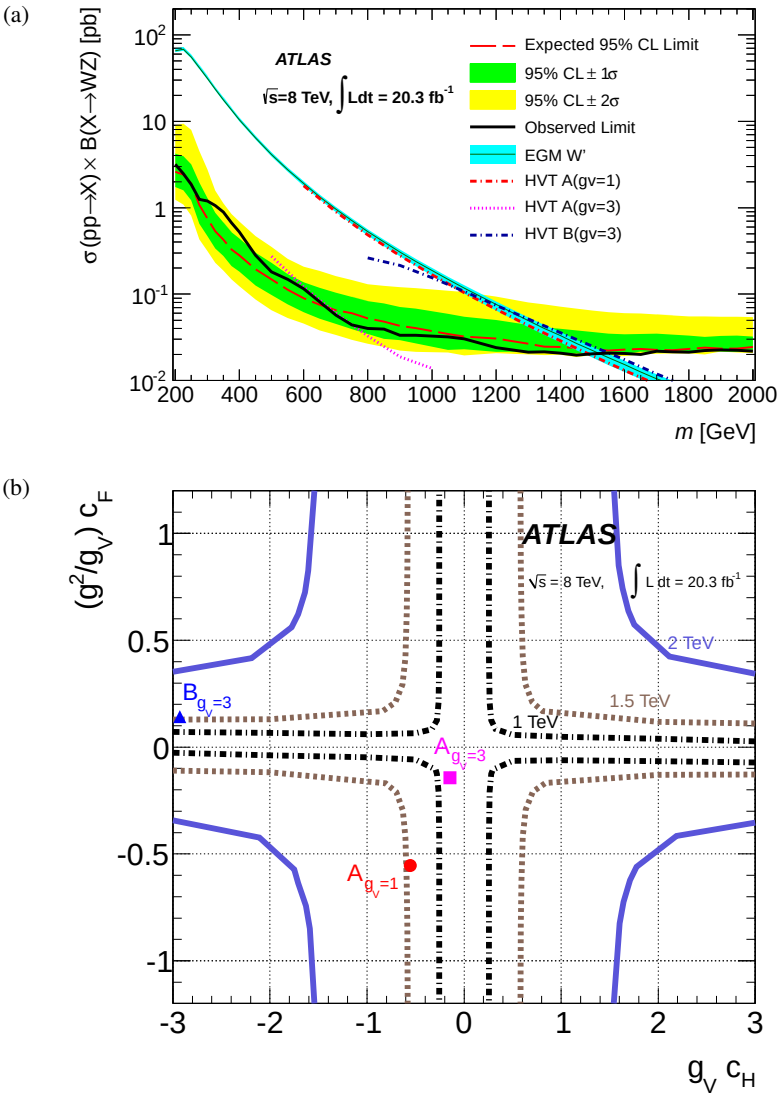

Figure 2.4: *(a)* Exclusion limit at the 95 % C.L. and EGM and HVT model for the W' production cross section times branching ratio in the leptonic final state. *(b)* Observed exclusion contours at 95 % C.L. in the HVT parameter space $(g^2/g_V)c_F$ *vs.* $g_V c_H$ for resonance masses of 1 TeV, 1.5 TeV, and 1.8 TeV [92].

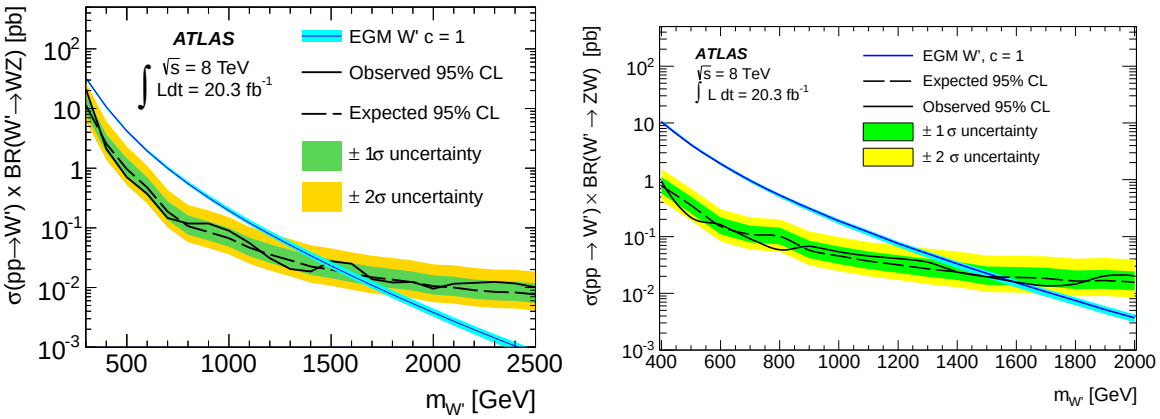

(a) (b)

Figure 2.5: Exclusion limits at the 95 % C.L. on the production cross section times branching ratio for $W' \to VV$ production in *(a)* $\ell\nu qq$ [89] and *(b)* $\ell\ell qq$ [91] final states obtained with the Run 1 LHC data. The prediction from the EGM W' model is shown for comparison.

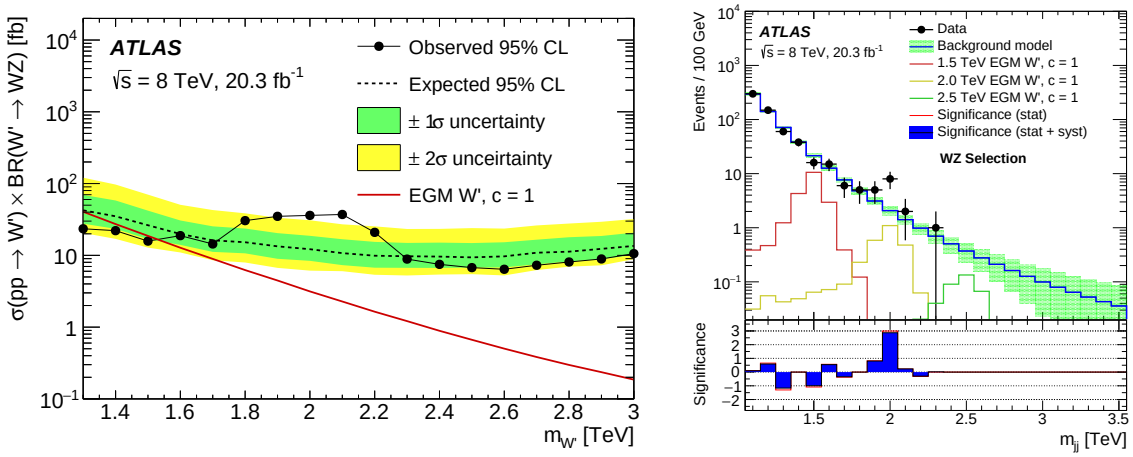

(a) (b)

Figure 2.6: *(a)* Exclusion limits at 95 % C.L. on the W' production cross section times branching ratio from the search with two boson-tagged jets in the final state. *(b)* Background-only hypothesis fit to the dijet mass (m_{jj}) distribution, showing an excess around 2 TeV [93].

corresponding distribution of the dijet mass, which is used as discriminating variable, is shown in Figure 2.6(b) fitted with the background expectation. The increased amount of data from LHC Run 2 is expected to resolve the origin of this excess, either due to a statistical fluctuation, or a new particle.

In a statistical combination of the searches described above, EGM W' masses of up to 1.81 TeV are excluded at the 95 % C.L. [95]. The combined results are shown in Figure 2.7. The significance of the excess around 2 TeV is estimated to be 2.9 standard deviations. Accounting for the probability that any

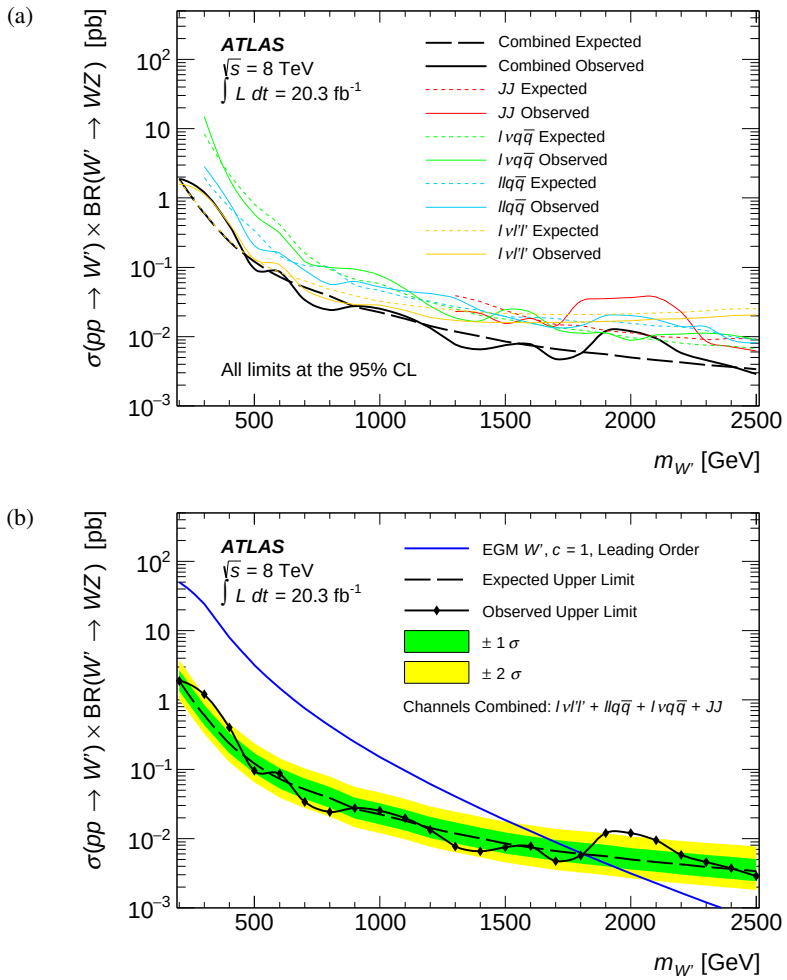

Figure 2.7: Expected and observed exclusion limits at 95 % C.L. from several analyses on the W' production cross section times branching ratio from Run 1 data recorded at $\sqrt{s} = 8$ TeV: *(a)* W' limits from the individual analyses and their combination and *(b)* combined result together with the EGM W' prediction [95].

channel could fluctuate reduces the significance of the excess to 2.6 standard deviations. Figure 2.7(b) shows the combined result together with the EGM W' prediction.

Searches for Vh resonances were conducted in the $\nu\nu bb$, $\ell\nu bb$, and $\ell\ell bb$ final states, with Higgs boson decays into a pair of b-quarks, $h \to bb$ [96]. The $\nu\nu$ and $\ell\ell$ channels were combined to determine upper limits on the cross section times branching ratio $\sigma(Z' \to Zh) \times \mathrm{BR}(h \to b\bar{b})$ of the new resonance. The result is shown in Figure 2.8(a). The $\ell\nu$ channel leads to the upper limits on $\sigma(W' \to Wh) \times \mathrm{BR}(h \to b\bar{b})$, shown in Figure 2.8(b). Masses above 1.36 TeV and 1.47 GeV for neutral and charged resonances, respectively, are excluded at the 95 % C.L., assuming the HVT Model A with $g_V = 1$. The exclusion contours for parameter combinations $(g^2/g_V)c_F$ and $g_V c_H$ for resonance masses of 1 TeV, 1.5 TeV, and 1.8 TeV are shown in Figure 2.9. Similar to the $VV \to \ell\nu\ell\ell$

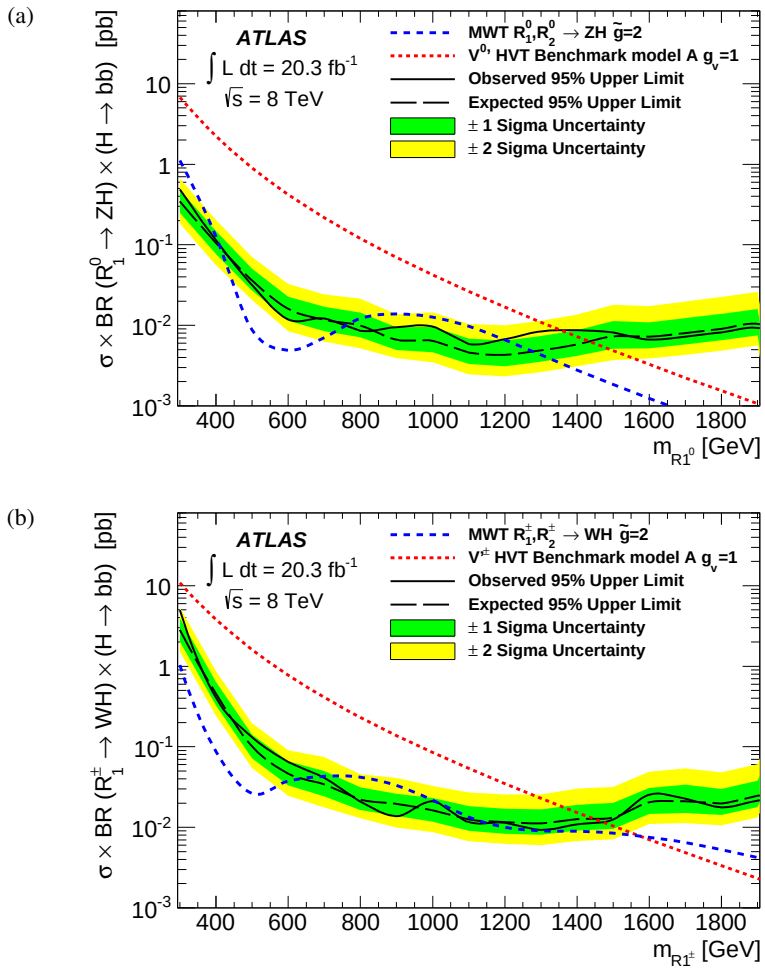

Figure 2.8: 95 % C.L. production cross section times branching ratio limits at 95 % C.L. as a function of the resonance mass *(a)* a neutral (with m_{R1^0}) and *(b)* a charged (with $m_{R1^\pm}$) heavy Vh resonance [96]. Theory predictions (red: HVT Model A, blue: Minimal Walking Technicolor (MWT)) are shown as dotted lines.

analysis, strong exclusion limits are observed for small resonance masses, while larger parts of the phase space remain unconstrained for larger masses.

2.2 Two-Higgs Doublet Model

While a single Higgs doublet is sufficient to complete the SM Higgs sector, a second Higgs doublet is a rather natural extension introduced in many theories beyond the Standard Model. It is introduced for example in the Minimal Supersymmetric extension of the standard model (MSSM) [97–101], in axion models [102], or in models addressing baryogenesis [103]. The following introduction to Two-Higgs

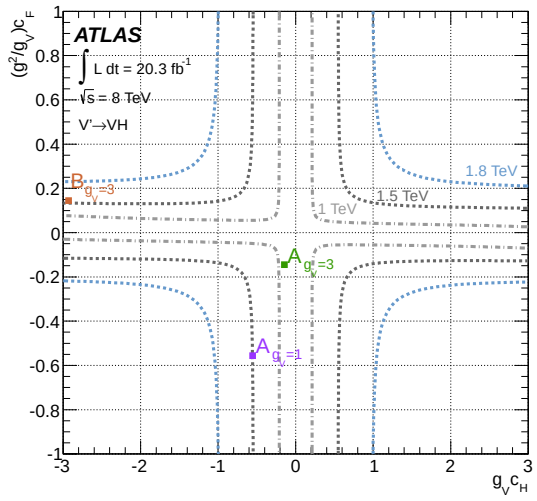

Figure 2.9: Observed exclusion contours at 95 % C.L. in the HVT parameter space $(g^2/g_V)c_F$ *vs.* $g_V c_H$ for resonances of mass 1 TeV, 1.5 TeV, and 1.8 TeV, from the search for $V' \to Vh$ decays [96]. The regions outside the curves are excluded. The squared markers indicate the benchmark models A ($g_V = 1$), A ($g_V = 3$) and B ($g_V = 3$).

Doublet Models is based on Ref. [11].

The general CP-conserving potential of two Higgs doublet fields Φ_1 and Φ_2 with hypercharge +1 is

$$V = m_{11}^2 \Phi_1^\dagger \Phi_1 + m_{22}^2 \Phi_2^\dagger \Phi_2 - m_{12}^2 \left(\Phi_1^\dagger \Phi_2 + \Phi_2^\dagger \Phi_1\right) + \frac{\lambda_1}{2}\left(\Phi_1^\dagger \Phi_1\right)^2 + \frac{\lambda_2}{2}\left(\Phi_2^\dagger \Phi_2\right)^2 + \lambda_3 \Phi_1^\dagger \Phi_1 \Phi_2^\dagger \Phi_2 + \lambda_4 \Phi_1^\dagger \Phi_2 \Phi_2^\dagger \Phi_1 + \frac{\lambda_5}{2}\left[\left(\Phi_1^\dagger \Phi_2\right)^2 + \left(\Phi_2^\dagger \Phi_1\right)^2\right], \tag{2.10}$$

with the mass parameters m_{ij} and Yukawa couplings λ_i $(i, j = 1, 2)$. As electroweak symmetry breaking minima of the potential the configurations

$$\langle \Phi_1 \rangle_0 = \begin{pmatrix} 0 \\ \frac{v_1}{\sqrt{2}} \end{pmatrix}, \qquad \langle \Phi_2 \rangle_0 = \begin{pmatrix} 0 \\ \frac{v_2}{\sqrt{2}} \end{pmatrix}, \tag{2.11}$$

can be chosen, where v_1 and v_2 are the vacuum expectation values of the first and the second doublet field respectively.

The two complex scalar SU(2) doublets Φ_a $(a = 1, 2)$ have eight degrees of freedom. Like in the SM, three of them give masses to the $W^\pm$ and Z^0 gauge bosons. Unlike in the SM, however, five physical Higgs fields remain instead of one. Two of them correspond to charged ($H^\pm$), two to neutral and CP-even (h, H) and one to a neutral and CP-odd (A) Higgs field. The 2HDM model has a rich

phenomenology, with the $A \rightarrow Zh$ decay channel being of particular interest for this thesis.

The two crucial parameters of the 2HDM are the angles α and β. The former describes the mixing of the neutral scalar fields h and H, while

$$\tan\beta \equiv \frac{v_2}{v_1} \tag{2.12}$$

is the ratio of the two vacuum expectation values. In particular, the SM Higgs boson is a superposition of h and H fields, given by $h^{\mathrm{SM}} = h\sin(\alpha-\beta) - H\cos(\alpha-\beta)$.

All 2HDMs allow in principle for flavour changing neutral currents (FCNCs) at tree level, which are mediated by neutral Higgs scalars ϕ via *e.g.* $\overline{d}s\phi$. As FCNCs are not observed at tree-level rates, they have to be suppressed also in 2HDMs. The Paschos-Glashow-Weinberg theorem [104, 105] states that FCNCs are eliminated under certain conditions that are fulfilled in benchmark scenarios. In the type 1 benchmark scenario quarks couple to just one of the Higgs doublets, whilst in type II all up-type quarks couple to one Higgs doublet, while the down-type quarks couple to the other one. In case of the type I 2HDM, the doublet to which the quarks couple is conventionally chosen to be Φ_2. In the type II 2HDM, the up-type quarks couple to Φ_2, while the down-type quarks couple to Φ_1. For both models, the leptons are assumed to behave analogously to their quark counterparts, but this is not a strict requirement of the theory. In the so-called lepton-specific 2HDM, the quarks couple to Φ_2 and the leptons to Φ_1. In the flipped 2HDM, the quarks behave just as in the type II 2HDM while the leptons couple to Φ_2 instead of Φ_1. These characteristics of the four mentioned models are summarised in Table 2.1.

Table 2.1: Overview of the fermion couplings in the four benchmark 2HDMs. All fields are implied to be right-handed. By convention, up-type quarks always couple to Φ_2.

Model	up-type quarks	down-type quarks	leptons
type I	Φ_2	Φ_2	Φ_2
type II	Φ_2	Φ_1	Φ_1
lepton-specific	Φ_2	Φ_2	Φ_1
flipped	Φ_2	Φ_1	Φ_2

The 2HDMs are described by a total of seven free parameters: the masses of the five Higgs bosons[2], m_h, $m_{H^\pm}$, m_H, and m_A, and the mixing angles α and β. More details about the phenomenology of the CP-odd 2HDM pseudoscalar A, which is of particular interest for the experimental searches performed in this thesis, can be found in Ref. [106].

[2] The measurement of the SM Higgs boson h^{SM} mass provides an external constraint, but as h^{SM} is a mixture of h and H, the masses m_h and m_H are not constrained to any particular value.

The dominant A production modes are gluon-gluon fusion (ggA) and in association with a b-quark pair (bbA). The corresponding leading-order (LO) Feynman diagrams are depicted in Figure 2.10. One possible A boson decay mode is through the coupling to the SM bosons Z and h. The ATLAS

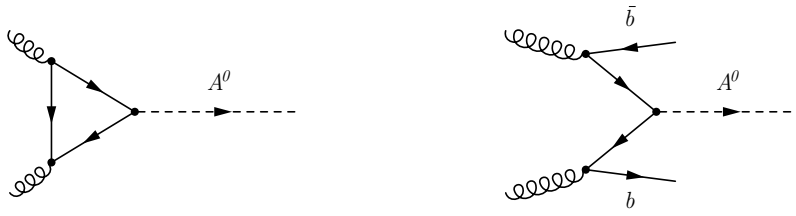

(a) (b)

Figure 2.10: Example leading order diagrams for *(a)* gluon-gluon fusion and *(b)* the b-quark pair associated production of the heavy CP-odd A.

experiment has performed searches for these decays using Run 1 data recorded at $\sqrt{s} = 8\,\text{TeV}$ [107], considering the $\ell\ell\tau\tau$, $\ell\ell bb$, and $\nu\nu bb$ final states. Upper limits on the production cross section times branching ratio were obtained for A boson masses between 200 GeV and 1000 GeV and are shown in Figure 2.11. They range between 0.098 pb and 0.013 pb for the $h \to \tau\tau$ decay mode and between 0.57 pb and 0.014 pb for the $h \to bb$ decay mode. Searches for the Zh decay mode are most sensitive for relatively light A boson resonances. For A boson masses above approximately 350 GeV, the $A \to t\bar{t}$ decay mode quickly becomes dominant [106].

In order to interpret the data in terms of 2HDM model parameters, exclusion contours at 95 % C.L. are derived in the $\{\cos(\beta-\alpha), \tan\beta\}$ parameter space for a fixed value of the resonance mass of $m_A = 300\,\text{GeV}$ (see Figure 2.12). With these results, strong constraints on the parameter space of all four types of 2HDM are imposed, particularly for $\tan\beta \lesssim 10$. However, the sensitivity close to the alignment limit ($\cos(\beta-\alpha) \to 0$) is limited and a significant part of the available phase space remains unconstrained. The vanishing sensitivity at the alignment limit can be partially compensated for by reinterpreting the results from the $A \to \tau\tau$ search [108], which are also shown in Figures 2.12 and 2.13.

The interpretation is also performed in the $\{m_A, \tan\beta\}$ parameter space, with the value of $\cos(\beta-\alpha)$ fixed to 0.1. The corresponding results are shown in Figure 2.13. A large fraction of this parameter plane remains unconstrained, particularly for A masses above 340 GeV.

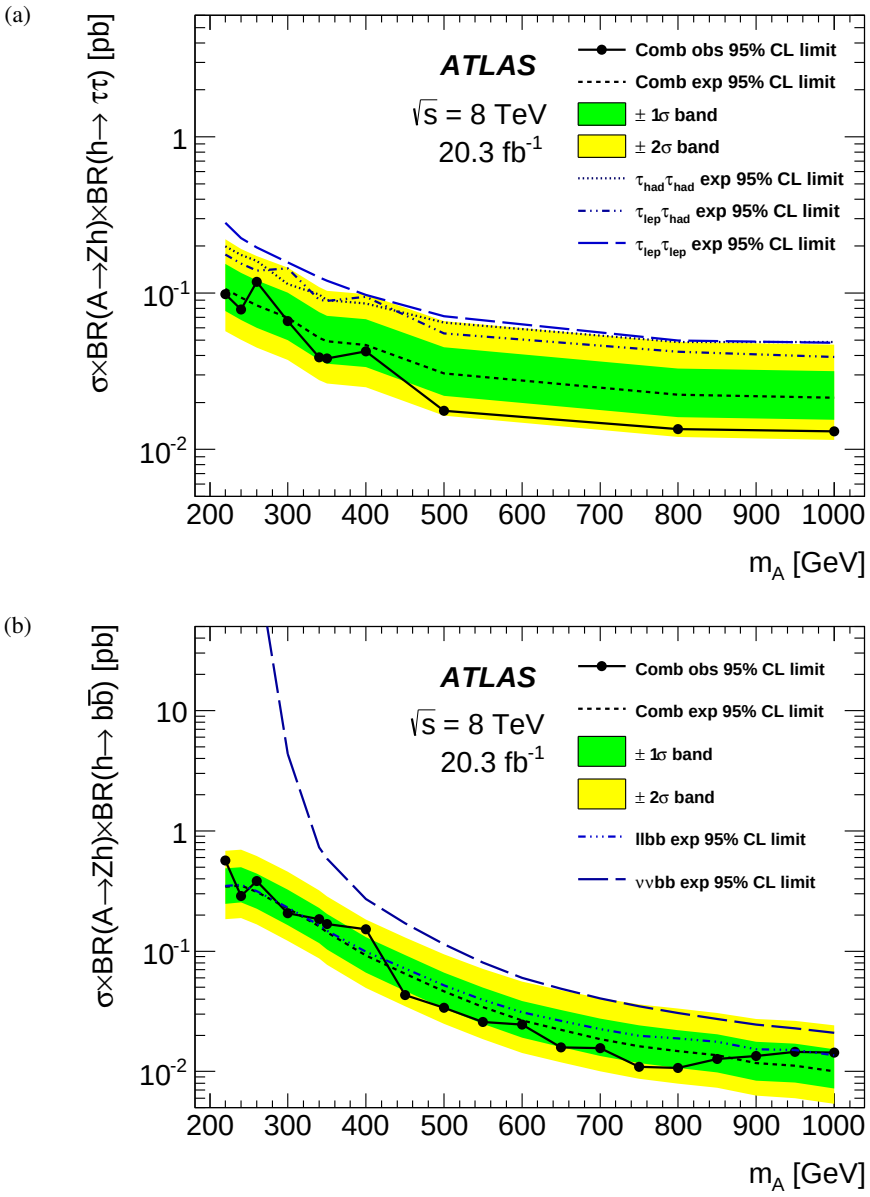

Figure 2.11: The expected and observed 95 % C.L. exclusion limits on the cross section times branching ratio for $A \rightarrow Zh$ production in the *(a)* $h \rightarrow \tau\tau$ and *(b)* $h \rightarrow bb$ decay channel [107]. The contributions from the individual searches in various sub-channels are also shown.

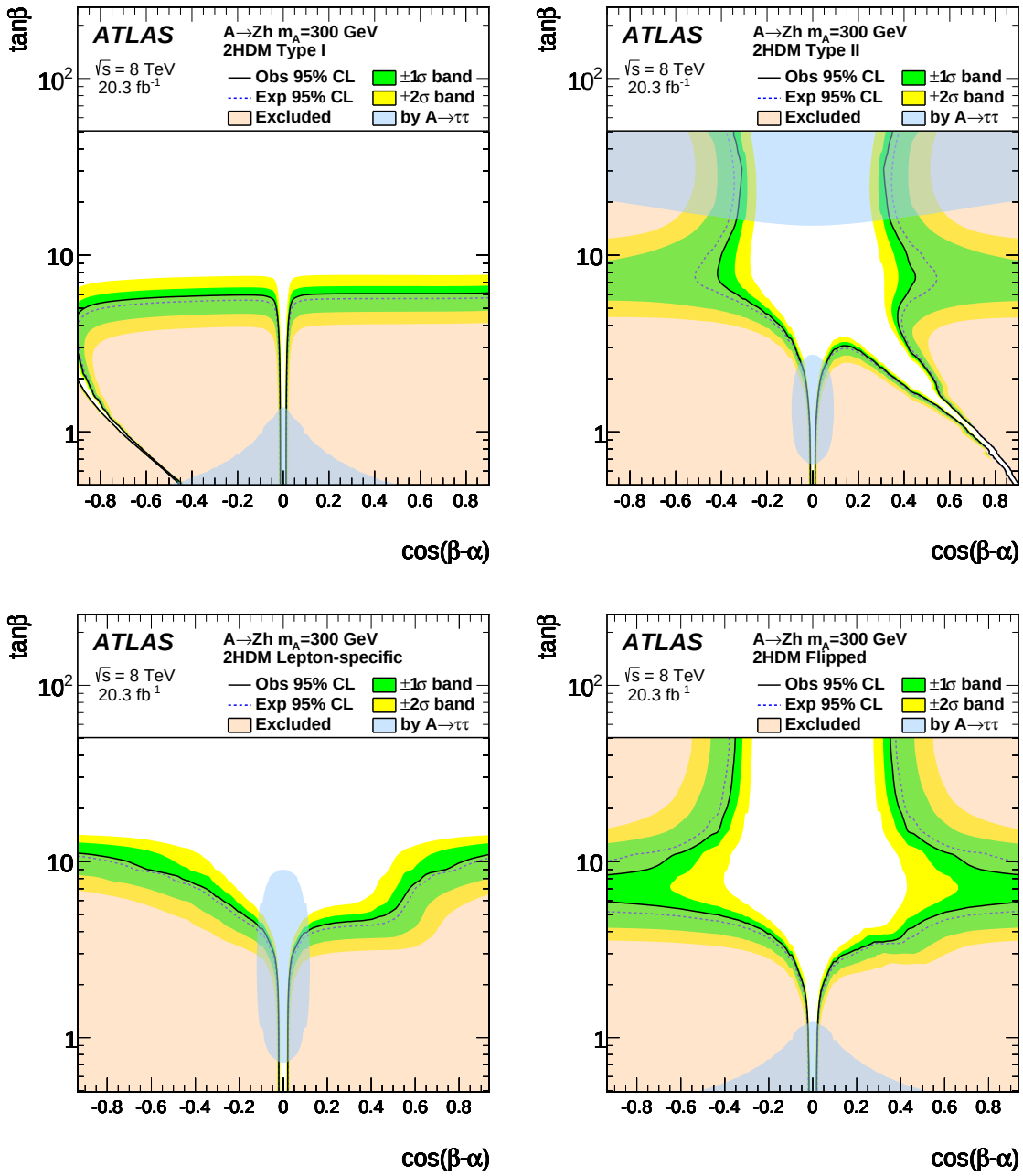

Figure 2.12: The interpretation of the cross section limits in the context of the various 2HDM types as a function of the parameters $\tan\beta$ and $\cos(\beta-\alpha)$ for $m_A = 300\,\text{GeV}$: *(a)* Type-I, *(b)* Type-II, *(c)* Lepton-specific, and *(d)* Flipped [107]. Variations of the natural width up to $\Gamma_A/m_A = 5\,\%$ are taken into account. For Type-II and Flipped 2HDM, the b-associated production is included in addition to the gluon fusion. The narrow regions with no exclusion power in Type-I and Type-II at low $\tan\beta$ and far from $\cos(\beta-\alpha) = 0$ are caused by vanishing branching ratios of $h \to bb$ and/or $h \to \tau\tau$. The blue shaded area denotes the area excluded by taking into account the constraints on the CP-odd Higgs boson derived by considering the $A \to \tau\tau$ decay mode after reinterpreting the results in Ref. [108]. Reproduced from Ref. [107].

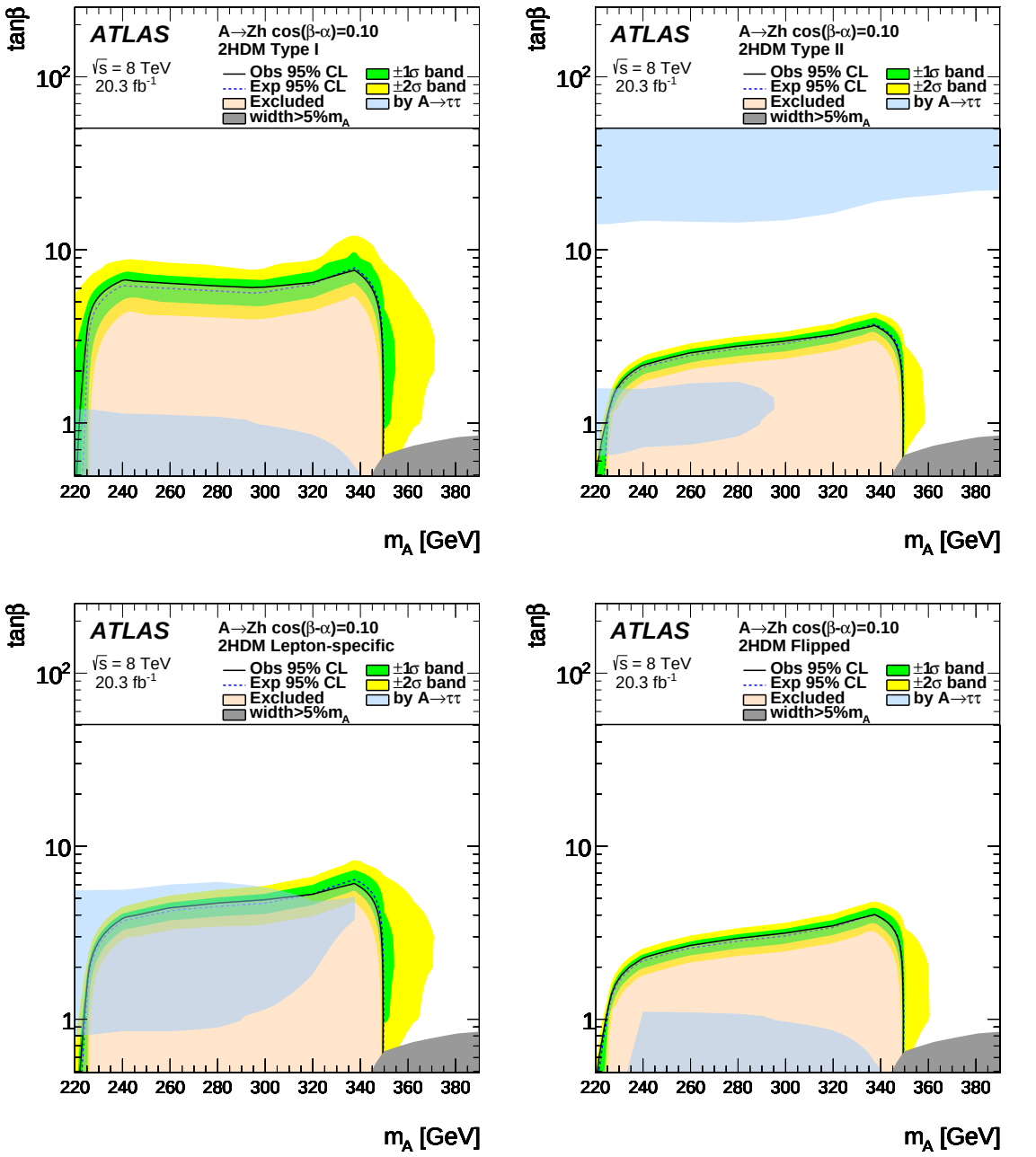

Figure 2.13: The interpretation of the cross section limits in the context of the various 2HDM types as a function of the parameters $\tan\beta$ and m_A for $\cos(\beta-\alpha) = 0.1$: *(a)* Type-I, *(b)* Type-II, *(c)* Lepton-specific, and *(d)* Flipped [107]. Variations of the natural width up to $\Gamma_A/m_A = 5\,\%$ are taken into account. The grey solid area indicates that the width is larger than 5 % of m_A. For Type-II and Flipped 2HDM, the b-associated production is included in addition to the gluon fusion. The blue shaded area denotes the area excluded by taking into account the constraints on the CP-odd Higgs boson derived by considering the $A \to \tau\tau$ decay mode after reinterpreting the results in Ref. [108]. Reproduced from Ref. [107].

CHAPTER THREE

THE ATLAS EXPERIMENT AT THE LARGE HADRON COLLIDER

In this chapter, the experimental infrastructure located the European Organization for Nuclear Research (CERN) near Geneva is discussed. Section 3.1 gives a brief overview of the Large Hadron Collider (LHC), and the accelerator complex required for its operation. The ATLAS detector is described in Section 3.2. The concept of Monte-Carlo simulation is introduced in Section 3.3. Finally, in Section 3.4 the reconstruction of physical objects in *pp* collisions in ATLAS is described, focusing on the requirements for the search for diboson resonances.

3.1 The Large Hadron Collider

The LHC [109–111] is the world's largest particle accelerator, located at CERN, near Geneva in Switzerland. With a circumference of 27 km it accelerates protons up to energies of 7 TeV. Between 2015 and 2018 (LHC Run 2), it was operated at a centre-of-mass energy of $\sqrt{s} = 13\,\text{TeV}$ for *pp* collisions, with a bunch collision frequency of 40 MHz (20 MHz in 2015). Superconducting radio frequency cavities operating at 400 MHz accelerate protons, increasing their energy by 485 keV at every turn. The beams are bent by 1232 superconducting dipole magnets. Cooled to 1.9 K, the magnet system constitutes the coldest extended place in the universe (the cosmic microwave background has a temperature of 2.76 K). With currents of up to 12 840 A, magnetic field strengths up to 9 T are achieved. In this condition, each dipole stores an energy of 8.11 MJ, which—for all dipoles combined—corresponds to the kinetic energy of an Airbus A340 at cruise speed.

The particles are injected into the LHC after a chain of pre-accelerators starting with a linear accelerator (LINAC), followed by the Proton Synchrotron Booster (PSB), the Proton Synchrotron (PS), and the Super Proton Synchrotron. For a proton run, bottled hydrogen is used as a starting point. In the LINAC the electrons are stripped away and the remaining protons are accelerated to an energy of 50 MeV. Subsequently, they enter the PSB, where they are accelerated to 1.4 GeV. The PS and the PSB are circular accelerators where the protons are brought to energies of 25 GeV and 450 GeV, respectively.

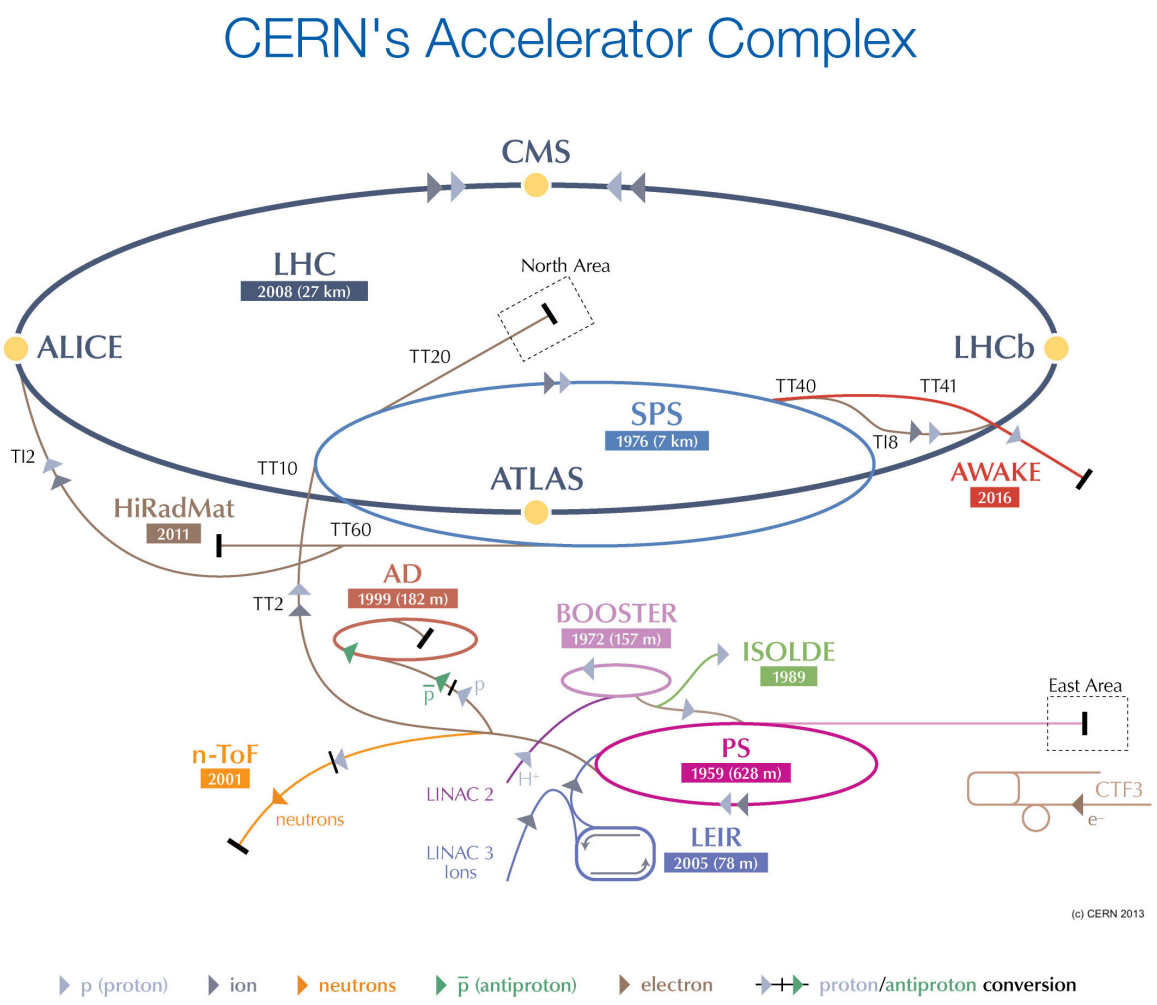

Figure 3.1: The CERN accelerator complex. Modified from [112].

Only then can they be injected into the LHC, where their final energy of currently 6.5 TeV is reached. The full CERN accelerator complex is shown in Figure 3.1.

Protons are injected as bunches into the LHC, each consisting of about 1.3×10^{11} protons. With the number of proton bunches varying between 2600 and 2800 per beam during the LHC Run 2, the instantaneous luminosity measured by ATLAS peaked at a value of $L = 2.1 \times 10^{34}\,\mathrm{cm}^{-2}\,\mathrm{s}^{-1}$ [113], as can be seen in Figure 3.2(a). This is more than twice the design value [109]. The beam intensity in the accelerator leads to multiple proton-proton interactions per bunch crossing, referred to as event pile-up. The mean number of interactions per bunch crossing depends strongly on the operating conditions and was as high as 70 [113]. The distribution over the Run 2 data taking periods can be seen in Figure 3.2(b).

In Run 2, the LHC delivered an unprecedented number of collisions to the experiments. For 2015

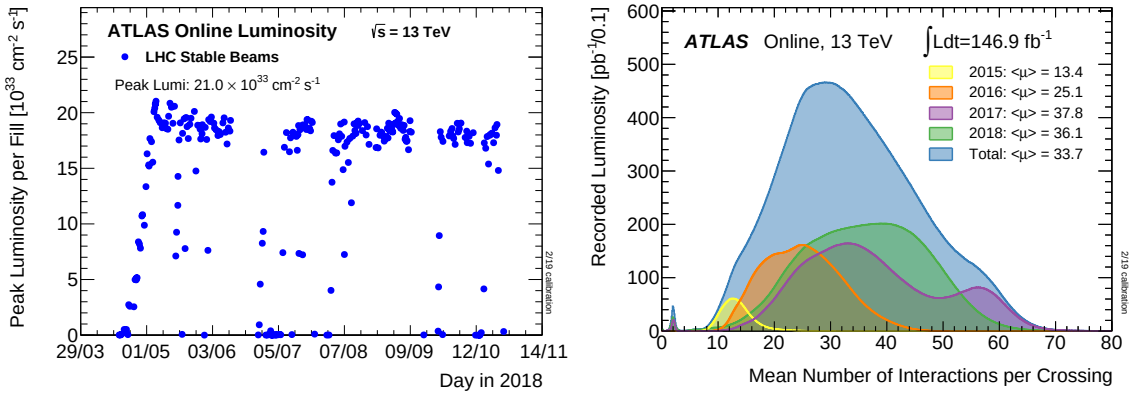

(a) (b)

Figure 3.2: *(a)* Peak luminosity per fill for the year 2018 as measured by ATLAS. *(b)* The distribution of the mean number of interactions per bunch crossing for data recorded during the LHC Run 2. Figures taken from Ref. [113].

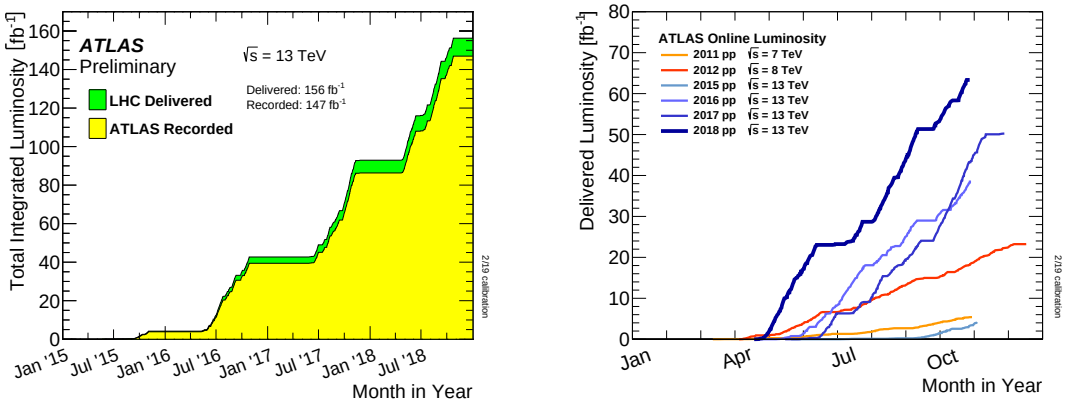

(a) (b)

Figure 3.3: *(a)* Incremental integrated luminosity over the Run 2 data taking period as delivered by the LHC (green) and recorded by ATLAS (yellow). *(b)* The integrated luminosity registered by ATLAS as a function of time in the years since the LHC startup. Figures taken from Ref. [113].

to 2018, the delivered integrated luminosity adds up to 156 fb^{-1}, out of which 147 fb^{-1} (or 94 %) were recorded by ATLAS (*cf.* Figure 3.3(a)). Owing to the large instantaneous luminosity that was delivered with great reliability, a steep rise in integrated luminosity is visible in both Figures 3.3(a) and 3.3(b).

3.2 The ATLAS experiment

The ATLAS experiment (A Toroidal LHC ApparatuS) is a multi-purpose detector for high-p_{T} processes at the LHC (*cf.* Figure 3.1). It is located about 100 m below ground at Point 1 of the LHC ring. With a length of 46 m and a height of 25 m it weighs about 7000 t, making it the biggest particle detector built so far. After the discovery of the Higgs boson [8] in 2012, SM precision measurements, recording Pb-Pb collision data, and searching for new physics phenomena at the TeV scale remain the main goals of the experiment.

The ATLAS coordinate system is right-handed, with the origin at the nominal beam interaction point. The x-axis points towards the centre of the LHC ring and the z-axis points along the beam pipe. Considering the cylindrical shape of the ATLAS detector around the beam pipe, cylindrical coordinates (r, θ, ϕ) are a natural choice, where r is the radial distance from the interaction point, θ is the polar angle with respect to the z-axis, and ϕ is the azimuthal angle around the z-axis.

A 3-momentum vector $\vec{p} = (p_x, p_y, p_z)$ has the transverse and longitudinal components $p_{\mathrm{T}} = |\vec{p}|\cos(\theta)$ and $p_z = |\vec{p}|\sin(\theta)$. It can thus be expressed as

$$\vec{p} = \left(p_{\mathrm{T}}\cos(\phi), p_{\mathrm{T}}\sin(\phi), p_z\right) . \tag{3.1}$$

With its additive nature, the rapidity y is a useful means when describing particle energies and momenta in a collider detector. The four-momentum $p^\mu = (E, \vec{p})$[1] is defined as

$$y = \frac{1}{2}\ln\left(\frac{E + p_z}{E - p_z}\right) . \tag{3.2}$$

Particles in the ATLAS detector are typically ultra-relativistic, where $|\vec{p}| \gg m$ and thus $E \simeq |\vec{p}|$. In this case, the pseudorapidity η coincides with y, *i.e.*

$$\lim_{|\vec{p}|\gg m} y = \eta = \frac{1}{2}\ln\left(\frac{E + E_z}{E - E_z}\right) = -\ln\left(\tan\left(\frac{\theta}{2}\right)\right) . \tag{3.3}$$

Using the pseudorapidity, the angular separation of two four-vectors p_1^μ, p_2^μ can be written as

[1] Throughout this text natural units are assumed.

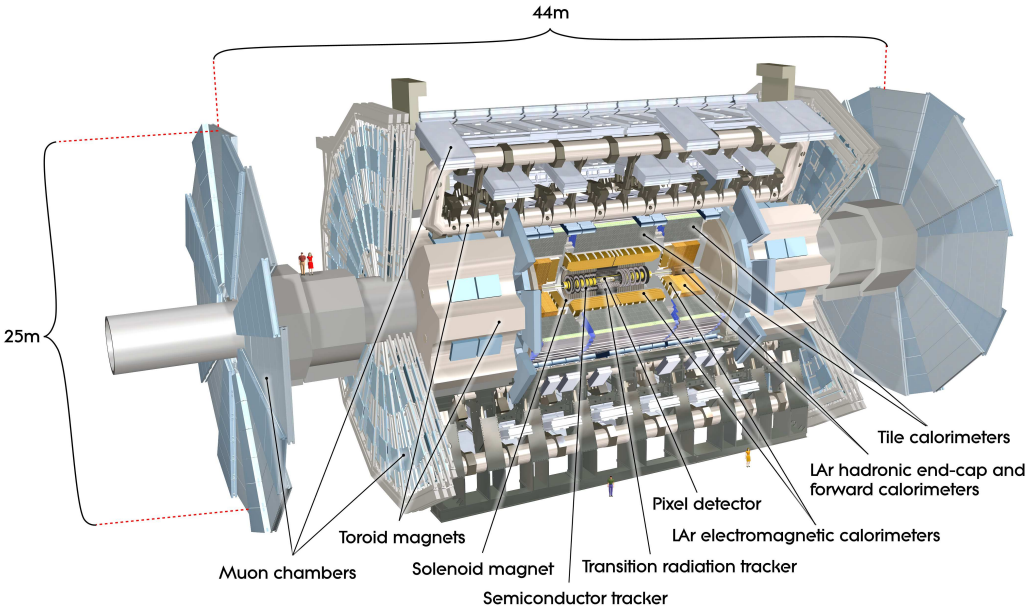

Figure 3.4: Cut-away view of the ATLAS detector [114]

$$\begin{aligned}\Delta R &= \sqrt{(\Delta\eta)^2 + (\Delta\phi)^2} \\ &= \sqrt{(\eta_2 - \eta_1)^2 + (\phi_2 - \phi_1)^2}.\end{aligned} \tag{3.4}$$

The ATLAS detector (Figure 3.4) is forward-backward symmetric with respect to the nominal interaction point and covers $|\eta|$ values of up to 4.9. Its coverage in ϕ is hermetic. It comprises multiple subsystems that are arranged in cylindrical layers around the interaction point, each dedicated to and optimised for a specific task. The innermost layer is formed by the ID (Section 3.2.1), followed by the calorimeters (Section 3.2.2), and, finally, the muon system (Section 3.2.3). These sections are focused on the detectors, neglecting the precise structure of the evenly important magnet systems. However, the characteristics of the magnetic fields are specified and the magnets themselves are shown in Figure 3.4.

3.2.1 The inner detector

The ATLAS inner detector [114] is immersed in a 2 T magnetic field. Consisting of the Insertable B-Layer (IBL) [115, 116], pixel detectors, Semi-Conductor Trackers (SCTs), and straw-tube-based Transition Radiation Trackers (TRTs), the ID is used for pattern recognition, momentum and vertex

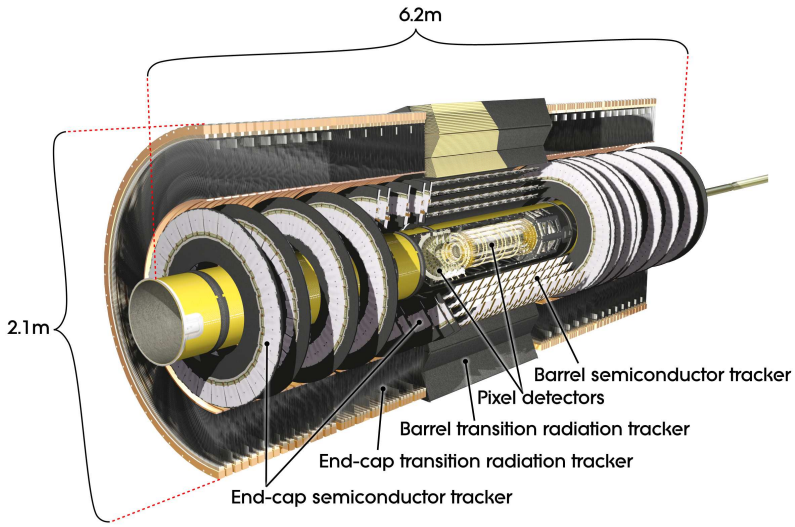

Figure 3.5: Cut-away view of the ATLAS inner detector [114].

measurements, and electron identification. It extends radially to a distance of 1150 mm from the beam and covers the pseudorapidities up to $|\eta| = 2.5$ for the precision detectors (pixels and SCT) and up to $|\eta| = 2.0$ for the TRT. The IBL has a coverage of up to $|\eta| = 2.58$, assuming moderate vertex spread [115]. In the barrel region, the detectors are aligned as concentric cylinders around the beam pipe, whilst in the end-cap region disks perpendicular to the beam axis are used (see Figure 3.5). Thus, the perpendicular direction for a given component is along r for barrel components and along z for end-cap components.

Totalling about 80.4 million readout channels, the pixel detectors have an intrinsic accuracy of 10 µm in the $r-\phi$ plane and 115 µm in their perpendicular directions. This is achieved using pixels with a nominal size in $r-\phi \times z$ of $50 \times 400\,\mu m^2$. About 10 % of the pixels are in the larger $50 \times 400\,\mu m^2$ format. The pixel detectors are based on oxygenated n-type wafers with pixel readout sensors on the n^+-implanted side. They measure the impact of ionising particles as they produce electron-hole pairs in the semiconductor material [117]. A bias voltage between 150 V and 600 V carries the holes to the n^+-doped side while the electrons travel to the n^{++} backplane[2]. Originally equipped with three layers, the IBL expands the pixel detector to a total of four layers. Moreover, the IBL is built using smaller $50 \times 250\,\mu m^2$ pixels.

The SCTs consist of strips with a pitch of approximately 80 µm. They use the cost-effective and radiation hard p-in-n technology [118, 119] and are AC-coupled to the readout strips. Biased with 150 V in the beginning and up to 350 V after ten years of irradiation, the detection principle is the same as in the pixel detectors, but with inverted intrinsic electric field. Bundled in about 6.8 million

[2] The higher voltage is required to account for radiation damages that occur over the lifetime of the detector.

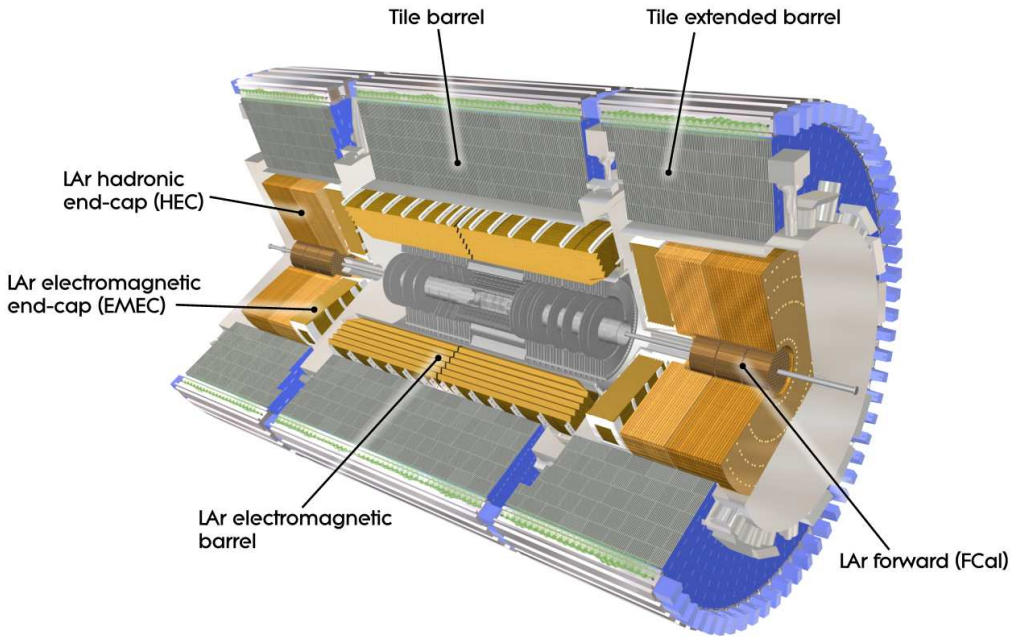

Figure 3.6: The ATLAS calorimeter system in a cut-away view [114]

channels, they give the detector an intrinsic accuracy of 17 µm in the $r-\phi$ plane and 580 µm in the perpendicular directions. The 351 000 straw drift tubes forming the TRT only measure the $r-\phi$ plane, for which an accuracy of 130 µm per straw is achieved.

Due to the magnetic field of 2 T, charged particles traversing the ID deposit energy along a bent trajectory. The particle's momentum can be calculated from the radius of the trajectory. The intrinsic spatial resolution of the ID detectors thus determines the momentum resolution in the reconstruction, which has a design goal of $\sigma_{p_T}/p_T = 0.05\,\%(p_T/\text{GeV}) \oplus 1\,\%$[3] [114].

3.2.2 The Calorimeter systems

ATLAS contains two calorimeter systems covering the range $|\eta| < 4.9$. They are shown in Figure 3.6. Dedicated to the energy measurement of electromagnetically interacting particles, the electromagnetic (EM) calorimeter [114] uses lead absorber planes with liquid-Argon filled gaps and as active medium. Divided into a barrel part ($|\eta| < 1.475$) and two-end cap parts ($1.375 < |\eta| < 3.2$)), the fine granularity of the EM calorimeter is ideal for precision electron and photon measurements. Its total thickness is more than 22 radiation lengths (X_0) in the barrel and more than $24X_0$ in the end-caps. This part of the detector has a design energy resolution of $\sigma_E/E = 10\,\%\sqrt{E/\text{GeV}} \oplus 0.7\,\%$ [114].

[3] The notation $a \oplus b$ denotes the quadratic addition of two uncertainties a and b according to $\sigma = \sqrt{a+b}$

The hadron calorimeter [114] consists of three parts: the tile calorimeter, the liquid Argon (LAr) hadronic end-cap calorimeter (HEC), and the LAr forward calorimeter (FCal). Placed directly next to the EM calorimeter, the tile barrel covers the range of $|\eta| < 1.0$ and the tile extended barrel covers $0.8 < |\eta| < 1.7$. Using steel as an absorber and scintillating tiles as active material, the tile calorimeter acts as a sampling calorimeter. It radially extends to $2.28\,\text{m} < r < 4.25\,\text{m}$ and segments into three layers that are about 1.5, 4.1, and 1.8 (1.5, 2.6, and 3.3) interaction lengths λ thick in the barrel (extended barrel). The tiles are read out by photomultiplier tubes.

The LAr hadronic end-cap calorimeter [114] is built from two independent wheels per end-cap and is installed directly behind the end-cap EM calorimeter, which allows using the same cryostat for both components. Extending up to $|\eta| = 3.2$, the HEC overlaps with the adjacent FCal. Similarly, by extending down to $|\eta| = 1.5$, it also overlaps with the tile calorimeter. This reduces the drop in material density in the transition regions. Its wheels have an inner and outer radius of 0.475 m and 2.03 m respectively. In the overlap region with the FCal, the inner radius is reduced to 0.372 m. Equipped with 32 identical copper wedges, the HEC consists of two segments per end-cap, each formed from four layers. The 8.5 mm gaps between the copper plates are filled with LAr, serving as the active medium. This setup is required to have an energy resolution better than $\sigma_E/E = 50\,\%/\sqrt{E/\text{GeV}} \oplus 3\,\%$ [114].

Integrated in the end-cap cryostats, the LAr forward calorimeter [114] unifies the calorimetric coverage and reduces the radiation background in the muon spectrometer. It has a thickness of approximately 10λ and is formed by three components in each end-cap. Built from copper, the innermost is optimised for electromagnetic measurements. The remaining two are made from tungsten and measure best hadronic interactions. An energy resolution of better than $\sigma_E/E = 100\,\%/\sqrt{E/\text{GeV}} \oplus 10\,\%$ is achieved [114].

3.2.3 Muon spectrometer

The ATLAS muon spectrometer [114] (shown in Figure 3.7) serves two purposes. Fast trigger chambers form the level-1 (L1) muon trigger and three layers of high precision tracking chambers measure charge and momentum of the muon. The MS is immersed in a magnetic field from superconducting toroidal magnets with field strengths between 0.3 T and 1.2 T.

Using Resistive Plate Chambers (RPCs) in the barrel region with $|\eta| \leq 1.05$ and Thin Gap Chambers (TGCs) in the end-cap regions with $1.05 \leq |\eta| \leq 2.4$, the trigger chambers provide fast signals that are achieved by sacrificing precision. In contrast, the high precision tracking chambers perform precise, but comparably slow measurements of the traversing particles. They consist of Monitored Drift Tube (MDT) chambers covering the region $|\eta| \leq 2.7$. In order to cope with the large background rates close to the beam pipe, Cathode Strip Chambers (CSCs) complement the MDT chambers in the forward

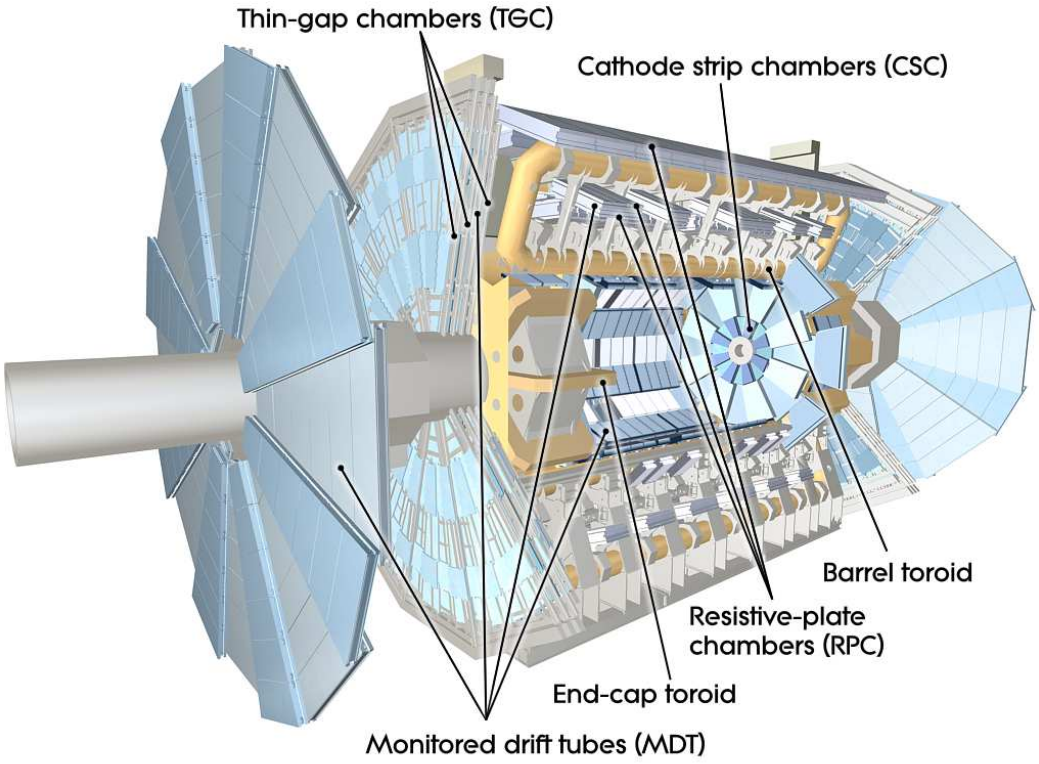

Figure 3.7: Cut-away view of the ATLAS muon system [114]

region above $|\eta| = 2.0$ in the inner end-cap layer. The design momentum resolution of the muon spectrometer is $\sigma_{p_T}/p_T = 10\,\%$ at $p_T = 1\,\text{TeV}$ [114].

3.2.4 Trigger and data acquisition system

With a 40 MHz interaction rate and assuming a typical event size of 1.5 MB, the ATLAS detector would generate several petabyte of raw data per second. Writing such vast amounts of data to disk is fortunately not necessary, as most events are of no interest to ATLAS analyses and thus can be disregarded. It is the task of the ATLAS Trigger and Data Acquisition system [114, 120] to pre-select interesting events and in doing so limit the outbound data rate to about one thousand events per second.

Figure 3.8 illustrates the TDAQ design for Run 2. Its structure and performance is described in detail in Ref. [120]. The first decision is made by the hardware-based L1 trigger. This component employs information from the L1 calorimeter trigger (L1Calo) and L1 muon trigger (L1Muon) systems, as well as from other systems as described in Ref. [121]. In 2016 a new topological trigger (L1Topo) was installed. Implemented as two field programmable gate array (FPGA) boards, it performs selections

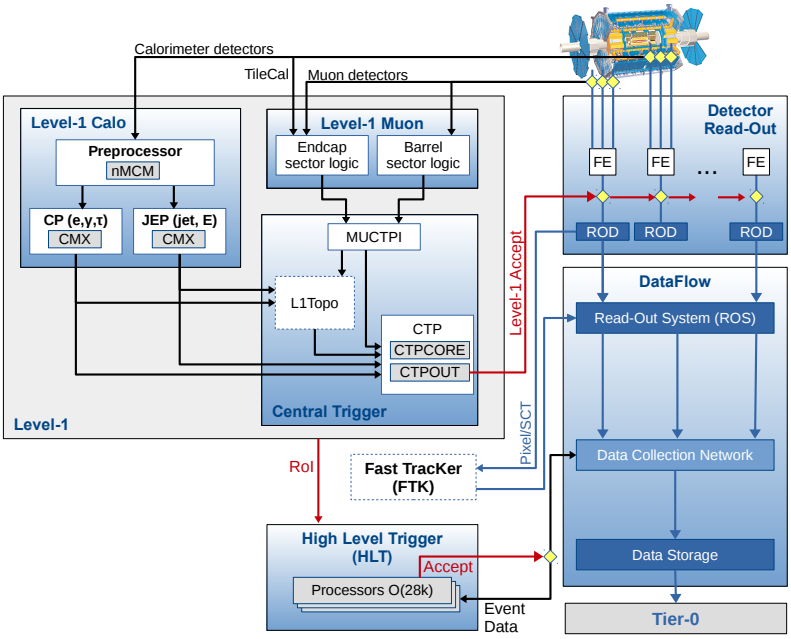

Figure 3.8: The ATLAS TDAQ system in Run 2 [120].

based on geometric or kinematic association of L1Calo and L1Muon trigger objects. Together with the Muon-to-CTP interface and the Central Trigger Processor the L1Topo forms the L1 Central Trigger.

For every successful selection the L1 trigger defines ranges in η and ϕ, called Region of Interest (RoI), that supposedly contain interesting features. Buffered in the Read-Out System, these events are transferred to the high-level trigger (HLT), where tracking information from the ID and MS as well as more precise calorimeter information is added. The HLT is a computer program realised in $O(4 \times 10^4)$ CPUs that perform calculations based on the more refined information [122]. The totality of these calculations (together with a set of configurations for the L1 Central Trigger) is referred to as trigger menu and the available menus for Run 2 are described in Refs. [120, 123, 124]. Pre-scaling is when an event is only accepted with a certain probability (defined by the pre-scaling value) even when it passes the HLT. Over the course of a LHC fill the instantaneous luminosity steadily decreases. Decreasing the pre-scaling value accordingly over a single LHC fill guarantees optimal usage of the available bandwidth and resources.

With an average decision time for accepting an event of 2.5 µs, the L1 trigger reduces the data rate

to 100 kHz. Within approximately 200 ms the HLT processes the buffered L1-accepted events and further reduces the rate to about 1 kHz. Events accepted by the HLT are transferred to the CERN Tier-0 computing centre for offline event reconstruction [122].

3.3 Monte-Carlo simulation

In order to interpret the recorded collision data, the observed data are usually compared to a prediction from simulated physics processes. The simulation of a given process comprises several steps from the event generation to a detailed simulation of the detector response. The first part of the event generation is the hard scattering, describing the transition from the initial to the final state particles. The elements of the scattering matrix $\mathcal{M}$ are calculated by Monte Carlo (MC) event generators based on a set of configurable parameters. The parameters incorporate the current knowledge about the SM as well as the assumptions that are made within the BSM theories. The scattering matrix allows for the calculation of the amplitude $\langle f|\mathcal{M}|i\rangle$, where $|i\rangle$ are the initial state proton constituents and $|f\rangle$ are the final state particles, all defined by their respective quantum numbers and four-momenta. Unstable particles (*e.g.* quarks) are then simulated to hadronise and/or decay further in a showering process until all produced particles can be considered as stable during their passage through the detector. The first step in this simulation chain is performed by a matrix element (ME) generator. The calculation of the hard scatter process is performed in the regime where the momentum transfer Q is large compared to the QCD scale, Λ_{QCD}. In this regime, the strong coupling constant is $\alpha_s(Q) \ll 1$, and the hadrons can be described as weakly interacting partons, using a parton distribution function (PDF). After the hard scattering, the partons can participate in a showering process. The description of this interaction step with a PDF is limited in generality, as softer processes can contribute significantly. By modifying the PDF tuning parameters, like *e.g.* the cutoff and hadronisation scales, a PDF can be tuned to adequately describe the showering process for a specific kinematic configuration (*e.g.* high-energetic Z bosons decaying into leptons). The combination of a PDF and a specific set of tuning parameters is called the PDF *tune*. Tunes are verified against experimental data in dedicated calibration studies and different tunes exist for the various kinematic scenarios of high-energy particle collisions. This particularly implies that different PDF sets might be used for the showering and the matrix element generation. Moreover, corrections from auxiliary tools can be incorporated. For example, a differential distribution generated at LO QCD precision can be re-weighted to match the predicted distribution of a next-to-leading-order (NLO) calculation, or the predicted LO cross section can be corrected to NLO precision in QCD.

The response of the ATLAS detector to the stable particles simulated taking into account all interactions with the detector. The ATLAS detector simulation software [125] is a detailed model of the ATLAS detector implemented in GEANT 4 [126]. An alternative to the detailed detector simulation is given

by the fast calorimeter simulation [127, 128], which provides a simulation of the particle energy response at the calorimeter read-out cell level at a fraction of the computing cost of GEANT 4. After simulating the detector response, the simulated events can be further processes as if they were real recorded data. The simulated detector response is fed through the same event reconstruction software as the actual collision data recorded by the ATLAS detector.

3.4 Object reconstruction

Hits deposit energy in the ID layers. From the ensemble of hits tracks are constructed with a track finding algorithm [129]. Defining characteristics for a track are its momentum, and the the transverse (d_0) and longitudinal (z_0) impact parameters, defined as the smallest distances of the track from the interaction point in transverse and longitudinal directions respectively. Tracks with $p_{\mathrm{T}} > 400\,\mathrm{GeV}$ and a sufficiently strong signature in the ID are used by a vertex finding algorithm based on a χ^2 fit [130]. If tracks incompatible with the primary vertex by more than 7σ are present, they can be used in a fit for another vertex. The vertex with the largest $\Sigma_{i\in\mathrm{tracks}} p_{\mathrm{T},\,i}$ defines the primary vertex. Events without a primary vertex are discarded.

Electrons in the region $|\eta| < 2.47$ are reconstructed from energy deposits in the EM calorimeter [131, 132]. The energy deposits are matched to tracks in the ID which in turn are required to have a minimum number of hits in the tracking system. Different electron identification working points are assigned to the electron candidates with a likelihood-based approach [131, 133]. The classes defined in Ref. [133] are *Loose LH*, *Medium LH*, and *Tight LH*. The electron efficiency for all working points increases with increasing transverse energies of the electron candidate, E_{T}, and ranges from 78 % (*Tight* at low E_{T}) up to 94 % (*Loose* at high E_{T}) [133]. Isolation variables [133] are defined to further discriminate electrons from heavy resonance decays such as $W \to e\nu$, or $Z \to ee$, from other, non-isolated electrons from *e.g.* converted photons produced hadron decays or heavy flavour decays. The calorimetric isolation, $I^{e}_{\mathrm{calo}} \equiv E_{\mathrm{T}}^{\mathrm{cone0.2}}$, is defined as the sum of the energies of all positive-energy, EM-calibrated topological clusters that lie within a cone of $\Delta R = 0.2$ around the electron candidate. This sum is corrected for the energy in the barycentre of the cone, electron energy leakage, and pileup effects as described in Refs. [132–134]. Electron track isolation, $I^{e}_{\mathrm{track}} \equiv p_{\mathrm{T}}^{\mathrm{varcone0.2}}$, is defined as the sum of track transverse momenta within a variable-sized cone of $\Delta R = \min(0.2, 10\,\mathrm{GeV}/E_{\mathrm{T}})$. The tracks have to be originating from the primary vertex and meet the quality requirements outlined in Ref. [133]. From these variables different working points are defined. The first class of working points are designed to select a fixed fraction of a test set of electrons, *i.e.* they have a fixed electron efficiency. They are called *LooseTrackOnly*, *Loose*, *Tight*, *Gradient*, and *GradientLoose*. The second class defines a fixed cut value on the isolation variables and the names of the working points are *FixedCutLoose*, *FixedCutTightTrackOnly*, and *FixedCutTight*. The efficiencies were calculated with

Table 3.1: Electron isolation working point (WP) definitions. The working point names and efficiency targets for the working points with a fixed electron efficiency are given in the upper part of the table. E_{T} is in GeV for the *Gradient* and *GradientLoose* workings points. The working point names and fixed cut values on the isolation variables for the fixed-cut working points are given in the lower part. Extracted from [133].

	Efficiency of fixed-efficiency WP		
Working Point	Calorimeter isolation	Track isolation	Total efficiency
LooseTrackOnly	—	99 %	99 %
Loose	99 %	99 %	~ 99 %
Tight	96 %	99 %	~ 98 %
Gradient	$0.1143\,\% \times E_{\mathrm{T}} + 92.14\,\%$		90/99 % at 25/60 GeV
GradientLoose	$0.057\,\% \times E_{\mathrm{T}} + 95.57\,\%$		95/99 % at 25/60 GeV
	Cut value of fixed-cut WP		
Working Point	Calorimeter isolation	Track isolation	
FixedCutLoose	0.20	0.15	
FixedCutTightTrackOnly	—	0.06	
FixedCutTight	0.06	0.06	

the tag-and-probe method for selections enriched in $J/\psi \to ee$ (for low E_{T}) and $Z \to ee$ (for high E_{T}) decays [131, 132]. The characteristics of the working points are summarised in Table 3.1.

The muon reconstruction [135] combines tracks from the ID with an analysis of MS hits. The latter starts with a Hough transform [136] in each chamber to identify hits aligned on a straight line in the bending plane of the MS. Based on a global χ^2 fit, hits from different layers are then combined into tracks. With a cut on the significance of the charge-over-momentum ratio $\sigma(q/p)/(q/p)$ muons with a bad fit quality are rejected after the combination of ID and MS tracks. Muons reconstructed this way, referred to as combined muons, use the best information available, since they combine independent information of two detector systems. However, more classes of muons exist. Segment-tagged muons are built from ID tracks that are extrapolated to and matched with at least one local track segment in the MDT or CSC chambers. Similarly, calorimeter-tagged muons are ID tracks that are matched to a minimum-ionising particle hit in the calorimeter. Having the lowest muon purity, this type is mostly useful in the $|\eta| < 0.1$ region where the MS is only partially instrumented. Lastly, extrapolated muons are MS muon tracks that can be loosely matched to the interaction point. The extrapolation considers the expected energy loss in the calorimeters. Extrapolated muons extend the acceptance of the MS into the region $2.5 < |\eta| < 2.7$, where no ID information is available. Working points at specific identification efficiency *vs.* background rejection points are defined [135], named *Loose*, *Medium*, *Tight*, and *High-p_T*. The acceptance ranges between 98.1 % (*Loose* with $20\,\mathrm{GeV} < p_{\mathrm{T}}^{\mu} < 100\,\mathrm{GeV}$) and 78.1 % (*High-$p_T$* with $4\,\mathrm{GeV} < p_{\mathrm{T}}^{\mu} < 20\,\mathrm{GeV}$). Furthermore, isolation variables [135] are defined to select muons originating from heavy particles, like vector or Higgs bosons. Similar

Table 3.2: Muon isolation working point (WP) definitions. The working point names and efficiency targets for the working points with a fixed electron efficiency are given in the upper part of the table. The working point names and fixed cut values on the isolation variables for the fixed-cut working points are given in the lower part. Extracted from [135].

	Composition of fixed-efficiency WP		
Working Point	Calorimeter isolation	Track isolation	Total efficiency
LooseTrackOnly	not required	required	99 %, constant in η and p_{T}
Loose	required	required	99 %, constant in η and p_{T}
Tight	required	required	96 %, constant in η and p_{T}
Gradient	required	required	$\geq$ 90/99 % at 25/60 GeV
GradientLoose	required	required	$\geq$ 95/99 % at 25/60 GeV
	Cut value of fixed-cut WP		
Working Point	Calorimeter isolation	Track isolation	
FixedCutTightTrackOnly	—	0.06	
FixedCutLoose	0.15	0.30	

to electrons, the track-based isolation, $I^{\mu}_{\mathrm{track}} \equiv p_{\mathrm{T}}^{\mathrm{varcone30}}$, is defined as the sum of track transverse momenta $> 1\,\mathrm{GeV}$ within variable-sized a cone of $\Delta R = \min(0.3, 10\,\mathrm{GeV}/p^{\mu}_{\mathrm{T}})$. The calorimetric isolation, $I^{\mu}_{\mathrm{calo}} \equiv E_{\mathrm{T}}^{\mathrm{topocone20}}$, is defined as the sum of the energies of all positive-energy, EM-calibrated topological clusters that lie within a cone of $\Delta R = 0.2$ around the muon candidate. The contribution of the muon candidate itself is subtracted and contributions from pileup and the underlying event are estimated and corrected for on an event-by-event basis with the ambient energy-density technique outlined in Ref [134]. Like for electrons, fixed-efficiency and fixed-cut working points are defined and they are summarised in Table 3.2

Jets are used to measure the properties of hadronic particle showers that are initiated by a single quark. At ATLAS either tracks measured in the inner detector (*track jets*) or calibrated and noise suppressed topological clusters of calorimeter cells (*calorimeter jets*) serve as an input to jet clustering algorithms. The calibration consists of several steps that mitigate a variety of effects, such as the non-compensating character of the calorimeter, or signal losses due to inactive material in the detector [137]. While a number of jet clustering algorithms exist, for example k_t [138], Cambridge/Aachen [139, 140], or SISCone [141], the anti-k_t clustering algorithm [142] has become the standard for ATLAS, as it is both infrared and collinear safe, and it produces easy-to-handle cone-shaped objects. It is implemented in the FastJet software package [143]. Being a member of the class of sequential recombination

algorithms, defining properties of the anti-k_t algorithm are the distance measures

$$d_{ij} = \min(p_{\mathrm{T},i}^{2p}, p_{\mathrm{T},j}^{2p}) \frac{\left(\Delta R_{ij}\right)^2}{R^2}, \quad \text{and} \tag{3.5}$$

$$d_{iB} = p_{\mathrm{T},i}^{2p}. \tag{3.6}$$

The radius parameter R is a free choice and ATLAS commonly uses values of 0.2, 0.4 and 1.0 for different categories of jets. The exponent p is the parameter that separates the various sequential recombination algorithms: k_t uses $p = 1$, Cambridge/Aachen $p = 0$, and the anti-k_t algorithm is defined by $p = -1$.

Variable radius (VR) track jets [144, 145] extend the anti-k_t idea by modifying Equation (3.6) with the dimensionless effective jet radius $R_{\mathrm{eff}}(p_{\mathrm{T}}) \equiv \rho / p_{\mathrm{T}}$,

$$d_{iB} = \frac{1}{p_{\mathrm{T},i}^2} \quad \rightarrow \quad d_{iB}^{\mathrm{VR}} = \frac{1}{p_{\mathrm{T},i}^2} R_{\mathrm{eff}}(p_{\mathrm{T},i})^2 = \frac{1}{p_{\mathrm{T},i}^2} \frac{\rho^2}{p_{\mathrm{T},i}^2} \tag{3.7}$$

The parameter ρ is a dimensionful constant, and it determines how fast the radius decreases with increasing transverse momentum of the jet. Studies suggest that a value of $\rho = 30\,\mathrm{GeV}$ maximises the reconstruction efficiency [146]. These objects are useful when reconstructing decays of heavily boosted objects with nearly collinear decay products. Requiring upper and lower bounds on the effective jet radius restores infrared and collinear safety and is implemented as

$$R_{\mathrm{eff}} = \min\left(\max\left(\rho / p_{\mathrm{T}}, R_{\mathrm{min}}\right), R_{\mathrm{max}}\right), \tag{3.8}$$

where $R_{\mathrm{min}} = 0.02$ and $R_{\mathrm{max}} = 0.4$ are typical values.

$R = 0.4$ jets are separated into *signal* and *forward* jets. Signal jets are reconstructed in the central η region and forward jets are reconstructed in $2.5 < |\eta| < 4.5$. Signal jets are further required to have either a p_{T} of at least 50 GeV or a p_{T} between 20 GeV and 50 GeV if their Jet Vertex Tagger (JVT) score is greater than 0.64. The JVT [147] uses information about the PV and jet and track p_{T} to construct a likelihood that separates pileup and hard scatter jets. The latter trend towards larger JVT scores. The selection requirements for the different jet types are summarised in Table 3.3.

Hadronically decaying taus τ_{had} are reconstructed by clustering topological cluster in the EM and hadronic calorimeters using $R = 0.4$ anti-k_t jets [148]. They have to satisfy $p_{\mathrm{T}} > 10\,\mathrm{GeV}$ and $|\eta| < 2.5$ to be accepted for the $\tau_{\text{had-vis}}$ reconstruction algorithm [148]. Final τ_{had} candidates are

Table 3.3: Selection requirements for forward and signal jets. The jet cleaning vetoes jets in regions with noisy calorimeter cells.

	Forward jets	Low-p_{T} signal jets	High-p_{T} signal jets
Quality	pass jet cleaning	pass jet cleaning	pass jet cleaning
p_{T} [GeV]	> 30	$[20, 50]$	> 50
$\lvert\eta\rvert$	$[2.5, 4.5]$	< 2.5	< 2.4

required to have at exactly one or three associated tracks and a $p_{\mathrm{T}} > 20\,\mathrm{GeV}$. The barrel/end-cap transition region $1.37 < |\eta| < 1.52$ is excluded.

3.4.1 Object definition

Contrary to collisions of elementary particles like e^+e^-, the momentum in the longitudinal direction is unknown in a pp interaction due to the partonic nature of the protons. However, since the protons carry no net transverse momentum, the missing transverse energy $E_{\mathrm{T}}^{\mathrm{miss}}$ can be reconstructed. $E_{\mathrm{T}}^{\mathrm{miss}}$ is caused for example by the neutrinos in the $Z \to \nu\bar{\nu}$ decay which leave the detector undetected, taking with them a certain transverse energy that is now missing from the sum of transverse energies of the reconstructed particles.

The $E_{\mathrm{T}}^{\mathrm{miss}}$ calculation [149] is based on reconstructed, calibrated *hard* objects and a *soft* term, which is calculated from energy deposits in either the ID or the calorimeters that are not associated to any hard object. Hard objects entering the calculation are electrons, muons, hadronically decaying taus, photons, and jets. The x and y components are defined as the negative sums over all the reconstructed objects

$$E_{x\,(y)}^{\mathrm{miss}} = -\sum_{\text{all } e} p_{x\,(y)}^{e} - \sum_{\text{all } \mu} p_{x\,(y)}^{\mu} - \sum_{\text{all } \tau_{\mathrm{had}}} p_{x\,(y)}^{\tau_{\mathrm{had}}} - \sum_{\text{all } \gamma} p_{x\,(y)}^{\gamma} - \sum_{\text{all jets}} p_{x\,(y)}^{\mathrm{jet}} - \sum_{\text{soft objects}} p_{x\,(y)}^{\mathrm{soft}}. \quad (3.9)$$

From this the $E_{\mathrm{T}}^{\mathrm{miss}}$ is calculated as

$$E_{\mathrm{T}}^{\mathrm{miss}} = \sqrt{\left(E_x^{\mathrm{miss}}\right)^2 + \left(E_y^{\mathrm{miss}}\right)^2}. \quad (3.10)$$

The track-based $E_{\mathrm{T}}^{\mathrm{miss}}$ (called $p_{\mathrm{T}}^{\mathrm{miss}}$) is a variation of the $E_{\mathrm{T}}^{\mathrm{miss}}$ calculation. Using only the track information of the hard objects, this quantity helps to suppress beam-induced and non-collision backgrounds.

A powerful tool in the interpretation of the $E_{\mathrm{T}}^{\mathrm{miss}}$ measurement is the object-based $E_{\mathrm{T}}^{\mathrm{miss}}$ significance, S [150]. Calculated on an event-by-event basis, this quantity evaluates the p-value that the observed $E_{\mathrm{T}}^{\mathrm{miss}}$ is compatible with the null hypothesis of zero real $E_{\mathrm{T}}^{\mathrm{miss}}$. A high S value indicates that the observed $E_{\mathrm{T}}^{\mathrm{miss}}$ indeed stems from undetected particles, like the neutrinos in the $Z \to \nu\bar{\nu}$ decay. It is defined as the measured $E_{\mathrm{T}}^{\mathrm{miss}}$ value divided by the $E_{\mathrm{T}}^{\mathrm{miss}}$ resolution. The latter, however, is inaccessible to measurements and thus ATLAS uses different proxies. Depending on the particular implementation, the object-based $E_{\mathrm{T}}^{\mathrm{miss}}$ significance can be defined as either

$$S = \frac{E_{\mathrm{T}}^{\mathrm{miss}}}{\sqrt{H_{\mathrm{T}}}}, \qquad \text{or} \qquad S = \frac{E_{\mathrm{T}}^{\mathrm{miss}}}{\sqrt{\sum E_{\mathrm{T}}}}. \tag{3.11}$$

Here, $\sum E_{\mathrm{T}}$ is the scalar sum of all transverse momenta from soft and hard objects, and H_{T} is the same sum but of the hard objects only.

Small radius jets are built from calorimeter cells clustered with the anti-k_t algorithm using a radius parameter $R = 0.4$. In some scenarios using large radius jets with $R = 1.0$ is preferred.

Track-CaloClusters (TCCs) [151] are large radius jets that are matched with track information from the ID. Tracks are extrapolated to calorimeter clusters and are combined into a TCC if the uncertainty on the extrapolation is smaller than the cluster width and if they overlap within the extrapolation uncertainty. TCCs combine the excellent energy resolution of the calorimeter [137] with the outstanding spatial resolution of the ID [152]. This is particularly useful in the high p_{T} scenario where large amounts of energy are deposited in small areas of the calorimeter. As such, TCCs are a powerful tool in the reconstruction of large-R jets, where the track information helps to identify jet substructures.

3.4.2 *b* tagging

For the identification of *e.g.* $h \to bb$ decays, b tagging is an essential tool. The b quarks hadronise and the resulting b hadrons travel a significant distance $\gamma c\tau \simeq \gamma \cdot 450\,\mu\mathrm{m}$ [42] in the laboratory frame. The displacement from the primary vertex in transversal and longitudinal directions is an essential ingredient in the identification of b jets. The distances of the closest approach are called transversal (d_0) and longitudinal (z_0) impact parameter in the $r{-}\phi$ plane and along the z direction, respectively. ATLAS utilises these impact parameters in unison with information about additional vertices in a procedure called b tagging [153]. Here, a multivariate algorithm calculates a score, based on which several selections are defined as working points. These have specific b jet efficiencies which are measured in control samples. For example, the 70 % working point of the MV2c10 algorithm selects

70 % of all possible b jets and has a rejection (defined as 1/efficiency) for c jets, τ jets, and light jets of 4.9, 15, and 110, respectively [153].

3.4.3 Overlap removal

The reconstruction of the introduced objects happens independently and so it can be that different objects are built from the same inputs, like energy clusters in the calorimeters, or ID tracks. As this would result in a double counting of energy, an overlap removal technique is applied [14]. First, τ leptons are considered. A τ is removed if it overlaps with a reconstructed electron within $\Delta R < 0.2$. It is also removed if it overlaps with a muon within $\Delta R < 0.2$, except if the tau-p_{T} is greater than 50 GeV and if the reconstructed muon is not a combined muon. Electrons are removed if they share an ID track with a muon. If a small-R jet overlaps with an electron or a muon within $\Delta R < 0.2$ it is removed if the lepton passes the isolation requirements introduced in Section 3.4.1. Since b hadrons can produce muons in their decay chain the jet is not removed if it overlaps with a muon and has at least three associated tracks, or if the jet and muon kinematics favour such a decay. This is the case if less than 70 % of the sum over the track p_{T} of the tracks associated to the jet comes from the muon and if the jet p_{T} is at least double the muon p_{T}. If after this step electrons or muons overlap with the remaining jets within $\Delta R < 0.4$ they are removed if their distance to any jet is smaller than $\Delta R = (0.04 + 10\,\mathrm{GeV}/p_{\mathrm{T}}^{\ell})$, where p_{T}^{ℓ} is the lepton p_{T}. Lastly, small-R jets within $\Delta R < 0.2$ of a hadronic tau candidate and large-R jets within $\Delta R < 1.2$ of any remaining electron are removed.

CHAPTER FOUR

SEARCH FOR HEAVY CHARGED VECTOR BOSONS IN THE $\ell\nu b\bar{b}$ DECAY CHANNEL

The existence of a new heavy charged vector boson decaying into a pair of lighter, known bosons is predicted by many theories beyond the Standard Model (see Chapter 2). A search for a charged $W'^{\pm}$ vector boson resonance decaying into a $W^{\pm}$ and a Higgs boson is conducted in the semileptonic $\ell^{\pm}\overset{(-)}{\nu}_{\ell}b\bar{b}$ final state, using 36 fb^{-1} of pp collision data at $\sqrt{s}$ = 13 TeV recorded during 2015 and 2016. The results are interpreted within the Heavy Vector Triplet (HVT) model.

Details on the signal topology and the summary of main background processes are given in Section 4.1. In order to formulate background-only and signal+background hypotheses that can be tested against the data in a statistical model, a signal+background prediction is made based on the simulated Monte Carlo (MC) samples introduced in Section 4.2. In Section 4.3 details about the data taking and the employed triggers are given. Next, the event reconstruction is summarised in Section 4.4. Since the kinematic region of interest corresponds only to a small portion of the simulated background events, the MC prediction is validated and corrected for via dedicated studies performed in control regions, containing background-enriched data that are disjoint from but as close as possible to the nominal signal event selection. Due to similar event selection requirements, the control regions are used for the validation of the background modelling. An overview of the background modelling studies is given in Section 4.5.

One particular study performed in dedicated control regions is the study of the V+jets ($V = W, Z$) background contribution. For an optimal description of this background process in the statistical analysis, V+jets events are grouped based on the flavour content of the associated jets and the optimisation of the categorisation according to the flavour is presented in Section 4.6. A second background study targets the expected contribution of multijet events to the total background prediction. Due to large statistical fluctuations in MC generated multijet samples, the prediction is based entirely on a data-driven method, which is explained in detail in Section 4.7. The goal of this study is a quantitative evaluation of the contribution of multijet events in the final event selection.

The final discriminant used for the statistical interpretation of data is the invariant mass of the W' candidate, m_{Wh} (see Section 4.4 for its deviation) and its distributions prior to the fit to data (pre-fit) are studied in Section 4.8. Both experimental and theoretical modelling uncertainties are considered in the statistical interpretation of the data. A summary of the various uncertainty sources is given in Section 4.9.

Apart from the validation studies, the control regions are also included in the final fit for the statistical interpretation, providing further constraints on the background contribution. Most notably, the overall normalisations, *i.e.* the predicted numbers of background events, for several background components are determined solely from the fit to data, as described in detail in Section 4.10. The results of the fit of the prediction to the observed data, are interpreted in terms of upper limits on the production cross section of heavy W' bosons. The consistency of the fit model is studied in detail by investigating the post-fit m_{Wh} and nuisance parameter distributions. These results are presented in Section 4.11.

4.1 The HVT W' signal and the main background processes

The dominant production mode for $W'^{\pm}$ bosons in the framework of the HVT model is quark annihilation in a Drell-Yan-like process (*cf.* Section 2.1). An exemplary LO Feynman diagram for this production process with a subsequent $\ell^{\pm(\mp)}\nu_\ell b\bar{b}$ decay via a Wh diboson decay channel is shown in Figure 4.1. Expected to be weaker by a few orders of magnitude, the VBF production is not considered for the presented search based on the partial dataset recorded in 2015 and 2016.

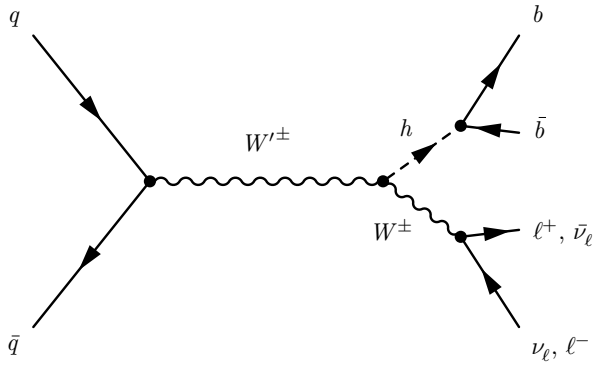

Figure 4.1: Leading-order Feynman diagram for the production of a $W'^{\pm}$ boson, decaying via a $W^{\pm}h$ diboson decay into a b-quark pair, a charged lepton, and a neutrino.

The semileptonic final state is chosen to combine the highest Higgs boson decay branching fraction from $h \to b\bar{b}$ decays with a strong background suppression due to the charged lepton (electron or muon) from the $W^{\pm} \to \ell^{\pm(\mp)}\nu_\ell$ decay.

Since only the transverse momentum can be directly reconstructed for the neutrino from the $W^{\pm} \to \ell^{\pm(-)}\nu_{\ell}$ decay, a W boson mass constraint is used to recover the z component of the neutrino momentum. Setting the x and y neutrino momentum components to the corresponding measured missing $p^{\nu}_{x,y} = E^{\text{miss}}_{x,y}$, and using the mass relation $m^2_W = (p_\ell + p_\nu) \cdot (p_\ell + p_\nu)$, where m_W is the W boson mass and $p_{\ell(\nu)}$ is the four-momentum of the charged lepton (neutrino), the z-component of the neutrino momentum can be expressed as

$$p^{\nu}_z = \frac{1}{2\left(p^{\ell}_{\text{T}}\right)^2}\left[p^{\ell}_z A + E_\ell\sqrt{A^2 - 4\left(p^{\ell}_{\text{T}}\right)^2\left(E^{\text{miss}}_{\text{T}}\right)^2}\right], \tag{4.1}$$

with $A = m^2_W + 2p^{\ell}_x E^{\text{miss}}_x + 2p^{\ell}_y E^{\text{miss}}_y$. For complex solutions of this expression, the real part of the solution is chosen as the p^{ν}_z component. If both solutions are real, the smaller of the two values is chosen.

Major background processes are $t\bar{t}$ and V+jets ($V = W, Z$). The $t\bar{t}$ process is relevant for all phase space regions of the event selection, in particular in regions containing events with b-tagged jets. The V+jets background contribution in different phase space regions depends on the flavour of the associated jets. The V+jets processes are therefore categorised according to their flavour information (Section 4.6) and are labelled V+hf, V+(bl, cl), and Vl for processes with two, one, or no heavy flavour quarks (b or c quarks), respectively. The components containing heavy flavour quarks are more dominant in regions of the event selection with b-tagged jets. Example leading order Feynman diagrams for the production of these background components are shown in Figure 4.2.

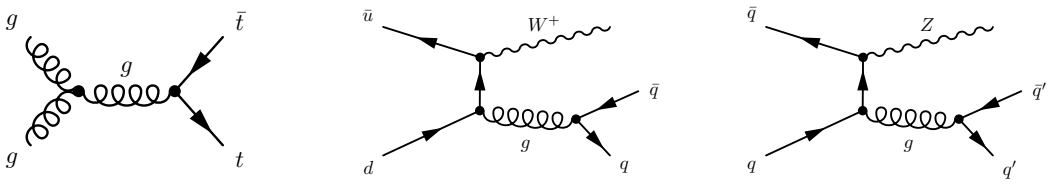

(a) $t\bar{t}$ (b) W+jets (c) Z+jets

Figure 4.2: Example leading order Feynman diagrams for the *(a)* $t\bar{t}$, *(b)* W+ jets, and *(c)* Z + jets production

Minor background processes are final states with a single top quark (Figure 4.3), top quark pairs produced in association with a vector or Higgs boson (Figure 4.2), diboson processes (Figure 4.5), as well as the non-resonant production of a Vh-pair (Figure 4.6).

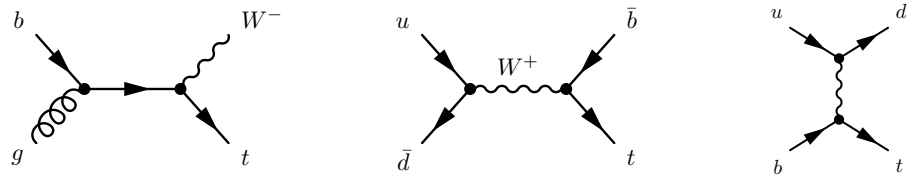

(a) Wt process (b) s-channel (c) t-channel

Figure 4.3: Example leading order Feynman diagrams for the single top quark production

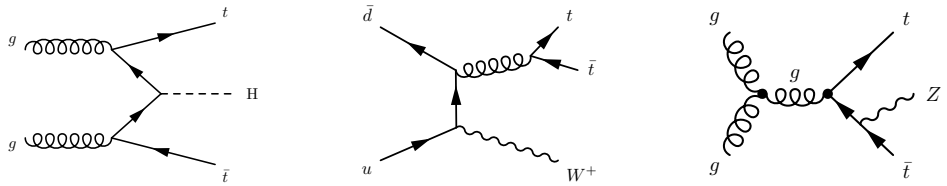

(a) $t\bar{t}H$ (b) $t\bar{t}$ + W (c) $t\bar{t}$ + Z

Figure 4.4: Example leading order Feynman diagrams for the$t\bar{t}$ production in association with a Higgs or a vector boson.

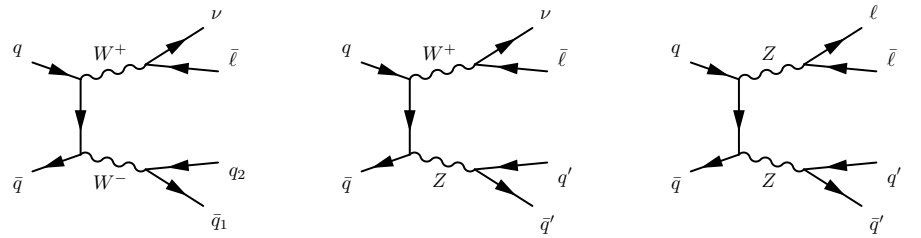

(a) WW (b) WZ (c) ZZ

Figure 4.5: Example leading order Feynman diagrams for the production of diboson pairs

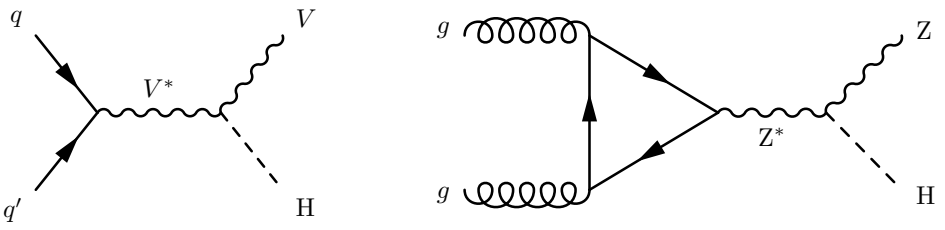

(a) Higgs strahlung (b) gluon fusion

Figure 4.6: Example Feynman diagrams for the non-resonant Vh production

4.2 Simulated signal and background processes

The HVT signal processes were generated by MadGraph5_aMC@NLO v2.2.2 [154, 155] using the NNPDF2.3 [156] LO PDF set, interfaced to Pythia 8.186 [157, 158] with the A14 [159] tune for the parton showering. A number of signal samples for various W' masses ranging from 500 GeV to 5 TeV (*cf.* Appendix A.1) were generated for the HVT benchmark model A (*cf.* Section 2.1). The differences in event kinematics between models A and B are expected to be smaller than the changes due to the detector response and thus the same signal samples are used for the interpretations within the HVT model B. The two models thus differ only by the predicted production and decay rates. The generated samples include both the $h \to b\bar{b}$ and $h \to c\bar{c}$ Higgs decay modes. The SM values of branching ratios $\mathcal{B}(h \to b\bar{b}) = 0.569$ and $\mathcal{B}(h \to c\bar{c}) = 0.0287$ and the Higgs boson mass of 125 GeV were assumed. The production cross sections for all simulated HVT signal processes are summarised in Appendix A.1.

Top quark pair events ($t\bar{t}$) were generated by Powheg-Box v2 v2 [160–162] at LO precision in QCD, interfaced to Pythia 6 [158] for the showering and using the Perugia 2012 [163] parton shower tune. The matrix elements were calculated with the CT10 [164] PDF set. The $t\bar{t}$ production cross section was normalised to next-to-next-to-leading-order (NNLO) QCD precision using the Top++2.0 software package [165–171], including soft gluon contributions up to next-to-next-to-leading-logarithm (NNLL) precision in QCD. The predicted p_{T} distributions of the $t\bar{t}$ events were corrected to the corresponding NNLO parton-level spectra [172].

Single top quark production processes were generated at NLO QCD precision by the same Powheg-Box v2 program interfaced to Pythia 6, and using the Perugia 2012 tune. The s- and t-channels as well as the Wt production were considered. Using the HATHOR v2.1 program [173, 174], the cross sections for the s- and t-channel production were calculated at NLO precision. The Wt process was approximated at NNLO precision based on soft-gluon resummation calculations at NNLL accuracy [175].

The production of top quark pairs in association with a Higgs or a vector boson ($t\bar{t}H, t\bar{t}V$) were simulated at NLO QCD precision by MadGraph5_aMC@NLO v2.3.2, with the NNPDF3.0 [176] NLO PDF set. Pythia 8.210 [158, 177] with the A14 tune was used for the parton showering. The top quark mass was assumed to be 172.5 GeV for all top quark processes.

Higgs bosons produced in association with a vector boson in a non-resonant SM quark-antiquark annihilation process ($q\bar{q} \to Zh, q\bar{q} \to Wh$) were simulated at LO QCD precision by Pythia 8.186 with the NNPDF2.3 LO PDF set. The loop-induced $gg \to Zh$ production was simulated at NLO in QCD by Powheg-Box v2 with the CT10 PDF set. Showering was performed by an AZNLO-tuned [178] version of Pythia 8.186, using the same PDF set as for the ME calculation.

Vector bosons production in association with jets (V+jets, where $V = W, Z$) were simulated by Sherpa 2.2.1 [179] with the NNPDF3.0 NNLO PDF set for both the calculation of the matrix elements and the showering. The Comix [180] and Open Loops [181] tools were used for the calculation of matrix elements, which were then matched to the parton shower using the ME+PS@NLO method [182]. Contributions with up to two additional parton emissions at the matrix-element level were simulated at NLO precision in QCD, while processes with up to four partons are provided at LO accuracy. The cross sections were normalised to NNLO accuracy in QCD [183].

The SM diboson processes (WW, ZW, ZZ) were generated using Sherpa 2.1.1 with the CT10 PDF set. At LO, diagrams with up to three additional partons were considered. Furthermore, for ZZ up to one additional parton was considered at NLO production. The cross sections were calculated at NLO accuracy.

EvtGen v1.2.0 [184] was used for the bottom and charm hadron decays for all samples produced by MadGraph5_aMC@NLOor Powheg, reducing potential differences of the decay properties between the two generators.

The impact of multiple pp interactions per bunch-crossing (*pile-up*) was taken into account by overlaying each signal and background event with minimum-bias events generated by Pythia 8.186 with the A2 tune [185] and the MSTW2008 LO PDF [186].

The response of the ATLAS detector was simulated by the ATLAS detector simulation software [125]. The simulated detector response is fed through the same event reconstruction software as the actual collision data recorded by the ATLAS detector (*cf.* Section 3.4).

Table 4.1 summarises all simulated signal and background samples that are employed in the presented analysis.

4.3 Data taking and trigger selection

The proton-proton collision data for the presented analysis were recorded during 2015 and 2016 at a centre-of-mass energy of $\sqrt{s} = 13\,\text{TeV}$. The integrated luminosity amounts to $36\,\text{fb}^{-1}$. A number of data quality criteria have to be met, ensuring that only data recorded with a fully operational ATLAS detector are used for further analysis. The Run 2 data quality operations are explained in more detail in Ref. [187].

The studied $\ell^{\pm}\overset{(-)}{\nu}_{\ell}b\bar{b}$ signal final state can be triggered by dedicated $E_{\text{T}}^{\text{miss}}$ and single-lepton triggers. The $E_{\text{T}}^{\text{miss}}$ triggers used for this search imposed varying lower thresholds of the $E_{\text{T}}^{\text{miss}}$ values during

Table 4.1: Summary of simulated MC samples used for the $W' \to Wh$ search together with the corresponding matrix element generators, PDFs, and parton shower (PS) tunes. The precision in QCD of the inclusive cross section calculation is included as well. MG is shorthand for MadGraph5_aMC@NLO.

Process	**ME generator**	**ME PDF**	**PS and hadronisation**	**MC tune**	**Cross section calc. order**
HVT W'	MG 2.2.2	NNPDF2.3 LO	Pythia 8.186	A14	LO
$t\bar{t}$	Powheg-Box v2	CT 10	Pythia 6.428	Perugia 2012	NNLO+NNLL
single top	Powheg-Box v2	CT 10	Pythia 6.428	Perugia 2012	NLO (Wt: approx. NNLO)
V + jets	Sherpa 2.2.1	NNPDF3.0 NNLO	Sherpa 2.2.1	Sherpa/MEPS@NLO	NNLO
WW, ZW, ZZ	Sherpa 2.1.1	CT 10	Sherpa 2.2.1	Sherpa/MEPS@NLO	NLO
$t\bar{t} + h$ and $t\bar{t} + V$	MG 2.3.2	NNPDF3.0 NLO	Pythia 8.210	A14	NLO
SM $q\bar{q} \to Vh$	Pythia 8.186	NNPDF2.3 LO	Pythia 8.186	A14	NNLO+NLO
SM $gg \to Vh$	Powheg-Box v2	CT 10	Pythia 8.186	AZNLO	NLO+NLL

online[1] data processing. For the 2015 data taking period this threshold was 70 GeV, while for the 2016 data taking before and after mid-June it was set to 90 GeV and 110 GeV, respectively. These are the un-prescaled $E_{\mathrm{T}}^{\mathrm{miss}}$ triggers with the lowest available thresholds.

The electron triggers used various requirements on the E_{T} of the HLT electron, electron likelihood, impact parameter, and isolation (*cf.* Section 3.4). For the 2015 data-taking period, the requirements were $E_{\mathrm{T}} > 24$ GeV and meeting the medium likelihood working point criteria. For 2016, the logical `or` of several triggers was used. They included E_{T} thresholds of 26, 60, 140, and 300 GeV. The higher E_{T} thresholds were added for a maximal trigger efficiency over the full E_{T} range. Moreover, they comprised looser identification criteria compared to the low-E_{T} triggers. A summary of all triggers and their corresponding event selection criteria is given in Table B.1.

Single-muon triggers, even though available, were not used for this search, as it was found that they had a negligible impact on the expected signal significance.

4.4 Event reconstruction

The particles from the recorded collisions and the corresponding simulated events are reconstructed using dedicated reconstruction algorithms and selection criteria described in Section 3.4.

[1] Here, the $E_{\mathrm{T}}^{\mathrm{miss}}$ value is calculated from jets reconstructed by the high-level trigger in real time.

Aiming at the $W \to \ell\nu$ decay, exactly one charged lepton (electron or muon) is required to be present in the event, with a p_{T} of at least 27 GeV and satisfying certain identification and isolation requirements (*cf.* Section 3.4.1): electrons (muons) are required to pass the FixedCutTight (FixedCutTightTrackOnly) isolation criteria and the TightLH (LooseLH) identification requirements.

The $h \to b\bar{b}$ Higgs decay candidates are reconstructed using dedicated jet reconstruction algorithms. For small resonance masses of $m_{W'} \lesssim 2\,\mathrm{TeV}$, the Higgs boson in the $W' \to Wh$ decay is produced with a relatively small Lorentz boost, resulting in a large opening angle between the two b quarks. In this scenario, the quarks hadronise in well separated regions of the detector and can be reconstructed as two small-radius (radius parameter $R = 0.4$) anti-k_t calorimeter jets. The separation of signal and background processes can be further enhanced by imposing b-tagging criteria on the reconstructed small-radius jets, as will be detailed later on. For larger resonance masses, the opening angle between the Higgs decay products is small and the angular separation of the corresponding small-radius jets can be less than 0.4. Even though the anti-k_t algorithm is robust enough to avoid double-counting calorimeter clusters, the substructure of the resulting jets no longer resembles the partonic structure of the initial quark system. The reconstruction of the $h \to b\bar{b}$ decay as a single large radius jet ($R = 1.0$) mitigates this problem. In order to access the information on the flavour composition within the large-radius jet, they are matched to track-based jets (*cf.* Section 3.4) which are within the large-radius jet. The track jets are built from ID tracks using the anti-k_t algorithm, with a fixed value of the radius parameter of $R = 0.2$. The b-tagging criteria are then applied on the track jets associated to the large-radius jets, similar to the small-radius jets. Signal candidate events reconstructed using small-radius jets are referred to as events within *resolved* topology, whilst *merged* event topology refers to events with a large-radius jet. The event selection criteria for the resolved topology require at least two and at most three signal jets (*cf.* Section 3.4.1). The presence of additional forward jets is allowed. The event selection for the merged topology requires at least one large-radius jet in the final state with at least one associated track jet.

Further requirements are imposed to suppress the overall background contamination. The requirements involve kinematic properties of the final state particles, such as $E_{\mathrm{T}}^{\mathrm{miss}}$ values or the jet p_{T}, as well as event-topology-inspired quantities, such as the presence of at least two small-radius jets in the resolved topology. All event selection requirements are summarised in Table 4.2

The first selection criterion is the trigger requirement described in Section 4.3. Trigger scale factors, correcting for differences between data and MC simulation due to trigger inefficiencies, are applied where necessary. Next, the $E_{\mathrm{T}}^{\mathrm{miss}}$ value is required to be above a given threshold, mainly to suppress the QCD backgrounds. With the signal having a real $E_{\mathrm{T}}^{\mathrm{miss}}$ contribution from the neutrino in the vector boson decay, this threshold trades background suppression for signal efficiency, and an optimal value in the resolved topology is found to be $E_{\mathrm{T}}^{\mathrm{miss}} > 30\,\mathrm{GeV}$ if the event contains an electron. The requirement is dropped if the event contains a muon. In contrast, the merged topology is mainly

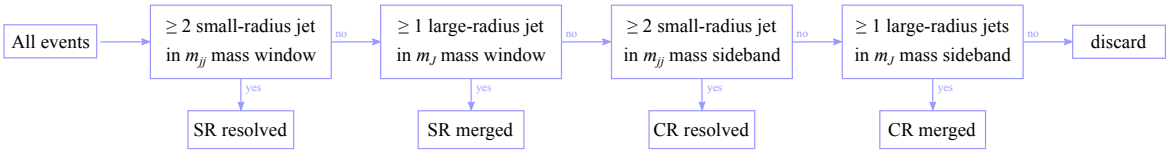

Figure 4.7: The analysis prioritisation scheme defining the categorisation of events into the signal regions (SRs) and sideband control regions (CRs) with the resolved and merged event topologies. The resolved topology selection is preferred over the one with the merged topology.

Table 4.2: Summary of the event selection criteria for the $W' \to Wh$ resonance search

Variable	**Resolved**	**Merged**
Number of jets	2 or 3 signal jets, ≥ 0 forward jets	≥1 large-radius jet
Associated track jets	—	≥ 1
Leading jet p_{T} [GeV]	> 45	> 250
Leading lepton p_{T} [GeV]	> 27	> 27
$E_{\mathrm{T}}^{\mathrm{miss}}$ [GeV]	> 30 (e channel), > 0 (μ channel)	> 100
$p_{\mathrm{T},W}$ [GeV]	$> \max[150,\ 710 - (3.3 \times 10^5\,\mathrm{GeV})/m_{Vh}]$	$> \max[150,\ 394 \cdot \ln(m_{Vh}/(1\,\mathrm{GeV})) - 2350]$
$m_{\mathrm{T},W}$ [GeV]	< 300	< 300
m_{jj} or m_J [GeV]	[110, 140]	[75, 145]

sensitive to high mass resonances producing a highly boosted neutrino, and therefore a threshold of $E_{\mathrm{T}}^{\mathrm{miss}} > 100\,\mathrm{GeV}$ is used. A lower threshold is also introduced on the transverse momentum of the W boson candidate, p_{T}^{W}, reconstructed from the final state lepton and $E_{\mathrm{T}}^{\mathrm{miss}}$. The threshold value depends on the mass of the hypothesised W' resonance. For the resolved topology, a maximal signal significance is expected for a p_{T}^{W} threshold value of $710 - (3.3 \times 10^5\,\mathrm{GeV})/m_{Wh}/(1\,\mathrm{GeV})$, with the minimal threshold value of 150 GeV. Similarly, in the merged topology the threshold value is given by the logarithmic function $394 \cdot \ln(m_{Wh}/(1\,\mathrm{GeV})) - 2350$, again with the minimal threshold of 150 GeV. The transverse component of the W boson mass, $m_{\mathrm{T},\,W}$, is required to be smaller than 300 GeV in both regimes, to avoid mismodelling in the tails of the $m_{\mathrm{T},\,W}$ distributions.

Events satisfying the above requirements are further categorised into signal regions (SRs) and control regions (CRs) based on the reconstructed Higgs boson candidate mass. In the kinematic regions with the resolved topology, the mass m_{jj} of the Higgs boson candidate is calculated by combining the four-momenta of the two highest-p_{T} signal jets. For the merged topology regime, the mass of the highest-p_{T} large-radius jet m_J is used instead. Mass windows are defined according to the experimentally measured Higgs boson mass of $m_h = 125\,\mathrm{GeV}$. In the regions with the resolved topology, the SR mass window is set to $110\,\mathrm{GeV} < m_{jj} < 140\,\mathrm{GeV}$ and for the merged topology to $75\,\mathrm{GeV} < m_J < 145\,\mathrm{GeV}$. Events with Higgs candidate mass values outside this window but still within $50\,\mathrm{GeV} < m_{jj/J} < 200\,\mathrm{GeV}$ define the low and high $m_{jj/J}$ mass sidebands.[2] These sidebands

[2] The symbol $m_{jj/J}$ is used synonymously for the Higgs candidate mass and corresponds to m_{jj} and m_J in the resolved

are combined into the $m_{jj/J}$ sideband CR and are employed to set constraints on the background contributions in the SRs. For events that can be reconstructed both as the resolved and the merged topology events, the selection criteria are chosen such that each event is uniquely assigned to one of the two categories by a dedicated prioritisation scheme, as outlined in Figure 4.7. If an event contains two small-radius signal jets with an invariant mass within the m_{jj} signal mass window, it is assigned to the resolved SR. Otherwise, if a large-radius jet is present in the event and has a mass within the m_J signal window, the event is assigned to the merged SR. If an event satisfies neither the resolved SR nor the merged SR requirements, it is considered a possible control region candidate, as long as the requirements in Table 4.2, with the notable exception of the $m_{jj/J}$ requirements, are still satisfied. If such an event contains two small-radius jets with a dijet invariant mass within the m_{jj} sideband mass window, it is assigned to the resolved sideband CR. Otherwise, if the highest-p_{T} large-radius jet has an invariant mass within the m_J sideband mass window, the event is assigned to the merged sideband CR. All other events are discarded from the analysis.

In order to better identify the Higgs boson candidates, the b-tagging procedure is applied on the jets, using the MV2c10 b-tagging algorithm at the 70 % b-tagging efficiency working point, as introduced in Section 3.4.2. Small-radius signal jets are tagged directly, whilst large-radius jets are matched to the smaller size track jets that can subsequently be b-tagged. The n-tag region in data is defined as a collection of events with n b-tagged small-radius jets (track jets) in the resolved (merged) event topology. A veto is applied on events with the merged topology in which additional b-tagged track jets not associated to the leading large-radius jet are present, which helps to suppress the contribution of $t\bar{t}$ background events.

The signal is searched for in data by looking for a localised excess of events (compared to the SM prediction) in the invariant mass distribution of the diboson resonance candidate, m_{Wh}. This final discriminant is calculated from the four-momenta of the final state particles, incorporating Equation (4.1) for the neutrino momentum,

$$m_{Wh} = \sqrt{\left(E_W + E_{\mathrm{T}}^{\mathrm{miss}} + E_h\right)^2 - \left(\vec{p}_W + \vec{p}_\nu + \vec{p}_h\right)^2}, \tag{4.2}$$

where the indices W, h, and ν indicate the corresponding particles. In order to improve the mass calibration of the Wh system in the resolved event topology, the invariant mass of the dijet system is rescaled by $125\,\mathrm{GeV}/m_{jj}$.

and merged event topologies respectively.

4.5 Background modelling

The modelling of all dominant SM background processes relies on the simulated MC samples introduced in Section 4.2. The validity of the MC predictions is studied in control regions, and, if necessary, mismodellings are addressed by dedicated modelling uncertainties that are included in the final fit model. In order to put tight constraints on the modelling uncertainties of these backgrounds, the corresponding sideband control regions for events with the resolved topology are included in the statistical interpretation. In particular, the normalisation of the $t\bar{t}$, W+hf, and W+(bl, cl) background components are determined entirely from the fit to data (*cf.* Section 4.10).

The simulated V+jets background components are grouped into categories according to the flavour of the associated jets in order to provide separate modelling and at the same time eliminate unconstrained degrees of freedom from the final fit to data. This study is described in Section 4.6.

Multijet background events can not be reliably simulated, and a data-driven method is established (*cf.* Section 4.7) by studying dedicated multijet control regions. With this method, the expected number of multijet events in the signal regions is determined together with a shape template of the m_{Wh} multijet background distribution and is included in the final statistical model. The background estimate also contains dedicated uncertainties on the modelling and normalisation of the multijet background contribution.

4.6 Optimisation of the V+jet background modelling

The background sources introduced in the previous section are not all treated independently in the statistical analysis of the data. Since the resonance candidate mass m_{Wh} is used as the final discriminant, processes that give similar shapes of this distribution can be treated as a single background template distribution, that is, they are affected by the same set of fit parameters in the final statistical interpretation of data (*cf.* Section 4.10). Generally, merging background templates is favourable, as it eliminates degrees of freedom in the fit and thus reduces ambiguities of the statistical interpretation. Very similar physics processes such as the different single top quark production modes are one example of processes that are merged into a single background template in this analysis. A second example are V+jets events ($V = W, Z$) with vector bosons produced in association with jets. This background comprises processes with different jet flavours, and there is some freedom whether different flavour components should be combined into a single template. The presented analysis implements an approach that combines flavour components based on their shape in the final discriminant, as described in detail below.

A flavour label specifies the jet flavour, and is based on particle-level information from the MC generator. This is in contrast to flavour tagging, which is based on detector information. The advantage of using particle-level information is that no uncertainty due to the inefficiency or misidentification rate of the b-tagging algorithm needs to be considered. Moreover, after choosing an adequate labelling scheme, no flavour labels in any given event can be missed. The latter is explained in greater detail below.

Two different approaches to assign a flavour label to a given jet in the event are studied, using either the so-called ΔR-matching method or the ghost association method. The former approach is based on the angular separation between the hadrons at particle (generator) level and each reconstructed jet in the event. If a generated b (c) quark at particle level has an angular distance $\Delta R \leq 0.3$ to the reconstructed jet, the b (c) flavour is assigned to that jet. In case multiple particle-level b or c hadrons can be matched to a single jet, the one with the smallest ΔR value is chosen for assigning the jet label. Finally, if no b or c quark is matched to the jet, the *light* (l) flavour label is assigned. The collection of reconstructed jets considered for the flavour labelling procedure differs for the resolved and merged event topologies. In the resolved (merged) event topology, small-radius jets (track jets associated to the large-radius jet) are used for the matching. In both cases only the two leading-p_{T} jets are considered. Since the event selection criteria for the merged topology also accepts events with only a single track jet associated to the large-radius jet, V+jets events with only a single label are possible in the case of if the ΔR-matching, even if there were two heavy flavour hadrons present at the particle-level.

In order to reach the additional flavour information in such special cases, the ghost association approach [188] is used. The ghost association procedure involves an additional step in which the existing reconstructed jets are re-clustered after adding generator-level particles to the original reconstructed clusters. In general, all generator-level particles are added, but in this case, only hadrons are considered. During the re-clustering, the p_{T} values of the generator-level particles are set to be vanishing, such that the re-clustered jet does not significantly differ from the original one. All generator-level particles that cluster with a given jet in this modified clustering step are considered to be *ghost associated* with the original jet. By counting all ghost associated, rather than ΔR-matched, particles for a given jet, more than one flavour label can be assigned even to events with a single track jet within the large-radius jet.

Following the ghost-association procedure, the V+jets events with a single track jet in a large-radius jet are then labelled using the following prioritisation:

1. Vbb: single track jet is ghost associated to two or more b hadrons;
2. Vbc: single track jet is ghost associated to one b and at least one c hadron;
3. Vbl: single track jet is ghost associated to one b hadron and no c hadrons;

4. Vcc: single track jet is ghost associated to two or more c hadrons;
5. Vcl: single track jet is ghost associated to one c hadron;
6. Vl: single track jet is ghost associated to neither a b nor a c hadron.

All other V+jets events are labelled using the ΔR-matching procedure.[3] With this hybrid strategy of ghost association for events with single track jets within a large-radius jet and ΔR-matching for all other events, the following components of the V+jets background are defined: Vbb, Vbc, Vcc, Vbl, Vcl, and Vl. The last component, Vl, also contains events with two light jets, *i.e.* Vll.

The advantage of this hybrid flavour labelling strategy can be seen in Figure 4.8, where the m_{Wh} distributions are shown for the W+hf (= W+bb + W+bc + W+cc), $W+(bl, cl)$ (= W+cl + W+bl), and W+l background components defined via ΔR-matching only or via the hybrid flavour matching procedure. In the case of ΔR-matching alone, if there is only a single b or c hadron matched to the jet, the event is included in the $W+(bl, cl)$ background component. The distributions are normalised to a unity integral, allowing for a direct shape comparison. The number of simulated events from each background component is quoted in the brackets. All events contributing to the analysis of the merged topology are included. The W+hf component defined with the hybrid labelling strategy contains significantly more events and has a harder m_{Wh} distribution than the component defined via ΔR matching alone. This is likely caused by the merging of the track jets in events with highly boosted Higgs boson candidates. The angular track jet separation in these events may be smaller than their radius parameter ($R = 0.2$) if the p_{T} of the Higgs boson candidate from which they originate is $\gtrsim 1.2$ TeV. In these cases of real heavy flavour decays with two or more heavy flavour track jets, only a single track jet is reconstructed and matched to the Higgs boson candidate large-radius jet. Therefore, with the ΔR-matching labelling approach, these events are assigned only a single jet flavour (W+c, W+b), although two heavy flavour bosons are present in the event. Consequently, these events are included in the $W+(bl, cl)$ component instead of the W+hf component. On average, these events have a larger m_{Wh} because of the mentioned jet boost. For the same reasoning, the $W+(bl, cl)$ component defined by the hybrid approach has fewer entries than from the ΔR-matching approach. This is supported by the fact that the m_{Wh} spectrum of the $W+(bl, cl)$ component obtained with the hybrid labelling approach is notably softer. The distributions of the W+l background components are hardly affected by the choice of the flavour labelling approach.

Overall, the hybrid matching approach significantly alters the m_{Wh} distributions of the W+jets background components with at least one heavy flavour quark, and generally allows for a better distinction between the W+hf and $W+(bl, cl)$ components. This can be clearly seen in Figure 4.9, where the m_{Wh} distributions from the three W+ jets background components are compared to each

[3] The ghost matching procedure is not required for the resolved topology, as the event selection requires at least two signal jets, which can be used in the ΔR-matching procedure.

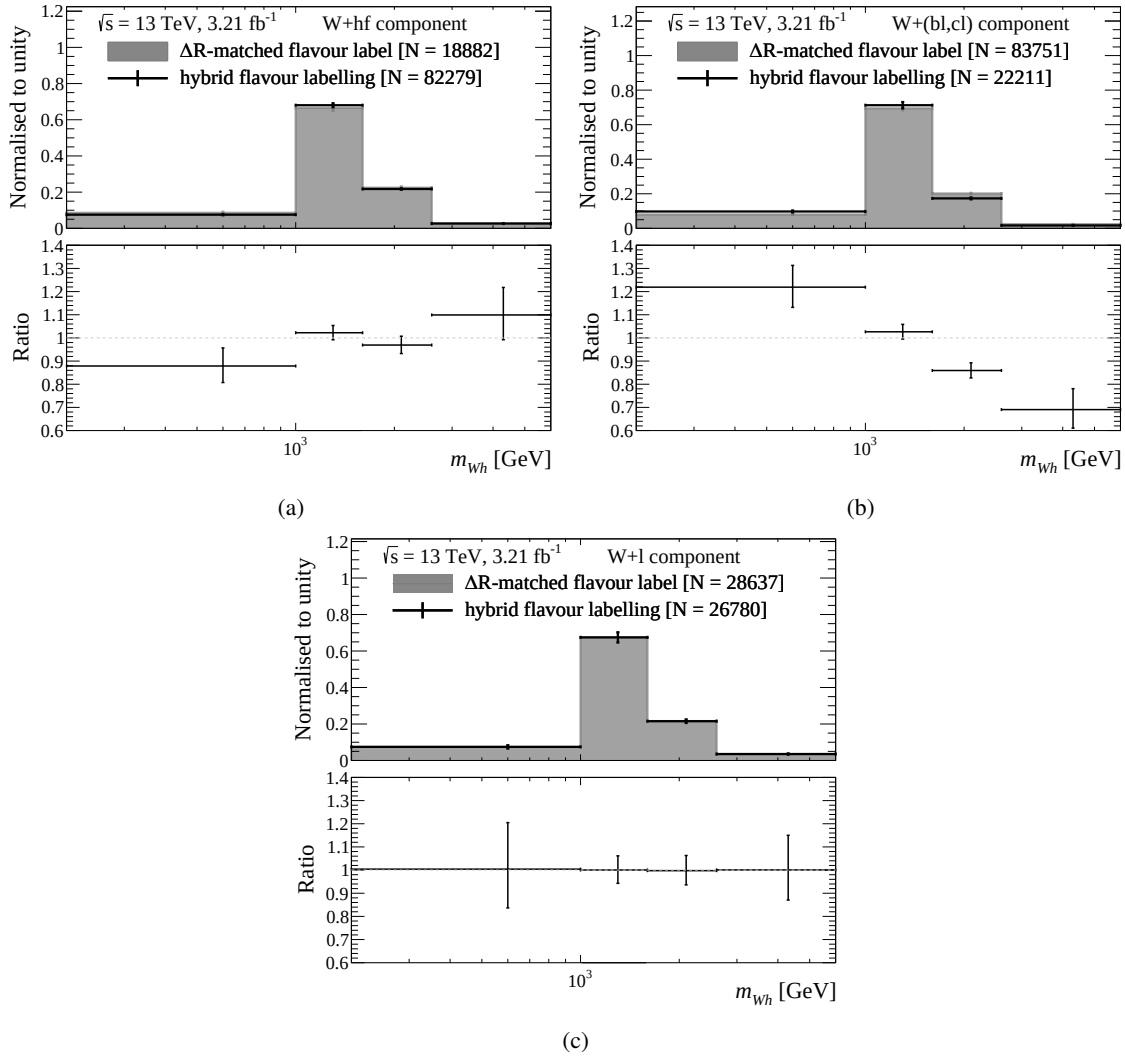

Figure 4.8: The expected normalised m_{Wh} distributions for different of W+ jets background components defined based on the ΔR-matching approach (grey filled histograms) and on the hybrid labelling approach (black dots): *(a)* W+hf, *(b)* $W+(bl, cl)$, and *(c)* $W+l$ component. In the lower panel, the ratio of the two distributions is shown. In both panels, only the statistical uncertainty of the background components defined by hybrid labelling approach (indicated by the markers) are shown, as the two samples are statistically strongly correlated. The number of events entering each component, N, is also provided in the legend. A subset of the simulated data is used, corresponding to an initial data taking period with an integrated luminosity of 3.21 fb^{-1}.

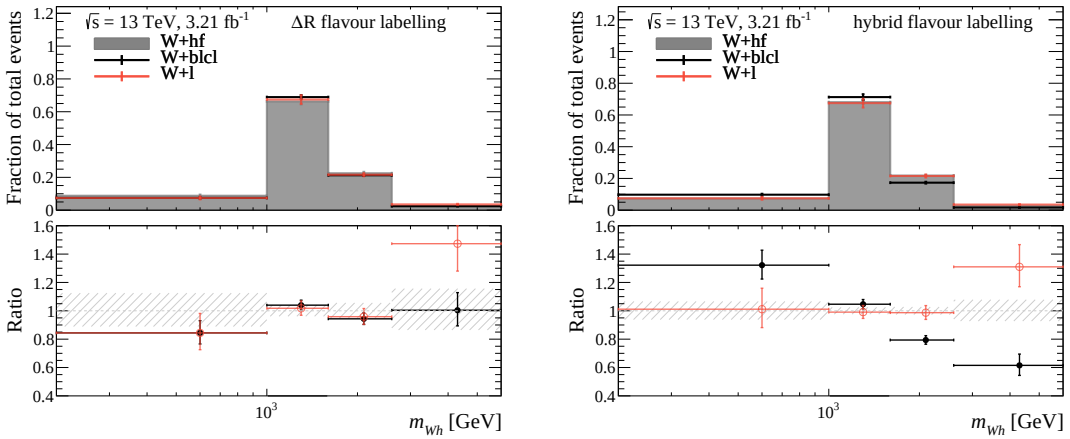

(a) (b)

Figure 4.9: Comparison of the shape of the m_{Wh} distributions for the various W+jets background components defined by the *(a)* ΔR-matching, and *(b)* hybrid matching flavour labelling approach. The lower panel shows the ratio of the W+hf to the $W+(bl, cl)$ (black full circles) and $W+l$ (red open circles) distribution, respectively. The statistical uncertainty is indicated by the grey hatched for the W+hf component area and by the error bars for the remaining components.

other for both flavour labelling approaches. Figure 4.9(a) shows the corresponding distributions obtained with the ΔR-matching labelling approach. The distributions of the three components are very similar, resulting in their ratio values being close to one. Thus, the background contributions from these three components cannot be easily distinguished from one another in the fit to the data, introducing a degree of degeneracy which limits the final signal sensitivity. On the other hand, the distributions obtained with the hybrid flavour labelling approach (Figure 4.9(b)) are significantly more distinct from each other, allowing in particular for better constraints on the W+hf and $W+(bl, cl)$ background components from the fit to data.

The hybrid flavour labelling approach is therefore chosen for the final statistical interpretation of the data (*cf.* Section 4.10).

Due to similarities of the Z+jets and W+jets background processes in terms of the event generation setup and the properties of final state products, the same flavour labelling strategy is chosen for the less dominant Z+jets background as well. The differences in the m_{Wh} distributions of the different Z+jets components, however, are found to be much less pronounced.

4.7 Estimate of the multijet background contribution

In pp collisions, the most likely interaction by far is an inelastic scattering of valence quarks, often resulting in relatively low energy (*soft*) jets in the final state. Such events are usually referred to

as QCD or multijet background. For every hard pp collision at 13 TeV in which a Higgs boson is produced, there are about 10 billion soft collisions. Even though the multijet events generally have a very different event topology and kinematic properties compared to the Higgs boson production or other hard-scatter processes, even a small imperfection in the detector response may lead to a significant contribution of the multijet background to virtually any final state. The $\ell^{\pm}\overset{(-)}{\nu}_{\ell}b\overline{b}$ final state studied in this thesis, for example, can be mimicked by a pion decay into a muon and a neutrino within a jet, accompanied by two additional jets, either originating from a b hadron, or being misidentified as b jets. Also, even with no pion decays into leptons, a jet itself may be misidentified as an electron.

Such multijet events are difficult to simulate, especially in the kinematic regions corresponding to the hard-scatter signal. Moreover, the efficiency of misidentifying a jet as a charged lepton is rather difficult to model as well. For this reason, multijet background distributions obtained from simulation often lack the statistical significance required for a proper estimate of this background contribution in the signal region (SR). Instead, estimates based on dedicated data in control regions (CRs) are required.

In this analysis, the so-called *template method* is used to determine a template of the m_{Wh} distribution from inelastic QCD events (*multijet template histogram*), which is used for the final statistical interpretation of the data. The method consists of two steps. First, the shape of the m_{Wh} multijet distribution is determined in a CR that is enriched in multijet events (so-called *shape template histogram*, see Section 4.7.1). For a proper shape estimate the CR should cover a similar (yet disjoint) portion of the phase space as the SR. The original normalisation of the shape template histogram corresponds to the number of multijet events in the dedicated CR. In order to extrapolate this contribution to the multijet contribution in the SR, the shape template histogram is normalised by a transfer factor in a second step (see Section 4.7.3). The transfer factor is obtained from a fit of the $E_{\mathrm{T}}^{\mathrm{miss}}$ distribution from the CR to the data in the nominal SR and $m_{jj/J}$ sidebands. The $E_{\mathrm{T}}^{\mathrm{miss}}$ distribution is chosen for two reasons. Firstly, it has negligible sensitivity to the potential HVT W' signals, which have relatively large $\Delta E_{\mathrm{T}}^{\mathrm{miss}}/E_{\mathrm{T}}^{\mathrm{miss}}$ values, and secondly, it has a very strong discriminating power between non-multijet and multijet backgrounds, as will be explained later on. The resulting normalised m_{Wh} template histogram is referred to as the *QCD template* and is used in the final statistical interpretation of the data (*cf.* Section 4.11). The impact of potential sources of uncertainties from this method is evaluated, and corresponding normalisation and shape uncertainties are assigned to the multijet template distribution for the final statistical interpretation.

4.7.1 Shape template histogram

An appropriate control region for the determination of the multijet shape template histogram is found by studying the charged lepton isolation properties. A charged lepton originating from a W boson

Table 4.3: Identification and isolation criteria of the charged leptons in the signal and in the isolation-inverted control regions.

	Criterion	Signal region	Isolation-inverted control region
Electrons	Identification WP	TightLH	TightLH
	Track-based isolation	$I^{e}_{\text{track}} < 0.06$	$I^{e}_{\text{track}} < 0.06$
	Calorimeter isolation	$I^{e}_{\text{calo}} < 0.06$	$I^{e}_{\text{calo}} > 0.06$
Muons	Identification WP	TightLH	TightLH
	Calorimeter-based isolation	$I^{\mu}_{\text{calo}} < 0.06$	$0.06 < I^{\mu}_{\text{calo}} < 0.15$

decay has a trajectory that is compatible with the primary vertex and carries a relatively high p_{T}. As such, prompt leptons are well isolated from hadronic activity in the inner detector and the calorimeters, justifying the choice of the tight isolation criteria for the selection of signal candidates. In contrast, leptons from multijet events often originate from weak decays inside the jet (*e.g.* the aforementioned pion decay into a muon and a neutrino) or from the misidentification of jets as leptons.

Isolation metrics quantifying the amount of hadronic activity around the lepton can be calculated based on the calorimetric and inner detector activity around the lepton candidate. The multijet CRs can therefore be defined by applying the same set of event selection criteria as in the case of the nominal event selection (*cf.* Table 4.2), except for the requirement on the calorimeter-based isolation, $I^{e,\mu}_{\text{calo}}$, which is inverted for both electron and muon events. In case of muon final states, an upper threshold of $I^{\mu}_{\text{calo}} < 0.15$ is required in addition to limit the phase space of the inverted region in order to be closer to the SR. The isolation requirements in the SRs and isolation inverted CRs are summarised in Table 4.3. Dedicated isolation-inverted CRs are defined separately for each of the corresponding signal and sideband control regions with resolved and merged event topologies and each n-tag category (*cf.* Section 4.4). In order to avoid the inconsistent requirements on the electron isolation in electron triggers used for the nominal event selection (Table B.1) and to cover the largest possible E_{T} range, only the electron trigger with the lowest available E_{T} threshold for any given data taking period is used for template method. Potential biases in the shape oft the determined electron multijet shape template histogram are addressed by a dedicated shape uncertainty, as described in Section 4.7.4.

The observed $E_{\text{T}}^{\text{miss}}$ and m_{Wh} distributions in the isolation-inverted region corresponding to 1 b-tag events with the resolved topology are shown in Figure 4.10, together with the MC prediction of the contributions from all other simulated processes. In the following, both distributions will be studied as the $E_{\text{T}}^{\text{miss}}$ distribution is used for the normalisation of the m_{Wh} template in the SR, which in turn is used in the final statistical interpretation of the data. Due to different origins of the reconstructed charged leptons from the multijet background, the final states with electrons and muons are analysed separately.

For both final states the difference between the observed and the simulated data is the largest at low $E_{\mathrm{T}}^{\mathrm{miss}}$ values, *i.e.* the multijet background contributes mainly to the region with $E_{\mathrm{T}}^{\mathrm{miss}}$ values below about 150 to 200 GeV. The same is true for events with 2 b-tags, as shown in Figure 4.11, but the relative contribution of multijet events to the total background is much smaller in the case of events with 2 b-tags. Smaller still is the contribution of multijet events in the regimes with merged event topology, mainly due to the increased $E_{\mathrm{T}}^{\mathrm{miss}}$ threshold requirement. The corresponding distributions from the isolation-inverted control regions with merged event topology are shown in Appendix B.2.

4.7.2 Background normalisation in the isolation-inverted control region

Each component of the simulated non-multijet background in Figures 4.10 and 4.11 is corrected for by using dedicated scale factors obtained from a fit to the data in the isolation-inverted control region. The fit is performed on the total simulated background sum in the high-$E_{\mathrm{T}}^{\mathrm{miss}}$ tail of the $E_{\mathrm{T}}^{\mathrm{miss}}$ distribution for reasons discussed below.

The impact of these scaling factors on the distributions of QCD observables in the isolation-inverted control region can be twofold. If each component of the simulated non-multijet backgrounds is scaled by an individual normalisation factor, the shape of the multijet distribution can change. In contrast, if all simulated non-multijet backgrounds are scaled by the same normalisation factor, the shape of a multijet distribution remains unchanged and only its normalisation is affected. The notable exception to the latter statement is the case where the difference between data and simulated non-multijet backgrounds is negative. Histograms with negative content correspond to a negative number of expected multijet events, and are truncated to zero, thus changing the original shape of the multijet distribution. By choosing an appropriate normalisation of the total simulated background, the number of template histogram bins with negative content can be minimised. Such bins are mainly observed in the tail of the $E_{\mathrm{T}}^{\mathrm{miss}}$ distribution, where the contribution of multijet events is expected to be small.

The $E_{\mathrm{T}}^{\mathrm{miss}}$ distribution is chosen for the scaling of the non-multijet backgrounds, since this distribution provides a good discrimination from the multijet process. In multijet events, the $E_{\mathrm{T}}^{\mathrm{miss}}$ mainly originates from imperfectly reconstructed jets rather than from neutrinos. As an example, a multijet event with three jets produced from a system at rest can be considered, as illustrated in Figure 4.12.[4] In this scenario, the net momentum of all jets is zero. However, if one of the jets is missed by the event reconstruction, the p_{T}-sum of the remaining two reconstructed jets is different from zero, leading to a finite value of $E_{\mathrm{T}}^{\mathrm{miss}} = \sqrt{(p_{j1}^{x} + p_{j2}^{x})^2 + (p_{j1}^{y} + p_{j2}^{y})^2}$. Instead or in addition to the jets missed completely by the jet reconstruction algorithms, mis-reconstructed jet energy can also contribute significantly to the wrongly reconstructed $E_{\mathrm{T}}^{\mathrm{miss}}$. The resulting $E_{\mathrm{T}}^{\mathrm{miss}}$ values are relatively small, *cf.*

[4] This is a somewhat constructed and unrealistic example. However, it can be easily extended to a more realistic scenario by allowing for some initial momentum in the system. This was omitted for the simplicity of the illustration.

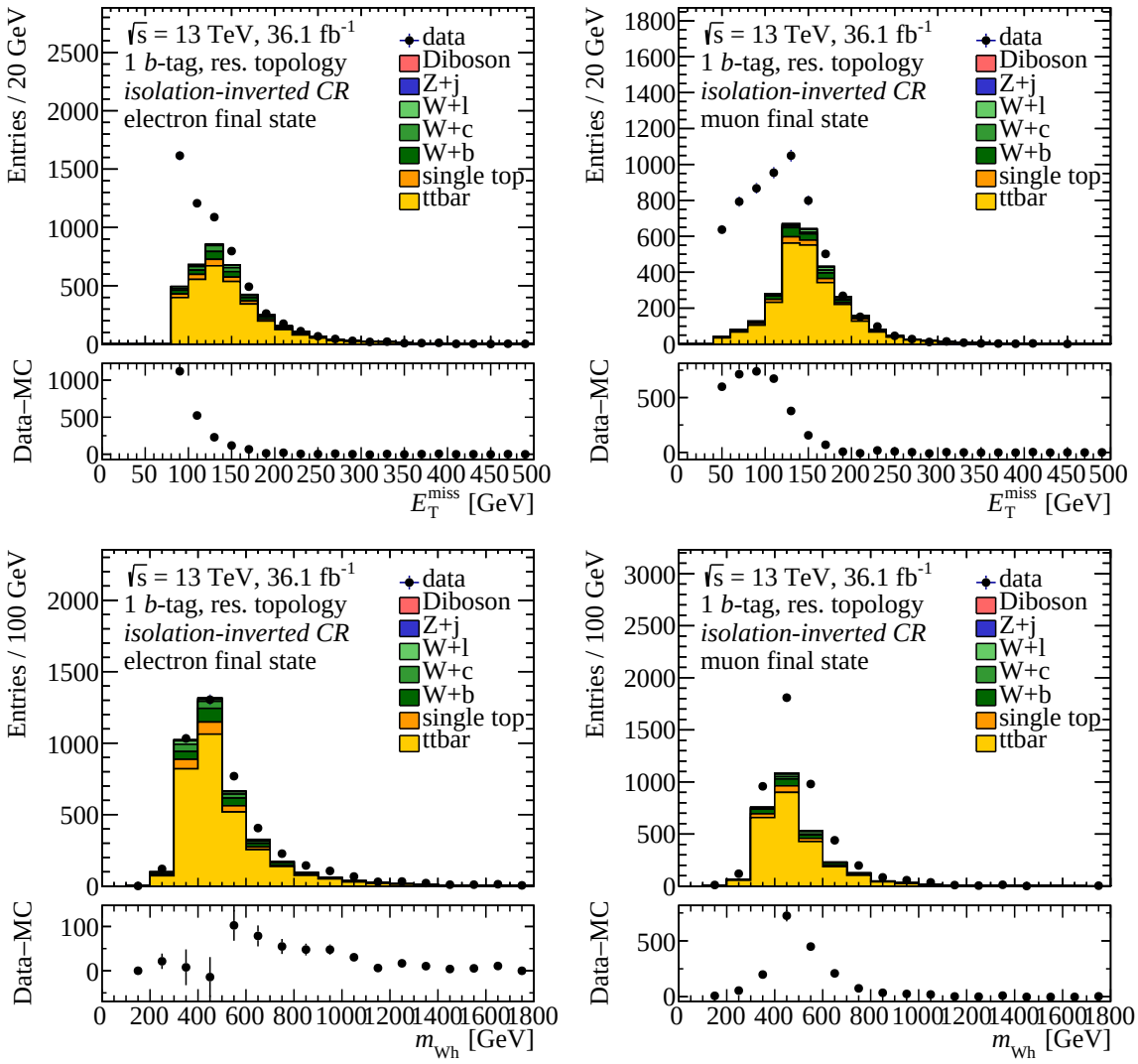

Figure 4.10: Observed distributions of the missing transverse energy (E_T^{miss}) and the mass of the Wh system (m_{Wh}) in the isolation-inverted control regions for events with 1 b-tag and the resolved topology for (left) the electron and (right) the muon final states. The expected MC non-multijet background contributions are shown as filled histograms. The difference between data and the MC prediction is shown in the lower panels. The total MC prediction is scaled to fit the data in the tail region with $E_T^{miss} > 200$ GeV, where the QCD contribution is expected to be negligible.

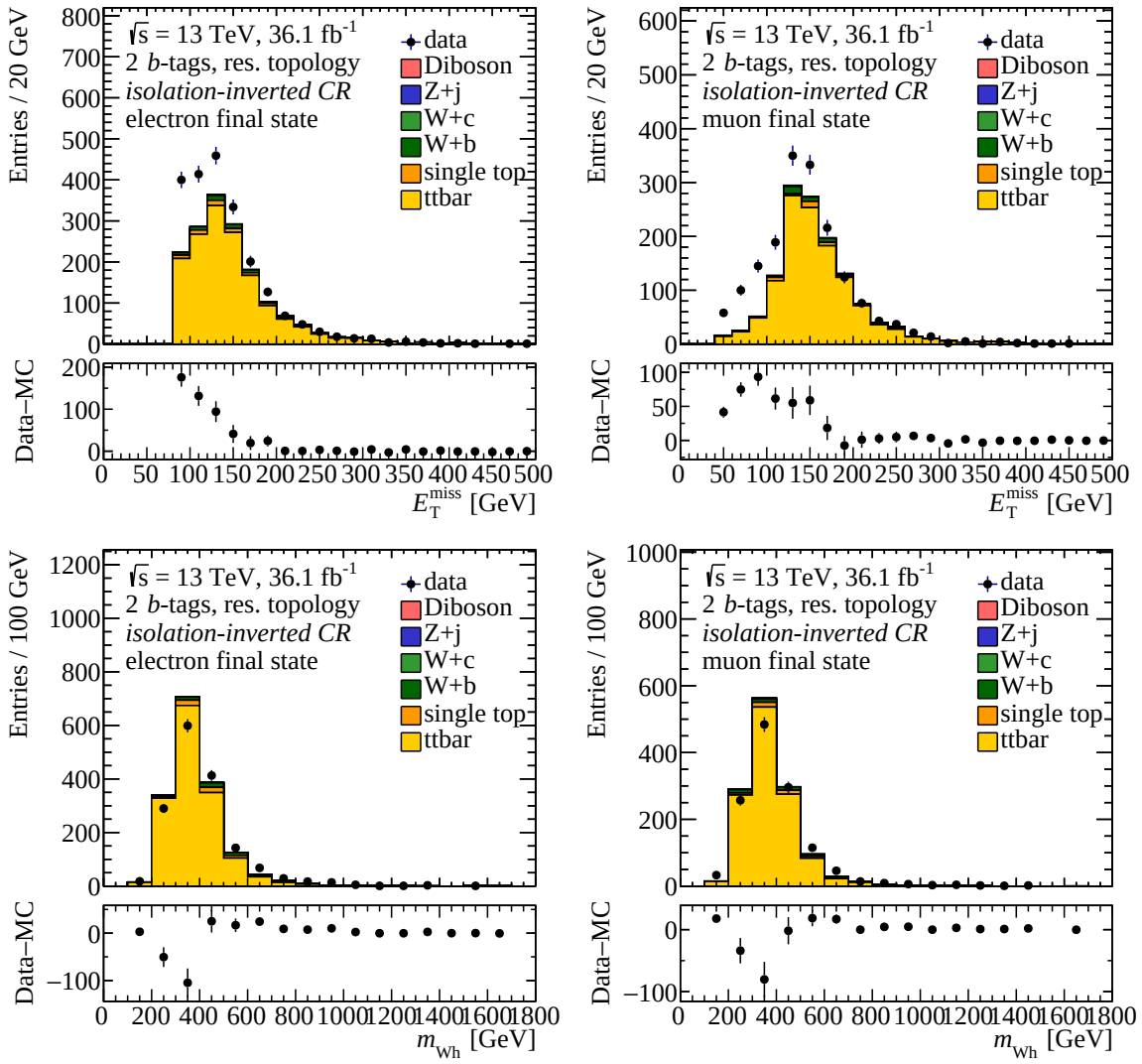

Figure 4.11: Observed distributions of the missing transverse energy ($E_{\mathrm{T}}^{\mathrm{miss}}$) and the mass of the Wh system (m_{Wh}) in the isolation-inverted control regions for events with 2 b-tag and the resolved topology for (left) the electron and (right) the muon final states. The expected MC non-multijet background contributions are shown as filled histograms. The difference between data and the MC prediction is shown in the lower panels. The total MC prediction is scaled to fit the data in the tail region with $E_{\mathrm{T}}^{\mathrm{miss}} > 200\,\mathrm{GeV}$, where the QCD contribution is expected to be negligible.

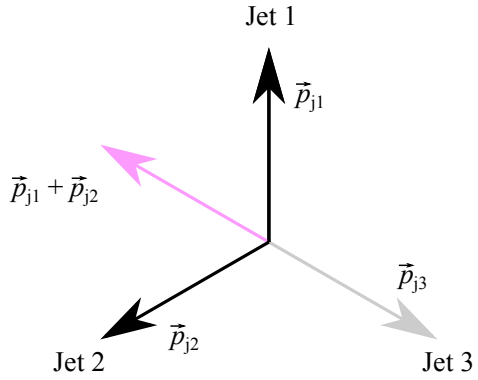

Figure 4.12: Illustration of $\vec{E}_{\mathrm{miss}}$ reconstruction due to mis-reconstructed jets. Jets 1, 2, and 3 are assumed to be produced together at rest. Jet 3 is missed by the event reconstruction. Therefore, the $E_{\mathrm{T}}^{\mathrm{miss}}$ is calculated only from Jets 1 and 2, leading to an $\vec{E}_{\mathrm{T}}^{\mathrm{miss}}$ vector with a value equal and the direction opposite to the transverse momentum vector of Jet 3.

Figures 4.10 and 4.11, where no multijet contribution is observed for sufficiently large $E_{\mathrm{T}}^{\mathrm{miss}}$ values. Based on this observation, the $E_{\mathrm{T}}^{\mathrm{miss}}$ distribution of the simulated total non-multijet backgrounds is fitted to the data above a certain $E_{\mathrm{T}}^{\mathrm{miss}}$ value in the isolation-inverted region to obtain a scaling of non-multijet backgrounds. Scale factors are determined for varying lower $E_{\mathrm{T}}^{\mathrm{miss}}$ thresholds between 150 and 300 GeV. The results of these fits are summarised in Table 4.4. For $E_{\mathrm{T}}^{\mathrm{miss}}$ thresholds above 200 GeV, the non-multijet normalisation factors are converging to a constant value, indicating that no multijet contribution is present at higher missing transverse momentum. The statistical precision decreases with higher $E_{\mathrm{T}}^{\mathrm{miss}}$ thresholds, since fewer events are available for the fit. As the best compromise between the non-multijet purity and the statistical precision, the normalisation scaling for the total simulated non-multijet background in Figures 4.10 and 4.11 is obtained from the fit in the $E_{\mathrm{T}}^{\mathrm{miss}}$ range above 200 GeV.

4.7.3 Normalisation of the multijet shape template histograms

With the procedure outlined above, multijet shape template histograms for the m_{Wh} distribution in the one and two b-tag regions are obtained. A similar procedure is also applied to obtain the shape of the multijet $E_{\mathrm{T}}^{\mathrm{miss}}$ distributions. The m_{Wh} template histograms can be employed to model the shapes of the corresponding distributions in the signal and sideband control regions with isolated leptons. However, as the normalisation of these distributions depends on the selection efficiency of multijet background in each region, this normalisation is expected to be very different between the regions with and without isolated leptons. One possibility to address this issue is to let the normalisation be a freely floating parameter in the final fit to data. The downside of this approach is that it is likely to be susceptible even to small statistical fluctuations in data, since the multijet background contribution is

Table 4.4: Normalisation factors for the total simulated non-multijet background contributions in the isolation-inverted CR, as obtained from the fit to the tails of the $E_{\mathrm{T}}^{\mathrm{miss}}$ distribution in that region. The fits are performed separately for different n-tag event categories. The first column indicates the lower $E_{\mathrm{T}}^{\mathrm{miss}}$ threshold defining the fit range. A dash "—" indicates a non-converging fit due to limited statistics. Only statistical uncertainties are considered in the fit. The resulting uncertainties on the normalisation factors are negligible, and therefore only the nominal values are reported.

	electron final state			muon final state		
Fit range	0 b-tag	1 b-tag	2 b-tag	0 b-tag	1 b-tag	2 b-tag
$E_{\mathrm{T}}^{\mathrm{miss}} > 160\,\mathrm{GeV}$	0.98	0.86	0.83	1.62	1.30	1.17
$E_{\mathrm{T}}^{\mathrm{miss}} > 180\,\mathrm{GeV}$	0.93	0.83	0.83	1.54	1.23	1.12
$E_{\mathrm{T}}^{\mathrm{miss}} > 190\,\mathrm{GeV}$	0.97	0.84	0.80	1.54	1.21	1.19
$E_{\mathrm{T}}^{\mathrm{miss}} > 200\,\mathrm{GeV}$	0.96	0.82	0.77	1.49	1.24	1.15
$E_{\mathrm{T}}^{\mathrm{miss}} > 220\,\mathrm{GeV}$	0.91	0.79	0.77	1.38	1.20	1.18
$E_{\mathrm{T}}^{\mathrm{miss}} > 250\,\mathrm{GeV}$	0.93	0.81	0.77	1.28	1.11	1.24
$E_{\mathrm{T}}^{\mathrm{miss}} > 300\,\mathrm{GeV}$	1.01	0.73	—	1.25	—	—

expected to be very small compared to these fluctuations. Moreover, if the original normalisation of the multijet shape template histogram is very different from the true value in the fitted data region, a typical fitting algorithm (*e.g.* gradient descent) can take a very long time to converge to the optimal value, thus making the fit unnecessarily ineffective and potentially unstable. A preferred approach is therefore to measure the normalisation of the multijet shape template histogram already before the fit to data in order to obtain a value which is as close as possible to the actual normalisation of the fitted region. This measured normalisation is then allowed to be varied in the fit only within a certain range of values, corresponding to the assigned uncertainties.

The normalisation of the multijet shape template histograms is therefore determined using a simplified fit of the expected $E_{\mathrm{T}}^{\mathrm{miss}}$ distribution to the data in the regions with isolated leptons. In this simplified fit, only two shape template histograms are defined, one for the multijet background and one for the total non-multijet background sum. The shape template for the multijet background is taken from the corresponding isolation-inverted region and the total non-multijet background is determined from simulated samples. Both template histograms are allowed to vary the shape within their bin-wise statistical uncertainties and the normalisation of each component is allowed to float freely. The ratio of the pre-fit and post-fit normalisations of the multijet template serve as the transfer factor from the isolation-inverted to the isolated region. Events with the resolved topology from the isolated signal region and the m_{jj} sidebands are combined, while separate fits are performed for each n-tag category and lepton flavour. The $E_{\mathrm{T}}^{\mathrm{miss}}$ observable is chosen for this fit as it provides good separation between the multijet and non-multijet background components (*cf.* Figure 4.13) and because of its negligible sensitivity to a potential W' signal. Since the shape of the $E_{\mathrm{T}}^{\mathrm{miss}}$ distribution of a hypothetical W' signal is very similar to that of the total non-multijet background sum, it becomes almost indistinguishable

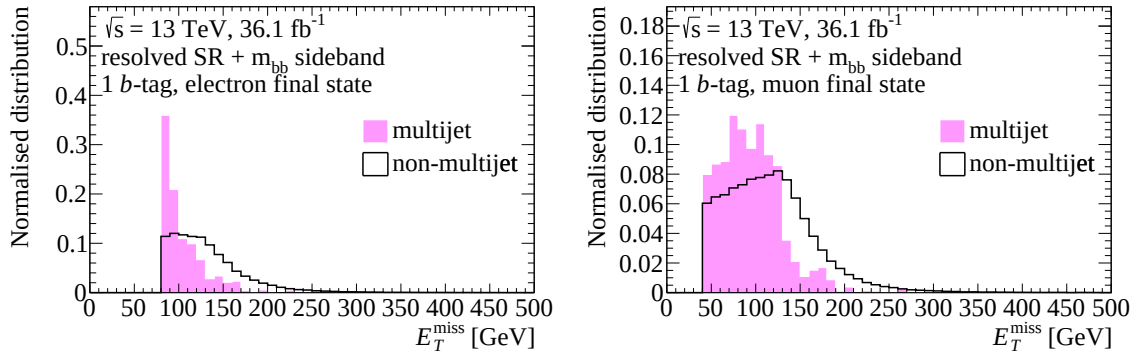

Figure 4.13: The $E_{\mathrm{T}}^{\mathrm{miss}}$ distributions of the multijet template histogram (filled, pink) and non-multijet background (black line) normalised to unity for the event selection corresponding to the signal region plus m_{jj} sideband control region with the resolved topology. Events in the electron (muon) final state are shown on the left (right).

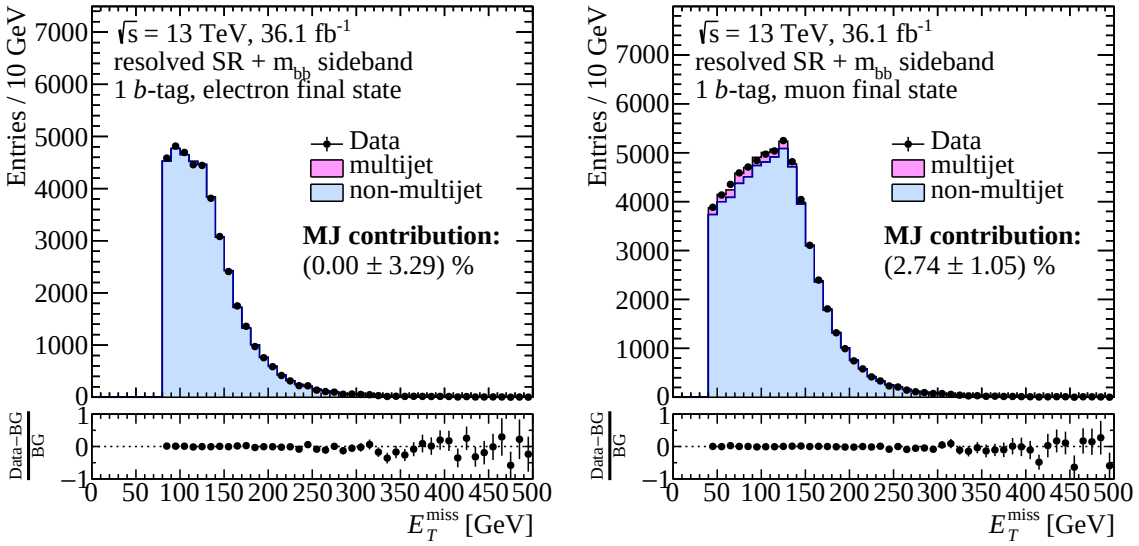

Figure 4.14: The $E_{\mathrm{T}}^{\mathrm{miss}}$ distribution in the combined signal and sideband regions with isolated leptons for events with 1 b-tag, the resolved topology, and the *(left)* electron, and *(right)* muon final state. The total non-mulitjet background and the multijet shape template histogram normalisations are floating freely in the fit to data. The determined fraction of multijet events in the total background (*MJ contribution*) for each final state is indicated in the figures.

from it in the fit and therefore (and because the signal is expected for the much smaller than the total background) has no relevant contribution to the normalisation of the multijet contribution. The fit results for the 1 b-tag data region are shown in Figure 4.14. With the normalisation of the multijet shape template obtained from the described fit, the multijet contribution ($N_{\mathrm{multijet}}/N_{\mathrm{total}}$) relative to the sum of all backgrounds can be calculated. In the electron channel, the relative multijet contribution is found to be negligible, while a relative contribution of (2.7 ± 1.0) % is measured in the muon channel.

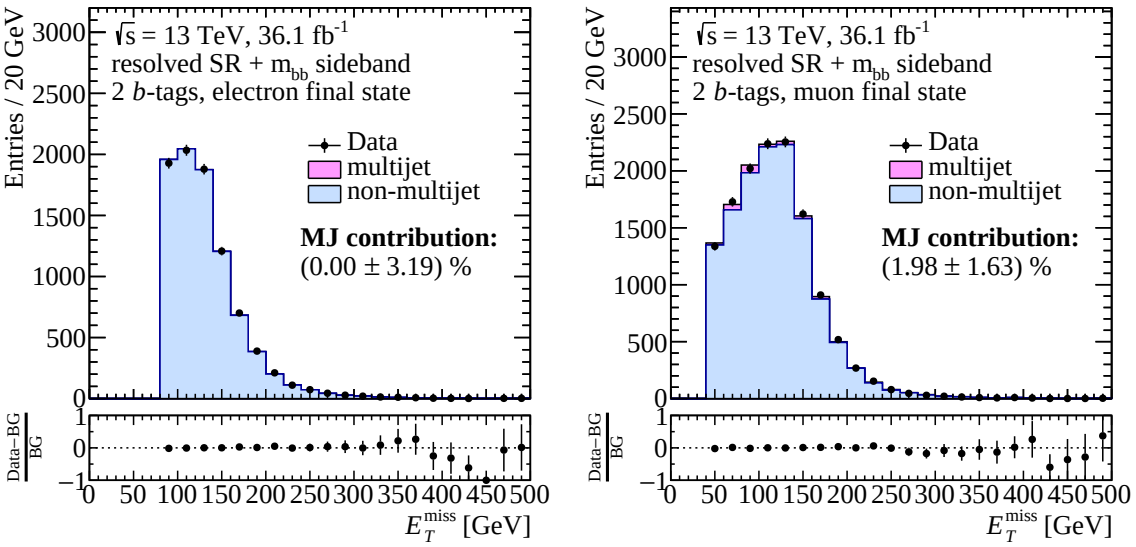

Figure 4.15: The $E_{\mathrm{T}}^{\mathrm{miss}}$ distribution in the combined signal and sideband regions with isolated leptons for events with 2 *b*-tags, the resolved topology, and the *(left)* electron, and *(right)* muon final state. The total non-mulitjet background and the multijet shape template histogram normalisations are floating freely in the fit to data. The determined fraction of multijet events in the total background (*MJ contribution*) for each final state is indicated in the figures.

The same fit procedure is repeated for the 2 *b*-tag region (shown in Figure 4.15), where the relative contribution in the electron channel is again found to be negligible and amounts to (2.0 ± 1.6) % in the muon channel. Applying the same fit procedure in the regions with merged event topologies (*cf.* Figures 4.16 and 4.17) results in unphysically large relative multijet contributions of 8 % or more, with an error 100 %. This can be attributed to large statistical uncertainties on the multijet shape template which is caused by the small event yield in the non-isolated region resulting in insufficient information for the fit to resolve the ambiguity between the multijet and non-multijet background shapes. As mentioned before, the multijet contribution to regions with the merged event topology is expected to be much smaller than to the corresponding regions with the resolved topology. Therefore, the multjiet contribution to events with the merged topology is not included in the final statistical analysis of the data. In Table 4.5 all relative multijet contributions as determined in the fit of the $E_{\mathrm{T}}^{\mathrm{miss}}$ distribution are summarised. The corresponding nominal transfer factors from the isolation-inverted to the isolated region are reported in Table 4.6.

In summary, multijet background shape templates are obtained in the isolation-inverted region for events with the resolved topology, separately for events with one and two *b*-tags. The shape templates are transformed to multijet background templates in the isolated signal region and m_{jj} sidebands by employing transfer factors (*cf.* Table 4.6) obtained from a fit of the $E_{\mathrm{T}}^{\mathrm{miss}}$ distribution to the observed data in the combined signal plus m_{bb} sideband regions with isolated leptons. Uncertainties on the shape

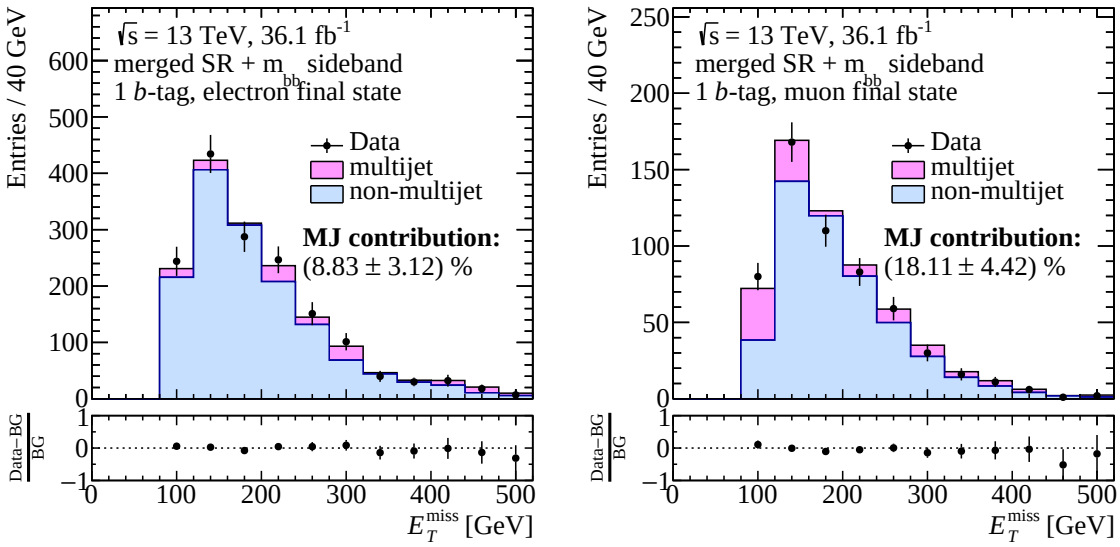

Figure 4.16: The $E_{\mathrm{T}}^{\mathrm{miss}}$ distribution in the combined signal and sideband regions with isolated leptons for events with 1 *b*-tag, the merged topology, and the *(left)* electron, and *(right)* muon final state. The total non-mulitjet background and the multijet shape template histogram normalisations are floating freely in the fit to data. The determined fraction of multijet events in the total background (*MJ contribution*) for each final state is indicated in the figures.

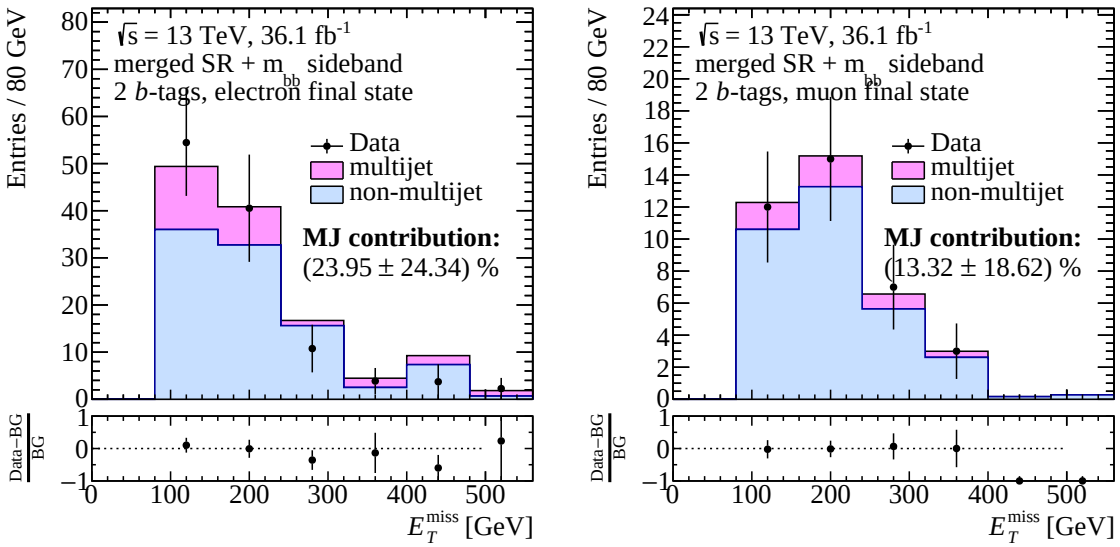

Figure 4.17: The $E_{\mathrm{T}}^{\mathrm{miss}}$ distribution in the combined signal and sideband regions with isolated leptons for events with 2 *b*-tags, the merged topology, and the *(left)* electron, and *(right)* muon final state. The total non-mulitjet background and the multijet shape template histogram normalisations are floating freely in the fit to data. The determined fraction of multijet events in the total background (*MJ contribution*) for each final state is indicated in the figures.

Table 4.5: Relative multijet background contribution to the total background in the different n-tag categories with the isolated leptons as obtained from the template fit.

	1 b-tag		2 b-tags	
	Electrons	Muons	Electrons	Muons
Resolved	(0.0 ± 1.7) %	(2.7 ± 1.0) %	(0.0 ± 3.2) %	(2.0 ± 1.6) %
Merged	(8.8 ± 3.1) %	(18.1 ± 4.4) %	(24.0 ± 24.3) %	(13.3 ± 18.6) %

Table 4.6: Nominal multijet background transfer factors

	1 b-tag		2 b-tags	
	Electrons	Muons	Electrons	Muons
Resolved	2.00×10^{-7}	9.22×10^{-1}	4.62×10^{-9}	2.03
Merged	7.48×10^{-1}	7.52×10^{-1}	5.16×10^{-1}	2.56×10^{-1}

and normalisation of the multijet background templates are obtained as described in the following.

4.7.4 Systematic uncertainties

Possible uncertainty sources for the multijet template method are assessed and translated into normalisation and shape uncertainties that are included in the final statistical analysis of the data. A conservative normalisation uncertainty is determined that combines several possible sources of uncertainty. Additionally, three different sources of shape variations are combined into a single shape uncertainty component by adding the individual sources in quadrature.

The transfer factor that is determined by the template fit does not consider systematic uncertainties from the non-multijet background components. Moreover, instead of separately addressing the physical processes comprising the non-multijet background, they are all combined into a single template, thus removing many degrees of freedom from the fit. These simplifications explain the residual post-fit disagreement between the predicted multijet and non-multijet background and the observed data (*cf.* Figures 4.14, 4.15, 4.16 and 4.17). The precision of the predicted multijet normalisation is further limited by the bin-wise statistical uncertainty of the shape template, which can be as high as 100 % in some bins. To account for all these factors, a very conservative multijet normalisation uncertainty of 50 % is used in the final fit to the data.

Sources of shape uncertainties are the trigger bias (*cf.* Section 4.7.1), shape variations in the total non-multijet background, and the residual ambiguity in the fit of the high $E_{\mathrm{T}}^{\mathrm{miss}}$ tails discussed in Section 4.7.3. Since the relative impact of the multijet background is small, the shape uncertainties are

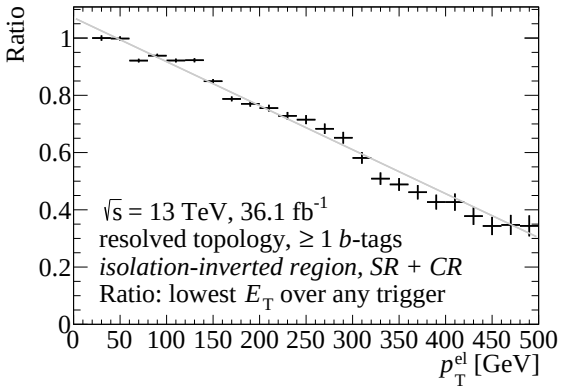

Figure 4.18: Ratio of the electron p_{T} distributions in the isolation-inverted region obtained by using only the lowest E_{T} threshold trigger and the logical "or" of all single electron triggers. Events with at least one b-tag and the resolved topology are included. The ratio is fitted with a linear function (shown by the grey line) which is used to parametrise the $p_{\mathrm{T}}^{\mathrm{el}}$-based reweighting uncertainty for the nominal m_{Vh} multijet distribution due to the trigger bias in the isolation-inverted region.

conservatively added in quadrature into a single shape uncertainty for the final statistical interpretation of the data.

The uncertainty due to the trigger bias applies only to events in the electron final state and is assessed by studying the distributions of the transverse momentum of the electron, $p_{\mathrm{T}}^{\mathrm{el}}$, in events selected by the lowest E_{T}-threshold trigger only and in event selected by a logical "or" of all un-prescaled single electron triggers (Section 4.3). The ratio of the two $p_{\mathrm{T}}^{\mathrm{el}}$ distributions obtained in this way is shown in Figure 4.18, and it is used as the uncertainty on the shape of the resulting multijet m_{Wh} template. It is propagated to the m_{Wh} multijet template distribution template by reweighting each event based on its respective $p_{\mathrm{T}}^{\mathrm{el}}$ value. The difference between the reweighted and the original multijet template histogram is taken as a corresponding shape uncertainty, which is in the order of 10 % for small m_{Wh} values and amounts to up to 50 % in the high-m_{Wh} tail.

For an estimate of the shape uncertainty due to variations in the relative composition of the non-multijet backgrounds, the template method procedure is repeated with scale factors applied separately to the dominant $t\bar{t}$ and W+jets background components. Analyses performed in similar regions of phase space [189, 190] determined scale factors between the pre-fit prediction and the fit to data as extreme as 0.9 and 1.6 for $t\bar{t}$ and W+jets, respectively. After employing the template method with these $t\bar{t}$ and W+jets normalisation factors, relative variations of the multijet shape of up to 30 % are obtained.

Finally, the impact of different fit configurations for the fit of the high $E_{\mathrm{T}}^{\mathrm{miss}}$ tail (*cf.* Section 4.7.3) is studied. Using different $E_{\mathrm{T}}^{\mathrm{miss}}$ thresholds for the fit results in slightly different final multijet shape template histograms. For a conservative estimate, the shape obtained by using the nominal $E_{\mathrm{T}}^{\mathrm{miss}}$ threshold (200 GeV) is compared to the shapes obtained from using the lowest and highest studied

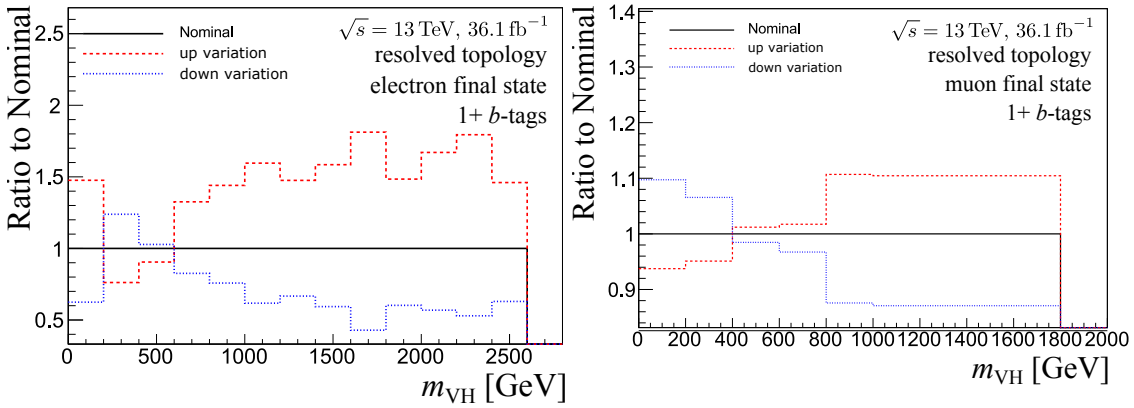

Figure 4.19: Shape variations of the multijet estimate in the *(left)* electron and *(right)* muon final state due to the uncertainties on the template method procedure. Events from the isolated signal regions with at least one b-tag are shown. All sources of shape uncertainties are added in quadrature, as explained in the text.

thresholds. The lowest threshold is 160 GeV and the highest threshold with a stable fit result is 300 GeV (250 GeV) for the electron (muon) channel. The lower threshold is used for the estimate of a downward variation, while the upper threshold is used for an upward variation of the shape template. Over the full m_{Wh} range, the corresponding uncertainty on the nominal multijet template shape is up to 40 %.

The quadratic sum of the shape uncertainties is shown in Figure 4.19, separately for events in the electron and muon final state.

4.8 Pre-fit distributions of the final m_{Wh} discriminant

Based on the selection criteria outlined in Section 4.4, the signal and control regions that are fitted simultaneously are defined, as summarised in Table 4.7. In order to validate the background modelling, the discriminant distributions in the $m_{jj/J}$ sideband CRs are studied before looking into the SR data, *i.e.*, prior to the final fit to the data. This allows for the correction of the potential mismodellings without introducing any bias from a potential signal in the SR. For completeness, Table 4.7 contains also the regions with the inverted charged lepton isolation requirements. These are, however, only used for the determination of the multijet template histograms as described in Section 4.7 and do not contribute to the final fit.

Figure 4.20 shows the expected and observed m_{Wh} distributions for the $m_{jj/J}$ sideband CRs and SRs, containing events with one and two b-tags for the resolved event topology. The corresponding distributions in the regions with merged topology are shown in Figure 4.21. The relative disagreement between data and the total MC prediction can be as large as about 12 %, as seen in the $m_{jj/J}$ sideband

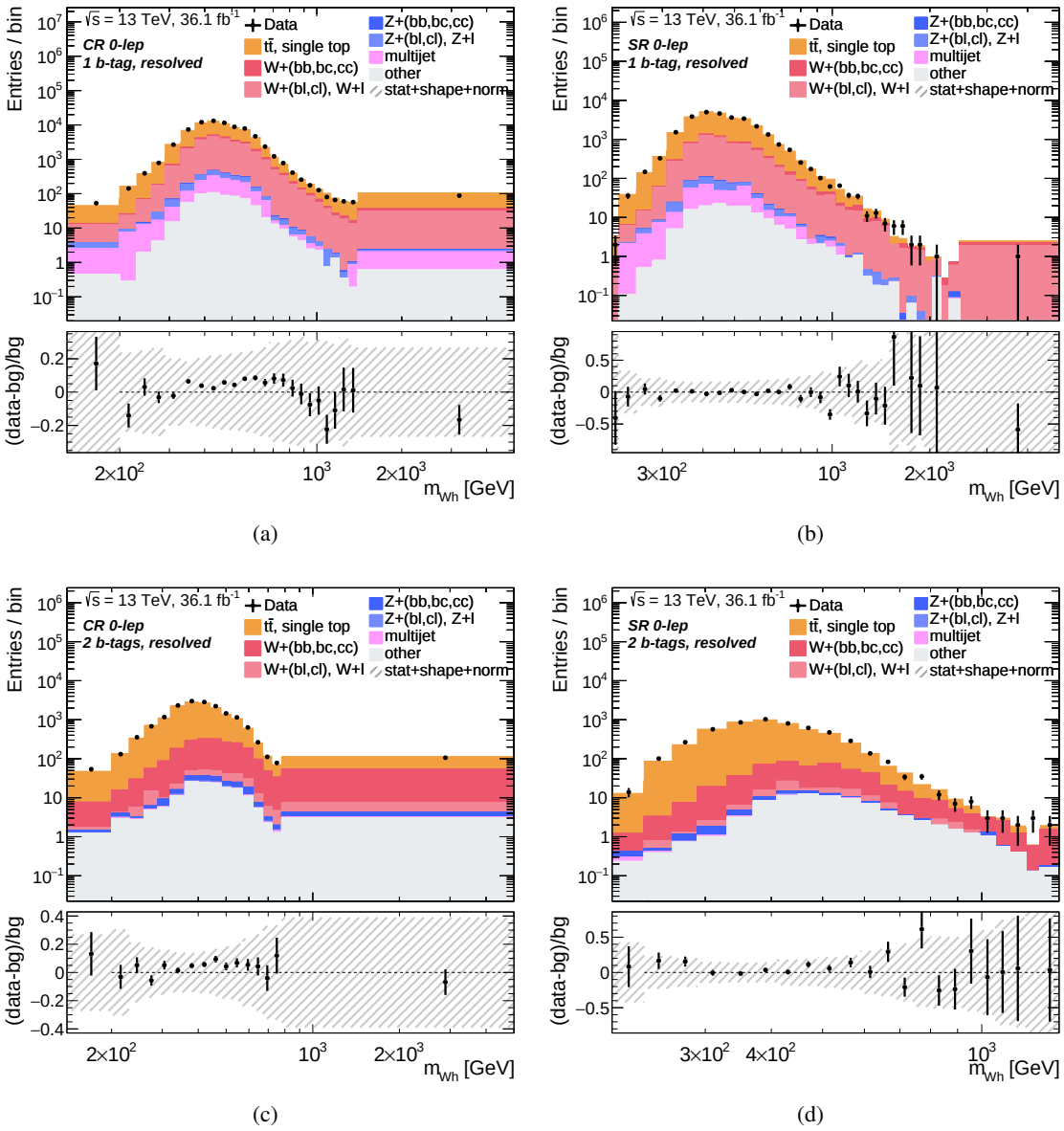

Figure 4.20: Observed and pre-fit expected m_{Wh} distributions in the data regions with resolved event topology: *(a)* 1 b-tag sideband CR and *(b)* SR, and the *(c)* 2 b-tag CR and *(d)* SR. The lower panels show the ratio between data after background subtraction (data − bg) and the total background prediction (bg). The uncertainties in the lower panels (hatched area) include the statistical and normalisation uncertainties, as well as the shape uncertainties of the different background components.

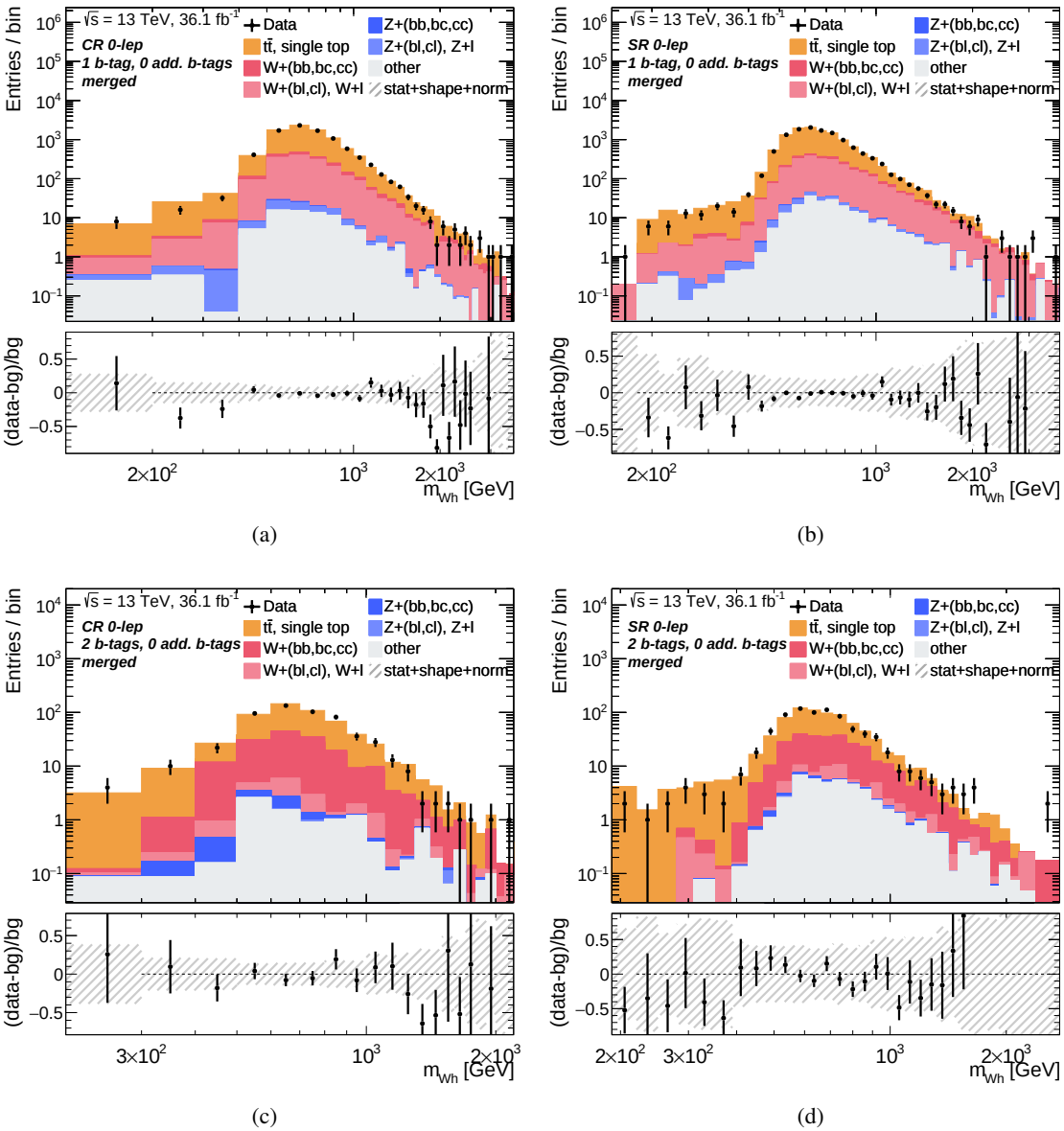

Figure 4.21: Observed and pre-fit expected m_{Wh} distributions in the data regions with merged event topology: *(a)* 1 *b*-tag sideband CR and *(b)* SR, and the *(c)* 2 *b*-tag CR and *(d)* SR. The lower panels show the ratio between data after background subtraction (data − bg) and the total background prediction (bg). The uncertainties in the lower panels (hatched area) include the statistical and normalisation uncertainties, as well as the shape uncertainties of the different background components.

Table 4.7: Summary of data regions employed in the presented analysis. The signal regions (SRs) are shown in the upper and the control regions (CRs) in the lower part of the table.

Event topology	$m_{jj/J}$ [GeV]	Number of b-tags	Lepton isolation	Comment	Used in the fit
resolved	[110, 140]	1	Nominal	$m_{jj/J}$ SR	✓
resolved	[110, 140]	2	Nominal	$m_{jj/J}$ SR	✓
merged	[75, 145]	1	Nominal	$m_{jj/J}$ SR	✓
merged	[75, 145]	2	Nominal	$m_{jj/J}$ SR	✓
resolved	[50, 110[$\vee$]140, 200]	1	Nominal	$m_{jj/J}$ CR	✓
resolved	[50, 110[$\vee$]140, 200]	2	Nominal	$m_{jj/J}$ CR	✓
resolved	[50, 200]	1	Inverted	multijet CR	—
resolved	[50, 200]	2	Inverted	multijet CR	—
merged	[50, 75[$\vee$]145, 200]	1	Nominal	$m_{jj/J}$ CR	—
merged	[50, 75[$\vee$]145, 200]	2	Nominal	$m_{jj/J}$ CR	—
merged	[50, 200]	1	Inverted	multijet CR	—
merged	[50, 200]	2	Inverted	multijet CR	—

CR with 1 b-tag and the resolved topology. However, the discrepancies between data and simulation are all covered by pre-fit uncertainties. Since there is no signal expected in the sideband CRs, the fit including these regions is expected to impose additional constraints on different background components, reducing the post-fit disagreement between data and MC, as well as constraining the post-fit uncertainties. The most dominant background process in all regions is the $t\bar{t}$ production. Its relative contribution to the total expected event yield ranges from 51 % in the resolved 1 b-tag sideband up to 71 % in the merged 1 b-tag SR. Other major background components are single top quark and W+jets events. A summary of the expected and observed event yields is given in Tables 4.8 and 4.9. No significant excess of observed above the expected number of events is observed.

4.9 Systematic uncertainties

The expected distributions of the final m_{Wh} fit discriminant in the fit regions (*cf.* Table 4.7) can be affected by both experimental and theory uncertainties. Possible sources of uncertainties are identified and their impact is quantified in dedicated studies, which are presented in this section.

4.9.1 Experimental uncertainties

Several sources of experimental uncertainties are considered. As a result of these uncertainties, both the shape and the normalisation of signal and background discriminant distributions are affected as

Table 4.8: Number of observed and expected (pre-fit) events in the signal regions of the analysis. The uncertainties are calculated as the quadratic sum of all pre-fit uncertainties and are therefore by construction conservative, as no correlations are taken into account. Possible differences between the sum of all contributions and the total background are due to the rounding of individual contributions.

	Resolved		Merged	
Process name	1 b-tag	2 b-tags	1 b-tag	2 b-tags
$t\bar{t}$	18 000 ± 1400	4000 ± 500	8900 ± 900	400 ± 150
single top	3760 ± 170	730 ± 70	1050 ± 100	108 ± 2
Z+l	35 ± 16	0.10 ± 0.14	12 ± 7	0.18 ± 0.30
Z+(bl,cl)	137 ± 21	0.9 ± 1.3	43 ± 8	0.38 ± 0.27
Z+(bb,bc,cc)	20 ± 5	13.4 ± 2.7	9.1 ± 1.9	3.8 ± 0.7
W+l	900 ± 350	9 ± 11	550 ± 320	0.13 ± 1.90
W+(bl,cl)	4400 ± 900	26 ± 12	1600 ± 400	20 ± 10
W+(bb,bc,cc)	590 ± 90	310 ± 40	320 ± 60	177 ± 25
Multijet	240 ± 60	1.9 ± 6.1	220 ± 60	45 ± 6
Other	148 ± 16	83 ± 7	—	—
Background sum	28 200 ± 1700	5200 ± 500	12 600 ± 1000	760 ± 150
Observed	28073	5348	12224	775

Table 4.9: Number of observed and expected (pre-fit) events in the $m_{jj/J}$ sideband regions of the analysis. The uncertainties are calculated as the quadratic sum of all pre-fit uncertainties and are therefore by construction conservative, as no correlations are taken into account. Possible differences between the sum of all contributions and the total background are due to the rounding of individual contributions.

	Resolved		Merged	
Process name	1 b-tag	2 b-tags	1 b-tag	2 b-tags
$t\bar{t}$	36 500 ± 2600	11 900 ± 1300	6400 ± 700	330 ± 130
single top	8600 ± 400	2170 ± 190	760 ± 70	65 ± 15
Z+l	160 ± 60	0.9 ± 0.9	13 ± 8	0.06 ± 0.10
Z+(bl,cl)	530 ± 80	6.1 ± 2.4	28 ± 6	0.24 ± 0.19
Z+(bb,bc,cc)	89 ± 15	60 ± 9	5.8 ± 1.4	3.3 ± 0.7
W+l	3200 ± 1200	15 ± 13	410 ± 230	1.6 ± 2.6
W+(bl,cl)	17 000 ± 4000	89 ± 34	1070 ± 300	7 ± 4
W+(bb,bc,cc)	2700 ± 400	1510 ± 160	270 ± 60	121 ± 20
Multijet	1070 ± 270	4 ± 13	—	—
Other	630 ± 120	161 ± 13	82 ± 19	10 ± 4
Background sum	71 000 ± 5000	15 900 ± 1300	9100 ± 800	540 ± 140
Observed	75153	16571	8787	546

quantified in dedicated studies, described below. For the analysis presented in this chapter, dominant sources of uncertainty are given by the calibration and resolution of the jet energy scale and mass, as well as uncertainties on the b-tagging identification and misidentification efficiencies. More details about the considered sources of uncertainties are listed in the following:

- The uncertainty on the integrated luminosity of the data set used in this analysis amounts to 3.2 % and has been determined using a methodology similar to the one detailed in Ref. [191]. This luminosity uncertainty is applied fully correlated to all signal and background samples.
- The performance of the trigger selection, as well as of the identification and reconstruction efficiency of electrons [133] and muons [192] was studied and the resulting recommended uncertainties are applied. These uncertainties were found to have negligible impact on the normalisation of the final m_{Wh} distributions and contribute only to the variation of the shape of these distributions.
- The pile-up profile used for the simulation of the signal and background events is re-weighted to match the actual pile-up distribution (*i.e.* the distribution of the number of pile-up interactions in each collision) measured in data. This method introduces residual biases related to the modelling of pile-up events.
- Small-radius jets are affected by uncertainties on the energy scale (JES) and resolution (JER), which are broken down into 21 uncorrelated components [193, 194], which affect both the normalisation and shape of the corresponding m_{Wh} distributions.
- Large-radius jets are subject to p_{T}-scale uncertainties that are determined from *in-situ* calibrations, similar to the ones outlined in Ref. [195]. In addition, the uncertainty on the jet energy resolution (JER) and mass resolution (JMR) are determined similarly to the small-radius jets [193, 194], and contribute with two uncorrelated uncertainty components.
- Corrections accounting for the difference between simulated and observed b-tagging efficiencies are determined separately for b-jets, c-jets, and light-flavour jets [196]. The corresponding uncertainties are parametrised as 16 uncorrelated components, which are defined separately for small-radius jets and track jets within a large-radius jet.
- The reconstruction of the missing transverse energy is affected by uncertainties on the $E_{\mathrm{T}}^{\mathrm{miss}}$ soft term and the reconstruction of the underlying event, pile-up, and the hard objects (jets, leptons, *etc.*), as detailed in Ref. [149].
- Uncertainties on the multijet background are evaluated as described in Section 4.7.4.

The impact of the experimental uncertainties on the final m_{Wh} discriminant for various processes is summarised in Table 4.10. Most sources of uncertainties alter the normalisation by not more

than 10 %, but a few edge cases with larger impact exist. These cases, however, are observed in low-statistics regions that have a negligible contribution to the overall result, since every given uncertainty contribution is correlated across all fit regions.

Table 4.10: Experimental systematic uncertainties for the various processes and their impact on the normalisation of the m_{Wh}distribution in the signal regions of the fit. An "S" indicates a shape variation. Uncertainties that are labelled only with "S" show a negligible impact on the overall normalisation of < 0.5 %.

Process	Uncertainty source	Value
Signal	Luminosity	3.2 %
	b-tagging	S
$t\bar{t}$	JES, JER, JMR	0–3 % + S
	b-tagging	0–30 % + S
	lepton ID & eff.	S
Single top quark	Luminosity	3.2 %
	JES, JER, JMR	0–2 % + S
	b-tagging	0–13 % + S
	lepton ID & eff.	S
Z+hf	Luminosity	3.2 %
	JES, JER, JMR	0–8 % + S
	b-tagging	0–11 % + S
	lepton ID & eff.	S
Z+(bl, cl)	Luminosity	3.2 %
	JES, JER, JMR	0–26 % + S
	b-tagging	0–11 % + S
	lepton ID & eff.	S
Z+l	Luminosity	3.2 %
	JES, JER, JMR	0–6 % + S
	b-tagging	0–55 % + S
	lepton ID & eff.	S
W+hf	JES, JER, JMR	S
	b-tagging	0–13 % + S
	lepton ID & eff.	S
W+(bl, cl)	JES, JER, JMR	S
	b-tagging	0–54 % + S
	lepton ID & eff.	S
W+l	Luminosity	3.2 %
	JES, JER, JMR	0–13 % + S
	b-tagging	0–79 % + S
	lepton ID & eff.	S
SM Vh	Luminosity	3.2 %
	JES, JER, JMR	0–3 % + S
	b-tagging	0–7 % + S
	lepton ID & eff.	S
Diboson	Luminosity	3.2 %
	JES, JER, JMR	0–10 % + S
	b-tagging	0–25 % + S
	lepton ID & eff.	S
Multijet	Luminosity	3.2 %
	Template method	50 % + S

4.9.2 Theory uncertainties

The impact of assumptions of a given theory model on the predicted cross sections, acceptance, and kinematic distributions of signal and background events is evaluated by comparison to alternative simulated samples or by applying dedicated event-based variation weights which are intrinsic to the nominal generator. Four major uncertainty sources are estimated.

1. The impact of uncertainties from a given PDF set is evaluated by means of event reweighting according to each of the 101 PDFs that are contained in the NNPDF set. Also, simulated samples with nominal and varied α_s values are compared for the nominal PDF set [176], as are the samples produced with the MMHT2014 NNLO and CT14 NNLO PDF sets [197] compared

to the sample with the nominal PDF set. For a conservative estimate, the final PDF uncertainty is given by the largest of these three impacts on the m_{Wh} discriminant.

2. The impact of QCD scale uncertainties is estimated by varying the renormalisation scale μ_R and factorisation scale μ_F by factors of two in both directions, resulting in six alternative (μ_R, μ_F) combinations additional to the nominal $(\mu_R, \mu_F) = (1.0, 1.0)$ choice. Per-event weights are calculated for every of the six alternative samples and applied to the nominal simulated sample. The largest of the six deviations from the nominal distribution is taken as the uncertainty. For hadronic processes, variations in the showering parameters are applied in order to account for increased or decreased initial- and final-state radiation (ISR/FSR).

3. The requirement of at most three signal jets limits the phase space in a way that leads to an underestimation of the QCD scale uncertainties that is accounted for by applying the Steward-Tackmann (ST) method [198]. Details on the implementation in the presented analysis are given in [199].

4. Matrix element (ME) and parton shower (PS) uncertainties are studied by comparison to alternative samples where the nominal ME or parton shower generator was replaced by an alternative one. ME uncertainties target the calculation of the ME itself as well as the matching of the ME to the parton shower. The PS uncertainties are also studied based on a comparison to a different set of tuned parameters for the same shower generator.

In addition to these uncertainty sources, relative uncertainties for the background selection efficiency between the $m_{jj/J}$ sideband and signal region are studied by comparing the obtained selection efficiency for the nominal and various alternative MC samples for a given process. The differences are translated into uncertainties on the ratio of the two corresponding event yields, which are applied only to the signal regions. Consequently, the normalisation of a given background processes in the $m_{jj/J}$ sideband region is decorrelated from the corresponding normalisation in the signal region to a degree that corresponds to the difference in the selection efficiencies in the $m_{jj/J}$ sideband and the signal region. Similarly, uncertainties on the ratios of background selection efficiency between events with resolved and merged topology are determined.

A summary of the impact of all studied theory uncertainties is shown in Table 4.11.

4.10 Fit model

The statistical interpretation of data, *i.e.* the test of the signal hypotheses, is performed via a fit of the expected signal and background m_{Wh} distributions to the observed data, simultaneously in all signal and sideband control regions summarised in Table 4.7.

Table 4.11: Theoretical uncertainties for the various processes and their impact on the normalisation of the m_{Wh}distribution in the signal regions of the fit. An "S" indicates a shape variation. Uncertainties on the relative normalisation are indicated by a forward slash "/" between the corresponding regions. "Normalisation" refers to the uncertainty on the total cross section × acceptance, and is determined entirely from data for processes indicated with "float".

Process	Uncertainty source	Value
$t\bar{t}$	normalisation	float
	$m_{jj/J}$ SR / $m_{jj/J}$ CR	5–7 %
	resolved / merged	26 %
	PS, ISR, FSR, ME, PDF	S
Single top quark	normalisation	19 %
	$m_{jj/J}$ SR / $m_{jj/J}$ CR	5–7 %
	resolved / merged	24 %
	PS, ISR, FSR, ME, PDF	S
Z+hf	normalisation	31 %
	resolved / merged	19 %
	$m_{jj/J}$ SR / $m_{jj/J}$ CR	6–8 %
Z+(bl, cl)	normalisation	20 %
	resolved / merged	28 %
	$m_{jj/J}$ SR / $m_{jj/J}$ CR	4–14 %
Z+l	normalisation	30 %
	resolved / merged	23 %
	$m_{jj/J}$ SR / $m_{jj/J}$ CR	5–6 %

Process	Uncertainty source	Value
W+hf	normalisation	float
	resolved / merged	28 %
	$m_{jj/J}$ SR / $m_{jj/J}$ CR	2–6 %
	ME/PS, matching, scale	S
W+(bl, cl)	normalisation	float
	resolved / merged	15 %
	$m_{jj/J}$ SR / $m_{jj/J}$ CR	1 %
	ME/PS, matching, scale	S
W+l	normalisation	3.2 %
	resolved / merged	16 %
	$m_{jj/J}$ SR / $m_{jj/J}$ CR	3–7 %
	ME/PS, matching, scale	S
$t\bar{t}H$, $t\bar{t}V$	normalisation	50 %
SM Vh	normalisation	50 %
Diboson	normalisation	11 %
Signal	normalisation	3–7 %

4.10.1 The binned maximum likelihood fit

A binned maximum likelihood fit is performed with the RooStats package [200], using the likelihood function $L(\mu, \vec{\theta})$, which is a function of the signal strength[5] μ and a set of nuisance parameters (NPs) $\vec{\theta}$, accounting for the systematic and statistical uncertainties (*cf.* Section 4.9). Depending on the type of uncertainty, a nuisance parameter can be unconstrained or log-normal constrained in the fit. The latter case assumes that the logarithm of the uncertainty is normally distributed, which is a good assumption for the shape and cross section uncertainties. Unconstrained nuisance parameters, on the other hand, are typically used for background normalisations, which should be determined entirely from control data. Unconstrained (constrained) uncertainties are denoted N_k (α_k) for a specific uncertainty source k of a given background. To constrain the nuisance parameters in the fit, auxiliary measurements are performed in dedicated calibration data and in the control sideband regions with negligible signal contribution. Correlations of uncertainty sources across various signal and sideband regions are accounted for by correlating the corresponding nuisance parameters. Statistical uncertainties are implemented as uncorrelated bin-by-bin uncertainties, γ_k. All nuisance parameters compose the

[5] The signal strength connects the actual to the simulated cross section via $\sigma_{\text{signal}} = \mu\sigma^{\text{MC}}_{\text{signal}}$.

components of the vector $\vec{\theta} = \{\vec{N}, \vec{\alpha}, \vec{\gamma}\}$. The explicit form of the likelihood function is a product of the Poissonian probabilities in each signal or sideband channel c and in bin b of the final distribution of m_{Wh}. This product is additionally multiplied by the constraints from the auxiliary measurements,

$$L(\mu, \vec{\theta}) = \prod_c \prod_b \text{Pois}\left(n_{cb}^{\text{obs}} \,|\, n_{cb}^{\text{sig}}(\mu, \vec{\theta}) + n_{cb}^{\text{bkg}}(\vec{\theta})\right) \prod_{p \in \mathbb{S}+\Gamma} f_p(w_p \,|\, \omega_p). \tag{4.3}$$

Here, n_{cb}^{obs} is the number of observed events, while n_{cb}^{sig} and n_{cb}^{bkg} are the expected signal and background events in the given channel and bin. The terms $f_p(w_p \,|\, \omega_p)$ are the constraints on the shape uncertainties $\mathcal{S} = \{\alpha_k\}$ and bin-by-bin uncertainties $\Gamma = \{\gamma_k\}$. Thereby, the w_p incorporates information about the nuisance parameter ω_p from an auxiliary measurement, such that a post-fit value $\omega_p \neq w_p$ introduces a penalty to the likelihood. The form of the penalty is defined by the functional form of f_p, which in the case of this analysis is a Gaussian function.

In order to avoid histogram bins with limited precision, a re-binning algorithm is applied, which merges neighbouring bins with low event yields. The re-binning procedure accounts for the expected signal m_{Wh} resolution and the expected number of events. Bins are required to have a width of at least two times the expected natural W' width at a given W' resonance mass. The bin width is then iteratively increased until the relative statistical uncertainty on the total expected background sum in the resized bin is smaller than 75 %.

For every shape uncertainty α_k and for every nominal signal or background distribution, there are two alternative m_{Wh} distributions, representing the up and down variations of the nominal m_{Wh} distribution for that process. The histograms are denoted $h_k^0(x)$, $h_k^+(x)$ and $h_k^-(x)$, for the nominal distribution, and its up and down variations, respectively. The up and down variations are determined by varying a given uncertainty source (*e.g.* the jet energy scale) by the corresponding $\pm 1\sigma$ uncertainty values. For a given α_k value, the modified nominal distribution is then given by

$$h_k(x) = \begin{cases} h_k^0(x) + \alpha_k \left(h_k^+(x) - h_k^0(x)\right), & \alpha_k \geq 0, \\ h_k^0(x) - \alpha_k \left(h_k^-(x) - h_k^0(x)\right), & \alpha_k < 0. \end{cases} \tag{4.4}$$

Unconstrained uncertainties N_k are allowed to float freely, *i.e.* they can assume any post-fit value without introducing extra penalty to the likelihood. However, as they strongly impact the post-fit number of expected background events, they nevertheless have a significant impact on the obtained likelihood. Without the large penalty, such floating nuisance parameters introduce a large amount of arbitrariness to the fit and should be avoided wherever possible. For most background contributions, reliable constraints on the cross section and modelling uncertainties exist. However, in some cases (such as events in extreme kinematic regions) the theoretical modelling is inadequate. For example, the

normalisation of the $t\bar{t}$, W+hf, and W+(bl, cl) background components are known to be mis-modelled in the phase space of this analysis, such that the corresponding uncertainty bounds are difficult to estimate. In such cases, the normalisation is left freely floating with the same nuisance parameters describing the normalisation in the SR and the sideband regions. In this way, the background components in the SR are constrained by the additional information from the sideband CRs.

To account for the slightly different phase space regions that are covered by the signal and control regions, additional log-normal constrained nuisance parameters are introduced for the normalisations of the $t\bar{t}$, W+hf, and W+(bl, cl) background components. These nuisance parameters are then only added to the signal regions, effectively decorrelating the normalisation in the signal and control regions. The larger the prior of the constraint, the larger the reduction of the correlation. Typical values for the prior are $\lesssim 10\,\%$.

4.10.2 Test statistic

The test statistic employed to test a given signal hypothesis is based on a profile likelihood ratio $\lambda(\mu)$ [201],

$$\lambda(\mu) = \frac{L\left(\mu, \hat{\hat{\theta}}\right)}{L\left(\hat{\mu}, \hat{\hat{\theta}}\right)}. \tag{4.5}$$

The numerator of the profile likelihood ratio corresponds to the conditional maximum likelihood fit, where $\hat{\hat{\theta}}$ is the set of nuisance parameter values that maximise the likelihood L for a given μ. The denominator is the unconditional maximum likelihood, where both $\hat{\mu}$ and $\hat{\hat{\theta}}$ are the free parameters of the fit, *i.e.* the maximum likelihood estimators of the likelihood L.

Further, the test statistic q_0 for the discovery of a positive signal is defined as

$$q_0 = \begin{cases} -2\ln\lambda(0), & \hat{\mu} \geq 0, \\ 0 & \hat{\mu} < 0, \end{cases} \tag{4.6}$$

where $\lambda(0)$ is the profile likelihood ratio as given in Equation (4.5) evaluated at $\mu = 0$. Based on the test statistic, the level of disagreement between the data and the $\mu = 0$ hypothesis can be calculated by the p_0 value,

$$p_0 = \int_{q_{0,\,\mathrm{obs}}}^{\infty} f(q_0|0)\,\mathrm{d}q_0. \tag{4.7}$$

It can be shown [201] that, under the Wald's approximation [202], the probability density function (p.d.f.) $f(q_0|0)$ reduces to a combination of the delta function and a chi-square distribution,

$$f(q_0|0) = \frac{1}{2}\delta(q_0) + \frac{1}{2}\frac{1}{\sqrt{2\pi}}\frac{1}{\sqrt{q_0}}e^{-q_0/2}, \tag{4.8}$$

whose cumulative distribution is given by the cumulative distribution of the standard Gaussian with zero mean and unit variance, $\Phi(x)$, as

$$F(q_0|0) = \Phi(\sqrt{q_0}) = \int_{-\infty}^{\sqrt{q_0}} \frac{1}{\sqrt{2\pi}} e^{-q^2}\,\mathrm{d}q. \tag{4.9}$$

Therefore, the p_0-value can be quickly obtained as $p_0 = 1 - F(q_0|0)$ and the discovery significance Z_0 is given by the formula

$$Z_0 = \Phi^{-1}(1 - p_0) = \sqrt{q_0}. \tag{4.10}$$

For the case in which the background only hypothesis can not be excluded and upper limits on the signal strength parameter μ need to be determined, the test statistic q_μ is defined

$$q_\mu = \begin{cases} -2\ln\lambda(\mu), & \hat{\mu} \leq \mu, \\ 0 & \hat{\mu} > \mu. \end{cases} \tag{4.11}$$

Similar to the background-only case, the level of agreement between the data and the hypothesised μ value is given by an integral that is (again using Wald's approximation) related to the cumulative distribution of the standard Gaussian

$$p_\mu = \int_{q_\mu}^{\infty} f(q_{\mu'}|\mu)\mathrm{d}q_{\mu'} = 1 - F(q_\mu|\mu) = 1 - \Phi(\sqrt{q_\mu}). \tag{4.12}$$

The value of μ is said to be excluded at a certain confidence level (C.L.) $(1-\alpha)$ if $p_\mu < (1-\alpha)$. That is, the upper limit of the signal strength that is excluded at the C.L. $(1-\alpha)$ is the largest μ for which $p_\mu = (1-\alpha)$. It can be calculated [201] as

$$\mu_{\mathrm{up}} = \hat{\mu} + \sigma\Phi^{-1}(1-\alpha), \tag{4.13}$$

where σ corresponds to the uncertainty on the signal strength and generally depends on the hypothesised μ. The value of σ for a given μ is determined from Asimov data [201].

Finally, the uncertainty band at the $(1-\alpha)$ C.L. corresponding to $\pm N$ standard variations at a given value of μ' can be calculated [201] using

$$\text{band}_{N\sigma} = \mu' + \sigma(\Phi^{-1}(1-\alpha) \pm N). \tag{4.14}$$

4.11 Results

In order to interpret the data by fully accounting for all uncertainties and their correlations across all signal and control regions, a fit of the expected to the observed m_{Wh} distributions is performed by minimising the negative log likelihood ratio $-2\ln\lambda(\mu)$, with $\lambda(\mu)$ being defined by Equation (4.5). The post-fit agreement between data and the expectation is studied in terms of pulls on the post-fit nuisance parameters (NPs).

The nuisance parameter pull is defined as the fitted nuisance parameter value $\hat{\theta}$ minus the pre-fit expectation θ_0, divided by the corresponding post-fit uncertainty $\sigma(\hat{\theta})$,

$$\text{pull} = \frac{\hat{\theta} - \theta_0}{\sigma(\hat{\theta})}. \tag{4.15}$$

For Gaussian uncertainties, the pull is expected to follow a Gaussian distribution, centred around zero and with a unit standard deviation [203]. A pull value different from zero indicates that the nuisance parameter is biased by the fit, meaning that the corresponding degree of freedom is required for an adequate description of the observed data.

Having only a single experiment, *i.e.* only one data set to fit, the post-fit standard deviation of a given nuisance parameter needs to be estimated from the covariance matrix of all fit nuisance parameters, which in turn is estimated from the inverse of the Hessian matrix [201]

$$\mathbf{cov}(i,j) = \left[-\frac{\partial^2 \ln\left(L\left(\hat{\mu}, \hat{\vec{\theta}}\right)\right)}{\partial\theta_i \partial\theta_j} \right]^{-1}. \tag{4.16}$$

The post-fit standard deviation for the NPs is estimated by the diagonal elements of this matrix, $\sigma(\theta_k) = \mathbf{cov}(k,k)$.

In case of post-fit standard deviations smaller than unity, the fit is able to impose additional constraints on the corresponding nuisance parameter. In general, this scenario is related to either one of two possible scenarios

- The pre-fit uncertainty was estimated too conservatively compared to the statistical fluctuations;

- The nuisance parameter describes a data-to-simulation disagreement that is also addressed by another nuisance parameter. The resulting degeneracy enables the fit to address the disagreement with a smaller overall penalty on the likelihood which is also reflected by stronger post-fit bounds on the nuisance parameter standard variation.

Post-fit standard deviations larger than unity generally indicate a problem with the implementation of this nuisance parameter in the fit model. Such a large value means that altering this nuisance parameter in a window of more than one (pre-fit) standard deviation shows no clear relationship with the obtained likelihood and further investigations of the nuisance parameter are required. The performance and the reliability of the fit is therefore verified by looking at the resulting nuisance parameter pulls.

All nuisance parameter pulls resulting from the fit are shown in Figures 4.22, 4.23 and 4.24. All post-fit uncertainties are ≤ 1. The NPs with the greatest pull deviations from zero are the ones encoding the uncertainty on the efficiency of tagging c-jets and light jets as b-jets in the resolved event topologies. The origin of these deviations can be found in the flavour tagging methodology [204]. The tagging efficiencies in the simulation are corrected to better match the data using data-to-simulation scale factors which are measured in two calibration data sets, comprising mainly the $t\bar{t}$ and W+c process, respectively. Figure 4.25 shows the corresponding scale factors for the 70 % b-tagging working point using the two measurement approaches. As can be seen, the uncertainty from the W+c measurement method is large compared to the $t\bar{t}$-based measurement. The flavour tagging nuisance parameter representing the b-tagging uncertainty has a pre-fit uncertainty corresponding to the difference of the central values from the two measurements added in quadrature. Considering that a negative post-fit pull corresponds to an increase in the applied scale factors, the obtained negative pull indicates that the fit prefers larger calibration factors, which are obtained from the $t\bar{t}$ method. The fit can converge to these values due to the large uncertainty of the W+c measurement method.

Larger pull values are also observed for a set of NPs describing uncertainties on the $t\bar{t}$ background modelling (*cf.* Figure 4.23). Since this is the dominant background component, a well-modelled $t\bar{t}$ prediction is crucial and the pulls should be carefully examined. There is a twofold explanation why $t\bar{t}$ NPs can be pulled (*i.e.* modifies the pre-fit $t\bar{t}$ prediction) and/or constrained (*i.e.* fit imposes additional constraints on the uncertainty component). First, the fit to the sideband CRs has a relatively high statistical power to constrain the theoretical uncertainties, which are determined by a conservative comparison of different generator configurations (*cf.* Section 4.9.2). Second, a small variation of these NPs can be expected to have a large impact on the likelihood. Any pre-fit mismodelling can hence be expected to be corrected for, as long as there are suitable NPs addressing the mismodellings. In particular, the NPs describing the matrix element, initial- and final-state radiation, and NNLO re-weighting uncertainties are pulled with pull values of -1.05, -0.81, and 0.89, respectively. The post-fit standard deviation of the matrix element and NNLO re-weighting uncertainties are also

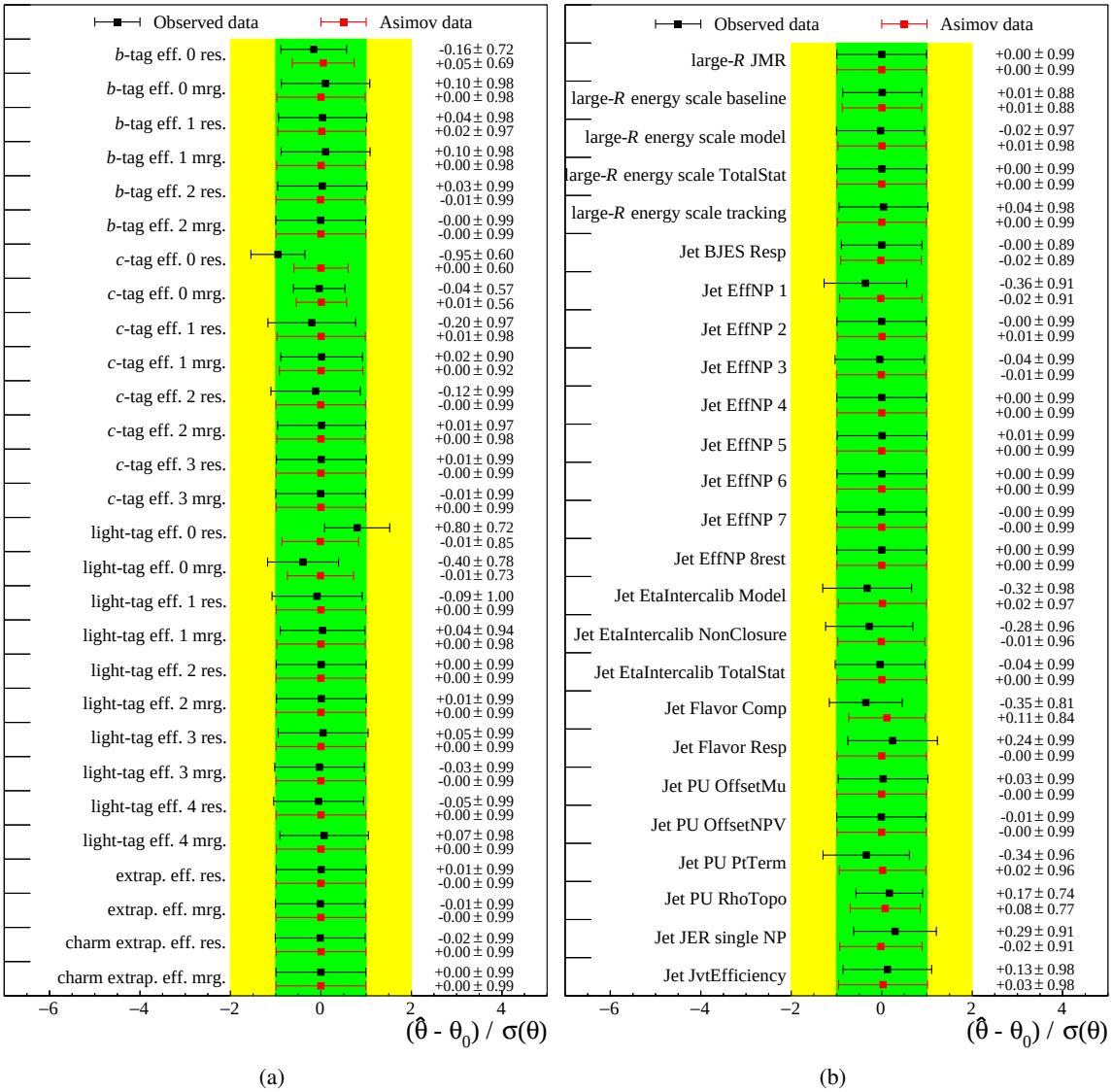

Figure 4.22: The pulls of various NPs after a fit to the expected (red) and observed data (black).The panels show *(a)* flavour tagging uncertainties and *(b)* jet reconstruction uncertainties. The meaning of each nuisance parameter is explained in more detail in Appendix B.3.

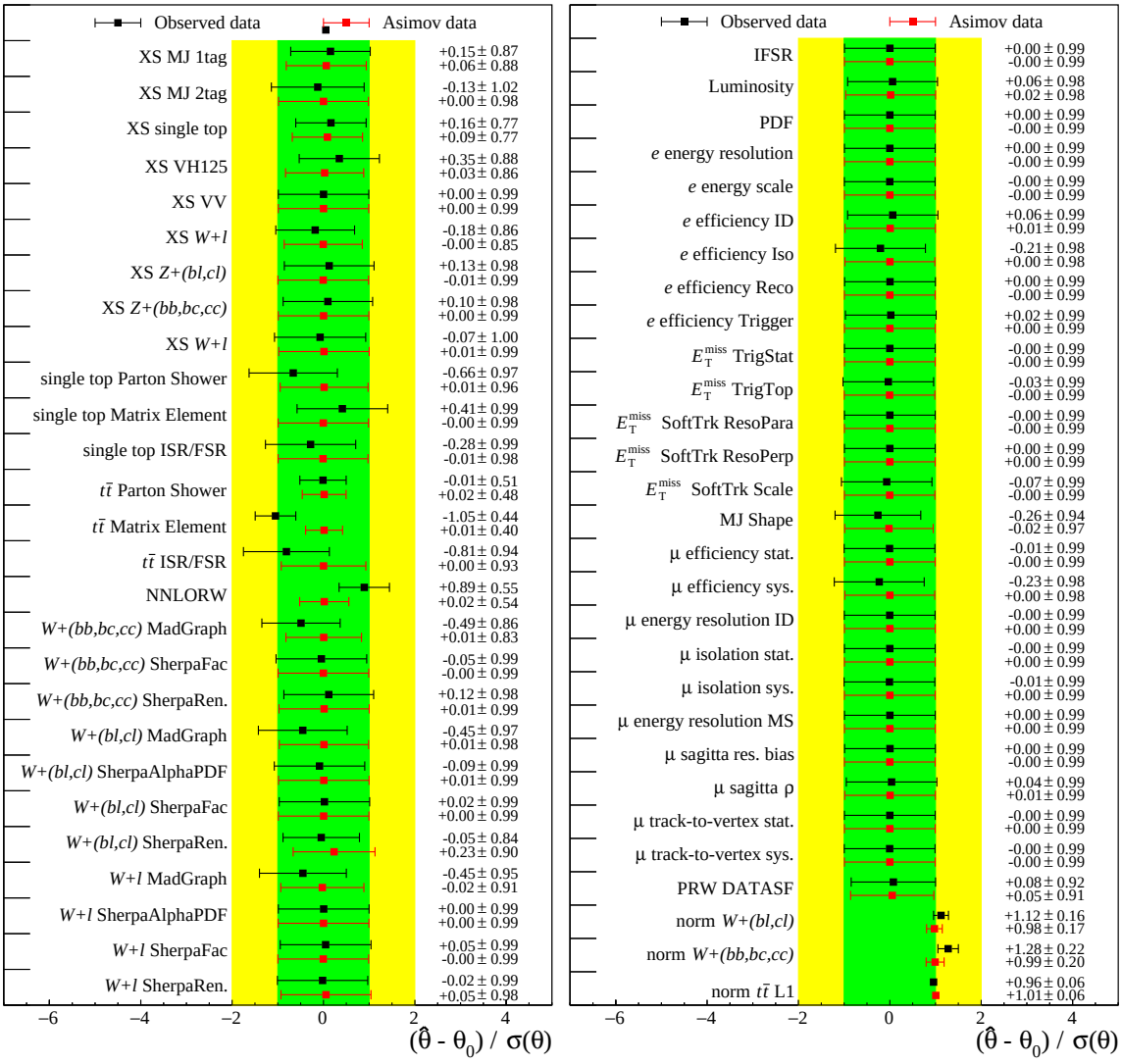

(a) (b)

Figure 4.23: The pulls of various NPs after a fit to the expected (red) and observed data (black). The panels show *(a)* other experimental and *(b)* cross section and theoretical uncertainties. The meaning of each nuisance parameter is explained in more detail in Appendix B.3.

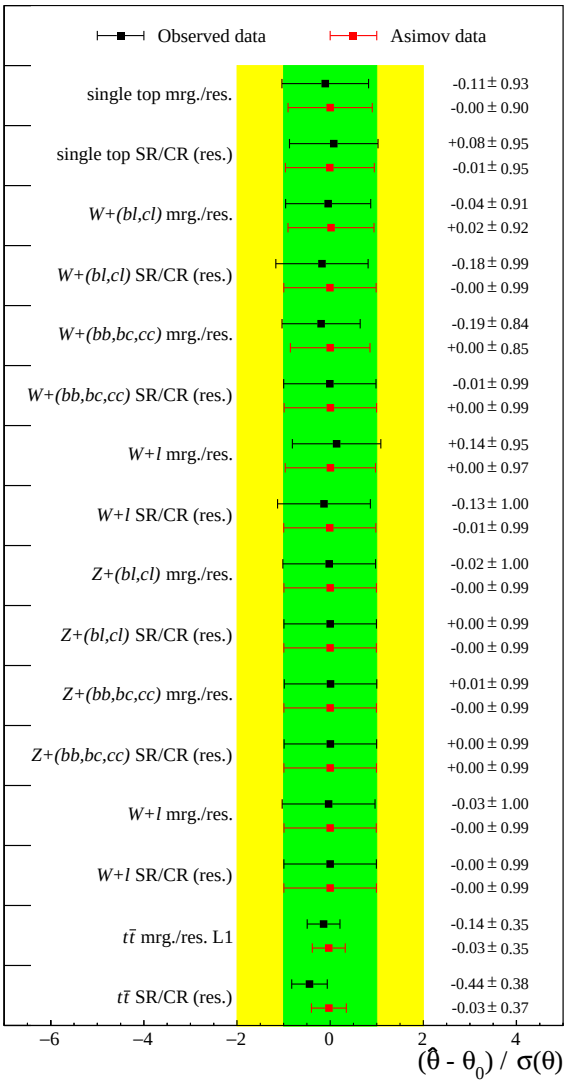

Figure 4.24: The pulls of various decorrelation NPs after a fit to the expected (red) and observed data (black). The meaning of each nuisance parameter is explained in more detail in Appendix B.3.

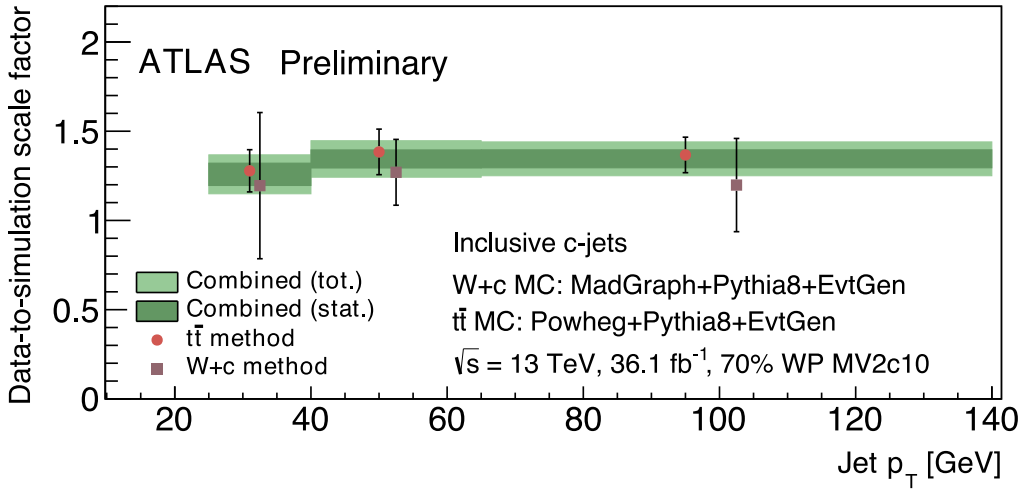

Figure 4.25: Data-to-simulation b-tagging scale factors for the inclusive c-jet sample, obtained by combining the results from the W+c and $t\bar{t}$ calibration samples for the 70 % b-tagging working point. The dark green band represents the statistical-only uncertainty of the combined data-to-simulation scale factor while the light green band shows the total (statistical+systematic) uncertainty. The red points (brown squares) indicate the results from the $t\bar{t}$ (W+c) measurement alone. Modified from Ref. [204].

constrained to values of ±0.44 and ±0.55, indicating overly conservative pre-fit estimates of these uncertainties. Therefore, a pull on these NPs is not considered biasing the fit results.

The impact of each nuisance parameter on the post-fit signal strength value, μ, is studied by comparing the fit result from an unconstrained fit to the result obtained by fixing the corresponding nuisance parameter to the $\pm 1\sigma$ values of the post-fit uncertainty. The largest impact is found for NPs related to the modelling of the $t\bar{t}$ background, the normalisation of the W+hf background component, and the uncertainty on the efficiency of tagging c-jets as b-jets in the resolved event topologies. For fits with signal hypotheses in the high-mass region ($m_{Wh} > 1.5$ TeV), the $m_{jj/J}$ CR / SR ratio uncertainties and W+l theory uncertainties become dominant as well.

The m_{Wh} distributions after the fit of the background-only hypothesis to the data can be seen in Figure 4.26. The lower panels in Figure 4.26 show the data-to-background ratio. Data are in good agreement with the background prediction, showing only sporadic statistical fluctuations in regions with few observed events. The agreement is supported by the values of the reduced[6] χ^2 between 0.4 and 0.9 in the different fit regions. The corresponding post-fit event yields are reported in Table 4.12.

[6] Reduced χ^2 is Pearson's χ^2 (see *e.g.* [203]) divided by the number of degrees of freedom (χ^2/ndf). Values $\gg 1$ indicate a poor agreement between data and the fitted expectation, values close to 1 a fit that describes the data well, and values $\ll 1$ indicate a fit with too many degrees of freedom, *i.e.* over-estimated uncertainties.

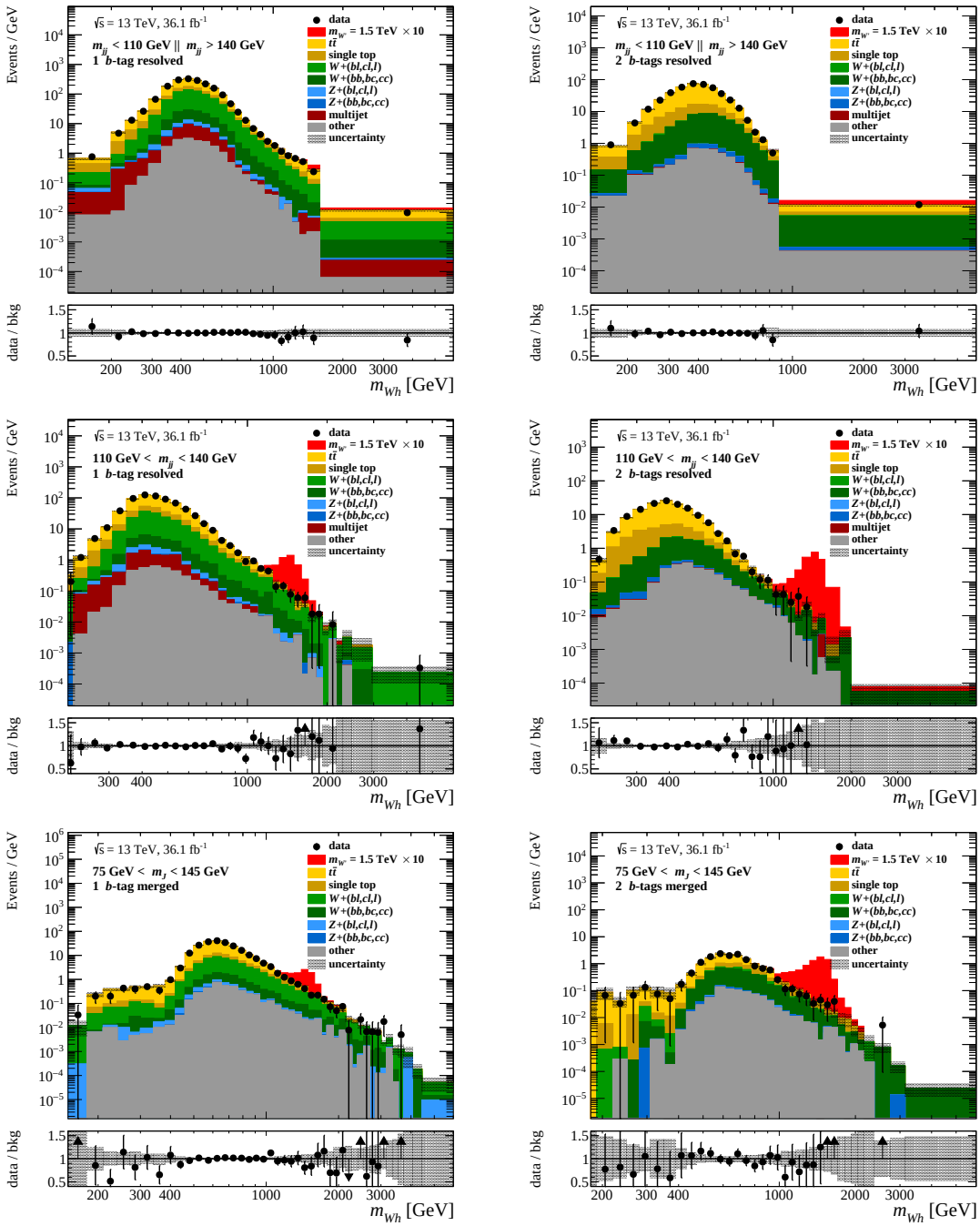

Figure 4.26: Observed and expected post-fit m_{Wh} distributions in the different control and signal regions. The number of events in each bin is divided by the bin width in GeV. The background prediction is shown with its uncertainties after an unconditional background-only binned maximum likelihood fit. The nominal signal prediction of a 1.5 TeV W' signal at a signal strength of $\mu = 10$ is added on top of the total background for reference. The lower panels show the ratio of data over background (black markers) together with the post-fit uncertainty on the background (shaded area).

Table 4.12: The observed and post-fit expected event yields in all four signal regions in the m_{Wh} mass range from 0 to 6 TeV. The reported numbers correspond to the background-only fit. The quoted uncertainties are the statistical and systematic post-fit uncertainties combined in quadrature. The uncertainty of the total background is smaller than the quadratic sum of the individual components due to correlations of the normalisation nuisance parameters.

	Resolved		Merged	
Process name	1 b-tag	2 b-tags	1 b-tag	2 b-tags
$t\bar{t}$	16 530 ± 200	3940 ± 40	8120 ± 80	382 ± 13
Single top quark	3820 ± 120	802 ± 28	1060 ± 50	107 ± 5
Diboson	111 ± 4	12.0 ± 0.5	219 ± 8	34.7 ± 1.4
Z+l	32 ± 4	0.083 ± 0.028	13.6 ± 1.6	0.19 ± 0.11
Z+(bl, cl)	152 ± 10	0.45 ± 0.27	43 ± 5	0.49 ± 0.11
Z+hf	21.9 ± 1.9	14.4 ± 1.2	9.41 ± 0.96	3.9 ± 0.4
W+l	570 ± 60	2.6 ± 2.0	640 ± 50	0.17 ± 0.07
W+(bl, cl)	5700 ± 130	22.6 ± 2.4	1720 ± 70	27.6 ± 2.6
W+hf	840 ± 28	450 ± 14	390 ± 21	210 ± 12
SM Vh	60 ± 5	85 ± 7	14.0 ± 1.0	11.1 ± 0.9
Multijet	283 ± 22	1.73 ± 0.32	—	—
Total	28 110 ± 120	5330 ± 50	12 220 ± 70	777 ± 17
Data	28073	5348	12224	775

Since no significant excess of events is observed in any region of the m_{Wh} mass distribution, exclusion limits for the HVT W' production cross section times the decay branching ratio are evaluated for the different signal masses using the methods described in Section 4.10. The result is shown in Figure 4.27. All cross section values below the observed upper limit (black line) are excluded at the 95 % C.L. The figure also shows the corresponding cross sections predicted by the HVT models A and B. Thus, the HVT W' resonances with masses up to 2.7 TeV and 2.9 TeV can be excluded at the 95 % C.L. for HVT Models A and B, respectively.

In an effort to constrain as much of the HVT parameter space as possible, the results of the $\ell^{\pm}\overset{(-)}{\nu}_{\ell}b\bar{b}$ final state are combined with the independent analyses of the $\nu\bar{\nu}b\bar{b}$ and $\ell^{\pm}\ell^{\mp}b\bar{b}$ final states [14]. Here, the scenario in which the W' and Z' masses are degenerate is assumed. As a result, an upper limit for the scaling factor (relative to the HVT Model A prediction) of the production cross-section for a V' boson ($V' = W', Z'$) times its branching fraction to Wh/Zh is determined. The result is shown in Figure 4.28. In this case, resonances with masses of up to 2.80 TeV (2.93 TeV) can be excluded at the 95 % C.L. for the HVT Model A (Model B).

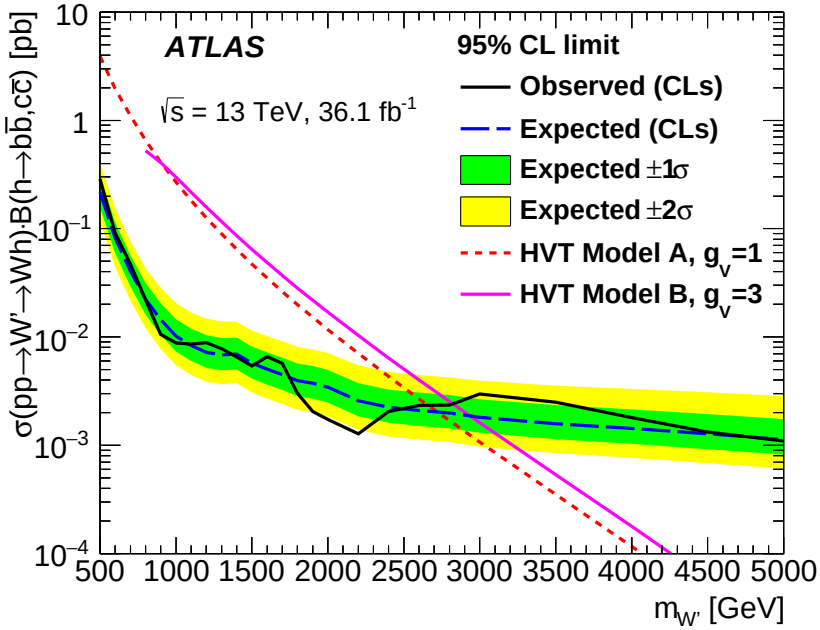

Figure 4.27: Upper limits as a function of the resonance mass at the 95 % C.L. for the production of a W' resonance and its subsequent decay into $Wh \to \ell\nu bb$. The production cross sections predicted by the HVT Model A and B are shown for comparison. Reproduced from [14].

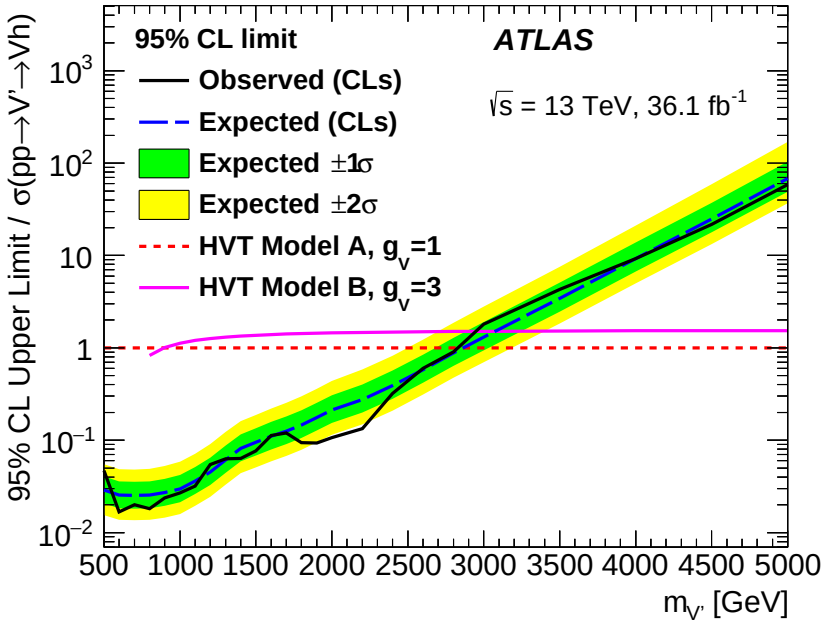

Figure 4.28: Upper limit for the scaling factor relative to HVT Model A of the production cross-section for a V' boson ($V' = W', Z'$) times its branching fraction to Wh/Zh [14].

CHAPTER FIVE

SEARCH FOR HEAVY NEUTRAL DIBOSON RESONANCES IN THE $\nu\bar{\nu}b\bar{b}$ FINAL STATE

A search for a new heavy neutral Zh resonance is conducted in the $\nu\bar{\nu}b\bar{b}$ final state. The search is performed with 139 fb^{-1} of pp collision data at $\sqrt{s}$ = 13 TeV recorded during the LHC Run 2 between 2015 and 2018. The results are interpreted within the two models introduced in Chapter 2: the Heavy Vector Triplet (HVT) model, which predicts the existence of a heavy Z' boson decaying into Zh, as well as the Two-Higgs Doublet Model (2HDM) in which the predicted heavy CP-odd A boson decays into Zh. For the latter, only the pure gluon-fusion production is considered in the standalone analysis of the $\nu\bar{\nu}b\bar{b}$ final state. Due to a more complicated description of the background processes, the b-associated production of the A boson is only studied in combination with the $\ell^{\pm}\ell^{\mp}b\bar{b}$ final state, as presented in Chapter 6.

All steps of the analysis are developed "blindly", *i.e.* based only on simulation and without looking into the signal region data before the final fit. In particular, data-driven background studies are performed using only control data to avoid biases from a potential signal contribution.

In Section 5.1, the signal and background processes are summarised. Subsequently, in Section 5.2, technical details about the simulated signal and background processes are given. Section 5.3 summarises the data set of the LHC Run 2 data taking period between 2015 and 2018 and the triggers that are used for the baseline event selection. The subsequent event reconstruction is discussed in Section 5.4. The shortcomings in the simulation-based description of the expected background contributions are studied and corrected for in Section 5.5. In this section, residual mismodellings that can not be corrected for on a pre-fit level are quantified in terms of additional modelling uncertainties that are included into the final statistical analysis of the data. Next, the systematic experimental and theoretical uncertainties contributing to the statistical analysis of the data are detailed Section 5.6. The presented analysis profits from employing track jets with a variable radius parameter (*cf.* Section 3.4) for the reconstruction of highly boosted Higgs decays, which provide a significant improvement with respect to the intermediate analysis of the partial data set recorded between 2015 and 2016 [14]. The

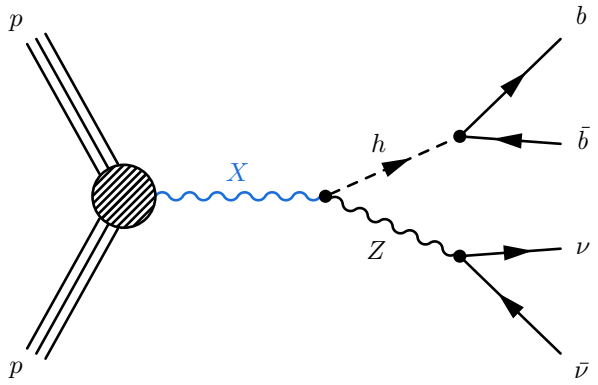

Figure 5.1: The signal process with the decay of a new resonance X, produced in a pp collision, into a Z boson and a Higgs boson that subsequently decay into pairs of neutrinos and b-quarks, respectively.

employment of variable-radius track jets is presented in Section 5.7. In the same section, studies targeting the V+jets and multijet background components are presented. It will be shown that a V+jets categorisation strategy similar to the one outlined in Section 4.6 can also be applied for the analysis of the $\nu\bar{\nu}b\bar{b}$ final state and that the multijet contribution can be suppressed to a negligible level by using optimised requirements on multijet-suppressing variables. A short summary of the fit model that is very similar to the one detailed in the analysis of the $\ell^{\pm(\mp)}\nu_\ell b\bar{b}$ final state (*cf.* Section 4.10) is given in Section 5.8. Finally, the observed results for the HVT Z' and 2HDM ggA analyses are shown in Sections 5.9.1 and 5.9.2, respectively.

5.1 The signal and the main background processes

The hypothetical new boson, X, predicted by the BSM theory models introduced in Chapter 2 frequently decays into a SM Z boson and a SM-like Higgs boson. Searches for such resonances are focusing on the final states with the dominant Higgs boson decay mode, $h \to b\bar{b}$, while simultaneously exploring several Z boson decay modes. In the presented analysis, the Z boson is assumed to decay into a neutrino-antineutrino-pair, while the Z boson decays into two charged leptons are considered elsewhere [15]. The searches in the two decay modes will be combined in Chapter 6. The signal process produced in a proton-proton collision is illustrated in Figure 5.1. Examples of tree-level Feynman diagrams for different production modes of the new heavy resonance X are shown in Figure 5.2. The heavy vector boson Z' predicted by the HVT model is predominantly produced in a Drell-Yan-like quark annihilation process, while the A boson predicted by the 2HDM model is expected to be predominantly produced via the ggA and bbA production.

Due to the two neutrinos in the final state, the four-momenta of the Z boson decay products cannot be

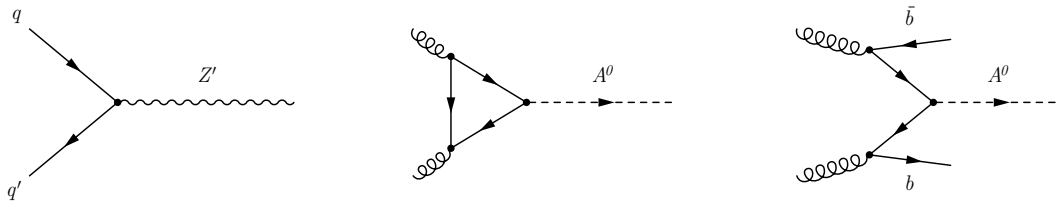

(a) Drell-Yan (b) ggA (c) bbA

Figure 5.2: Example tree-level Feynman diagrams for the production of a Zh resonance: *(a)* Drell-Yan like production of a Z' boson within the HVT model, and the production of a pseudoscalar A boson from the 2HDM via *(a)* gluon fusion (ggA production), and via *(c)* associated production with b-quarks (bbA production).

fully reconstructed. Thus, the invariant mass of the Zh diboson system also cannot be reconstructed, and is therefore approximated with the transverse component of the resonance mass, $m_{\mathrm{T},\,Vh}$, relying on the total transverse missing energy $\vec{E}_{\mathrm{T}}^{\mathrm{miss}} = (E_{\mathrm{T,\,x}}^{\mathrm{miss}}, E_{\mathrm{T,\,y}}^{\mathrm{miss}})$ from the two neutrinos:

$$m_{\mathrm{T},\,Vh} = \sqrt{\left(p_{\mathrm{T}}^{h} + E_{\mathrm{T}}^{\mathrm{miss}}\right)^2 - \left(\vec{p}_{\mathrm{T}}^{\,h} + \vec{E}_{\mathrm{T}}^{\mathrm{miss}}\right)^2}, \tag{5.1}$$

where $\vec{p}_{\mathrm{T}}^{\,h}$ is the transverse momentum of the Higgs boson candidate, reconstructed from the final state (flavour-tagged) jets.

Since the new physics is expected to occur at the TeV scale, this presented search considers X resonance masses of at least 300 GeV. The search for a heavy vector boson as predicted by the HVT model is only limited by the available amount of LHC Run 2 data, which allows for searches up to resonance masses of 5 TeV. The search for the CP-odd A boson, however, is only conducted up to 2 TeV as the branching fraction of the $A \to t\bar{t}$ decay mode quickly dominates the relative branching fractions once the $t\bar{t}$ mass threshold is surpassed, in which case the Zh decay mode is only relevant for a narrow window of model parameters [106]. Moreover, the design of the A boson study in the bbA production mode is optimised for combination with other final states, in particular $\ell^{\pm}\ell^{\mp}b\bar{b}$. This is motivated by the small excess at $m_A = 440$ GeV, which was previously observed at a local (global) significance level of 3.6σ (2.4σ) [14]. Since the $\ell^{\pm}\ell^{\mp}b\bar{b}$ final state has much higher sensitivity in this region of phase space, event reconstruction choices which are suboptimal for the $\nu\bar{\nu}b\bar{b}$ standalone analysis are deliberately kept, as long as they are expected to benefit the subsequent combination with the $\ell^{\pm}\ell^{\mp}b\bar{b}$ final state.

The $\nu\bar{\nu}b\bar{b}$ final state is subject to the same background processes that were introduced for the $\ell^{\pm(-)}\nu_{\ell}b\bar{b}$ final state in Section 4.1.

5.2 Simulated signal and background processes

Generally, the production of simulated background samples followed an approach similar to that of the analysis of the $\ell^{\pm}\overset{(-)}{\nu}_{\ell}b\bar{b}$ final state (*cf.* Section 4.2). However, small modifications in terms of generator parameter tunes and software package versions have been made. Only the production of the HVT signal and of vector bosons in association with jets was done with the identical setup from Section 4.2.

The ggA signal process within the 2HDM model was generated under the narrow width approximation (NWA) at LO precision in QCD using the MadGraph5_aMC@NLO v2.2.2. [154] generator, with the 2HDM FeynRules model [205, 206], and the NNPDF2.3LO PDF set [176]. The parton shower is modelled using Pythia 8.186 [157, 177] with the A14 set of tuned parameters [159]. The bbA signal process was generated in the four-flavour scheme at NLO QCD precision by the MadGraph5_aMC@NLO v2.2.2 generator using the same NNPDF2.3 NLO PDF set for the matrix element modelling, and Pythia 8.186 with the A14 tune for the parton shower. A number of mass points between 300 GeV and 2 TeV were simulated for each signal process, as listed in more detail in Appendix A.2.

The top quark pair background ($t\bar{t}$) was generated with by Powheg-Box [160–162], interfaced to Pythia 8.230 [158, 177] with the A14 tune for the parton showering. The matrix elements were calculated at NLO QCD precision using the NNPDF3.0 NLO [176] PDF set. The top mass was set to $m_t = 172.5$ GeV and the hdamp parameter [207], which describes the damping scale of high-p_{T} radiation, was fixed to $1.5\,m_t$. The $t\bar{t}$ production cross section was normalised to the state-of-the-art calculation at NNLO precision in perturbative QCD using Top++2.0 [170], including soft gluon contributions up to NNLL precision in QCD [171]. Particle-level information was used to separate the $t\bar{t}$ background events into two broad categories: $t\bar{t}$+hf and $t\bar{t}$+lf. The former (latter) relates to $t\bar{t}$ pairs that are (are not) produced in association with heavy flavour (b or c) quarks. The $t\bar{t}$+hf events are mainly produced via gluon splitting from the initial- or final-state radiation or via the heavy-flavour content of the proton [208, 209]. The theoretical description of these processes in Monte Carlo simulation is shown to be suboptimal [210, 211]. The categorisation according to the heavy flavour content allows for further constraints of each component using dedicated data-based modelling corrections. The categorisation was performed according to the number of b-quarks not originating from $t \to Wb$ decays and the number of c-quarks not originating from W boson decays. If at least one such heavy flavour quark was found, the event was classified as a $t\bar{t}$+hf, and otherwise as a $t\bar{t}$+lf event.

Single top quark production was also generated at NLO QCD precision by the Powheg-Box program using the NNPDF3.0 NLO PDF set, and with Pythia 8.230 with the A14 tune for the parton shower.

The s- and t-channel as well as Wt production modes were considered. Potential overlaps of Feynman diagrams were removed using a diagram removal scheme [212].

The production of top quark pairs in association with a Higgs or a vector boson ($t\bar{t}H$ and $t\bar{t}V$) were simulated at NLO QCD precision by MadGraph5_aMC@NLO v2.3.2, with the NNPDF3.0 NLO PDF set and Pythia 8.210 [158, 177] with the A14 tune for the parton showering. The top quark mass was assumed to be 172.5 GeV for all top quark processes.

The SM diboson processes (WW, ZW, ZZ) were produced separately for the gg and $q\bar{q}$ production modes using Sherpa 2.2.1 with the NNPDF3.0 NNLO PDF set. Feynman diagrams with up to one (up to three) additional emission(s) were considered at NLO (LO) accuracy. In the gg production mode, diboson production is possible only at loop level. These processes were generated using OpenLoops2 [213] interfaced with Sherpa 2.2.2, using the NNPDF3.0 NNLO PDF set.

The non-resonant SM production of a Higgs boson in association with a vector boson is an additional background process which was simulated separately for the $q\bar{q} \to Zh$ and $gg \to Zh$ production modes. The $q\bar{q}$-initiated production was simulated using the Powheg-Box+GoSam+MiNLO generator [214, 215], with the NNPDF3.0 NLO PDF set, resulting in NLO precision in QCD. A scale factor that depends on the transverse momentum of the vector boson is applied to account for electroweak (EW) corrections at NLO, thereby relying on the differential cross-section computed with the Hawk program [216, 217]. The inclusive $pp \to Zh$ cross section was calculated at NNLO in QCD and NLO for EW contributions. The gg-initiated production was generated by Powheg-Box with the NNPDF3.0 NLO tune, calculating the cross section at NLO precision and including soft gluon resummation up to NLL. For both production modes Pythia 8.212 [158, 177] was used with the AZNLO [178] tune for the showering.

The EvtGen v1.2.0 [184] program was used for the simulation of bottom and charm hadron decays for all samples generated with MadGraph5_aMC@NLO or Powheg-Box reducing potential differences of the decay properties between the two generators.

The impact of multiple pp interactions per bunch-crossing (*pile-up*) was taken into account by overlaying each signal and background event with minimum-bias events generated using Pythia 8.186 with the A2 tune [185] and the MSTW2008 LO PDF [186].

The detailed response of the ATLAS detector was simulated by the GEANT 4-based [126] ATLAS detector simulation software [125]. The simulated detector response undergoes the same event reconstruction as the collision data recorded by the ATLAS detector (*cf.* Section 3.4).

The simulated signal and background Monte Carlo samples are summarised in Table 5.1.

Table 5.1: Summary of simulated MC samples used for the $Z' \to Zh \to \nu\bar{\nu}b\bar{b}$ search together with the corresponding matrix element generators, PDFs, and parton shower (PS) tunes. The precision in QCD of the inclusive cross section calculation is included as well. MG is shorthand for MadGraph5_aMC@NLO.

Process	**ME generator**	**ME PDF**	**PS and hadronisation**	**MC tune**	**Cross section calc. order in QCD**
HVT Z'	MG 2.2.2	NNPDF2.3 LO	Pythia 8.186	A14	LO
2HDM ggA	MG 2.2.2	NNPDF2.3 LO	Pythia 8.186	A14	LO
2HDM bbA	MG 2.2.2	NNPDF2.3 LO	Pythia 8.186	A14	LO
$t\bar{t}$	Powheg-Box	NNPDF3.0 NLO	Pythia 8.230	A14	NNLO+NNLL
single top	Powheg-Box	NNPDF3.0 NLO	Pythia 8.230	A14	NLO
V + jets	Sherpa 2.2.1	NNPDF3.0 NNLO	Sherpa 2.2.1	Sherpa/MEPS@NLO	NNLO
WW, ZW, ZZ	Sherpa 2.2.1	NNPDF3.0 NNLO	Sherpa 2.2.1	Sherpa/MEPS@NLO	NLO
$t\bar{t}+h$ and $t\bar{t}+V$	MG 2.3.2	NNPDF3.0 NLO	Pythia 8.210	A14	NLO
SM $q\bar{q} \to Zh$	Powheg-Box	NNPDF3.0 NLO	Pythia 8.186	AZNLO	NNLO (QCD) + NLO (EW)
SM $gg \to Zh$	Powheg-Box	NNPDF3.0 NLO	Pythia 8.186	AZNLO	NLO+NLL

5.3 Data taking and trigger selection

This section contains a short summary of the ATLAS Run 2 data set and presents the triggers that were employed for the baseline event selection.

5.3.1 The ATLAS Run 2 dataset

Collected between 2015 and 2018, the ATLAS Run 2 data set of pp collisions at $\sqrt{s} = 13\,\text{TeV}$ corresponds to an integrated luminosity of $(139.0 \pm 2.4)\,\text{fb}^{-1}$ [218, 219]. The data are required to meet a number of data quality requirements, ensuring that all detector components were in good operating conditions during the data taking. More details about the data quality requirements are given in Ref. [187]. The evolution of the integrated luminosity over the Run 2 data taking period is shown in Figure 5.3. A total integrated luminosity of $156\,\text{fb}^{-1}$ was delivered by the LHC to the ATLAS experiment, out of which 94 % ($147\,\text{fb}^{-1}$) were recorded. Almost 95 % ($139\,\text{fb}^{-1}$) of the recorded data satisfy the quality requirements.

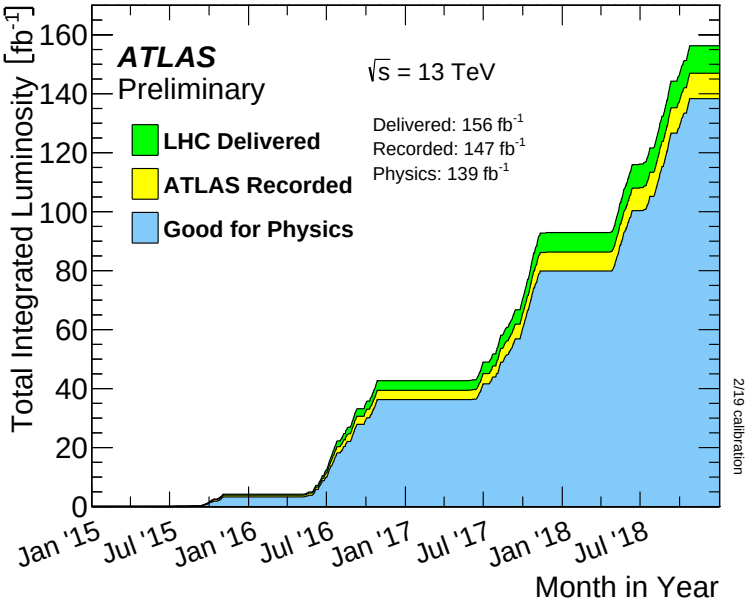

Figure 5.3: The integrated luminosity over the Run 2 data taking period for pp collisions [113]. The luminosity delivered by the LHC is shown in green. ATLAS recorded more than 94 % of these data, as shown in yellow, out of which 139 fb^{-1} are marked as good for physics analysis (blue).

5.3.2 Trigger requirements and trigger efficiency

The data for the analysis of the $\nu\bar{\nu}b\bar{b}$ final state are collected using $E_{\mathrm{T}}^{\mathrm{miss}}$ triggers with varying lower thresholds, depending on the data taking period. The $E_{\mathrm{T}}^{\mathrm{miss}}$ value thereby is calculated from HLT objects (*online* $E_{\mathrm{T}}^{\mathrm{miss}}$). For the data recorded in 2015, a lower threshold of 70 GeV was required. For 2016, the threshold varied between 90 GeV and 110 GeV. Finally, a threshold of 110 GeV was applied in data from 2017 and 2018. The triggers are also summarised in Table C.1.

For the jet-based $E_{\mathrm{T}}^{\mathrm{miss}}$ trigger, referred to as the *mht* trigger [220], the missing transverse energy is calculated from the vector sum of the negative transverse momenta of all jets above a threshold of 7 GeV before calibration. The jets are clustered with the anti-k_t algorithm, using calibrated topological calorimeter clusters as inputs. This method uses all energy clusters in the calorimeter and therefore has a significant pileup dependency. The *pufit* (pileup fit) algorithm [120], on the other hand, greatly reduces the pileup dependency. In this algorithm, the clusters are grouped into η-ϕ patches with a size that roughly corresponds to that of a jet with $R = 0.4$, which are individually corrected for pile-up effects on a per-event basis. The correction accounts for the deposited energy and its spatial fluctuations in the calorimeter [220], which allows the *pufit* algorithm to outperform other trigger algorithms, like *e.g.* the *mht* algorithm. In order to compare the two algorithms, the so-called trigger cross section is defined, which is the product of the measured instantaneous luminosity and the online

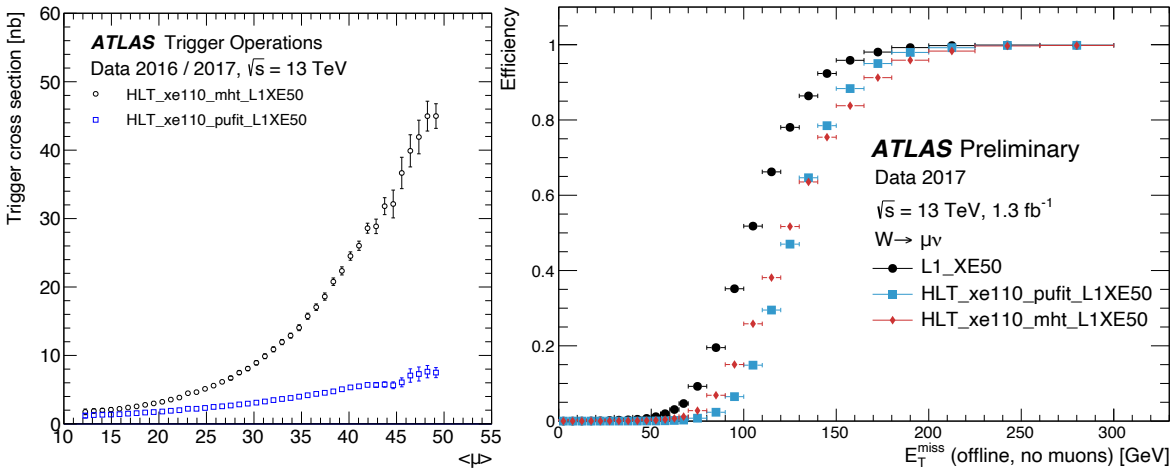

(a) (b)

Figure 5.4: *(a)* Trigger cross section as a function of the average number of pile-up interactions per proton-proton bunch crossing. *(b)* $E_{\mathrm{T}}^{\mathrm{miss}}$ trigger efficiency as a function of the $E_{\mathrm{T}}^{\mathrm{miss}}$ value calculated during the offline reconstruction. The black dots show the L1 trigger with a $E_{\mathrm{T}}^{\mathrm{miss}}$ requirement of 50 GeV. The red and turquoise dots show the HLT trigger with a threshold of online $E_{\mathrm{T}}^{\mathrm{miss}} > 110$ GeV for the *mht* and *pufit* algorithms, respectively. Originally published in Ref. [221].

trigger rate. In an ideal setting, this quantity should be independent of the average number of pile-up events $\langle\mu\rangle$ per bunch-crossing. The dependency of the trigger cross section on $\langle\mu\rangle$ is shown in Figure 5.4(a) for both algorithms. A strong dependency of the trigger cross section on the $\langle\mu\rangle$ value can be observed for the *mht* algorithm, while the *pufit* algorithm is a lot more resilient against pile-up effects. Since the values of $\langle\mu\rangle = 50$ have been on average exceeded during the 2017 and 2018 data taking periods (*cf.* Figure 3.2, p. 30), the *pufit* algorithm is used for this data taking period, allowing for more than a factor of six smaller trigger cross sections, compared to the *mht* algorithm. At the same time, the trigger efficiency with the *pufit* algorithm remains very similar to the efficiency of the *mht* algorithm, as can be seen in Figure 5.4(b). The figure shows the corresponding trigger efficiencies as measured in $W \rightarrow \mu\nu$ events. At an offline $E_{\mathrm{T}}^{\mathrm{miss}}$ value of 150 GeV both algorithms reach an efficiency of 80 % and both are fully efficient at $E_{\mathrm{T}}^{\mathrm{miss}} \gtrsim 230$ GeV. The *mht* trigger algorithm reaches the 60 % efficiency mark a bit faster, but at that mark the *pufit* algorithm catches up and reaches the full efficiency plateau sooner than the *mht* algorithm.

Since the analysis considers events with offline $E_{\mathrm{T}}^{\mathrm{miss}}$ values in the steeply rising *turn-on* region of the $E_{\mathrm{T}}^{\mathrm{miss}}$ triggers between roughly 50 and 230 GeV, a bias from the non-unity efficiency of the trigger is introduced, as events with a $E_{\mathrm{T}}^{\mathrm{miss}}$ value below 230 GeV are systematically selected at a lower rate. To correct for this systematic effect, dedicated trigger scale factors were determined in the framework of the search for the non-resonant SM Zh production [222], which can also be employed for the presented analysis. The scale factors are obtained by comparing the number of events selected by the

$E_{\mathrm{T}}^{\mathrm{miss}}$ trigger to the number of events selected by other control triggers, that are known to have no systematic dependency on the $E_{\mathrm{T}}^{\mathrm{miss}}$ value. In this particular analysis, $W \to \mu\nu$+jets events are studied both in simulated data and in data control regions which are enriched in events of this process. The alternative trigger is the single muon trigger which can select the muon from the W boson decay, and it is independent of the momentum of the final state neutrino, which induces the $E_{\mathrm{T}}^{\mathrm{miss}}$ in the final state. Dedicated uncertainties describing the impact of the limited size of the control data sample, as well as the dependency on the physical process that is used for comparison are provided by the authors of Ref. [222] and are included in the final statistical analysis of the data.

5.4 Event reconstruction

The reconstruction of the Higgs boson decay into a pair of b-quarks is similar to the one in the Wh resonance search described in Section 4.4. Thus, similar signal and control regions with resolved and merged event topology are defined. Notable differences, however, are the signal mass window for resolved-topology events, which is defined to be $100 < m_{jj} < 140\,\mathrm{GeV}$, and the usage of track jets with a variable, p_{T}-dependent radius parameter (VR track jets, *cf.* Sections 3.4 and 5.7.1) instead of the track jets with a fixed ($R = 0.2$) radius parameter. Referring to the notation of Section 5.7.1, the effective radius parameter of the VR track jets is $R_{\mathrm{min}} = 0.02 < R_{\mathrm{eff}} < 0.4 = R_{\mathrm{max}}$. The classification of events into signal and control regions is prioritised using the same prioritisation scheme as in the Wh diboson resonance search, as summarised in Figure 4.7.

Events with merged topology containing overlapping VR track jets are vetoed, as required by the calibration of the b-tagging algorithm. Two track jets are considered to overlap if the angular separation of their jet axes is smaller than the smaller jet radius, *i.e.* jets i and j with radii $R_{i,j}$ are overlapping if $\Delta R(j_i, j_j) < \min(R_i, R_j)$. The index i runs over all VR track jets that are used for applying b-tags and the index j considers all VR track jets in the event with a p_{T} of at least 5 GeV[1] and at least two associated tracks, even if the track jet does not meet the remaining requirements specified in this section. In all cases $i \neq j$.

Since there are no charged leptons produced in the signal process, events with charged leptons (electrons or muons) reconstructed at the *Loose* working point are vetoed.

A veto is also applied on events with a hadronically decaying tau candidate satisfying the *Medium* working point. This veto targets the backgrounds processes with hadronic τ decays, such as the $W \to \tau\nu_\tau$ decays in the W+jets, $t\bar{t}$, and diboson background components.

[1] In contrast, track jets matched to large-radius jets are required to have a p_{T} of at least 7 GeV.

Signal candidate events are expected to have a large $E_{\mathrm{T}}^{\mathrm{miss}}$ value due to the $Z \to \nu\nu$ decay and are selected using the triggers introduced in Section 5.3.2. The events are further required to have $E_{\mathrm{T}}^{\mathrm{miss}} > 150\,\mathrm{GeV}$ ($> 200\,\mathrm{GeV}$) in the resolved (merged) event topology. These lower thresholds are chosen such that the contribution of multijet background events are suppressed efficiently without loosing too much sensitivity to the hypothesised signals at lower resonance masses. The multijet background contribution is further suppressed by requiring thresholds on the track-based missing energy, $p_{\mathrm{T}}^{\mathrm{miss}} > 60\,\mathrm{GeV}$; the angular separation between $\vec{E}_{\mathrm{T}}^{\mathrm{miss}}$ and $\vec{p}_{\mathrm{T}}^{\mathrm{miss}}$, $\Delta\phi(\vec{E}_{\mathrm{T}}^{\mathrm{miss}}, \vec{p}_{\mathrm{T}}^{\mathrm{miss}}) < \pi/2$; the angular separation between $\vec{E}_{\mathrm{T}}^{\mathrm{miss}}$ and the Higgs candidate, $\Delta\phi(\vec{E}_{\mathrm{T}}^{\mathrm{miss}}, \vec{p}_{h}) > 2\pi/3$; and on the minimal angular separation between $\vec{E}_{\mathrm{T}}^{\mathrm{miss}}$ and the small-radius jets in the event, $\min[\Delta\phi(\vec{p}_{\mathrm{jet}}, \vec{E}_{\mathrm{T}}^{\mathrm{miss}})] > \pi/9$ ($> \pi/6$) for events with up to three (more than three) jets. Finally, the $m_{\mathrm{T},\,Vh}$-dependent threshold on the $E_{\mathrm{T}}^{\mathrm{miss}}$ significance is applied, as described in more detail in Section 5.7.3.

The events are further categorised into the $m_{jj/J}$ signal and sideband control regions. For the signal region with resolved topology, the reconstructed mass of the dijet system is required to be $100 < m_{jj} < 140\,\mathrm{GeV}$, whilst for the merged topology the reconstructed leading large-radius jet mass is required to be $75 < m_{J} < 145\,\mathrm{GeV}$. Events with $m_{jj/J}$ values outside these windows are selected for the sideband control region, as long as their respective $m_{jj/J}$ values are not smaller than 50 GeV and not larger than 200 GeV.

A summary of all selection requirements is given in Table 5.2.

Following these requirements, the b-tagging procedure is applied on the jets from the candidate Higgs decay, based on the MV2c10 algorithm and using the 70 % working point as introduced in Section 3.4.2. The tagging is applied directly on either small-radius signal jets or VR track jets for events with resolved and merged topology, respectively. The n-tag signal or sideband region then contains events with n b-tagged small-radius jets (VR track jets) in the resolved (merged) event topology. In the merged topology, all jets are counted, including those that are not matched to the leading large-radius jet. Events are then grouped based on the number of counted b-tags. In the resolved event topology, regions with exactly one, exactly two, and with three or more b-tags are defined, whilst regions with exactly one and with exactly two b-tagged VR track jets are introduced in the merged event topology. In the latter case, additional b-tagged jets outside the large-radius jet are also allowed in order to increase the sensitivity to the bbA signal process. However, these regions with and without additional b-tagged VR track jets are analysed separately.

Based on the outlined requirements, the regions summarised in Table 5.3 are defined. The table also includes the regions used in the statistical interpretation on the 2HDM bbA signal model, which will be presented in Chapter 6.

For the signal regions with the resolved and merged topologies of the different b-tag multiplicities, the overall signal selection efficiency, *i.e.* the signal acceptance times reconstruction efficiency, is

Table 5.2: Summary of the event selection criteria for the signal regions of the Zh diboson resonance search in the $\nu\bar{\nu}b\bar{b}$ channel. The requirement on the Higgs candidate mass $m_{jj/J}$ is inverted for the sideband control regions.

Observable	Resolved topology	Merged topology
$m_{jj/J}$ [GeV]	110–140	75–145
Leading jet p_{T} [GeV]	> 45	> 250
$E_{\mathrm{T}}^{\mathrm{miss}}$ [GeV]	> 150	> 200
$\Delta\phi_{jj}$	$< 7\pi/9$	—
Number of jets	≥ 2 small-radius jets	≥ 1 large-radius jet
$N_{e,\mu,\tau_{\mathrm{had}}}$	0	
$\min[\Delta\phi(\vec{p}_{\mathrm{jet}}, \vec{E}_{\mathrm{T}}^{\mathrm{miss}})]$	$> \pi/9$ (2 or 3 jets), $> \pi/6$ (≥ 4 jets)	
$p_{\mathrm{T}}^{\mathrm{miss}}$[GeV]	> 30	
$\Delta\phi(\vec{E}_{\mathrm{T}}^{\mathrm{mis}}, \vec{p}_{\mathrm{T}}^{\mathrm{mis}})$	$< \pi/2$	
$\Delta\phi(\vec{E}_{\mathrm{T}}^{\mathrm{mis}}, \vec{p}_{h})$	$> 2\pi/3$	
$E_{\mathrm{T}}^{\mathrm{miss}}$ significance	$\begin{cases} > 9 & m_{\mathrm{T},\,Vh} < 400, \\ > 6.6 + 0.01 \cdot m_{\mathrm{T},\,Vh} & 400 < m_{\mathrm{T},\,Vh} < 700, \\ > 13.6 & m_{\mathrm{T},\,Vh} > 700, \end{cases}$	

Table 5.3: Summary of data regions employed in the presented analysis. The signal regions (SRs) are shown in the upper and the control regions (CRs) in the lower part of the table. The number of additional b-tagged track jets in the merged topology that are not matched to the leading large-radius jet is abbreviated with "add.".

Event topology	$m_{jj/J}$ [GeV]	Number of b-tags	Comment	Used in the Z', ggA fit	Used in the bbA fit
resolved	[110, 140]	1	$m_{jj/J}$ SR	✓	✓
resolved	[110, 140]	2	$m_{jj/J}$ SR	✓	✓
resolved	[110, 140]	3+	$m_{jj/J}$ SR	—	✓
merged	[75, 145]	1, 0 add.	$m_{jj/J}$ SR	✓	✓
merged	[75, 145]	2, 0 add.	$m_{jj/J}$ SR	✓	✓
merged	[75, 145]	2, 1+ add.	$m_{jj/J}$ SR	—	✓
resolved	$[50, 110[\vee]140, 200]$	1	$m_{jj/J}$ CR	✓	—
resolved	$[50, 110[\vee]140, 200]$	2	$m_{jj/J}$ CR	✓	—
merged	$[50, 75[\vee]145, 200]$	1, 0 add.	$m_{jj/J}$ CR	✓	—
merged	$[50, 75[\vee]145, 200]$	2, 0 add.	$m_{jj/J}$ CR	✓	—

studied for different signal models, as shown in Figure 5.5. As a result of the selection requirements, the selection efficiency of A (Z') bosons is relatively small up to a resonance mass of about 400 GeV (600 GeV), which is mainly driven by the required $E_{\mathrm{T}}^{\mathrm{miss}}$ threshold, which implies a sufficiently large boost of the Z boson. However, for these relatively light resonances, the theory models also predict relatively large production cross sections, such that a competitive measurement is possible, even if the signal efficiency is small. Peak selection efficiencies of about 35–55 % are reached at intermediate resonance masses, with similar values expected for both the resolved and the merged regime. At very high resonance masses, the signal selection efficiency drops again due to a reduced number of events with resolved topology and due to losses in the signal regions with high b-tag multiplicity. Nevertheless, also here the efficiency remains at a high level of 30–40 %.

5.5 Control data for background estimates

In this section, the modelling of major background processes is studied by comparing the predicted distributions of key observables to the observed data in the sideband regions outside the $m_{jj/J}$ mass window and in the regions with exactly zero b-tags, in which the V+jets processes (in particular V+light jets) are ubiquitous. Moreover, the agreement between data and prediction is evaluated in validation regions in which the veto on hadronically decaying τ-leptons (τ_{had}) is replaced by requiring exactly one τ_{had}. The main background process in these regions is $t\bar{t}$.

Two ways of addressing potential disagreements are realised in this analysis. In the first approach, differences between the predicted and observed data are parametrised and the original prediction is replaced by an alternative, corrected prediction. This method is applied to the mismodelling of the distribution of the dijet pair transverse momentum, $p_{\mathrm{T}}^{b\bar{b}}$. The second approach only defines alternative distributions based on the difference between predicted and observed data and these alternative distributions are then included as additional uncertainties in the fit model. This is done for the residual disagreements observed in the $p_{\mathrm{T}}^{\mathrm{miss}}$ distributions and for a mismodelling observed in the p_{T} description of the leading large-radius jet in events with merged topology.

The main reason why these two approaches are chosen is that in the former case the observed mismodelling can be clearly attributed to a specific background process, while in latter case no such attribution is possible. Therefore, the additional degrees of freedom from the residual mismodellings are included in the statistical model, where they can be constrained by the additional correlations that are taken into account by the final fit to data.

The studies and the evaluation of the applied corrections are described in more detail below.

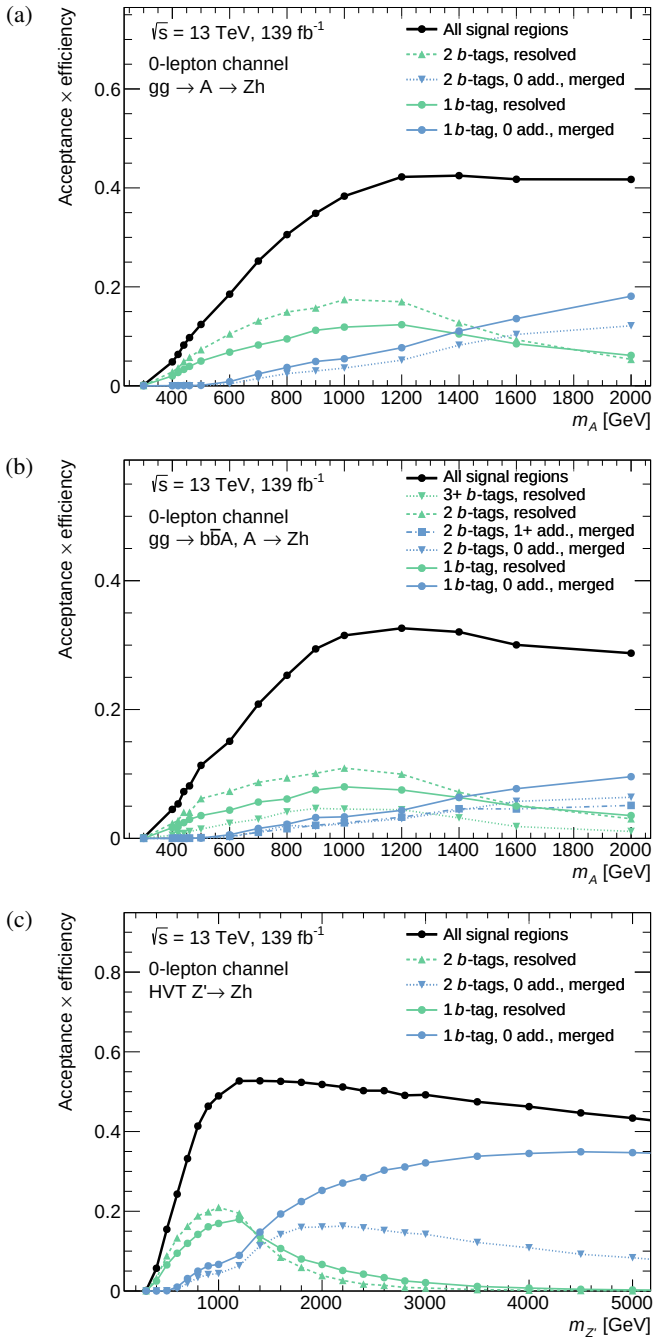

Figure 5.5: Product of signal acceptance and reconstruction efficiency for the various signals as a function of the resonance mass. The signal modes are *(a)* $gg \to A \to Zh \to \nu\bar{\nu}b\bar{b}$, *(b)* $gg \to bbA, A \to Zh \to \nu\bar{\nu}b\bar{b}$, and *(c)* $Z' \to Zh \to \nu\bar{\nu}b\bar{b}$. The total product of acceptance and efficiency (black full circle markers) are shown together with the separate values for each of the signal regions. The number of additional b-tagged jets not matched to the leading large-radius jet in the merged topology is abbreviated with "add." in the legends.

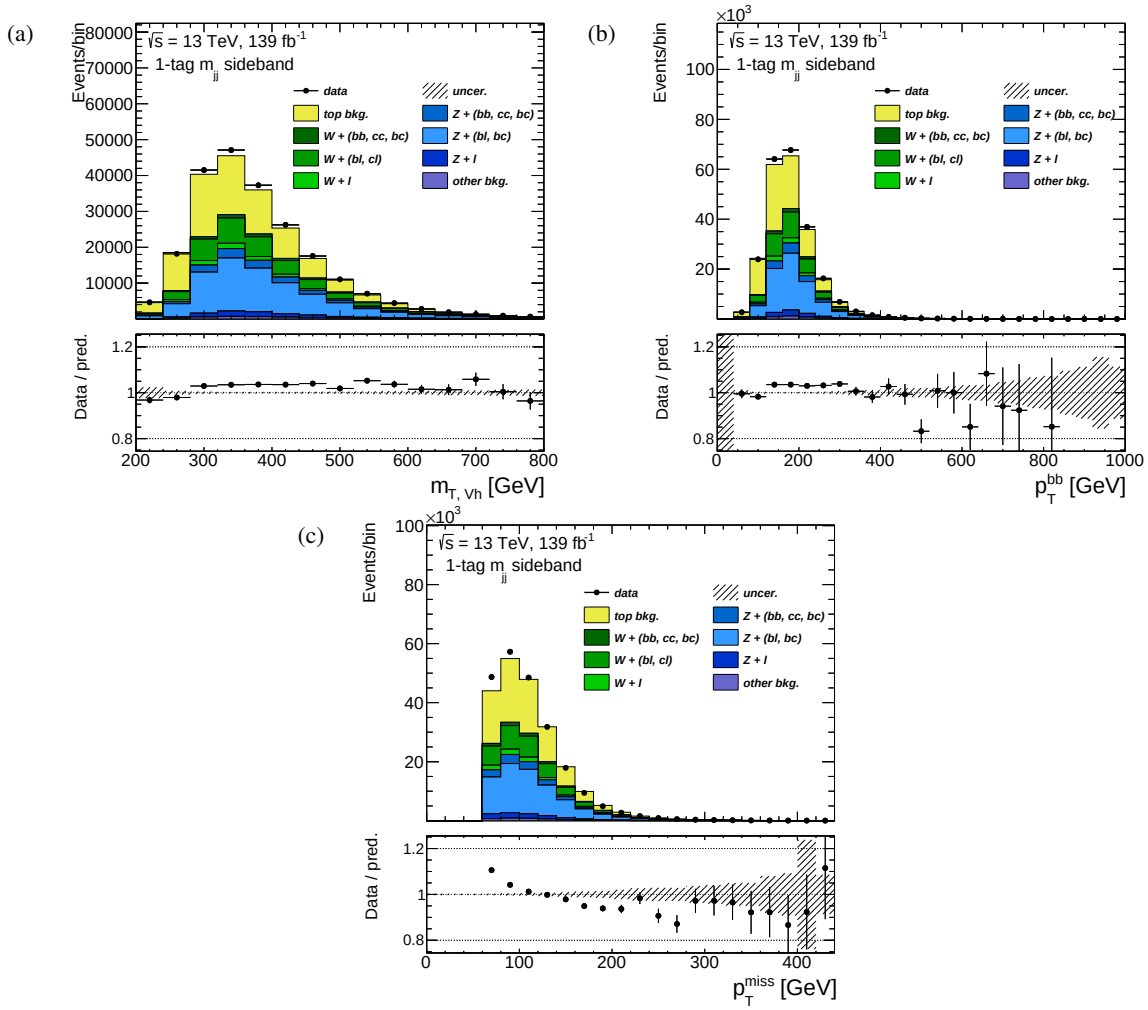

Figure 5.6: Observed and expected background distributions of discriminating observables in the resolved-topology m_{jj} sideband regions with exactly one b-tagged jet per event after applying the $p_{\mathrm{T}}^{b\bar{b}}$-based event reweighting: *(a)* $m_{\mathrm{T},\,Vh}$, *(b)* $p_{\mathrm{T}}^{b\bar{b}}$ and *(c)* $p_{\mathrm{T}}^{\mathrm{miss}}$ distributions. The lower panels show the ratio between data and total background prediction. The uncertainty bands show only the statistical uncertainties.

5.5.1 Background modelling corrections from different kinematic distributions

In order to evaluate the quality of the pre-fit modelling of the individual background processes, the data-to-prediction ratio of different kinematic distributions in the sideband control regions is studied. Figure 5.6 shows the distributions of $m_{\mathrm{T},\,Vh}$, $p_{\mathrm{T}}^{b\bar{b}}$, and $p_{\mathrm{T}}^{\mathrm{miss}}$ in the m_{jj} sideband regions with exactly one b-tagged jet per event in the resolved event topology. While the $m_{\mathrm{T},\,Vh}$ distribution is the discriminant distribution that is used in the final fit to the data, the remaining distributions are shown as well since there are significant pre-fit data-to-prediction disagreements identified for them. For the $p_{\mathrm{T}}^{\mathrm{miss}}$ distribution, a clear slope in the data-to-prediction ratio with a trend towards smaller ratio values

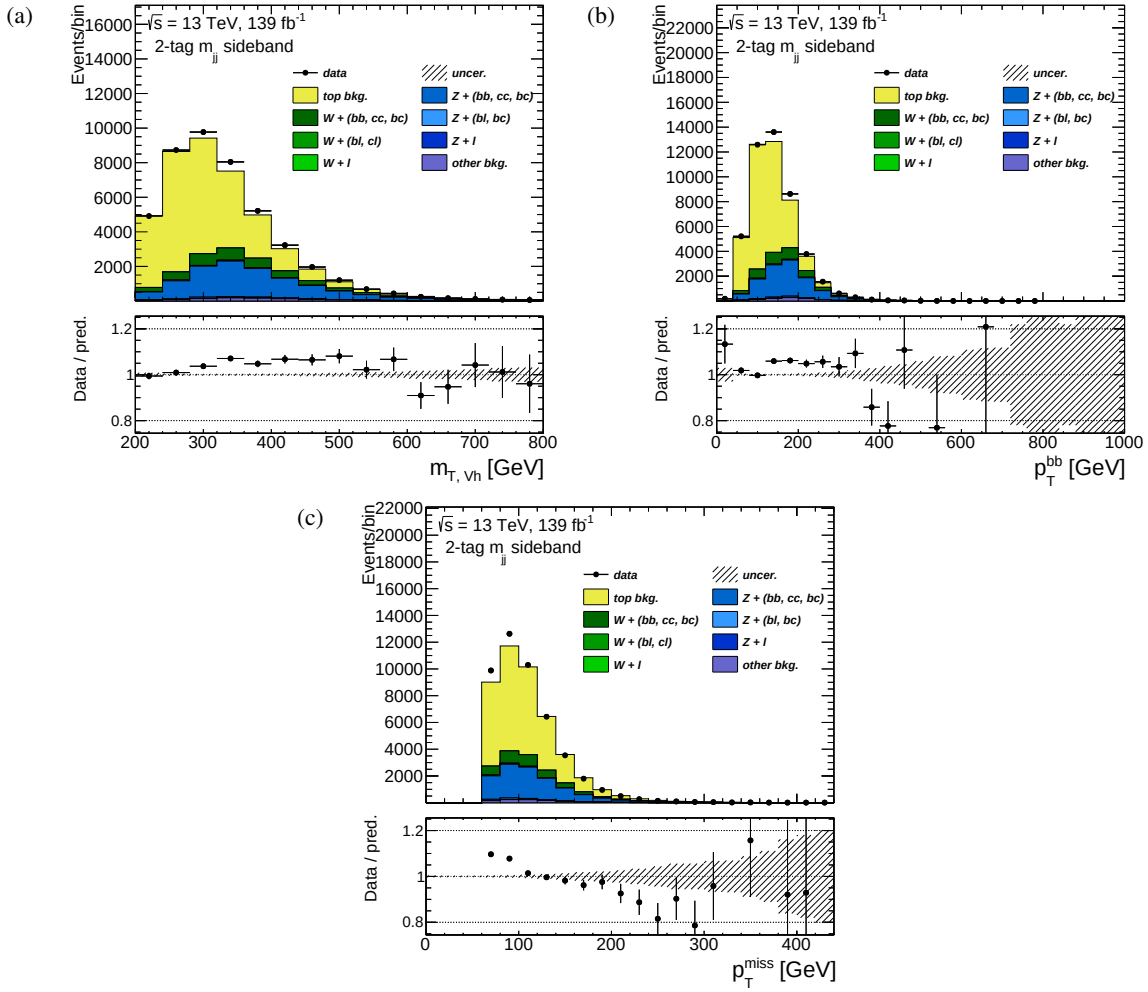

Figure 5.7: Observed and expected background distributions of discriminating observables in the resolved-topology m_{jj} sideband regions with exactly two b-tagged jets per event after applying the $p_{\mathrm{T}}^{b\bar{b}}$-based event reweighting: *(a)* $m_{\mathrm{T},\,Vh}$, *(b)* $p_{\mathrm{T}}^{b\bar{b}}$ and *(c)* $p_{\mathrm{T}}^{\mathrm{miss}}$ distributions. The lower panels show the ratio between data and total background prediction. The uncertainty bands show only the statistical uncertainties.

for larger $p_{\mathrm{T}}^{\mathrm{miss}}$ values is visible up to $p_{\mathrm{T}}^{\mathrm{miss}}$ values of about 200 GeV, while the data-to-prediction disagreements for the $m_{\mathrm{T},\,Vh}$ and $p_{\mathrm{T}}^{b\bar{b}}$ distributions show a more localised disagreement between data and prediction in the bins with the highest numbers of contributing events. Additionally, a trend towards smaller values can be observed in the tail of the respective distribution. Similar effects are also observed in the resolved sideband regions with two b-tagged jets, shown in Figure 5.7. The description of the $m_{\mathrm{T},\,Vh}$ observable in the region with two b-tagged jets is worse than in the region with one b-tagged jet, with the ratio of data and prediction exhibiting a slope towards positive values.

Since the presented analysis is designed for the combination with the $\ell^{\pm}\ell^{\mp}b\bar{b}$ final state and since a

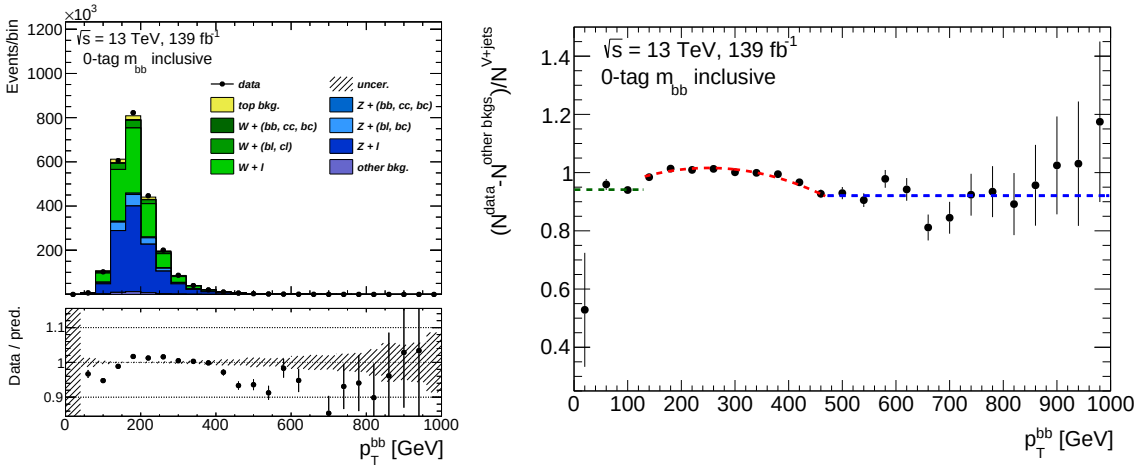

(a) (b)

Figure 5.8: *(a)* Pre-fit distribution of the $p_{\mathrm{T}}^{b\bar{b}}$ observable in events with resolved topology and a veto on b-tagged jets. All events within $50 < m_{bb}/\mathrm{GeV} < 200$ are shown. The ratio of data and the prediction from simulation, "data/prediction", is shown in the bottom panel, where the impact of the statistical uncertainty of the simulation is indicated by the grey hatched area.*(b)* A fit to the ratio of data and V+jets prediction after subtracting all but the V+jets background predictions from data.

significant mismodelling of the corresponding $p_{\mathrm{T}}^{b\bar{b}}$ distribution is found in this final state, the $p_{\mathrm{T}}^{b\bar{b}}$ mismodelling shown in Figures 5.6 and 5.7 is studied first. The main background contribution in the $\ell^{\pm}\ell^{\mp}b\bar{b}$ final state is from V+jets events ($V = W, Z$), which is why the mismodelling of the $p_{\mathrm{T}}^{b\bar{b}}$ distribution is attributed to this background component. The $\ell^{\pm}\ell^{\mp}b\bar{b}$ and $\nu\bar{\nu}b\bar{b}$ final states cover similar phase space regions, and therefore the $p_{\mathrm{T}}^{b\bar{b}}$ mismodelling is also attributed to the V+jets background processes in the presented analysis. Therefore, the disagreement between the V+jets prediction and the observed data after subtracting all but the V+jets predictions, $(N_{\mathrm{data}} - N_{\mathrm{other\ BGs}})/N_{\mathrm{V+jets}}$, is studied. Moreover, this ratio is studied in the event selection with a veto on b-tagged jets, where the V+jets background components are by far dominant. The $p_{\mathrm{T}}^{b\bar{b}}$ distribution for these events is shown in Figure 5.8(a), and the corresponding ratio in Figure 5.8(b). Figure 5.8(b) also includes an overlay of the fit function that is obtained by a three-component fit to the ratio. The three components represent the parametrisation of the V+jets modelling corrections, which are applied as weights to each V+jets event:

$$w\left(p_{\mathrm{T}}^{b\bar{b}}\right) = \begin{cases} 0.946 & \text{for} \quad 0 < p_{\mathrm{T}}^{b\bar{b}} \leq 130, \\ 0.888 + 0.001\,\frac{p_{\mathrm{T}}^{b\bar{b}}}{1\,\mathrm{GeV}} - 2.003 \cdot 10^{-6}\left(\frac{p_{\mathrm{T}}^{b\bar{b}}}{1\,\mathrm{GeV}}\right)^2 & \text{for} \quad 130 < p_{\mathrm{T}}^{b\bar{b}} \leq 470, \\ 0.917 & \text{for} \quad p_{\mathrm{T}}^{b\bar{b}} \geq 470. \end{cases} \tag{5.2}$$

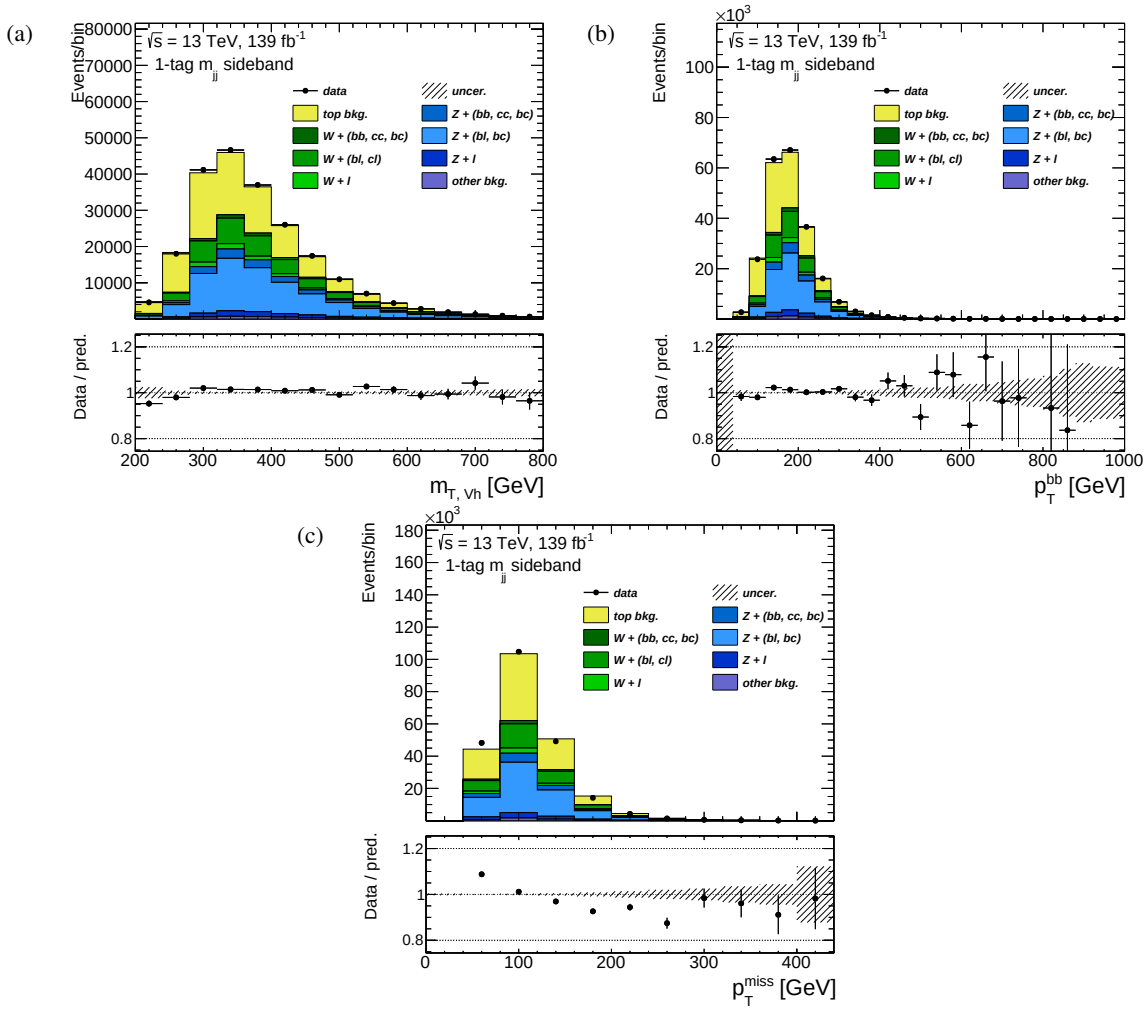

Figure 5.9: Observed and expected background distributions of discriminating observables in the m_{jj} sideband regions with exactly one b-tagged jet per event: *(a)* $m_{\mathrm{T},\,Vh}$, *(b)* $p_{\mathrm{T}}^{b\bar{b}}$ and *(c)* $p_{\mathrm{T}}^{\mathrm{miss}}$ distributions. The lower panels show the ratio between data and total background prediction. The uncertainty bands show only the statistical uncertainties.

After applying the $p_{\mathrm{T}}^{b\bar{b}}$ corrections, new $m_{\mathrm{T},\,Vh}$, $p_{\mathrm{T}}^{b\bar{b}}$ and $p_{\mathrm{T}}^{\mathrm{miss}}$ distributions are obtained for the resolved-topology events with one and two b-tagged jets, shown in Figures 5.9 and 5.10. Compared to the distributions before the $p_{\mathrm{T}}^{b\bar{b}}$ correction, the agreement between data and prediction from simulation improved for the $m_{\mathrm{T},\,Vh}$ distributions. However, the mismodelling observed for the $p_{\mathrm{T}}^{\mathrm{miss}}$ distribution remains for both the region with one and with two b-tagged jets.

In contrast to the $p_{\mathrm{T}}^{b\bar{b}}$ mismodelling, the mismodelling of the $p_{\mathrm{T}}^{\mathrm{miss}}$ distribution can not be clearly attributed to the V+jets backgrounds alone, as becomes clear when studying the corresponding distributions in the τ_{had} sideband validation regions. In these sideband regions, the veto on hadronically

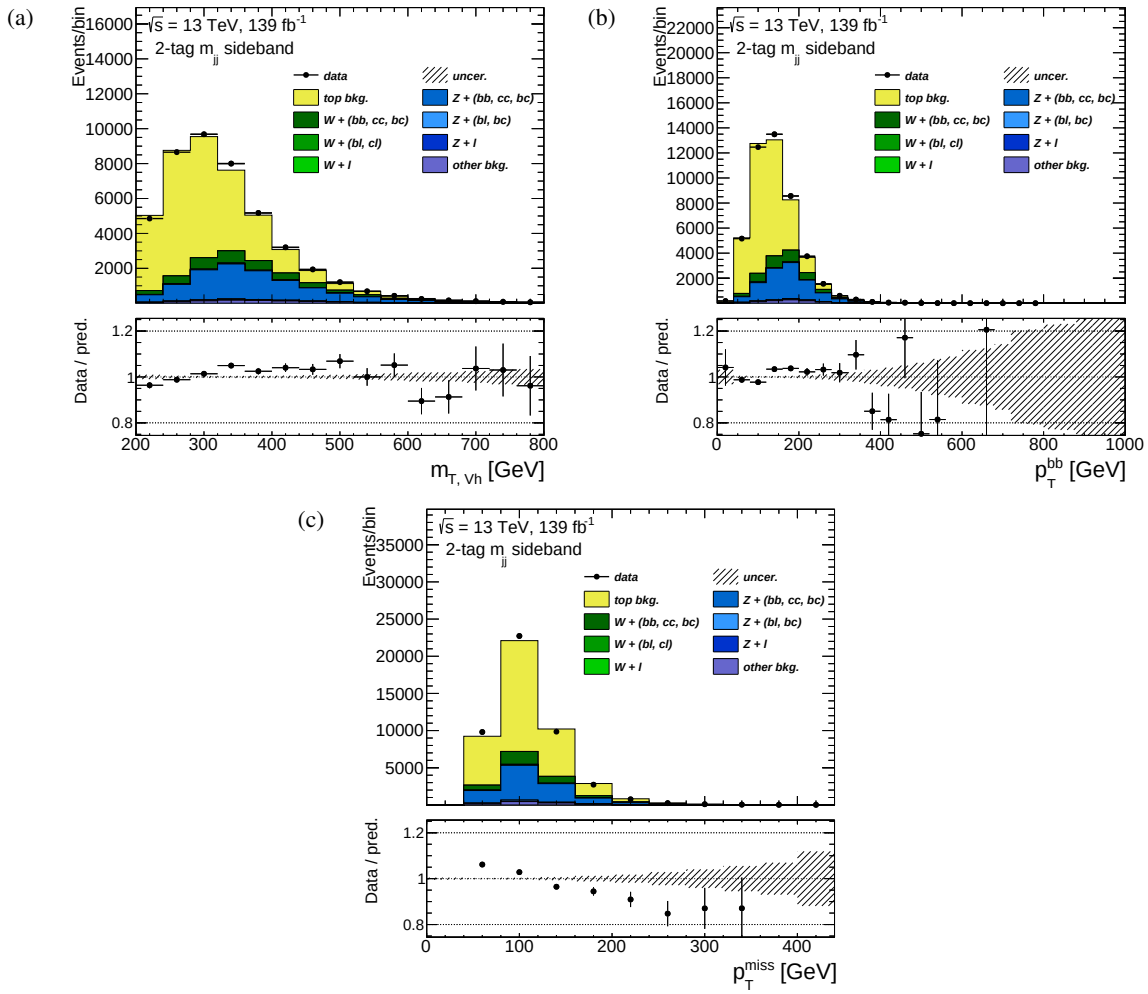

Figure 5.10: Observed and expected background distributions of discriminating observables in the m_{jj} sideband regions with exactly two b-tagged jets per event: *(a)* $m_{\mathrm{T,}\,Vh}$, *(b)* $p_{\mathrm{T}}^{b\bar{b}}$ and *(c)* $p_{\mathrm{T}}^{\mathrm{miss}}$ distributions. The lower panels show the ratio between data and total background prediction. The uncertainty bands show only the statistical uncertainties.

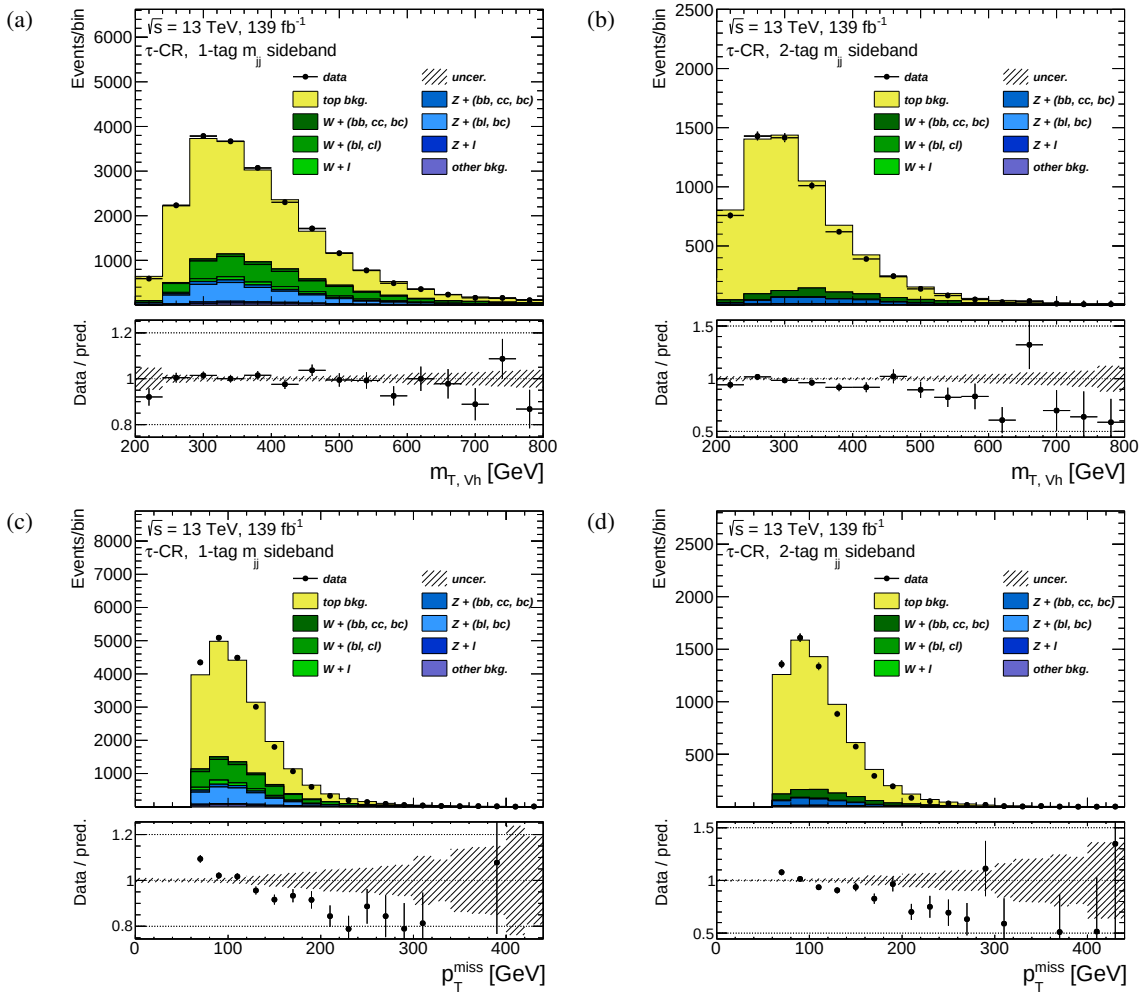

Figure 5.11: Observed and expected background distributions in validation regions with a τ_{had} requirement per event after applying the $p_{\text{T}}^{b\bar{b}}$-based event reweighting: the *(a)* m_{Vh}, 1 *b*-tag *(b)* m_{Vh}, 2 *b*-tags *(c)* $p_{\text{T}}^{\text{miss}}$, 1 *b*-tag *(d)* $p_{\text{T}}^{\text{miss}}$, 2 *b*-tags distributions. The uncertainty bands account only for the statistical uncertainties.

decaying tau leptons is inverted by requiring exactly one of them in the event. The main background contribution in these regions stems from $t\bar{t}$ events. As can be seen in Figure 5.11, a good modelling of the $m_{\text{T, }Vh}$ distribution is observed, while a similar mismodelling as in the nominal sideband regions is found for the $p_{\text{T}}^{\text{miss}}$ distribution. This implies that the cause of the mis-modelled $p_{\text{T}}^{\text{miss}}$ distribution also affects the $t\bar{t}$ background component to a similar extent as it affects the combination of all backgrounds that is studied in the nominal sideband regions. Thus, based on the available control and validation data, no individual background component can be identified as the source of the mismodelling, and instead of applying a correction to a certain background process, an overall modelling uncertainty based on the observed slope is defined. This modelling uncertainty is included separately (*i.e.* uncorrelated) for every background component in the final fit to the data, which can impose additional constraints on

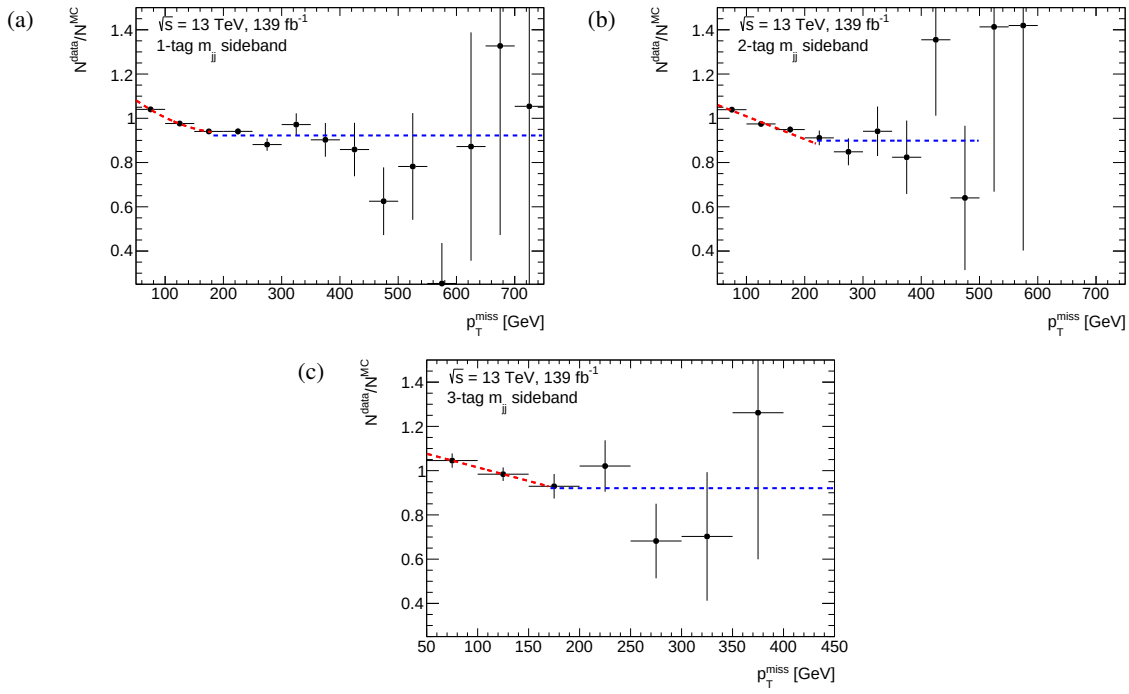

Figure 5.12: A fit to the ratio of data and background prediction from simulation for the $p_{\mathrm{T}}^{\mathrm{miss}}$ distributions in the resolved-topology regions after applying the $p_{\mathrm{T}}^{b\bar{b}}$-based event reweighting with: *(a)* 1, *(b)* 2, and *(c)* 3 b-tagged jets. The stepwise continuous functions resulting from a fit to the ratio are overlaid on top of the data points.

the background modelling uncertainties based on the full correlation scheme (*cf.* Section 5.6).

In order to obtain a quantitative description of the $p_{\mathrm{T}}^{\mathrm{miss}}$ modelling uncertainty, the residual mismodelling of the $p_{\mathrm{T}}^{\mathrm{miss}}$ distribution in the resolved topology is studied, separately in the sideband control regions with one, two, and more than two b-tagged jets. Correction functions are obtained from a fit to the data-to-prediction ratio, shown in Figure 5.12, and summarised in Table 5.4. Based on these reweighting functions, the nominal background predictions are reweighted and the resulting alternative distributions are used to define an additional modelling uncertainties on the simulated predictions of the background processes.

The impact of the obtained reweighting functions on the $m_{\mathrm{T},\,Vh}$ and $p_{\mathrm{T}}^{\mathrm{miss}}$ distributions in the signal regions is visualised in Figure 5.13. While the $p_{\mathrm{T}}^{b\bar{b}}$ correction only has a very small impact on both the $m_{\mathrm{T},\,Vh}$ and $p_{\mathrm{T}}^{\mathrm{miss}}$ distributions, the $p_{\mathrm{T}}^{\mathrm{miss}}$ correction shows a larger impact and significantly modifies the $m_{\mathrm{T},\,Vh}$ distribution. Deviations from the nominal distribution of about 10 % are observed in the high-$m_{\mathrm{T},\,Vh}$ tail.

Similar to the $p_{\mathrm{T}}^{\mathrm{miss}}$ uncertainty determination, a residual mismodelling observed in the p_{T}-distributions of the leading large-radius jet is addressed. The ratios between data and simulated prediction from

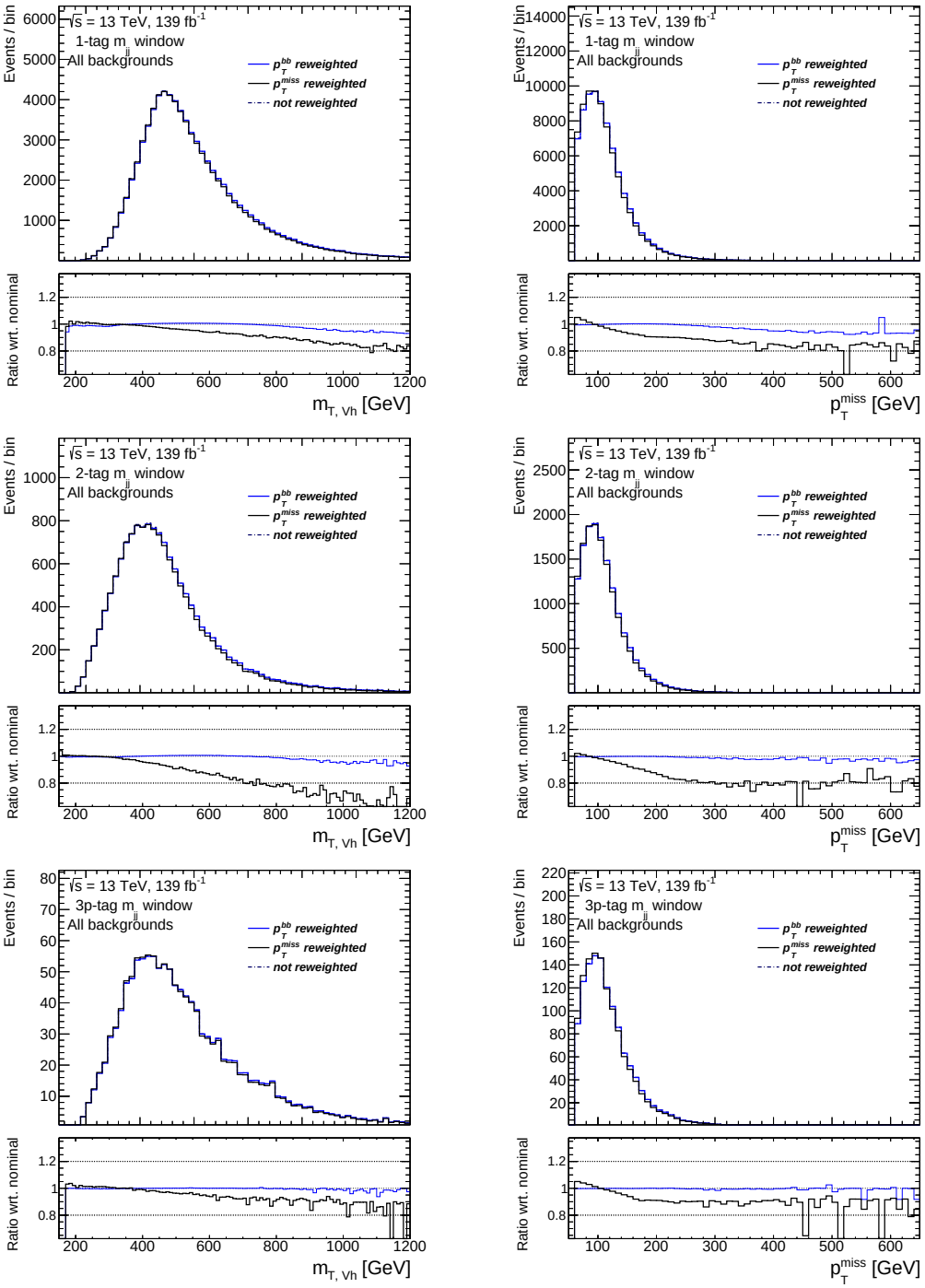

Figure 5.13: The *(left)* $m_{\mathrm{T,}\,Vh}$ and *(right)* $p_{\mathrm{T}}^{\mathrm{miss}}$ distributions of the sum of all simulated backgrounds before any correction (dashed line), after the $p_{\mathrm{T}}^{b\bar{b}}$ correction (blue solid line), and after the $p_{\mathrm{T}}^{\mathrm{miss}}$ correction (black solid line). The distributions are shown for events with the resolved topology, within the m_{jj} mass signal window, and with (from top to bottom) one, two, or more than two b-tagged jets. The bottom panels show the ratio of the corrected to the original distribution.

Table 5.4: Summary of correction (reweighting) functions that address the residual $p_{\mathrm{T}}^{\mathrm{miss}}$ mismodelling of all background processes after the $p_{\mathrm{T}}^{b\bar{b}}$ correction was applied on the V+jets process. In the relevant $p_{\mathrm{T}}^{\mathrm{miss}}$ range the correction is always smaller than 10 %.

Number of b-tags	Weight formula	$p_{\mathrm{T}}^{\mathrm{miss}}$ range in GeV
1	$1.200 - 0.003\,\frac{p_{\mathrm{T}}^{\mathrm{miss}}}{1\,\mathrm{GeV}} + 5.801 \times 10^{-6} \left(\frac{p_{\mathrm{T}}^{\mathrm{miss}}}{1\,\mathrm{GeV}}\right)^2$	50–180
	0.926	> 180
2	$1.116 - 0.001\,\frac{p_{\mathrm{T}}^{\mathrm{miss}}}{1\,\mathrm{GeV}}$	50–220
	0.901	> 220
3+	$1.140 - 0.001\,\frac{p_{\mathrm{T}}^{\mathrm{miss}}}{1\,\mathrm{GeV}}$	50–170
	0.92	> 170

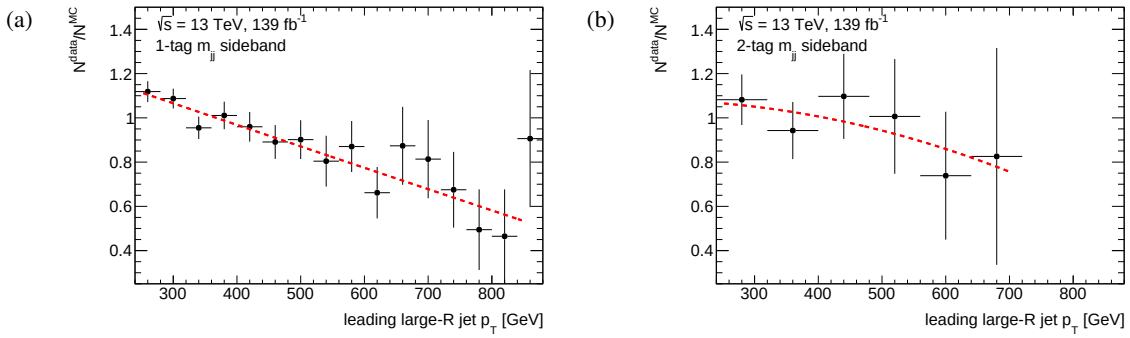

Figure 5.14: A fit to the ratio of data and background prediction from simulation for the p_{T}-distributions of the leading large radius jets in the merged-topology regions with merged topology and: *(a)* 1, and *(b)* 2 b-tagged track jets. The continuous functions resulting from a fit to the ratio are overlaid on top of the data points.

events in the merged topology with one and two b-tagged track jets are fitted separately with a quadratic function. The corresponding ratios are shown in Figure 5.14 and the resulting fit functions defining the event weights are parametrised as follows:

$$w(p_{\mathrm{T,J}}) = \begin{cases} 1.3651 - 0.0010 \cdot \frac{p_{\mathrm{T,J}}}{1\,\mathrm{GeV}} + 3.4051 \cdot 10^{-8} \left(\frac{p_{\mathrm{T,J}}}{1\,\mathrm{GeV}}\right)^2 & \text{for } 250\,\mathrm{GeV} < p_{\mathrm{T,J}} \leq 850\,\mathrm{GeV}, \\ 0.5340 & \text{for } p_{\mathrm{T,J}} \geq 850\,\mathrm{GeV}, \end{cases} \tag{5.3}$$

for events with one b-tagged track jet, and

$$w(p_{\mathrm{T,J}}) = \begin{cases} 1.0622 + 0.0002 \cdot \frac{p_{\mathrm{T,J}}}{1\,\mathrm{GeV}} - 1.0254 \cdot 10^{-6} \left(\frac{p_{\mathrm{T,J}}}{1\,\mathrm{GeV}}\right)^2 & \text{for } 250\,\mathrm{GeV} < p_{\mathrm{T,J}} \leq 700\,\mathrm{GeV}, \\ 0.7499 & \text{for } p_{\mathrm{T,J}} \geq 700\,\mathrm{GeV}, \end{cases} \tag{5.4}$$

Table 5.5: Number of observed and expected (pre-fit) events in the signal and sideband regions of the $Z' \to Zh \to \nu\bar{\nu}b\bar{b}$ analysis at an integrated luminosity of 139 fb^{-1}. Possible differences between the sum of all background contributions and the total background are due to the rounding of individual contributions and correlations of the uncertainties.

Signal regions	resolved event topology		merged event topology	
Process name	1 b-tag	2 b-tags	1 b-tag	2 b-tags
top quarks	44 800 ± 500	11 130 ± 100	2500 ± 140	90 ± 4
Z+hf	2910 ± 110	2283 ± 97	530 ± 40	242 ± 13
Z+(bl, cl)	17 300 ± 1200	102 ± 10	2390 ± 180	17.5 ± 1.4
Z+l	1890 ± 180	6.8 ± 1.6	660 ± 50	2.48 ± 0.27
W+hf	930 ± 60	680 ± 40	223 ± 28	97 ± 15
W+(bl, cl)	8500 ± 900	77 ± 9	1000 ± 160	7.5 ± 0.8
W+l	1970 ± 180	13.8 ± 2.5	335 ± 32	1.11 ± 0.13
SM Vh	192 ± 14	251 ± 18	20.5 ± 1.5	12.7 ± 0.9
SM Diboson	720 ± 50	103 ± 7	433 ± 32	117 ± 9
Total	79 170 ± 310	14 650 ± 80	8090 ± 70	587 ± 12
Data	80 110	14 681	7260	584

Sideband regions	resolved event topology		merged event topology	
Process name	1 b-tag	2 b-tags	1 b-tag	2 b-tags
top quarks	86 800 ± 2100	30 200 ± 400	670 ± 60	21.54 ± 0.97
Z+hf	11 400 ± 600	9100 ± 500	273 ± 25	102 ± 7
Z+(bl, cl)	63 000 ± 7000	360 ± 50	1210 ± 130	7.9 ± 0.6
Z+l	7300 ± 1000	21 ± 6	460 ± 40	1.24 ± 0.16
W+hf	4200 ± 400	3390 ± 260	124 ± 17	48 ± 7
W+(bl, cl)	30 000 ± 5000	220 ± 40	450 ± 110	2.53 ± 0.29
W+l	6300 ± 900	25 ± 6	220 ± 26	0.50 ± 0.11
SM Vh	220 ± 28	131 ± 15	2.50 ± 0.30	0.380 ± 0.032
SM Diboson	3800 ± 500	1010 ± 110	95 ± 10	8.9 ± 0.8
Total	212 800 ± 1200	44 440 ± 230	3510 ± 50	193 ± 8
Data	222 882	46 277	3435	230

for events with two b-tagged track jets. Once more, alternative $m_{\mathrm{T},\,Vh}$ distributions are obtained by applying the weights from the corresponding fit function and are used as an additional modelling uncertainty in the final fit to data.

With these corrections applied, the pre-fit yields as reported in Table 5.5 are obtained.

5.5.2 Post-fit background prediction in the $m_{jj/J}$ sideband regions

The described corrections of the background modelling and all systematic uncertainties (*cf.* Section 5.6) including their correlations are taken into account in the final fit of the expected to the observed data, simultaneously in all signal and control regions (*cf.* Section 5.8).

The agreement between data and background prediction is also studied in signal-depleted data regions after the final fit to data (post-fit background distributions). For this purpose, the fit is performed under a background-only hypothesis, *i.e.* assuming no signal contributions. The expected post-fit $m_{\mathrm{T},\,Vh}$ distributions and the corresponding observations are shown in Figure 5.15 for different sideband regions, using one of the two different fit scenarios.

In the first scenario, all background processes with top quarks are treated as a single background component, whilst in the second scenario the $t\bar{t}$+hf process is fitted separately from the remaining top quark background components. The first fit scenario is applied in the resolved and merged mass sideband regions with exactly one or exactly two b-tagged jets (shown in Figures 5.15(a), 5.15(b), 5.15(c) and 5.15(d)). In the resolved (merged) regions with three or more b-tagged jets (two b-tagged jets inside and at least one outside the large-radius jet), the second fit scenario is applied (shown in Figures 5.15(e) and 5.15(f)). This is motivated by the fact that the first four regions are included in the final fit targeting the HVT Z' and 2HDM ggA signal hypotheses, covered in this section (*cf.* Table 5.3). The regions with more than two b-tagged jets are only used in the search for the bbA production, which is performed in combination with the $\ell^{\pm}\ell^{\mp}b\bar{b}$ final state and has a slightly modified fit strategy (*cf.* Chapter 6).

In all cases, the prediction is in good agreement with the observation. In particular, no residual slopes can be seen in the distributions of the ratio of data to the background prediction. The few remaining small discrepancies are all within the range of statistical fluctuations.

5.6 Systematic uncertainties

The expected distributions of the final $m_{\mathrm{T},\,Vh}$ fit discriminant in the fit regions can be affected by both experimental and theory uncertainties. Possible sources of uncertainties are identified and their impact is quantified in dedicated studies, which are presented in this section. Very similar uncertainty sources as for the $\ell^{\pm}\overset{(-)}{\nu}_{\ell}b\bar{b}$ final state presented in Section 4.9 are considered. However, small differences exist, mainly due to the different final state and the larger (full Run 2) data set that is used for the full Run 2 analysis of the $\nu\bar{\nu}b\bar{b}$ final state.

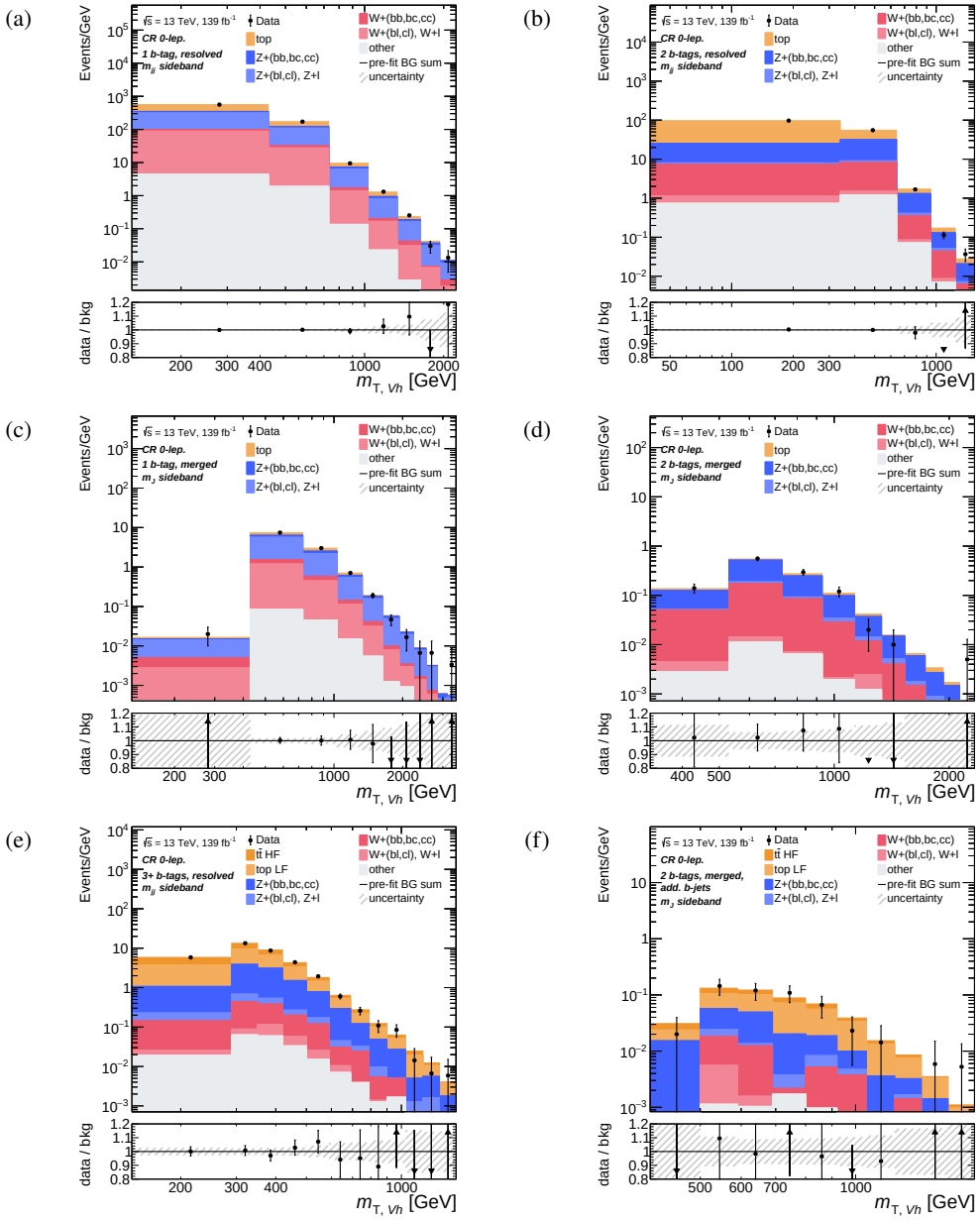

Figure 5.15: Observed and expected (post-fit) distributions of the transverse Vh mass, $m_{\mathrm{T},\,Vh}$, after a background-only fit to data in the $m_{jj/J}$ mass sideband regions with different numbers of b-tagged jets in the resolved topology: with *(a)* one, *(c)* two, and *(e)* more than two b-tagged jets, as well as in the merged topology with *(b)* one, and *(d, f)* two b-tagged track jets within the leading large-radius jet. The results in the latter case are obtained for events *(d)* without and *(f)* with additional b-tagged track jets that are not marched to the leading large-radius jet. The bottom panels show the ratio of data over the post-fit background expectation and the hatched area indicates the total post-fit uncertainty.

5.6.1 Experimental uncertainties

Similar to Section 4.9, experimental uncertainty sources are studied and included in the statistical interpretation. Dominant uncertainty sources are associated with the calibration and resolution of the jet energy scale and mass, and with the identification efficiency and misidentification rate of *e.g.* leptons and b-jets. Details for all estimated uncertainties are listed below.

- The Run-2 integrated luminosity is $(139.0 \pm 2.4)\,\text{fb}^{-1}$ [218, 219]. This corresponds to an uncertainty of 1.7 % (*cf.* Section 5.3.1), which is applied globally to the normalisation of all signal and background processes.
- The uncertainties on the $E_{\text{T}}^{\text{miss}}$ trigger are described in Section 5.3.2.
- The efficiency of the veto on hadronically decaying τ leptons is affected by the uncertainty on the efficiency of the reconstruction and identification of hadronically decaying τ-leptons, together with their energy scale and resolution measurements at the given τ-identification working point (*cf.* Section 5.4).
- An uncertainty on the pile-up re-weighting procedure is introduced similar to Section 4.9.
- Small-radius jets are subject to a number of uncertainty sources. A total of 125 uncorrelated uncertainty sources are considered for the jet energy scale (JES) [223], targeting effects from pile-up, jet flavour dependence, η intercalibration, and *in situ* calibrations. They are then reduced to a set of 30 effective components by following the reduction scheme outlined in Ref. [223]. This procedure preserves the total uncertainty and reduces the number of components at the cost of a small loss of correlation information. The jet energy resolution (JER) comprises 8 effective components, which are determined from jet energy resolution measurements in dijet events, as well as from measurements of the noise that is induced by pile-up and electronics-related effects, as detailed in Ref. [223].
- Uncertainties on the p_{T}-scale of the large-radius jet are determined from data-driven calibrations of the calorimeter- and track-based jet energy and jet mass measurements [195, 224]. The impact of the uncertainties from the jet mass resolution measurement is evaluated by randomly smearing the reconstructed large-radius jet mass by up to 20 %.
- The flavour-tagging efficiency is measured in control data and simulation and is translated to correction factors that are applied to b-jets, c-jets, as well as light-flavour jets. An extrapolation for the efficiency of tagging jets with high-p_{T} is also performed [153, 225, 226]. The uncertainties are decomposed into a set of three, four, and five uncorrelated uncertainty components for the b-, c-, and light-flavour jets, respectively. The uncertainty from the extrapolation to large jet

p_{T}-values is accounted for by two additional uncertainty components. All uncertainties are determined separately for small- and large-radius jets.

- The reconstruction of the missing transverse energy is affected by the same uncertainties that are introduced in Section 4.9.

The impact of experimental uncertainties on the various signal and background processes is summarised in Table 5.6. Only the uncertainty sources that have a significant impact (either on the $m_{\mathrm{T},\,Vh}$ shape distribution or the normalisation) of 0.5 % on average are shown. Most uncertainties affect the signal or background normalisation by not more than 10 %, but in few cases there is a larger impact. These cases, however, mostly affect data regions with small amount of data, and therefore only marginally affect the final result of the analysis.

Table 5.6: Impact of different experimental systematic uncertainties on the shape and normalisation of the $m_{\mathrm{T},\,Vh}$ distribution from the various signal and background processes in the signal and control regions. The values are obtained for an integrated luminosity of 139 fb^{-1}. The impact on the normalisation is calculated as the average normalisation change due to a given uncertainty over all fit regions with at least 100 events of the given background component. An "S" indicates the shape-only uncertainties.

Process	Uncertainty source	Value
Signal	Luminosity	1.7 %
	JES, JER	S
	b-tagging	S
top quarks	$E_{\mathrm{T}}^{\mathrm{miss}}$ trigger	S
	JES, JER	1.6 % + S
	b-tagging	1.8 % + S
	$E_{\mathrm{T}}^{\mathrm{miss}}$, τ_{had}	S
Z+hf	JES, JER	6.0 % + S
	b-tagging	2.1 % + S
Z+(bl, cl)	$E_{\mathrm{T}}^{\mathrm{miss}}$ trigger	S
	JES, JER	6.7 % + S
	b-tagging	3.5 % + S
Z+l	Luminosity	1.7 %
	$E_{\mathrm{T}}^{\mathrm{miss}}$ trigger	S
	JES, JER	4.7 % + S
	b-tagging	34.6 % + S
W+hf	Luminosity	1.7 %
	$E_{\mathrm{T}}^{\mathrm{miss}}$ trigger	S
	JES, JER	5.1 % + S
	b-tagging	2.0 % + S
W+(bl, cl)	Luminosity	1.7 %
	$E_{\mathrm{T}}^{\mathrm{miss}}$ trigger	S
	JES, JER	6.8 % + S
	b-tagging	3.6 % + S
W+l	Luminosity	1.7 %
	$E_{\mathrm{T}}^{\mathrm{miss}}$ trigger	S
	JES, JER	5.7 % + S
	b-tagging	34.1 % + S
	$E_{\mathrm{T}}^{\mathrm{miss}}$, τ_{had}	S
SM Vh	Luminosity	1.7 %
	$p_{\mathrm{T}}^{\mathrm{miss}}$ reweight.	S
SM Diboson	Luminosity	1.7 %
	$p_{\mathrm{T}}^{\mathrm{miss}}$ reweight.	S

5.6.2 Theory uncertainties

The study of theory uncertainties follows the steps outlined in Section 4.9.2. As no upper threshold on the number of signal jets is defined for the analysis presented in this chapter, the Stewart-Tackmann method is not applied to the QCD scale uncertainties. On the other hand, the background modelling studies presented in Section 5.5 give rise to additional uncertainties on the shape of certain background distributions. The uncertainty on the shape of the $m_{\mathrm{T},\,Vh}$ distribution from V+jets processes is determined by comparing the simulated distribution to the one obtained after the $p_{\mathrm{T}}^{b\bar{b}}$-dependent event reweighting. Similarly, the differences between the original and reweighted $p_{\mathrm{T}}^{\mathrm{miss}}$ distributions are accounted as additional uncertainties. The $p_{\mathrm{T}}^{b\bar{b}}$ uncertainty component is correlated for all background processes, while individual components of the $p_{\mathrm{T}}^{\mathrm{miss}}$-related uncertainty are defined separately for the different types of background processes (top quarks, $Z+$jets, $W+$jets, *etc.*). Additionally, the alternative distributions based on the large-radius jet p_{T}-reweighting are also added as additional uncertainties that are correlated for all background processes.

For the V+jets backgrounds, combined ME+PS uncertainties are determined from the comparison to alternative samples produced with MadGraph5_aMC@NLO 2.2.2, interfaced to Pythia 8.186 using the CKKW-L merging procedure [227, 228], the A14 set of tuned parton shower parameters, and the NNPDF 2.3 LO PDF set. The QCD scale uncertainties are evaluated from the variations of renormalisation and factorisation scales as described in Section 4.9.2.

ME and PS uncertainties for the $t\bar{t}$ background are determined by comparison to alternative dedicated samples. For the uncertainty related to the ME calculation and to the matching to the PS, a comparison to a sample produced with MadGraph5_aMC@NLO instead of Powheg-Box is made. The PS uncertainty is estimated from a comparison to an alternative sample where Pythia 8 is replaced by Herwig++ 2.7.1 [229]. Variations in the amount of initial- and final-state radiation are addressed by changing the renormalisation and factorisation scales in combination with using dedicated intrinsic ISR/FSR eigenvariations of the A14 tune [159]. The renormalisation and factorisation (renormalisation only) scales are varied by factors of two in the ISR (FSR) case.

As an example, the impact of the Z+jets theoretical modelling uncertainties on the shape of the $m_{\mathrm{T},\,Vh}$ distribution is shown in Figure 5.16, using the signal regions with one b-tagged jet in resolved and merged event topologies. Similar input is seen also in the regions with more b-tags. The nominal distributions from Z+hf events are shown together with relative changes due to different uncertainty sources. Throughout all signal and control regions, the $m_{\mathrm{T},\,Vh}$ shape can vary up to 10 %, 2 %, and 4 % due to the ME+PS, QCD scale, and α_s uncertainties, respectively. Only a subset of six intrinsic PDF variations within the NNPDF set is shown in the figure. The average of all 100 intrinsic variations, which is used as the uncertainty in the final fit to data, is indicated by the grey area. The α_s, intrinsic

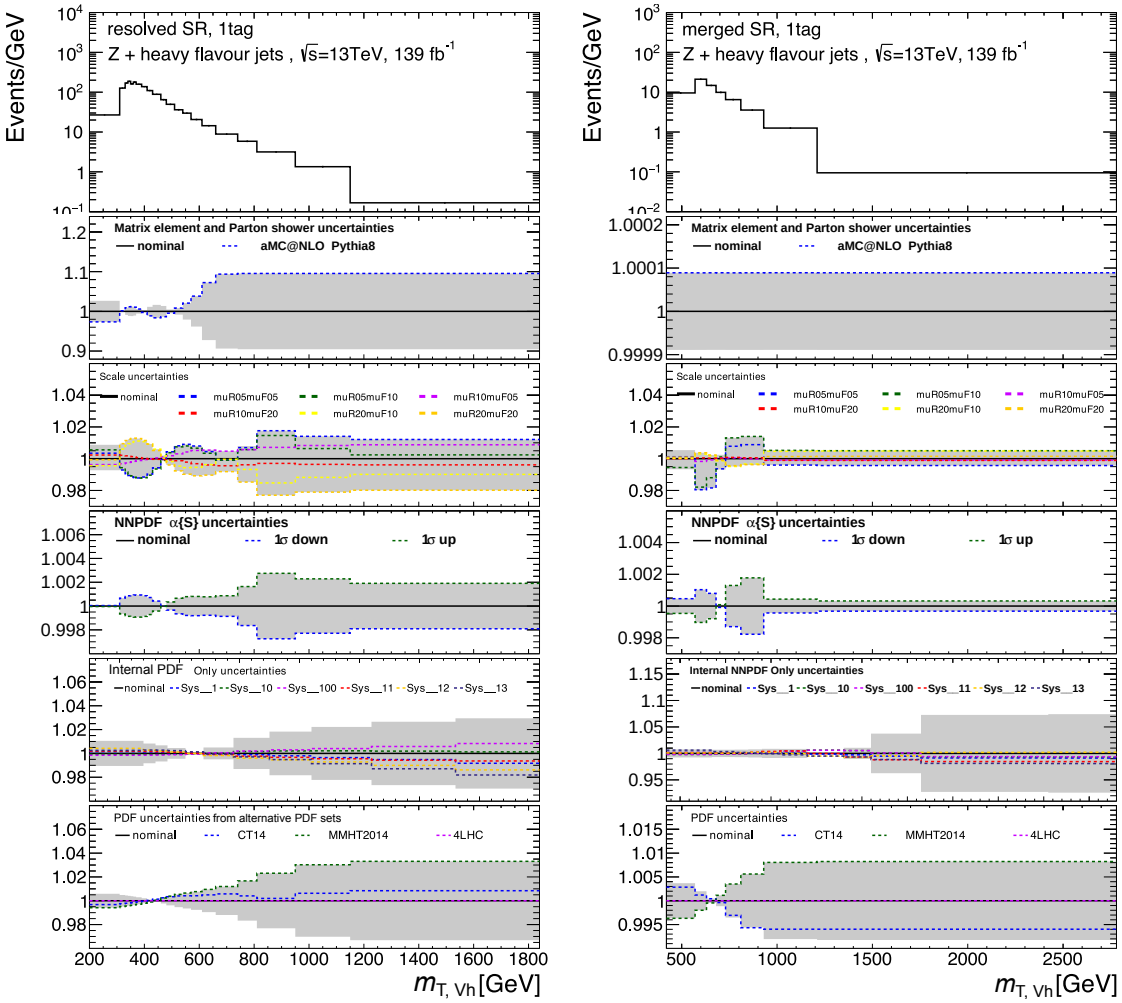

Figure 5.16: Impact of various modelling uncertainties on the shape of the $m_{\mathrm{T,}\,Vh}$ distribution from Z+hf events. The left-hand (right-hand) side corresponds to signal regions with resolved (merged) event topology with one b-tagged jet per event. The nominal distributions are shown in the first panel on the top, and below are the relative changes due to the uncertainties from: the ME and PS modelling; the renormalisation and factorisation scales; α_s; intrinsic PDF variations; different PDF sets. The grey area in the ratio panels is obtained as an envelope of the corresponding uncertainty components and defines the $\pm 1\sigma$ interval of the given uncertainty.

NNPDF, and external PDF uncertainties are combined into a single, conservative uncertainty by choosing the one of the three components with the largest deviation from the nominal value.

To account for uncertainties in the composition of the top quark background, an additional normalisation uncertainty of 19 % (50 %) is assumed for the single top quark ($t\bar{t}H/t\bar{t}V$) production. The uncertainty value for the single top quark production is obtained from comparisons of different MC generator setups, while the very subdominant $t\bar{t}V/t\bar{t}H$ processes are addressed by a conservative uncertainty in order to give the fit a large enough freedom to adjust their post-fit normalisation. The CMS collaboration recently reported the observation of the SM Vh process [222] with an uncertainty on the

signal strength in the order of 20 %, which is taken as a statistically independent estimate for the cross section uncertainty of the SM Vh process.

Similarly as for the Z+hf background, the impact of the $t\bar{t}$ modelling uncertainties on the shape of the $m_{\mathrm{T},\,Vh}$ distribution of $t\bar{t}$ events can be seen in Figure 5.17. Generally, the impact of the theory uncertainties on the background modelling is below 10 % in the bulk of the $t\bar{t}$ distribution.

For all signal and background processes, the obtained uncertainties are expressed in terms of additional nuisance fit parameters (*cf.* Section 5.8) for the shape and overall normalisation of the fitted distributions. Single-sided variations, *i.e.* variations with only an upward or a downward fluctuation, are symmetrised around the nominal values.

A summary of all estimated theory uncertainties is shown in Table 5.7.

Table 5.7: Impact of theoretical systematic uncertainties on the selection of signal and background processes. The values are obtained for an integrated luminosity of 139 fb^{-1}. The label "S" indicates a shape-only variation. The normalisations between two kinematic regions, *i.e.* the migration of events from one region to another, are indicated by a forward slash "/". "Normalisation" refers on the total event yield, and is determined entirely from data for processes indicated with "float". Uncertainties targeting the relative composition of a background category are indicated by "comp.".

Process	Uncertainty source	Value
top	normalisation	float
	resolved / merged migration	9–46 %
	SR / CR migration	2 %
	PS, ISR, FSR, ME, PDF	S
	single top comp.	19 %
	$t\bar{t}H/t\bar{t}V$ comp.	50 %
	p_{T}^{J}, $p_{\mathrm{T}}^{\mathrm{miss}}$ reweight.	S
Z+hf	normalisation	float
	resolved / merged migration	10–14 %
	SR / CR migration	5–6 %
	ME/PS, matching, scale	S
	$p_{\mathrm{T}}^{b\bar{b}}$, p_{T}^{J}, $p_{\mathrm{T}}^{\mathrm{miss}}$ reweight.	S
Z+(bl, cl)	normalisation	float
	resolved / merged migration	15–21 %
	SR / CR migration	4–20 %
	ME/PS, matching, scale	S
	$p_{\mathrm{T}}^{b\bar{b}}$, p_{T}^{J}, $p_{\mathrm{T}}^{\mathrm{miss}}$ reweight.	S
Z+l	normalisation	19 %
	resolved / merged migration	8–50 %
	SR / CR migration	5–20 %
	ME/PS, matching, scale	S
	$p_{\mathrm{T}}^{b\bar{b}}$, p_{T}^{J}, $p_{\mathrm{T}}^{\mathrm{miss}}$ reweight.	S

Process	Uncertainty source	Value
W+hf	normalisation	20 %
	resolved / merged migration	46 %
	SR / CR migration	5–7 %
	ME/PS, matching, scale	S
	$p_{\mathrm{T}}^{b\bar{b}}$, p_{T}^{J}, $p_{\mathrm{T}}^{\mathrm{miss}}$ reweight.	S
W+(bl, cl)	normalisation	30 %
	resolved / merged migration	20–43 %
	SR / CR migration	10–20 %
	ME/PS, matching, scale	S
	$p_{\mathrm{T}}^{b\bar{b}}$, p_{T}^{J}, $p_{\mathrm{T}}^{\mathrm{miss}}$ reweight.	S
W+l	normalisation	30 %
	resolved / merged migration	18–24 %
	SR / CR migration	5–20 %
	ME/PS, matching, scale	S
	$p_{\mathrm{T}}^{b\bar{b}}$, p_{T}^{J}, $p_{\mathrm{T}}^{\mathrm{miss}}$ reweight.	S
SM Vh	normalisation	20 %
Diboson	normalisation	50 %
Signal	normalisation	2–7 %
	PS, ISR-FSR, PDF	S

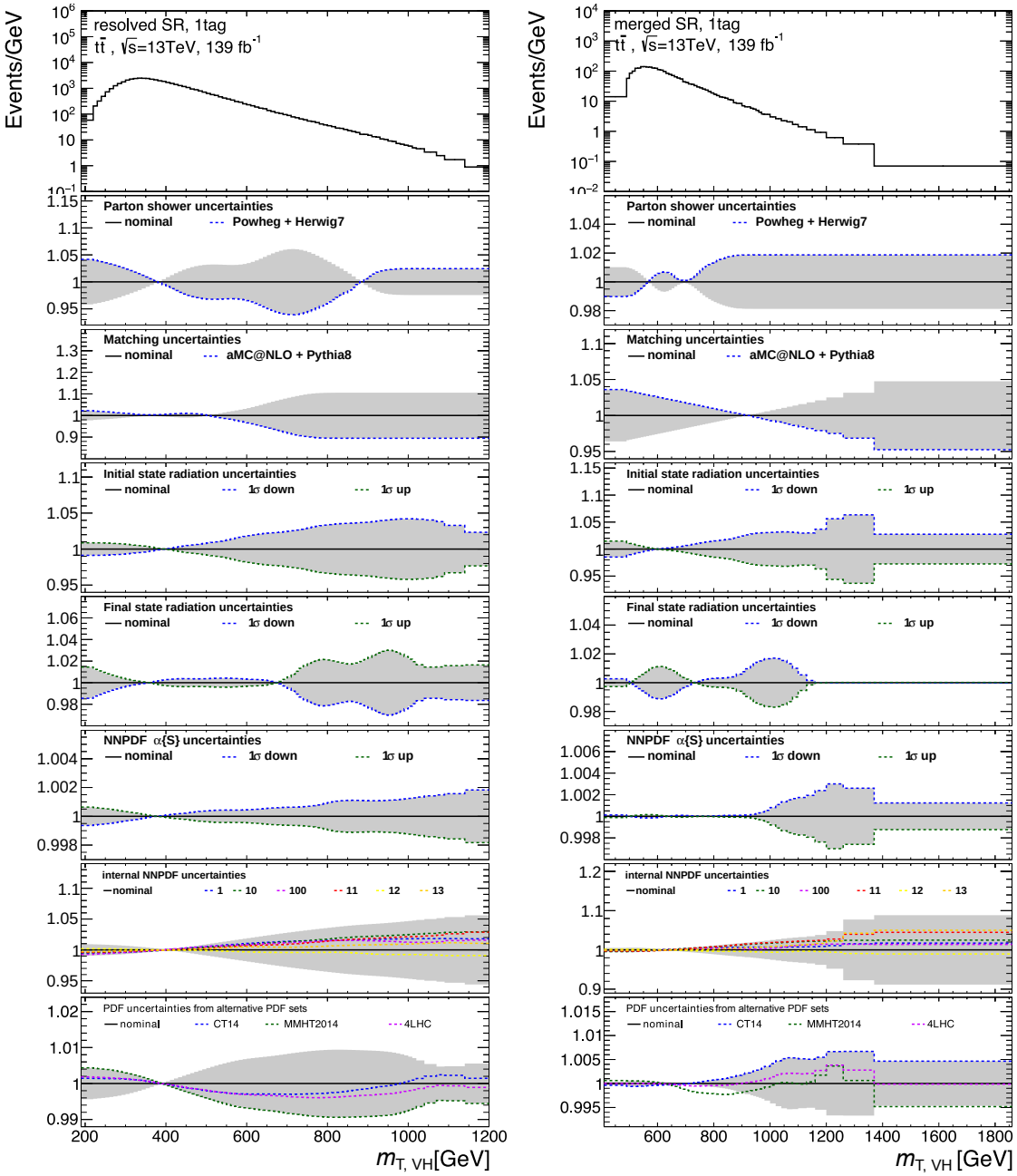

Figure 5.17: Impact of various modelling uncertainties on the shape of the $m_{T,Vh}$ distribution from $t\bar{t}$ events. The left-hand (right-hand) side corresponds to signal regions with resolved (merged) event topology with one b-tagged jet per event. The nominal distributions are shown in the first panel from the top, and below them the relative changes due to the uncertainties from: the PS; the ME matching; ISR; FSR; α_s; intrinsic PDF variations; different PDF sets. The grey area in the ratio panels is obtained as an envelope of the corresponding uncertainty components and defines the $\pm 1\sigma$ interval of the given uncertainty.

5.7 Optimisation studies

5.7.1 Track jets with variable radius parameter

Track jets with a variable radius parameter (*cf.* Section 3.4.1) are introduced to increase the signal reconstruction efficiency in events with highly boosted Higgs bosons. The effective radius of the jets from the Higgs boson decay decreases significantly at large Higgs boson momenta. In order to improve the reconstruction of track jets, an anti-k_t algorithm is used with a radius parameter depending on the track jet p_{T}, rather than using a fixed radius parameter of $R = 0.2$. A comparison of the signal efficiency in the merged event topology for each of the two types of track jets can seen in Figure 5.18. Here, similar to Figure 5.5, the acceptance times efficiency, $A \times \varepsilon$, is shown for events with different b-jet multiplicities. In contrast to Figure 5.5, the number of b-jets are counted based on generator-level flavour information, thus eliminating potential biases arising from the employed b-tagging algorithm. Only the two leading-p_{T} track jets in the event are considered, even if more than two track jets are reconstructed. The comparison shows that the total $A \times \varepsilon$ after summing over all signal regions with merged topology is the same for both track jet collections and for all three signal processes. However, a significant fraction of events migrates from the one b-jet to the two b-jet region at large resonance masses. This is particularly prominent for the HVT Z' signal with masses of $m_{Z'} > 2\,\mathrm{TeV}$. While the events with one b-jet become dominant at $m_{Z'} > 3\,\mathrm{TeV}$ in the case of track jets with a fixed radius parameter, these events partially migrate to the region with two b-jets. This leads to an increased signal sensitivity due to the small background contamination in the two b-tag region.

5.7.2 Optimisation of the V+jet background modelling

The modelling of the V+jets ($V = W, Z$) background processes depends on the flavour content of the associated jets. This background contribution is therefore classified into several categories according to the flavour content, while at the same time combining the components with similar shapes of the $m_{\mathrm{T},\,Vh}$ distribution to reduce the number of degrees of freedom in the fit to data. Similarly as in the study presented in Section 4.6, different groupings of V+jets background components are studied.

Figure 5.19 shows the $m_{\mathrm{T},\,Vh}$ distributions of different V+jets background components normalised to unit area. In Figure 5.19(a), the shape of the $m_{\mathrm{T},\,Vh}$ distribution is shown for the Z+hf process, and the corresponding individual sub-contributions from the Z+bb, Z+bc, and Z+cc processes. The ratio panel shows that all distributions are compatible with each other over the largest part of the $m_{\mathrm{T},\,Vh}$ range, allowing for the combination of the individual components into a single Z+hf background category. The corresponding distributions of the remaining Z+jets background components are shown in Figure 5.19(b). The shape of the Z boson plus at least one light jet (Z+l) component differs

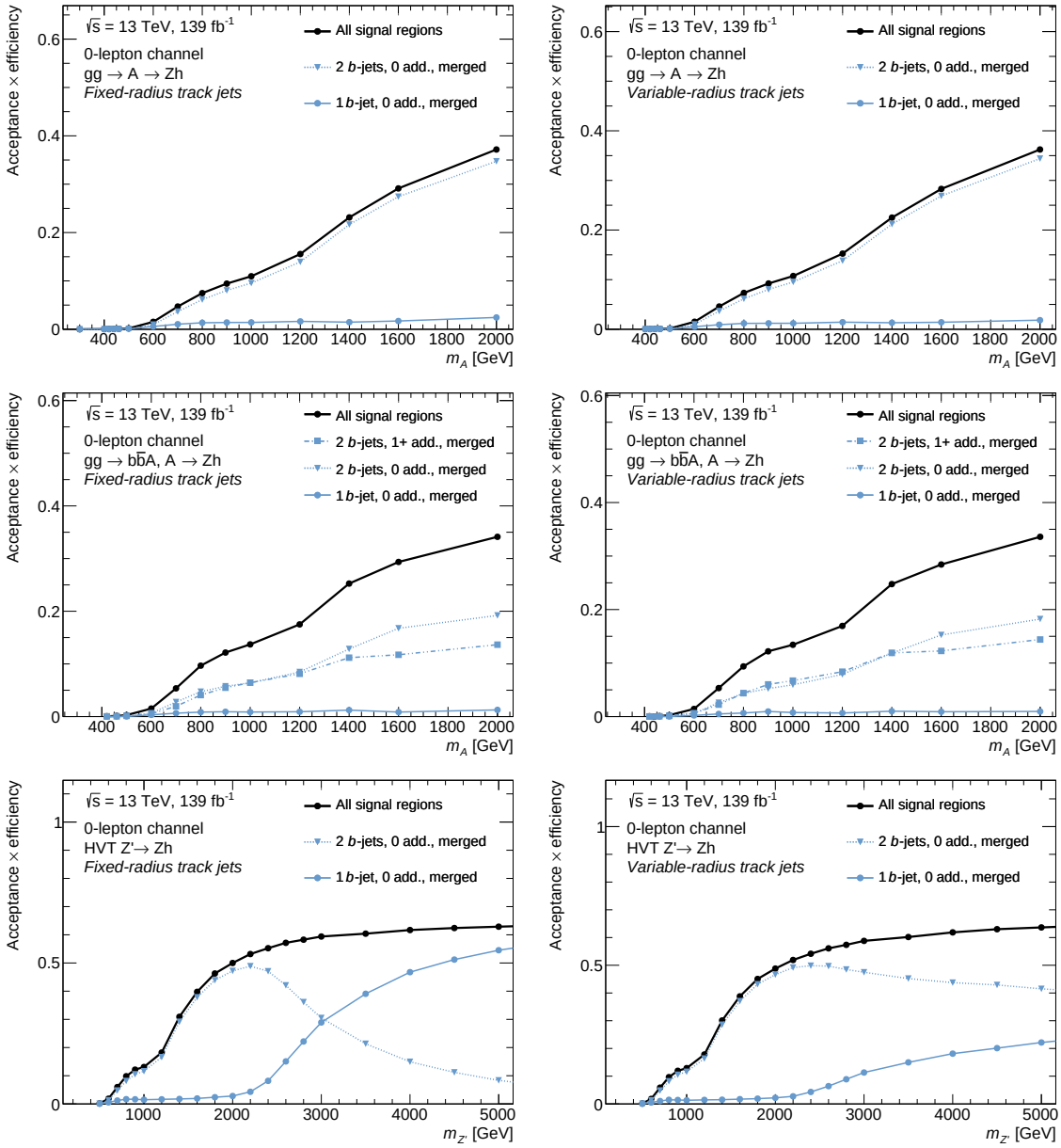

Figure 5.18: Product of signal acceptance and reconstruction efficiency in the merged event topology when using track jets with a *(left-hand side)* fixed and *(right-hand side)* variable radius parameter for the various signal processes as a function of the resonance mass. The signal modes are: *(top row)* $gg \to A \to Zh \to \nu\bar{\nu}b\bar{b}$; *(middle row)* $gg \to bbA, A \to Zh \to \nu\bar{\nu}b\bar{b}$; and *(bottom row)* $q\bar{q} \to Z' \to Zh \to \nu\bar{\nu}b\bar{b}$. The total product of acceptance and efficiency (black full circle markers) are shown together with the separate values for each of the signal regions. The number of additional b-tagged jets not matched to the leading large-radius jet is abbreviated with "add." in the legends.

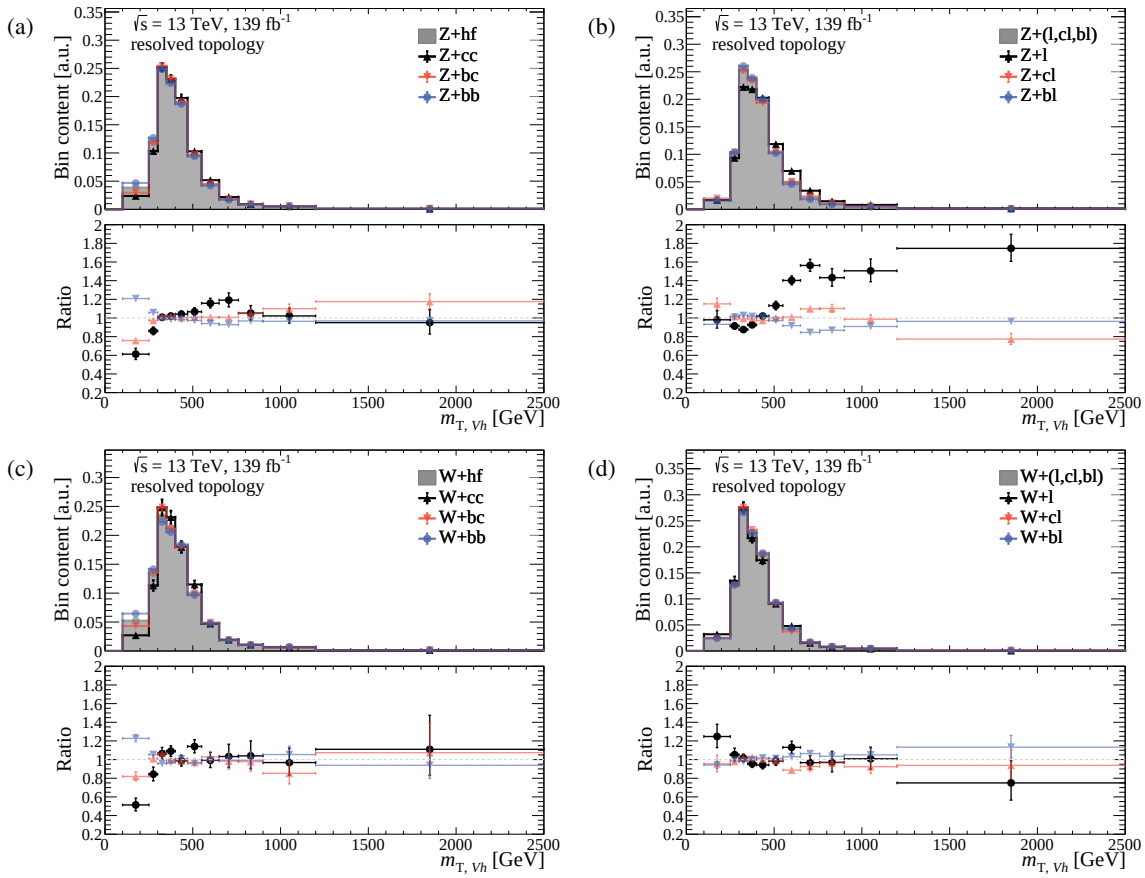

Figure 5.19: The expected shape of the $m_{\mathrm{T},\,Vh}$distributions for the different V+jets background components in events with resolved event topology, shown for: Z boson production with *(a)* two heavy flavour jets, and *(b)* fewer than two heavy flavour jets; and W boson production with *(c)* two heavy flavour jets, and *(d)* fewer than two heavy flavour jets. The lower panels show the ratio with respect to the filled histogram.

significantly from the corresponding distributions from a Z boson plus exactly one heavy flavour (b or c) and one light jet (Z+bl or Z+cl) at large $m_{\mathrm{T},\,Vh}$ values. Therefore, two additional categories are defined: Z+(bl, cl) and Z+l.

The corresponding distributions for the W+ jets background processes are shown in Figures 5.19(c) and 5.19(d). Similar to the Z+hf category, the W+hf category containing W+bb, W+bc, and W+cc processes is defined. In contrast to the differences between the Z+l and Z+(bl, cl) background components, however, the shape of the $m_{\mathrm{T},\,Vh}$ distribution of the W+l component is in good agreement with the shape of the distributions from the W+(bl, cl) processes. However, for a consistent treatment of W+jets and Z+jets processes, the same splitting into W+(bl, cl) and W+l categories is used.

In summary, the following six V+jets background components are modelled and fitted separately to the data in the presented analysis: Z+hf, Z+(bl, cl), Z+l, W+hf, W+(bl, cl), and W+l.

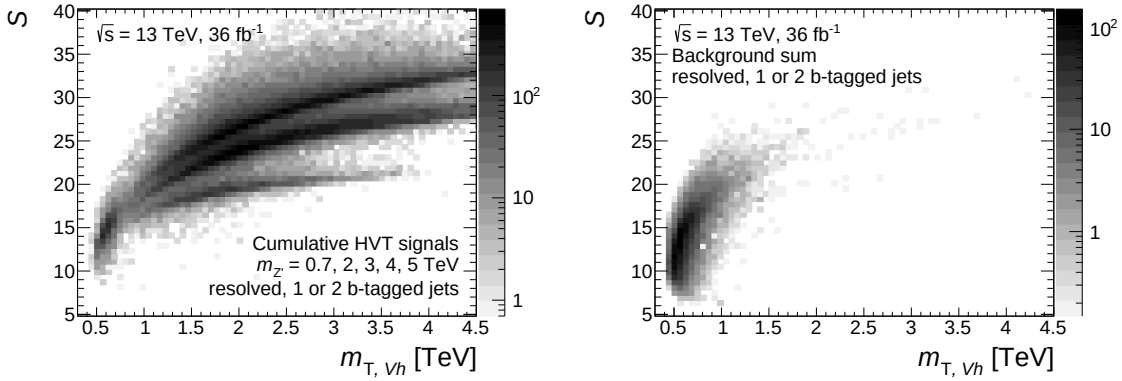

Figure 5.20: Two-dimensional distributions of the $E_{\mathrm{T}}^{\mathrm{miss}}$ significance S for simulated *(left)* signal and *(right)* background processes in dependence on $m_{\mathrm{T},\,Vh}$. Resolved-topology events with one or two b-tagged jets and the nominal selection requirements except for the S requirement are shown. The data correspond to an integrated luminosity of 36 fb^{-1} and the z-axis shows the number of selected events.

5.7.3 Suppression of multijet background using the $E_{\mathrm{T}}^{\mathrm{miss}}$ significance

The contribution of multijet background processes with multiple jets in the final state is expected to be small in the introduced signal regions. Similar previous analyses found the multijet background contribution to be negligible [150, 230], especially when employing requirements on the object-based $E_{\mathrm{T}}^{\mathrm{miss}}$ significance (S, *cf.* Section 3.4.1) for the event selection. The employment of this discriminant variable is therefore studied also in the presented analysis. In a first step, an optimal lower threshold on S is determined, which maximises the expected signal significance. In a second step, the efficacy of the S requirement is evaluated in a data-driven measurement of the multijet background contribution (*cf.* Section 5.7.4).

A large value of S indicates that the observed $E_{\mathrm{T}}^{\mathrm{miss}}$ does not originate solely from detector resolution effects and suggests that an unobserved particle such as a neutrino escaped the detector without any interaction with the detector material. Thus, a lower threshold on S allows for the discrimination between the signal and the background processes with minor or no neutrino contributions. The distribution of S in dependence of $m_{\mathrm{T},\,Vh}$ is shown in Figure 5.20, separately for the signal and the total background contribution. Here, only HVT Z' signal processes are included. However, the 2HDM signal processes are expected to behave analogously, as the $E_{\mathrm{T}}^{\mathrm{miss}}$ stems from the same $Z \to \nu\bar{\nu}$ decay. It can be seen that a lower threshold on S can be used to suppress background contributions in the $m_{\mathrm{T},\,Vh}$ region below approximately 1 TeV. The goal is therefore to find the optimal value of the lower threshold on S in this region, without compromising the signal selection efficiency by a significant amount.

In order to find the optimal S-threshold value, the $m_{\mathrm{T},\,Vh}$ slices corresponding to $m_{\mathrm{T},\,Vh}$ bins with a

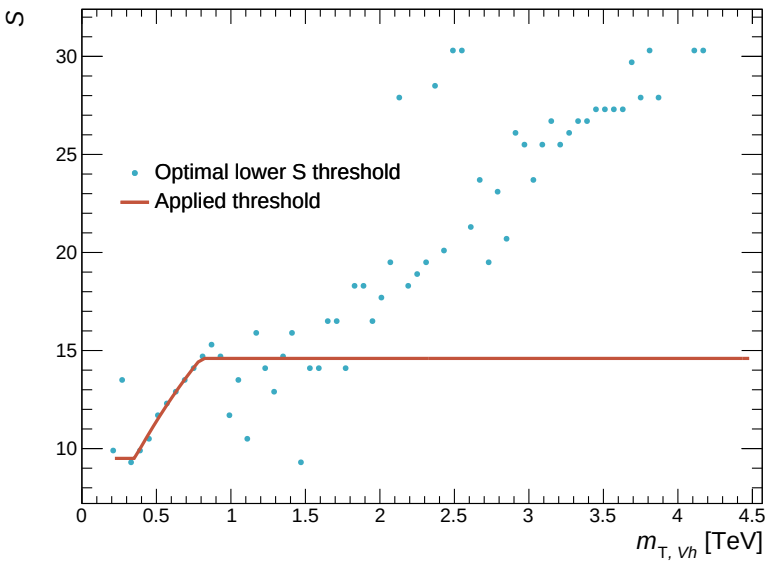

Figure 5.21: Optimal lower threshold on S (blue dots) which maximises the expected $Z' \to Zh \to \nu\bar{\nu}b\bar{b}$ signal significance for the given $m_{T,\,Vh}$ value. The simplified threshold dependence on $m_{T,\,Vh}$, as applied in the analysis, is also shown (full red line).

width of 60 GeV in Figure 5.20 are studied separately. In each slice, the expected significance Z is calculated for varying S thresholds using the expression [231]

$$Z(n, b, \sigma) = \sqrt{2\left(n \ln\left[\frac{n(b+\sigma^2)}{b^2+n\sigma^2}\right] - \frac{b^2}{\sigma^2}\ln\left[1+\frac{\sigma^2(n-b)}{b(b+\sigma^2)}\right]\right)}, \tag{5.5}$$

where n is the total number of expected events, defined as $n = s + b$, with s being the expected number of signal and b the expected number of background events. The quantity b is only known with an uncertainty σ, which is assumed to be 10 % in all cases[2]. This formula assumes $n > b$, *i.e.* a positive number of signal events.

For every $m_{T,\,Vh}$ slice, the range $0 < S < 60$ is divided into 100 bins of equal width. Given the lower threshold value on the E_T^{miss} significance in the i-th bin, S_i, the expected significance Z_i is calculated using Equation (5.5) for all signal and background events that satisfy $S \geq S_i$ in a given $m_{T,\,Vh}$ slice. The optimal lower threshold S^{opt} for a given $m_{T,\,Vh}$ yields a maximum signal significance Z. The resulting threshold values in each $m_{T,\,Vh}$ slice are shown as the blue dots in Figure 5.21 for the HVT Z' signal process. The figure also shows the simplified S threshold dependence on $m_{T,\,Vh}$ as actually applied in the data analysis. In the mass window below 300 GeV, the lower threshold of $S^{thr} = 9$

[2] The study was also repeated using a significantly higher value of $\sigma = 50$ % and the impact on the outcome was found to be negligible.

is applied, as no significant amount of signal events is observed below this value. The quadratic dependence of S^{opt} on $m_{\text{T, }Vh}$ in the mass window 300 GeV $< m_{\text{T, }Vh} <$ 800 GeV is obtained from the fit to S^{opt} values, resulting in the following parametrisation:

$$S(m_{\text{T, }Vh}) = 4.06 + 17.1\frac{m_{\text{T, }Vh}}{1\,\text{TeV}} - 5.96\frac{(m_{\text{T, }Vh})^2}{1\,\text{TeV}^2}. \tag{5.6}$$

With increasing $m_{\text{T, }Vh}$ values, the background contribution decreases, which is why the requirement on S can be kept at a constant level of $S^{\text{thr}} = 15.56$ for $m_{\text{T, }Vh} > 800$ GeV. This value corresponds to the S^{thr} value from Equation (5.6) at $m_{\text{T, }Vh} = 0.8$ TeV.

5.7.4 Multijet background measurement using the ABCD template method

The total number of multijet events in each signal region of the analysis is expected to be very small and is estimated using the so-called ABCD method, based on the extrapolation from three control regions (B, C, and D) in data into the signal region A. The regions, A, B, C, and D are defined by the requirements on the multijet-sensitive discriminating variables S and $\min[\Delta\phi(\vec{p}_{\text{jet}}, \vec{E}_{\text{T}}^{\text{miss}})]$.

Region A is the signal region with events fulfilling all requirements specified in Table 5.2. The number of multijet events in this target region of the ABCD method is estimated from the other three regions. In region D, the requirements on S and $\min[\Delta\phi(\vec{p}_{\text{jet}}, \vec{E}_{\text{T}}^{\text{miss}})]$ are both inverted compared to the nominal selection, *i.e.* $S < S^{\text{thr}}$ and $\min[\Delta\phi(\vec{p}_{\text{jet}}, \vec{E}_{\text{T}}^{\text{miss}})] < \pi/9$ or $\pi/6$, depending on the number of jets in the event (*cf.* Section 5.4). In region B, the requirement on S is inverted, while the $\min[\Delta\phi(\vec{p}_{\text{jet}}, \vec{E}_{\text{T}}^{\text{miss}})]$ requirement is not, and vice versa for the region C. The definition of each region is illustrated in Figure 5.22. Regions B, C, and D are signal-depleted, while also having an enhanced contribution of multijet background events compared to other background processes. Assuming that the discriminating variables S and $\min[\Delta\phi(\vec{p}_{\text{jet}}, \vec{E}_{\text{T}}^{\text{miss}})]$ are uncorrelated, the following equation holds for the number of multijet background events N_A in the signal region A:

$$N_A = \frac{N_C}{N_D} N_B, \tag{5.7}$$

where $N_i \in \{B, C, D\}$ is the number of multijet events in the regions B, C, and D, respectively. Assuming signal-free regions B, C, and D, the number of multijet background events in each region is obtained from the difference between observed data and predicted non-multijet contributions. Therefore, Equation (5.7) can be written as

$$N_A = \frac{N_C^{\text{data}} - N_C^{\text{MC}}}{N_D^{\text{data}} - N_D^{\text{MC}}}(N_B^{\text{data}} - N_B^{\text{MC}}), \tag{5.8}$$

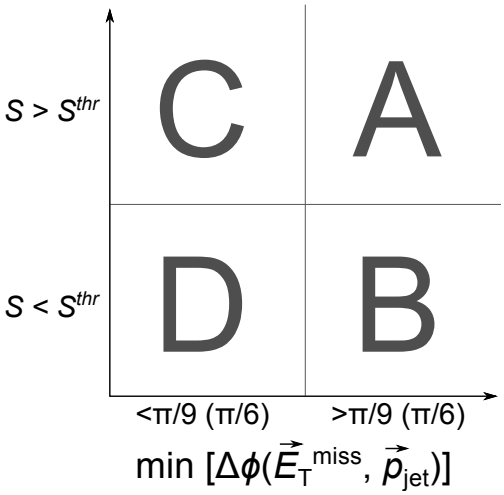

Figure 5.22: Definition of the data regions A, B, C, and D used for the data-driven measurement of the multijet background contribution. The regions are distinguished based on two discriminating variables: $\min[\Delta\phi(\vec{p}_{\text{jet}}, \vec{E}_{\text{T}}^{\text{miss}})]$ and the $E_{\text{T}}^{\text{miss}}$ significance S. The threshold on $\min[\Delta\phi(\vec{p}_{\text{jet}}, \vec{E}_{\text{T}}^{\text{miss}})]$ is $\pi/9$ or $\pi/6$, depending on the number of jets in the event, as described in the text.

where N_i^{data} is the total number of events observed in the region i and N_i^{MC} is the non-multijet background contribution predicted from simulation in that region. The latter is considered as contamination of the multijet control regions B, C, and D and needs to be subtracted to obtain the pure multijet component in each control region. The expression in Equation (5.8) can also be generalised to determine the multijet content in each bin of the $m_{\text{T, }Vh}$ distribution separately. The procedure is first applied for the signal regions with the resolved topology, since the multijet contribution in the signal regions with merged topology can in general be assumed to be smaller, mainly due to the stricter $E_{\text{T}}^{\text{miss}}$ requirement. The $m_{\text{T, }Vh}$ distributions for data and all simulated non-multjiet backgrounds are determined separately for the regions B, C, and D. The difference between data and simulation in region B is referred to as the multijet template, and is expected to have the same shape as the multijet $m_{\text{T, }Vh}$ distribution in the signal region A, but with a different normalisation. The transfer factor, *i.e.* the normalisation scaling, from region B to region A is derived by dividing the corresponding number of multijet background events (determined from the "data−MC" distributions) in regions C and D. Figures 5.23 and 5.24 show the resulting multijet templates for the signal regions with one and two b-tagged jets, respectively.

The total number of estimated multijet events in each region is reported in Table 5.8. With an estimated 66.9 ± 14.5 events in the 1 b-tag channel and 26.2 ± 8.3 events in the 2 b-tag channel, the expected multijet contribution is about an order of magnitude smaller than the statistical uncertainty on the total expected number of events in the signal region (*cf.* Table 5.5), implying a negligible impact of the multijet contribution to the signal sensitivity. The multijet contribution in the signal regions with merged topology can therefore also be neglected.

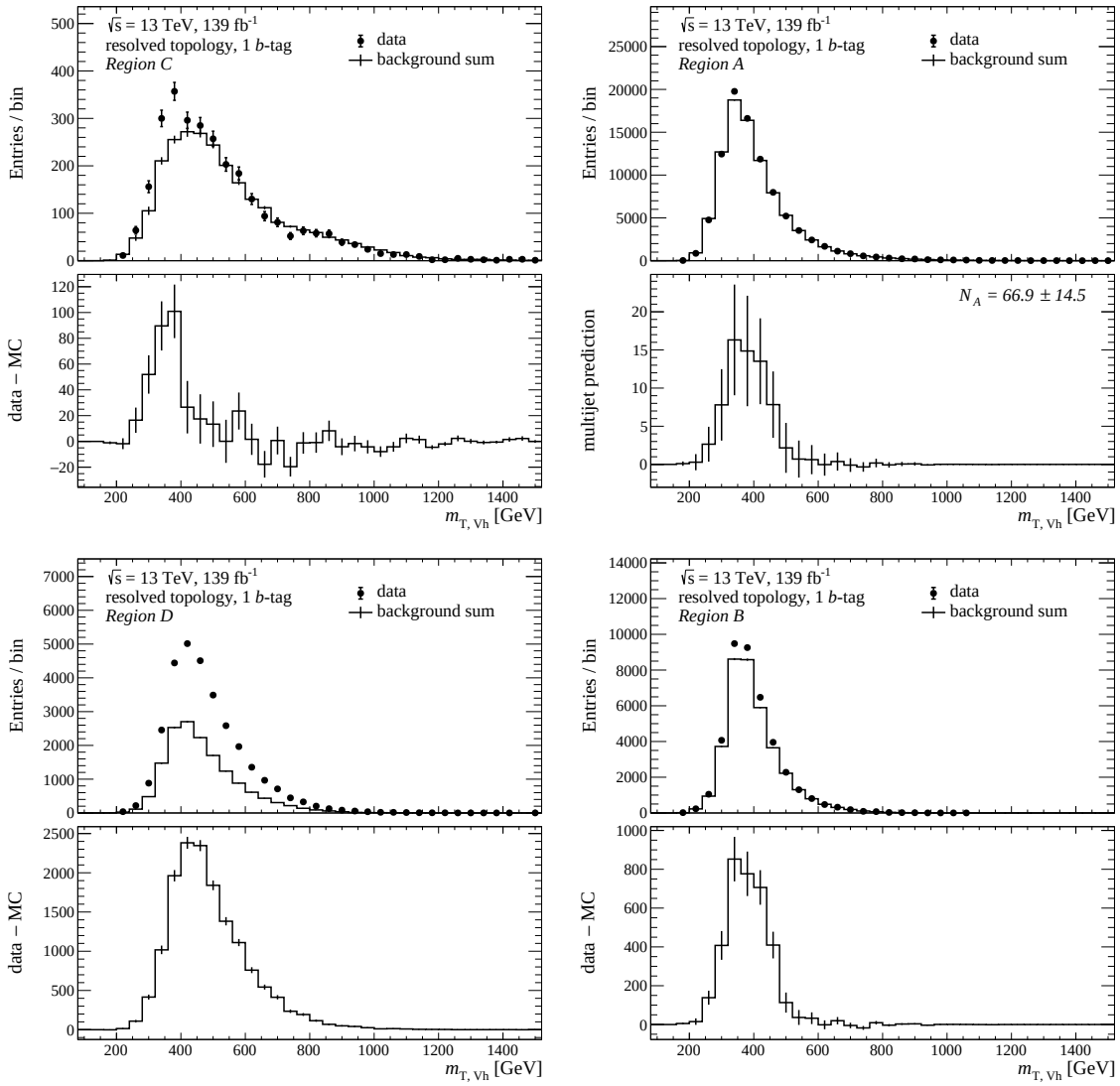

Figure 5.23: The $m_{\mathrm{T,}\,Vh}$ distribution in the signal region A and the multijet control regions B, C, and D for events with a dijet mass of 110 GeV $< m_{jj} <$ 140 GeV in the resolved topology with exactly one b-tagged jet. The upper panels show the observed data and the sum of all non-multijet backgrounds in the corresponding region. For the control regions B, C, and D, the bottom panels show the multijet template defined as the difference between observed data and non-multijet backgrounds ("data−MC"). For the signal region A, the bottom panel shows the multijet template from region B scaled with the transfer factor ("multijet prediction") as described in the text. The obtained number of multijet events N_A is also quoted.

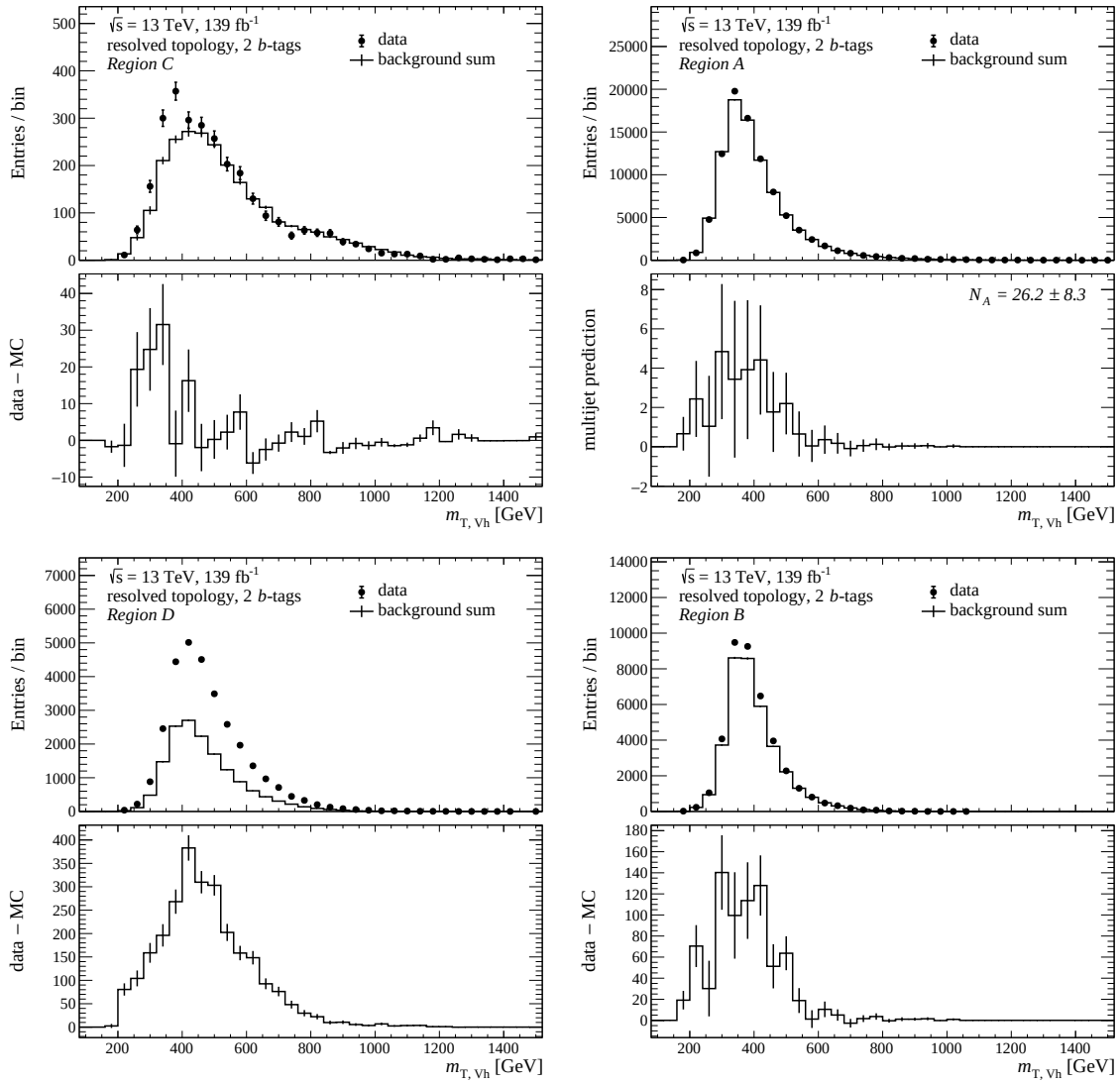

Figure 5.24: The $m_{\mathrm{T},Vh}$ distribution in the signal region A and the multijet control regions B, C, and D for events with a dijet mass of 110 GeV $< m_{jj} <$ 140 GeV in the resolved topology with exactly two b-tagged jets. The upper panels show the observed data and the sum of all non-multijet backgrounds in the corresponding region. For the control regions B, C, and D, the bottom panels show the multijet template defined as the difference between observed data and non-multijet backgrounds ("data−MC"). For the signal region A, the bottom panel shows the multijet template from region B scaled with the transfer factor ("multijet prediction") as described in the text. The obtained number of multijet events N_A is also quoted.

Table 5.8: Number of multijet events in the control regions B, C, and D, and the determined number of multijet events in the signal region N_A for events with the resolved topology and one or two b-tagged jets at an integrated luminosity of 139 fb^{-1}.

b-tags	$N_B^{\text{data}-\text{MC}}$	$N_C^{\text{data}-\text{MC}}$	$N_D^{\text{data}-\text{MC}}$	N_A
1	3498 ± 229	288 ± 59	15072 ± 183	66.9 ± 14.5
2	758 ± 85	90.8 ± 26.8	2631 ± 72	26.2 ± 8.3

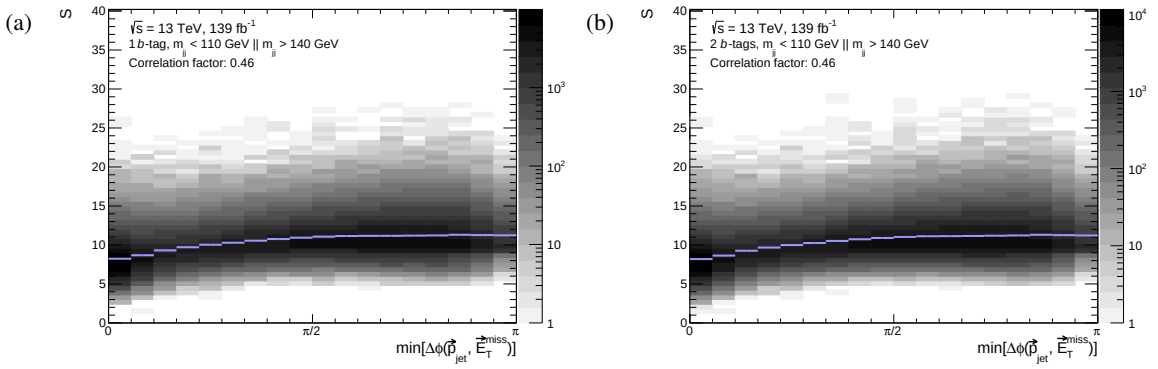

Figure 5.25: Two-dimensional distribution of $\min[\Delta\phi(\vec{p}_{\text{jet}}, \vec{E}_{\text{T}}^{\text{miss}})]$ and S in observed data for the sideband regions with the resolved event topology and with *(a)* 1 b-tag, and *(b)* 2 b-tags. In every $\min[\Delta\phi(\vec{p}_{\text{jet}}, \vec{E}_{\text{T}}^{\text{miss}})]$ slice, the mean S value is overlaid (blue line). A correlation between the two variables of 46 % is observed in both cases.

Several cross-checks are performed to confirm the validity of this result. The first cross-check investigates the impact of the correlations between the two chosen discriminant observables, S and $\min[\Delta\phi(\vec{p}_{\text{jet}}, \vec{E}_{\text{T}}^{\text{miss}})]$. These are not fully uncorrelated, reaching correlation values of more than 40 %, as can be seen in Figure 5.25. In order to understand the effect of this correlation on the multijet estimate, the regions C and D that fail the $\min[\Delta\phi(\vec{p}_{\text{jet}}, \vec{E}_{\text{T}}^{\text{miss}})]$ requirement are further divided into four new regions, labelled A′, B′, C′, and D′, as illustrated in Figure 5.26. Each event in these regions fails the $\min[\Delta\phi(\vec{p}_{\text{jet}}, \vec{E}_{\text{T}}^{\text{miss}})]$ requirement from Table 5.2. The regions C′ and D′ select events with $\min[\Delta\phi(\vec{p}_{\text{jet}}, \vec{E}_{\text{T}}^{\text{miss}})] < 5°$, whereas regions A′ and B′ select events with $5° < \min[\Delta\phi(\vec{p}_{\text{jet}}, \vec{E}_{\text{T}}^{\text{miss}})] < 20°(30°)$, depending on the number of jets in the event. Since the region A′ is disjoint from the signal region A, the observed number of events in the region A′ is not blinded and can be looked at and compared to the estimate from the regions B′, C′, and D′. The ABCD method applied to these modified regions of data predicts 190 ± 27 multijet events in the region A′, while only 96 ± 53 are observed. Conservatively, this difference could be used as a non-closure uncertainty on the normalisation of the multijet template. This would yield a normalisation uncertainty in the normalisation not larger than a factor of two, which is still an order of magnitude below the statistical uncertainty on the total number of expected events in the signal region.

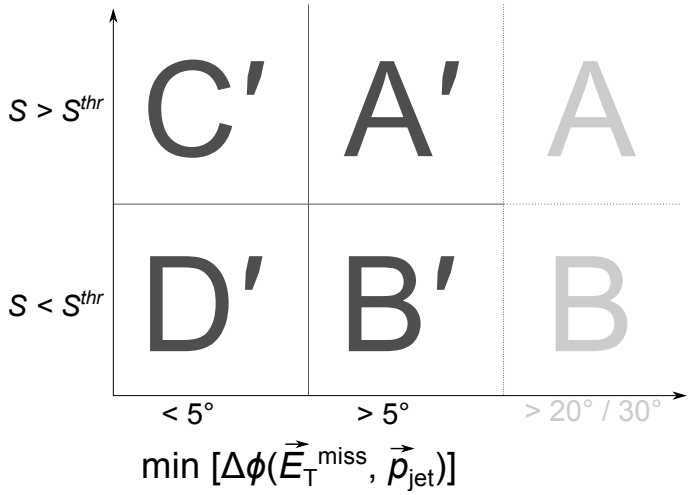

Figure 5.26: Modified regions A′, B′, C′, and D′ used for the validation of the multijet background estimate. All regions fail the $\min[\Delta\phi(\vec{p}_{\text{jet}}, \vec{E}_{\text{T}}^{\text{miss}})]$ cut of 20° or 30° (depending on the number of jets in the event), and are divided by the $\min[\Delta\phi(\vec{p}_{\text{jet}}, \vec{E}_{\text{T}}^{\text{miss}})]$ threshold at 5°.

In another cross-check, the number of multijet events is predicted from the m_{jj} sidebands. Here, outside the mass window, more events are predicted by simulation than there are observed in the data (*cf.* Table 5.5). If the discrepancy is assumed to come only from the multijet background, this would yield a negative number of multijet events, and the multijet contribution can therefore be considered negligible. Nevertheless, ABCD sideband regions are defined by repeating the approach sketched in Figure 5.22 and a predicted number of multijet events in the sideband region of $N_A^{\text{sideband}} = 292 \pm 25$ (88 ± 12) is obtained for events with one (two) b-tagged jet(s). Once more, the ABCD template method predicts a number of multijet background events that can be considered both conservative (*i.e.* larger than the one obtained from the "data−MC" value in the sideband region A) and negligible (*i.e.* much smaller than the statistical uncertainty on the predicted number of background events in the sideband region A).

Ultimately, the multijet background is not considered for the final interpretation of data.

5.8 Fit model for the statistical interpretation of data

The statistical analysis is based on the maximisation of the likelihood function from Equation (4.3), which is achieved by minimising the test statistic from Equation (4.6). The nuisance parameters in the likelihood function account for the statistical uncertainty of simulated signal and background samples as well the experimental and theoretical systematic uncertainties outlined in Section 5.6.

The fit is performed using the $m_{\mathrm{T},\,Vh}$ distribution as the final discriminant simultaneously in the signal and control regions introduced in Table 5.3. This section summarises the fitted background components, as well as the nuisance parameters employed in the fit.

Nuisance parameters related to uncertainties in background normalisations are implemented as scale factors for individual or groups of background processes. They are either unconstrained or log-normal constrained. Nuisance parameters related to the shape of the $m_{\mathrm{T},\,Vh}$ distributions are log-normal constrained and are also implemented either for individual or groups of background processes. Unconstrained nuisance parameters are initialised to unity and then allowed to float freely, while log-normal constrained nuisance parameters are initialised to zero and their post-fit deviation from zero correlates with the post-fit size of the corresponding uncertainty. More details about the types of nuisance parameters are given in Section 4.10.

5.8.1 General fit configuration

For the HVT Z' boson and 2HDM A pseudo-scalar interpretations, all signal and $m_{jj/J}$ sideband regions with exactly one or two b-tagged (track) jets are simultaneously fitted (*cf.* Table 5.3). For the merged event topology, only those signal and sideband regions without additional b-tagged track jets that are not matched to the leading large-radius jet are considered.

The background processes are grouped as follows

- top quark processes, consisting of $t\bar{t}$, single top quark, $t\bar{t}V$, and $t\bar{t}H$ processes;
- Z+hf, comprising events with a Z boson and the heavy flavour jet combinations bb, bc, and cc;
- Z+(bl, cl), comprising events with a Z boson and one b- or c-jet, accompanied by zero or more light-flavour jets (= u, d, s quark, or a gluon);
- Z+l, comprising events with a Z boson and zero or more light-flavour jets;
- W+hf, comprising events with a W boson and the heavy flavour jet combinations bb, bc, and cc;
- W+(bl, cl), comprising events with a W boson and one b- or c-jet, accompanied by zero or more light-flavour jets;
- W+l, comprising events with a W boson and zero or more light-flavour jets;
- SM diboson events, comprising the diboson production processes $qq \to WW/ZZ/WZ$ and $gg \to ZZ/WW$;

- SM Vh background, comprising the SM Vh production in the channels $qq \to Zh/Wh$ and $gg \to Zh$, with subsequent $h \to b\bar{b}$ Higgs boson decays. The Higgs boson mass of 125 GeV is assumed.

5.8.2 Normalisation-related nuisance parameters

Normalisation-related nuisance parameters allow for modifications of the original normalisation of a given background process, defined by its production cross section times the acceptance times the reconstruction efficiency. The nuisance parameters account for both the uncertainty on the total cross section, and on the acceptances in different kinematic regions of the analysis.

The normalisation uncertainties for all top quark, Z+hf and Z+(bl, cl) processes are described by unconstrained nuisance parameters, separately for each process. This allows for the data-driven fit of the corresponding background normalisations from the control regions in data. These normalisation parameters are applied globally in all signal and sideband regions.

The normalisation nuisance parameters are defined according to Tables 5.6 and 5.7. Unconstrained nuisance parameters are defined for the processes marked with "float" and for the others the pre-fit constraint is given by the specified value.

5.8.3 Shape-related nuisance parameters

Shape-related nuisance parameters allow for the modification of the nominal shape of the $m_{\mathrm{T},\,Vh}$ distribution of a given background or signal sample. Each shape uncertainty is implemented in terms of an alternative distribution corresponding to a 1σ uncertainty. The amount of the modification after the fit (*i.e.* the morphing between the nominal and alternative shapes) is given by the post-fit value ("pull") on the corresponding nuisance parameter. A pull of zero corresponds to using only the nominal distribution and a pull of one to the 1σ deviation from the nominal shape (*i.e.* to the alternative shape). All other pull values correspond to a morphing between the nominal and alternative distributions by an appropriate amount by means of linear inter- and extrapolation. At pre-fit level, all shape nuisance parameters are set to zero.

The main sources of $m_{\mathrm{T},\,Vh}$ shape variations are the experimental uncertainties, in particular the b-tagging and jet uncertainties (*cf.* Section 5.6.1). Moreover, modelling uncertainties obtained with alternative signal and background samples (*cf.* Section 5.6.2) are also translated into shape nuisance parameters. Finally, the residual mismodelling of some background processes (*cf.* Section 5.5) is also translated into shape uncertainties.

5.9 Results

This section contains the results of the statistical interpretation of the Run 2 dataset within the framework of the HVT and 2HDM models. In Section 5.9.1, the results of the search for a HVT Z' boson resonance in the $\nu\bar{\nu}b\bar{b}$ final state are shown. The results of the search for a 2HDM A boson resonance produced via gluon fusion (ggA) in the same final state are presented in Section 5.9.2. The results are reproduced from the data published in [15].

5.9.1 Results of the HVT Z' boson search

In the search for a Z' boson as predicted by the HVT model, a fit to data is performed according to the strategy outlined in the previous sections. In general, the expected post-fit background-only event yields are compatible with the observed data within the uncertainties, as reported in Table 5.9. The observed data and the expected post-fit $m_{\mathrm{T},\,Vh}$ distributions are shown in Figure 5.27 for the signal regions and in Figure 5.28 for the $m_{jj/J}$ sideband regions. For comparison, the distributions also show the total expected background prior to the fit (pre-fit). The largest differences (up to approximately a factor of two) with respect to the total post-fit background are observed in the tails of the $m_{\mathrm{T},\,Vh}$ spectra, where the modelling uncertainties are non-negligible.

The signal distribution is employed in the signal-plus-background fit to data to determine the upper limit on the signal cross section in an iterative procedure, starting with a reference cross section $\sigma(pp \to Z') \times \mathcal{B}(Z' \to Zh) \times \mathcal{B}(h \to b\bar{b}, c\bar{c}) \times \mathcal{B}(Z \to \nu\bar{\nu}) = 0.0002\,\mathrm{pb}$. The signal strength is then varied in steps until the signal is excluded at the 95 % C.L., which is calculated using Equation (4.13). A dedicated constrained fit is performed at every step to obtain an updated estimate of the post-fit uncertainties σ. For the example signal shown in Figure 5.27 with a Z' resonance mass of $m_{Z'} = 700\,\mathrm{GeV}$, this method yields an upper limit at the 95 % C.L. on the cross section of

$$\sigma_{\mathrm{up}}(pp \to Z') \times \mathcal{B}(Z' \to Zh) \equiv \sigma^{\mathrm{up}}_{pp\to Z'\to Zh} = 3.3 \times 10^{-2}\,\mathrm{pb}, \tag{5.9}$$

where the SM values for $\mathcal{B}(Z \to \nu\bar{\nu}) = 0.2$ and $\mathcal{B}(h \to b\bar{b}, c\bar{c}) = 0.5977$ are assumed.

Similarly, the expected upper limit is obtained from the signal-plus-background fit to the expected background only distribution—with nuisance parameters set to the values obtained from the background-only fit to the data—yielding $\sigma^{\mathrm{up,\,exp.}}_{pp\to Z'\to Zh} = 2.89^{+1.14}_{-0.81} \times 10^{-2}\,\mathrm{pb}$. The uncertainties thereby correspond to the Gaussian quantile at the signal strength $\mu' = 0$ (*cf.* Equation (4.14)).

The limit calculation is repeated for all signal mass hypotheses. The resulting observed and expected cross section limits together with the corresponding uncertainties are quoted in Table 5.10 and

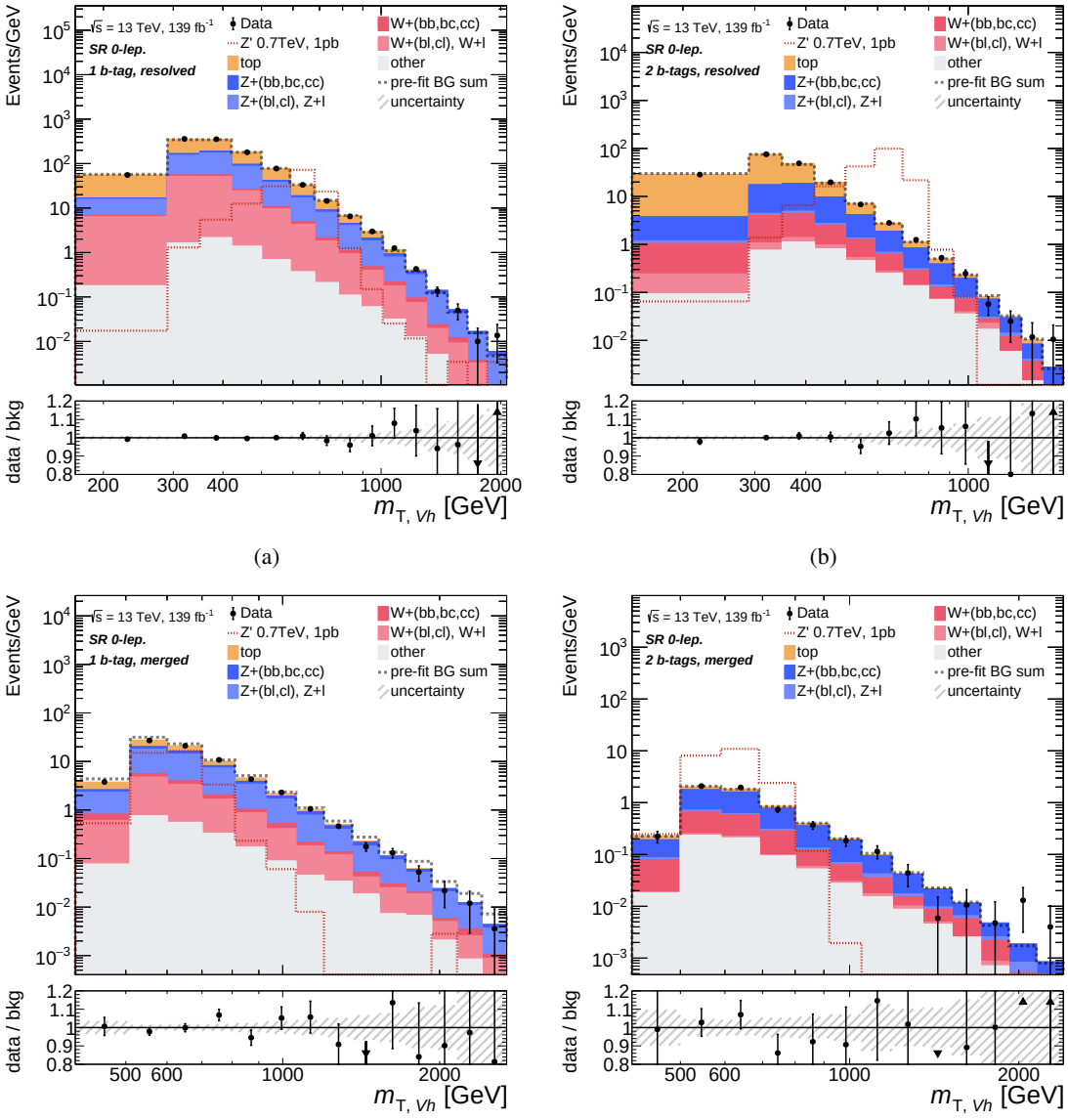

Figure 5.27: Observed and expected post-fit $m_{\mathrm{T},\,Vh}$ distributions in the signal regions of the $Zh \to \nu\bar{\nu}b\bar{b}$ resonance search. Events from the resolved event selection are shown in panels *(a)* and *(b)*, whilst panels *(c)* and *(d)* show events from the merged event selection. Panels *(a)* and *(c)* contain events with one b-tag and panels *(b)* and *(d)* events with two b-tags. The total pre-fit background sum is indicated by the dashed black line and the expected signal distribution of a 700 GeV HVT Z' boson with $\sigma(pp \to Z') \times \mathcal{B}(Z' \to Zh) \times \mathcal{B}(Z \to \nu\bar{\nu}) \times \mathcal{B}(h \to b\bar{b}, c\bar{c}) = 1$ pb is shown as the dotted red line. The data-to-background ratio together with the post-fit background uncertainty is shown in the bottom panels.

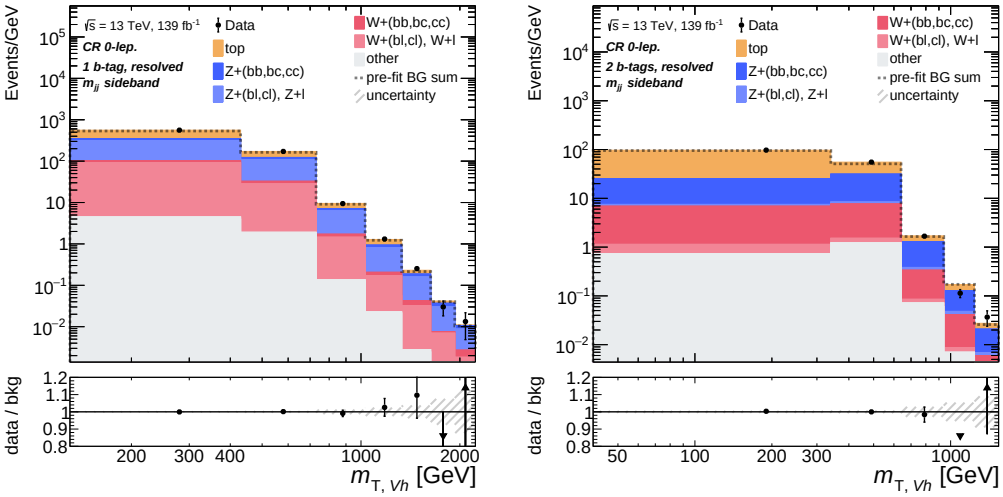

(a)

(b)

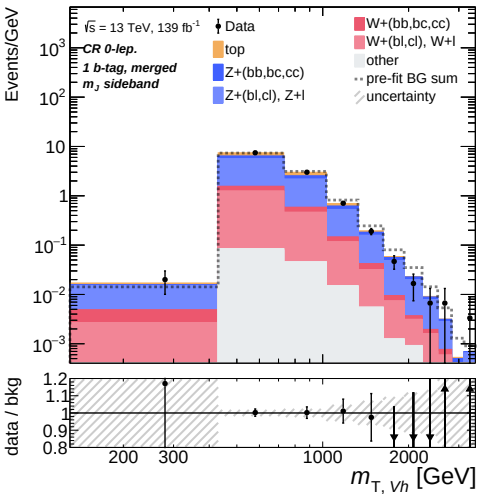

(c)

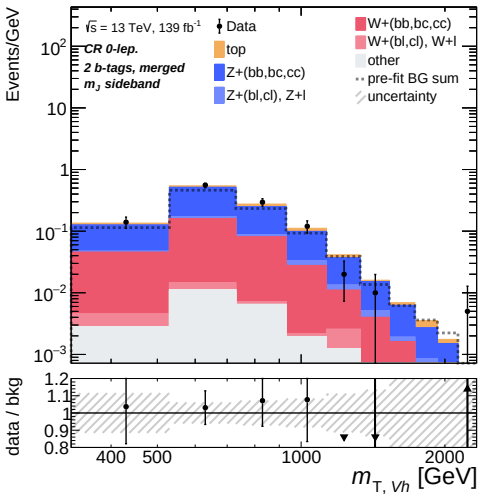

(d)

Figure 5.28: Observed and expected post-fit $m_{\mathrm{T},Vh}$ distributions in the sideband regions of the $Zh \to \nu\bar{\nu}b\bar{b}$ resonance search. Events from the resolved event selection are shown in panels *(a)* and *(b)*, whilst panels *(c)* and *(d)* show events from the merged event selection. Panels *(a)* and *(c)* contain events with one b-tag and panels *(b)* and *(d)* events with two b-tags. The total pre-fit background sum is indicated by the dashed black line. The data-to-background ratio together with the post-fit background uncertainty is shown in the bottom panels.

Table 5.9: The number of observed and expected (post-fit) events in the various signal and mass sideband regions of the HVT Z' boson and 2HDM ggA pseudoscalar searches for an integrated luminosity of 139 fb^{-1}. Numbers are individually rounded and therefore the *Total* background can be different from the sum of the individual components.

	Signal regions			
	resolved topology		merged topology	
Process name	1 b-tag	2 b-tags	1 b-tag	2 b-tags
top quarks	39 900 ± 500	10 340 ± 110	1650 ± 110	66.3 ± 3.4
Z+hf	3900 ± 140	3140 ± 110	680 ± 50	313 ± 18
Z+(bl, cl)	22 800 ± 1200	124 ± 15	3090 ± 190	14.4 ± 1.6
Z+l	1580 ± 170	4.6 ± 1.6	370 ± 40	0.53 ± 0.28
W+hf	990 ± 60	740 ± 40	252 ± 33	117 ± 19
W+(bl, cl)	8500 ± 1100	69 ± 9	800 ± 160	4.3 ± 0.8
W+l	1920 ± 200	12.2 ± 3.0	201 ± 32	0.30 ± 0.13
SM Vh	194 ± 14	254 ± 18	20.6 ± 1.6	12.90 ± 0.97
Diboson	330 ± 50	49 ± 7	200 ± 33	56 ± 9
Total background	80 070 ± 230	14 740 ± 80	7270 ± 60	585 ± 13
Data	80 110	14 681	7260	584

	$m_{jj/J}$ sideband regions			
	resolved topology		merged topology	
Process name	1 b-tag	2 b-tags	1 b-tag	2 b-tags
top quarks	78 900 ± 2100	28 800 ± 400	510 ± 50	17.5 ± 0.8
Z+hf	15 300 ± 800	12 500 ± 600	360 ± 34	137 ± 9
Z+(bl, cl)	82 000 ± 6000	420 ± 70	1610 ± 140	6.6 ± 0.7
Z+l	6100 ± 1000	15 ± 6	260 ± 40	0.27 ± 0.14
W+hf	4400 ± 400	3670 ± 310	142 ± 21	60 ± 9
W+(bl, cl)	28 000 ± 6000	190 ± 40	380 ± 110	1.30 ± 0.29
W+l	6100 ± 900	21 ± 7	128 ± 26	0.18 ± 0.09
SM Vh	222 ± 29	132 ± 16	2.52 ± 0.31	0.384 ± 0.033
Diboson	1800 ± 500	480 ± 120	44 ± 10	4.6 ± 0.8
Total background	222 900 ± 500	46 220 ± 200	3430 ± 50	227 ± 9
Data	222 882	46 277	3435	230

Table 5.10: Expected and observed upper limit on the HVT Z' signal cross section $\sigma^{\text{up}}_{pp\to Z'\to Zh}$ at the 95 % C.L., together with the $\pm1\sigma$ and $\pm2\sigma$ uncertainty bands for the different $m_{Z'}$ mass points. The values are obtained for an integrated luminosity of 139 fb^{-1}.

Z' mass [GeV]	$\sigma^{\text{up, exp.}}_{pp\to Z'\to Zh}$ [fb]	-2σ [fb]	-1σ [fb]	$+1\sigma$ [fb]	$+2\sigma$ [fb]	$\sigma^{\text{up, obs.}}_{pp\to Z'\to Zh}$ [fb]
300	4.50×10^{4}	2.42×10^{4}	3.24×10^{4}	6.24×10^{4}	8.35×10^{4}	3.14×10^{4}
400	6.16×10^{2}	3.31×10^{2}	4.44×10^{2}	8.55×10^{2}	1.14×10^{3}	9.39×10^{2}
500	1.31×10^{2}	7.05×10^{1}	9.46×10^{1}	1.83×10^{2}	2.45×10^{2}	1.28×10^{2}
600	5.51×10^{1}	2.96×10^{1}	3.97×10^{1}	7.67×10^{1}	1.03×10^{2}	3.18×10^{1}
700	2.89×10^{1}	1.55×10^{1}	2.08×10^{1}	4.03×10^{1}	5.44×10^{1}	3.31×10^{1}
800	1.59×10^{1}	8.53	1.15×10^{1}	2.23×10^{1}	3.02×10^{1}	2.17×10^{1}
900	1.05×10^{1}	5.62	7.55	1.47×10^{1}	2.01×10^{1}	1.15×10^{1}
1000	8.17	4.39	5.89	1.15×10^{1}	1.57×10^{1}	8.85
1200	5.25	2.82	3.78	7.45	1.03×10^{1}	4.10
1400	4.41	2.36	3.17	6.26	8.68	3.04
1600	3.39	1.82	2.44	4.84	6.79	2.51
1800	2.57	1.38	1.85	3.69	5.23	2.10
2000	2.04	1.09	1.47	2.95	4.23	2.70
2200	1.64	8.81×10^{-1}	1.18	2.39	3.46	2.61
2400	1.38	7.39×10^{-1}	9.93×10^{-1}	2.01	2.93	2.13
2600	1.15	6.16×10^{-1}	8.27×10^{-1}	1.68	2.47	1.65
2800	9.81×10^{-1}	5.27×10^{-1}	7.07×10^{-1}	1.44	2.15	1.22
3000	8.31×10^{-1}	4.46×10^{-1}	5.99×10^{-1}	1.23	1.85	8.68×10^{-1}
3500	6.50×10^{-1}	3.49×10^{-1}	4.69×10^{-1}	9.69×10^{-1}	1.49	5.52×10^{-1}
4000	5.26×10^{-1}	2.82×10^{-1}	3.79×10^{-1}	7.92×10^{-1}	1.24	4.06×10^{-1}
4500	4.59×10^{-1}	2.46×10^{-1}	3.31×10^{-1}	6.96×10^{-1}	1.11	3.54×10^{-1}
5000	4.12×10^{-1}	2.21×10^{-1}	2.97×10^{-1}	6.28×10^{-1}	1.02	3.24×10^{-1}

visualised in Figure 5.29. All observed upper limits are compatible with the respective expected upper limit within the $\pm2\sigma$ uncertainty bands, indicating that there is no signal present in the data. Based on the model predictions (*cf.* Appendix A.1), Z' boson resonances with masses of up to 2.8 TeV (3.3 TeV) are excluded for HVT Model A (Model B) at the 95 % C.L. Independently of the assumed model, Z' production cross sections $\sigma_{pp\to Z'\to Zh}$ between 32 pb (at $m_{Z'} = 300$ GeV) and 0.5 fb (at $m_{Z'} = 5$ TeV) are excluded at the 95 % C.L.

The agreement between the background-only hypothesis and the observed data is further confirmed by the measured probability p_0 (*cf.* Figure 5.30), *i.e.* the probability that the observed excess of events in the data above the expected background originates from background fluctuations alone. The p_0 values are referred to as "local" because they are calculated for a given fixed value of the resonance mass,

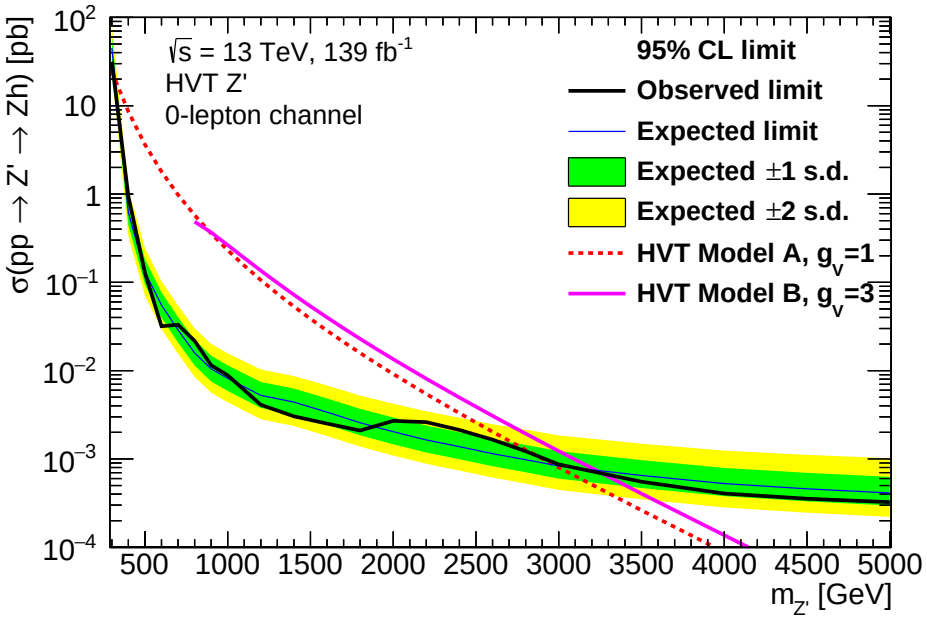

Figure 5.29: The observed (full black line) and expected (full blue line) 95 % C.L. upper limits on the product of the cross section and branching ratio, $\sigma_{pp\to Z'\to Zh}$ in the $\nu\bar{\nu}q\bar{q}$ final state. SM branching fractions of $\mathcal{B}(h \to \bar{b}b, \bar{c}c) = 0.5977$ and $\mathcal{B}(Z \to \nu\bar{\nu}) = 0.2$ are assumed. The green and yellow bands indicate the $\pm 1\sigma$ and $\pm 2\sigma$ uncertainties on the expected upper cross section limit, respectively. For comparison, the corresponding signal production cross sections predicted by the HVT Models A and B are overlaid.

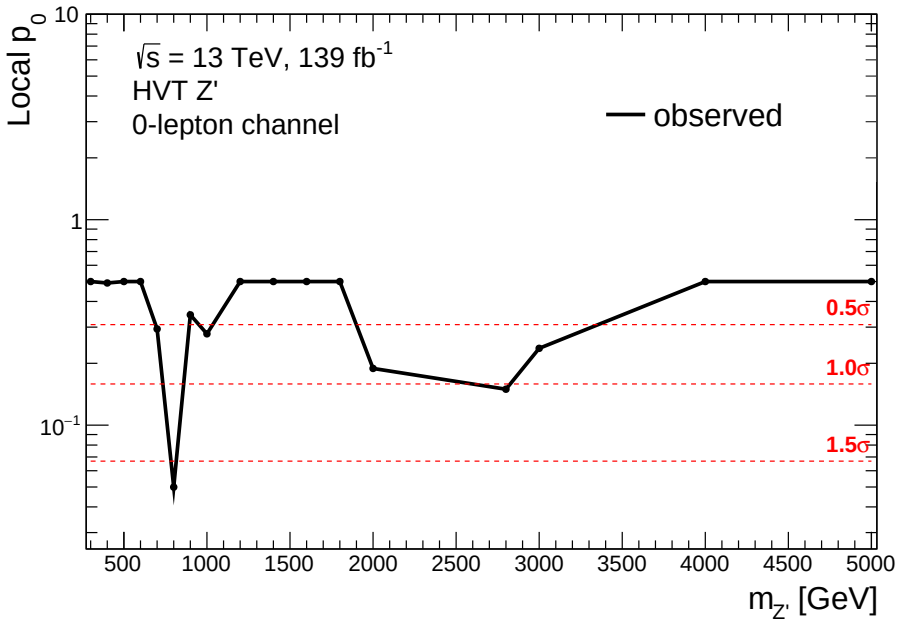

Figure 5.30: The observed local p_0-values for the HVT Z' signal masses between 300 GeV and 5 TeV. For reference, the signal significance levels of 0.5σ, 1σ, and 1.5σ are indicated by the red dotted lines.

rather than in a global mass-independent way. Values above $p_0 = 0.5$ are truncated, since in that case the background-only hypothesis is at least as likely as a signal-plus-background hypothesis, and the background-only hypothesis is preferred. The largest deviation from the background-only hypothesis is observed for the 800 GeV signal mass point with a local p_0 value of 0.05, corresponding to a signal significance of 1.64 standard deviations.

In order to evaluate the robustness of the presented results, the impact of the nuisance parameters on the signal significance is also studied by looking at their impact on the best-fit signal strength $\hat{\mu}$, which results from an unconditional maximum likelihood fit of the signal-plus-background hypothesis to the observed data. In this process, the nuisance parameters are each varied by ±1 (post-fit) standard variations around their respective best-fit values. Then, the fit is repeated twice with the nuisance parameter constrained to the plus and minus one (post-fit) standard deviation, respectively, and the corresponding impact $\Delta\hat{\mu}$ is obtained from the difference of the $\hat{\mu}$ values from the two constrained fits with respect to the unconstrained fit. The 20 nuisance parameters with the largest $\Delta\hat{\mu}$ impact obtained with this procedure are shown in Figures 5.31 and 5.32 for the 700 GeV and 2 TeV signal mass hypotheses, respectively. The impact is measured relative to the total impact of all statistical and systematic uncertainty sources, $\Delta\hat{\mu}_{\text{tot}}$. For the 700 GeV signal mass point, the most impactful nuisance parameters are due to the W+hf matrix element and parton showering uncertainties (ME+PS), followed by the $p_{\text{T}}^{b\bar{b}}$-based reweighting of the V+jets background events, and the Z+hf ME+PS uncertainties. These nuisance parameters correspond to approximately 40 %, 30 %, and 20 % of $\Delta\hat{\mu}_{\text{tot}}$. The most impactful nuisance parameters for the 2 TeV signal mass point are related to the Z+l and W+l ME+PS uncertainties, and the uncertainties on the extrapolation of b-tagging scale factors from low- to high-p_{T} jets in the merged regime. For the higher resonance mass, the impact of the systematic uncertainties is significantly smaller (below 5 % for all nuisance parameters), as only few background events contribute to the corresponding kinematic region of the discriminant variable. The analysis is thus dominated by the statistical uncertainty on the data for large resonance masses. For completeness, the pull distributions of all nuisance parameters are shown in Appendix C.2.

Finally, the expected and observed correlations between the fitted nuisance parameters in the background-only fit are shown in Figures 5.33 and 5.34, respectively. The correlations of the normalisation and the cross section nuisance parameters, which both affect the absolute normalisation of a given background process, indicate a limitation of the statistical fit model for this analysis. Since all major background components contribute to all signal and control regions, no single component can be fitted independently of the others, introducing residual correlations of both the normalisation and the shape uncertainties of individual background components. For example, the freely floating normalisation nuisance parameter for the Z+(bl, cl) background component is highly anti-correlated with the Gaussian constrained cross section (XS) nuisance parameter of the W+(bl, cl) background component, with an observed correlation coefficient of $r = -75$ %. Similarly, the normalisation of the

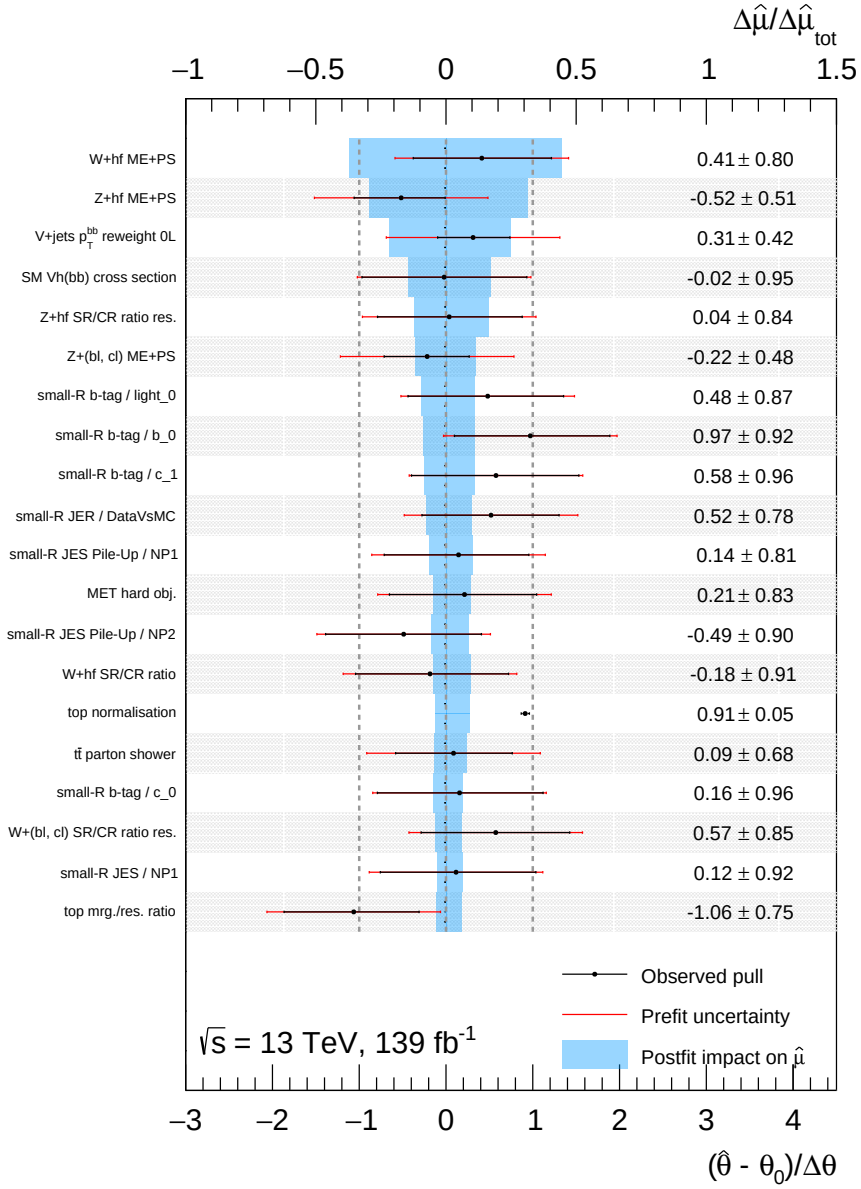

Figure 5.31: The impact $\Delta\hat{\mu}$ of each of the 20 most relevant nuisance parameters on the best-fit signal strength $\hat{\mu}$ with respect to the best-fit value. The best-fit value $\hat{\mu}$ is obtained from an unconstrained fit to the data using a signal-plus-background hypothesis with a signal mass of $m_{Z'} = 700\,\text{GeV}$ and $\sigma_{pp\to Z'\to Zh} = 20\,\text{fb}$. The impact $\Delta\hat{\mu}$ is obtained by repeating the fit with the respective nuisance parameter being modified by ±1 (post-fit) standard deviation around their best-fit values. The nuisance parameter standard deviations are indicated in the figure by black bars. The post-fit pull $(\hat{\theta} - \theta_0)/\Delta\theta$ on a given nuisance parameter θ is indicated by the black dot. The exact pull values are written explicitly next to each nuisance parameter. A value of $\Delta\hat{\mu} = 1$ corresponds to a change in the production cross section of 20 fb.

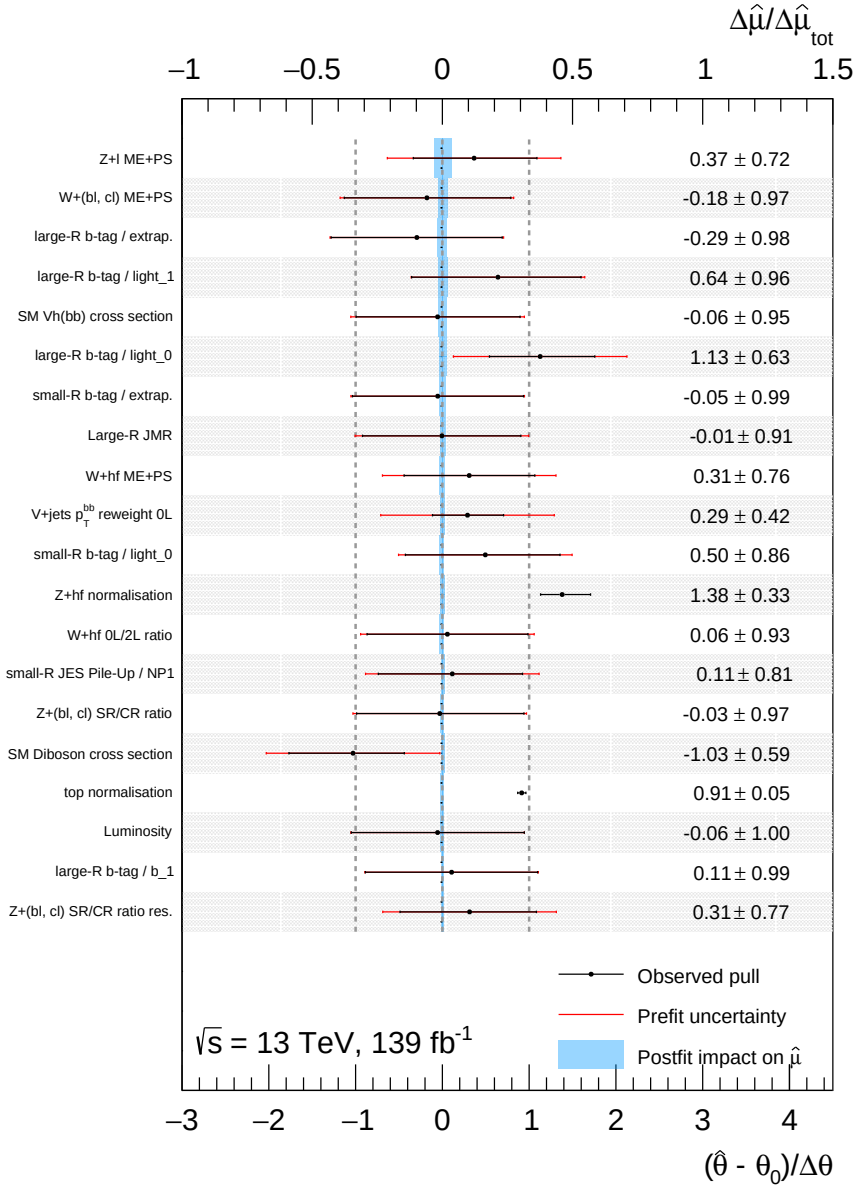

Figure 5.32: The impact $\Delta\hat{\mu}$ of each of the 20 most relevant nuisance parameters on the best-fit signal strength $\hat{\mu}$ with respect to the best-fit value. The best-fit value $\hat{\mu}$ is obtained from an unconstrained fit to the data using a signal-plus-background hypothesis with a signal mass of $m_{Z'} = 2$ TeV and $\sigma_{pp\to Z'\to Zh} = 2$ fb. The impact $\Delta\hat{\mu}$ is obtained by repeating the fit with the respective nuisance parameter being modified by ±1 (post-fit) standard deviation around their best-fit values. The nuisance parameter standard deviations are indicated in the figure by black bars. The post-fit pull $(\hat{\theta} - \theta_0)/\Delta\theta$ on a given nuisance parameter θ is indicated by the black dot. The exact pull values are written explicitly next to each nuisance parameter. A value of $\Delta\hat{\mu} = 1$ corresponds to a change in the production cross section of 2 fb.

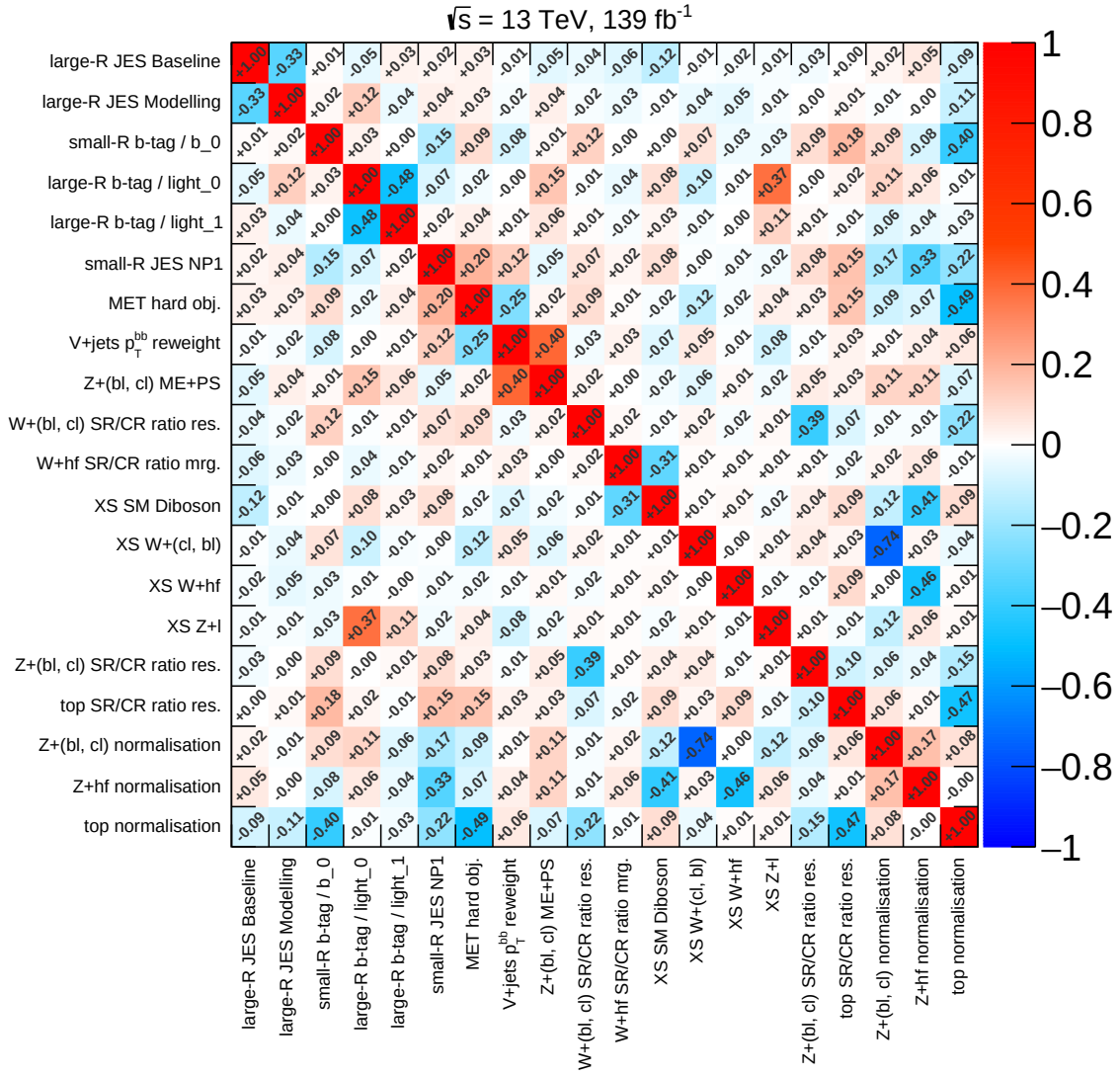

Figure 5.33: Expected correlation coefficients obtained from a fit to expected pseudo-data for the background-only hypothesis for the 20 nuisance parameters with the largest correlations.

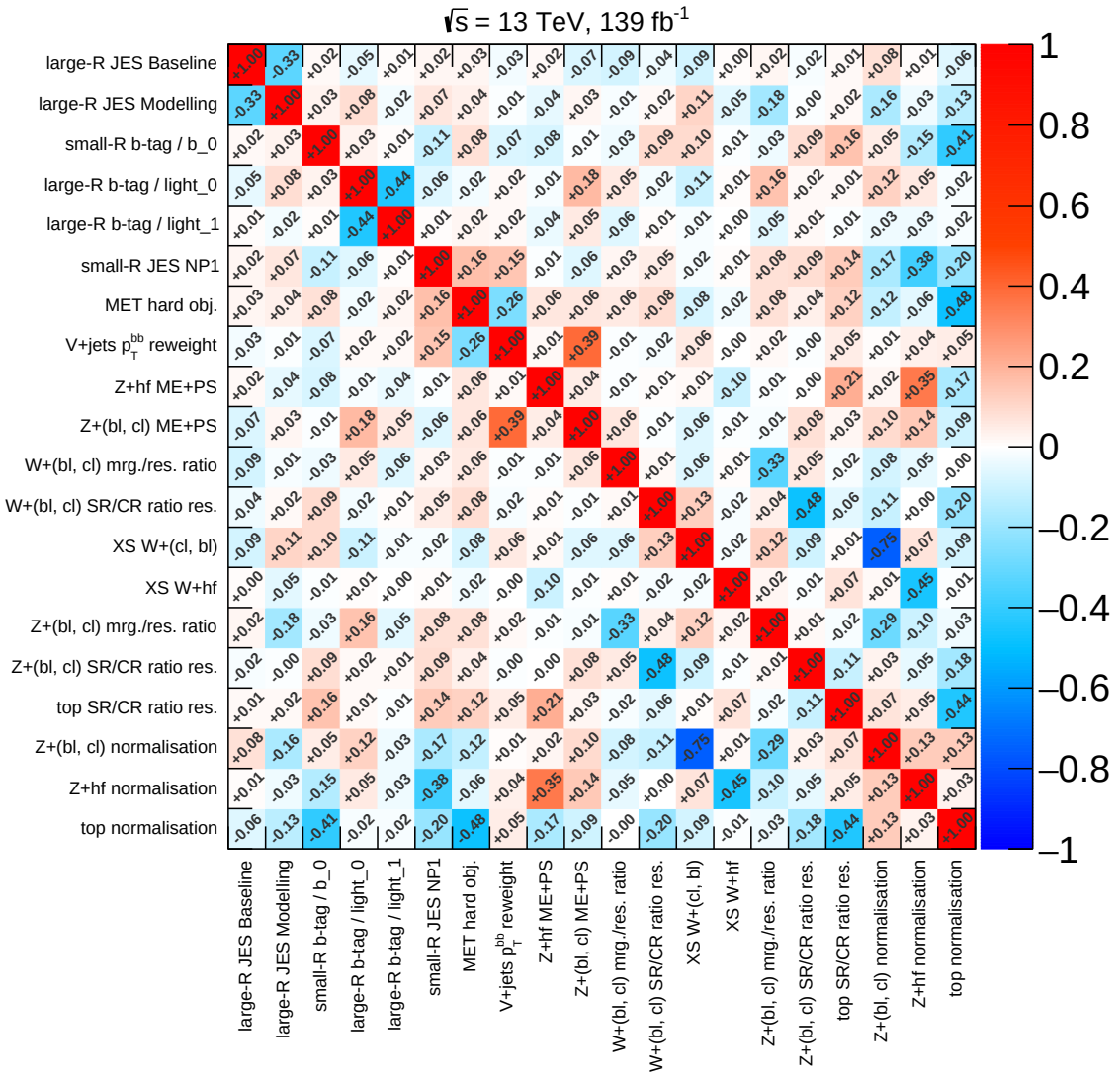

Figure 5.34: Observed correlation coefficients obtained from a fit to the observed data for the background-only hypothesis for the 20 nuisance parameters with the largest correlations.

Z+hf component is correlated with the one of the W+hf component ($r = -45\,\%$). Effectively, this indicates that these background components cannot be well distinguished in the fit, which ultimately may reduce the signal sensitivity. A combination of the search in the 0-lepton channel with searches in other final states, for example with the $\ell^{\pm}\ell^{\mp}b\bar{b}$ channel, which is dominated by the Z + jets background components, will introduce additional information to the fit, thereby reducing correlations between the individual nuisance parameters, and improving the fit sensitivity. Other sources of correlation are indicated by nuisance parameters describing the shape uncertainties. For instance, the Z+hf nuisance parameter describing the matrix element and parton shower uncertainties (ME+PS) is correlated with the nuisance parameter that corresponds to the uncertainty of the $p_{\mathrm{T}}^{b\bar{b}}$ mismodelling of the V+jets background components. When the nominal MC-based background prediction contains residual mismodellings of the shape of a given distribution, the fit tries to compensate the deviation from the observed distribution by pulling the corresponding shape nuisance parameters. Since the matrix element and parton shower uncertainty is determined by comparison of a nominal to an alternative MC generator and the $p_{\mathrm{T}}^{b\bar{b}}$-reweighting uncertainty by comparison to the observed data in control regions, both of these uncertainties allow to pull the nominal distribution closer to the observed data in the fit, resulting in the observed correlation coefficient of $r = 40\,\%$. In this case, the correlations are introduced by construction and reflect the limited knowledge at the pre-fit level and ultimately also limit the total sensitivity of the fit. In future, they can be reduced either by more accurate MC modelling samples that show fewer residual mismodellings or by additional modelling corrections with dedicated control regions of data.

5.9.2 Results of the search for a 2HDM A boson produced via gluon fusion

In the search for a pseudoscalar A boson produced to 100 % via gluon fusion (ggA), within the 2HDM model, the same fit model is used as in the case of the HVT Z' search, with only the signal model being replaced.

The observed and expected upper limits on the cross section $\sigma(gg \to A \to Zh)$ are summarised in Table 5.11 and visualised in Figure 5.35. Similar as in Section 5.9.1, the branching ratios of $Z \to \nu\bar{\nu}$ and $h \to b\bar{b}$ decays are assumed to correspond to the SM predictions. Again, all observed limits are compatible with the background-only expectation within the $\pm 2\sigma$ uncertainty bands. No significant excess of events above the expected background is found, as seen by the local p_0 values in Figure 5.36. Production cross sections below 15 pb (3.8 fb) are excluded at the 95 % C.L. for an A boson mass of 300 GeV (2 TeV).

Compared to the limits obtained for the HVT Z' resonance, similar limits on the cross-section are also obtained for the ggA production. The differences observed between the two are due to small differences in the signal acceptances × efficiency for the two production modes (quark annihilation

Table 5.11: The expected and observed upper limit on the 2HDM ggA signal cross section $\sigma^{\text{up}}_{gg\to A\to Zh}$ at the 95 % C.L., together with the $\pm1\sigma$ and $\pm2\sigma$ uncertainty bands for the different m_A mass points. The values are obtained for an integrated luminosity of 139 fb^{-1}.

A mass [GeV]	$\sigma^{\text{up, exp.}}_{gg\to A\to Zh}$ [10 fb]	-2σ [10 fb]	-1σ [10 fb]	$+1\sigma$ [10 fb]	$+2\sigma$ [10 fb]	$\sigma^{\text{up, obs.}}_{gg\to A\to Zh}$ [10 fb]
300	2.93×10^{3}	1.57×10^{3}	2.11×10^{3}	4.07×10^{3}	5.45×10^{3}	1.51×10^{3}
400	7.99×10^{1}	4.29×10^{1}	5.76×10^{1}	1.11×10^{2}	1.48×10^{2}	1.15×10^{2}
420	5.20×10^{1}	2.79×10^{1}	3.75×10^{1}	7.21×10^{1}	9.64×10^{1}	7.84×10^{1}
440	3.69×10^{1}	1.98×10^{1}	2.66×10^{1}	5.11×10^{1}	6.83×10^{1}	5.36×10^{1}
460	3.42×10^{1}	1.84×10^{1}	2.46×10^{1}	4.75×10^{1}	6.36×10^{1}	4.71×10^{1}
500	1.81×10^{1}	9.74	1.31×10^{1}	2.53×10^{1}	3.40×10^{1}	1.90×10^{1}
600	7.75	4.16	5.58	1.08×10^{1}	1.45×10^{1}	4.50
700	3.99	2.14	2.88	5.57	7.52	4.34
800	2.29	1.23	1.65	3.22	4.38	3.13
900	1.52	8.16×10^{-1}	1.10	2.14	2.92	1.72
1000	1.13	6.08×10^{-1}	8.16×10^{-1}	1.59	2.17	1.21
1200	7.13×10^{-1}	3.83×10^{-1}	5.14×10^{-1}	1.01	1.40	5.52×10^{-1}
1400	6.02×10^{-1}	3.23×10^{-1}	4.34×10^{-1}	8.55×10^{-1}	1.19	4.18×10^{-1}
1600	4.81×10^{-1}	2.58×10^{-1}	3.47×10^{-1}	6.87×10^{-1}	9.62×10^{-1}	3.72×10^{-1}
2000	3.02×10^{-1}	1.62×10^{-1}	2.17×10^{-1}	4.36×10^{-1}	6.24×10^{-1}	3.86×10^{-1}

in the HVT model *vs.* gluon fusion in 2HDM), as studied in Section 5.4. Generally, more jets are expected in the final state in case of the ggA signal. This results in a higher probability to select a wrong jet pair for the Higgs boson candidate, and thus reduces the event reconstruction efficiency within the Higgs mass window. For this reason, the upper limit on the ggA production is never lower than the corresponding limit on the HVT Z' production cross section.

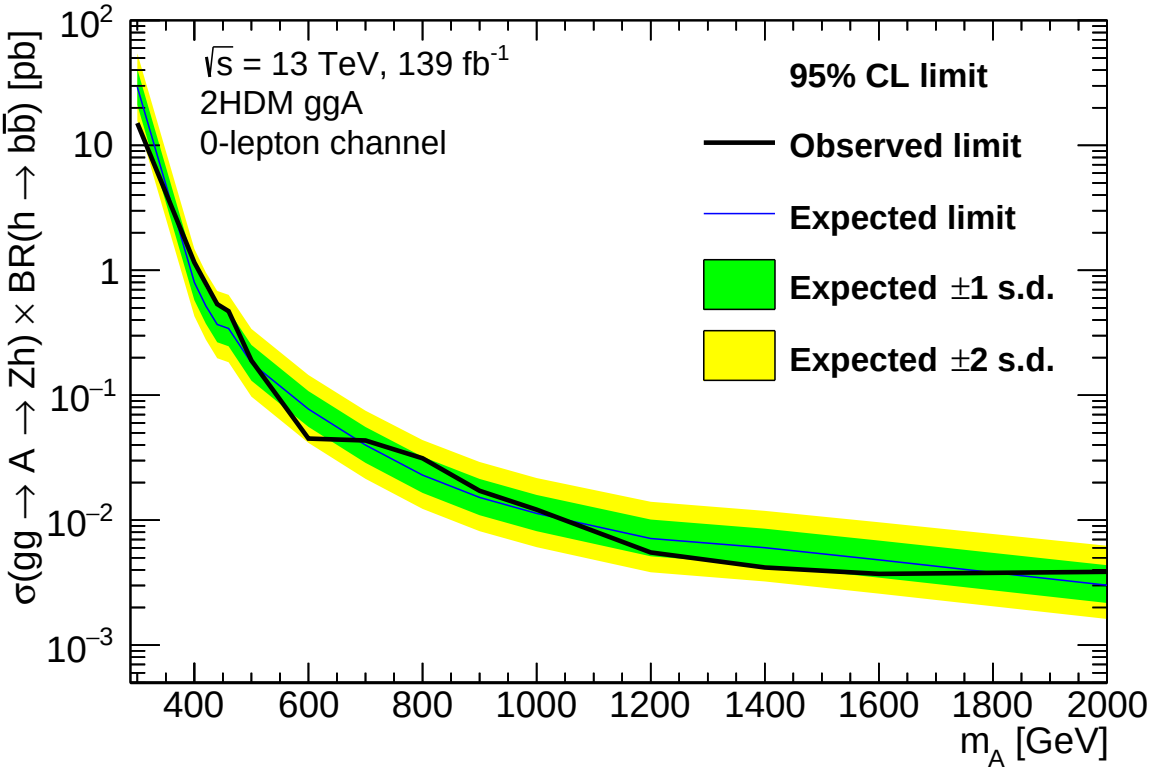

Figure 5.35: The observed (full black line) and expected (full blue line) 95 % C.L. upper limits on the product of the cross section and branching ratio, $\sigma_{gg\to A\to Zh}$ in the $\nu\bar{\nu}b\bar{b}$ final state. SM branching fractions of $\mathcal{B}(h \to \bar{b}b) = 0.569$ and $\mathcal{B}(Z \to \nu\bar{\nu}) = 0.2$ are assumed. The green and yellow bands indicate the $\pm 1\sigma$ and $\pm 2\sigma$ uncertainties on the expected upper cross section, respectively.

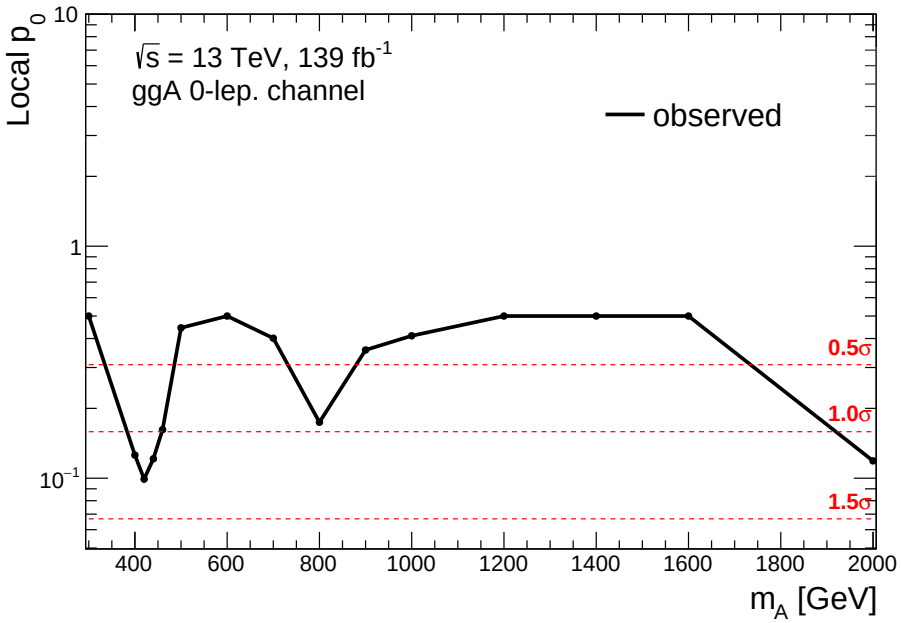

Figure 5.36: The observed local p_0-values for the 2HDM ggA-produced A boson with signal masses between 300 GeV and 2 TeV. For reference, the signal significance levels of 0.5σ, 1σ, and 1.5σ are indicated by the red dotted lines.

CHAPTER SIX

THE SEARCH FOR HEAVY BOSONS IN THE COMBINATION OF $\nu\bar{\nu}b\bar{b}$ AND $\ell^{\pm}\ell^{\mp}b\bar{b}$ FINAL STATES

Similar to the $\nu\bar{\nu}b\bar{b}$ final state that was presented in Chapter 5, the final state with two charged leptons ($\ell = e, \mu$) is also analysed in terms of the searches for a HVT Z' boson and 2HDM pseudoscalar A boson. In this chapter, the two final states are combined in the final fit to the observed data. The analysis strategy is based on the results presented in Ref. [15].

The general strategy of the combination effort is outlined in Section 6.1. In Section 6.2, the main differences between the 0- and the 2-lepton final states and the corresponding differences in the event reconstruction are summarised. In Section 6.3, the combined fit model is introduced. A study employing simulated pseudo-data with signal contributions ("injected signal") quantifies the expected discovery potential for the combined fit to the data and the results of these sensitivity studies are presented in Section 6.4. It will be shown that the set of simulated signal samples with different resonance masses is not sufficient to fully cover the entire mass range, resulting in an underestimated discovery potential for resonance masses in the intermediate range between simulated points. In order to recover the sensitivity drop for these intermediate resonance mass points, additional signal samples for more mass points are generated by means of a morphing technique, which is described in Section 6.5. Finally, the results of the combined 0- and 2-lepton final state analysis with the full Run 2 data set are shown in Section 6.6. The results are reproduced from the data published in [15]. The differences with respect to the published results are summarised in Appendix D.1.

6.1 Motivation and general strategy of the combination

The standalone analysis of the $\nu\bar{\nu}b\bar{b}$ final state that was presented in detail in Chapter 5 is combined with the analysis of the $\ell^{\pm}\ell^{\mp}b\bar{b}$ final state [15]. On its own, this final state provides a similar signal sensitivity as the $\nu\bar{\nu}b\bar{b}$ final state. The combination of the two final states is expected to add several beneficial contributions to the separate results. Firstly, the main background component in the $\ell^{\pm}\ell^{\mp}b\bar{b}$

final state is composed of Z+jets events that also significantly contribute to the $\nu\bar{\nu}b\bar{b}$ final state. Therefore, correlating the Z+jets contributions in both analyses is expected to significantly reduce the post-fit Z+jets uncertainties, thus improving the fit sensitivity. Secondly, the $\ell^{\pm}\ell^{\mp}b\bar{b}$ final state can be fully reconstructed, as it does not contain neutrinos that cannot be detected by the ATLAS detector. Therefore, the invariant mass resolution of the $\ell^{\pm}\ell^{\mp}b\bar{b}$ resonance candidate is significantly improved with respect to the $\nu\bar{\nu}b\bar{b}$ analysis, which also improves the discrimination between the signal and the background processes in kinematic regions with significant background contributions. Finally, the correlated treatment of experimental and theoretical uncertainty sources also reduces the post-fit uncertainties, again improving the fit sensitivity.

The combination is performed on the fully reconstructed invariant mass distributions of the resonance candidates ($m_{\mathrm{T},\,Vh}$ in the $\nu\bar{\nu}b\bar{b}$ final state and $m_{Vh} \equiv m_{\ell\ell bb}$ in the $\ell^{\pm}\ell^{\mp}b\bar{b}$ final state) and is realised by correlating the nuisance parameters that enter the common fit model. Since the two final states cover very similar phase space regions, the uncertainty sources are generally assumed to be mutually compatible within the precision of the measurement and therefore the corresponding nuisance parameters can be correlated. The fit model is described in more detail in Section 6.3.

As mentioned in Section 5.1, the combination is performed for the interpretations in the framework of three signal models: the HVT Z' boson, the 2HDM A pseudoscalar produced via gluon fusion, and, additionally, the 2HDM A pseudoscalar produced in association with b-quarks. The latter signal model was not included in the standalone analysis of the $\nu\bar{\nu}b\bar{b}$ final state, since the background contributions in the signal regions with additional b-jets can only be fully constrained in a combined fit of the two final states.

6.2 Overview of the $\ell^{\pm}\ell^{\mp}b\bar{b}$ analysis

The analysis strategy for the $\ell^{\pm}\ell^{\mp}b\bar{b}$ final state is described in detail in Ref. [15]. It is optimised for the search for a new Zh resonance, produced by the BSM theories introduced in Chapter 2, using the same signal hypotheses that were introduced in Section 5.1. The main difference with respect to the $\nu\bar{\nu}b\bar{b}$ final state is that the Z boson is required to decay into a pair of charged same-flavour leptons (electrons or muons) rather than a pair of neutrinos and that therefore the full mass of the resonance candidate, m_{Vh}, can be reconstructed. In consequence, the same signal and simulated background processes as presented in Chapter 5 are also employed in the analysis of the $\ell^{\pm}\ell^{\mp}b\bar{b}$ final state.

Table 6.1: Summary of the event selection criteria for the signal regions of the Zh diboson resonance search in the $\ell^{\pm}\ell^{\mp}b\bar{b}$ final state. The requirement on the Higgs candidate mass $m_{jj/J}$ is inverted for the sideband control regions.

Observable	Resolved topology	Merged topology
$m_{jj/J}$ [GeV]	100–145	75–145
Leading jet p_{T} [GeV]	> 45	> 250
Leading lepton p_{T} [GeV]	> 27	> 27
Sub-leading lepton p_{T} [GeV]	> 20	> 25
$E_{\mathrm{T}}^{\mathrm{miss}}/\sqrt{H_{\mathrm{T}}}$ [$\sqrt{\mathrm{GeV}}$]	$< 1.15 + 8 \times 10^{-3} m_{Vh}/1\,\mathrm{GeV}$	
$p_{\mathrm{T}}^{\ell\ell}$ [GeV]	$> 20 + 9\sqrt{m_{Vh}/1\,\mathrm{GeV} - 320}$	for $m_{Vh} \geq 320\,\mathrm{GeV}$
$m_{\ell\ell}$ [GeV]	$\left[\max[40, 87 - 0.030 m_{Vh}/1\,\mathrm{GeV}], 97 + 0.013 m_{Vh}/1\,\mathrm{GeV}\right]$	
Number of jets	≥ 2 small-radius jets	≥ 1 large-radius jet

6.2.1 Event reconstruction

The reconstruction of signal candidate events is—similar to the strategy presented in Section 5.4—based on a set of consecutive requirements on kinematic properties of final state products, thereby mainly relying on a veto on events with large $E_{\mathrm{T}}^{\mathrm{miss}}$ values, and on kinematic properties of the final state leptons. Here, the $E_{\mathrm{T}}^{\mathrm{miss}}$ is divided by the square-root of the scalar sum of all transverse momenta p_{T} from leptons and small-radius jets in the event, $H_{\mathrm{T}} \equiv \sum_{i \in \{\text{leptons, jets}\}} p_{\mathrm{T},\,i}$, which was found to improve the suppression of multijet events. The exact signal selection requirements are summarised in Table 6.1.

Again, $m_{jj/J}$ signal and control regions are defined, where events in the signal (control) region are required to satisfy (fail) the requirement on the $m_{jj/J}$ values specified in Table 6.1. An additional CR is defined for events with resolved topology containing opposite-flavour leptons, which is $> 99\,\%$ pure in $t\bar{t}$ events and is thus used as a dedicated CR for the $t\bar{t}$ process. In this CR, the m_{jj} requirement is the same as for the nominal signal region.

After the event reconstruction, b-tagging is applied on the small-radius jets (VR track jets) in the resolved (merged) event topology using the 70 % working point of the MV2c10 algorithm, and the events are categorised according to their b-tag multiplicity in the same was as for the analysis of the $\nu\bar{\nu}b\bar{b}$ final state.

6.2.2 Experimental and theoretical systematic uncertainties

Due to the similar phase space covered by the $\ell^{\pm}\ell^{\mp}b\bar{b}$ final state, the identical uncertainty sources as presented in Section 5.6 are studied and contribute as nuisance parameters to the combined fit model. Moreover, the $\ell^{\pm}\ell^{\mp}b\bar{b}$ final state also has implemented dedicated modelling uncertainties based on studies of the pre-fit $p_{\mathrm{T}}^{b\bar{b}}$ (p_{T} of the leading large-radius jet) distributions in the resolved (merged) event topology, which are determined analogously to the corresponding uncertainties in the $\nu\bar{\nu}b\bar{b}$ final state (*cf.* Section 5.5).

The impact of experimental uncertainties on the various signal and background processes in the $\ell^{\pm}\ell^{\mp}b\bar{b}$ final state is shown in Table 6.2. As for the $\nu\bar{\nu}b\bar{b}$ analysis, dominant uncertainty contributions arise from the calibration and resolution of the jet energy scale and mass, and from the identification efficiency and misidentification rate of *e.g.* leptons and b-jets. The corresponding impact of theoretical

Table 6.2: Impact of different experimental systematic uncertainties on the shape and normalisation of the m_{Vh} distribution from the various signal and background processes in the signal and control regions of the $\ell^{\pm}\ell^{\mp}b\bar{b}$ final state. The values are obtained for an integrated luminosity of 139 fb^{-1}. The impact on the normalisation is calculated as the average normalisation change due to a given uncertainty over all fit regions with at least 100 events of the given background component. An "S" indicates the shape-only uncertainties.

Process	Uncertainty source	Value
Signal	Luminosity	1.7 %
	JES, JER	S
	b-tagging	S
top quarks	JES, JER	0.9 % + S
	b-tagging	1.1 % + S
	lepton ID & trigger	1.0 % + S
$t\bar{t}$+hf	JES, JER	3.2 % + S
	b-tagging	0.9 % + S
	lepton ID & trigger	1.0 % + S
Z+hf	JES, JER	3.5 % + S
	b-tagging	3.1 % + S
	lepton ID & trigger	1.0 % + S
Z+(bl, cl)	JES, JER	5.1 % + S
	b-tagging	6.9 % + S
	lepton ID & trigger	1.0 % + S
Z+l	Luminosity	1.7 %
	JES, JER	4.0 % + S
	b-tagging	33 % + S
	lepton ID & trigger	1.0 % + S

Process	Uncertainty source	Value
W+hf	Luminosity	1.7 %
	JES, JER	S
	b-tagging	S
	lepton ID & trigger	1.0 % + S
W+(bl, cl)	Luminosity	1.7 %
	JES, JER	S
	b-tagging	S
	lepton ID & trigger	1.0 % + S
W+l	Luminosity	1.7 %
	JES, JER	S
	b-tagging	S
	lepton ID & trigger	1.0 % + S
SM Vh	Luminosity	1.7 %
	JES, JER	2.1 % + S
	b-tagging	0.9 % + S
	lepton ID & trigger	1.0 % + S
SM Diboson	Luminosity	1.7 %
	JES, JER	3.9 % + S
	b-tagging	6.1 % + S
	lepton ID & trigger	1.0 % + S

uncertainties is shown in Table 6.3. All uncertainty contributions are smaller than 10 % in the bulk of

Table 6.3: Impact of theoretical systematic uncertainties on the selection of signal and background processes in the $\ell^{\pm}\ell^{\mp}b\bar{b}$ final state. The values are obtained for an integrated luminosity of 139 fb^{-1}. The label "S" indicates a shape-only variation. The normalisations between two kinematic regions, *i.e.* the migration of events from one region to another, are indicated by a forward slash "/". "Normalisation" refers on the total event yield, and is determined entirely from data for processes indicated with "float". Uncertainties targeting the relative composition of a background category are indicated by "comp.".

Process	Uncertainty source	Value
top quarks	normalisation	float
	resolved / merged migration	18 %
	SR / CR migration	0.2 %
	PS, ISR, FSR, ME, PDF	S
	single top comp.	19 %
	$t\bar{t}H/t\bar{t}V$ comp.	50 %
	p_{T}^{J} reweight.	S
Z+hf	normalisation	float
	resolved / merged migration	19–28 %
	SR / CR migration	5–6 %
	ME/PS, matching, scale	S
	$p_{\mathrm{T}}^{b\bar{b}}$, p_{T}^{J} reweight.	S
Z+(bl, cl)	normalisation	float
	resolved / merged migration	15–21 %
	SR / CR migration	4–20 %
	ME/PS, matching, scale	S
	$p_{\mathrm{T}}^{b\bar{b}}$, p_{T}^{J} reweight.	S
Z+l	normalisation	19 %
	resolved / merged migration	8–50 %
	SR / CR migration	5–20 %
	ME/PS, matching, scale	S
	$p_{\mathrm{T}}^{b\bar{b}}$, p_{T}^{J} reweight.	S

Process	Uncertainty source	Value
W+hf	normalisation	30 %
	resolved / merged migration	14 %
	SR / CR migration	5–7 %
	ME/PS, matching, scale	S
	$p_{\mathrm{T}}^{b\bar{b}}$, p_{T}^{J} reweight.	S
W+(bl, cl)	normalisation	30 %
	resolved / merged migration	19 %
	SR / CR migration	10–20 %
	ME/PS, matching, scale	S
	$p_{\mathrm{T}}^{b\bar{b}}$, p_{T}^{J} reweight.	S
W+l	normalisation	19 %
	resolved / merged migration	17 %
	SR / CR migration	5–20 %
	ME/PS, matching, scale	S
	$p_{\mathrm{T}}^{b\bar{b}}$, p_{T}^{J} reweight.	S
SM Vh	normalisation	20 %
Diboson	normalisation	50 %
Signal	normalisation	2–7 %
	PS, ISR-FSR, PDF	S

the m_{Vh} distributions and larger values are only obtained for regions or background components with small numbers of contributing events, which have negligible impact on the result of the final statistical interpretation of data.

6.3 The combined fit model

Two general fit configurations are distinguished for the combination of the $\nu\bar{\nu}b\bar{b}$ and $\ell^{\pm}\ell^{\mp}b\bar{b}$ final states. The first configuration targets the signal hypotheses with a HVT Z' boson and a 2HDM A pseudoscalar produced via gluon fusion (ggA production), and it is based on the standalone analysis of the $\nu\bar{\nu}b\bar{b}$ final state that was presented in Section 5.8. This setup is referred to as the Z'/ggA fit in the following. The second configuration targets the 2HDM A pseudoscalar produced in association with a b-quark pair (bbA production) and includes additional, dedicated signal regions with a high b-tag

Table 6.4: Summary of data regions employed in the combined fit of the $\nu\bar{\nu}b\bar{b}$ and $\ell^{\pm}\ell^{\mp}b\bar{b}$ final states, distinguished below by the number of final state leptons. The signal regions (SRs) are shown in the upper and the control regions (CRs) in the lower part of the table. The opposite-flavour control region is abbreviated by "OF CR". The number of additional b-tagged track jets in the merged topology that are not matched to the leading large-radius jet is abbreviated with "add.".

Event topology	$m_{jj/J}$ [GeV]	Number of leptons	Number of b-tags	Comment	Used in the Z'/ggA fit	Used in the bbA fit
resolved	$[110, 140]$	0	1	$m_{jj/J}$ SR	✓	✓
resolved	$[110, 140]$	0	2	$m_{jj/J}$ SR	✓	✓
resolved	$[110, 140]$	0	3+	$m_{jj/J}$ SR	—	✓
merged	$[75, 145]$	0	1, 0 add.	$m_{jj/J}$ SR	✓	✓
merged	$[75, 145]$	0	2, 0 add.	$m_{jj/J}$ SR	✓	✓
merged	$[75, 145]$	0	2, 1+ add.	$m_{jj/J}$ SR	—	✓
resolved	$[100, 145]$	2	1	$m_{jj/J}$ SR	✓	✓
resolved	$[100, 145]$	2	2	$m_{jj/J}$ SR	✓	✓
resolved	$[100, 145]$	2	3+	$m_{jj/J}$ SR	—	✓
merged	$[75, 145]$	2	1, 0 add.	$m_{jj/J}$ SR	✓	✓
merged	$[75, 145]$	2	2, 0 add.	$m_{jj/J}$ SR	✓	✓
merged	$[75, 145]$	2	1+, 1+ add.	$m_{jj/J}$ SR	—	✓
resolved	$[50, 110[\vee]140, 200]$	0	1	$m_{jj/J}$ CR	✓	—
resolved	$[50, 110[\vee]140, 200]$	0	2	$m_{jj/J}$ CR	✓	—
merged	$[50, 75[\vee]145, 200]$	0	1, 0 add.	$m_{jj/J}$ CR	✓	—
merged	$[50, 75[\vee]145, 200]$	0	2, 0 add.	$m_{jj/J}$ CR	✓	—
resolved	$[100, 145]$	2	1 & 2	OF CR	✓	✓

multiplicity requirement. Due to the additional b-tags, the selected part of the phase space in these additional signal regions is quite different from the remaining signal regions, such that the constraints on the background contributions can not be fully correlated. Since the overall number of contributing background events is also small, the dominant Z+jets and $t\bar{t}$ background components can only be constrained in a combined fit of both final states. In the following, this fit configuration is referred to as the bbA fit. The fit regions that are defined for the two setups based on the event reconstruction requirements outlined in Sections 5.4 and 6.2 and are summarised in Table 6.4.

In order to account for the different phase space region selected by requiring a high b-tag multiplicity in the bbA fit, the uncertainties on the background components with heavy flavour quark content are addressed with dedicated nuisance parameters. As mentioned in Section 5.2, the description of the $t\bar{t}$+hf background process in MC simulation is found to be suboptimal. Therefore, a dedicated floating normalisation nuisance parameter—correlated over the $\nu\bar{\nu}b\bar{b}$ and $\ell^{\pm}\ell^{\mp}b\bar{b}$ final states—is defined for the $t\bar{t}$+hf shape templates. Moreover, nuisance parameters targeting theoretical shape uncertainties are decorrelated from the remaining background processes containing top quarks, thus allowing the fit to determine independent normalisation and shape corrections for the $t\bar{t}$+hf background component. Similarly, a floating normalisation and dedicated shape nuisance parameters are defined for the Z+hf

background process in the regions with three or more b-tagged (track) jets. Since the Z+hf process is by far dominant in these regions and thus the Z+(bl, cl) and Z+l processes have only negligible impact on the overall result, a combined template of Z + jets background processes is used instead of the separate (Z+hf, Z+(bl, cl), Z+l) components to reduce the number of free parameters. The different treatments of background with heavy flavour content in the two fit setups are summarised in Table 6.5.

Table 6.5: Differences in the treatment of the uncertainties on the background components with heavy flavour content in the Z'/ggA and bbA fit configurations. The "low b-tag" ("high b-tag") refers to the signal regions with at most (more than) two b-tags.

Process	Z'/ggA fit	bbA fit (low b-tag SR)	bbA fit (high b-tag SR)
$t\bar{t}$+hf	combined with top quark background component	dedicated uncertainties	
Z+jets	separate Z+hf, Z+(bl, cl), Z+l uncertainties	separate Z+hf, Z+(bl, cl), Z+l uncertainties	combined Z + jets uncertainties

6.4 Expected sensitivity from signal injection studies

The expected discovery potential from the combined analysis is determined from a fit to pseudo-data that consist of the nominal simulated background contributions and a signal with a known resonance mass and production cross section. The addition of the BSM signal to the SM expectation is referred to as the signal injection. By studying the local p_0 values resulting from fits with injected signal, the discovery potential for a given model is evaluated. The study is performed using the bbA signal model, but is expected to generalise also to the other signal models, as the relevant quantity affecting shape of the signal distributions is the natural width of the resonance mass distribution, which is similar for all signal models, with maximum differences below 10 %.

There are three sets of pseudo-data with injected signal defined, for resonance mass hypotheses of m_A = 440, 1200, and 1600 GeV. The final discriminant distributions of injected signals are normalised to the production cross section $\sigma_{gg\to b\bar{b}A\to b\bar{b}Zh}$ of 0.23 pb, 0.017 pb, and 0.011 pb for the injected signal masses of 440 GeV, 1200 GeV, and 1600 GeV, respectively. The values roughly correspond to the upper cross section exclusion limits at the 95 % C.L. obtained with the partial data set recorded in 2015 and 2016 [14]. The corresponding local p_0 values obtained by performing the fit to pseudo-data for a range of signal mass hypotheses, m_A, are shown in Figure 6.1.

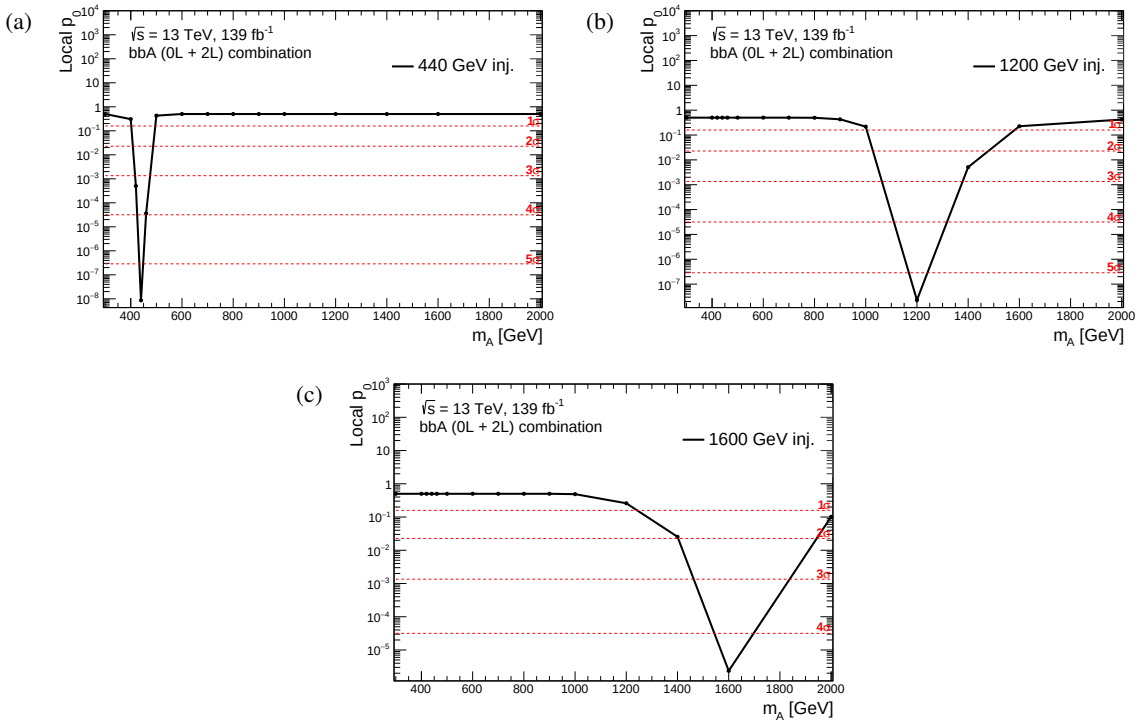

Figure 6.1: The local p_0 values in dependence on the signal mass hypothesis, m_A, as obtained from combined fits (bbA fit configuration) to pseudo-data with an injected bbA signal with a mass of *(a)* $m_A = 440\,\text{GeV}$, *(b)* $m_A = 1200\,\text{GeV}$, and *(c)* $m_A = 1600\,\text{GeV}$. For reference, the signal significance levels up to 5σ are indicated by the red dotted lines.

As expected, the probability p_0 of the background-only hypothesis in each m_A scan is smallest for the hypothesised signal mass value m_A, corresponding to the mass of the injected signal. At this mass point, the background-only hypothesis is ruled out with a significance of 4 standard deviations (4σ) or more. However, already a small variation of the mass hypothesis leads to a significant increase of the p_0 value. For example, the p_0 value at $m_A = 440\,\text{GeV}$ for the fit with a 440 GeV injected signal (*cf.* Figure 6.1(a)) is approximately 1×10^{-8}. On the other hand, for very close-by simulated signal mass hypotheses of 420 GeV and 460 GeV, the p_0 values of approximately 5×10^{-4} and 3×10^{-5}, respectively, are obtained from the corresponding fits. This shows that if the simulated signal in the fit model has a mass that is only 20 GeV different from the true value in the data, the discovery potential is reduced from a significance well above 5σ to a value that is only between 3σ and 4σ.

The same holds also for the injected signals with resonance masses of 1200 GeV and 1600 GeV (*cf.* Figures 6.1(b) and 6.1(c)). However, for these injected signals, some residual sensitivity is observed even for the signal mass hypotheses that are 200 GeV away from the injected mass. For such large resonance masses, the combined sensitivity is mainly driven by the $\nu\bar{\nu}b\bar{b}$ final state (*cf.* Section 6.6). Since the resolution of the $m_{\text{T, }Vh}$ discriminant in the $\nu\bar{\nu}b\bar{b}$ final state is substantially

worse than the corresponding resolution of the m_{Vh} discriminant in the $\ell^{\pm}\ell^{\mp}b\bar{b}$ final state, the signal is smeared out over a wider $m_{\mathrm{T},\,Vh}$ range, causing the residual sensitivity even if the signal mass hypothesis is more than 10 % different from the true value in data.

In summary, this study shows that for relatively small resonance masses a narrow grid of simulated mass points (*i.e.* $\Delta m \simeq 10 - 20\,\mathrm{GeV}$) is required for optimum coverage of all signal masses. For larger resonance masses, especially above approximately 1.2 TeV, a slightly wider grid ($\Delta m \simeq 50 - 100\,\mathrm{GeV}$) is sufficient.

6.5 Signal modelling using morphing techniques

Generating a grid of signal samples in which the distance between the simulated mass points approximately corresponds to the resonance mass resolution in the most sensitive channel (Section 6.4) is computationally expensive and inefficient. A dedicated signal interpolation technique (referred to as *morphing*) is therefore introduced to emulate additional signal samples with intermediate mass points between the ones in the original grid of samples.

In this section, the moment morphing technique [232] is discussed. It is used to emulate the so-called morphed signal samples from a set of original simulated ones. In order to validate the morphing procedure, an additional set of morphed validation samples is generated and compared to the detailed MC-based simulation of the detector response. For brevity, they are referred to as morphed and simulated samples, respectively. These comparisons between morphed and validation signal predictions are performed separately for each signal model, *i.e.* HVT Z', 2HDM ggA, and 2HDM bbA processes. The simulated signal samples of each signal model are divided into two sets (referred to as training and testing class, respectively): the first set of samples in a given signal sample is used to generate the morphed validation samples and second to compare the morphed validation samples to the simulated samples.

For the final fit to data, an optimal compromise between additional computing cost and the recovery of expected signal sensitivity is found for the set of the simulated and the additional morphed samples with resonance mass distances as summarised in Table 6.6.

6.5.1 Overview of the morphing technique

This analysis makes use of the moment morphing technique introduced in Ref. [232]. The technique introduces a morphing p.d.f. $f(\vec{x}|m)$ that transforms the set of observables $\vec{x}$ based on the single morphing parameter m. While the method is able to transform several observables $\vec{x} = (x_1, x_2, x_3, \ldots)$ at once, its application in this analysis is limited to the single observable, *i.e.* the (transverse) invariant

Table 6.6: Optimal distance Δm between the simulated resonance mass points. The first column specifies the resonance mass range and the remaining columns indicate the Δm with which signal samples (either originally simulated or morphed) are produced. A dash "—" indicates that no signal sample is available for the specified resonance mass range.

	Δm [GeV]		
Resonance mass range	HVT Z'	2HDM ggA	2HDM bbA
300 GeV – 350 GeV	100	50	50
350 GeV – 390 GeV	—	10	10
400 GeV – 490 GeV	25	10	10
500 GeV – 780 GeV	25	20	20
800 GeV – 1000 GeV	50	50	50
1050 GeV – 3000 GeV	50	—	—
3100 GeV – 5000 GeV	100	—	—

mass of the candidate Vh system. The morphing parameter m is the resonance mass of the hypothesised signal ($m_{Z'}$ or m_A). For the p.d.f. $f(\vec{x}|m)$, the authors of Ref. [232] suggest using a Taylor series up to order $(n-1)$ around a reference mass point m_0. Given n known (simulated) values of m, one can write the vector equation

$$f(\vec{x}|m_i) \approx \sum_{j=0}^{n-1}(m_i - m_0)^j f'_j(\vec{x}|m_0) = \sum_{j=0}^{n-1} M_{ij} f'_j(\vec{x}|m_0), \tag{6.1}$$

where M_{ij} is the $n \times n$ transformation matrix $M_{ij} = (m_i - m_0)^j$, and $f(\vec{x}|m_i)$ and $f'_j(\vec{x}|m_0)$ are the distributions of the set of observables $\vec{x}$ of the n known values of m_i ($i = 0, 1, \ldots, n-1$) and the reference mass point m_0, respectively. The inversion of the transformation matrix allows to predict the template shape at any given model parameter (*i.e.* mass point) m'

$$f_{\text{pred}}(\vec{x}|m') = \sum_{j=0}^{n-1} c_i(m') f(\vec{x}|m_i). \tag{6.2}$$

where, in the case of this analysis, the $f(\vec{x}|m_i)$ p.d.f.s are given by the originally simulated signal samples for the various mass points m_i and the coefficients $c_i(m')$ are obtained from the inverted transformation matrix,

$$c_i(m') = \sum_{j=0}^{n-1}(m' - m_0)(M^{-1})_{ji}. \tag{6.3}$$

In summary, the moment morphing technique consists of the following steps:

1. Determination of the transformation matrix based on n given simulated samples,
2. Inversion of the transformation matrix,
3. Definition of $(n-1)$ p.d.f.s $f(\vec{x}|m_i)$ based on the simulated samples, and
4. Predictions of $f(\vec{x}|m_i)$ for any value of m' using Equation (6.2).

Since this technique does not consider the statistical uncertainties of the input distributions, the statistical uncertainty of the resulting morphed signal shape template is calculated from average statistical uncertainties of the two neighbouring originally simulated signal samples (one at the lower and one at the higher signal mass point). Using their respective integrals I_{low} and I_{high} and statistical uncertainties σ_{low} and σ_{high}, the statistical uncertainty of the morphed sample at a mass point M is defined as

$$\frac{\sigma_M}{I_M} = \frac{1}{\sqrt{2}} \left(\frac{\sigma_{\text{low}}}{I_{\text{low}}} + \frac{\sigma_{\text{high}}}{I_{\text{high}}} \right), \tag{6.4}$$

which is equivalent to the arithmetic mean of the statistical uncertainties of the neighbouring simulated samples, increased by a factor of $\sqrt{2}$, which is added to account for potential residual correlations between the simulated samples.

Systematic uncertainties for the morphed signal samples are obtained by repeating the moment morphing technique with the $m_{\text{T, }Vh}/m_{Vh}$ distributions modified with respect to the nominal ones according to the corresponding systematic uncertainties.

6.5.2 Validation of the morphed signal samples for the HVT Z' model

The 22 simulated mass points for the HVT Z' signal hypothesis are divided into training and testing samples as summarised in Table 6.7. Based on the training signal samples, the morphing p.d.f. is

Table 6.7: Training and testing classes for the validation of the Z' signal morphing.

Group	Z' Signal Mass Points [GeV]	Total
train	300, 500, 700, 900, 1200, 1600, 2000, 2400, 2800, 3500, 4500	11
test	400, 600, 800, 1000, 1400, 1800, 2200, 2600, 3000, 4000	10

calculated, from which signal samples corresponding to the same mass points as in the testing group are generated. The comparison of these simulated testing and morphed signal samples is given in Figure 6.2 for a selected subset of the morphed mass points and signal regions. The subset of mass points and signal regions is chosen such that it contains examples of all typical observations made

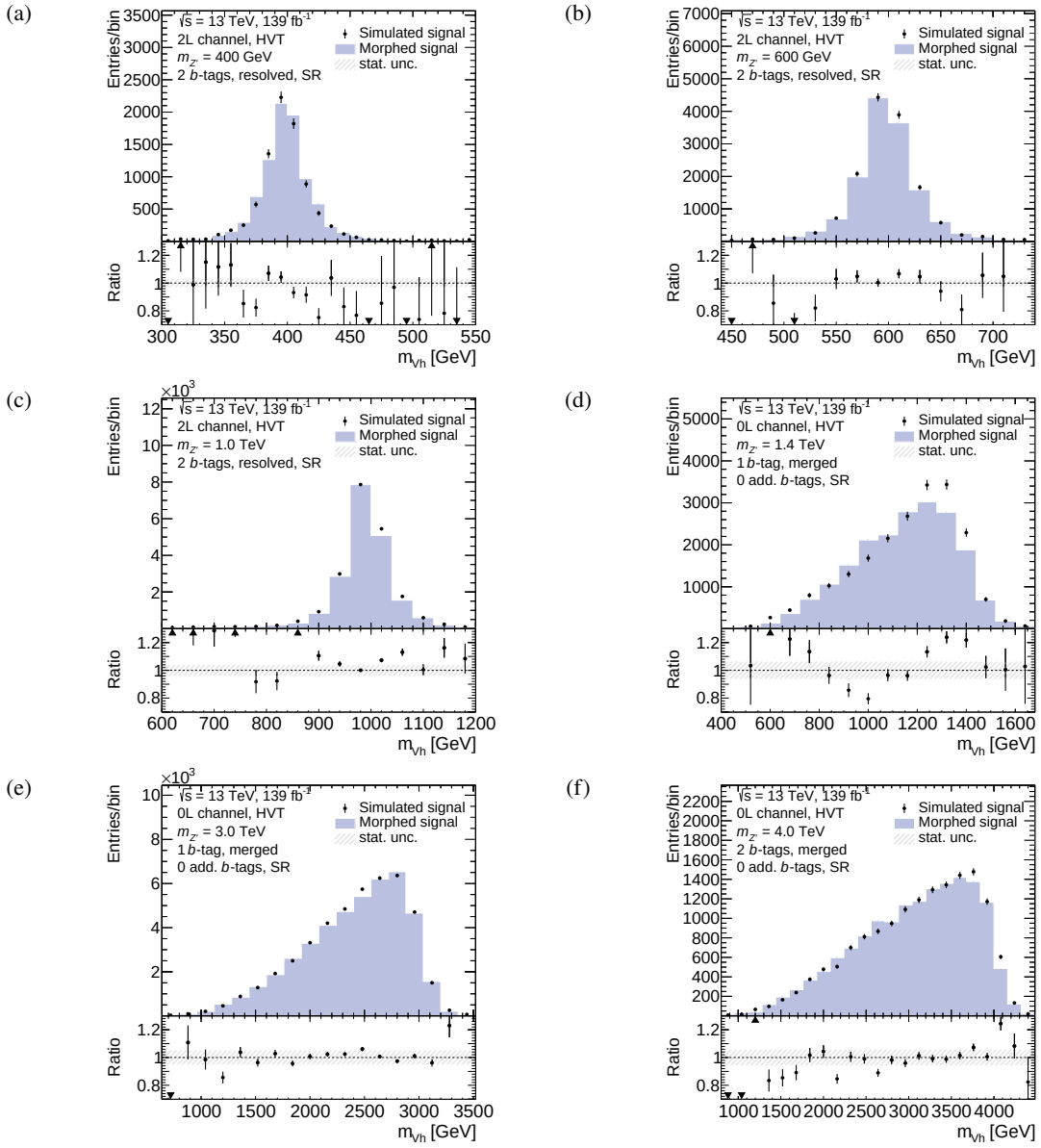

Figure 6.2: Comparison of simulated and morphed distributions of the reconstructed resonance candidate mass for the HVT Z' boson signal with a resonance mass of *(a)* $m_{Z'} = 400\,\text{GeV}$ in the $\ell^{\pm}\ell^{\mp}b\bar{b}$ 1 b-tag resolved-topology signal region, *(b)* $m_{Z'} = 600\,\text{GeV}$ in the $\ell^{\pm}\ell^{\mp}b\bar{b}$ 2 b-tag resolved-topology signal region, *(c)* $m_{Z'} = 1.0\,\text{TeV}$ in the $\ell^{\pm}\ell^{\mp}b\bar{b}$ 2 b-tag resolved-topology signal region, *(d)* $m_{Z'} = 1.4\,\text{TeV}$ in the $\nu\bar{\nu}b\bar{b}$ 1 b-tag merged-topology signal region, *(e)* $m_{Z'} = 3.0\,\text{TeV}$ in the $\nu\bar{\nu}b\bar{b}$ 1 b-tag merged-topology signal region, and *(f)* $m_{Z'} = 4.0\,\text{TeV}$ in the $\nu\bar{\nu}b\bar{b}$ 1 b-tag merged-topology signal region. The morphed distributions are shown as the full histograms. The distributions from simulated samples are shown as the full markers with the corresponding statistical uncertainty. The bottom panels show the ratio of the morphed distribution over the simulated reference, with the statistical uncertainties corresponding to the uncertainty of the morphed sample.

when comparing the reference simulated to the morphed signal samples. At several presented mass points, the peak value of the morphed mass distribution is shifted with respect to the simulated validation distribution. In these cases, an "S"-shape is observed for the ratio of the two distributions (*e.g.* Figures 6.2(b) and 6.2(d)). The corresponding difference between the two samples can be as large as 20 %. These differences are expected to decrease with a finer grid of training samples, since the training samples represent only half of all samples that will be used for the final morphing (the other half being the testing samples). The final morphing based on both training and testing samples is expected to significantly decrease the described mismodelling. In some cases (*e.g.* Figure 6.2(c)), the overall normalisation of the morphed sample is smaller compared to the corresponding simulated sample, *i.e.* the morphed signal sample predicts a smaller number of signal events. In the statistical analysis this leads to more conservative (weaker) exclusion limits. For the reported example, the normalisation of the morphed distribution 20 % smaller than the original one, which is well within the expected uncertainty expected from the final fit to the data. In most cases, however, the morphed distributions agree well with the original simulation (*cf.* Figures 6.2(e) and 6.2(f)).

6.5.3 Validation of the morphed signal samples for the 2HDM *A* model

For the 2HDM *A* pseudoscalar signal, 15 simulated samples are produced in each of the two production modes (ggA mode and bbA mode). They are each divided into training and testing classes as summarised in Table 6.8. Morphed signal distributions are produced from the training set, separately for each production mode. The simulated distributions from testing samples are again compared to

Table 6.8: Training and testing classes for the validation of the 2HDM *A* signal morphing.

Group	ggA Signal Mass Points [GeV]	Total
train	300, 420, 460, 600, 800, 1000, 1400, 2000	8
test	400, 440, 500, 700, 900, 1200, 1600	7

the corresponding morphed distributions based on selected subsets of distributions in Figures 6.3 and 6.4 for the 2HDM *A* pseudoscalar produced in gluon fusion and in association with *b*-quarks, respectively. Similar observations as for the HVT Z' signals (*cf.* Section 6.5.2) are made. In addition, the bbA distributions are in general subject to larger statistical uncertainties due to a smaller signal reconstruction efficiency compared to signal events from other signal models (*cf.* Figure 5.5).

6.5.4 Precision of morphed signal predictions

Upper limits μ_{up} on the signal strength μ obtained at the 95 % C.L. using simulated signal samples are compared to the corresponding limits obtained using a morphed signal sample at a given resonance

mass (*cf.* Table 6.9). In most cases, the expected upper limit on the signal strength obtained both from

Table 6.9: Upper limits μ_{up} on the signal strength μ at the 95 % C.L. obtained from the simulated and the corresponding morphed signal samples for selected mass points within three signal models. The values are obtained from the fit to pseudo-data corresponding to an integrated luminosity of 139 fb^{-1}.

Signal process and mass	$\mu_{\text{up}}^{\text{simulated}}$	$\mu_{\text{up}}^{\text{morphed}}$	$(\mu_{\text{up}}^{\text{morphed}}/\mu_{\text{up}}^{\text{simulated}}) - 1$
Z', $m_{Z'} = 500\,\text{GeV}$	7.687×10^{1}	8.139×10^{1}	+5.9 %
Z', $m_{Z'} = 2\,\text{GeV}$	1.227	1.230	+0.2 %
Z', $m_{Z'} = 4\,\text{TeV}$	3.528×10^{-1}	3.657×10^{-1}	+3.7 %
ggA, $m_A = 400\,\text{GeV}$	9.007×10^{-1}	7.920×10^{-1}	−12 %
ggA, $m_A = 800\,\text{GeV}$	2.547×10^{-2}	2.584×10^{-2}	+1.5 %
ggA, $m_A = 1.6\,\text{TeV}$	6.911×10^{-3}	6.888×10^{-3}	−0.3 %
bbA, $m_A = 400\,\text{GeV}$	1.135	1.143	+0.7 %
bbA, $m_A = 800\,\text{GeV}$	3.199×10^{-2}	3.456×10^{-2}	+8.0 %
bbA, $m_A = 1.6\,\text{TeV}$	6.428×10^{-3}	9.987×10^{-3}	+55 %

simulated and from morphed signal samples agree within 5 %–10 %, with a tendency towards slightly higher (*i.e.* more conservative) limits in case of the morphed signal samples. The largest differences are seen for the expected limit on the ggA signal with a signal mass of $m_A = 400\,\text{GeV}$ and for the bbA signal with a signal mass of $m_A = 1.6\,\text{TeV}$. However, only a single simulated signal sample is available with lower (higher) resonance mass for the $m_A = 400\,\text{GeV}$ ($m_A = 1.6\,\text{TeV}$) morphed signal, indicating that the precision of the morphing method is significantly decreased in such edge cases. Therefore, morphed samples are only used in the final fit to the data if at least two simulated signal samples with lower and two with higher resonance mass are available.

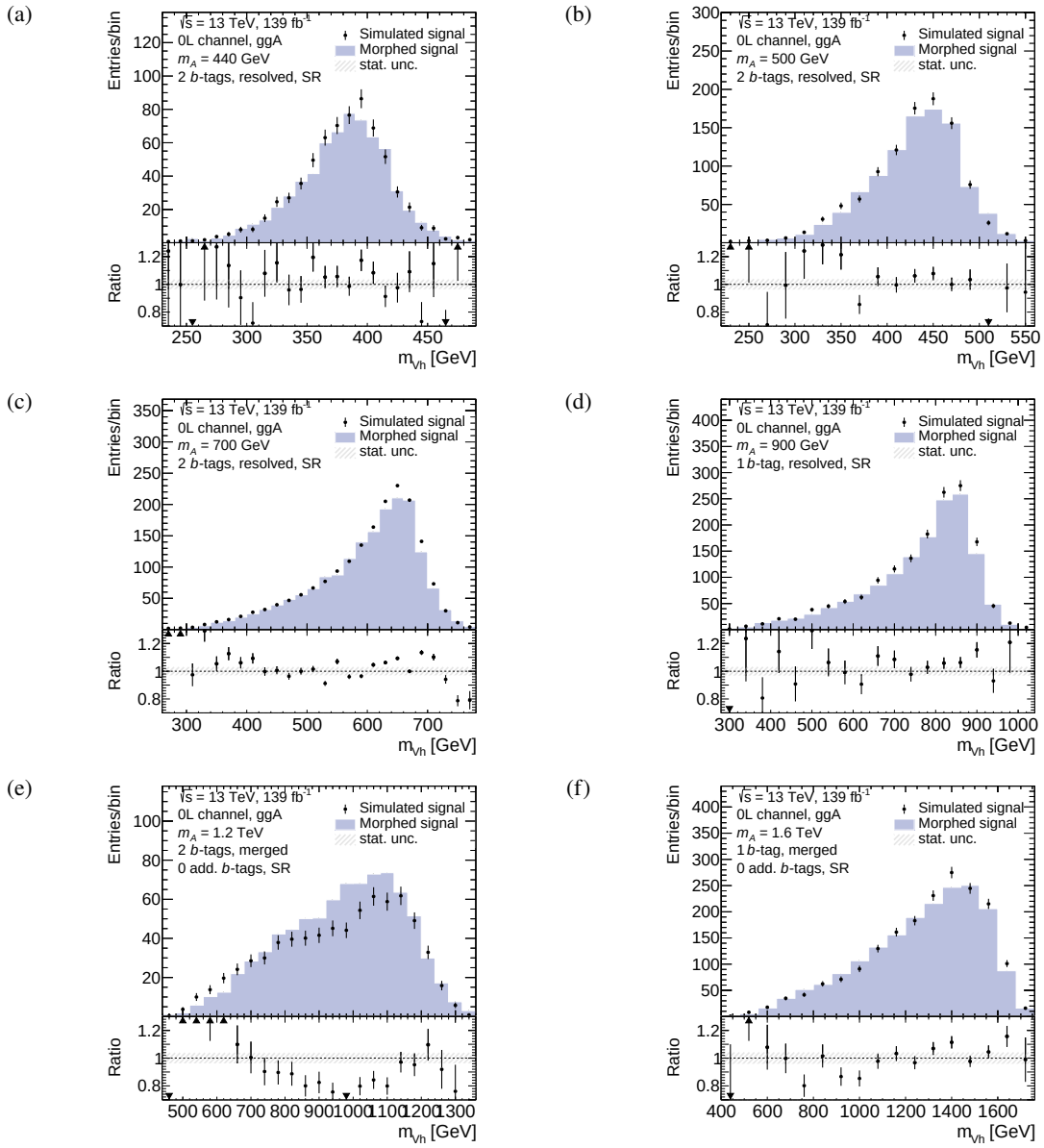

Figure 6.3: Comparison of simulated and morphed distributions of the reconstructed resonance candidate mass for the 2HDM A pseudoscalar produced in pure gluon fusion with a resonance mass of *(a)* $m_A = 440\,\text{GeV}$ in the $\nu\bar{\nu}b\bar{b}$ 2 b-tag resolved-topology signal region, *(b)* $m_A = 500\,\text{GeV}$ in the $\nu\bar{\nu}b\bar{b}$ 2 b-tag resolved-topology signal region, *(c)* $m_A = 700\,\text{GeV}$ in the $\nu\bar{\nu}b\bar{b}$ 2 b-tag resolved-topology signal region, *(d)* $m_A = 900\,\text{GeV}$ in the $\nu\bar{\nu}b\bar{b}$ 1 b-tag resolved-topology signal region, *(e)* $m_A = 1.2\,\text{TeV}$ in the $\nu\bar{\nu}b\bar{b}$ 2 b-tag merged-topology signal region, and *(f)* $m_A = 1.6\,\text{TeV}$ in the $\nu\bar{\nu}b\bar{b}$ 1 b-tag merged-topology signal region. The morphed distributions are shown as the full histograms. The distributions from simulated samples are shown as the full markers with the corresponding statistical uncertainty. The bottom panels show the ratio of the morphed distribution over the simulated reference, with the statistical uncertainties corresponding to the uncertainty of the morphed sample.

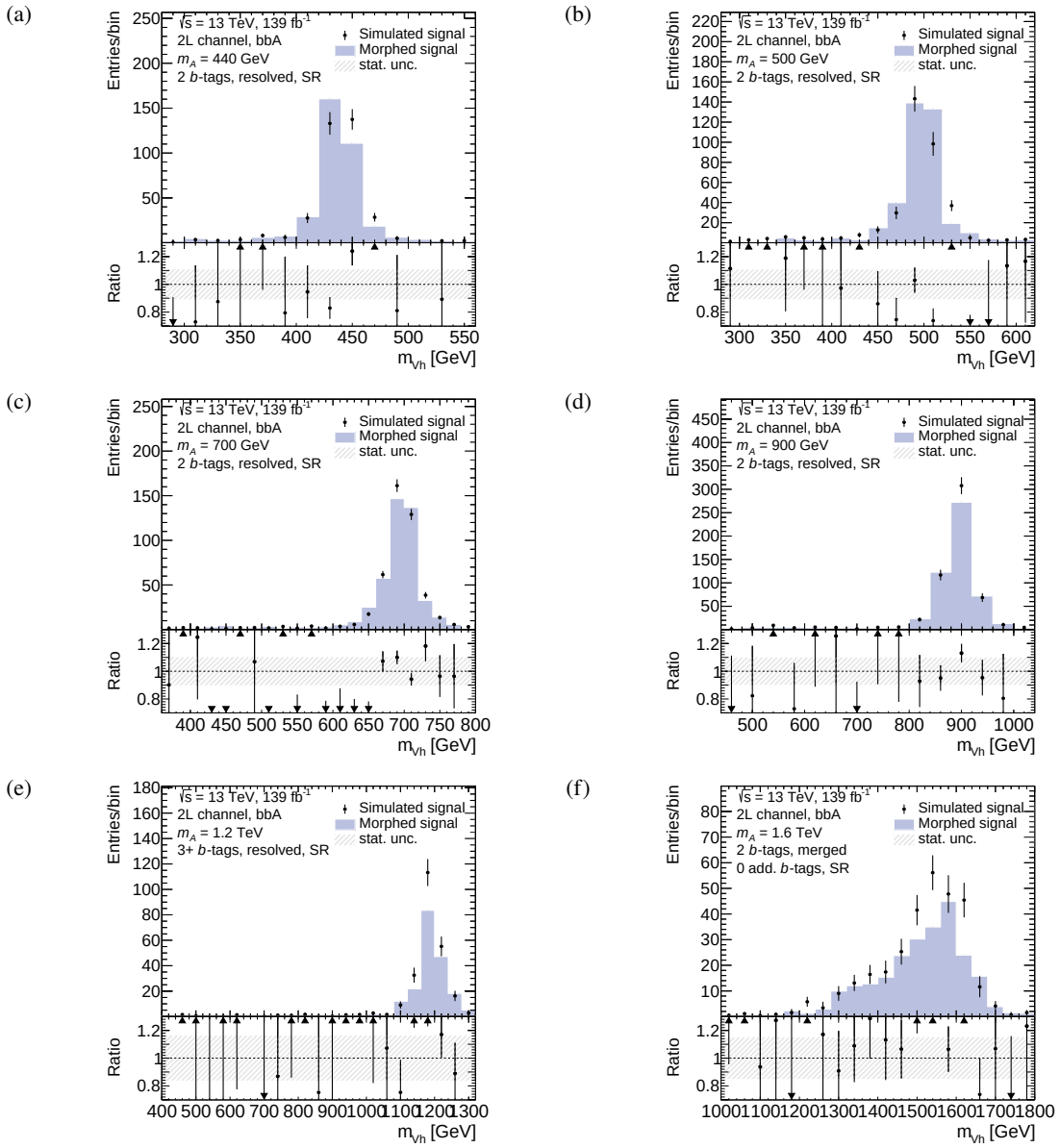

Figure 6.4: Comparison of simulated and morphed distributions of the reconstructed resonance candidate mass for the 2HDM A pseudoscalar produced in association with b-quarks with a resonance mass of *(a)* $m_A = 440\,\text{GeV}$ in the $\nu\bar{\nu}b\bar{b}$ 2 b-tag resolved-topology signal region, *(b)* $m_A = 500\,\text{GeV}$ in the $\nu\bar{\nu}b\bar{b}$ 2 b-tag resolved-topology signal region, *(c)* $m_A = 700\,\text{GeV}$ in the $\nu\bar{\nu}b\bar{b}$ 2 b-tag resolved-topology signal region, *(d)* $m_A = 900\,\text{GeV}$ in the $\nu\bar{\nu}b\bar{b}$ 1 b-tag resolved-topology signal region, *(e)* $m_A = 1.2\,\text{TeV}$ in the $\nu\bar{\nu}b\bar{b}$ 2 b-tag merged-topology signal region, and *(f)* $m_A = 1.6\,\text{TeV}$ in the $\nu\bar{\nu}b\bar{b}$ 1 b-tag merged-topology signal region. The morphed distributions are shown as the full histograms. The distributions from simulated samples are shown as the full markers with the corresponding statistical uncertainty. The bottom panels show the ratio of the morphed distribution over the simulated reference, with the statistical uncertainties corresponding to the uncertainty of the morphed sample.

6.6 Results of the combined analysis

This section presents the results of the combined fits of the expected final discriminant distributions in the $\nu\bar{\nu}b\bar{b}$ and $\ell^{\pm}\ell^{\mp}b\bar{b}$ final states to the observed data from the LHC Run 2 dataset of pp collisions at $\sqrt{s} = 13\,\text{TeV}$ with an integrated luminosity of $139\,\text{fb}^{-1}$. In general, all observations are compatible with the background-only expectation and therefore upper limits on the signal cross section are derived, similarly to the results presented in Sections 4.11 and 5.9. The results are also interpreted in terms of limits on the selected parameters of the HVT model, in particular in the two-dimensional parameter space spanned by the model parameters $(g^2/g_V)c_F$ and $g_V c_H$, similar as for the previous results which are summarised in Chapter 2 (*cf.* Figure 2.9). In addition to the results of the search for a HVT Z' boson, which is presented in Section 6.6.1, the searches for a 2HDM A boson produced via gluon fusion (ggA) and in association with b-quarks (bbA) are shown in Sections 6.6.2 and 6.6.3, respectively. The results of the search for the 2HDM A boson produced via both the ggA and the bbA production mode is presented in Section 6.6.4.

6.6.1 Results of the HVT Z' boson search

The observed and expected numbers of background events in the signal regions of the Z'/ggA fit setup are shown in Table 6.10. The corresponding numbers in the $\nu\bar{\nu}b\bar{b}$ sideband control regions are given in Table 6.11. The expected values are obtained from a background-only fit to the data simultaneously in all signal and control regions. All observed event yields are compatible with the corresponding expected value within the post-fit uncertainties. The post-fit distributions of the final discriminant variables are shown in Figures 6.5, 6.6 and 6.7 for the $\nu\bar{\nu}b\bar{b}$ signal regions, $\ell^{\pm}\ell^{\mp}b\bar{b}$ signal regions, and control regions from both final states, respectively. The numbers of expected background events and $m_{\text{T, }Vh}$ distributions corresponding to the $\nu\bar{\nu}b\bar{b}$ signal and control regions are very similar to the corresponding ones obtained from the standalone analysis of the $\nu\bar{\nu}b\bar{b}$ final state, yet small differences exist due to the slightly different best-fit values of the contributing nuisance parameters. No excess of events beyond the background-only expectation is observed and therefore upper limits on the HVT $Z' \to Zh$ cross section are determined at the 95 % C.L., as summarised in Table 6.12 and visualised in Figure 6.8. The observed upper cross section limits are in agreement with the expectation within the 2σ uncertainty band for all Z' boson mass hypotheses, except at $m_{Z'} = 500\,\text{GeV}$, where a small excess of events with a significance of 2.14 standard deviations above the SM background is observed. The local probabilities of the background-only hypothesis, p_0, are shown for all signal mass hypotheses in Figure 6.9.

Based on these observations and in combination with the predicted cross sections of the HVT Models A and B (*cf.* Appendix A.1), Z' boson resonances with masses of up to 2.8 TeV and 3.3 GeV, respectively,

Table 6.10: The number of observed and expected (post-fit) events in the various $\nu\bar{\nu}b\bar{b}$ and $\ell^{\pm}\ell^{\mp}b\bar{b}$ signal regions in the Z'/ggA fit setup. The reported numbers correspond to an integrated luminosity of 139 fb^{-1}. Numbers are individually rounded and therefore the *Total* background can be different from the sum of the individual components. Cells are marked with a dash "—" if fewer than 1 event of the corresponding process is expected.

	$\nu\bar{\nu}b\bar{b}$ signal regions			
	resolved topology		merged topology	
Process	1 b-tag	2 b-tags	1 b-tag	2 b-tags
top quarks	39 700 ± 500	10 380 ± 90	1710 ± 80	66.8 ± 2.5
Z+hf	3670 ± 120	2980 ± 80	670 ± 40	303 ± 13
Z+(bl, cl)	22 100 ± 500	115 ± 15	2650 ± 80	12.8 ± 1.4
Z+l	1510 ± 200	4.0 ± 1.8	372 ± 34	—
W+hf	1110 ± 50	840 ± 40	268 ± 28	122 ± 15
W+(bl, cl)	9490 ± 310	75 ± 9	1140 ± 90	5.8 ± 0.6
W+l	1910 ± 230	11 ± 4	215 ± 29	—
SM Vh	211 ± 7	276 ± 9	22.5 ± 0.8	14.1 ± 0.5
Diboson	367 ± 27	54.3 ± 3.5	220 ± 17	62 ± 5
Total background	80 070 ± 220	14 740 ± 80	7260 ± 60	588 ± 13
Data	80 110	14 681	7260	584

	$\ell^{\pm}\ell^{\mp}b\bar{b}$ signal regions			
	resolved topology		merged topology	
Process	1 b-tag	2 b-tags	1 b-tag	2 b-tags
top quarks	8090 ± 50	6130 ± 60	47 ± 4	3.25 ± 0.32
Z+hf	22 190 ± 310	17 000 ± 110	213 ± 6	100.7 ± 3.4
Z+(bl, cl)	104 100 ± 800	430 ± 40	728 ± 17	4.11 ± 0.21
Z+l	6600 ± 700	23 ± 9	156 ± 10	—
W+hf	4.2 ± 0.8	1.48 ± 0.08	—	—
W+(bl, cl)	21.0 ± 1.7	—	1.43 ± 0.06	—
SM Vh	321 ± 8	402 ± 11	5.08 ± 0.20	2.60 ± 0.12
Diboson	1354 ± 29	383.1 ± 9.7	77.1 ± 1.8	17.5 ± 0.6
Total background	142 670 ± 270	24 370 ± 90	1229 ± 16	128 ± 4
Data	142 672	24 371	1220	133

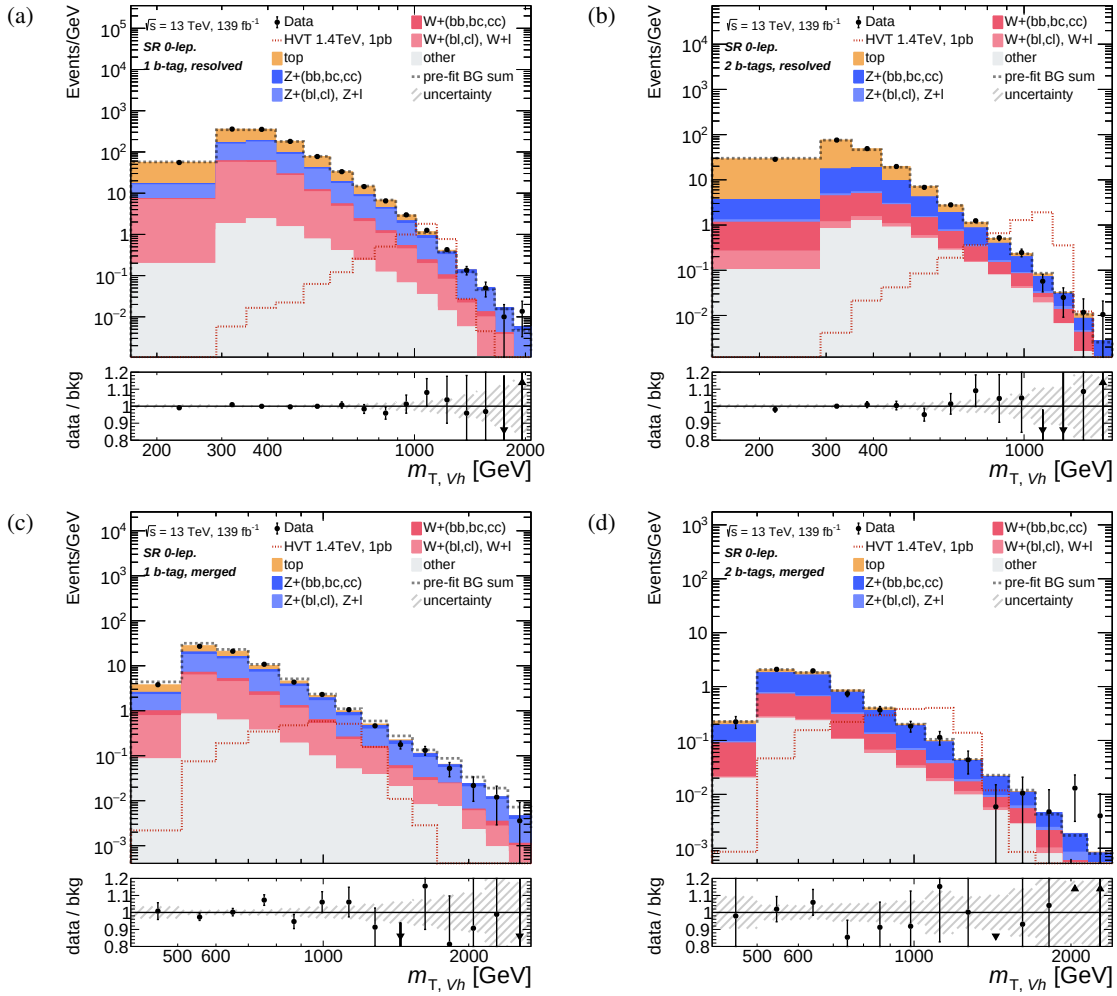

Figure 6.5: Observed and expected post-fit $m_{T,\,Vh}$ distributions obtained from the Z'/ggA fit setup in the $\nu\bar{\nu}b\bar{b}$ signal regions, with *(a)* 1 b-tag and *(b)* 2 b-tag events with the resolved topology and *(c)* 1 b-tag and *(d)* 2 b-tag events with the merged topology. The total pre-fit background contribution is indicated by the dashed black line and the expected signal distribution from a HVT Z' boson with a mass of 1.4 TeV and $\sigma_{pp\to Z'\to Zh} = 1$ pb is shown as the dotted red line. The data-to-background ratio where the hatched area indicates the post-fit background uncertainty is shown in the bottom panels.

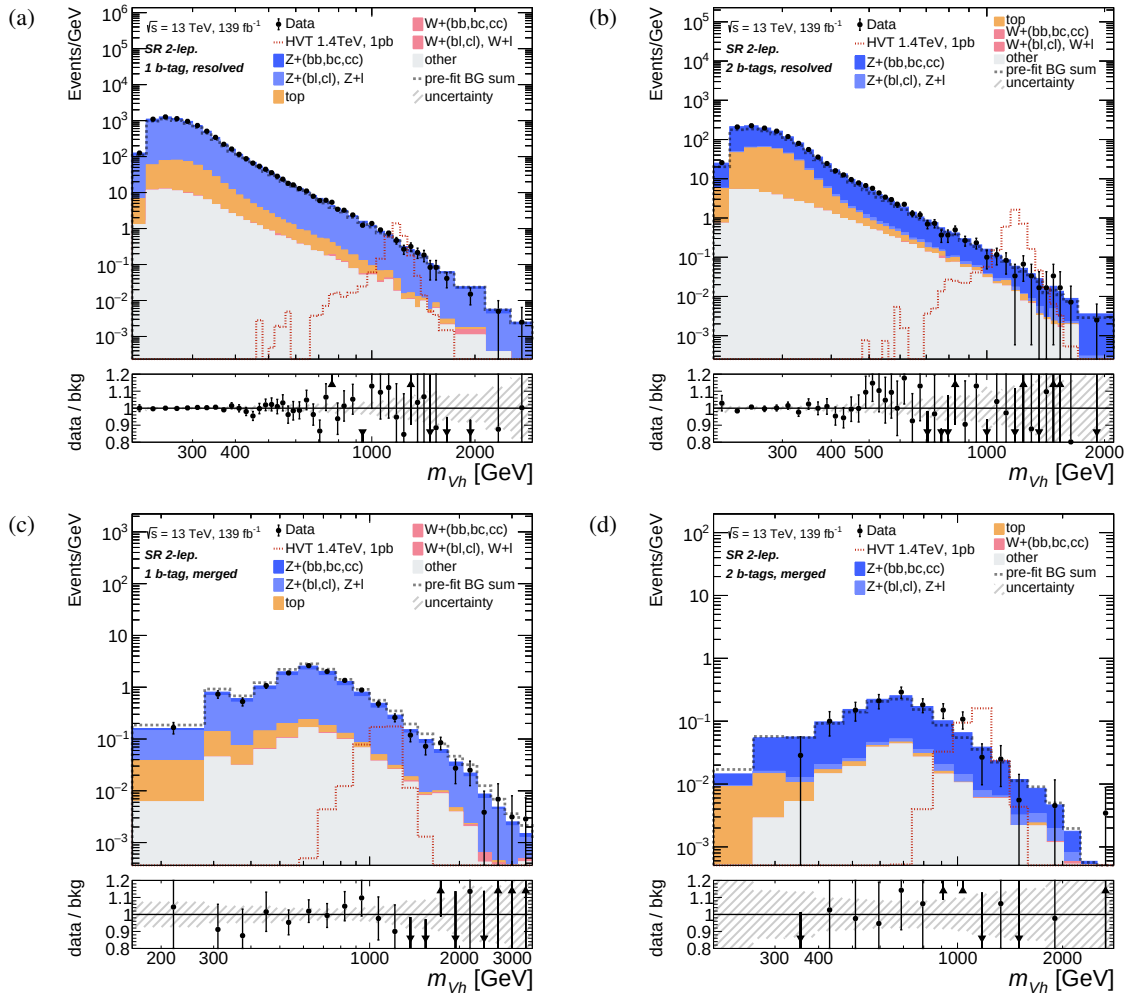

Figure 6.6: Observed and expected post-fit m_{Vh} distributions obtained from the Z'/ggA fit setup in the $\ell^{\pm}\ell^{\mp}b\bar{b}$ signal regions, with *(a)* 1 b-tag and *(b)* 2 b-tag events with the resolved topology and *(c)* 1 b-tag and *(d)* 2 b-tag events with the merged topology. The total pre-fit background contribution is indicated by the dashed black line and the expected signal distribution from a HVT Z' boson with a mass of 1.4 TeV and $\sigma_{pp\to Z'\to Zh} = 1$ pb is shown as the dotted red line. The data-to-background ratio where the hatched area indicates the post-fit background uncertainty is shown in the bottom panels.

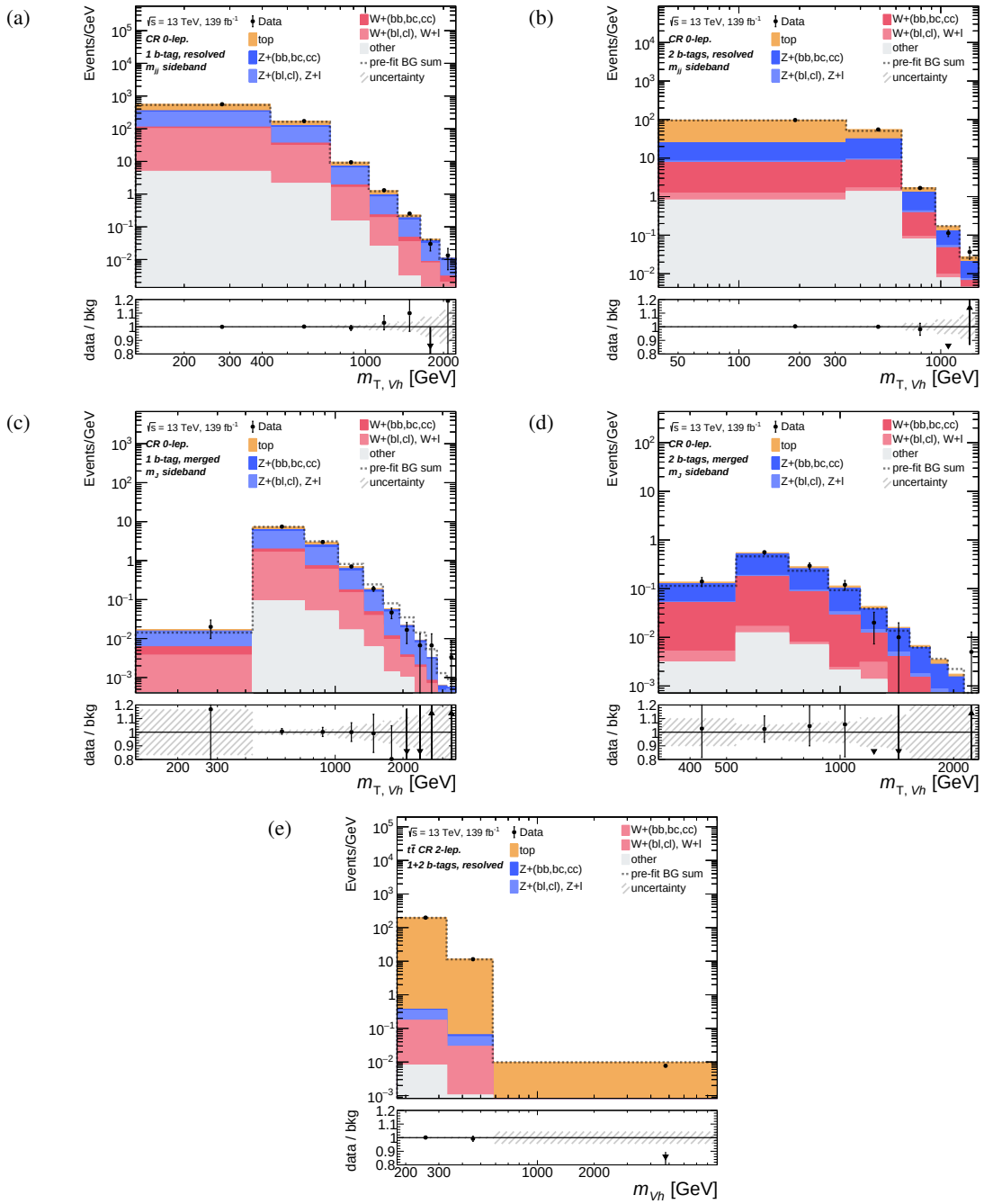

Figure 6.7: Observed and expected post-fit $m_{\mathrm{T},\,Vh}$ and m_{Vh} distributions obtained from the Z'/ggA fit setup in the $\nu\bar{\nu}b\bar{b}$ and $\ell^{\pm}\ell^{\mp}b\bar{b}$ control regions, with *(a)* 1 b-tag and *(b)* 2 b-tag events in the sideband control regions with the resolved topology, and *(c)* 1 b-tag and *(d)* 2 b-tag events in the sideband control regions with the merged topology of the $\nu\bar{\nu}b\bar{b}$ final state, and *(e)* 1 and 2 b-tag events in the opposite-flavour control region with resolved topology in the $\ell^{\pm}\ell^{\mp}b\bar{b}$ final state. The total pre-fit background contribution is indicated by the dashed black line. The data-to-background ratio where the hatched area indicates the post-fit background uncertainty is shown in the bottom panels.

Table 6.11: The number of observed and expected (post-fit) events in the $\nu\bar{\nu}b\bar{b}$ sideband control regions in the Z'/ggA fit setup. The reported numbers correspond to an integrated luminosity of 139 fb^{-1}. Numbers are individually rounded and therefore the *Total* background can be different from the sum of the individual components. Cells are marked with a dash "—" if fewer than 1 event of the corresponding process is expected.

	$\nu\bar{\nu}b\bar{b}$ sideband control regions			
	resolved topology		merged topology	
Process	1 b-tag	2 b-tags	1 b-tag	2 b-tags
top quarks	78 800 ± 1700	28 900 ± 400	530 ± 40	17.9 ± 0.7
Z+hf	14 300 ± 600	11 800 ± 400	359 ± 19	135 ± 7
Z+(bl, cl)	79 300 ± 3100	390 ± 70	1400 ± 60	5.4 ± 0.5
Z+l	5800 ± 1200	13 ± 6	256 ± 30	—
W+hf	4980 ± 350	4150 ± 290	155 ± 16	65 ± 7
W+(bl, cl)	31 600 ± 1200	210 ± 40	540 ± 60	1.69 ± 0.17
W+l	6000 ± 1200	20 ± 9	141 ± 23	—
SM Vh	242 ± 15	144 ± 8	2.75 ± 0.16	—
Diboson	1940 ± 240	530 ± 60	48 ± 5	5.0 ± 0.4
Total background	222 900 ± 500	46 210 ± 200	3420 ± 50	230 ± 8
Data	222 882	46 277	3435	230

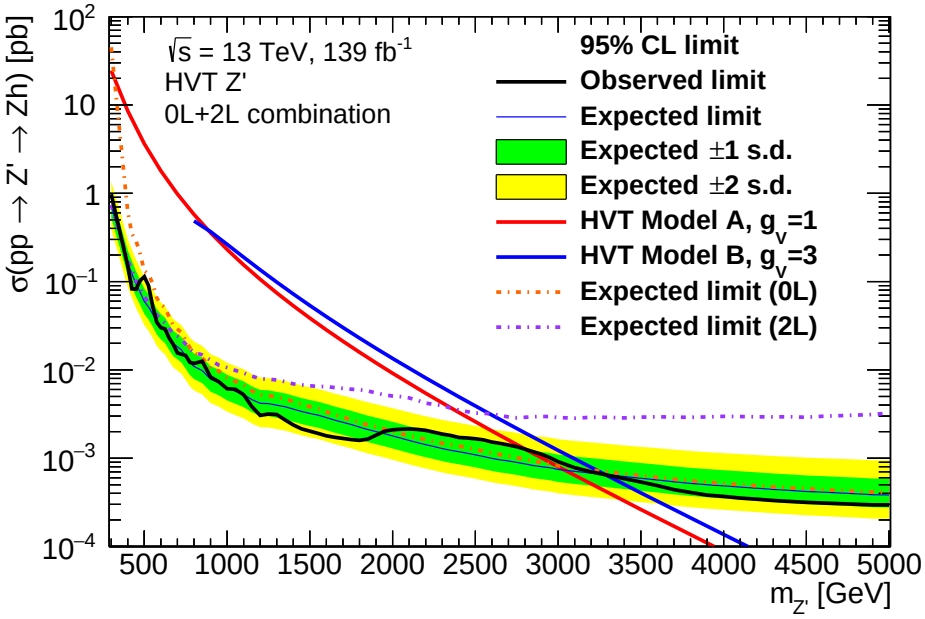

Figure 6.8: The observed (full black line) and expected (full blue line) 95 % C.L. upper limits on the cross section times branching ratio, $\sigma_{pp\to Z'\to Zh}$, for the combination of the $\nu\bar{\nu}b\bar{b}$ (0L, dashed orange line) and $\ell^{\pm}\ell^{\mp}b\bar{b}$ (2L, dashed purple line) final states. SM branching fractions of $\mathcal{B}(h\to b\bar{b}) = 0.569$, $\mathcal{B}(Z\to\nu\bar{\nu}) = 0.2$, and $\mathcal{B}(Z\to\ell^{+}\ell^{-}) = 0.1$ are assumed. The green and yellow bands indicate the $\pm1\sigma$ and $\pm2\sigma$ uncertainties on the expected cross section limit, respectively. For comparison, the corresponding signal production cross sections predicted by the HVT Models A and B are overlaid.

Table 6.12: The observed and the expected 95 % C.L. upper limit on the HVT $Z' \to Zh$ signal cross section $\sigma^{\text{up}}_{pp\to Z'\to Zh}$ with $\pm1\sigma$ and $\pm2\sigma$ uncertainty bands for the different Z' masses. The results are obtained from the combined analysis of the $\nu\bar{\nu}b\bar{b}$ and $\ell^{\pm}\ell^{\mp}b\bar{b}$ final states using the LHC Run 2 pp data set at $\sqrt{s} = 13$ TeV with an integrated luminosity of 139 fb^{-1}. Only the mass points corresponding to simulated signal samples are shown.

Z' mass [GeV]	$\sigma^{\text{up, exp.}}_{pp\to Z'\to Zh}$ [fb]	-2σ [fb]	-1σ [fb]	$+1\sigma$ [fb]	$+2\sigma$ [fb]	$\sigma^{\text{up, obs.}}_{pp\to Z'\to Zh}$ [fb]
300	7.32×10^{2}	3.93×10^{2}	5.28×10^{2}	1.02×10^{3}	1.37×10^{3}	9.77×10^{2}
400	1.62×10^{2}	8.71×10^{1}	1.17×10^{2}	2.26×10^{2}	3.05×10^{2}	1.51×10^{2}
500	5.97×10^{1}	3.20×10^{1}	4.30×10^{1}	8.34×10^{1}	1.13×10^{2}	1.14×10^{2}
600	3.07×10^{1}	1.65×10^{1}	2.21×10^{1}	4.29×10^{1}	5.80×10^{1}	3.01×10^{1}
700	1.83×10^{1}	9.81	1.32×10^{1}	2.56×10^{1}	3.47×10^{1}	1.56×10^{1}
800	1.09×10^{1}	5.87	7.88	1.53×10^{1}	2.09×10^{1}	1.18×10^{1}
900	7.86	4.22	5.66	1.10×10^{1}	1.51×10^{1}	8.30
1000	6.27	3.36	4.52	8.81	1.20×10^{1}	6.12
1200	4.18	2.24	3.01	5.92	8.20	3.05
1400	3.60	1.93	2.59	5.10	7.05	2.38
1600	2.89	1.55	2.08	4.11	5.74	1.79
1800	2.25	1.21	1.62	3.22	4.54	1.59
2000	1.79	9.59×10^{-1}	1.29	2.58	3.68	2.10
2200	1.42	7.64×10^{-1}	1.03	2.07	2.98	2.07
2400	1.19	6.36×10^{-1}	8.54×10^{-1}	1.73	2.51	1.72
2600	9.95×10^{-1}	5.34×10^{-1}	7.17×10^{-1}	1.45	2.13	1.52
2800	8.61×10^{-1}	4.62×10^{-1}	6.21×10^{-1}	1.26	1.87	1.27
3000	7.46×10^{-1}	4.00×10^{-1}	5.38×10^{-1}	1.10	1.64	9.14×10^{-1}
3500	5.92×10^{-1}	3.18×10^{-1}	4.26×10^{-1}	8.82×10^{-1}	1.34	5.37×10^{-1}
4000	4.86×10^{-1}	2.61×10^{-1}	3.50×10^{-1}	7.32×10^{-1}	1.14	3.69×10^{-1}
4500	4.20×10^{-1}	2.25×10^{-1}	3.02×10^{-1}	6.37×10^{-1}	1.01	3.16×10^{-1}
5000	3.83×10^{-1}	2.06×10^{-1}	2.76×10^{-1}	5.86×10^{-1}	9.45×10^{-1}	2.96×10^{-1}

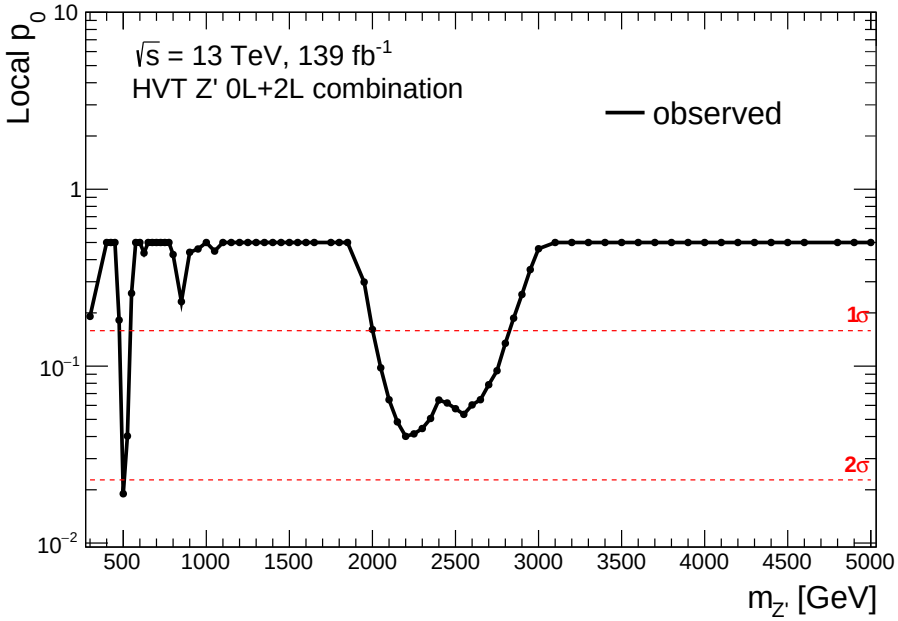

Figure 6.9: The observed local p_0-values for the HVT Z' signal mass hypotheses between 300 GeV and 5 TeV. For reference, the signal significance levels of 1σ and 2σ are indicated by the red dotted lines.

are excluded at the 95 % C.L. The excluded mass values are similar to the ones obtained in the $\nu\bar{\nu}b\bar{b}$ standalone analysis, since the combined signal sensitivity is dominated by the $\nu\bar{\nu}b\bar{b}$ final state in the case of an almost background-free kinematic region with $m_{\mathrm{T},\,Vh} \gtrsim 2$ TeV. For higher resonance masses, the signal-to-background ratio saturates, as only very few background events are expected for $m_{\mathrm{T},\,Vh}$ and m_{Vh} values above 1.5 TeV. This reduces the impact of the post-fit uncertainties on the result such that the $\nu\bar{\nu}b\bar{b}$ final state drives the combined sensitivity due to the larger number of events in the $\nu\bar{\nu}b\bar{b}$ than in the $\ell^{\pm}\ell^{\mp}b\bar{b}$ signal regions with merged topology. For lower signal masses, particularly in the intermediate region between $m_{Z'} = 700$ GeV and $m_{Z'} = 1500$ GeV, the combined result is significantly better than the corresponding results from either of the two individual analyses. In this kinematic region, there are still substantial contributions from background processes, and thus the reduced post-fit uncertainties due to the correlated treatment of uncertainty sources improve the combined sensitivity. For even smaller resonance masses, the $\ell^{\pm}\ell^{\mp}b\bar{b}$ standalone analysis is significantly more sensitive than the $\nu\bar{\nu}b\bar{b}$ analysis, such that the benefit of the combined analysis is negligible. In total, the combined expected upper cross section limit is always better than the ones from each individual analysis over the full $m_{Z'}$ range. Cross sections for the production of a HVT Z' boson decaying into Zh, $\sigma_{pp\to Z'\to Zh}$, that are above 0.98 pb at $m_{Z'} = 300$ GeV and above 0.30 fb at $m_{Z'} = 5$ TeV are excluded at the 95 % C.L.

The observed upper cross section limits are also compared to the signal cross sections predicted

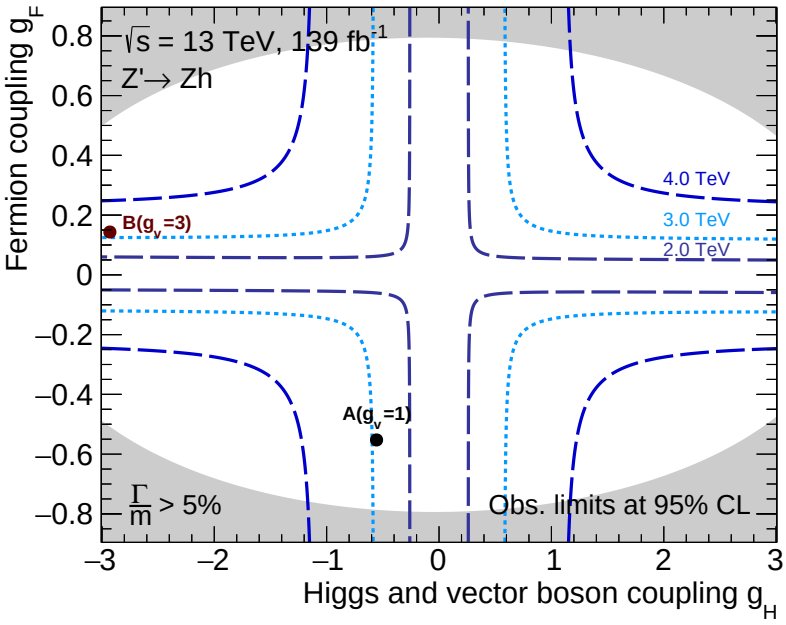

Figure 6.10: The observed contours at the 95 % C.L. of excluded HVT model parameter combinations $g_H = g_V c_H$ and $g_F = (g^2/g_V)c_F$ for HVT Z' signals with resonance masses of 2 TeV (inner dashed line), 3 TeV (dotted line), and 4 TeV (outer dashed line). Areas outside the contours (*i.e.* larger absolute values of the parameters g_F and g_V) are excluded. The parameter settings corresponding to the reference HVT Models A and B are indicated by the full dots. The grey area indicates the model parameter space in which the approximation of a narrow width resonance is no longer valid, *i.e.* $\Gamma/m > 5\,\%$.

by a general HVT model, *i.e.* in terms of fermion coupling $g_F = (g^2/g_V)c_F$ and the Higgs and vector boson coupling $g_H = g_V c_H$ (*cf.* Section 2.1). The corresponding (g_F, g_V) exclusion contours obtained at the 95 % C.L. for resonance masses of 2 TeV, 3 TeV, and 4 TeV are shown in Figure 6.10. The largest part of the (g_F, g_V) parameter space with narrow width resonances is excluded for a resonance with $m_{Z'} = 2$ TeV. With increasing resonance masses, *e.g.* 3 TeV and 4 GeV, the excluded regions become smaller. Figure 6.10 also shows the (g_F, g_V) points corresponding to the HVT reference Models A and B. In agreement with the observation in Figure 6.8, the HVT Z' boson with $m_{Z'} = 3$ TeV is almost excluded (is excluded) at the 95 % C.L. for the reference Model A (Model B).

The impact $\Delta\hat{\mu}$ of the individual nuisance parameters on the best fit signal strength $\hat{\mu}$ is quantified relative to the total impact $\Delta\hat{\mu}_{\text{tot}}$ of all uncertainties, as shown in Figures 6.11 and 6.12 for the fits to the observed data with a signal mass of $m_{Z'} = 700$ GeV and $m_{Z'} = 2$ TeV, respectively. Compared to the standalone fit in the $\nu\bar{\nu}b\bar{b}$ final state, the overall impact of the systematic uncertainties decreased in the combined fit and is now below approximately 20 % (2 %) for any given nuisance parameter at $m_{Z'} = 700$ GeV (2 TeV). This shows that the correlated treatment of uncertainty sources significantly decreases the post-fit uncertainties. For the 700 GeV signal mass point, the W+hf matrix element and parton shower (ME+PS) uncertainties have the largest relative impact of approximately 20 %.

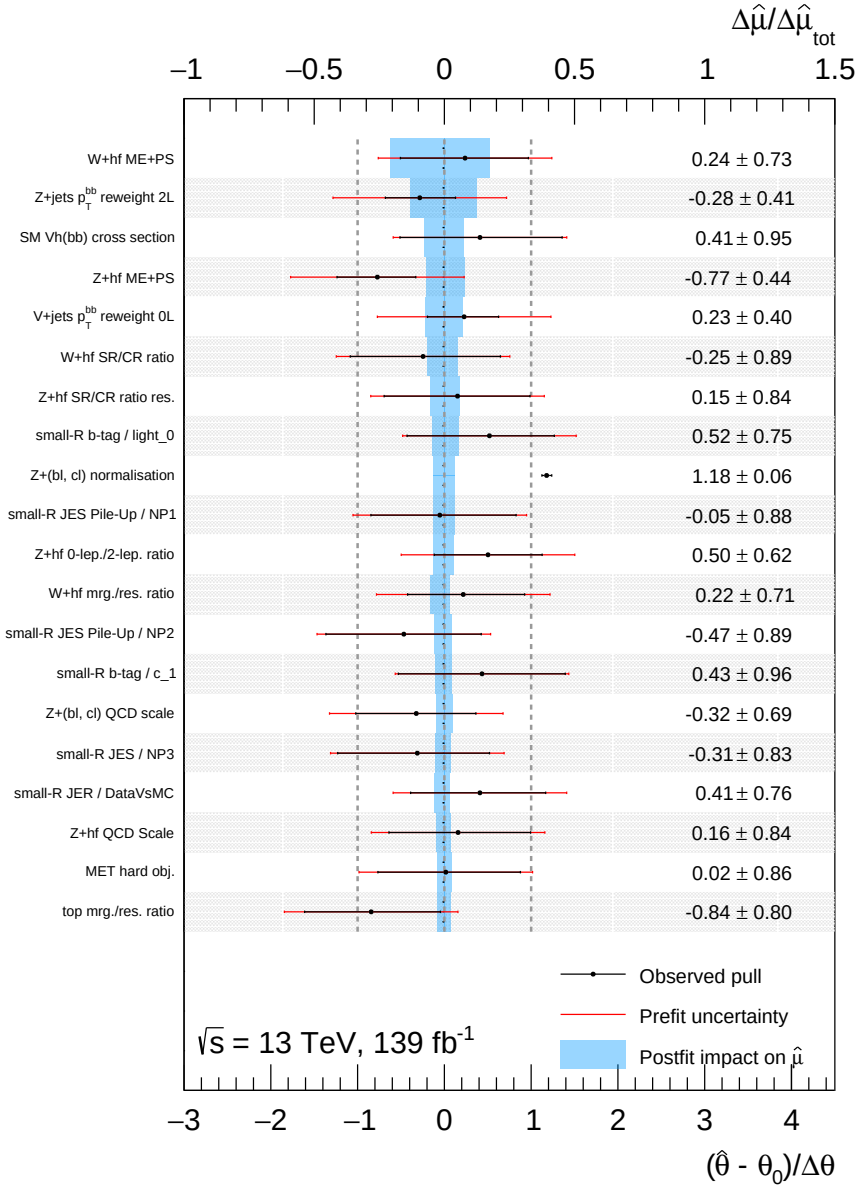

Figure 6.11: The individual impact $\Delta\hat{\mu}$ of the 20 most relevant nuisance parameters on the best-fit HVT Z' boson signal strength $\hat{\mu}$ with respect to the nominal best-fit value, obtained from an unconstrained fit to the data of the signal-plus-background hypothesis with a signal mass $m_{Z'} = 700\,\text{GeV}$ and $\sigma_{pp\to Z'\to Zh} = 20\,\text{fb}$. The $\Delta\hat{\mu}$ are given relative to the total impact $\Delta\hat{\mu}_{\text{tot}}$ of all systematic and statistical uncertainties. They are obtained by repeating the fit with nuisance parameters being shifted by ± 1 standard deviation with respect to their best-fit values. The post-fit pulls $(\hat{\theta} - \theta_0)/\Delta\theta$ of the nuisance parameters θ are indicated by the black dots with black error bars $\Delta\theta$.

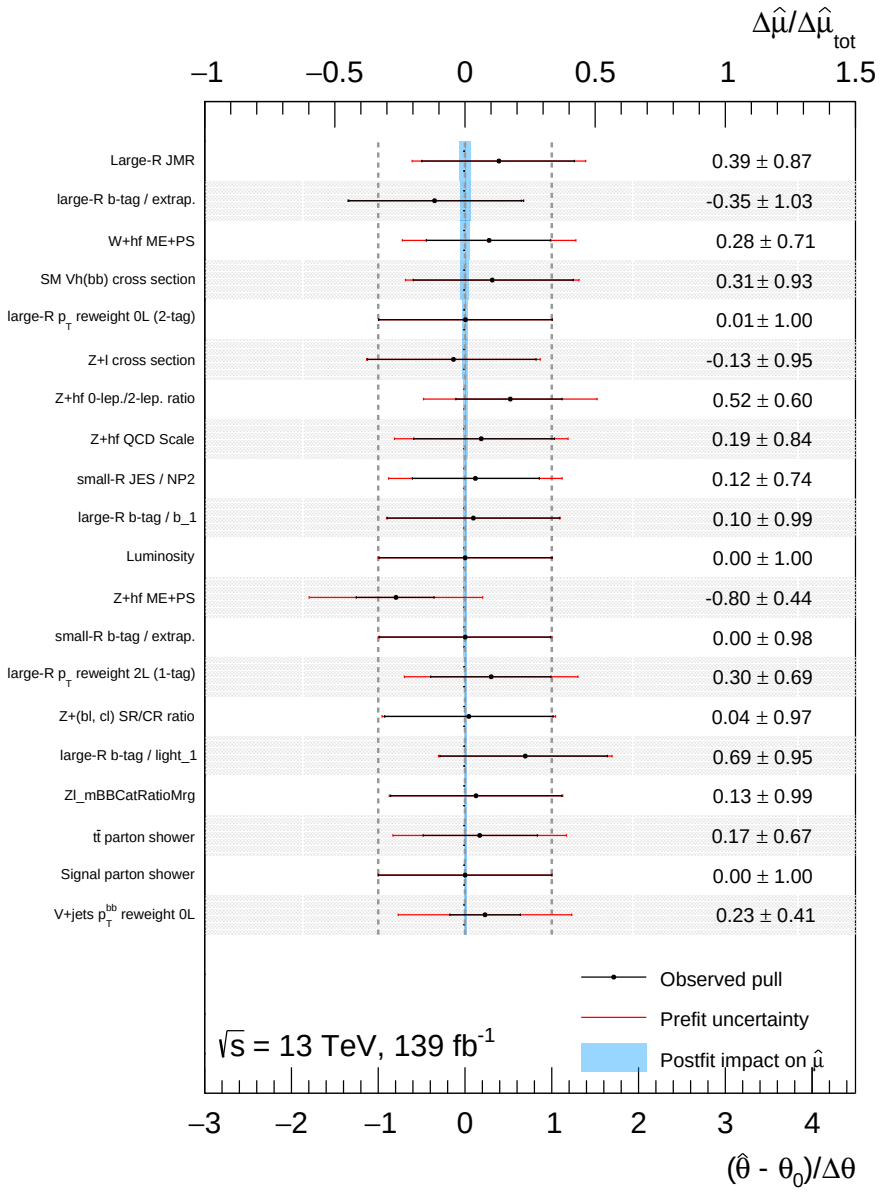

Figure 6.12: The individual impact $\Delta\hat{\mu}$ of the 20 most relevant nuisance parameters on the best-fit HVT Z' boson signal strength $\hat{\mu}$ with respect to the nominal best-fit value, obtained from an unconstrained fit to the data of the signal-plus-background hypothesis with a signal mass $m_{Z'} = 2\,\text{TeV}$ and $\sigma_{pp\to Z'\to Zh} = 2\,\text{fb}$. The $\Delta\hat{\mu}$ are given relative to the total impact $\Delta\hat{\mu}_{\text{tot}}$ of all systematic and statistical uncertainties. They are obtained by repeating the fit with nuisance parameters being shifted by ± 1 standard deviation with respect to their best-fit values. The post-fit pulls $(\hat{\theta} - \theta_0)/\Delta\theta$ of the nuisance parameters θ are indicated by the black dots with black error bars $\Delta\theta$.

Further dominant uncertainty sources are related to the Z+jets $p_{\mathrm{T}}^{b\bar{b}}$-based reweighting in the $\ell^{\pm}\ell^{\mp}b\bar{b}$ final state and to the predicted cross section of the SM Vh process. The relative importance of the remaining uncertainties targeting the Z+jets background components is decreased compared to the standalone analysis of the $\nu\bar{\nu}b\bar{b}$ final state due to the constraints from the $\ell^{\pm}\ell^{\mp}b\bar{b}$ final state. For the 2 TeV signal mass point, uncertainties on the mass resolution of large-radius jets and the extrapolation of the b-tagging efficiency calibration to high-p_{T} large-radius jets are dominant. The W+hf ME+PS modelling uncertainties contribute as the third-highest ranking nuisance parameter. However, this analysis is strongly limited by the statistical uncertainties, as even the highest-ranking nuisance parameter contributes only about 2 % to the total change of $\Delta\hat{\mu}_{\mathrm{tot}}$.

The impact of a set of related nuisance parameters on the total uncertainty of the best-fit signal strength $\hat{\mu}$ is evaluated by comparing two fit results: one with the full set of nuisance parameters (yielding the uncertainty σ_{tot}) and one with a particular set of nuisance parameters excluded (yielding the uncertainty $\sigma_{\vec{\theta}_i\text{excluded}}$, with $\vec{\theta}_i$ indicating the set of excluded nuisance parameters). The exclusion of nuisance parameters from the fit is achieved by setting the values of the corresponding nuisance parameters to their best-fit values and not allowing these values to be changed by the fit. The impact of the given set of nuisance parameters on $\hat{\mu}$ is then defined via the quadratic difference of the two obtained uncertainties on $\hat{\mu}$

$$\sigma_{\theta_i} = \sqrt{\sigma^2_{\mathrm{tot}} - \sigma^2_{\theta_i\ \mathrm{excluded}}}. \tag{6.5}$$

The nuisance parameters are grouped corresponding to the uncertainty sources presented in Sections 5.6 and 6.2.2. The obtained uncertainty values for the fits with pseudo-data containing signal masses of 700 GeV and 2 TeV are summarised in Table 6.13. For both signal mass points, the dominant contribution to the total uncertainty originates from statistical uncertainties on the data set. For completeness, the pull distributions of all nuisance parameters are shown in Appendix D.2.1.

The observed and expected correlation between the nuisance parameters are shown in Figures 6.13 and 6.14, respectively. Even though additional constraints on the Z + jets background components are available from the $\ell^{\pm}\ell^{\mp}b\bar{b}$ final state (with respect to the standalone fit of the $\nu\bar{\nu}b\bar{b}$ signal regions), a large correlation is observed between the normalisation of the top quark and the Z+hf background processes, indicating that constraints on the Z+jets background components alone are not sufficient to resolve the residual redundancy in the statistical description of these background components. Most of the other remaining correlations are related to the V+jets background components and the similarity in the shapes of the respective final fit discriminant. This is especially pronounced in the $\nu\bar{\nu}b\bar{b}$ final state, due to the worse resonance mass resolution.

Table 6.13: The expected uncertainties on the best-fit signal strength $\hat{\mu}$ at an integrated luminosity of 139 fb^{-1} for the combined analysis of the $\nu\bar{\nu}b\bar{b}$ and $\ell^{\pm}\ell^{\mp}b\bar{b}$ final states in the Z'/ggA fit setup with two different signal mass points. The uncertainty on the signal strength is given for a specific set of uncertainty sources, for the sum of all systematic uncertainties, and for the statistical uncertainties on the data. The values are obtained from an unconstrained fit to pseudo-data containing an HVT Z' signal with $\sigma_{pp\to Z'\to Zh}$ = 20 fb (2 fb) at $m_{Z'}$ = 700 GeV (2 TeV).

	Uncertainty on $\hat{\mu}$ [%]	
Uncertainty source	$m_{Z'}$ = 700 GeV	$m_{Z'}$ = 2 TeV
b-tagging (small-radius jets)	2.6	0.6
b-tagging (track jets)	0.6	1.5
top quark normalisation	0.7	0.2
Z+hf normalisation	0.1	0.2
Z+(bl, cl) normalisation	1.2	0.1
Jets	0.8	0.6
Leptons	0.1	0.0
Taus	0.1	0.0
$E_{\mathrm{T}}^{\mathrm{miss}}$	1.1	0.1
Luminosity	1.9	1.7
Pileup	0.2	0.1
$p_{\mathrm{T}}^{\mathrm{miss}}$ reweight	0.6	0.3
$p_{\mathrm{T}}^{b\bar{b}}$ reweight	4.8	0.5
large-radius p_{T}-based reweighting	0.2	2.6
Theory uncertainties (top quarks)	1.5	0.2
Theory uncertainties (Z+jets)	4.5	1.2
Theory uncertainties (W+jets)	7.0	1.2
Theory uncertainties (signal)	1.0	2.0
Diboson normalisation	1.2	1.1
SM Vh normalisation	2.8	0.7
MC stat.	6.4	2.4
Total syst.	16.8	5.5
Data stat.	22.1	22.3
Total	27.8	22.9

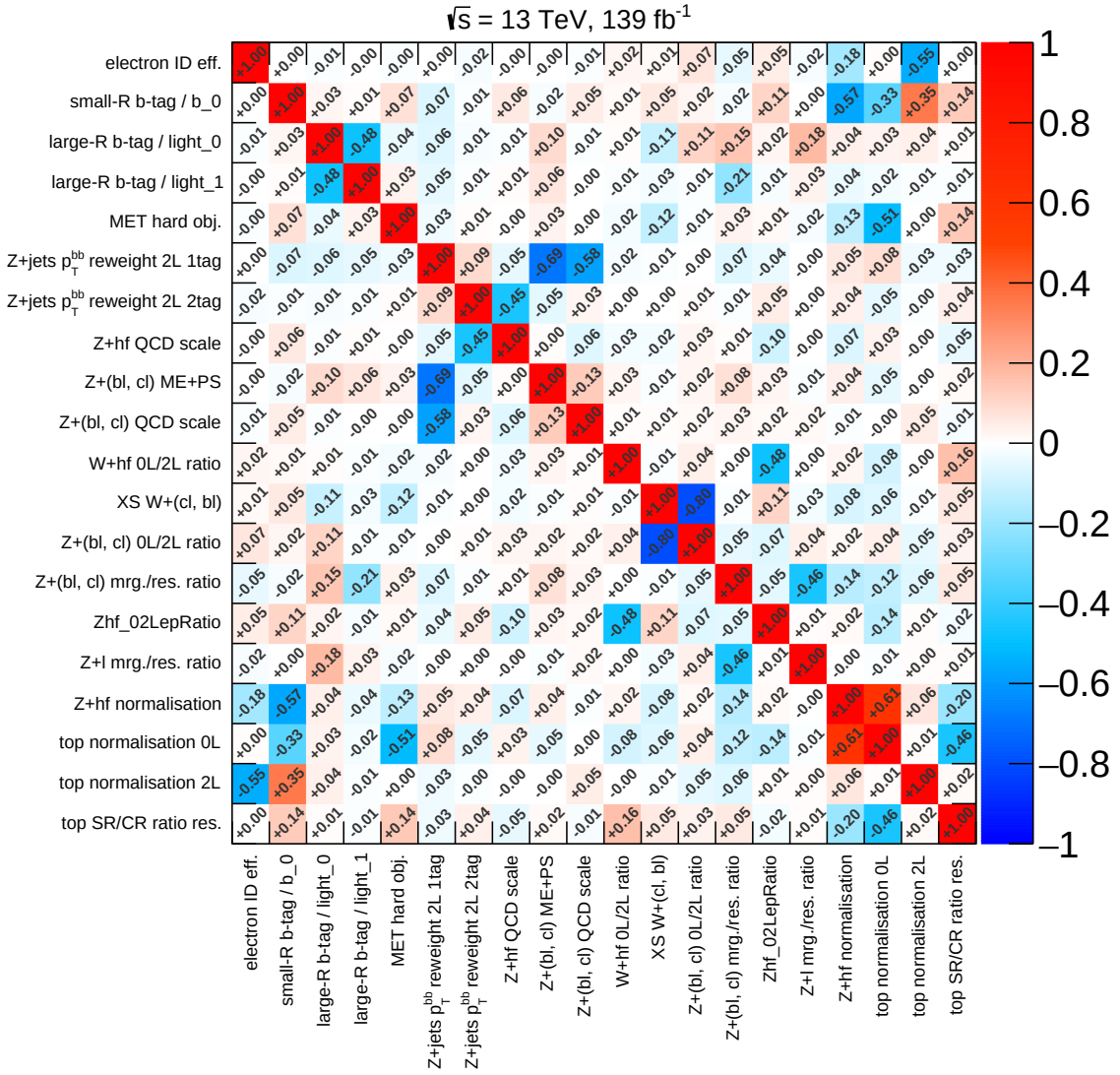

Figure 6.13: Expected correlation coefficients between the 20 nuisance parameters with the largest correlations, obtained from a fit to expected pseudo-data for the background-only hypothesis in the Z'/ggA fit setup.

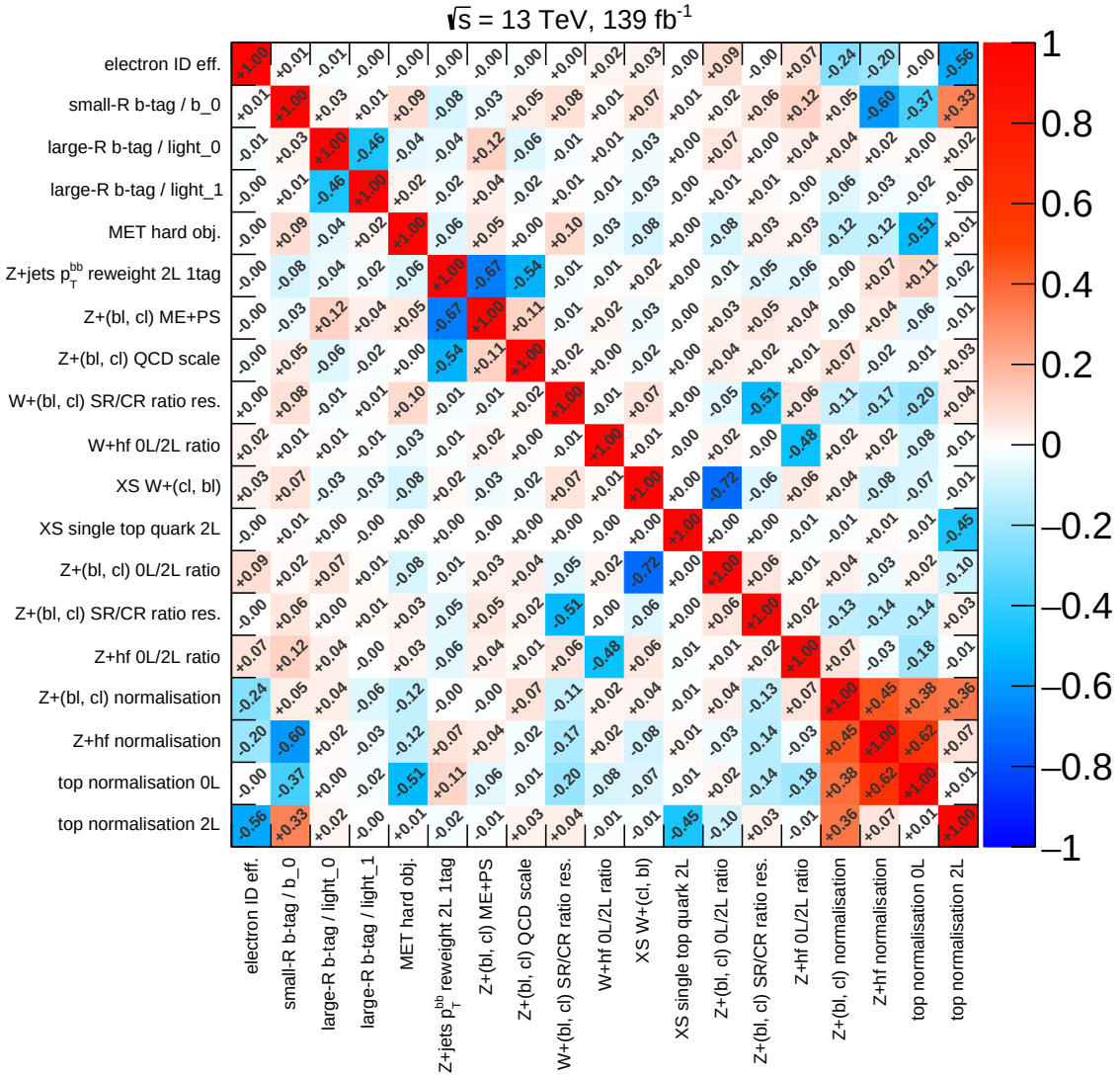

Figure 6.14: Observed correlation coefficients between the 20 nuisance parameters with the largest correlations, obtained from a fit to the observed data for the background-only hypothesis in the Z'/ggA fit setup.

Table 6.14: The observed and the expected 95 % C.L. upper limits on the 2HDM $A \to Zh$ signal cross section $\sigma^{\text{up}}_{gg\to A\to Zh}$ with $\pm1\sigma$ and $\pm2\sigma$ uncertainty bands for different A masses. The A boson is assumed to be exclusively produced in gluon fusion (ggA). The results are obtained from the combined analysis of the $\nu\bar{\nu}b\bar{b}$ and $\ell^{\pm}\ell^{\mp}b\bar{b}$ final states using the LHC Run 2 pp data set at $\sqrt{s} = 13\,\text{TeV}$ with an integrated luminosity of $139\,\text{fb}^{-1}$. Only the mass points corresponding to simulated signal samples are shown.

A mass [GeV]	$\sigma^{\text{up, exp.}}_{gg\to A\to Zh}$ [fb]	-2σ [fb]	-1σ [fb]	$+1\sigma$ [fb]	$+2\sigma$ [fb]	$\sigma^{\text{up, obs.}}_{gg\to A\to Zh}$ [fb]
300	4.50×10^2	2.42×10^2	3.24×10^2	6.26×10^2	8.40×10^2	5.94×10^2
400	1.22×10^2	6.52×10^1	8.76×10^1	1.70×10^2	2.29×10^2	1.06×10^2
420	1.05×10^2	5.63×10^1	7.55×10^1	1.46×10^2	1.98×10^2	6.74×10^1
440	8.94×10^1	4.80×10^1	6.44×10^1	1.25×10^2	1.69×10^2	6.40×10^1
460	7.48×10^1	4.01×10^1	5.39×10^1	1.05×10^2	1.41×10^2	7.16×10^1
500	5.41×10^1	2.90×10^1	3.90×10^1	7.57×10^1	1.03×10^2	1.04×10^2
600	2.97×10^1	1.59×10^1	2.14×10^1	4.17×10^1	5.67×10^1	3.12×10^1
700	1.83×10^1	9.82	1.32×10^1	2.57×10^1	3.52×10^1	1.39×10^1
800	1.20×10^1	6.46	8.68	1.70×10^1	2.33×10^1	1.19×10^1
900	9.46	5.08	6.82	1.33×10^1	1.82×10^1	1.02×10^1
1000	7.21	3.87	5.19	1.02×10^1	1.40×10^1	6.75
1200	4.90	2.63	3.53	6.96	9.68	3.51
1400	4.26	2.29	3.07	6.06	8.45	2.99
1600	3.60	1.93	2.59	5.13	7.17	2.28
2000	2.46	1.32	1.77	3.54	5.03	2.66

6.6.2 Results of the search for a 2HDM A boson produced via gluon fusion

The search for a 2HDM A pseudoscalar produced via gluon fusion (ggA mode, *cf.* Figure 5.2(b)) is performed using the same fit configuration as the search presented in the previous section (Z'/ggA fit setup). Therefore, the same numbers of post-fit expected and observed events are obtained and no excess of events above the background-only expectation is observed. Based on the dedicated ggA signal samples, upper limits at the 95 % C.L. are determined on the production cross section of an A boson produced via gluon fusion, $\sigma^{\text{up}}_{gg\to A\to Zh}$, as summarised in Table 6.14 and visualised in Figure 6.15. All observed limits are compatible with the respective expected limit within the $\pm2\sigma$ uncertainty band, except for the signal mass hypothesis of $m_A = 500\,\text{GeV}$ hypothesis, where a small excess of events with a significance of 2.14 standard deviations is observed. Production cross sections above 450 fb at $m_A = 300\,\text{GeV}$ and above 2.46 fb at $m_A = 2\,\text{TeV}$ are excluded at the 95 % C.L. The observed local p_0 values of the background-only hypothesis are shown in Figure 6.16. The values are very similar to the corresponding ones obtained from the HVT Z' analysis (*cf.* Section 6.6.1), underlining the similarity of the two signal models in terms of their respective distributions of the

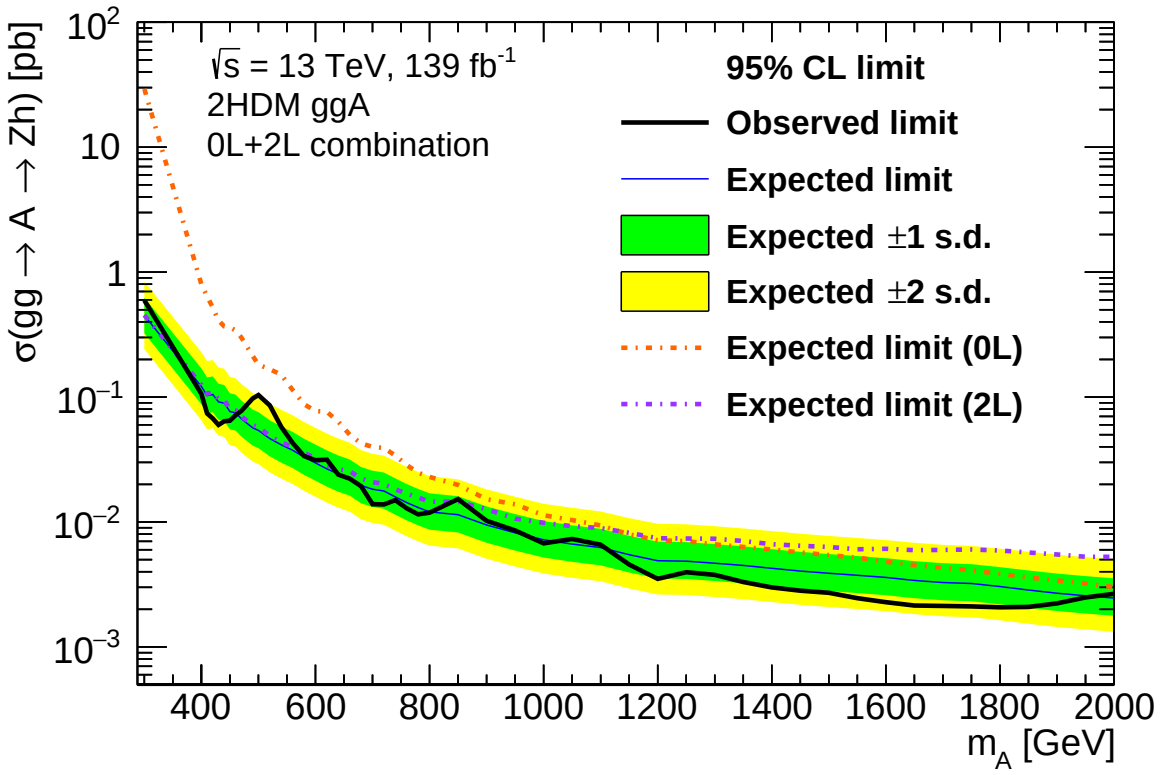

Figure 6.15: The observed (full black line) and expected (full blue line) 95 % C.L. upper limits on the cross section times branching ratio, $\sigma_{gg\to A\to Zh}$, for the combination of the $\nu\bar{\nu}b\bar{b}$ (0L, dashed orange line) and $\ell^{\pm}\ell^{\mp}b\bar{b}$ (2L, dashed purple line) final states. SM branching fractions of $\mathcal{B}(h \to \bar{b}b) = 0.569$, $\mathcal{B}(Z \to \nu\bar{\nu}) = 0.2$, and $\mathcal{B}(Z \to \ell^{+}\ell^{-}) = 0.1$ are assumed. The green and yellow bands indicate the $\pm 1\sigma$ and $\pm 2\sigma$ uncertainties on the expected cross section limit, respectively.

final discriminating variables.

6.6.3 Results of the search for a 2HDM A boson produced with b quarks

A dedicated fit to the observed data including additional signal regions is performed when searching for a 2HDM A boson produced in association with a b-quark pair (bbA mode, *cf.* Figure 5.2(c)), as described in Section 6.3. All observed numbers of events in the various signal regions are compatible with the background-only post-fit expectation (*cf.* Table 6.15). The observed and post-fit expected background distributions of the final discriminating variables are shown in Figures 6.17, 6.18 and 6.19 for the $\nu\bar{\nu}b\bar{b}$ signal regions, the $\ell^{\pm}\ell^{\mp}b\bar{b}$ signal regions with resolved topology, and the $\ell^{\pm}\ell^{\mp}b\bar{b}$ signal regions with merged topology, respectively. As no significant excess of events beyond the background-only expectation is observed, upper limits at the 95 % C.L. are obtained on the bbA signal cross section, as reported in Table 6.16 and visualised in Figure 6.20. All observed cross section

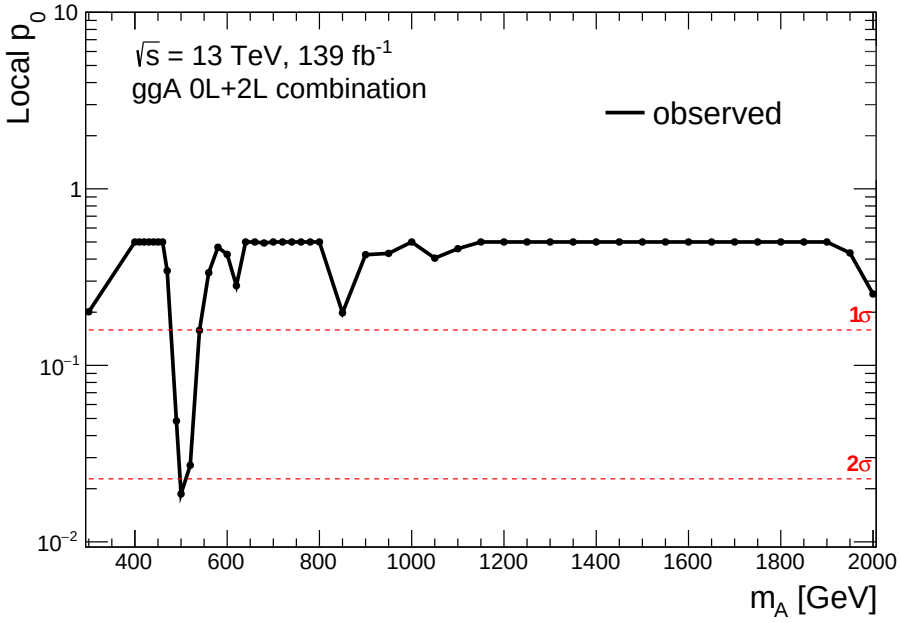

Figure 6.16: The observed local p_0-values for the 2HDM A (produced via gluon fusion) signal mass hypotheses between 300 GeV and 2 TeV. For reference, the signal significance levels of 1σ and 2σ are indicated by the red dotted lines.

limits are compatible with the corresponding expected limits within the $\pm 2\sigma$ uncertainty band. Cross sections for the production of a 2HDM A boson produced in association with b-quarks and decaying into Zh, $\sigma_{gg\to b\bar{b}A\to b\bar{b}Zh}$, that are above 0.42 pb at $m_A = 300$ GeV and above 2.7 fb at $m_A = 2$ TeV are excluded at the 95 % C.L. The compatibility of the observed data with the background-only hypothesis is further emphasised by the local p_0 values, which are all well below a significance level of 2 standard deviations (2σ), as shown in Figure 6.21.

The nuisance parameters with the largest impact on the best-fit $\hat{\mu}$ are summarised in Figures 6.22 and 6.23 for the $m_A = 400$ GeV and $m_A = 1.6$ TeV bbA signal mass points, respectively. For the lower mass point, where there are significant background contributions to the $m_{\mathrm{T},\,Vh}/m_{Vh}$, the dedicated treatment of the Z+jets background components in the high b-tag signal regions with resolved topology has the largest impact on the best-fit $\hat{\mu}$ value of about 10 %, indicating that these regions have the overall largest sensitivity in the analysis. Other dominant nuisance parameters are related to the QCD scale uncertainties of Z+hf events (8 %) and the parton shower tune in signal events (7 %). For the fit at the 1.6 TeV bbA signal mass point, the uncertainties on the predicted cross sections of the SM diboson processes have the largest impact on $\hat{\mu}$, about 15 %, indicating that the corresponding distributions of the discriminating variables are to some extent mutually indistinguishable. The second- and third-highest ranking nuisance parameters describe the theoretical uncertainties on the signal

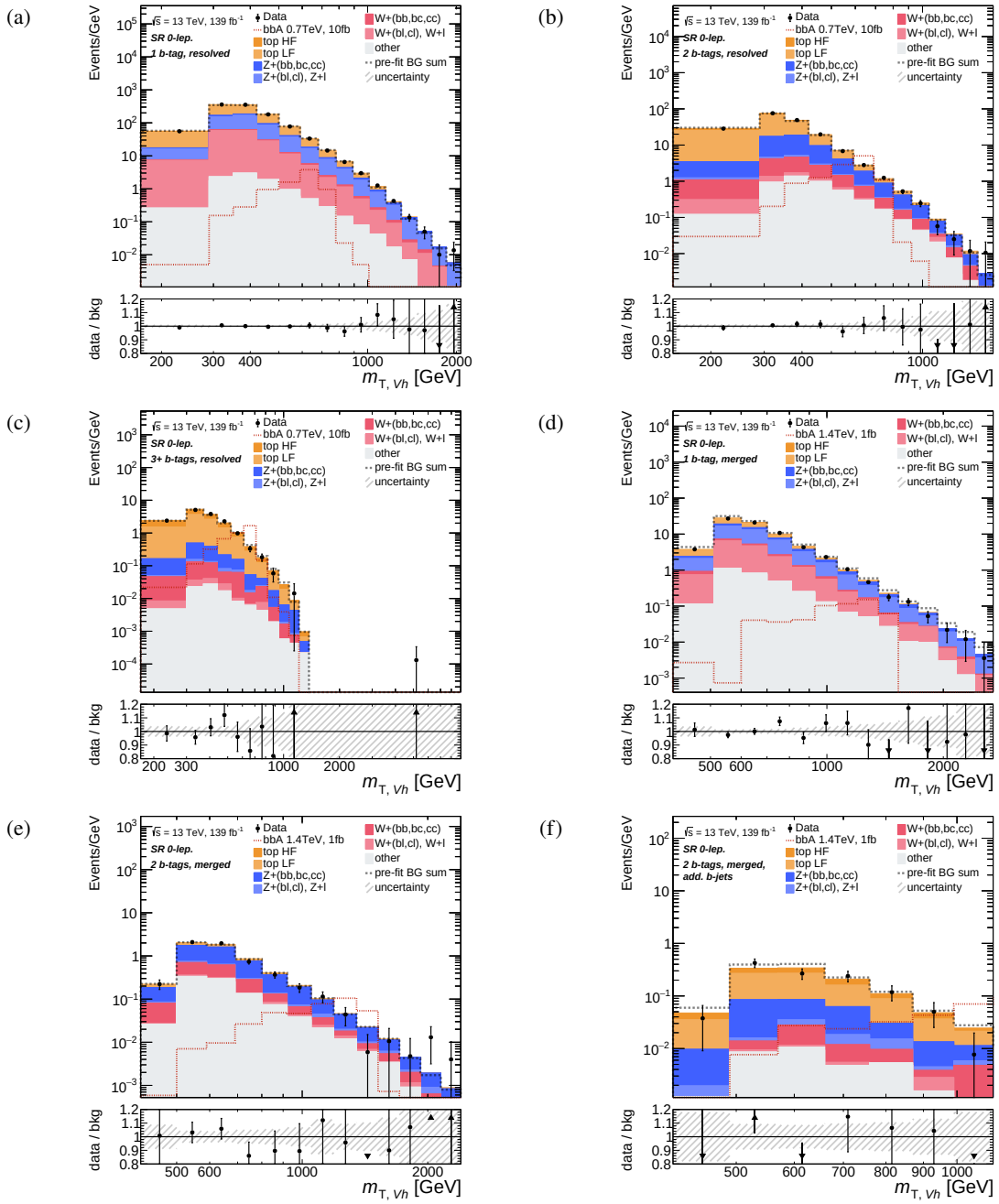

Figure 6.17: Observed and expected post-fit $m_{\mathrm{T},\,Vh}$ distributions obtained from the bbA fit setup in the $\nu\bar{\nu}b\bar{b}$ signal regions, with *(a)* 1 b-tag, *(b)* 2 b-tag, and *(c)* 3 or more b-tag events with the resolved topology, and *(d)* 1 b-tag, *(e)* 2 b-tag, and *(f)* 2 b-tag with additional b-tagged track jets not matched to the leading large-radius jet events with the merged topology. The total pre-fit background contribution is indicated by the dashed black line and the expected signal distribution from a 2HDM A boson (ggA mode) with a mass of 700 GeV (1.4 TeV) and $\sigma_{gg\to b\bar{b}A\to b\bar{b}Zh} = 10\,\mathrm{fb}$ (1 fb) is shown as the dotted red line for the distributions corresponding to events in the resolved (merged) topology. The data-to-background ratio where the hatched area indicates the post-fit background uncertainty is shown in the bottom panels.

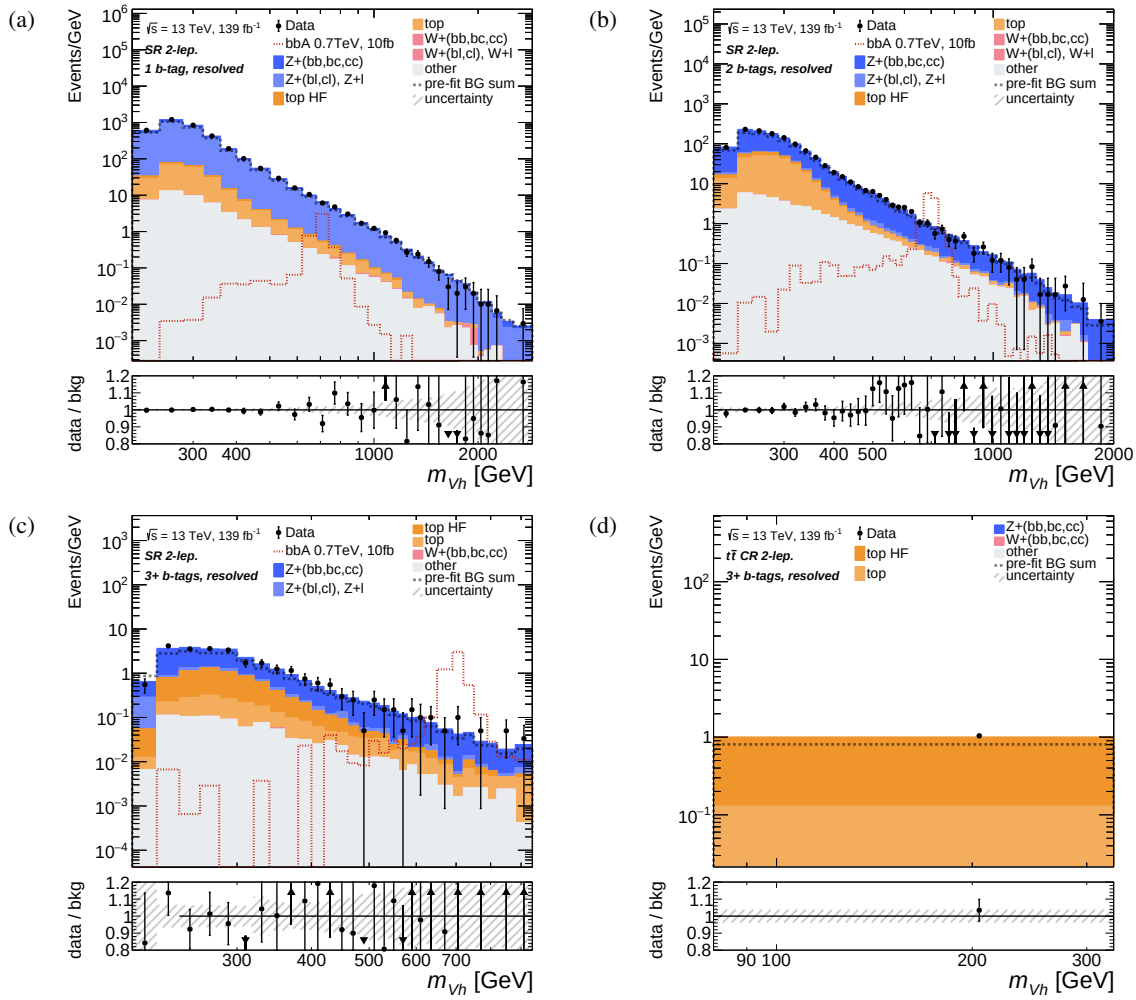

Figure 6.18: Observed and expected post-fit m_{Vh} distributions obtained from the bbA fit setup in the $\ell^{\pm}\ell^{\mp}b\bar{b}$ signal regions with resolved topology and *(a)* 1 b-tag, *(b)* 2 b-tag, and *(c)* 3 or more b-tag events. In *(d)*, the m_{Vh} distribution obtained from events with 1 or 2 b-tagged jets in the $t\bar{t}$ control region with opposite-flavour leptons is shown. The total pre-fit background contribution is indicated by the dashed black line and the expected signal distribution of a 700 GeV 2HDM A boson produced in association with a b-quark pair with $\sigma_{gg\to b\bar{b}A\to b\bar{b}Zh} = 10$ fb is shown as the dotted red line. The data-to-background ratio where the hatched area indicates the post-fit background uncertainty is shown in the bottom panels.

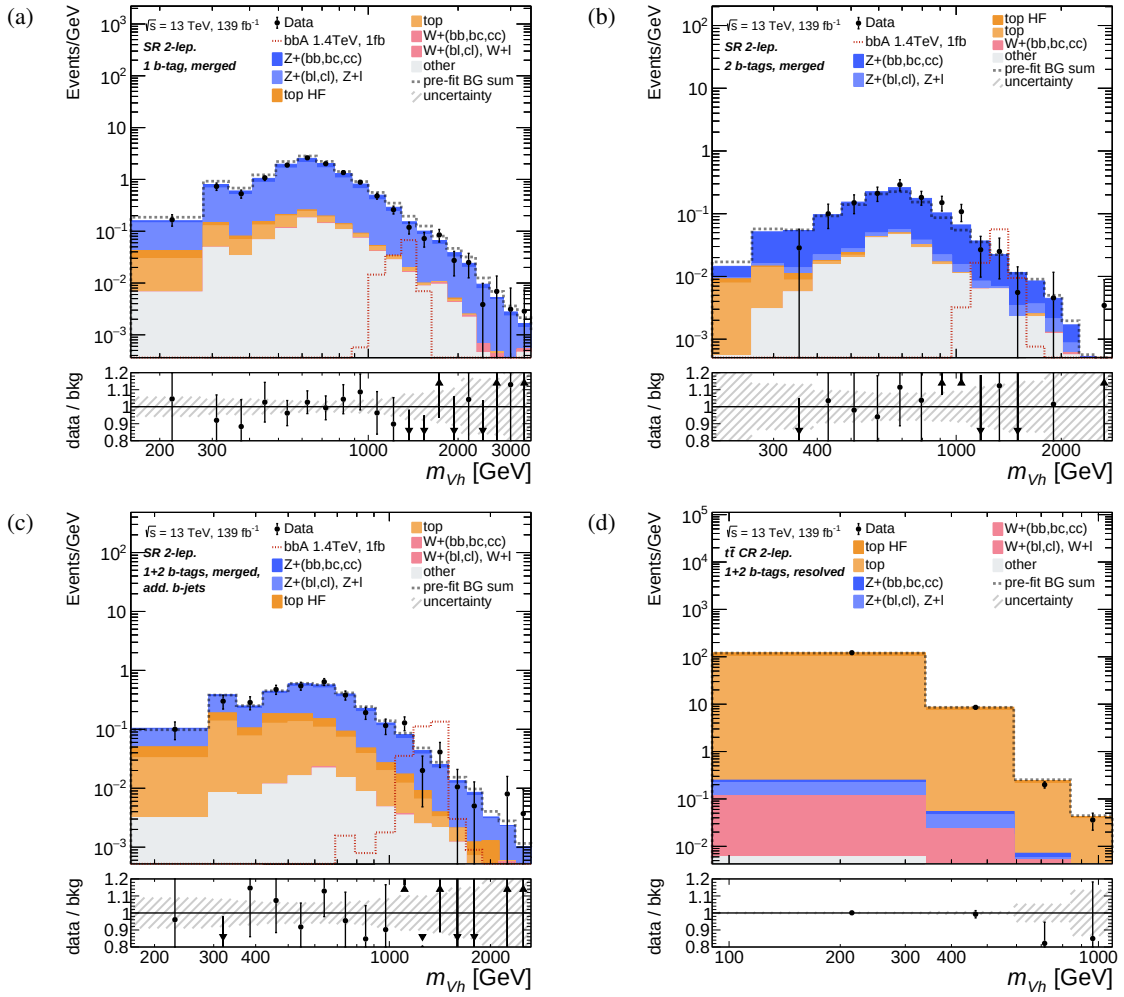

Figure 6.19: Observed and expected post-fit m_{Vh} distributions obtained from the bbA fit setup in the $\ell^{\pm}\ell^{\mp}b\bar{b}$ signal regions with merged topology and events with *(a)* 1 b-tag, *(b)* 2 b-tags, and *(c)* 1 or more b-tags together with additional b-tagged track jets not matched to the leading large-radius jet. In *(d)*, the m_{Vh} distribution obtained from events with 1 or 2 b-tagged track jets matched to the leading large-radius jet in the $t\bar{t}$ control region with opposite-flavour leptons is shown. The total pre-fit background contribution is indicated by the dashed black line and the expected signal distribution of a 1.4 TeV 2HDM A boson produced in association with a b-quark pair with $\sigma_{gg\to b\bar{b}A\to b\bar{b}Zh} = 1$ fb is shown as the dotted red line. The data-to-background ratio where the hatched area indicates the post-fit background uncertainty is shown in the bottom panels.

Table 6.15: The number of observed and expected (post-fit) events in the various $\nu\bar{\nu}b\bar{b}$ and $\ell^{\pm}\ell^{\mp}b\bar{b}$ signal regions in the bbA fit setup. The reported numbers correspond to an integrated luminosity of 139 fb^{-1}. Numbers are individually rounded and therefore the *Total* background can be different from the sum of the individual components. Cells are marked with a dash "—" if fewer than 1 event of the corresponding process is expected. The number of additional b-tagged VR track jets not matched to the leading large-radius track jet is abbreviated with "add.".

	$\nu\bar{\nu}b\bar{b}$ signal regions					
	resolved topology			merged topology		
Process	1 b-tag	2 b-tags	3+ b-tags	1 b-tag	2 b-tags, 0 add.	2 b-tags, 1+ add.
$t\bar{t}$+hf	4070 ± 310	1310 ± 110	406 ± 21	280 ± 40	14.4 ± 2.2	22.9 ± 3.4
top quarks	36 300 ± 500	8990 ± 120	736 ± 20	1690 ± 70	57.5 ± 2.3	53.9 ± 2.5
Z+hf	3776 ± 97	3000 ± 70	81.7 ± 3.3	665 ± 28	304 ± 12	19.2 ± 1.3
Z+(bl, cl)	20 800 ± 400	113 ± 15	5.92 ± 0.95	2340 ± 70	12.5 ± 0.9	2.39 ± 0.23
Z+l	1690 ± 230	5.8 ± 2.2	—	388 ± 31	—	—
W+hf	1000 ± 40	750 ± 40	27.8 ± 1.4	213 ± 17	94 ± 8	3.6 ± 0.5
W+(bl, cl)	9780 ± 310	89.0 ± 9.6	3.8 ± 0.6	1120 ± 90	6.0 ± 0.6	—
W+l	2030 ± 270	14 ± 4	—	239 ± 29	—	—
SM Vh	226 ± 14	295 ± 18	3.77 ± 0.21	24.5 ± 1.7	15.4 ± 1.1	—
Diboson	500 ± 60	73 ± 8	4.0 ± 0.5	300 ± 40	83 ± 11	2.75 ± 0.32
Total	80 110 ± 220	14 650 ± 90	1270 ± 21	7250 ± 60	587 ± 13	106 ± 5
Data	80 110	14 681	1265	7260	584	105

	$\ell^{\pm}\ell^{\mp}b\bar{b}$ signal regions					
	resolved topology			merged topology		
Process	1 b-tag	2 b-tags	3+ b-tags	1 b-tag	2 b-tags, 0 add.	1+ b-tags, 1+ add.
$t\bar{t}$+hf	1280 ± 70	1137 ± 35	106.1 ± 3.2	10.5 ± 0.5	—	25.7 ± 1.3
top quarks	6750 ± 100	4860 ± 90	27.8 ± 1.9	38.9 ± 2.4	2.66 ± 0.20	58 ± 4
Z+hf	23 000 ± 500	17 050 ± 110	333 ± 9	213 ± 7	99 ± 4	33.5 ± 2.2
Z+(bl, cl)	102 400 ± 1200	470 ± 40	22.1 ± 2.3	724 ± 18	4.66 ± 0.22	164 ± 7
Z+l	7300 ± 1100	35 ± 11	0	152 ± 12	—	18.8 ± 1.7
W+hf	4.66 ± 0.99	1.51 ± 0.13	—	—	—	—
W+(bl, cl)	22.9 ± 3.2	—	—	1.368 ± 0.034	—	—
W+l	—	—	—	—	—	—
SM Vh	331 ± 14	402 ± 13	5.18 ± 0.19	5.08 ± 0.25	2.59 ± 0.13	—
Diboson	1540 ± 80	426 ± 19	12.3 ± 0.6	84.3 ± 2.9	18.8 ± 0.8	10.1 ± 0.4
Total	142 680 ± 310	24 387 ± 95	506 ± 12	1230 ± 16	129 ± 4	311 ± 7
Data	142 672	24 371	505	1220	133	311

parton shower modelling (10 %) and the matching of the matrix element to parton shower generator (ME-to-PS) for the top quark processes (10 %).

The expected impact of different sets of nuisance parameters on the best-fit uncertainty on the signal strength is determined following Equation (6.5) and is shown in Table 6.17. For both investigated signal mass points, the statistical uncertainty of the recorded data set is the dominant contributor to the total uncertainty. The uncertainty due to the statistical fluctuations in data is particularly large for the 400 GeV signal mass point, indicating that the dominant contribution to the signal strength μ stems from the less populated resolved-topology signal regions with three or more b-tagged jets. In these regions, there is only a very limited number of contributing events compared to other signal regions with resolved topology. The post-fit pull values for complete set of nuisance parameters are shown in Appendix D.2.2.

Table 6.16: The observed and the expected 95 % C.L. upper limits on the 2HDM $A \to Zh$ signal cross section $\sigma^{\text{up}}_{gg\to b\bar{b}A\to b\bar{b}Zh}$ with $\pm1\sigma$ and $\pm2\sigma$ uncertainty bands for different A masses. The A boson is assumed to be exclusively produced in association with b-quarks (bbA). The results are obtained from the combined analysis of the $\nu\bar{\nu}b\bar{b}$ and $\ell^{\pm}\ell^{\mp}b\bar{b}$ final states using the LHC Run 2 pp data set at $\sqrt{s} = 13$ TeV with an integrated luminosity of 139 fb^{-1}. Only the mass points corresponding to simulated signal samples are shown.

A mass [GeV]	$\sigma^{\text{up, exp.}}_{gg\to b\bar{b}A\to b\bar{b}Zh}$ [fb]	-2σ [fb]	-1σ [fb]	$+1\sigma$ [fb]	$+2\sigma$ [fb]	$\sigma^{\text{up, obs.}}_{gg\to b\bar{b}A\to b\bar{b}Zh}$ [fb]
300	4.15×10^2	2.23×10^2	2.99×10^2	5.79×10^2	7.84×10^2	3.56×10^2
400	1.14×10^2	6.14×10^1	8.25×10^1	1.61×10^2	2.22×10^2	1.20×10^2
420	1.01×10^2	5.41×10^1	7.26×10^1	1.42×10^2	1.95×10^2	1.32×10^2
440	8.28×10^1	4.45×10^1	5.97×10^1	1.17×10^2	1.61×10^2	9.65×10^1
460	6.87×10^1	3.69×10^1	4.95×10^1	9.71×10^1	1.34×10^2	6.97×10^1
500	5.54×10^1	2.97×10^1	3.99×10^1	7.84×10^1	1.08×10^2	9.29×10^1
600	3.20×10^1	1.72×10^1	2.30×10^1	4.55×10^1	6.36×10^1	4.35×10^1
700	1.87×10^1	1.01×10^1	1.35×10^1	2.68×10^1	3.78×10^1	1.87×10^1
800	1.30×10^1	6.97	9.36	1.85×10^1	2.60×10^1	1.17×10^1
900	1.00×10^1	5.39	7.23	1.43×10^1	1.99×10^1	8.91
1000	8.48	4.55	6.11	1.21×10^1	1.68×10^1	5.85
1200	5.57	2.99	4.01	7.93	1.10×10^1	3.65
1400	4.40	2.36	3.17	6.34	9.03	3.23
1600	3.77	2.02	2.72	5.44	7.77	2.50
2000	2.67	1.43	1.92	3.92	5.79	2.48

The expected and observed correlations between nuisance parameters are shown in Figures 6.24 and 6.25, respectively. Once more, the largest correlations are observed across the normalisations of the V+jets and top quark background components.

6.6.4 Combined interpretation of the 2HDM ggA and bbA production modes

The signal hypotheses presented in Sections 6.6.2 and 6.6.3 correspond to the 2HDM A being produced exclusively via gluon fusion and in association with b-quarks, respectively. Within the 2HDM model, the relative contribution of the two production modes are fixed for any given set of 2HDM parameters. Thus, a simultaneous fit of both ggA and bbA signal contributions will provide direct constraints on the 2HDM parameter space. In order to allow for a simultaneous fit of signal contributions from both production modes in the statistical analysis of the observed data, a dedicated fit is performed with both production modes included in the signal hypothesis. For this fit, the number of expected signal events

Table 6.17: The expected uncertainties on the best-fit signal strength $\hat{\mu}$ at an integrated luminosity of 139 fb^{-1} for the combined analysis of the $\nu\bar{\nu}b\bar{b}$ and $\ell^{\pm}\ell^{\mp}b\bar{b}$ final states in the bbA fit setup with two different signal mass points. The uncertainty on the signal strength is given for a specific set of uncertainty sources, for the sum of all systematic uncertainties, and for the statistical uncertainties on the data. The values are obtained from an unconstrained fit to pseudo-data containing a 2HDM A signal produced in association with b-quarks with $\sigma_{gg\to b\bar{b}A\to b\bar{b}Zh}$ = 120 fb (14 fb) at m_A = 400 GeV (1.6 TeV).

	Uncertainty on $\hat{\mu}$ [%]	
Uncertainty source	m_A = 400 GeV	m_A = 1.6 TeV
b-tagging (small-radius jets)	2.6	1.8
b-tagging (track jets)	0.4	2.2
Jets	0.8	1.1
Leptons	0.2	0.1
Taus	0.3	0.1
$E_{\mathrm{T}}^{\mathrm{miss}}$	0.6	0.1
Luminosity	1.6	0.3
Pileup	0.3	0.0
$p_{\mathrm{T}}^{\mathrm{miss}}$ reweight	2.3	0.6
$p_{\mathrm{T}}^{b\bar{b}}$ reweight	2.3	1.0
large-radius p_{T}-based reweighting	0.1	0.7
Theory uncertainties (top quarks)	5.3	0.9
Theory uncertainties (Z+jets)	4.5	1.3
Theory uncertainties (W+jets)	3.3	0.6
Theory uncertainties (signal)	1.6	0.9
top quark normalisation	2.8	0.2
Z+hf normalisation	0.1	0.4
Z+(bl, cl) normalisation	1.8	0.6
Diboson normalisation	1.6	0.9
SM Vh normalisation	3.3	1.1
MC stat.	12.5	2.2
Total syst.	26.9	5.8
Data stat.	43.7	15.1
Total	51.3	16.2

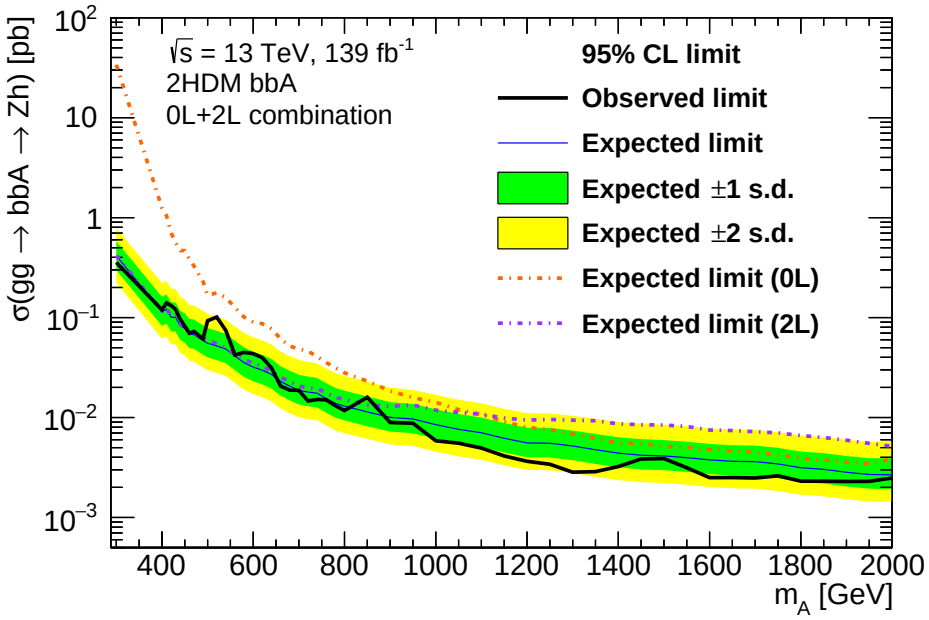

Figure 6.20: The observed (full black line) and expected (full blue line) 95 % C.L. upper limits on the cross section times branching ratio, $\sigma_{gg\to b\bar{b}A\to b\bar{b}Zh}$, for the combination of the $\nu\bar{\nu}b\bar{b}$ (0L, dashed orange line) and $\ell^{\pm}\ell^{\mp}b\bar{b}$ (2L, dashed purple line) final states. SM branching fractions of $\mathcal{B}(h\to\bar{b}b) = 0.569$, $\mathcal{B}(Z\to\nu\bar{\nu}) = 0.2$, and $\mathcal{B}(Z\to\ell\bar{\ell}) = 0.1$ are assumed. The green and yellow bands indicate the $\pm1\sigma$ and $\pm2\sigma$ uncertainties on the expected cross section limit, respectively.

from Equation (4.3) is modified to

$$n_{cb}^{\text{sig}} \quad\to\quad n_{cb}^{\text{sig, total}} = f_{\text{ggA}}\cdot n_{cb}^{\text{sig, ggA}} + f_{\text{bbA}}\cdot n_{cb}^{\text{sig, bbA}}, \tag{6.6}$$

where the signal fractions f_{ggA} and f_{bbA} are introduced as configurable parameters to individually scale the fraction of signal events produced exclusively via gluon fusion ($n_{cb}^{\text{sig, ggA}}$) and in association with a b-quark pair ($n_{cb}^{\text{sig, bbA}}$).

By scanning simultaneously over the two signal fractions and calculating the test statistic value (*cf.* Equation (4.6)) at each point $(f_{\text{ggA}}, f_{\text{bbA}})$, two-dimensional upper cross section limits are obtained (*i.e.* simultaneous cross section limits depending on $\sigma^{\text{up}}_{gg\to A\to Zh}$ *vs.* $\sigma^{\text{up}}_{gg\to b\bar{b}A\to b\bar{b}Zh}$). For simulated background-only pseudo-data, the resulting expected limits on the two cross sections are shown in Figure 6.26. The best-fit value (point of the highest probability) coincides with the origin at $(f_{\text{ggA}}, f_{\text{bbA}}) = (0, 0)$ by construction, and the 68 % and 95 % C.L. intervals correspond to the smallest areas that contain the corresponding probability.[1] The corresponding observed exclusion contours are shown in Figure 6.27, where the background-only scenario (*i.e.* $(0, 0)$) is contained within the 68 %

[1] These values do not necessarily coincide with the one-dimensional upper cross section limits at the 95 % C.L. as described in more detail in Ref. [233].

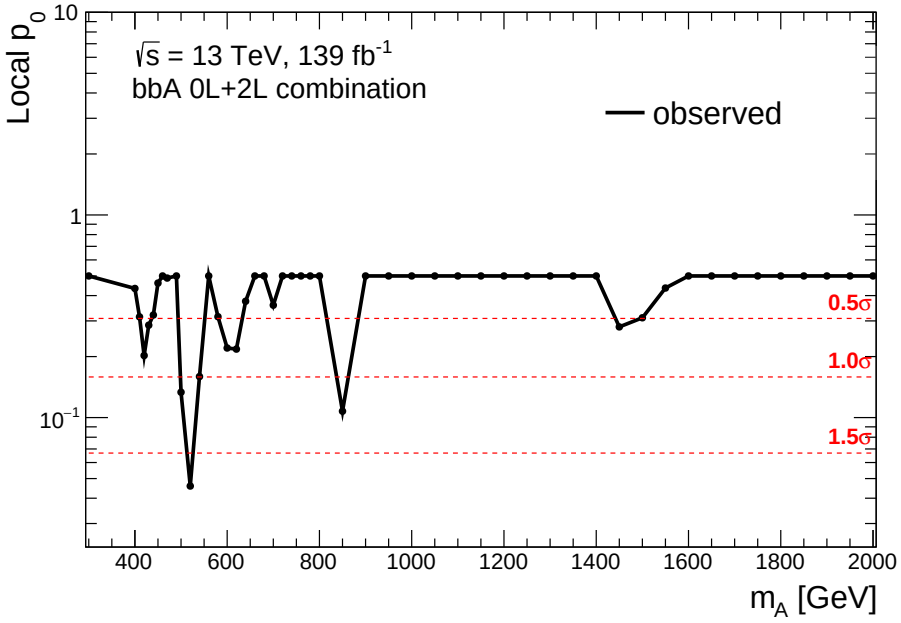

Figure 6.21: The observed local p_0-values for the 2HDM bbA-produced A boson with signal masses between 300 GeV and 2 TeV. For reference, the signal significance levels of 0.5σ, 1σ, and 1.5σ are indicated by the red dotted lines.

C.L. contour for all tested values of m_A.

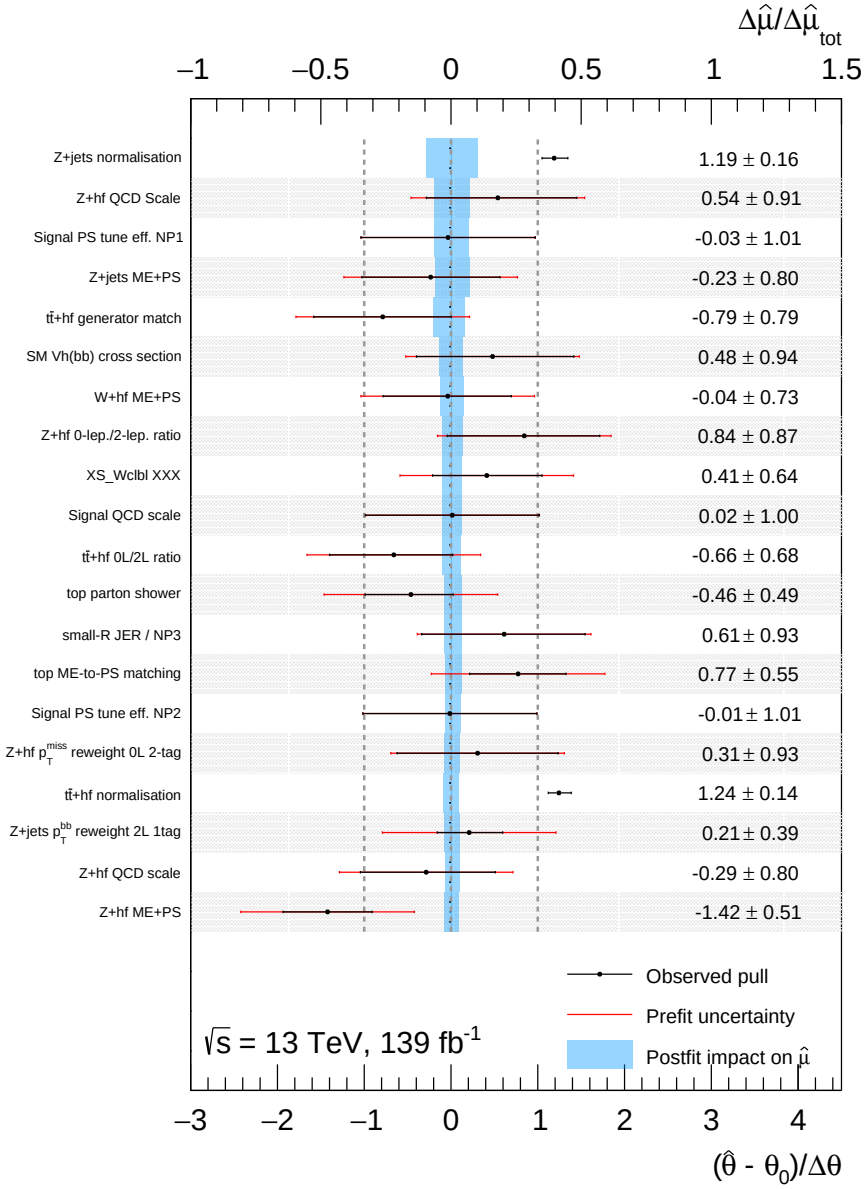

Figure 6.22: The impact $\Delta\hat{\mu}$ of each of the 20 most relevant nuisance parameters on the best-fit signal strength $\hat{\mu}$ with respect to the nominal best-fit value. The best-fit value $\hat{\mu}$ is obtained from an unconstrained fit to the data using a signal-plus-background hypothesis (for the 2HDM A boson produced in association with b-quarks) with a signal mass of $m_A = 400\,\text{GeV}$ and $\sigma_{gg\to A\to Zh} = 120\,\text{fb}$. The impact $\Delta\hat{\mu}$ is obtained by repeating the fit with the respective nuisance parameter being modified by ±1 (post-fit) standard deviation around their best-fit values. The nuisance parameter standard deviations are indicated in the figure by black bars. The post-fit pull $(\hat{\theta} - \theta_0)/\Delta\theta$ on a given nuisance parameter θ is indicated by the black dot. The exact pull values are written explicitly next to each nuisance parameter.

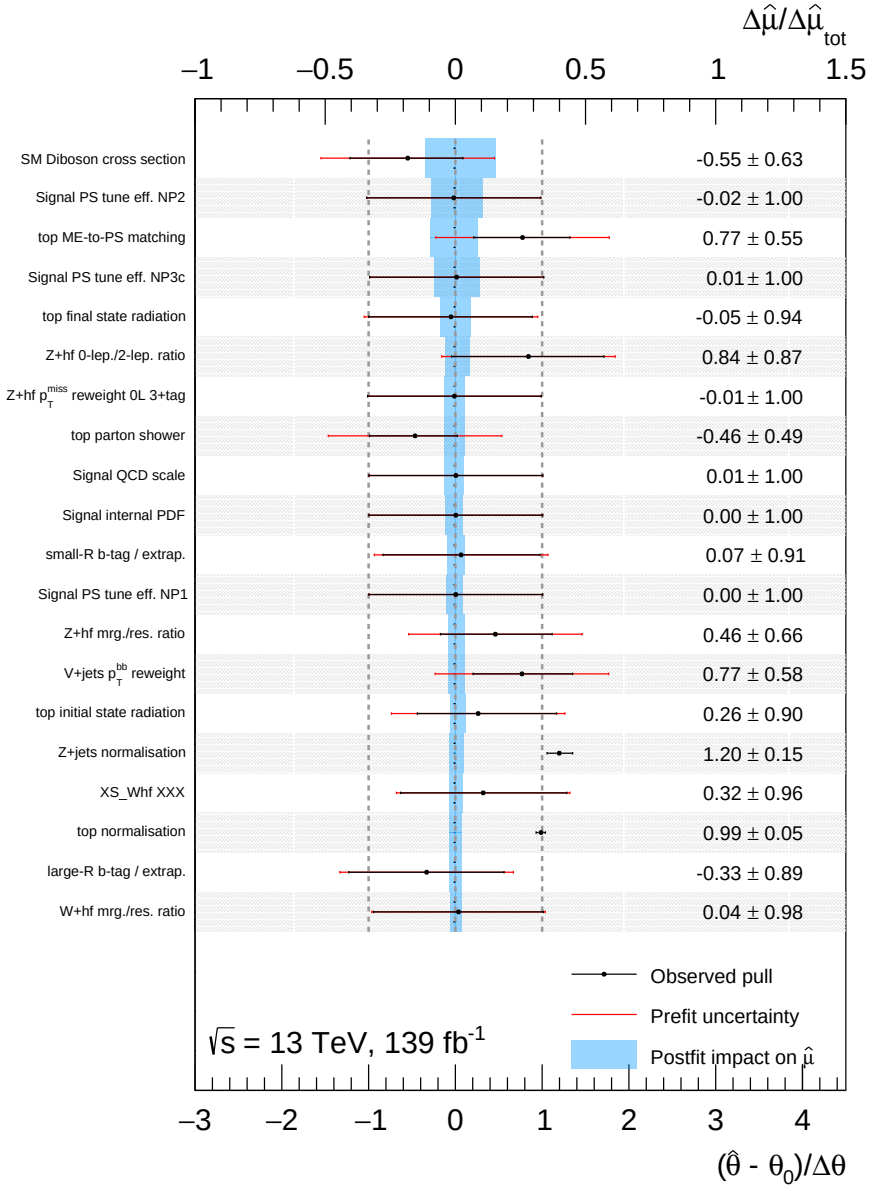

Figure 6.23: The impact $\Delta\hat{\mu}$ of each of the 20 most relevant nuisance parameters on the best-fit signal strength $\hat{\mu}$ with respect to the nominal best-fit value. The best-fit value $\hat{\mu}$ is obtained from an unconstrained fit to the data using a signal-plus-background hypothesis (for the 2HDM A boson produced in association with b-quarks) with a signal mass of $m_A = 1.6\,\text{TeV}$ and $\sigma_{gg\to A\to Zh} = 14\,\text{fb}$. The impact $\Delta\hat{\mu}$ is obtained by repeating the fit with the respective nuisance parameter being modified by ± 1 (post-fit) standard deviation around their best-fit values. The nuisance parameter standard deviations are indicated in the figure by black bars. The post-fit pull $(\hat{\theta} - \theta_0)/\Delta\theta$ on a given nuisance parameter θ is indicated by the black dot. The exact pull values are written explicitly next to each nuisance parameter.

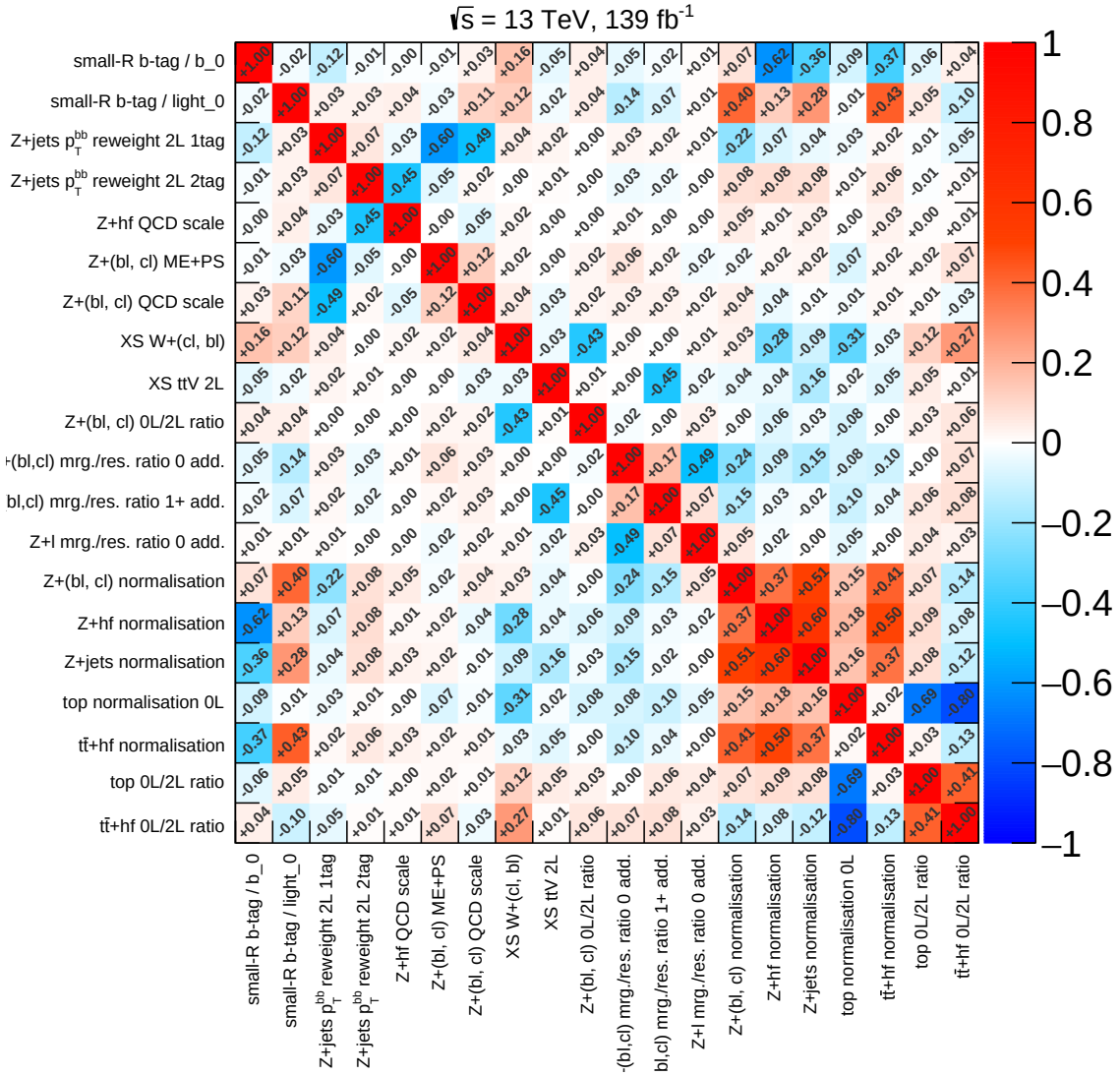

Figure 6.24: Expected correlation coefficients between the 20 nuisance parameters with the largest correlations, obtained from a fit to expected pseudo-data for the background-only hypothesis in the bbA fit setup.

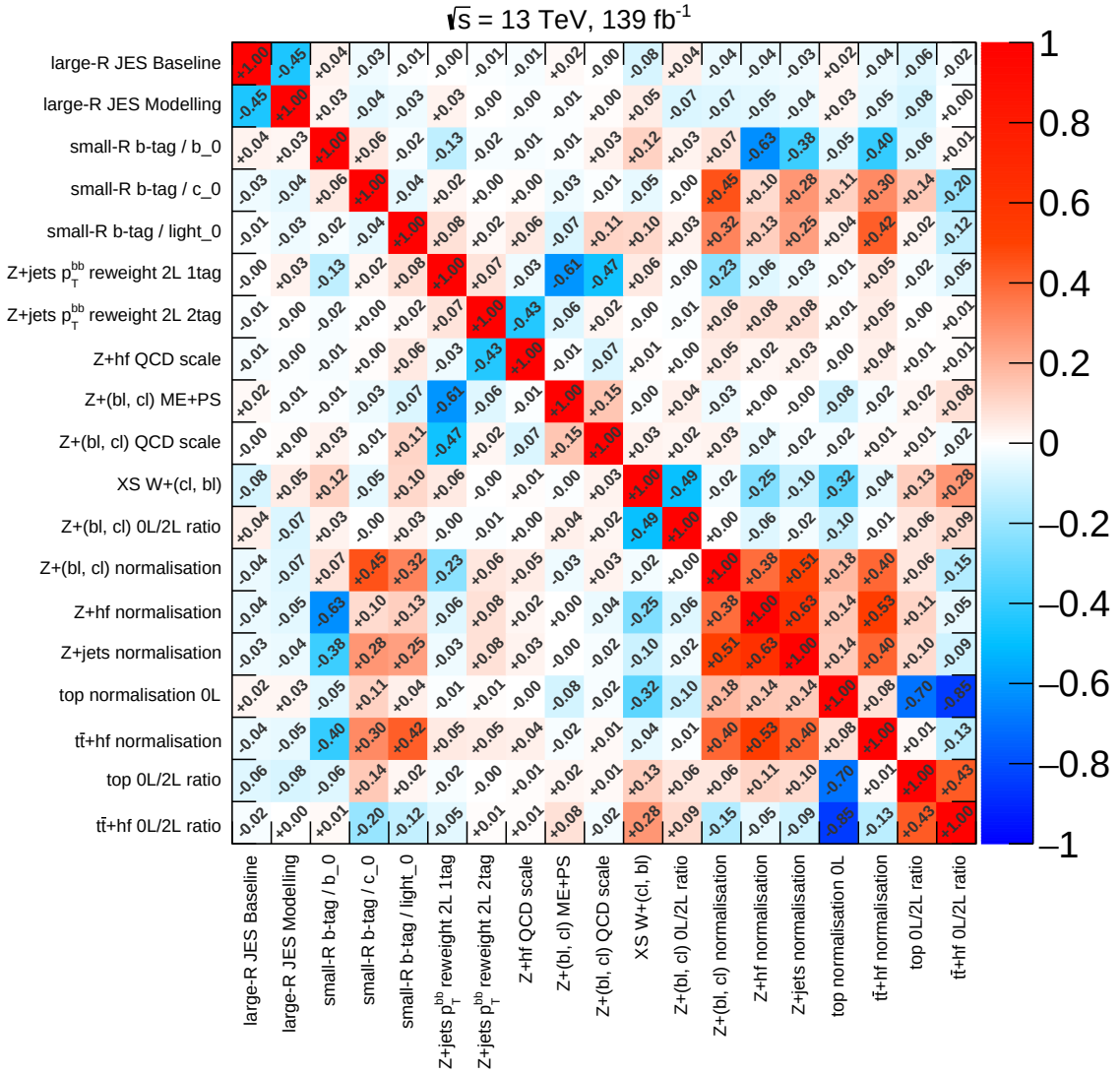

Figure 6.25: Observed correlation coefficients between the 20 nuisance parameters with the largest correlations, obtained from a fit to the observed data for the background-only hypothesis in the bbA fit setup.

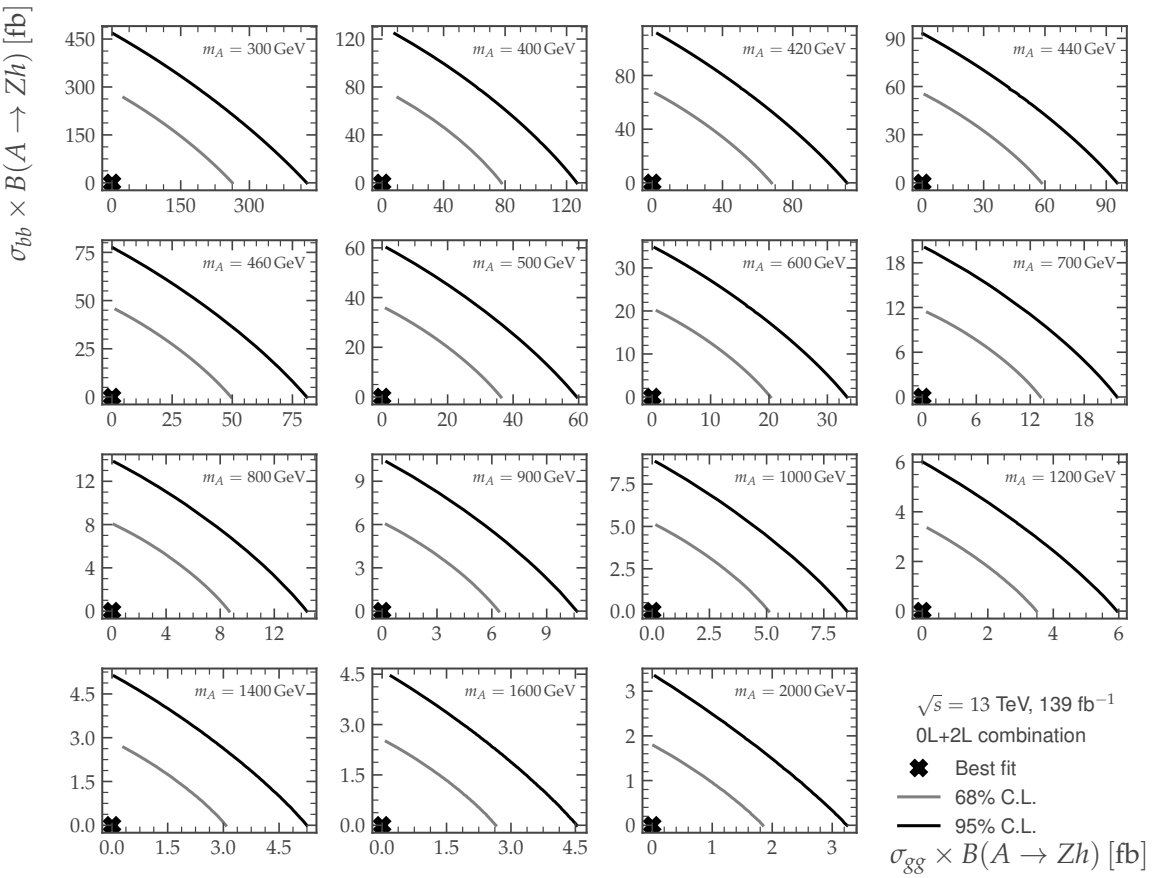

Figure 6.26: The expected upper limit contours at 68 % C.L. (grey) and 95 % C.L. (black) on the cross sections for the gluon fusion, $\sigma^{\text{up}}_{gg\to A\to Zh}$, and the b-quark associated signal production, $\sigma^{\text{up}}_{gg\to b\bar{b}A\to b\bar{b}Zh}$, obtained from a combined fit of the $\nu\bar{\nu}b\bar{b}$ and $\ell^{\pm}\ell^{\mp}b\bar{b}$ final state fit regions to background-only pseudo-data. Both cross sections are multiplied with the branching fraction for an A boson into a Zh boson pair, $B(A \to Zh)$. The best-fit value is indicated by the black cross. The area on the top-right above each contour line is excluded at the corresponding confidence level. SM branching fractions of $\mathcal{B}(h \to b\bar{b}) = 0.569$, $\mathcal{B}(Z \to \nu\bar{\nu}) = 0.2$, and $\mathcal{B}(Z \to \ell^{+}\ell^{-}) = 0.1$ are assumed. The scan is performed for A boson masses between 300 GeV and 2000 GeV.

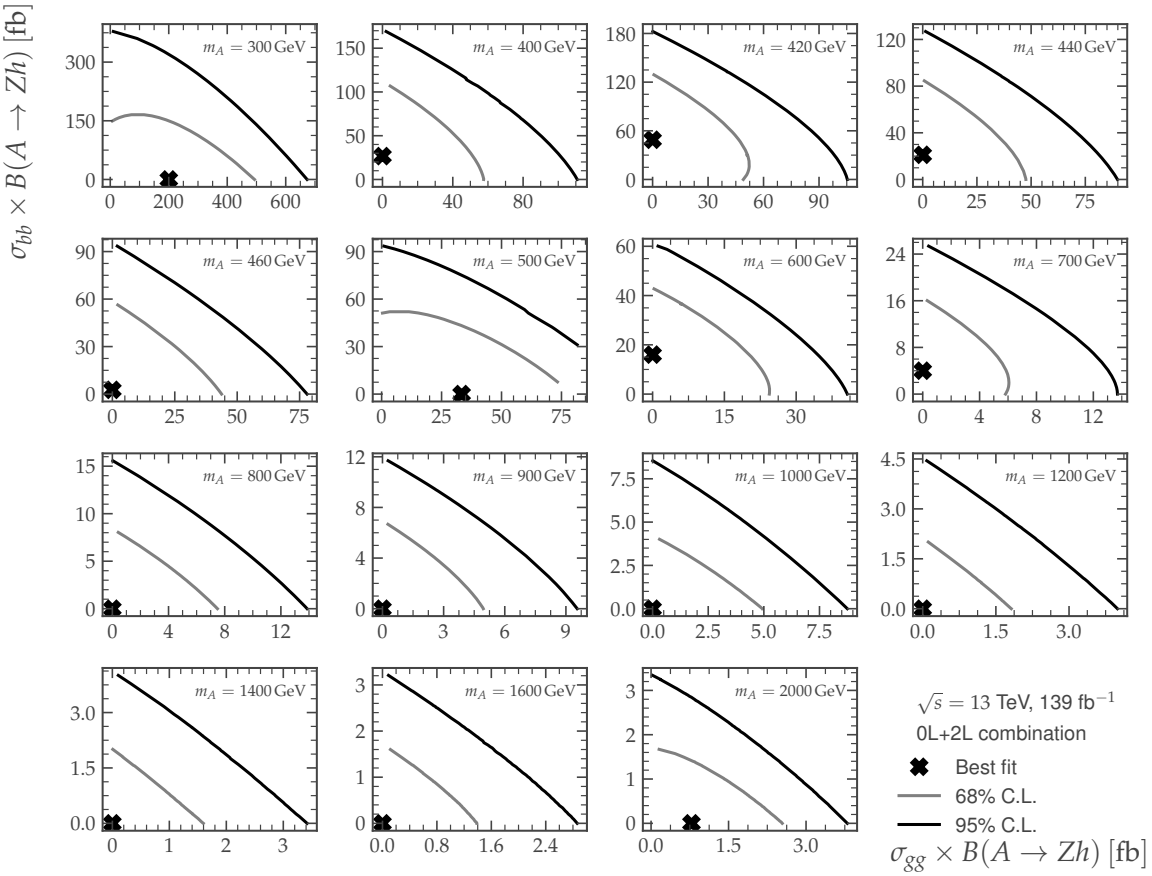

Figure 6.27: The observed upper limit contours at 68 % C.L. (grey) and 95 % C.L. (black) on the cross sections for the gluon fusion, $\sigma^{\text{up}}_{gg\to A\to Zh}$, and the b-quark associated signal production, $\sigma^{\text{up}}_{gg\to b\bar{b}A\to b\bar{b}Zh}$, obtained from a combined fit of the $\nu\bar{\nu}b\bar{b}$ and $\ell^{\pm}\ell^{\mp}b\bar{b}$ final state fit regions to the recorded data. Both cross sections are multiplied with the branching fraction for an A boson into a Zh boson pair, $B(A \to Zh)$. The best-fit value is indicated by the black cross. The area on the top-right above each contour line is excluded at the corresponding confidence level. SM branching fractions of $\mathcal{B}(h \to b\bar{b}) = 0.569$, $\mathcal{B}(Z \to \nu\bar{\nu}) = 0.2$, and $\mathcal{B}(Z \to \ell^{+}\ell^{-}) = 0.1$ are assumed. The scan is performed for A boson masses between 300 GeV and 2000 GeV.

CHAPTER SEVEN

CONCLUSIONS AND OUTLOOK

Since its discovery in 2012, the Higgs boson has become a key probe for the exploration of new physics scenarios beyond the Standard Model (BSM). In addition to the measurement of Higgs boson properties and searching for deviations from SM predictions, the SM Higgs boson may also be produced in decays of new BSM particles. The discovered Higgs boson could, for example, be part of an extended scalar sector with additional Higgs bosons—like a pseudoscalar A boson—as described by Two-Higgs Doublet Models (2HDMs). Other extensions of the Standard Model—such as the Heavy Vector Triplet (HVT) model—predict the existence of additional heavy vector bosons $W'^{\pm}$ and Z', which couple to the SM Higgs boson h. Searches for new heavy resonances decaying into the Higgs boson strongly constrain many extensions of the Standard Model. In this thesis, searches for such resonances ($W'^{\pm}$, Z', A) decaying into a weak vector boson and a Higgs boson have been performed, using the LHC Run-2 (2015–2018) pp collision data recorded by the ATLAS experiment at a centre-of-mass energy of 13 TeV.

The search for a new heavy charged vector boson W' in $W' \to Wh$ decays predicted by the HVT model was performed in the $\ell^{\pm}\overset{(-)}{\nu}_{\ell} b\bar{b}$ final state using the dataset of pp collisions recorded in 2015 and 2016 that corresponds to an integrated luminosity of 36.1 fb^{-1}. The focus of this thesis for this search was on the modelling of the background processes. The contribution of multijet background was estimated using a dedicated data-driven method. The V+jets background was classified according to their jet flavour, in order to optimise the modelling of this background. No significant excess of events over the expected background contribution was observed. Therefore, 95 % C.L. upper limits on the production cross time branching fraction, $\sigma_{pp\to W'\to Wh} \times \mathcal{B}(h \to b\bar{b}, c\bar{c})$, of a heavy $W' \to Wh$ vector boson resonance were set for representative W' masses. Values of $\sigma_{pp\to W'\to Wh} \times \mathcal{B}(h \to b\bar{b}, c\bar{c})$ above 0.29 pb and 1.1 fb are excluded for W' resonance masses of 300 GeV and 5 TeV, respectively. Correspondingly, W' boson masses above 2.7 TeV and 2.8 TeV are excluded at 95 % C.L. in the HVT reference models A and B, respectively. In a combined analysis of the $\nu\bar{\nu}b\bar{b}$, $\ell^{\pm}\overset{(-)}{\nu}_{\ell} b\bar{b}$, and $\ell^{\pm}\ell^{\mp}b\bar{b}$ final states, assuming degenerated Z' and W' boson masses in the HVT model, resonance masses above 2.8 TeV and 2.9 TeV are excluded at 95 % C.L. for the HVT models A and B, respectively.

The searches for a neutral pseudoscalar A and a heavy vector Z' boson have been performed in the $\nu\bar{\nu}b\bar{b}$ final state using the full Run-2 dataset with an integrated luminosity of 139 fb^{-1}. Compared to the preceding analysis based on the 2015 and 2016 dataset, significant improvements to the analysis strategy have been made within the context of this thesis, increasing the search sensitivity beyond the mere improvement of the statistical precision of the recorded dataset. The employment of track jets with a variable, p_{T}-dependent radius parameter greatly improves the search sensitivity for large resonance masses. A threshold on the object-based $E_{\mathrm{T}}^{\mathrm{miss}}$ significance allowed for the efficient suppression of the multijet background to a negligible level, as demonstrated by a new data-driven background estimation method. The V+jets background was classified similarly to the analysis of the $\ell^{\pm}\overset{(-)}{\nu}_{\ell}b\bar{b}$ final state. The work done within the context of this thesis also contributed the complete statistical interpretation of the data, including the calculation of 95 % C.L. upper cross section limits. No significant excess over the background-only expectation was observed. Consequently, 95 % C.L. upper limits on the signal production cross section times branching ratio are derived for the 2HDM A boson and the HVT Z' boson resonances decaying subsequently into the SM Higgs boson and a Z boson ($X \to Zh$). The interpretation in terms of a 2HDM pseudoscalar A is limited to the A boson production via gluon fusion. Production cross sections times branching ratios $\sigma_{pp\to Z'\to Zh}$ of 31 pb, 2.7 fb, and 0.32 fb are excluded at the 95 % C.L. for HVT Z' resonances with masses of 300 GeV, 2 TeV, and 5 TeV, respectively. These limits are up to a factor of two lower for 2HDM A boson production via gluon fusion.

The combined statistical interpretation of the data in the $\nu\bar{\nu}b\bar{b}$ and the $\ell^{\pm}\ell^{\mp}b\bar{b}$ final states was performed as a part of this thesis. It allows for up to 30-fold stronger constraints on new heavy boson production compared to the limits from the $\nu\bar{\nu}b\bar{b}$ final state alone. Additionally, the combination also provides sensitivity to A boson production in association with b-quarks by employing dedicated signal regions. In an effort to restore the sensitivity to new signals with resonance masses in the range between the simulated signal mass points, a morphing signal modelling technique was implemented. As no excess over the background in either of the two final states was observed, combined upper limits on the production cross section times branching ratio of new heavy resonances were determined. Values of $\sigma_{pp\to Z'\to Zh}$ larger than 0.98 pb, 2.1 fb, and 0.30 fb are excluded at 95 % C.L. for resonance masses of 300 GeV, 2 TeV, and 5 TeV, respectively. Differences of approximately a factor of two are observed in the 2HDM interpretations. The results are also translated into exclusion contours in the two-dimensional parameter space of couplings of the new heavy boson to W, Z, and Higgs bosons (g_H) and to fermions (g_F) in the HVT model. The results of the interpretations of 2HDM A boson production via gluon fusion (ggA) and in association with b-quarks (bbA) are combined to obtain exclusion contours in the plane $\sigma_{gg\to A\to Zh}$ *vs.* $\sigma_{gg\to b\bar{b}A\to b\bar{b}Zh}$. The Standard Model background-only hypothesis is contained within the 68 % C.L. exclusion contours for all tested 2HDM A boson resonance masses between 300 GeV and 2 TeV.

The presented upper limits on the production cross sections of new resonances are obtained using only minimal assumptions about the tested theoretical models. The main assumption is that the natural decay width Γ of the new heavy boson with mass m is small enough, $\Gamma/m \lesssim 5\,\%$, allowing for these particles to observed as a narrow resonance on top of the smoothly falling background spectrum. Therefore, the results can be re-interpreted in terms of various other models with spin-0 or spin-1 resonances decaying to Wh or Zh.

Searches for heavy diboson resonances have also been carried out in other decay modes. New results for searches in the fully hadronic $Vh \to q\bar{q}b\bar{b}$ ($V = W, Z$) final state [234], and in the semileptonic VV decay mode [235] have recently been published. The former search sets particularly strong upper cross section limits for resonance masses below 3 TeV, while the latter provides very similar limits to those presented in this thesis over the full range of resonance masses. By accepting a certain model dependence related to the relative branching fractions for different resonance decay modes, the statistical combination of these searches will further strengthen the constraints on the production of new heavy resonances. Such a combination was published with the partial dataset recorded in 2015 and 2016 [236] and the update with the full Run-2 dataset is expected to exclude HVT Model A and B resonances for masses beyond 4 TeV.

In the future, the search for Vh resonances can be significantly improved by further increasing the signal reconstruction efficiency. The current reconstruction of the $h \to b\bar{b}$ Higgs boson decay candidates often leads to the selection of a wrong jet pair. Especially in the case of 2HDM A boson production in association with a b-quark pair, the selection of the correct $h \to b\bar{b}$ candidate is challenging and a large fraction of the signal does not pass the signal selection criteria. By including more information on the kinematic properties of the final state jets using multivariate analysis methods leveraging the correlations between the jet properties, the signal acceptance can be significantly improved. Moreover, additional Higgs boson decay modes, like $h \to \tau\tau$, can be included in the search. A major advantage of this Higgs decay mode is that a clear distinction between the Higgs decay products and the b-quarks produced in association with the A boson is possible. With a branching ratio of $\mathcal{B}(h \to \tau\tau) = 6.3\,\%$ in the Standard Model [237], this decay mode provides a relatively large number of signal events, while the background contributions are smaller compared to the $b\bar{b}$ final state. For highly boosted Higgs boson decays, the $h \to WW$ decay mode into two hadronically decaying W bosons, with SM branching fraction $\mathcal{B}(h \to WW \to \text{jets}) = 0.21 \cdot (0.67)^2 = 9.4\,\%$, can also be considered for future searches. In the case of a highly boosted Higgs boson decay, all final state products can be contained within a single large-radius jet. Efforts in this direction can be based on preceding work, presented for instance in Refs. [238, 239], where large-radius jets incorporating track jet information [240] are used to extract substructure information from the large-radius jet.

Nine years after the discovery of the Higgs boson, no new heavy particle beyond the Standard Model has been observed at the LHC. Instead, the experiments at the LHC provide increasingly stronger

constraints on all extensions of the Standard Model. With no clear preference for any model, it is important to provide the search results in an unbiased, largely model-independent way. Based on the published results from LHC Run 1 and Run 2 data, the models have evolved and many possibilities for finding new particles at yet unexplored mass scales exist for the upcoming Run 3 of the LHC and for the high-luminosity LHC upgrade. With the possibility for direct observation and fairly model-independent selection of new particles, the search for Vh resonances will continue to play an important role in the future ATLAS and LHC physics programme.

Appendix

CHAPTER A

SIGNAL CROSS SECTION TABLES

A.1 HVT production cross sections

The production cross sections for heavy vector boson resonances are calculated using the software tools provided in Ref. [12]. The predicted values $\sigma_{pp\to Z'\to Zh}$ within the HVT benchmark Model A and Model B are shown in Table A.1. The corresponding values for a W' resonance are summarised in Table A.2.

	300 GeV	400 GeV	500 GeV	600 GeV	700 GeV	800 GeV	900 GeV
Model A	$2.45 \cdot 10^{1}$	8.6	3.6	1.79	$9.81 \cdot 10^{-1}$	$5.8 \cdot 10^{-1}$	$3.6 \cdot 10^{-1}$
Model B	—	—	—	—	—	$4.9 \cdot 10^{-1}$	$3.7 \cdot 10^{-1}$
	1000 GeV	1100 GeV	1200 GeV	1300 GeV	1400 GeV	1500 GeV	1600 GeV
Model A	$2.31 \cdot 10^{-1}$	$1.55 \cdot 10^{-1}$	$1.06 \cdot 10^{-1}$	$7.4 \cdot 10^{-2}$	$5.3 \cdot 10^{-2}$	$3.9 \cdot 10^{-2}$	$2.84 \cdot 10^{-2}$
Model B	$2.64 \cdot 10^{-1}$	$1.89 \cdot 10^{-1}$	$1.36 \cdot 10^{-1}$	$9.86 \cdot 10^{-2}$	$7.2 \cdot 10^{-2}$	$5.4 \cdot 10^{-2}$	$4.0 \cdot 10^{-2}$
	1700 GeV	1800 GeV	1900 GeV	2000 GeV	2100 GeV	2200 GeV	2300 GeV
Model A	$2.11 \cdot 10^{-2}$	$1.58 \cdot 10^{-2}$	$1.20 \cdot 10^{-2}$	$9.2 \cdot 10^{-3}$	$7.0 \cdot 10^{-3}$	$5.4 \cdot 10^{-3}$	$4.2 \cdot 10^{-3}$
Model B	$3.02 \cdot 10^{-2}$	$2.29 \cdot 10^{-2}$	$1.75 \cdot 10^{-2}$	$1.35 \cdot 10^{-2}$	$1.04 \cdot 10^{-2}$	$8.1 \cdot 10^{-3}$	$6.3 \cdot 10^{-3}$
	2400 GeV	2500 GeV	2600 GeV	2700 GeV	2800 GeV	2900 GeV	3000 GeV
Model A	$3.30 \cdot 10^{-3}$	$2.58 \cdot 10^{-3}$	$2.03 \cdot 10^{-3}$	$1.60 \cdot 10^{-3}$	$1.27 \cdot 10^{-3}$	$1.01 \cdot 10^{-3}$	$8.0 \cdot 10^{-4}$
Model B	$5.0 \cdot 10^{-3}$	$3.9 \cdot 10^{-3}$	$3.08 \cdot 10^{-3}$	$2.44 \cdot 10^{-3}$	$1.93 \cdot 10^{-3}$	$1.54 \cdot 10^{-3}$	$1.23 \cdot 10^{-3}$
	3100 GeV	3200 GeV	3300 GeV	3400 GeV	3500 GeV	3600 GeV	3700 GeV
Model A	$6.4 \cdot 10^{-4}$	$5.1 \cdot 10^{-4}$	$4.1 \cdot 10^{-4}$	$3.27 \cdot 10^{-4}$	$2.62 \cdot 10^{-4}$	$2.11 \cdot 10^{-4}$	$1.69 \cdot 10^{-4}$
Model B	$9.79 \cdot 10^{-4}$	$7.8 \cdot 10^{-4}$	$6.3 \cdot 10^{-4}$	$5.0 \cdot 10^{-4}$	$4.0 \cdot 10^{-4}$	$3.25 \cdot 10^{-4}$	$2.62 \cdot 10^{-4}$
	3800 GeV	3900 GeV	4000 GeV	4100 GeV	4200 GeV	4300 GeV	4400 GeV
Model A	$1.36 \cdot 10^{-4}$	$1.10 \cdot 10^{-4}$	$8.8 \cdot 10^{-5}$	$7.1 \cdot 10^{-5}$	$5.7 \cdot 10^{-5}$	$4.6 \cdot 10^{-5}$	$3.7 \cdot 10^{-5}$
Model B	$2.11 \cdot 10^{-4}$	$1.70 \cdot 10^{-4}$	$1.37 \cdot 10^{-4}$	$1.10 \cdot 10^{-4}$	$8.9 \cdot 10^{-5}$	$7.2 \cdot 10^{-5}$	$5.8 \cdot 10^{-5}$
	4500 GeV	4600 GeV	4700 GeV	4800 GeV	4900 GeV	5000 GeV	5100 GeV
Model A	$3.00 \cdot 10^{-5}$	$2.42 \cdot 10^{-5}$	$1.95 \cdot 10^{-5}$	$1.57 \cdot 10^{-5}$	$1.27 \cdot 10^{-5}$	$1.02 \cdot 10^{-5}$	$8.2 \cdot 10^{-6}$
Model B	$4.7 \cdot 10^{-5}$	$3.8 \cdot 10^{-5}$	$3.04 \cdot 10^{-5}$	$2.45 \cdot 10^{-5}$	$1.97 \cdot 10^{-5}$	$1.59 \cdot 10^{-5}$	$1.28 \cdot 10^{-5}$
	5200 GeV	5300 GeV	5400 GeV	5500 GeV	5600 GeV	5700 GeV	5800 GeV
Model A	$6.6 \cdot 10^{-6}$	$5.3 \cdot 10^{-6}$	$4.2 \cdot 10^{-6}$	$3.40 \cdot 10^{-6}$	$2.72 \cdot 10^{-6}$	$2.18 \cdot 10^{-6}$	$1.74 \cdot 10^{-6}$
Model B	$1.03 \cdot 10^{-5}$	$8.3 \cdot 10^{-6}$	$6.6 \cdot 10^{-6}$	$5.3 \cdot 10^{-6}$	$4.3 \cdot 10^{-6}$	$3.41 \cdot 10^{-6}$	$2.72 \cdot 10^{-6}$
	5900 GeV	6000 GeV	6100 GeV	6200 GeV	6300 GeV	6400 GeV	6500 GeV
Model A	$1.39 \cdot 10^{-6}$	$1.11 \cdot 10^{-6}$	$8.8 \cdot 10^{-7}$	$7.0 \cdot 10^{-7}$	$5.5 \cdot 10^{-7}$	$4.4 \cdot 10^{-7}$	$3.45 \cdot 10^{-7}$
Model B	$2.17 \cdot 10^{-6}$	$1.73 \cdot 10^{-6}$	$1.38 \cdot 10^{-6}$	$1.09 \cdot 10^{-6}$	$8.7 \cdot 10^{-7}$	$6.9 \cdot 10^{-7}$	$5.4 \cdot 10^{-7}$
	6600 GeV	6700 GeV	6800 GeV	6900 GeV	7000 GeV	7100 GeV	7200 GeV
Model A	$2.72 \cdot 10^{-7}$	$2.14 \cdot 10^{-7}$	$1.68 \cdot 10^{-7}$	$1.31 \cdot 10^{-7}$	$1.02 \cdot 10^{-7}$	$8.0 \cdot 10^{-8}$	$6.2 \cdot 10^{-8}$
Model B	$4.3 \cdot 10^{-7}$	$3.35 \cdot 10^{-7}$	$2.63 \cdot 10^{-7}$	$2.06 \cdot 10^{-7}$	$1.61 \cdot 10^{-7}$	$1.25 \cdot 10^{-7}$	$9.70 \cdot 10^{-8}$
	7300 GeV	7400 GeV	7500 GeV	7600 GeV	7700 GeV	7800 GeV	7900 GeV
Model A	$4.8 \cdot 10^{-8}$	$3.7 \cdot 10^{-8}$	$2.84 \cdot 10^{-8}$	$2.18 \cdot 10^{-8}$	$1.66 \cdot 10^{-8}$	$1.27 \cdot 10^{-8}$	$9.60 \cdot 10^{-9}$
Model B	$7.5 \cdot 10^{-8}$	$5.8 \cdot 10^{-8}$	$4.5 \cdot 10^{-8}$	$3.41 \cdot 10^{-8}$	$2.61 \cdot 10^{-8}$	$1.99 \cdot 10^{-8}$	$1.51 \cdot 10^{-8}$

Table A.1: Production cross sections times Zh branching fraction, $\sigma_{pp \to Z' \to Zh}$, in pb of a neutral Z' heavy vector boson in the HVT Model A and B benchmarks. The values are generated with the tools provided in Ref. [12].

	300 GeV	400 GeV	500 GeV	600 GeV	700 GeV	800 GeV	900 GeV
Model A	$3.9 \cdot 10^{1}$	$1.43 \cdot 10^{1}$	6.4	3.23	1.80	1.08	$6.8 \cdot 10^{-1}$
Model B	—	—	—	—	—	$8.8 \cdot 10^{-1}$	$6.9 \cdot 10^{-1}$
	1000 GeV	1100 GeV	1200 GeV	1300 GeV	1400 GeV	1500 GeV	1600 GeV
Model A	$4.4 \cdot 10^{-1}$	$3.00 \cdot 10^{-1}$	$2.08 \cdot 10^{-1}$	$1.47 \cdot 10^{-1}$	$1.06 \cdot 10^{-1}$	$7.8 \cdot 10^{-2}$	$5.8 \cdot 10^{-2}$
Model B	$5.0 \cdot 10^{-1}$	$3.6 \cdot 10^{-1}$	$2.65 \cdot 10^{-1}$	$1.94 \cdot 10^{-1}$	$1.44 \cdot 10^{-1}$	$1.08 \cdot 10^{-1}$	$8.1 \cdot 10^{-2}$
	1700 GeV	1800 GeV	1900 GeV	2000 GeV	2100 GeV	2200 GeV	2300 GeV
Model A	$4.3 \cdot 10^{-2}$	$3.28 \cdot 10^{-2}$	$2.50 \cdot 10^{-2}$	$1.93 \cdot 10^{-2}$	$1.49 \cdot 10^{-2}$	$1.16 \cdot 10^{-2}$	$9.1 \cdot 10^{-3}$
Model B	$6.2 \cdot 10^{-2}$	$4.7 \cdot 10^{-2}$	$3.6 \cdot 10^{-2}$	$2.83 \cdot 10^{-2}$	$2.20 \cdot 10^{-2}$	$1.72 \cdot 10^{-2}$	$1.35 \cdot 10^{-2}$
	2400 GeV	2500 GeV	2600 GeV	2700 GeV	2800 GeV	2900 GeV	3000 GeV
Model A	$7.1 \cdot 10^{-3}$	$5.6 \cdot 10^{-3}$	$4.4 \cdot 10^{-3}$	$3.50 \cdot 10^{-3}$	$2.78 \cdot 10^{-3}$	$2.21 \cdot 10^{-3}$	$1.77 \cdot 10^{-3}$
Model B	$1.07 \cdot 10^{-2}$	$8.4 \cdot 10^{-3}$	$6.7 \cdot 10^{-3}$	$5.3 \cdot 10^{-3}$	$4.2 \cdot 10^{-3}$	$3.38 \cdot 10^{-3}$	$2.70 \cdot 10^{-3}$
	3100 GeV	3200 GeV	3300 GeV	3400 GeV	3500 GeV	3600 GeV	3700 GeV
Model A	$1.41 \cdot 10^{-3}$	$1.13 \cdot 10^{-3}$	$9.0 \cdot 10^{-4}$	$7.2 \cdot 10^{-4}$	$5.8 \cdot 10^{-4}$	$4.6 \cdot 10^{-4}$	$3.7 \cdot 10^{-4}$
Model B	$2.16 \cdot 10^{-3}$	$1.73 \cdot 10^{-3}$	$1.39 \cdot 10^{-3}$	$1.11 \cdot 10^{-3}$	$8.9 \cdot 10^{-4}$	$7.2 \cdot 10^{-4}$	$5.7 \cdot 10^{-4}$
	3800 GeV	3900 GeV	4000 GeV	4100 GeV	4200 GeV	4300 GeV	4400 GeV
Model A	$2.98 \cdot 10^{-4}$	$2.39 \cdot 10^{-4}$	$1.92 \cdot 10^{-4}$	$1.54 \cdot 10^{-4}$	$1.23 \cdot 10^{-4}$	$9.85 \cdot 10^{-5}$	$7.9 \cdot 10^{-5}$
Model B	$4.6 \cdot 10^{-4}$	$3.7 \cdot 10^{-4}$	$2.97 \cdot 10^{-4}$	$2.38 \cdot 10^{-4}$	$1.91 \cdot 10^{-4}$	$1.53 \cdot 10^{-4}$	$1.22 \cdot 10^{-4}$
	4500 GeV	4600 GeV	4700 GeV	4800 GeV	4900 GeV	5000 GeV	5100 GeV
Model A	$6.3 \cdot 10^{-5}$	$5.0 \cdot 10^{-5}$	$4.0 \cdot 10^{-5}$	$3.19 \cdot 10^{-5}$	$2.54 \cdot 10^{-5}$	$2.02 \cdot 10^{-5}$	$1.60 \cdot 10^{-5}$
Model B	$9.79 \cdot 10^{-5}$	$7.8 \cdot 10^{-5}$	$6.2 \cdot 10^{-5}$	$5.0 \cdot 10^{-5}$	$4.0 \cdot 10^{-5}$	$3.15 \cdot 10^{-5}$	$2.50 \cdot 10^{-5}$
	5200 GeV	5300 GeV	5400 GeV	5500 GeV	5600 GeV	5700 GeV	5800 GeV
Model A	$1.27 \cdot 10^{-5}$	$1.00 \cdot 10^{-5}$	$7.9 \cdot 10^{-6}$	$6.2 \cdot 10^{-6}$	$4.9 \cdot 10^{-6}$	$3.9 \cdot 10^{-6}$	$3.02 \cdot 10^{-6}$
Model B	$1.98 \cdot 10^{-5}$	$1.57 \cdot 10^{-5}$	$1.24 \cdot 10^{-5}$	$9.75 \cdot 10^{-6}$	$7.7 \cdot 10^{-6}$	$6.0 \cdot 10^{-6}$	$4.7 \cdot 10^{-6}$
	5900 GeV	6000 GeV	6100 GeV	6200 GeV	6300 GeV	6400 GeV	6500 GeV
Model A	$2.36 \cdot 10^{-6}$	$1.84 \cdot 10^{-6}$	$1.43 \cdot 10^{-6}$	$1.11 \cdot 10^{-6}$	$8.6 \cdot 10^{-7}$	$6.6 \cdot 10^{-7}$	$5.1 \cdot 10^{-7}$
Model B	$3.7 \cdot 10^{-6}$	$2.87 \cdot 10^{-6}$	$2.23 \cdot 10^{-6}$	$1.73 \cdot 10^{-6}$	$1.34 \cdot 10^{-6}$	$1.03 \cdot 10^{-6}$	$8.0 \cdot 10^{-7}$
	6600 GeV	6700 GeV	6800 GeV	6900 GeV	7000 GeV	7100 GeV	7200 GeV
Model A	$3.9 \cdot 10^{-7}$	$2.99 \cdot 10^{-7}$	$2.28 \cdot 10^{-7}$	$1.73 \cdot 10^{-7}$	$1.32 \cdot 10^{-7}$	$9.96 \cdot 10^{-8}$	$7.5 \cdot 10^{-8}$
Model B	$6.1 \cdot 10^{-7}$	$4.7 \cdot 10^{-7}$	$3.6 \cdot 10^{-7}$	$2.72 \cdot 10^{-7}$	$2.06 \cdot 10^{-7}$	$1.56 \cdot 10^{-7}$	$1.18 \cdot 10^{-7}$
	7300 GeV	7400 GeV	7500 GeV	7600 GeV	7700 GeV	7800 GeV	7900 GeV
Model A	$5.7 \cdot 10^{-8}$	$4.2 \cdot 10^{-8}$	$3.18 \cdot 10^{-8}$	$2.37 \cdot 10^{-8}$	$1.77 \cdot 10^{-8}$	$1.32 \cdot 10^{-8}$	$9.78 \cdot 10^{-9}$
Model B	$8.9 \cdot 10^{-8}$	$6.7 \cdot 10^{-8}$	$5.0 \cdot 10^{-8}$	$3.7 \cdot 10^{-8}$	$2.78 \cdot 10^{-8}$	$2.07 \cdot 10^{-8}$	$1.53 \cdot 10^{-8}$

Table A.2: Production cross sections times Zh branching fraction, $\sigma_{pp \to W' \to Zh}$, in pb of a charged W' heavy vector boson in the HVT Model A and B benchmarks. The values are generated with the tools provided in Ref. [12].

A.2 2HDM production cross sections

The predicted production cross sections for a pseudoscalar A produced via gluon fusion as predicted by the 2HDM are calculated for several values of $\tan\beta$ and for masses between 300 GeV and 2 TeV for the four types of 2HDM. The values for the type I, type II, type III, and type IV scenario are shown in Tables A.3, A.4, A.5 and A.6, respectively.

The values corresonding to the b-associated production for the four respective models are shown in Tables A.7, A.8, A.9 and A.10.

	production cross section in pb												
$\tan\beta$	300 GeV	400 GeV	420 GeV	440 GeV	460 GeV	500 GeV	600 GeV	700 GeV	800 GeV	900 GeV	1000 GeV	1200 GeV	1400 GeV
0.10	3.13×10^{3}	2.77×10^{3}	2.13×10^{3}	1.66×10^{3}	1.31×10^{3}	8.32×10^{2}	3.04×10^{2}	1.26×10^{2}	5.73×10^{1}	2.80×10^{1}	1.45×10^{1}	4.44	1.55
0.12	2.17×10^{3}	1.93×10^{3}	1.48×10^{3}	1.15×10^{3}	9.08×10^{2}	5.78×10^{2}	2.11×10^{2}	8.74×10^{1}	3.98×10^{1}	1.95×10^{1}	1.01×10^{1}	3.08	1.08
0.14	1.60×10^{3}	1.41×10^{3}	1.09×10^{3}	8.47×10^{2}	6.67×10^{2}	4.25×10^{2}	1.55×10^{2}	6.42×10^{1}	2.92×10^{1}	1.43×10^{1}	7.40	2.26	7.90×10^{-1}
0.16	1.22×10^{3}	1.08×10^{3}	8.33×10^{2}	6.49×10^{2}	5.11×10^{2}	3.25×10^{2}	1.19×10^{2}	4.92×10^{1}	2.24×10^{1}	1.09×10^{1}	5.67	1.73	6.05×10^{-1}
0.18	9.65×10^{2}	8.56×10^{2}	6.58×10^{2}	5.13×10^{2}	4.04×10^{2}	2.57×10^{2}	9.37×10^{1}	3.89×10^{1}	1.77×10^{1}	8.65	4.48	1.37	4.78×10^{-1}
0.20	7.82×10^{2}	6.93×10^{2}	5.33×10^{2}	4.15×10^{2}	3.27×10^{2}	2.08×10^{2}	7.59×10^{1}	3.15×10^{1}	1.43×10^{1}	7.00	3.63	1.11	3.87×10^{-1}
0.24	5.43×10^{2}	4.81×10^{2}	3.70×10^{2}	2.88×10^{2}	2.27×10^{2}	1.45×10^{2}	5.27×10^{1}	2.19×10^{1}	9.95	4.86	2.52	7.70×10^{-1}	2.69×10^{-1}
0.28	3.99×10^{2}	3.54×10^{2}	2.72×10^{2}	2.12×10^{2}	1.67×10^{2}	1.06×10^{2}	3.87×10^{1}	1.61×10^{1}	7.31	3.57	1.85	5.66×10^{-1}	1.97×10^{-1}
0.32	3.05×10^{2}	2.71×10^{2}	2.08×10^{2}	1.62×10^{2}	1.28×10^{2}	8.13×10^{1}	2.97×10^{1}	1.23×10^{1}	5.60	2.74	1.42	4.33×10^{-1}	1.51×10^{-1}
0.36	2.41×10^{2}	2.14×10^{2}	1.65×10^{2}	1.28×10^{2}	1.01×10^{2}	6.42×10^{1}	2.34×10^{1}	9.71	4.42	2.16	1.12	3.42×10^{-1}	1.19×10^{-1}
0.40	1.95×10^{2}	1.73×10^{2}	1.33×10^{2}	1.04×10^{2}	8.17×10^{1}	5.20×10^{1}	1.90×10^{1}	7.87	3.58	1.75	9.07×10^{-1}	2.77×10^{-1}	9.68×10^{-2}
0.46	1.48×10^{2}	1.31×10^{2}	1.01×10^{2}	7.85×10^{1}	6.18×10^{1}	3.93×10^{1}	1.44×10^{1}	5.95	2.71	1.32	6.86×10^{-1}	2.10×10^{-1}	7.32×10^{-2}
0.52	1.16×10^{2}	1.03×10^{2}	7.88×10^{1}	6.14×10^{1}	4.83×10^{1}	3.08×10^{1}	1.12×10^{1}	4.66	2.12	1.04	5.36×10^{-1}	1.64×10^{-1}	5.73×10^{-2}
0.58	9.30×10^{1}	8.24×10^{1}	6.34×10^{1}	4.94×10^{1}	3.89×10^{1}	2.47×10^{1}	9.03	3.74	1.70	8.33×10^{-1}	4.31×10^{-1}	1.32×10^{-1}	4.60×10^{-2}
0.64	7.63×10^{1}	6.77×10^{1}	5.21×10^{1}	4.05×10^{1}	3.19×10^{1}	2.03×10^{1}	7.41	3.07	1.40	6.84×10^{-1}	3.54×10^{-1}	1.08×10^{-1}	3.78×10^{-2}
0.70	6.38×10^{1}	5.66×10^{1}	4.35×10^{1}	3.39×10^{1}	2.67×10^{1}	1.70×10^{1}	6.20	2.57	1.17	5.72×10^{-1}	2.96×10^{-1}	9.05×10^{-2}	3.16×10^{-2}
0.80	4.89×10^{1}	4.33×10^{1}	3.33×10^{1}	2.59×10^{1}	2.04×10^{1}	1.30×10^{1}	4.74	1.97	8.95×10^{-1}	4.38×10^{-1}	2.27×10^{-1}	6.93×10^{-2}	2.42×10^{-2}
0.90	3.86×10^{1}	3.42×10^{1}	2.63×10^{1}	2.05×10^{1}	1.61×10^{1}	1.03×10^{1}	3.75	1.55	7.07×10^{-1}	3.46×10^{-1}	1.79×10^{-1}	5.48×10^{-2}	1.91×10^{-2}
1.0	3.13×10^{1}	2.77×10^{1}	2.13×10^{1}	1.66×10^{1}	1.31×10^{1}	8.32	3.04	1.26	5.73×10^{-1}	2.80×10^{-1}	1.45×10^{-1}	4.44×10^{-2}	1.55×10^{-2}
1.2	2.17×10^{1}	1.93×10^{1}	1.48×10^{1}	1.15×10^{1}	9.08	5.78	2.11	8.74×10^{-1}	3.98×10^{-1}	1.95×10^{-1}	1.01×10^{-1}	3.08×10^{-2}	1.08×10^{-2}
1.4	1.60×10^{1}	1.41×10^{1}	1.09×10^{1}	8.47	6.67	4.25	1.55	6.42×10^{-1}	2.92×10^{-1}	1.43×10^{-1}	7.40×10^{-2}	2.26×10^{-2}	7.90×10^{-3}
1.6	1.22×10^{1}	1.08×10^{1}	8.33	6.49	5.11	3.25	1.19	4.92×10^{-1}	2.24×10^{-1}	1.09×10^{-1}	5.67×10^{-2}	1.73×10^{-2}	6.05×10^{-3}
1.8	9.65	8.56	6.58	5.13	4.04	2.57	9.37×10^{-1}	3.89×10^{-1}	1.77×10^{-1}	8.65×10^{-2}	4.48×10^{-2}	1.37×10^{-2}	4.78×10^{-3}
2.0	7.82	6.93	5.33	4.15	3.27	2.08	7.59×10^{-1}	3.15×10^{-1}	1.43×10^{-1}	7×10^{-2}	3.63×10^{-2}	1.11×10^{-2}	3.87×10^{-3}
2.2	6.46	5.73	4.41	3.43	2.70	1.72	6.27×10^{-1}	2.60×10^{-1}	1.18×10^{-1}	5.79×10^{-2}	3×10^{-2}	9.16×10^{-3}	3.20×10^{-3}
2.4	5.43	4.81	3.70	2.88	2.27	1.44	5.27×10^{-1}	2.19×10^{-1}	9.95×10^{-2}	4.86×10^{-2}	2.52×10^{-2}	7.70×10^{-3}	2.69×10^{-3}
2.6	4.63	4.10	3.15	2.46	1.93	1.23	4.49×10^{-1}	1.86×10^{-1}	8.48×10^{-2}	4.14×10^{-2}	2.15×10^{-2}	6.56×10^{-3}	2.29×10^{-3}
2.8	3.99	3.54	2.72	2.12	1.67	1.06	3.87×10^{-1}	1.61×10^{-1}	7.31×10^{-2}	3.57×10^{-2}	1.85×10^{-2}	5.66×10^{-3}	1.97×10^{-3}
3.0	3.47	3.08	2.37	1.85	1.45	9.25×10^{-1}	3.37×10^{-1}	1.40×10^{-1}	6.37×10^{-2}	3.11×10^{-2}	1.61×10^{-2}	4.93×10^{-3}	1.72×10^{-3}
3.4	2.71	2.40	1.84	1.44	1.13	7.20×10^{-1}	2.63×10^{-1}	1.09×10^{-1}	4.96×10^{-2}	2.42×10^{-2}	1.25×10^{-2}	3.84×10^{-3}	1.34×10^{-3}
3.8	2.17	1.92	1.48	1.15	9.05×10^{-1}	5.76×10^{-1}	2.10×10^{-1}	8.72×10^{-2}	3.97×10^{-2}	1.94×10^{-2}	1×10^{-2}	3.07×10^{-3}	1.07×10^{-3}
4.2	1.77	1.57	1.21	9.41×10^{-1}	7.41×10^{-1}	4.72×10^{-1}	1.72×10^{-1}	7.14×10^{-2}	3.25×10^{-2}	1.59×10^{-2}	8.22×10^{-3}	2.51×10^{-3}	8.78×10^{-4}
4.6	1.48	1.31	1.01	7.85×10^{-1}	6.18×10^{-1}	3.93×10^{-1}	1.44×10^{-1}	5.95×10^{-2}	2.71×10^{-2}	1.32×10^{-2}	6.86×10^{-3}	2.10×10^{-3}	7.32×10^{-4}
5.0	1.25	1.11	8.53×10^{-1}	6.64×10^{-1}	5.23×10^{-1}	3.33×10^{-1}	1.21×10^{-1}	5.04×10^{-2}	2.29×10^{-2}	1.12×10^{-2}	5.80×10^{-3}	1.77×10^{-3}	6.19×10^{-4}
6.0	8.69×10^{-1}	7.70×10^{-1}	5.92×10^{-1}	4.61×10^{-1}	3.63×10^{-1}	2.31×10^{-1}	8.43×10^{-2}	3.50×10^{-2}	1.59×10^{-2}	7.78×10^{-3}	4.03×10^{-3}	1.23×10^{-3}	4.30×10^{-4}
7.0	6.38×10^{-1}	5.66×10^{-1}	4.35×10^{-1}	3.39×10^{-1}	2.67×10^{-1}	1.70×10^{-1}	6.20×10^{-2}	2.57×10^{-2}	1.17×10^{-2}	5.72×10^{-3}	2.96×10^{-3}	9.05×10^{-4}	3.16×10^{-4}
8.0	4.89×10^{-1}	4.33×10^{-1}	3.33×10^{-1}	2.59×10^{-1}	2.04×10^{-1}	1.30×10^{-1}	4.74×10^{-2}	1.97×10^{-2}	8.95×10^{-3}	4.38×10^{-3}	2.27×10^{-3}	6.93×10^{-4}	2.42×10^{-4}
9.0	3.86×10^{-1}	3.42×10^{-1}	2.63×10^{-1}	2.05×10^{-1}	1.61×10^{-1}	1.03×10^{-1}	3.75×10^{-2}	1.55×10^{-2}	7.07×10^{-3}	3.46×10^{-3}	1.79×10^{-3}	5.48×10^{-4}	1.91×10^{-4}
10	3.13×10^{-1}	2.77×10^{-1}	2.13×10^{-1}	1.66×10^{-1}	1.31×10^{-1}	8.32×10^{-2}	3.04×10^{-2}	1.26×10^{-2}	5.73×10^{-3}	2.80×10^{-3}	1.45×10^{-3}	4.44×10^{-4}	1.55×10^{-4}
15	1.39×10^{-1}	1.23×10^{-1}	9.48×10^{-2}	7.38×10^{-2}	5.81×10^{-2}	3.70×10^{-2}	1.35×10^{-2}	5.60×10^{-3}	2.55×10^{-3}	1.25×10^{-3}	6.45×10^{-4}	1.97×10^{-4}	6.88×10^{-5}
20	7.82×10^{-2}	6.93×10^{-2}	5.33×10^{-2}	4.15×10^{-2}	3.27×10^{-2}	2.08×10^{-2}	7.59×10^{-3}	3.15×10^{-3}	1.43×10^{-3}	7×10^{-4}	3.63×10^{-4}	1.11×10^{-4}	3.87×10^{-5}
25	5×10^{-2}	4.44×10^{-2}	3.41×10^{-2}	2.66×10^{-2}	2.09×10^{-2}	1.33×10^{-2}	4.86×10^{-3}	2.01×10^{-3}	9.17×10^{-4}	4.48×10^{-4}	2.32×10^{-4}	7.10×10^{-5}	2.48×10^{-5}
30	3.47×10^{-2}	3.08×10^{-2}	2.37×10^{-2}	1.85×10^{-2}	1.45×10^{-2}	9.25×10^{-3}	3.37×10^{-3}	1.40×10^{-3}	6.37×10^{-4}	3.11×10^{-4}	1.61×10^{-4}	4.93×10^{-5}	1.72×10^{-5}
35	2.55×10^{-2}	2.26×10^{-2}	1.74×10^{-2}	1.36×10^{-2}	1.07×10^{-2}	6.79×10^{-3}	2.48×10^{-3}	1.03×10^{-3}	4.68×10^{-4}	2.29×10^{-4}	1.18×10^{-4}	3.62×10^{-5}	1.26×10^{-5}
40	1.95×10^{-2}	1.73×10^{-2}	1.33×10^{-2}	1.04×10^{-2}	8.17×10^{-3}	5.20×10^{-3}	1.90×10^{-3}	7.87×10^{-4}	3.58×10^{-4}	1.75×10^{-4}	9.07×10^{-5}	2.77×10^{-5}	9.70×10^{-6}
45	1.54×10^{-2}	1.37×10^{-2}	1.05×10^{-2}	8.20×10^{-3}	6.46×10^{-3}	4.11×10^{-3}	1.50×10^{-3}	6.22×10^{-4}	2.83×10^{-4}	1.38×10^{-4}	7.16×10^{-5}	2.19×10^{-5}	7.60×10^{-6}
50	1.25×10^{-2}	1.11×10^{-2}	8.53×10^{-3}	6.64×10^{-3}	5.23×10^{-3}	3.33×10^{-3}	1.21×10^{-3}	5.04×10^{-4}	2.29×10^{-4}	1.12×10^{-4}	5.80×10^{-5}	1.77×10^{-5}	6.20×10^{-6}

Table A.3: Production cross section in pb of a pseudoscalar A produced via the gluon-fusion mode for several mass points in a type I 2HDM [241–245].

	production cross section in pb												
$\tan\beta$	300 GeV	400 GeV	420 GeV	440 GeV	460 GeV	500 GeV	600 GeV	700 GeV	800 GeV	900 GeV	1000 GeV	1200 GeV	1400 GeV
0.1	3.09×10^{3}	2.77×10^{3}	2.13×10^{3}	1.66×10^{3}	1.31×10^{3}	8.35×10^{2}	3.05×10^{2}	1.27×10^{2}	5.76×10^{1}	2.82×10^{1}	1.46×10^{1}	4.46	1.56
0.12	2.15×10^{3}	1.93×10^{3}	1.48×10^{3}	1.16×10^{3}	9.10×10^{2}	5.80×10^{2}	2.12×10^{2}	8.79×10^{1}	4.00×10^{1}	1.96×10^{1}	1.01×10^{1}	3.10	1.08
0.14	1.58×10^{3}	1.42×10^{3}	1.09×10^{3}	8.49×10^{2}	6.69×10^{2}	4.26×10^{2}	1.56×10^{2}	6.45×10^{1}	2.94×10^{1}	1.44×10^{1}	7.44	2.28	7.94×10^{-1}
0.16	1.21×10^{3}	1.08×10^{3}	8.34×10^{2}	6.50×10^{2}	5.12×10^{2}	3.26×10^{2}	1.19×10^{2}	4.94×10^{1}	2.25×10^{1}	1.10×10^{1}	5.70	1.74	6.08×10^{-1}
0.18	9.54×10^{2}	8.56×10^{2}	6.59×10^{2}	5.14×10^{2}	4.05×10^{2}	2.58×10^{2}	9.41×10^{1}	3.90×10^{1}	1.78×10^{1}	8.69	4.50	1.38	4.80×10^{-1}
0.2	7.72×10^{2}	6.94×10^{2}	5.34×10^{2}	4.16×10^{2}	3.28×10^{2}	2.09×10^{2}	7.63×10^{1}	3.16×10^{1}	1.44×10^{1}	7.04	3.65	1.12	3.89×10^{-1}
0.24	5.36×10^{2}	4.82×10^{2}	3.71×10^{2}	2.89×10^{2}	2.28×10^{2}	1.45×10^{2}	5.30×10^{1}	2.20×10^{1}	1.00×10^{1}	4.89	2.53	7.74×10^{-1}	2.70×10^{-1}
0.28	3.94×10^{2}	3.54×10^{2}	2.72×10^{2}	2.12×10^{2}	1.67×10^{2}	1.07×10^{2}	3.89×10^{1}	1.61×10^{1}	7.35	3.59	1.86	5.69×10^{-1}	1.99×10^{-1}
0.32	3.02×10^{2}	2.71×10^{2}	2.09×10^{2}	1.63×10^{2}	1.28×10^{2}	8.16×10^{1}	2.98×10^{1}	1.24×10^{1}	5.63	2.75	1.42	4.36×10^{-1}	1.52×10^{-1}
0.36	2.38×10^{2}	2.14×10^{2}	1.65×10^{2}	1.28×10^{2}	1.01×10^{2}	6.44×10^{1}	2.35×10^{1}	9.77	4.45	2.17	1.13	3.44×10^{-1}	1.20×10^{-1}
0.4	1.93×10^{2}	1.73×10^{2}	1.34×10^{2}	1.04×10^{2}	8.19×10^{1}	5.22×10^{1}	1.91×10^{1}	7.91	3.60	1.76	9.12×10^{-1}	2.79×10^{-1}	9.74×10^{-2}
0.46	1.46×10^{2}	1.31×10^{2}	1.01×10^{2}	7.87×10^{1}	6.20×10^{1}	3.95×10^{1}	1.44×10^{1}	5.98	2.72	1.33	6.90×10^{-1}	2.11×10^{-1}	7.36×10^{-2}
0.52	1.14×10^{2}	1.03×10^{2}	7.90×10^{1}	6.16×10^{1}	4.85×10^{1}	3.09×10^{1}	1.13×10^{1}	4.68	2.13	1.04	5.40×10^{-1}	1.65×10^{-1}	5.76×10^{-2}
0.58	9.15×10^{1}	8.25×10^{1}	6.35×10^{1}	4.95×10^{1}	3.90×10^{1}	2.48×10^{1}	9.08	3.77	1.71	8.39×10^{-1}	4.34×10^{-1}	1.33×10^{-1}	4.64×10^{-2}
0.64	7.51×10^{1}	6.77×10^{1}	5.21×10^{1}	4.07×10^{1}	3.20×10^{1}	2.04×10^{1}	7.46	3.09	1.41	6.89×10^{-1}	3.57×10^{-1}	1.09×10^{-1}	3.81×10^{-2}
0.7	6.27×10^{1}	5.66×10^{1}	4.36×10^{1}	3.40×10^{1}	2.68×10^{1}	1.71×10^{1}	6.24	2.59	1.18	5.76×10^{-1}	2.98×10^{-1}	9.12×10^{-2}	3.18×10^{-2}
0.8	4.79×10^{1}	4.34×10^{1}	3.34×10^{1}	2.60×10^{1}	2.05×10^{1}	1.31×10^{1}	4.78	1.98	9.03×10^{-1}	4.42×10^{-1}	2.29×10^{-1}	6.99×10^{-2}	2.44×10^{-2}
0.9	3.78×10^{1}	3.43×10^{1}	2.64×10^{1}	2.06×10^{1}	1.62×10^{1}	1.03×10^{1}	3.78	1.57	7.14×10^{-1}	3.49×10^{-1}	1.81×10^{-1}	5.53×10^{-2}	1.93×10^{-2}
1.0	3.06×10^{1}	2.78×10^{1}	2.14×10^{1}	1.67×10^{1}	1.31×10^{1}	8.38	3.06	1.27	5.79×10^{-1}	2.83×10^{-1}	1.47×10^{-1}	4.48×10^{-2}	1.56×10^{-2}
1.2	2.11×10^{1}	1.93×10^{1}	1.49×10^{1}	1.16×10^{1}	9.13	5.82	2.13	8.85×10^{-1}	4.03×10^{-1}	1.97×10^{-1}	1.02×10^{-1}	3.12×10^{-2}	1.09×10^{-2}
1.4	1.54×10^{1}	1.42×10^{1}	1.09×10^{1}	8.52	6.72	4.29	1.57	6.52×10^{-1}	2.97×10^{-1}	1.45×10^{-1}	7.52×10^{-2}	2.30×10^{-2}	8.03×10^{-3}
1.6	1.17×10^{1}	1.09×10^{1}	8.37	6.53	5.15	3.29	1.20	5×10^{-1}	2.28×10^{-1}	1.12×10^{-1}	5.77×10^{-2}	1.77×10^{-2}	6.16×10^{-3}
1.8	9.20	8.58	6.62	5.17	4.08	2.60	9.54×10^{-1}	3.97×10^{-1}	1.81×10^{-1}	8.84×10^{-2}	4.58×10^{-2}	1.40×10^{-2}	4.89×10^{-3}
2.0	7.39	6.95	5.37	4.19	3.31	2.11	7.76×10^{-1}	3.22×10^{-1}	1.47×10^{-1}	7.19×10^{-2}	3.72×10^{-2}	1.14×10^{-2}	3.98×10^{-3}
2.2	6.05	5.75	4.44	3.47	2.74	1.75	6.43×10^{-1}	2.68×10^{-1}	1.22×10^{-1}	5.97×10^{-2}	3.09×10^{-2}	9.46×10^{-3}	3.30×10^{-3}
2.4	5.03	4.83	3.74	2.92	2.31	1.48	5.43×10^{-1}	2.26×10^{-1}	1.03×10^{-1}	5.04×10^{-2}	2.61×10^{-2}	7.99×10^{-3}	2.79×10^{-3}
2.6	4.24	4.12	3.19	2.50	1.97	1.26	4.65×10^{-1}	1.93×10^{-1}	8.82×10^{-2}	4.32×10^{-2}	2.24×10^{-2}	6.84×10^{-3}	2.39×10^{-3}
2.8	3.61	3.56	2.75	2.16	1.71	1.09	4.02×10^{-1}	1.68×10^{-1}	7.65×10^{-2}	3.74×10^{-2}	1.94×10^{-2}	5.93×10^{-3}	2.07×10^{-3}
3.0	3.11	3.10	2.40	1.88	1.49	9.56×10^{-1}	3.52×10^{-1}	1.47×10^{-1}	6.70×10^{-2}	3.28×10^{-2}	1.70×10^{-2}	5.20×10^{-3}	1.81×10^{-3}
3.4	2.36	2.42	1.88	1.48	1.17	7.51×10^{-1}	2.77×10^{-1}	1.16×10^{-1}	5.28×10^{-2}	2.59×10^{-2}	1.34×10^{-2}	4.10×10^{-3}	1.43×10^{-3}
3.8	1.83	1.94	1.51	1.19	9.44×10^{-1}	6.07×10^{-1}	2.25×10^{-1}	9.40×10^{-2}	4.29×10^{-2}	2.10×10^{-2}	1.09×10^{-2}	3.34×10^{-3}	1.16×10^{-3}
4.2	1.46	1.60	1.25	9.82×10^{-1}	7.80×10^{-1}	5.03×10^{-1}	1.87×10^{-1}	7.82×10^{-2}	3.57×10^{-2}	1.75×10^{-2}	9.08×10^{-3}	2.78×10^{-3}	9.69×10^{-4}
4.6	1.18	1.34	1.05	8.26×10^{-1}	6.57×10^{-1}	4.25×10^{-1}	1.58×10^{-1}	6.63×10^{-2}	3.03×10^{-2}	1.49×10^{-2}	7.71×10^{-3}	2.36×10^{-3}	8.23×10^{-4}
5.0	9.65×10^{-1}	1.14	8.94×10^{-1}	7.07×10^{-1}	5.63×10^{-1}	3.65×10^{-1}	1.36×10^{-1}	5.72×10^{-2}	2.62×10^{-2}	1.28×10^{-2}	6.66×10^{-3}	2.04×10^{-3}	7.11×10^{-4}
6.0	6.25×10^{-1}	8.08×10^{-1}	6.39×10^{-1}	5.08×10^{-1}	4.06×10^{-1}	2.65×10^{-1}	9.98×10^{-2}	4.20×10^{-2}	1.93×10^{-2}	9.45×10^{-3}	4.90×10^{-3}	1.50×10^{-3}	5.23×10^{-4}
7.0	4.40×10^{-1}	6.12×10^{-1}	4.88×10^{-1}	3.90×10^{-1}	3.14×10^{-1}	2.06×10^{-1}	7.81×10^{-2}	3.30×10^{-2}	1.51×10^{-2}	7.43×10^{-3}	3.85×10^{-3}	1.18×10^{-3}	4.10×10^{-4}
8.0	3.42×10^{-1}	4.89×10^{-1}	3.93×10^{-1}	3.16×10^{-1}	2.54×10^{-1}	1.68×10^{-1}	6.44×10^{-2}	2.72×10^{-2}	1.25×10^{-2}	6.14×10^{-3}	3.19×10^{-3}	9.73×10^{-4}	3.39×10^{-4}
9.0	2.96×10^{-1}	4.10×10^{-1}	3.31×10^{-1}	2.68×10^{-1}	2.17×10^{-1}	1.44×10^{-1}	5.53×10^{-2}	2.35×10^{-2}	1.08×10^{-2}	5.29×10^{-3}	2.74×10^{-3}	8.37×10^{-4}	2.91×10^{-4}
10	2.87×10^{-1}	3.57×10^{-1}	2.91×10^{-1}	2.36×10^{-1}	1.92×10^{-1}	1.28×10^{-1}	4.93×10^{-2}	2.09×10^{-2}	9.61×10^{-3}	4.71×10^{-3}	2.44×10^{-3}	7.43×10^{-4}	2.58×10^{-4}
15	5.29×10^{-1}	2.84×10^{-1}	2.33×10^{-1}	1.90×10^{-1}	1.55×10^{-1}	1.03×10^{-1}	3.95×10^{-2}	1.66×10^{-2}	7.55×10^{-3}	3.67×10^{-3}	1.89×10^{-3}	5.67×10^{-4}	1.94×10^{-4}
20	1.05	3.44×10^{-1}	2.78×10^{-1}	2.23×10^{-1}	1.80×10^{-1}	1.17×10^{-1}	4.36×10^{-2}	1.80×10^{-2}	8.04×10^{-3}	3.86×10^{-3}	1.96×10^{-3}	5.80×10^{-4}	1.96×10^{-4}
25	1.77	4.65×10^{-1}	3.68×10^{-1}	2.92×10^{-1}	2.32×10^{-1}	1.49×10^{-1}	5.38×10^{-2}	2.17×10^{-2}	9.59×10^{-3}	4.55×10^{-3}	2.29×10^{-3}	6.68×10^{-4}	2.24×10^{-4}
30	2.67	6.31×10^{-1}	4.93×10^{-1}	3.86×10^{-1}	3.05×10^{-1}	1.93×10^{-1}	6.81×10^{-2}	2.71×10^{-2}	1.18×10^{-2}	5.57×10^{-3}	2.79×10^{-3}	8.03×10^{-4}	2.67×10^{-4}
35	3.73	8.34×10^{-1}	6.46×10^{-1}	5.03×10^{-1}	3.94×10^{-1}	2.47×10^{-1}	8.59×10^{-2}	3.38×10^{-2}	1.46×10^{-2}	6.85×10^{-3}	3.41×10^{-3}	9.75×10^{-4}	3.22×10^{-4}
40	4.97	1.07	8.25×10^{-1}	6.39×10^{-1}	4.99×10^{-1}	3.11×10^{-1}	1.07×10^{-1}	4.17×10^{-2}	1.80×10^{-2}	8.38×10^{-3}	4.15×10^{-3}	1.18×10^{-3}	3.88×10^{-4}
45	6.38	1.35	1.03	7.96×10^{-1}	6.19×10^{-1}	3.84×10^{-1}	1.31×10^{-1}	5.08×10^{-2}	2.18×10^{-2}	1.01×10^{-2}	5.01×10^{-3}	1.42×10^{-3}	4.65×10^{-4}
50	7.95	1.65	1.26	9.71×10^{-1}	7.55×10^{-1}	4.66×10^{-1}	1.58×10^{-1}	6.10×10^{-2}	2.61×10^{-2}	1.21×10^{-2}	5.97×10^{-3}	1.68×10^{-3}	5.51×10^{-4}

Table A.4: Production cross section in pb of a pseudoscalar A produced via the gluon-fusion mode for several mass points in a type II 2HDM [241–245].

	production cross section in pb												
$\tan\beta$	300 GeV	400 GeV	420 GeV	440 GeV	460 GeV	500 GeV	600 GeV	700 GeV	800 GeV	900 GeV	1000 GeV	1200 GeV	1400 GeV
0.1	3.13×10^{3}	2.77×10^{3}	2.13×10^{3}	1.66×10^{3}	1.31×10^{3}	8.32×10^{2}	3.04×10^{2}	1.26×10^{2}	5.73×10^{1}	2.80×10^{1}	1.45×10^{1}	4.44	1.55
0.12	2.17×10^{3}	1.93×10^{3}	1.48×10^{3}	1.15×10^{3}	9.08×10^{2}	5.78×10^{2}	2.11×10^{2}	8.74×10^{1}	3.98×10^{1}	1.95×10^{1}	1.01×10^{1}	3.08	1.08
0.14	1.60×10^{3}	1.41×10^{3}	1.09×10^{3}	8.47×10^{2}	6.67×10^{2}	4.25×10^{2}	1.55×10^{2}	6.42×10^{1}	2.92×10^{1}	1.43×10^{1}	7.40	2.26	7.90×10^{-1}
0.16	1.22×10^{3}	1.08×10^{3}	8.33×10^{2}	6.49×10^{2}	5.11×10^{2}	3.25×10^{2}	1.19×10^{2}	4.92×10^{1}	2.24×10^{1}	1.09×10^{1}	5.67	1.73	6.05×10^{-1}
0.18	9.65×10^{2}	8.56×10^{2}	6.58×10^{2}	5.13×10^{2}	4.04×10^{2}	2.57×10^{2}	9.37×10^{1}	3.89×10^{1}	1.77×10^{1}	8.65	4.48	1.37	4.78×10^{-1}
0.2	7.82×10^{2}	6.93×10^{2}	5.33×10^{2}	4.15×10^{2}	3.27×10^{2}	2.08×10^{2}	7.59×10^{1}	3.15×10^{1}	1.43×10^{1}	7.00	3.63	1.11	3.87×10^{-1}
0.24	5.43×10^{2}	4.81×10^{2}	3.70×10^{2}	2.88×10^{2}	2.27×10^{2}	1.45×10^{2}	5.27×10^{1}	2.19×10^{1}	9.95	4.86	2.52	7.70×10^{-1}	2.69×10^{-1}
0.28	3.99×10^{2}	3.54×10^{2}	2.72×10^{2}	2.12×10^{2}	1.67×10^{2}	1.06×10^{2}	3.87×10^{1}	1.61×10^{1}	7.31	3.57	1.85	5.66×10^{-1}	1.97×10^{-1}
0.32	3.05×10^{2}	2.71×10^{2}	2.08×10^{2}	1.62×10^{2}	1.28×10^{2}	8.13×10^{1}	2.97×10^{1}	1.23×10^{1}	5.60	2.74	1.42	4.33×10^{-1}	1.51×10^{-1}
0.36	2.41×10^{2}	2.14×10^{2}	1.65×10^{2}	1.28×10^{2}	1.01×10^{2}	6.42×10^{1}	2.34×10^{1}	9.71	4.42	2.16	1.12	3.42×10^{-1}	1.19×10^{-1}
0.4	1.95×10^{2}	1.73×10^{2}	1.33×10^{2}	1.04×10^{2}	8.17×10^{1}	5.20×10^{1}	1.90×10^{1}	7.87	3.58	1.75	9.07×10^{-1}	2.77×10^{-1}	9.68×10^{-2}
0.46	1.48×10^{2}	1.31×10^{2}	1.01×10^{2}	7.85×10^{1}	6.18×10^{1}	3.93×10^{1}	1.44×10^{1}	5.95	2.71	1.32	6.86×10^{-1}	2.10×10^{-1}	7.32×10^{-2}
0.52	1.16×10^{2}	1.03×10^{2}	7.88×10^{1}	6.14×10^{1}	4.83×10^{1}	3.08×10^{1}	1.12×10^{1}	4.66	2.12	1.04	5.36×10^{-1}	1.64×10^{-1}	5.73×10^{-2}
0.58	9.30×10^{1}	8.24×10^{1}	6.34×10^{1}	4.94×10^{1}	3.89×10^{1}	2.47×10^{1}	9.03	3.74	1.70	8.33×10^{-1}	4.31×10^{-1}	1.32×10^{-1}	4.60×10^{-2}
0.64	7.63×10^{1}	6.77×10^{1}	5.21×10^{1}	4.05×10^{1}	3.19×10^{1}	2.03×10^{1}	7.41	3.07	1.40	6.84×10^{-1}	3.54×10^{-1}	1.08×10^{-1}	3.78×10^{-2}
0.7	6.38×10^{1}	5.66×10^{1}	4.35×10^{1}	3.39×10^{1}	2.67×10^{1}	1.70×10^{1}	6.20	2.57	1.17	5.72×10^{-1}	2.96×10^{-1}	9.05×10^{-2}	3.16×10^{-2}
0.8	4.89×10^{1}	4.33×10^{1}	3.33×10^{1}	2.59×10^{1}	2.04×10^{1}	1.30×10^{1}	4.74	1.97	8.95×10^{-1}	4.38×10^{-1}	2.27×10^{-1}	6.93×10^{-2}	2.42×10^{-2}
0.9	3.86×10^{1}	3.42×10^{1}	2.63×10^{1}	2.05×10^{1}	1.61×10^{1}	1.03×10^{1}	3.75	1.55	7.07×10^{-1}	3.46×10^{-1}	1.79×10^{-1}	5.48×10^{-2}	1.91×10^{-2}
1.0	3.13×10^{1}	2.77×10^{1}	2.13×10^{1}	1.66×10^{1}	1.31×10^{1}	8.32	3.04	1.26	5.73×10^{-1}	2.80×10^{-1}	1.45×10^{-1}	4.44×10^{-2}	1.55×10^{-2}
1.2	2.17×10^{1}	1.93×10^{1}	1.48×10^{1}	1.15×10^{1}	9.08	5.78	2.11	8.74×10^{-1}	3.98×10^{-1}	1.95×10^{-1}	1.01×10^{-1}	3.08×10^{-2}	1.08×10^{-2}
1.4	1.60×10^{1}	1.41×10^{1}	1.09×10^{1}	8.47	6.67	4.25	1.55	6.42×10^{-1}	2.92×10^{-1}	1.43×10^{-1}	7.40×10^{-2}	2.26×10^{-2}	7.90×10^{-3}
1.6	1.22×10^{1}	1.08×10^{1}	8.33	6.49	5.11	3.25	1.19	4.92×10^{-1}	2.24×10^{-1}	1.09×10^{-1}	5.67×10^{-2}	1.73×10^{-2}	6.05×10^{-3}
1.8	9.65	8.56	6.58	5.13	4.04	2.57	9.37×10^{-1}	3.89×10^{-1}	1.77×10^{-1}	8.65×10^{-2}	4.48×10^{-2}	1.37×10^{-2}	4.78×10^{-3}
2.0	7.82	6.93	5.33	4.15	3.27	2.08	7.59×10^{-1}	3.15×10^{-1}	1.43×10^{-1}	7×10^{-2}	3.63×10^{-2}	1.11×10^{-2}	3.87×10^{-3}
2.2	6.46	5.73	4.41	3.43	2.70	1.72	6.27×10^{-1}	2.60×10^{-1}	1.18×10^{-1}	5.79×10^{-2}	3×10^{-2}	9.16×10^{-3}	3.20×10^{-3}
2.4	5.43	4.81	3.70	2.88	2.27	1.44	5.27×10^{-1}	2.19×10^{-1}	9.95×10^{-2}	4.86×10^{-2}	2.52×10^{-2}	7.70×10^{-3}	2.69×10^{-3}
2.6	4.63	4.10	3.15	2.46	1.93	1.23	4.49×10^{-1}	1.86×10^{-1}	8.48×10^{-2}	4.14×10^{-2}	2.15×10^{-2}	6.56×10^{-3}	2.29×10^{-3}
2.8	3.99	3.54	2.72	2.12	1.67	1.06	3.87×10^{-1}	1.61×10^{-1}	7.31×10^{-2}	3.57×10^{-2}	1.85×10^{-2}	5.66×10^{-3}	1.97×10^{-3}
3.0	3.47	3.08	2.37	1.85	1.45	9.25×10^{-1}	3.37×10^{-1}	1.40×10^{-1}	6.37×10^{-2}	3.11×10^{-2}	1.61×10^{-2}	4.93×10^{-3}	1.72×10^{-3}
3.4	2.71	2.40	1.84	1.44	1.13	7.20×10^{-1}	2.63×10^{-1}	1.09×10^{-1}	4.96×10^{-2}	2.42×10^{-2}	1.25×10^{-2}	3.84×10^{-3}	1.34×10^{-3}
3.8	2.17	1.92	1.48	1.15	9.05×10^{-1}	5.76×10^{-1}	2.10×10^{-1}	8.72×10^{-2}	3.97×10^{-2}	1.94×10^{-2}	1×10^{-2}	3.07×10^{-3}	1.07×10^{-3}
4.2	1.77	1.57	1.21	9.41×10^{-1}	7.41×10^{-1}	4.72×10^{-1}	1.72×10^{-1}	7.14×10^{-2}	3.25×10^{-2}	1.59×10^{-2}	8.22×10^{-3}	2.51×10^{-3}	8.78×10^{-4}
4.6	1.48	1.31	1.01	7.85×10^{-1}	6.18×10^{-1}	3.93×10^{-1}	1.44×10^{-1}	5.95×10^{-2}	2.71×10^{-2}	1.32×10^{-2}	6.86×10^{-3}	2.10×10^{-3}	7.32×10^{-4}
5.0	1.25	1.11	8.53×10^{-1}	6.64×10^{-1}	5.23×10^{-1}	3.33×10^{-1}	1.21×10^{-1}	5.04×10^{-2}	2.29×10^{-2}	1.12×10^{-2}	5.80×10^{-3}	1.77×10^{-3}	6.19×10^{-4}
6.0	8.69×10^{-1}	7.70×10^{-1}	5.92×10^{-1}	4.61×10^{-1}	3.63×10^{-1}	2.31×10^{-1}	8.43×10^{-2}	3.50×10^{-2}	1.59×10^{-2}	7.78×10^{-3}	4.03×10^{-3}	1.23×10^{-3}	4.30×10^{-4}
7.0	6.38×10^{-1}	5.66×10^{-1}	4.35×10^{-1}	3.39×10^{-1}	2.67×10^{-1}	1.70×10^{-1}	6.20×10^{-2}	2.57×10^{-2}	1.17×10^{-2}	5.72×10^{-3}	2.96×10^{-3}	9.05×10^{-4}	3.16×10^{-4}
8.0	4.89×10^{-1}	4.33×10^{-1}	3.33×10^{-1}	2.59×10^{-1}	2.04×10^{-1}	1.30×10^{-1}	4.74×10^{-2}	1.97×10^{-2}	8.95×10^{-3}	4.38×10^{-3}	2.27×10^{-3}	6.93×10^{-4}	2.42×10^{-4}
9.0	3.86×10^{-1}	3.42×10^{-1}	2.63×10^{-1}	2.05×10^{-1}	1.61×10^{-1}	1.03×10^{-1}	3.75×10^{-2}	1.55×10^{-2}	7.07×10^{-3}	3.46×10^{-3}	1.79×10^{-3}	5.48×10^{-4}	1.91×10^{-4}
10	3.13×10^{-1}	2.77×10^{-1}	2.13×10^{-1}	1.66×10^{-1}	1.31×10^{-1}	8.32×10^{-2}	3.04×10^{-2}	1.26×10^{-2}	5.73×10^{-3}	2.80×10^{-3}	1.45×10^{-3}	4.44×10^{-4}	1.55×10^{-4}
15	1.39×10^{-1}	1.23×10^{-1}	9.48×10^{-2}	7.38×10^{-2}	5.81×10^{-2}	3.70×10^{-2}	1.35×10^{-2}	5.60×10^{-3}	2.55×10^{-3}	1.25×10^{-3}	6.45×10^{-4}	1.97×10^{-4}	6.88×10^{-5}
20	7.82×10^{-2}	6.93×10^{-2}	5.33×10^{-2}	4.15×10^{-2}	3.27×10^{-2}	2.08×10^{-2}	7.59×10^{-3}	3.15×10^{-3}	1.43×10^{-3}	7×10^{-4}	3.63×10^{-4}	1.11×10^{-4}	3.87×10^{-5}
25	5×10^{-2}	4.44×10^{-2}	3.41×10^{-2}	2.66×10^{-2}	2.09×10^{-2}	1.33×10^{-2}	4.86×10^{-3}	2.01×10^{-3}	9.17×10^{-4}	4.48×10^{-4}	2.32×10^{-4}	7.10×10^{-5}	2.48×10^{-5}
30	3.47×10^{-2}	3.08×10^{-2}	2.37×10^{-2}	1.85×10^{-2}	1.45×10^{-2}	9.25×10^{-3}	3.37×10^{-3}	1.40×10^{-3}	6.37×10^{-4}	3.11×10^{-4}	1.61×10^{-4}	4.93×10^{-5}	1.72×10^{-5}
35	2.55×10^{-2}	2.26×10^{-2}	1.74×10^{-2}	1.36×10^{-2}	1.07×10^{-2}	6.79×10^{-3}	2.48×10^{-3}	1.03×10^{-3}	4.68×10^{-4}	2.29×10^{-4}	1.18×10^{-4}	3.62×10^{-5}	1.26×10^{-5}
40	1.95×10^{-2}	1.73×10^{-2}	1.33×10^{-2}	1.04×10^{-2}	8.17×10^{-3}	5.20×10^{-3}	1.90×10^{-3}	7.87×10^{-4}	3.58×10^{-4}	1.75×10^{-4}	9.07×10^{-5}	2.77×10^{-5}	9.70×10^{-6}
45	1.54×10^{-2}	1.37×10^{-2}	1.05×10^{-2}	8.20×10^{-3}	6.46×10^{-3}	4.11×10^{-3}	1.50×10^{-3}	6.22×10^{-4}	2.83×10^{-4}	1.38×10^{-4}	7.16×10^{-5}	2.19×10^{-5}	7.60×10^{-6}
50	1.25×10^{-2}	1.11×10^{-2}	8.53×10^{-3}	6.64×10^{-3}	5.23×10^{-3}	3.33×10^{-3}	1.21×10^{-3}	5.04×10^{-4}	2.29×10^{-4}	1.12×10^{-4}	5.80×10^{-5}	1.77×10^{-5}	6.20×10^{-6}

Table A.5: Production cross section in pb of a pseudoscalar A produced via the gluon-fusion mode for several mass points in a type III 2HDM [241–245].

	production cross section in pb												
$\tan\beta$	300 GeV	400 GeV	420 GeV	440 GeV	460 GeV	500 GeV	600 GeV	700 GeV	800 GeV	900 GeV	1000 GeV	1200 GeV	1400 GeV
0.1	3.09×10^{3}	2.77×10^{3}	2.13×10^{3}	1.66×10^{3}	1.31×10^{3}	8.35×10^{2}	3.05×10^{2}	1.27×10^{2}	5.76×10^{1}	2.82×10^{1}	1.46×10^{1}	4.46	1.56
0.12	2.15×10^{3}	1.93×10^{3}	1.48×10^{3}	1.16×10^{3}	9.10×10^{2}	5.80×10^{2}	2.12×10^{2}	8.79×10^{1}	4.00×10^{1}	1.96×10^{1}	1.01×10^{1}	3.10	1.08
0.14	1.58×10^{3}	1.42×10^{3}	1.09×10^{3}	8.49×10^{2}	6.69×10^{2}	4.26×10^{2}	1.56×10^{2}	6.45×10^{1}	2.94×10^{1}	1.44×10^{1}	7.44	2.28	7.94×10^{-1}
0.16	1.21×10^{3}	1.08×10^{3}	8.34×10^{2}	6.50×10^{2}	5.12×10^{2}	3.26×10^{2}	1.19×10^{2}	4.94×10^{1}	2.25×10^{1}	1.10×10^{1}	5.70	1.74	6.08×10^{-1}
0.18	9.54×10^{2}	8.56×10^{2}	6.59×10^{2}	5.14×10^{2}	4.05×10^{2}	2.58×10^{2}	9.41×10^{1}	3.90×10^{1}	1.78×10^{1}	8.69	4.50	1.38	4.80×10^{-1}
0.2	7.72×10^{2}	6.94×10^{2}	5.34×10^{2}	4.16×10^{2}	3.28×10^{2}	2.09×10^{2}	7.63×10^{1}	3.16×10^{1}	1.44×10^{1}	7.04	3.65	1.12	3.89×10^{-1}
0.24	5.36×10^{2}	4.82×10^{2}	3.71×10^{2}	2.89×10^{2}	2.28×10^{2}	1.45×10^{2}	5.30×10^{1}	2.20×10^{1}	1.00×10^{1}	4.89	2.53	7.74×10^{-1}	2.70×10^{-1}
0.28	3.94×10^{2}	3.54×10^{2}	2.72×10^{2}	2.12×10^{2}	1.67×10^{2}	1.07×10^{2}	3.89×10^{1}	1.61×10^{1}	7.35	3.59	1.86	5.69×10^{-1}	1.99×10^{-1}
0.32	3.02×10^{2}	2.71×10^{2}	2.09×10^{2}	1.63×10^{2}	1.28×10^{2}	8.16×10^{1}	2.98×10^{1}	1.24×10^{1}	5.63	2.75	1.42	4.36×10^{-1}	1.52×10^{-1}
0.36	2.38×10^{2}	2.14×10^{2}	1.65×10^{2}	1.28×10^{2}	1.01×10^{2}	6.44×10^{1}	2.35×10^{1}	9.77	4.45	2.17	1.13	3.44×10^{-1}	1.20×10^{-1}
0.4	1.93×10^{2}	1.73×10^{2}	1.34×10^{2}	1.04×10^{2}	8.19×10^{1}	5.22×10^{1}	1.91×10^{1}	7.91	3.60	1.76	9.12×10^{-1}	2.79×10^{-1}	9.74×10^{-2}
0.46	1.46×10^{2}	1.31×10^{2}	1.01×10^{2}	7.87×10^{1}	6.20×10^{1}	3.95×10^{1}	1.44×10^{1}	5.98	2.72	1.33	6.90×10^{-1}	2.11×10^{-1}	7.36×10^{-2}
0.52	1.14×10^{2}	1.03×10^{2}	7.90×10^{1}	6.16×10^{1}	4.85×10^{1}	3.09×10^{1}	1.13×10^{1}	4.68	2.13	1.04	5.40×10^{-1}	1.65×10^{-1}	5.76×10^{-2}
0.58	9.15×10^{1}	8.25×10^{1}	6.35×10^{1}	4.95×10^{1}	3.90×10^{1}	2.48×10^{1}	9.08	3.77	1.71	8.39×10^{-1}	4.34×10^{-1}	1.33×10^{-1}	4.64×10^{-2}
0.64	7.51×10^{1}	6.77×10^{1}	5.21×10^{1}	4.07×10^{1}	3.20×10^{1}	2.04×10^{1}	7.46	3.09	1.41	6.89×10^{-1}	3.57×10^{-1}	1.09×10^{-1}	3.81×10^{-2}
0.7	6.27×10^{1}	5.66×10^{1}	4.36×10^{1}	3.40×10^{1}	2.68×10^{1}	1.71×10^{1}	6.24	2.59	1.18	5.76×10^{-1}	2.98×10^{-1}	9.12×10^{-2}	3.18×10^{-2}
0.8	4.79×10^{1}	4.34×10^{1}	3.34×10^{1}	2.60×10^{1}	2.05×10^{1}	1.31×10^{1}	4.78	1.98	9.03×10^{-1}	4.42×10^{-1}	2.29×10^{-1}	6.99×10^{-2}	2.44×10^{-2}
0.9	3.78×10^{1}	3.43×10^{1}	2.64×10^{1}	2.06×10^{1}	1.62×10^{1}	1.03×10^{1}	3.78	1.57	7.14×10^{-1}	3.49×10^{-1}	1.81×10^{-1}	5.53×10^{-2}	1.93×10^{-2}
1.0	3.06×10^{1}	2.78×10^{1}	2.14×10^{1}	1.67×10^{1}	1.31×10^{1}	8.38	3.06	1.27	5.79×10^{-1}	2.83×10^{-1}	1.47×10^{-1}	4.48×10^{-2}	1.56×10^{-2}
1.2	2.11×10^{1}	1.93×10^{1}	1.49×10^{1}	1.16×10^{1}	9.13	5.82	2.13	8.85×10^{-1}	4.03×10^{-1}	1.97×10^{-1}	1.02×10^{-1}	3.12×10^{-2}	1.09×10^{-2}
1.4	1.54×10^{1}	1.42×10^{1}	1.09×10^{1}	8.52	6.72	4.29	1.57	6.52×10^{-1}	2.97×10^{-1}	1.45×10^{-1}	7.52×10^{-2}	2.30×10^{-2}	8.03×10^{-3}
1.6	1.17×10^{1}	1.09×10^{1}	8.37	6.53	5.15	3.29	1.20	5×10^{-1}	2.28×10^{-1}	1.12×10^{-1}	5.77×10^{-2}	1.77×10^{-2}	6.16×10^{-3}
1.8	9.20	8.58	6.62	5.17	4.08	2.60	9.54×10^{-1}	3.97×10^{-1}	1.81×10^{-1}	8.84×10^{-2}	4.58×10^{-2}	1.40×10^{-2}	4.89×10^{-3}
2.0	7.39	6.95	5.37	4.19	3.31	2.11	7.76×10^{-1}	3.22×10^{-1}	1.47×10^{-1}	7.19×10^{-2}	3.72×10^{-2}	1.14×10^{-2}	3.98×10^{-3}
2.2	6.05	5.75	4.44	3.47	2.74	1.75	6.43×10^{-1}	2.68×10^{-1}	1.22×10^{-1}	5.97×10^{-2}	3.09×10^{-2}	9.46×10^{-3}	3.30×10^{-3}
2.4	5.03	4.83	3.74	2.92	2.31	1.48	5.43×10^{-1}	2.26×10^{-1}	1.03×10^{-1}	5.04×10^{-2}	2.61×10^{-2}	7.99×10^{-3}	2.79×10^{-3}
2.6	4.24	4.12	3.19	2.50	1.97	1.26	4.65×10^{-1}	1.93×10^{-1}	8.82×10^{-2}	4.32×10^{-2}	2.24×10^{-2}	6.84×10^{-3}	2.39×10^{-3}
2.8	3.61	3.56	2.75	2.16	1.71	1.09	4.02×10^{-1}	1.68×10^{-1}	7.65×10^{-2}	3.74×10^{-2}	1.94×10^{-2}	5.93×10^{-3}	2.07×10^{-3}
3.0	3.11	3.10	2.40	1.88	1.49	9.56×10^{-1}	3.52×10^{-1}	1.47×10^{-1}	6.70×10^{-2}	3.28×10^{-2}	1.70×10^{-2}	5.20×10^{-3}	1.81×10^{-3}
3.4	2.36	2.42	1.88	1.48	1.17	7.51×10^{-1}	2.77×10^{-1}	1.16×10^{-1}	5.28×10^{-2}	2.59×10^{-2}	1.34×10^{-2}	4.10×10^{-3}	1.43×10^{-3}
3.8	1.83	1.94	1.51	1.19	9.44×10^{-1}	6.07×10^{-1}	2.25×10^{-1}	9.40×10^{-2}	4.29×10^{-2}	2.10×10^{-2}	1.09×10^{-2}	3.34×10^{-3}	1.16×10^{-3}
4.2	1.46	1.60	1.25	9.82×10^{-1}	7.80×10^{-1}	5.03×10^{-1}	1.87×10^{-1}	7.82×10^{-2}	3.57×10^{-2}	1.75×10^{-2}	9.08×10^{-3}	2.78×10^{-3}	9.69×10^{-4}
4.6	1.18	1.34	1.05	8.26×10^{-1}	6.57×10^{-1}	4.25×10^{-1}	1.58×10^{-1}	6.63×10^{-2}	3.03×10^{-2}	1.49×10^{-2}	7.71×10^{-3}	2.36×10^{-3}	8.23×10^{-4}
5.0	9.65×10^{-1}	1.14	8.94×10^{-1}	7.07×10^{-1}	5.63×10^{-1}	3.65×10^{-1}	1.36×10^{-1}	5.72×10^{-2}	2.62×10^{-2}	1.28×10^{-2}	6.66×10^{-3}	2.04×10^{-3}	7.11×10^{-4}
6.0	6.25×10^{-1}	8.08×10^{-1}	6.39×10^{-1}	5.08×10^{-1}	4.06×10^{-1}	2.65×10^{-1}	9.98×10^{-2}	4.20×10^{-2}	1.93×10^{-2}	9.45×10^{-3}	4.90×10^{-3}	1.50×10^{-3}	5.23×10^{-4}
7.0	4.40×10^{-1}	6.12×10^{-1}	4.88×10^{-1}	3.90×10^{-1}	3.14×10^{-1}	2.06×10^{-1}	7.81×10^{-2}	3.30×10^{-2}	1.51×10^{-2}	7.43×10^{-3}	3.85×10^{-3}	1.18×10^{-3}	4.10×10^{-4}
8.0	3.42×10^{-1}	4.89×10^{-1}	3.93×10^{-1}	3.16×10^{-1}	2.54×10^{-1}	1.68×10^{-1}	6.44×10^{-2}	2.72×10^{-2}	1.25×10^{-2}	6.14×10^{-3}	3.19×10^{-3}	9.73×10^{-4}	3.39×10^{-4}
9.0	2.96×10^{-1}	4.10×10^{-1}	3.31×10^{-1}	2.68×10^{-1}	2.17×10^{-1}	1.44×10^{-1}	5.53×10^{-2}	2.35×10^{-2}	1.08×10^{-2}	5.29×10^{-3}	2.74×10^{-3}	8.37×10^{-4}	2.91×10^{-4}
10	2.87×10^{-1}	3.57×10^{-1}	2.91×10^{-1}	2.36×10^{-1}	1.92×10^{-1}	1.28×10^{-1}	4.93×10^{-2}	2.09×10^{-2}	9.61×10^{-3}	4.71×10^{-3}	2.44×10^{-3}	7.43×10^{-4}	2.58×10^{-4}
15	5.29×10^{-1}	2.84×10^{-1}	2.33×10^{-1}	1.90×10^{-1}	1.55×10^{-1}	1.03×10^{-1}	3.95×10^{-2}	1.66×10^{-2}	7.55×10^{-3}	3.67×10^{-3}	1.89×10^{-3}	5.67×10^{-4}	1.94×10^{-4}
20	1.05	3.44×10^{-1}	2.78×10^{-1}	2.23×10^{-1}	1.80×10^{-1}	1.17×10^{-1}	4.36×10^{-2}	1.80×10^{-2}	8.04×10^{-3}	3.86×10^{-3}	1.96×10^{-3}	5.80×10^{-4}	1.96×10^{-4}
25	1.77	4.65×10^{-1}	3.68×10^{-1}	2.92×10^{-1}	2.32×10^{-1}	1.49×10^{-1}	5.38×10^{-2}	2.17×10^{-2}	9.59×10^{-3}	4.55×10^{-3}	2.29×10^{-3}	6.68×10^{-4}	2.24×10^{-4}
30	2.67	6.31×10^{-1}	4.93×10^{-1}	3.86×10^{-1}	3.05×10^{-1}	1.93×10^{-1}	6.81×10^{-2}	2.71×10^{-2}	1.18×10^{-2}	5.57×10^{-3}	2.79×10^{-3}	8.03×10^{-4}	2.67×10^{-4}
35	3.73	8.34×10^{-1}	6.46×10^{-1}	5.03×10^{-1}	3.94×10^{-1}	2.47×10^{-1}	8.59×10^{-2}	3.38×10^{-2}	1.46×10^{-2}	6.85×10^{-3}	3.41×10^{-3}	9.75×10^{-4}	3.22×10^{-4}
40	4.97	1.07	8.25×10^{-1}	6.39×10^{-1}	4.99×10^{-1}	3.11×10^{-1}	1.07×10^{-1}	4.17×10^{-2}	1.80×10^{-2}	8.38×10^{-3}	4.15×10^{-3}	1.18×10^{-3}	3.88×10^{-4}
45	6.38	1.35	1.03	7.96×10^{-1}	6.19×10^{-1}	3.84×10^{-1}	1.31×10^{-1}	5.08×10^{-2}	2.18×10^{-2}	1.01×10^{-2}	5.01×10^{-3}	1.42×10^{-3}	4.65×10^{-4}
50	7.95	1.65	1.26	9.71×10^{-1}	7.55×10^{-1}	4.66×10^{-1}	1.58×10^{-1}	6.10×10^{-2}	2.61×10^{-2}	1.21×10^{-2}	5.97×10^{-3}	1.68×10^{-3}	5.51×10^{-4}

Table A.6: Production cross section in pb of a pseudoscalar A produced via the gluon-fusion mode for several mass points in a type IV 2HDM [241–245].

	production cross section in pb												
$\tan\beta$	300 GeV	400 GeV	420 GeV	440 GeV	460 GeV	500 GeV	600 GeV	700 GeV	800 GeV	900 GeV	1000 GeV	1200 GeV	1400 GeV
0.1	2.20	6.60×10^{-1}	5.34×10^{-1}	4.35×10^{-1}	3.57×10^{-1}	2.45×10^{-1}	1.04×10^{-1}	4.94×10^{-2}	2.52×10^{-2}	1.37×10^{-2}	7.90×10^{-3}	3.04×10^{-3}	1.49×10^{-3}
0.12	1.53	4.58×10^{-1}	3.71×10^{-1}	3.02×10^{-1}	2.48×10^{-1}	1.70×10^{-1}	7.26×10^{-2}	3.43×10^{-2}	1.75×10^{-2}	9.54×10^{-3}	5.49×10^{-3}	2.11×10^{-3}	1.03×10^{-3}
0.14	1.12	3.37×10^{-1}	2.72×10^{-1}	2.22×10^{-1}	1.82×10^{-1}	1.25×10^{-1}	5.33×10^{-2}	2.52×10^{-2}	1.29×10^{-2}	7.01×10^{-3}	4.03×10^{-3}	1.55×10^{-3}	7.59×10^{-4}
0.16	8.59×10^{-1}	2.58×10^{-1}	2.08×10^{-1}	1.70×10^{-1}	1.39×10^{-1}	9.56×10^{-2}	4.08×10^{-2}	1.93×10^{-2}	9.85×10^{-3}	5.37×10^{-3}	3.09×10^{-3}	1.19×10^{-3}	5.81×10^{-4}
0.18	6.79×10^{-1}	2.04×10^{-1}	1.65×10^{-1}	1.34×10^{-1}	1.10×10^{-1}	7.56×10^{-2}	3.22×10^{-2}	1.52×10^{-2}	7.78×10^{-3}	4.24×10^{-3}	2.44×10^{-3}	9.38×10^{-4}	4.59×10^{-4}
0.2	5.50×10^{-1}	1.65×10^{-1}	1.33×10^{-1}	1.09×10^{-1}	8.92×10^{-2}	6.12×10^{-2}	2.61×10^{-2}	1.23×10^{-2}	6.31×10^{-3}	3.43×10^{-3}	1.98×10^{-3}	7.59×10^{-4}	3.72×10^{-4}
0.24	3.82×10^{-1}	1.15×10^{-1}	9.27×10^{-2}	7.55×10^{-2}	6.20×10^{-2}	4.25×10^{-2}	1.81×10^{-2}	8.57×10^{-3}	4.38×10^{-3}	2.38×10^{-3}	1.37×10^{-3}	5.27×10^{-4}	2.58×10^{-4}
0.28	2.81×10^{-1}	8.42×10^{-2}	6.81×10^{-2}	5.55×10^{-2}	4.55×10^{-2}	3.12×10^{-2}	1.33×10^{-2}	6.30×10^{-3}	3.22×10^{-3}	1.75×10^{-3}	1.01×10^{-3}	3.87×10^{-4}	1.90×10^{-4}
0.32	2.15×10^{-1}	6.44×10^{-2}	5.21×10^{-2}	4.25×10^{-2}	3.49×10^{-2}	2.39×10^{-2}	1.02×10^{-2}	4.82×10^{-3}	2.46×10^{-3}	1.34×10^{-3}	7.71×10^{-4}	2.97×10^{-4}	1.45×10^{-4}
0.36	1.70×10^{-1}	5.09×10^{-2}	4.12×10^{-2}	3.36×10^{-2}	2.75×10^{-2}	1.89×10^{-2}	8.06×10^{-3}	3.81×10^{-3}	1.95×10^{-3}	1.06×10^{-3}	6.10×10^{-4}	2.34×10^{-4}	1.15×10^{-4}
0.4	1.37×10^{-1}	4.12×10^{-2}	3.34×10^{-2}	2.72×10^{-2}	2.23×10^{-2}	1.53×10^{-2}	6.53×10^{-3}	3.08×10^{-3}	1.58×10^{-3}	8.59×10^{-4}	4.94×10^{-4}	1.90×10^{-4}	9.30×10^{-5}
0.46	1.04×10^{-1}	3.12×10^{-2}	2.52×10^{-2}	2.06×10^{-2}	1.69×10^{-2}	1.16×10^{-2}	4.94×10^{-3}	2.33×10^{-3}	1.19×10^{-3}	6.49×10^{-4}	3.73×10^{-4}	1.44×10^{-4}	7.03×10^{-5}
0.52	8.14×10^{-2}	2.44×10^{-2}	1.97×10^{-2}	1.61×10^{-2}	1.32×10^{-2}	9.06×10^{-3}	3.86×10^{-3}	1.83×10^{-3}	9.33×10^{-4}	5.08×10^{-4}	2.92×10^{-4}	1.12×10^{-4}	5.50×10^{-5}
0.58	6.54×10^{-2}	1.96×10^{-2}	1.59×10^{-2}	1.29×10^{-2}	1.06×10^{-2}	7.28×10^{-3}	3.11×10^{-3}	1.47×10^{-3}	7.50×10^{-4}	4.08×10^{-4}	2.35×10^{-4}	9.03×10^{-5}	4.42×10^{-5}
0.64	5.37×10^{-2}	1.61×10^{-2}	1.30×10^{-2}	1.06×10^{-2}	8.71×10^{-3}	5.98×10^{-3}	2.55×10^{-3}	1.21×10^{-3}	6.16×10^{-4}	3.35×10^{-4}	1.93×10^{-4}	7.42×10^{-5}	3.63×10^{-5}
0.7	4.49×10^{-2}	1.35×10^{-2}	1.09×10^{-2}	8.88×10^{-3}	7.28×10^{-3}	5×10^{-3}	2.13×10^{-3}	1.01×10^{-3}	5.15×10^{-4}	2.80×10^{-4}	1.61×10^{-4}	6.20×10^{-5}	3.04×10^{-5}
0.8	3.44×10^{-2}	1.03×10^{-2}	8.34×10^{-3}	6.80×10^{-3}	5.58×10^{-3}	3.83×10^{-3}	1.63×10^{-3}	7.71×10^{-4}	3.94×10^{-4}	2.15×10^{-4}	1.23×10^{-4}	4.75×10^{-5}	2.33×10^{-5}
0.9	2.72×10^{-2}	8.15×10^{-3}	6.59×10^{-3}	5.37×10^{-3}	4.41×10^{-3}	3.02×10^{-3}	1.29×10^{-3}	6.09×10^{-4}	3.11×10^{-4}	1.70×10^{-4}	9.75×10^{-5}	3.75×10^{-5}	1.84×10^{-5}
1.0	2.20×10^{-2}	6.60×10^{-3}	5.34×10^{-3}	4.35×10^{-3}	3.57×10^{-3}	2.45×10^{-3}	1.04×10^{-3}	4.94×10^{-4}	2.52×10^{-4}	1.37×10^{-4}	7.90×10^{-5}	3.04×10^{-5}	1.49×10^{-5}
1.2	1.53×10^{-2}	4.58×10^{-3}	3.71×10^{-3}	3.02×10^{-3}	2.48×10^{-3}	1.70×10^{-3}	7.26×10^{-4}	3.43×10^{-4}	1.75×10^{-4}	9.54×10^{-5}	5.49×10^{-5}	2.11×10^{-5}	1.03×10^{-5}
1.4	1.12×10^{-2}	3.37×10^{-3}	2.72×10^{-3}	2.22×10^{-3}	1.82×10^{-3}	1.25×10^{-3}	5.33×10^{-4}	2.52×10^{-4}	1.29×10^{-4}	7.01×10^{-5}	4.03×10^{-5}	1.55×10^{-5}	7.60×10^{-6}
1.6	8.59×10^{-3}	2.58×10^{-3}	2.08×10^{-3}	1.70×10^{-3}	1.39×10^{-3}	9.56×10^{-4}	4.08×10^{-4}	1.93×10^{-4}	9.85×10^{-5}	5.37×10^{-5}	3.09×10^{-5}	1.19×10^{-5}	5.80×10^{-6}
1.8	6.79×10^{-3}	2.04×10^{-3}	1.65×10^{-3}	1.34×10^{-3}	1.10×10^{-3}	7.56×10^{-4}	3.22×10^{-4}	1.52×10^{-4}	7.78×10^{-5}	4.24×10^{-5}	2.44×10^{-5}	9.40×10^{-6}	4.60×10^{-6}
2.0	5.50×10^{-3}	1.65×10^{-3}	1.33×10^{-3}	1.09×10^{-3}	8.92×10^{-4}	6.12×10^{-4}	2.61×10^{-4}	1.23×10^{-4}	6.31×10^{-5}	3.43×10^{-5}	1.98×10^{-5}	7.60×10^{-6}	3.70×10^{-6}
2.2	4.55×10^{-3}	1.36×10^{-3}	1.10×10^{-3}	8.99×10^{-4}	7.37×10^{-4}	5.06×10^{-4}	2.16×10^{-4}	1.02×10^{-4}	5.21×10^{-5}	2.84×10^{-5}	1.63×10^{-5}	6.30×10^{-6}	3.10×10^{-6}
2.4	3.82×10^{-3}	1.15×10^{-3}	9.27×10^{-4}	7.55×10^{-4}	6.20×10^{-4}	4.25×10^{-4}	1.81×10^{-4}	8.57×10^{-5}	4.38×10^{-5}	2.38×10^{-5}	1.37×10^{-5}	5.30×10^{-6}	2.60×10^{-6}
2.6	3.25×10^{-3}	9.76×10^{-4}	7.90×10^{-4}	6.43×10^{-4}	5.28×10^{-4}	3.62×10^{-4}	1.55×10^{-4}	7.30×10^{-5}	3.73×10^{-5}	2.03×10^{-5}	1.17×10^{-5}	4.50×10^{-6}	2.20×10^{-6}
2.8	2.81×10^{-3}	8.42×10^{-4}	6.81×10^{-4}	5.55×10^{-4}	4.55×10^{-4}	3.12×10^{-4}	1.33×10^{-4}	6.30×10^{-5}	3.22×10^{-5}	1.75×10^{-5}	1.01×10^{-5}	3.90×10^{-6}	1.90×10^{-6}
3.0	2.44×10^{-3}	7.33×10^{-4}	5.93×10^{-4}	4.83×10^{-4}	3.97×10^{-4}	2.72×10^{-4}	1.16×10^{-4}	5.48×10^{-5}	2.80×10^{-5}	1.53×10^{-5}	8.80×10^{-6}	3.40×10^{-6}	1.70×10^{-6}
3.4	1.90×10^{-3}	5.71×10^{-4}	4.62×10^{-4}	3.76×10^{-4}	3.09×10^{-4}	2.12×10^{-4}	9.04×10^{-5}	4.27×10^{-5}	2.18×10^{-5}	1.19×10^{-5}	6.80×10^{-6}	2.60×10^{-6}	1.30×10^{-6}
3.8	1.52×10^{-3}	4.57×10^{-4}	3.70×10^{-4}	3.01×10^{-4}	2.47×10^{-4}	1.70×10^{-4}	7.24×10^{-5}	3.42×10^{-5}	1.75×10^{-5}	9.50×10^{-6}	5.50×10^{-6}	2.10×10^{-6}	1×10^{-6}
4.2	1.25×10^{-3}	3.74×10^{-4}	3.03×10^{-4}	2.47×10^{-4}	2.02×10^{-4}	1.39×10^{-4}	5.92×10^{-5}	2.80×10^{-5}	1.43×10^{-5}	7.80×10^{-6}	4.50×10^{-6}	1.70×10^{-6}	8×10^{-7}
4.6	1.04×10^{-3}	3.12×10^{-4}	2.52×10^{-4}	2.06×10^{-4}	1.69×10^{-4}	1.16×10^{-4}	4.94×10^{-5}	2.33×10^{-5}	1.19×10^{-5}	6.50×10^{-6}	3.70×10^{-6}	1.40×10^{-6}	7×10^{-7}
5.0	8.80×10^{-4}	2.64×10^{-4}	2.13×10^{-4}	1.74×10^{-4}	1.43×10^{-4}	9.79×10^{-5}	4.18×10^{-5}	1.97×10^{-5}	1.01×10^{-5}	5.50×10^{-6}	3.20×10^{-6}	1.20×10^{-6}	6×10^{-7}
6.0	6.11×10^{-4}	1.83×10^{-4}	1.48×10^{-4}	1.21×10^{-4}	9.91×10^{-5}	6.80×10^{-5}	2.90×10^{-5}	1.37×10^{-5}	7×10^{-6}	3.80×10^{-6}	2.20×10^{-6}	8×10^{-7}	4×10^{-7}
7.0	4.49×10^{-4}	1.35×10^{-4}	1.09×10^{-4}	8.88×10^{-5}	7.28×10^{-5}	5×10^{-5}	2.13×10^{-5}	1.01×10^{-5}	5.10×10^{-6}	2.80×10^{-6}	1.60×10^{-6}	6×10^{-7}	3×10^{-7}
8.0	3.44×10^{-4}	1.03×10^{-4}	8.34×10^{-5}	6.80×10^{-5}	5.58×10^{-5}	3.83×10^{-5}	1.63×10^{-5}	7.70×10^{-6}	3.90×10^{-6}	2.10×10^{-6}	1.20×10^{-6}	5×10^{-7}	2×10^{-7}
9.0	2.72×10^{-4}	8.15×10^{-5}	6.59×10^{-5}	5.37×10^{-5}	4.41×10^{-5}	3.02×10^{-5}	1.29×10^{-5}	6.10×10^{-6}	3.10×10^{-6}	1.70×10^{-6}	1×10^{-6}	4×10^{-7}	2×10^{-7}
10	2.20×10^{-4}	6.60×10^{-5}	5.34×10^{-5}	4.35×10^{-5}	3.57×10^{-5}	2.45×10^{-5}	1.04×10^{-5}	4.90×10^{-6}	2.50×10^{-6}	1.40×10^{-6}	8×10^{-7}	3×10^{-7}	1×10^{-7}
15	9.78×10^{-5}	2.93×10^{-5}	2.37×10^{-5}	1.93×10^{-5}	1.59×10^{-5}	1.09×10^{-5}	4.60×10^{-6}	2.20×10^{-6}	1.10×10^{-6}	6×10^{-7}	4×10^{-7}	1×10^{-7}	1×10^{-7}
20	5.50×10^{-5}	1.65×10^{-5}	1.33×10^{-5}	1.09×10^{-5}	8.90×10^{-6}	6.10×10^{-6}	2.60×10^{-6}	1.20×10^{-6}	6×10^{-7}	3×10^{-7}	2×10^{-7}	1×10^{-7}	0.00
25	3.52×10^{-5}	1.06×10^{-5}	8.50×10^{-6}	7×10^{-6}	5.70×10^{-6}	3.90×10^{-6}	1.70×10^{-6}	8×10^{-7}	4×10^{-7}	2×10^{-7}	1×10^{-7}	0.00	0.00
30	2.44×10^{-5}	7.30×10^{-6}	5.90×10^{-6}	4.80×10^{-6}	4×10^{-6}	2.70×10^{-6}	1.20×10^{-6}	5×10^{-7}	3×10^{-7}	2×10^{-7}	1×10^{-7}	0.00	0.00
35	1.80×10^{-5}	5.40×10^{-6}	4.40×10^{-6}	3.60×10^{-6}	2.90×10^{-6}	2×10^{-6}	9×10^{-7}	4×10^{-7}	2×10^{-7}	1×10^{-7}	1×10^{-7}	0.00	0.00
40	1.37×10^{-5}	4.10×10^{-6}	3.30×10^{-6}	2.70×10^{-6}	2.20×10^{-6}	1.50×10^{-6}	7×10^{-7}	3×10^{-7}	2×10^{-7}	1×10^{-7}	0.00	0.00	0.00
45	1.09×10^{-5}	3.30×10^{-6}	2.60×10^{-6}	2.10×10^{-6}	1.80×10^{-6}	1.20×10^{-6}	5×10^{-7}	2×10^{-7}	1×10^{-7}	1×10^{-7}	0.00	0.00	0.00
50	8.80×10^{-6}	2.60×10^{-6}	2.10×10^{-6}	1.70×10^{-6}	1.40×10^{-6}	1×10^{-6}	4×10^{-7}	2×10^{-7}	1×10^{-7}	1×10^{-7}	0.00	0.00	0.00

Table A.7: Production cross section in pb of a pseudoscalar A produced via the b-associated production mode for several mass points in a type I 2HDM [241–245].

	production cross section in pb												
$\tan\beta$	300 GeV	400 GeV	420 GeV	440 GeV	460 GeV	500 GeV	600 GeV	700 GeV	800 GeV	900 GeV	1000 GeV	1200 GeV	1400 GeV
0.1	5.75×10^{-5}	6.09×10^{-5}	5.09×10^{-5}	4.23×10^{-5}	3.51×10^{-5}	2.44×10^{-5}	1.04×10^{-5}	4.90×10^{-6}	2.50×10^{-6}	1.40×10^{-6}	8×10^{-7}	3×10^{-7}	1×10^{-7}
0.12	1.54×10^{-4}	8.99×10^{-5}	7.44×10^{-5}	6.15×10^{-5}	5.08×10^{-5}	3.51×10^{-5}	1.50×10^{-5}	7.10×10^{-6}	3.60×10^{-6}	2×10^{-6}	1.10×10^{-6}	4×10^{-7}	2×10^{-7}
0.14	2.67×10^{-4}	1.24×10^{-4}	1.02×10^{-4}	8.41×10^{-5}	6.94×10^{-5}	4.79×10^{-5}	2.05×10^{-5}	9.70×10^{-6}	4.90×10^{-6}	2.70×10^{-6}	1.50×10^{-6}	6×10^{-7}	3×10^{-7}
0.16	3.98×10^{-4}	1.64×10^{-4}	1.34×10^{-4}	1.10×10^{-4}	9.08×10^{-5}	6.26×10^{-5}	2.67×10^{-5}	1.26×10^{-5}	6.50×10^{-6}	3.50×10^{-6}	2×10^{-6}	8×10^{-7}	4×10^{-7}
0.18	5.47×10^{-4}	2.09×10^{-4}	1.70×10^{-4}	1.40×10^{-4}	1.15×10^{-4}	7.92×10^{-5}	3.38×10^{-5}	1.60×10^{-5}	8.20×10^{-6}	4.50×10^{-6}	2.60×10^{-6}	1×10^{-6}	5×10^{-7}
0.2	7.13×10^{-4}	2.59×10^{-4}	2.11×10^{-4}	1.73×10^{-4}	1.42×10^{-4}	9.78×10^{-5}	4.18×10^{-5}	1.97×10^{-5}	1.01×10^{-5}	5.50×10^{-6}	3.20×10^{-6}	1.20×10^{-6}	6×10^{-7}
0.24	1.10×10^{-3}	3.75×10^{-4}	3.05×10^{-4}	2.49×10^{-4}	2.05×10^{-4}	1.41×10^{-4}	6.02×10^{-5}	2.84×10^{-5}	1.45×10^{-5}	7.90×10^{-6}	4.60×10^{-6}	1.70×10^{-6}	9×10^{-7}
0.28	1.55×10^{-3}	5.12×10^{-4}	4.16×10^{-4}	3.40×10^{-4}	2.79×10^{-4}	1.92×10^{-4}	8.19×10^{-5}	3.87×10^{-5}	1.98×10^{-5}	1.08×10^{-5}	6.20×10^{-6}	2.40×10^{-6}	1.20×10^{-6}
0.32	2.08×10^{-3}	6.70×10^{-4}	5.44×10^{-4}	4.44×10^{-4}	3.65×10^{-4}	2.51×10^{-4}	1.07×10^{-4}	5.05×10^{-5}	2.58×10^{-5}	1.41×10^{-5}	8.10×10^{-6}	3.10×10^{-6}	1.50×10^{-6}
0.36	2.67×10^{-3}	8.50×10^{-4}	6.89×10^{-4}	5.62×10^{-4}	4.62×10^{-4}	3.17×10^{-4}	1.35×10^{-4}	6.40×10^{-5}	3.27×10^{-5}	1.78×10^{-5}	1.02×10^{-5}	3.90×10^{-6}	1.90×10^{-6}
0.4	3.33×10^{-3}	1.05×10^{-3}	8.51×10^{-4}	6.95×10^{-4}	5.70×10^{-4}	3.92×10^{-4}	1.67×10^{-4}	7.90×10^{-5}	4.04×10^{-5}	2.20×10^{-5}	1.26×10^{-5}	4.90×10^{-6}	2.40×10^{-6}
0.46	4.46×10^{-3}	1.39×10^{-3}	1.13×10^{-3}	9.19×10^{-4}	7.55×10^{-4}	5.18×10^{-4}	2.21×10^{-4}	1.04×10^{-4}	5.34×10^{-5}	2.91×10^{-5}	1.67×10^{-5}	6.40×10^{-6}	3.10×10^{-6}
0.52	5.74×10^{-3}	1.78×10^{-3}	1.44×10^{-3}	1.17×10^{-3}	9.64×10^{-4}	6.62×10^{-4}	2.83×10^{-4}	1.33×10^{-4}	6.82×10^{-5}	3.71×10^{-5}	2.14×10^{-5}	8.20×10^{-6}	4×10^{-6}
0.58	7.19×10^{-3}	2.21×10^{-3}	1.79×10^{-3}	1.46×10^{-3}	1.20×10^{-3}	8.24×10^{-4}	3.51×10^{-4}	1.66×10^{-4}	8.48×10^{-5}	4.62×10^{-5}	2.66×10^{-5}	1.02×10^{-5}	5×10^{-6}
0.64	8.78×10^{-3}	2.70×10^{-3}	2.18×10^{-3}	1.78×10^{-3}	1.46×10^{-3}	1×10^{-3}	4.28×10^{-4}	2.02×10^{-4}	1.03×10^{-4}	5.63×10^{-5}	3.24×10^{-5}	1.24×10^{-5}	6.10×10^{-6}
0.7	1.05×10^{-2}	3.23×10^{-3}	2.61×10^{-3}	2.13×10^{-3}	1.75×10^{-3}	1.20×10^{-3}	5.12×10^{-4}	2.42×10^{-4}	1.24×10^{-4}	6.73×10^{-5}	3.87×10^{-5}	1.49×10^{-5}	7.30×10^{-6}
0.8	1.38×10^{-2}	4.21×10^{-3}	3.41×10^{-3}	2.78×10^{-3}	2.28×10^{-3}	1.57×10^{-3}	6.69×10^{-4}	3.16×10^{-4}	1.61×10^{-4}	8.79×10^{-5}	5.06×10^{-5}	1.94×10^{-5}	9.50×10^{-6}
0.9	1.75×10^{-2}	5.34×10^{-3}	4.32×10^{-3}	3.52×10^{-3}	2.89×10^{-3}	1.98×10^{-3}	8.46×10^{-4}	4×10^{-4}	2.04×10^{-4}	1.11×10^{-4}	6.40×10^{-5}	2.46×10^{-5}	1.21×10^{-5}
1.0	2.17×10^{-2}	6.59×10^{-3}	5.33×10^{-3}	4.35×10^{-3}	3.57×10^{-3}	2.45×10^{-3}	1.04×10^{-3}	4.94×10^{-4}	2.52×10^{-4}	1.37×10^{-4}	7.90×10^{-5}	3.04×10^{-5}	1.49×10^{-5}
1.2	3.13×10^{-2}	9.49×10^{-3}	7.68×10^{-3}	6.26×10^{-3}	5.14×10^{-3}	3.53×10^{-3}	1.50×10^{-3}	7.11×10^{-4}	3.63×10^{-4}	1.98×10^{-4}	1.14×10^{-4}	4.37×10^{-5}	2.14×10^{-5}
1.4	4.26×10^{-2}	1.29×10^{-2}	1.05×10^{-2}	8.52×10^{-3}	6.99×10^{-3}	4.80×10^{-3}	2.05×10^{-3}	9.67×10^{-4}	4.94×10^{-4}	2.69×10^{-4}	1.55×10^{-4}	5.95×10^{-5}	2.92×10^{-5}
1.6	5.57×10^{-2}	1.69×10^{-2}	1.37×10^{-2}	1.11×10^{-2}	9.13×10^{-3}	6.27×10^{-3}	2.67×10^{-3}	1.26×10^{-3}	6.46×10^{-4}	3.52×10^{-4}	2.02×10^{-4}	7.78×10^{-5}	3.81×10^{-5}
1.8	7.06×10^{-2}	2.14×10^{-2}	1.73×10^{-2}	1.41×10^{-2}	1.16×10^{-2}	7.93×10^{-3}	3.39×10^{-3}	1.60×10^{-3}	8.17×10^{-4}	4.45×10^{-4}	2.56×10^{-4}	9.84×10^{-5}	4.82×10^{-5}
2.0	8.72×10^{-2}	2.64×10^{-2}	2.13×10^{-2}	1.74×10^{-2}	1.43×10^{-2}	9.79×10^{-3}	4.18×10^{-3}	1.97×10^{-3}	1.01×10^{-3}	5.49×10^{-4}	3.16×10^{-4}	1.22×10^{-4}	5.95×10^{-5}
2.2	1.06×10^{-1}	3.19×10^{-2}	2.58×10^{-2}	2.10×10^{-2}	1.73×10^{-2}	1.19×10^{-2}	5.06×10^{-3}	2.39×10^{-3}	1.22×10^{-3}	6.65×10^{-4}	3.82×10^{-4}	1.47×10^{-4}	7.20×10^{-5}
2.4	1.26×10^{-1}	3.80×10^{-2}	3.07×10^{-2}	2.50×10^{-2}	2.06×10^{-2}	1.41×10^{-2}	6.02×10^{-3}	2.84×10^{-3}	1.45×10^{-3}	7.91×10^{-4}	4.55×10^{-4}	1.75×10^{-4}	8.57×10^{-5}
2.6	1.47×10^{-1}	4.46×10^{-2}	3.61×10^{-2}	2.94×10^{-2}	2.41×10^{-2}	1.66×10^{-2}	7.06×10^{-3}	3.34×10^{-3}	1.70×10^{-3}	9.29×10^{-4}	5.34×10^{-4}	2.05×10^{-4}	1.01×10^{-4}
2.8	1.71×10^{-1}	5.17×10^{-2}	4.18×10^{-2}	3.41×10^{-2}	2.80×10^{-2}	1.92×10^{-2}	8.19×10^{-3}	3.87×10^{-3}	1.98×10^{-3}	1.08×10^{-3}	6.19×10^{-4}	2.38×10^{-4}	1.17×10^{-4}
3.0	1.96×10^{-1}	5.93×10^{-2}	4.80×10^{-2}	3.91×10^{-2}	3.21×10^{-2}	2.20×10^{-2}	9.40×10^{-3}	4.44×10^{-3}	2.27×10^{-3}	1.24×10^{-3}	7.11×10^{-4}	2.73×10^{-4}	1.34×10^{-4}
3.4	2.52×10^{-1}	7.62×10^{-2}	6.17×10^{-2}	5.03×10^{-2}	4.13×10^{-2}	2.83×10^{-2}	1.21×10^{-2}	5.71×10^{-3}	2.92×10^{-3}	1.59×10^{-3}	9.13×10^{-4}	3.51×10^{-4}	1.72×10^{-4}
3.8	3.15×10^{-1}	9.52×10^{-2}	7.70×10^{-2}	6.28×10^{-2}	5.15×10^{-2}	3.54×10^{-2}	1.51×10^{-2}	7.13×10^{-3}	3.64×10^{-3}	1.98×10^{-3}	1.14×10^{-3}	4.39×10^{-4}	2.15×10^{-4}
4.2	3.85×10^{-1}	1.16×10^{-1}	9.41×10^{-2}	7.67×10^{-2}	6.29×10^{-2}	4.32×10^{-2}	1.84×10^{-2}	8.71×10^{-3}	4.45×10^{-3}	2.42×10^{-3}	1.39×10^{-3}	5.36×10^{-4}	2.62×10^{-4}
4.6	4.62×10^{-1}	1.40×10^{-1}	1.13×10^{-1}	9.20×10^{-2}	7.55×10^{-2}	5.18×10^{-2}	2.21×10^{-2}	1.04×10^{-2}	5.34×10^{-3}	2.91×10^{-3}	1.67×10^{-3}	6.43×10^{-4}	3.15×10^{-4}
5.0	5.46×10^{-1}	1.65×10^{-1}	1.33×10^{-1}	1.09×10^{-1}	8.92×10^{-2}	6.12×10^{-2}	2.61×10^{-2}	1.23×10^{-2}	6.31×10^{-3}	3.43×10^{-3}	1.98×10^{-3}	7.59×10^{-4}	3.72×10^{-4}
6.0	7.86×10^{-1}	2.37×10^{-1}	1.92×10^{-1}	1.57×10^{-1}	1.28×10^{-1}	8.81×10^{-2}	3.76×10^{-2}	1.78×10^{-2}	9.08×10^{-3}	4.95×10^{-3}	2.84×10^{-3}	1.09×10^{-3}	5.36×10^{-4}
7.0	1.07	3.23×10^{-1}	2.61×10^{-1}	2.13×10^{-1}	1.75×10^{-1}	1.20×10^{-1}	5.12×10^{-2}	2.42×10^{-2}	1.24×10^{-2}	6.73×10^{-3}	3.87×10^{-3}	1.49×10^{-3}	7.29×10^{-4}
8.0	1.40	4.22×10^{-1}	3.41×10^{-1}	2.78×10^{-1}	2.28×10^{-1}	1.57×10^{-1}	6.69×10^{-2}	3.16×10^{-2}	1.61×10^{-2}	8.79×10^{-3}	5.06×10^{-3}	1.94×10^{-3}	9.52×10^{-4}
9.0	1.77	5.34×10^{-1}	4.32×10^{-1}	3.52×10^{-1}	2.89×10^{-1}	1.98×10^{-1}	8.46×10^{-2}	4×10^{-2}	2.04×10^{-2}	1.11×10^{-2}	6.40×10^{-3}	2.46×10^{-3}	1.21×10^{-3}
10	2.18	6.59×10^{-1}	5.33×10^{-1}	4.35×10^{-1}	3.57×10^{-1}	2.45×10^{-1}	1.04×10^{-1}	4.94×10^{-2}	2.52×10^{-2}	1.37×10^{-2}	7.90×10^{-3}	3.04×10^{-3}	1.49×10^{-3}
15	4.91	1.48	1.20	9.78×10^{-1}	8.03×10^{-1}	5.51×10^{-1}	2.35×10^{-1}	1.11×10^{-1}	5.67×10^{-2}	3.09×10^{-2}	1.78×10^{-2}	6.83×10^{-3}	3.35×10^{-3}
20	8.74	2.64	2.13	1.74	1.43	9.79×10^{-1}	4.18×10^{-1}	1.97×10^{-1}	1.01×10^{-1}	5.49×10^{-2}	3.16×10^{-2}	1.22×10^{-2}	5.95×10^{-3}
25	1.36×10^{1}	4.12	3.33	2.72	2.23	1.53	6.53×10^{-1}	3.08×10^{-1}	1.58×10^{-1}	8.59×10^{-2}	4.94×10^{-2}	1.90×10^{-2}	9.30×10^{-3}
30	1.97×10^{1}	5.93	4.80	3.91	3.21	2.20	9.40×10^{-1}	4.44×10^{-1}	2.27×10^{-1}	1.24×10^{-1}	7.11×10^{-2}	2.73×10^{-2}	1.34×10^{-2}
35	2.68×10^{1}	8.08	6.54	5.33	4.37	3.00	1.28	6.05×10^{-1}	3.09×10^{-1}	1.68×10^{-1}	9.68×10^{-2}	3.72×10^{-2}	1.82×10^{-2}
40	3.49×10^{1}	1.05×10^{1}	8.54	6.96	5.71	3.92	1.67	7.90×10^{-1}	4.04×10^{-1}	2.20×10^{-1}	1.26×10^{-1}	4.86×10^{-2}	2.38×10^{-2}
45	4.42×10^{1}	1.34×10^{1}	1.08×10^{1}	8.81	7.23	4.96	2.12	1.00	5.11×10^{-1}	2.78×10^{-1}	1.60×10^{-1}	6.15×10^{-2}	3.01×10^{-2}
50	5.46×10^{1}	1.65×10^{1}	1.33×10^{1}	1.09×10^{1}	8.92	6.12	2.61	1.23	6.31×10^{-1}	3.43×10^{-1}	1.98×10^{-1}	7.59×10^{-2}	3.72×10^{-2}

Table A.8: Production cross section in pb of a pseudoscalar A produced via the b-associated production mode for several mass points in a type II 2HDM [241–245].

	production cross section in pb												
$\tan\beta$	300 GeV	400 GeV	420 GeV	440 GeV	460 GeV	500 GeV	600 GeV	700 GeV	800 GeV	900 GeV	1000 GeV	1200 GeV	1400 GeV
0.1	2.20	6.60×10^{-1}	5.34×10^{-1}	4.35×10^{-1}	3.57×10^{-1}	2.45×10^{-1}	1.04×10^{-1}	4.94×10^{-2}	2.52×10^{-2}	1.37×10^{-2}	7.90×10^{-3}	3.04×10^{-3}	1.49×10^{-3}
0.12	1.53	4.58×10^{-1}	3.71×10^{-1}	3.02×10^{-1}	2.48×10^{-1}	1.70×10^{-1}	7.26×10^{-2}	3.43×10^{-2}	1.75×10^{-2}	9.54×10^{-3}	5.49×10^{-3}	2.11×10^{-3}	1.03×10^{-3}
0.14	1.12	3.37×10^{-1}	2.72×10^{-1}	2.22×10^{-1}	1.82×10^{-1}	1.25×10^{-1}	5.33×10^{-2}	2.52×10^{-2}	1.29×10^{-2}	7.01×10^{-3}	4.03×10^{-3}	1.55×10^{-3}	7.59×10^{-4}
0.16	8.59×10^{-1}	2.58×10^{-1}	2.08×10^{-1}	1.70×10^{-1}	1.39×10^{-1}	9.56×10^{-2}	4.08×10^{-2}	1.93×10^{-2}	9.85×10^{-3}	5.37×10^{-3}	3.09×10^{-3}	1.19×10^{-3}	5.81×10^{-4}
0.18	6.79×10^{-1}	2.04×10^{-1}	1.65×10^{-1}	1.34×10^{-1}	1.10×10^{-1}	7.56×10^{-2}	3.22×10^{-2}	1.52×10^{-2}	7.78×10^{-3}	4.24×10^{-3}	2.44×10^{-3}	9.38×10^{-4}	4.59×10^{-4}
0.2	5.50×10^{-1}	1.65×10^{-1}	1.33×10^{-1}	1.09×10^{-1}	8.92×10^{-2}	6.12×10^{-2}	2.61×10^{-2}	1.23×10^{-2}	6.31×10^{-3}	3.43×10^{-3}	1.98×10^{-3}	7.59×10^{-4}	3.72×10^{-4}
0.24	3.82×10^{-1}	1.15×10^{-1}	9.27×10^{-2}	7.55×10^{-2}	6.20×10^{-2}	4.25×10^{-2}	1.81×10^{-2}	8.57×10^{-3}	4.38×10^{-3}	2.38×10^{-3}	1.37×10^{-3}	5.27×10^{-4}	2.58×10^{-4}
0.28	2.81×10^{-1}	8.42×10^{-2}	6.81×10^{-2}	5.55×10^{-2}	4.55×10^{-2}	3.12×10^{-2}	1.33×10^{-2}	6.30×10^{-3}	3.22×10^{-3}	1.75×10^{-3}	1.01×10^{-3}	3.87×10^{-4}	1.90×10^{-4}
0.32	2.15×10^{-1}	6.44×10^{-2}	5.21×10^{-2}	4.25×10^{-2}	3.49×10^{-2}	2.39×10^{-2}	1.02×10^{-2}	4.82×10^{-3}	2.46×10^{-3}	1.34×10^{-3}	7.71×10^{-4}	2.97×10^{-4}	1.45×10^{-4}
0.36	1.70×10^{-1}	5.09×10^{-2}	4.12×10^{-2}	3.36×10^{-2}	2.75×10^{-2}	1.89×10^{-2}	8.06×10^{-3}	3.81×10^{-3}	1.95×10^{-3}	1.06×10^{-3}	6.10×10^{-4}	2.34×10^{-4}	1.15×10^{-4}
0.4	1.37×10^{-1}	4.12×10^{-2}	3.34×10^{-2}	2.72×10^{-2}	2.23×10^{-2}	1.53×10^{-2}	6.53×10^{-3}	3.08×10^{-3}	1.58×10^{-3}	8.59×10^{-4}	4.94×10^{-4}	1.90×10^{-4}	9.30×10^{-5}
0.46	1.04×10^{-1}	3.12×10^{-2}	2.52×10^{-2}	2.06×10^{-2}	1.69×10^{-2}	1.16×10^{-2}	4.94×10^{-3}	2.33×10^{-3}	1.19×10^{-3}	6.49×10^{-4}	3.73×10^{-4}	1.44×10^{-4}	7.03×10^{-5}
0.52	8.14×10^{-2}	2.44×10^{-2}	1.97×10^{-2}	1.61×10^{-2}	1.32×10^{-2}	9.06×10^{-3}	3.86×10^{-3}	1.83×10^{-3}	9.33×10^{-4}	5.08×10^{-4}	2.92×10^{-4}	1.12×10^{-4}	5.50×10^{-5}
0.58	6.54×10^{-2}	1.96×10^{-2}	1.59×10^{-2}	1.29×10^{-2}	1.06×10^{-2}	7.28×10^{-3}	3.11×10^{-3}	1.47×10^{-3}	7.50×10^{-4}	4.08×10^{-4}	2.35×10^{-4}	9.03×10^{-5}	4.42×10^{-5}
0.64	5.37×10^{-2}	1.61×10^{-2}	1.30×10^{-2}	1.06×10^{-2}	8.71×10^{-3}	5.98×10^{-3}	2.55×10^{-3}	1.21×10^{-3}	6.16×10^{-4}	3.35×10^{-4}	1.93×10^{-4}	7.42×10^{-5}	3.63×10^{-5}
0.7	4.49×10^{-2}	1.35×10^{-2}	1.09×10^{-2}	8.88×10^{-3}	7.28×10^{-3}	5×10^{-3}	2.13×10^{-3}	1.01×10^{-3}	5.15×10^{-4}	2.80×10^{-4}	1.61×10^{-4}	6.20×10^{-5}	3.04×10^{-5}
0.8	3.44×10^{-2}	1.03×10^{-2}	8.34×10^{-3}	6.80×10^{-3}	5.58×10^{-3}	3.83×10^{-3}	1.63×10^{-3}	7.71×10^{-4}	3.94×10^{-4}	2.15×10^{-4}	1.23×10^{-4}	4.75×10^{-5}	2.33×10^{-5}
0.9	2.72×10^{-2}	8.15×10^{-3}	6.59×10^{-3}	5.37×10^{-3}	4.41×10^{-3}	3.02×10^{-3}	1.29×10^{-3}	6.09×10^{-4}	3.11×10^{-4}	1.70×10^{-4}	9.75×10^{-5}	3.75×10^{-5}	1.84×10^{-5}
1.0	2.20×10^{-2}	6.60×10^{-3}	5.34×10^{-3}	4.35×10^{-3}	3.57×10^{-3}	2.45×10^{-3}	1.04×10^{-3}	4.94×10^{-4}	2.52×10^{-4}	1.37×10^{-4}	7.90×10^{-5}	3.04×10^{-5}	1.49×10^{-5}
1.2	1.53×10^{-2}	4.58×10^{-3}	3.71×10^{-3}	3.02×10^{-3}	2.48×10^{-3}	1.70×10^{-3}	7.26×10^{-4}	3.43×10^{-4}	1.75×10^{-4}	9.54×10^{-5}	5.49×10^{-5}	2.11×10^{-5}	1.03×10^{-5}
1.4	1.12×10^{-2}	3.37×10^{-3}	2.72×10^{-3}	2.22×10^{-3}	1.82×10^{-3}	1.25×10^{-3}	5.33×10^{-4}	2.52×10^{-4}	1.29×10^{-4}	7.01×10^{-5}	4.03×10^{-5}	1.55×10^{-5}	7.60×10^{-6}
1.6	8.59×10^{-3}	2.58×10^{-3}	2.08×10^{-3}	1.70×10^{-3}	1.39×10^{-3}	9.56×10^{-4}	4.08×10^{-4}	1.93×10^{-4}	9.85×10^{-5}	5.37×10^{-5}	3.09×10^{-5}	1.19×10^{-5}	5.80×10^{-6}
1.8	6.79×10^{-3}	2.04×10^{-3}	1.65×10^{-3}	1.34×10^{-3}	1.10×10^{-3}	7.56×10^{-4}	3.22×10^{-4}	1.52×10^{-4}	7.78×10^{-5}	4.24×10^{-5}	2.44×10^{-5}	9.40×10^{-6}	4.60×10^{-6}
2.0	5.50×10^{-3}	1.65×10^{-3}	1.33×10^{-3}	1.09×10^{-3}	8.92×10^{-4}	6.12×10^{-4}	2.61×10^{-4}	1.23×10^{-4}	6.31×10^{-5}	3.43×10^{-5}	1.98×10^{-5}	7.60×10^{-6}	3.70×10^{-6}
2.2	4.55×10^{-3}	1.36×10^{-3}	1.10×10^{-3}	8.99×10^{-4}	7.37×10^{-4}	5.06×10^{-4}	2.16×10^{-4}	1.02×10^{-4}	5.21×10^{-5}	2.84×10^{-5}	1.63×10^{-5}	6.30×10^{-6}	3.10×10^{-6}
2.4	3.82×10^{-3}	1.15×10^{-3}	9.27×10^{-4}	7.55×10^{-4}	6.20×10^{-4}	4.25×10^{-4}	1.81×10^{-4}	8.57×10^{-5}	4.38×10^{-5}	2.38×10^{-5}	1.37×10^{-5}	5.30×10^{-6}	2.60×10^{-6}
2.6	3.25×10^{-3}	9.76×10^{-4}	7.90×10^{-4}	6.43×10^{-4}	5.28×10^{-4}	3.62×10^{-4}	1.55×10^{-4}	7.30×10^{-5}	3.73×10^{-5}	2.03×10^{-5}	1.17×10^{-5}	4.50×10^{-6}	2.20×10^{-6}
2.8	2.81×10^{-3}	8.42×10^{-4}	6.81×10^{-4}	5.55×10^{-4}	4.55×10^{-4}	3.12×10^{-4}	1.33×10^{-4}	6.30×10^{-5}	3.22×10^{-5}	1.75×10^{-5}	1.01×10^{-5}	3.90×10^{-6}	1.90×10^{-6}
3.0	2.44×10^{-3}	7.33×10^{-4}	5.93×10^{-4}	4.83×10^{-4}	3.97×10^{-4}	2.72×10^{-4}	1.16×10^{-4}	5.48×10^{-5}	2.80×10^{-5}	1.53×10^{-5}	8.80×10^{-6}	3.40×10^{-6}	1.70×10^{-6}
3.4	1.90×10^{-3}	5.71×10^{-4}	4.62×10^{-4}	3.76×10^{-4}	3.09×10^{-4}	2.12×10^{-4}	9.04×10^{-5}	4.27×10^{-5}	2.18×10^{-5}	1.19×10^{-5}	6.80×10^{-6}	2.60×10^{-6}	1.30×10^{-6}
3.8	1.52×10^{-3}	4.57×10^{-4}	3.70×10^{-4}	3.01×10^{-4}	2.47×10^{-4}	1.70×10^{-4}	7.24×10^{-5}	3.42×10^{-5}	1.75×10^{-5}	9.50×10^{-6}	5.50×10^{-6}	2.10×10^{-6}	1×10^{-6}
4.2	1.25×10^{-3}	3.74×10^{-4}	3.03×10^{-4}	2.47×10^{-4}	2.02×10^{-4}	1.39×10^{-4}	5.92×10^{-5}	2.80×10^{-5}	1.43×10^{-5}	7.80×10^{-6}	4.50×10^{-6}	1.70×10^{-6}	8×10^{-7}
4.6	1.04×10^{-3}	3.12×10^{-4}	2.52×10^{-4}	2.06×10^{-4}	1.69×10^{-4}	1.16×10^{-4}	4.94×10^{-5}	2.33×10^{-5}	1.19×10^{-5}	6.50×10^{-6}	3.70×10^{-6}	1.40×10^{-6}	7×10^{-7}
5.0	8.80×10^{-4}	2.64×10^{-4}	2.13×10^{-4}	1.74×10^{-4}	1.43×10^{-4}	9.79×10^{-5}	4.18×10^{-5}	1.97×10^{-5}	1.01×10^{-5}	5.50×10^{-6}	3.20×10^{-6}	1.20×10^{-6}	6×10^{-7}
6.0	6.11×10^{-4}	1.83×10^{-4}	1.48×10^{-4}	1.21×10^{-4}	9.91×10^{-5}	6.80×10^{-5}	2.90×10^{-5}	1.37×10^{-5}	7×10^{-6}	3.80×10^{-6}	2.20×10^{-6}	8×10^{-7}	4×10^{-7}
7.0	4.49×10^{-4}	1.35×10^{-4}	1.09×10^{-4}	8.88×10^{-5}	7.28×10^{-5}	5×10^{-5}	2.13×10^{-5}	1.01×10^{-5}	5.10×10^{-6}	2.80×10^{-6}	1.60×10^{-6}	6×10^{-7}	3×10^{-7}
8.0	3.44×10^{-4}	1.03×10^{-4}	8.34×10^{-5}	6.80×10^{-5}	5.58×10^{-5}	3.83×10^{-5}	1.63×10^{-5}	7.70×10^{-6}	3.90×10^{-6}	2.10×10^{-6}	1.20×10^{-6}	5×10^{-7}	2×10^{-7}
9.0	2.72×10^{-4}	8.15×10^{-5}	6.59×10^{-5}	5.37×10^{-5}	4.41×10^{-5}	3.02×10^{-5}	1.29×10^{-5}	6.10×10^{-6}	3.10×10^{-6}	1.70×10^{-6}	1×10^{-6}	4×10^{-7}	2×10^{-7}
10	2.20×10^{-4}	6.60×10^{-5}	5.34×10^{-5}	4.35×10^{-5}	3.57×10^{-5}	2.45×10^{-5}	1.04×10^{-5}	4.90×10^{-6}	2.50×10^{-6}	1.40×10^{-6}	8×10^{-7}	3×10^{-7}	1×10^{-7}
15	9.78×10^{-5}	2.93×10^{-5}	2.37×10^{-5}	1.93×10^{-5}	1.59×10^{-5}	1.09×10^{-5}	4.60×10^{-6}	2.20×10^{-6}	1.10×10^{-6}	6×10^{-7}	4×10^{-7}	1×10^{-7}	1×10^{-7}
20	5.50×10^{-5}	1.65×10^{-5}	1.33×10^{-5}	1.09×10^{-5}	8.90×10^{-6}	6.10×10^{-6}	2.60×10^{-6}	1.20×10^{-6}	6×10^{-7}	3×10^{-7}	2×10^{-7}	1×10^{-7}	0.00
25	3.52×10^{-5}	1.06×10^{-5}	8.50×10^{-6}	7×10^{-6}	5.70×10^{-6}	3.90×10^{-6}	1.70×10^{-6}	8×10^{-7}	4×10^{-7}	2×10^{-7}	1×10^{-7}	0.00	0.00
30	2.44×10^{-5}	7.30×10^{-6}	5.90×10^{-6}	4.80×10^{-6}	4×10^{-6}	2.70×10^{-6}	1.20×10^{-6}	5×10^{-7}	3×10^{-7}	2×10^{-7}	1×10^{-7}	0.00	0.00
35	1.80×10^{-5}	5.40×10^{-6}	4.40×10^{-6}	3.60×10^{-6}	2.90×10^{-6}	2×10^{-6}	9×10^{-7}	4×10^{-7}	2×10^{-7}	1×10^{-7}	1×10^{-7}	0.00	0.00
40	1.37×10^{-5}	4.10×10^{-6}	3.30×10^{-6}	2.70×10^{-6}	2.20×10^{-6}	1.50×10^{-6}	7×10^{-7}	3×10^{-7}	2×10^{-7}	1×10^{-7}	0.00	0.00	0.00
45	1.09×10^{-5}	3.30×10^{-6}	2.60×10^{-6}	2.10×10^{-6}	1.80×10^{-6}	1.20×10^{-6}	5×10^{-7}	2×10^{-7}	1×10^{-7}	1×10^{-7}	0.00	0.00	0.00
50	8.80×10^{-6}	2.60×10^{-6}	2.10×10^{-6}	1.70×10^{-6}	1.40×10^{-6}	1×10^{-6}	4×10^{-7}	2×10^{-7}	1×10^{-7}	1×10^{-7}	0.00	0.00	0.00

Table A.9: Production cross section in pb of a pseudoscalar A produced via the b-associated production mode for several mass points in a type II 2HDM [241–245].

	production cross section in pb												
$\tan\beta$	300 GeV	400 GeV	420 GeV	440 GeV	460 GeV	500 GeV	600 GeV	700 GeV	800 GeV	900 GeV	1000 GeV	1200 GeV	1400 GeV
0.1	5.75×10^{-5}	6.09×10^{-5}	5.09×10^{-5}	4.23×10^{-5}	3.51×10^{-5}	2.44×10^{-5}	1.04×10^{-5}	4.90×10^{-6}	2.50×10^{-6}	1.40×10^{-6}	8×10^{-7}	3×10^{-7}	1×10^{-7}
0.12	1.54×10^{-4}	8.99×10^{-5}	7.44×10^{-5}	6.15×10^{-5}	5.08×10^{-5}	3.51×10^{-5}	1.50×10^{-5}	7.10×10^{-6}	3.60×10^{-6}	2×10^{-6}	1.10×10^{-6}	4×10^{-7}	2×10^{-7}
0.14	2.67×10^{-4}	1.24×10^{-4}	1.02×10^{-4}	8.41×10^{-5}	6.94×10^{-5}	4.79×10^{-5}	2.05×10^{-5}	9.70×10^{-6}	4.90×10^{-6}	2.70×10^{-6}	1.50×10^{-6}	6×10^{-7}	3×10^{-7}
0.16	3.98×10^{-4}	1.64×10^{-4}	1.34×10^{-4}	1.10×10^{-4}	9.08×10^{-5}	6.26×10^{-5}	2.67×10^{-5}	1.26×10^{-5}	6.50×10^{-6}	3.50×10^{-6}	2×10^{-6}	8×10^{-7}	4×10^{-7}
0.18	5.47×10^{-4}	2.09×10^{-4}	1.70×10^{-4}	1.40×10^{-4}	1.15×10^{-4}	7.92×10^{-5}	3.38×10^{-5}	1.60×10^{-5}	8.20×10^{-6}	4.50×10^{-6}	2.60×10^{-6}	1×10^{-6}	5×10^{-7}
0.2	7.13×10^{-4}	2.59×10^{-4}	2.11×10^{-4}	1.73×10^{-4}	1.42×10^{-4}	9.78×10^{-5}	4.18×10^{-5}	1.97×10^{-5}	1.01×10^{-5}	5.50×10^{-6}	3.20×10^{-6}	1.20×10^{-6}	6×10^{-7}
0.24	1.10×10^{-3}	3.75×10^{-4}	3.05×10^{-4}	2.49×10^{-4}	2.05×10^{-4}	1.41×10^{-4}	6.02×10^{-5}	2.84×10^{-5}	1.45×10^{-5}	7.90×10^{-6}	4.60×10^{-6}	1.70×10^{-6}	9×10^{-7}
0.28	1.55×10^{-3}	5.12×10^{-4}	4.16×10^{-4}	3.40×10^{-4}	2.79×10^{-4}	1.92×10^{-4}	8.19×10^{-5}	3.87×10^{-5}	1.98×10^{-5}	1.08×10^{-5}	6.20×10^{-6}	2.40×10^{-6}	1.20×10^{-6}
0.32	2.08×10^{-3}	6.70×10^{-4}	5.44×10^{-4}	4.44×10^{-4}	3.65×10^{-4}	2.51×10^{-4}	1.07×10^{-4}	5.05×10^{-5}	2.58×10^{-5}	1.41×10^{-5}	8.10×10^{-6}	3.10×10^{-6}	1.50×10^{-6}
0.36	2.67×10^{-3}	8.50×10^{-4}	6.89×10^{-4}	5.62×10^{-4}	4.62×10^{-4}	3.17×10^{-4}	1.35×10^{-4}	6.40×10^{-5}	3.27×10^{-5}	1.78×10^{-5}	1.02×10^{-5}	3.90×10^{-6}	1.90×10^{-6}
0.4	3.33×10^{-3}	1.05×10^{-3}	8.51×10^{-4}	6.95×10^{-4}	5.70×10^{-4}	3.92×10^{-4}	1.67×10^{-4}	7.90×10^{-5}	4.04×10^{-5}	2.20×10^{-5}	1.26×10^{-5}	4.90×10^{-6}	2.40×10^{-6}
0.46	4.46×10^{-3}	1.39×10^{-3}	1.13×10^{-3}	9.19×10^{-4}	7.55×10^{-4}	5.18×10^{-4}	2.21×10^{-4}	1.04×10^{-4}	5.34×10^{-5}	2.91×10^{-5}	1.67×10^{-5}	6.40×10^{-6}	3.10×10^{-6}
0.52	5.74×10^{-3}	1.78×10^{-3}	1.44×10^{-3}	1.17×10^{-3}	9.64×10^{-4}	6.62×10^{-4}	2.83×10^{-4}	1.33×10^{-4}	6.82×10^{-5}	3.71×10^{-5}	2.14×10^{-5}	8.20×10^{-6}	4×10^{-6}
0.58	7.19×10^{-3}	2.21×10^{-3}	1.79×10^{-3}	1.46×10^{-3}	1.20×10^{-3}	8.24×10^{-4}	3.51×10^{-4}	1.66×10^{-4}	8.48×10^{-5}	4.62×10^{-5}	2.66×10^{-5}	1.02×10^{-5}	5×10^{-6}
0.64	8.78×10^{-3}	2.70×10^{-3}	2.18×10^{-3}	1.78×10^{-3}	1.46×10^{-3}	1×10^{-3}	4.28×10^{-4}	2.02×10^{-4}	1.03×10^{-4}	5.63×10^{-5}	3.24×10^{-5}	1.24×10^{-5}	6.10×10^{-6}
0.7	1.05×10^{-2}	3.23×10^{-3}	2.61×10^{-3}	2.13×10^{-3}	1.75×10^{-3}	1.20×10^{-3}	5.12×10^{-4}	2.42×10^{-4}	1.24×10^{-4}	6.73×10^{-5}	3.87×10^{-5}	1.49×10^{-5}	7.30×10^{-6}
0.8	1.38×10^{-2}	4.21×10^{-3}	3.41×10^{-3}	2.78×10^{-3}	2.28×10^{-3}	1.57×10^{-3}	6.69×10^{-4}	3.16×10^{-4}	1.61×10^{-4}	8.79×10^{-5}	5.06×10^{-5}	1.94×10^{-5}	9.50×10^{-6}
0.9	1.75×10^{-2}	5.34×10^{-3}	4.32×10^{-3}	3.52×10^{-3}	2.89×10^{-3}	1.98×10^{-3}	8.46×10^{-4}	4×10^{-4}	2.04×10^{-4}	1.11×10^{-4}	6.40×10^{-5}	2.46×10^{-5}	1.21×10^{-5}
1.0	2.17×10^{-2}	6.59×10^{-3}	5.33×10^{-3}	4.35×10^{-3}	3.57×10^{-3}	2.45×10^{-3}	1.04×10^{-3}	4.94×10^{-4}	2.52×10^{-4}	1.37×10^{-4}	7.90×10^{-5}	3.04×10^{-5}	1.49×10^{-5}
1.2	3.13×10^{-2}	9.49×10^{-3}	7.68×10^{-3}	6.26×10^{-3}	5.14×10^{-3}	3.53×10^{-3}	1.50×10^{-3}	7.11×10^{-4}	3.63×10^{-4}	1.98×10^{-4}	1.14×10^{-4}	4.37×10^{-5}	2.14×10^{-5}
1.4	4.26×10^{-2}	1.29×10^{-2}	1.05×10^{-2}	8.52×10^{-3}	6.99×10^{-3}	4.80×10^{-3}	2.05×10^{-3}	9.67×10^{-4}	4.94×10^{-4}	2.69×10^{-4}	1.55×10^{-4}	5.95×10^{-5}	2.92×10^{-5}
1.6	5.57×10^{-2}	1.69×10^{-2}	1.37×10^{-2}	1.11×10^{-2}	9.13×10^{-3}	6.27×10^{-3}	2.67×10^{-3}	1.26×10^{-3}	6.46×10^{-4}	3.52×10^{-4}	2.02×10^{-4}	7.78×10^{-5}	3.81×10^{-5}
1.8	7.06×10^{-2}	2.14×10^{-2}	1.73×10^{-2}	1.41×10^{-2}	1.16×10^{-2}	7.93×10^{-3}	3.39×10^{-3}	1.60×10^{-3}	8.17×10^{-4}	4.45×10^{-4}	2.56×10^{-4}	9.84×10^{-5}	4.82×10^{-5}
2.0	8.72×10^{-2}	2.64×10^{-2}	2.13×10^{-2}	1.74×10^{-2}	1.43×10^{-2}	9.79×10^{-3}	4.18×10^{-3}	1.97×10^{-3}	1.01×10^{-3}	5.49×10^{-4}	3.16×10^{-4}	1.22×10^{-4}	5.95×10^{-5}
2.2	1.06×10^{-1}	3.19×10^{-2}	2.58×10^{-2}	2.10×10^{-2}	1.73×10^{-2}	1.19×10^{-2}	5.06×10^{-3}	2.39×10^{-3}	1.22×10^{-3}	6.65×10^{-4}	3.82×10^{-4}	1.47×10^{-4}	7.20×10^{-5}
2.4	1.26×10^{-1}	3.80×10^{-2}	3.07×10^{-2}	2.50×10^{-2}	2.06×10^{-2}	1.41×10^{-2}	6.02×10^{-3}	2.84×10^{-3}	1.45×10^{-3}	7.91×10^{-4}	4.55×10^{-4}	1.75×10^{-4}	8.57×10^{-5}
2.6	1.47×10^{-1}	4.46×10^{-2}	3.61×10^{-2}	2.94×10^{-2}	2.41×10^{-2}	1.66×10^{-2}	7.06×10^{-3}	3.34×10^{-3}	1.70×10^{-3}	9.29×10^{-4}	5.34×10^{-4}	2.05×10^{-4}	1.01×10^{-4}
2.8	1.71×10^{-1}	5.17×10^{-2}	4.18×10^{-2}	3.41×10^{-2}	2.80×10^{-2}	1.92×10^{-2}	8.19×10^{-3}	3.87×10^{-3}	1.98×10^{-3}	1.08×10^{-3}	6.19×10^{-4}	2.38×10^{-4}	1.17×10^{-4}
3.0	1.96×10^{-1}	5.93×10^{-2}	4.80×10^{-2}	3.91×10^{-2}	3.21×10^{-2}	2.20×10^{-2}	9.40×10^{-3}	4.44×10^{-3}	2.27×10^{-3}	1.24×10^{-3}	7.11×10^{-4}	2.73×10^{-4}	1.34×10^{-4}
3.4	2.52×10^{-1}	7.62×10^{-2}	6.17×10^{-2}	5.03×10^{-2}	4.13×10^{-2}	2.83×10^{-2}	1.21×10^{-2}	5.71×10^{-3}	2.92×10^{-3}	1.59×10^{-3}	9.13×10^{-4}	3.51×10^{-4}	1.72×10^{-4}
3.8	3.15×10^{-1}	9.52×10^{-2}	7.70×10^{-2}	6.28×10^{-2}	5.15×10^{-2}	3.54×10^{-2}	1.51×10^{-2}	7.13×10^{-3}	3.64×10^{-3}	1.98×10^{-3}	1.14×10^{-3}	4.39×10^{-4}	2.15×10^{-4}
4.2	3.85×10^{-1}	1.16×10^{-1}	9.41×10^{-2}	7.67×10^{-2}	6.29×10^{-2}	4.32×10^{-2}	1.84×10^{-2}	8.71×10^{-3}	4.45×10^{-3}	2.42×10^{-3}	1.39×10^{-3}	5.36×10^{-4}	2.62×10^{-4}
4.6	4.62×10^{-1}	1.40×10^{-1}	1.13×10^{-1}	9.20×10^{-2}	7.55×10^{-2}	5.18×10^{-2}	2.21×10^{-2}	1.04×10^{-2}	5.34×10^{-3}	2.91×10^{-3}	1.67×10^{-3}	6.43×10^{-4}	3.15×10^{-4}
5.0	5.46×10^{-1}	1.65×10^{-1}	1.33×10^{-1}	1.09×10^{-1}	8.92×10^{-2}	6.12×10^{-2}	2.61×10^{-2}	1.23×10^{-2}	6.31×10^{-3}	3.43×10^{-3}	1.98×10^{-3}	7.59×10^{-4}	3.72×10^{-4}
6.0	7.86×10^{-1}	2.37×10^{-1}	1.92×10^{-1}	1.57×10^{-1}	1.28×10^{-1}	8.81×10^{-2}	3.76×10^{-2}	1.78×10^{-2}	9.08×10^{-3}	4.95×10^{-3}	2.84×10^{-3}	1.09×10^{-3}	5.36×10^{-4}
7.0	1.07	3.23×10^{-1}	2.61×10^{-1}	2.13×10^{-1}	1.75×10^{-1}	1.20×10^{-1}	5.12×10^{-2}	2.42×10^{-2}	1.24×10^{-2}	6.73×10^{-3}	3.87×10^{-3}	1.49×10^{-3}	7.29×10^{-4}
8.0	1.40	4.22×10^{-1}	3.41×10^{-1}	2.78×10^{-1}	2.28×10^{-1}	1.57×10^{-1}	6.69×10^{-2}	3.16×10^{-2}	1.61×10^{-2}	8.79×10^{-3}	5.06×10^{-3}	1.94×10^{-3}	9.52×10^{-4}
9.0	1.77	5.34×10^{-1}	4.32×10^{-1}	3.52×10^{-1}	2.89×10^{-1}	1.98×10^{-1}	8.46×10^{-2}	4×10^{-2}	2.04×10^{-2}	1.11×10^{-2}	6.40×10^{-3}	2.46×10^{-3}	1.21×10^{-3}
10	2.18	6.59×10^{-1}	5.33×10^{-1}	4.35×10^{-1}	3.57×10^{-1}	2.45×10^{-1}	1.04×10^{-1}	4.94×10^{-2}	2.52×10^{-2}	1.37×10^{-2}	7.90×10^{-3}	3.04×10^{-3}	1.49×10^{-3}
15	4.91	1.48	1.20	9.78×10^{-1}	8.03×10^{-1}	5.51×10^{-1}	2.35×10^{-1}	1.11×10^{-1}	5.67×10^{-2}	3.09×10^{-2}	1.78×10^{-2}	6.83×10^{-3}	3.35×10^{-3}
20	8.74	2.64	2.13	1.74	1.43	9.79×10^{-1}	4.18×10^{-1}	1.97×10^{-1}	1.01×10^{-1}	5.49×10^{-2}	3.16×10^{-2}	1.22×10^{-2}	5.95×10^{-3}
25	1.36×10^{1}	4.12	3.33	2.72	2.23	1.53	6.53×10^{-1}	3.08×10^{-1}	1.58×10^{-1}	8.59×10^{-2}	4.94×10^{-2}	1.90×10^{-2}	9.30×10^{-3}
30	1.97×10^{1}	5.93	4.80	3.91	3.21	2.20	9.40×10^{-1}	4.44×10^{-1}	2.27×10^{-1}	1.24×10^{-1}	7.11×10^{-2}	2.73×10^{-2}	1.34×10^{-2}
35	2.68×10^{1}	8.08	6.54	5.33	4.37	3.00	1.28	6.05×10^{-1}	3.09×10^{-1}	1.68×10^{-1}	9.68×10^{-2}	3.72×10^{-2}	1.82×10^{-2}
40	3.49×10^{1}	1.05×10^{1}	8.54	6.96	5.71	3.92	1.67	7.90×10^{-1}	4.04×10^{-1}	2.20×10^{-1}	1.26×10^{-1}	4.86×10^{-2}	2.38×10^{-2}
45	4.42×10^{1}	1.34×10^{1}	1.08×10^{1}	8.81	7.23	4.96	2.12	1.00	5.11×10^{-1}	2.78×10^{-1}	1.60×10^{-1}	6.15×10^{-2}	3.01×10^{-2}
50	5.46×10^{1}	1.65×10^{1}	1.33×10^{1}	1.09×10^{1}	8.92	6.12	2.61	1.23	6.31×10^{-1}	3.43×10^{-1}	1.98×10^{-1}	7.59×10^{-2}	3.72×10^{-2}

Table A.10: Production cross section in pb of a pseudoscalar A produced via the b-associated production mode for several mass points in a type IV 2HDM [241–245].

CHAPTER B

ADDITIONAL CONTENT FROM THE W' ANALYSIS

B.1 Trigger isolation

The isolation requirements of the various triggers used for the 2016 data taking period are summarised in Table B.1.

B.2 Additional plots from the multijet study in the $W' \to Wh$ analysis

The multijet control plots from events with merged topology and one and two b-tagged jets are shown in Figures B.1 and B.2, respectively.

B.3 Additional information about the uncertainties in the W' analysis

The methods of determining the experimental uncertainties are described in additional literature and Table B.2 summarises the various sources considered in this analysis together with the appropriate references. The uncertainties with the largest impact on the parameter of interest, μ, were found to be the ones related to the small- and large-R jet energy scale and resolution, its mass, and flavour tagging.

Trigger name	HLT E_{T} [GeV]	Electron LH	Impact parameter cut	Electron isolation
`e26_lhtight_nod0_ivarloose`	26	Tight	no	$p_{\mathrm{T}}^{\mathrm{varcone20}}/p_{\mathrm{T}} < 0.1$
`e60_lhmedium_nod0`	60	Medium	no	—
`e140_lhloose_nod0`	140	Loose	no	—
`e300_etcut`	300	—	yes	—

Table B.1: Summary of single electron triggers used for the 2016 data taking period. The impact parameter cut (if applied) consists of a cut on $d_0/\sigma_{d_0} < 5$ and $\Delta z_0 \sin\theta < 0.5\,\mathrm{mm}$.

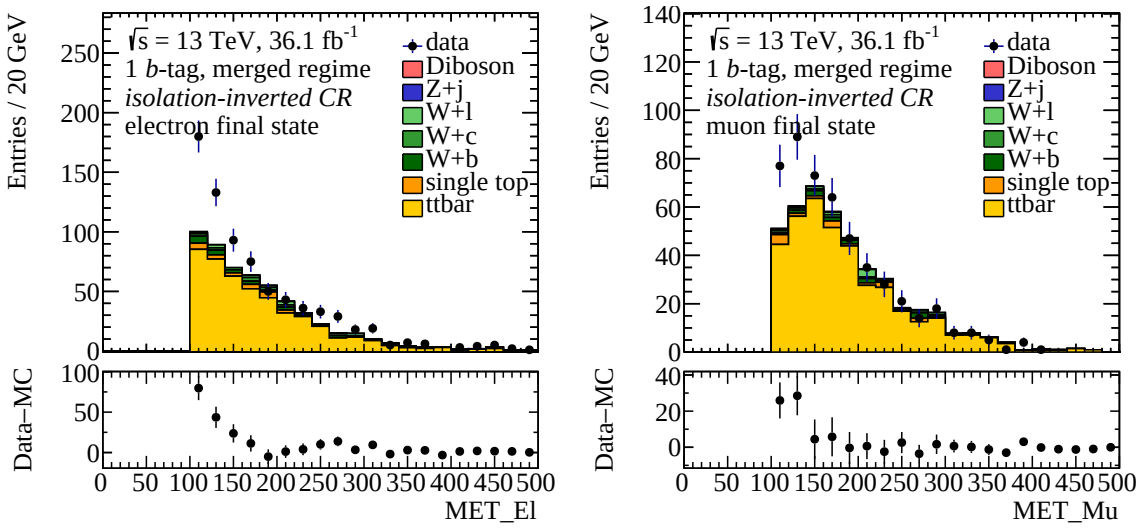

Figure B.1: Observed distributions of the missing transverse energy in the isolation-inverted regions with 1 b-tag events in the merged regime for the electron (left) and the muon (right) final states. The expected simulated non-multijet background contributions are shown as filled histograms. The difference between data and the MC prediction, defining the QCD shape template, is shown in the lower panel. The total MC prediction is normalised by scaling it such that it fits the data in the tail region with $E_{\mathrm{T}}^{\mathrm{miss}} > 200\,\mathrm{GeV}$, where the QCD contribution is expected to be negligible.

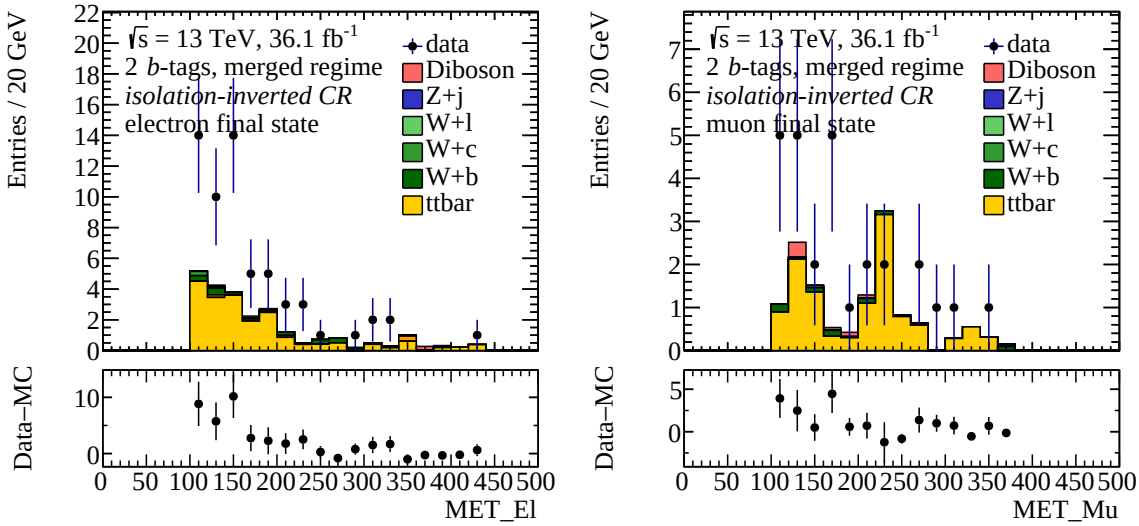

Figure B.2: Observed distributions of the missing transverse energy in the isolation-inverted regions with 2 b-tag events in the merged regime for the electron (left) and the muon (right) final states. The expected simulated non-multijet background contributions are shown as filled histograms. The difference between data and the MC prediction, defining the QCD shape template, is shown in the lower panel. The total MC prediction is normalised by scaling it such that it fits the data in the tail region with $E_{\mathrm{T}}^{\mathrm{miss}} > 200\,\mathrm{GeV}$, where the QCD contribution is expected to be negligible.

Table B.2: Summary of experimental uncertainties applied in this analysis. The table is split into blocks addressing the individual sources of uncertainties outlined in the text.

Systematic uncertainty	Description	Reference
PRW_SF	Pile-up re-weighting uncertainty	[246]
	Electrons	
EL_EFF_Trigger_TOTAL_1NPCOR_PLUS_UNCOR	Trigger efficiency uncertainty	[133]
EL_EFF_Reco_TOTAL_1NPCOR_PLUS_UNCOR	Reconstruction efficiency uncertainty	[133]
EL_EFF_ID_TOTAL_1NPCOR_PLUS_UNCOR	ID efficiency uncertainty	[133]
EL_EFF_Iso_TOTAL_1NPCOR_PLUS_UNCOR	Isolation efficiency uncertainty	[133]
EG_SCALE_ALL	Energy scale uncertainty	[133, 247, 248]
EG_RESOLUTION_ALL	Energy resolution uncertainty	[133, 247, 248]
	Muons	
MUON_EFF_STAT + _SYS	Reconstruction and ID efficiency uncertainty, $p_{\mathrm{T}}^{\mu} > 15\,\mathrm{GeV}$	[192]
MUON_EFF_STAT_LOWPT + _SYS_LOWPT	Reconstruction and ID efficiency uncertainty, $p_{\mathrm{T}}^{\mu} \leq 15\,\mathrm{GeV}$	[192]
MUON_ISO_STAT + _SYS	Isolation efficiency uncertainty	[192]
MUON_TTVA_STAT + _SYS	Track-to-vertex association efficiency uncertainty	[249]
MUONS_SCALE	Energy scale uncertainty	[192]
MUONS_ID	Energy resolution uncertainty from inner detector	[192]
MUONS_MS	Energy resolution uncertainty from muon system	[192]
	Small-R jets	
JET	Energy scale uncertainty split into 21 components	[250–252]
JET_JER_SINGLE_NP	Energy resolution uncertainty	[253]
JvtEfficiency	JVT efficiency uncertainty	—
FT_EFF_Eigen_B	b-tagging efficiency uncertainties; 3 components for b-jets	[196, 254–256]
FT_EFF_Eigen_C	b-tagging efficiency uncertainties; 4 components for c-jets	[196, 254–256]
FT_EFF_Eigen_L	b-tagging efficiency uncertainties; 5 components for light jets	[196, 254–256]
FT_EFF_Eigen_extrapolation	b-tagging efficiency uncertainty for the extrapolation to high p_{T} jets	[196, 254–256]
FT_EFF_Eigen_from_charm	b-tagging efficiency uncertainty on tau jets	[196, 254–256]
	Large-R jets	
SysJET_Comb_Baseline_Kin	Energy scale uncertainties (p_{T} and mass scales fully correlated)	[257–259]
SysJET_Comb_Modelling_Kin		[257–259]
SysJET_Comb_TotalStat_Kin		[257–259]
SysJET_Comb_Tracking_Kin		[257–259]
FATJET_JER	Energy resolution uncertainty	[257–259]
FATJET_JMR	Mass resolution uncertainty	[257–259]
	Track jets	
FT_EFF_Eigen_B	b-tagging efficiency uncertainties; 3 components for b-jets	[196, 254–256]
FT_EFF_Eigen_C	b-tagging efficiency uncertainties; 4 components for c-jets	[196, 254–256]
FT_EFF_Eigen_L	b-tagging efficiency uncertainties; 5 components for light jets	[196, 254–256]
FT_EFF_Eigen_extrapolation	b-tagging efficiency uncertainty for the extrapolation to high p_{T} jets	[196, 254–256]
FT_EFF_Eigen_from_charm	b-tagging efficiency uncertainty on tau jets	[196, 254–256]
	$E_{\mathrm{T}}^{\mathrm{miss}}$	
METTrigStat	Trigger efficiency uncertainty	—
METTrigTop/Z	Trigger efficiency uncertainty	—
MET_SoftTrk_ResoPara	Track-based soft term related longitudinal resolution uncertainty	[149]
MET_SoftTrk_ResoPara	Track-based soft term related transverse resolution uncertainty	[149]
MET_SoftTrk_ResoPara	Track-based soft term related longitudinal scale uncertainty	[149]
MET_SoftTrk_ResoPara	Track $E_{\mathrm{T}}^{\mathrm{miss}}$ scale uncertainty due to tracks in jets	[149]

CHAPTER C

ADDITIONAL CONTENT FROM THE $\nu\bar{\nu}b\bar{b}$ ANALYSIS

C.1 Trigger requirements of the Run 2 data taking period

Table C.1 shows the trigger requirements for the various data taking runs of the LHC Run 2 between 2015 and 2018. The $E_{\mathrm{T}}^{\mathrm{miss}}$ type distinguishes between the classical *mht* calculation and the novel *pufit* algorithm, explained in more detail in Section 5.3.

Table C.1: The 0 lepton $E_{\mathrm{T}}^{\mathrm{miss}}$ triggers for the different data taking periods

Data taking period	Online $E_{\mathrm{T}}^{\mathrm{miss}}$ threshold [GeV]	L1 $E_{\mathrm{T}}^{\mathrm{miss}}$ threshold [GeV]	$E_{\mathrm{T}}^{\mathrm{miss}}$ type
2015	70	50	*mht*
2016 (Jan – mid Jun)	90	50	*mht*
2016 (mid Jun – Dec)	110	50	*mht*
2017	110	50	*pufit*
2018	110	50	*pufit*

C.2 Pull distributions

The pull distributions of all nuisance parameters in the $\nu\bar{\nu}b\bar{b}$ analysis are shown in the Figures C.1 and C.2. For a better overview, the nuisance parameters are presented in groups. The first three groups are b-tagging, jet, and decorrelation nuisance parameters and are shown in Figure C.1. The final two groups are cross section and normalisation, and theory model uncertainties and are shown in Figure C.2. The pull distributions are based on a fit to the observed data with the $m_{Z'} = 700\,\mathrm{GeV}$ signal hypothesis.

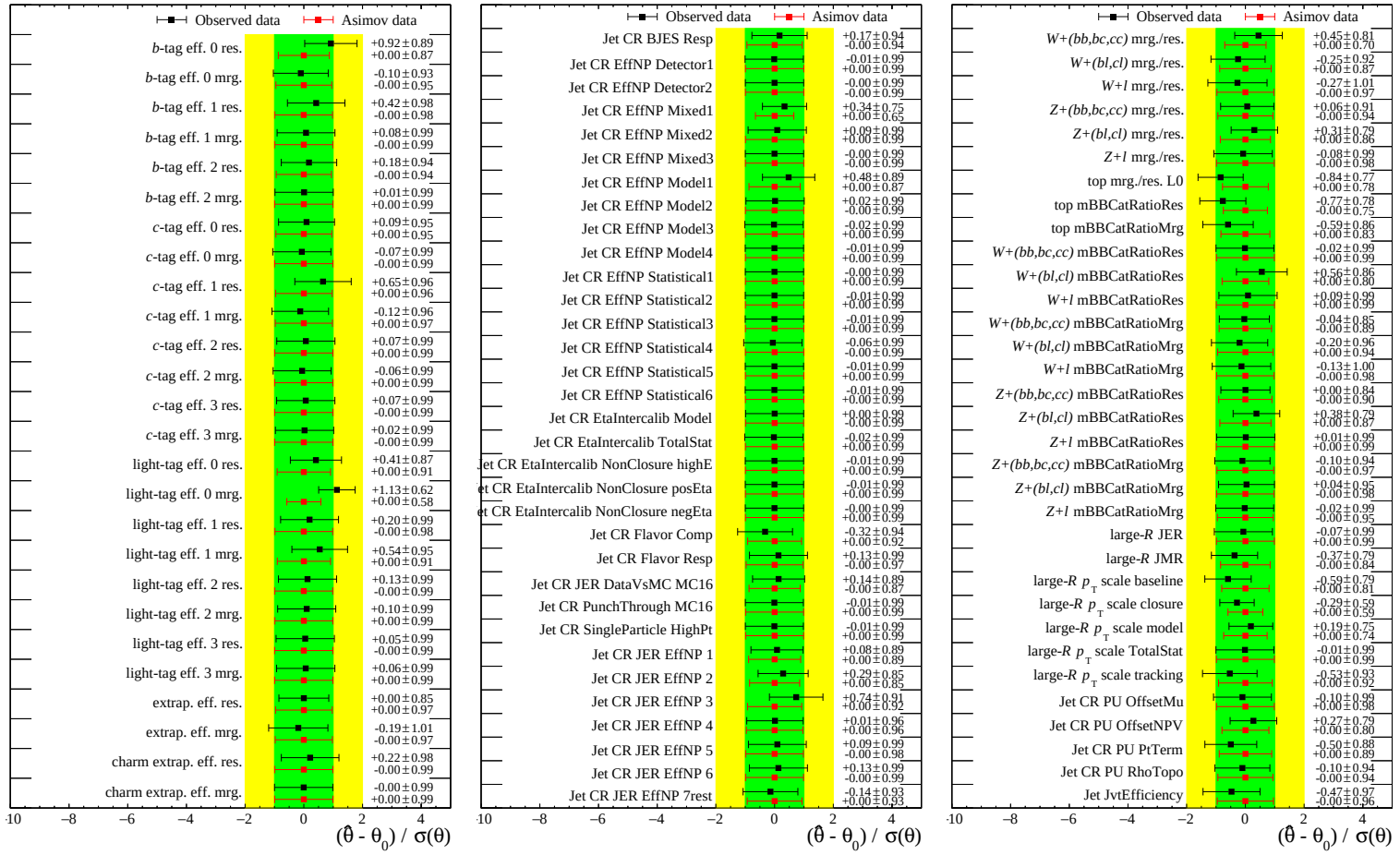

Figure C.1: Plots visualising the nuisance parameter pulls after a fit to Asimov data (red) and observed data (black). The panels show (from left to right): flavour tagging uncertainties, jet-related experimental uncertainties, and large-radius jet related and decorrelation uncertainties. The green and yellow bands correspond to the one and two sigma uncertainty intervals.

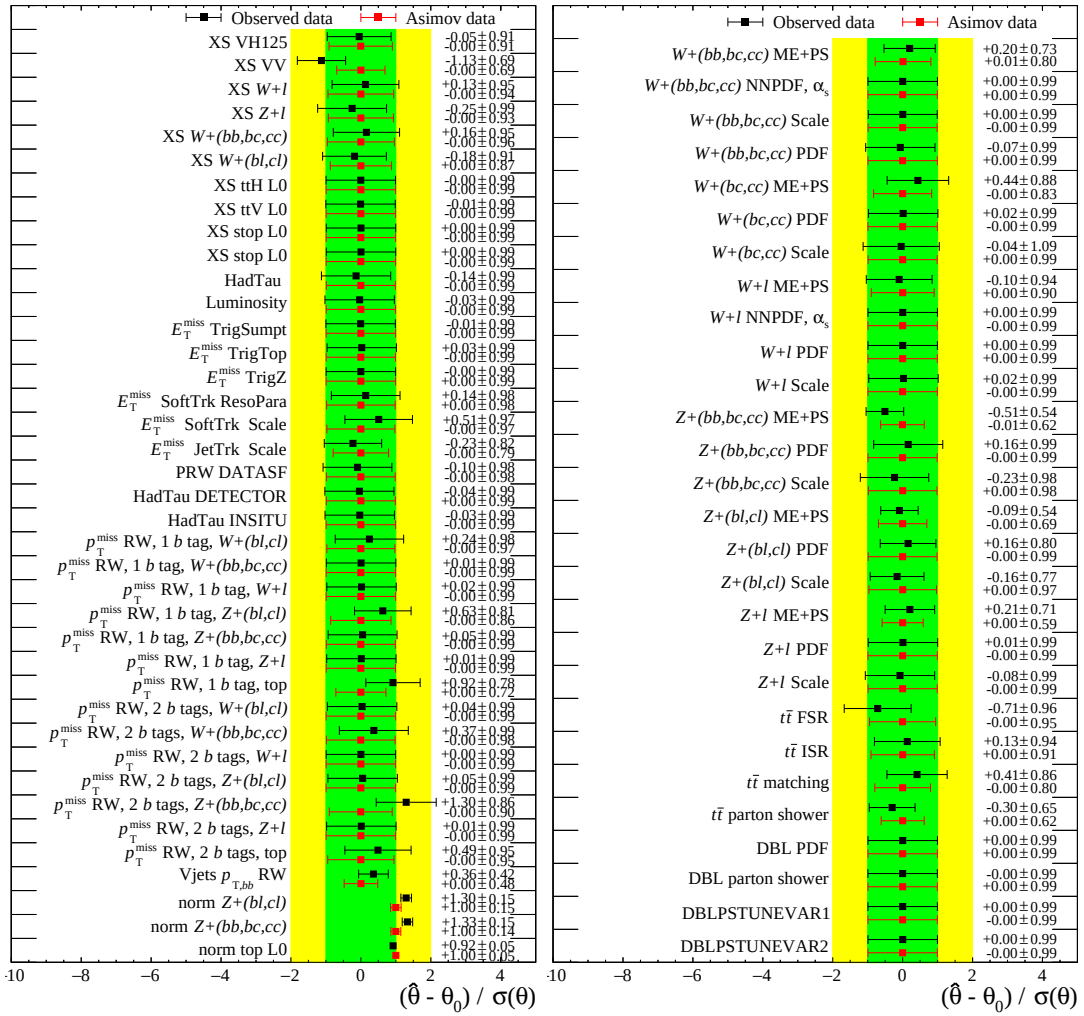

Figure C.2: Plots visualising the nuisance parameter pulls after a fit to Asimov data (red) and observed data (black) for the HVT Z' interpretation in the 0-lepton channel. The left panel shows cross section and normalisation uncertainties, as well as the $p_{\mathrm{T}}^{b\bar{b}}$ and $p_{\mathrm{T}}^{\mathrm{miss}}$ modelling uncertainties, decorrelated for different background components and tag multiplicities. The right panel shows the theory modelling uncertainties. The green and yellow bands correspond to the one and two sigma uncertainty intervals.

CHAPTER D

ADDITIONAL CONTENT FROM THE COMBINATION OF THE $\nu\bar{\nu}b\bar{b}$ AND $\ell^{\pm}\ell^{\mp}b\bar{b}$ ANALYSES

D.1 Comparison to the published results

All results contained in this thesis were reproduced from the published data [15] after adding the morphed signal samples (*cf.* Section 6.5) and re-evaluation of the theoretical signal uncertainties based on additional simulated samples. Small changes ($\sim 1\,\%$) are observed in the observed and predicted event yields due to these changes and after a switch to a newer ATLAS software release [260]. The published expected and observed yields are presented in Figure D.1. The results in the bbA fit setup are also based on the published data, with the addition of the signal regions with high b-tag multiplicity (three or more b-tags).

The distributions of the discriminating variable after a fit to the observed data in the publication correspond to an unconditional signal-plus-background fit for a HVT Z' $m_{Z'} = 2\,\text{TeV}$ mass hypothesis, while the corresponding distributions presented in this thesis are obtained from a conditional background-only fit. Additionally, the bins are optimised to avoid bins with large statistical fluctuations. The resulting differences are small. For completeness, the published figures are attached in Figures D.2, D.3 and D.4.

The results of the signal acceptance times reconstruction efficiency study presented in Section 5.4 are identical for the HVT Z' and 2HDM ggA signal processes (*cf.* Figure D.5), but new signal masses were added. The study of the 2HDM bbA signal was newly added.

The exclusion limits presented in Sections 6.6.1 and 6.6.2 correspond to those from Ref. [15] (*cf.* Figure D.6) for overlapping mass points.

	Resolved		Merged	
0-lepton	1 b-tag	2 b-tag	1 b-tag	2 b-tag
Top	38000 ± 500	9700 ± 110	1440 ± 80	55.9 ± 2.8
Diboson	420 ± 40	62 ± 5	252 ± 30	69 ± 8
Zl	1950 ± 130	7.6 ± 1.6	453 ± 40	0.9 ± 0.2
Z+hl	23100 ± 900	149 ± 14	3210 ± 150	18.4 ± 1.7
Z+hf	4730 ± 160	3860 ± 110	810 ± 60	365 ± 18
Wl	2170 ± 160	19.2 ± 2.6	223 ± 33	0.2 ± 0.1
W+hl	9300 ± 1000	76 ± 7	760 ± 120	5.7 ± 1.1
W+hf	970 ± 50	720 ± 40	175 ± 26	68 ± 13
SM Vh	190 ± 20	252 ± 26	20.7 ± 2.8	12.7 ± 1.6
Total	80730 ± 180	14850 ± 70	7340 ± 60	596 ± 13
Data	80798	14839	7351	590
2-lepton	1 b-tag	2 b-tag	1 b-tag	2 b-tag
Top	7800 ± 40	5740 ± 60	34.3 ± 2.6	2.5 ± 0.3
Diboson	1820 ± 100	459 ± 29	115 ± 7	25.3 ± 1.7
Zl	9000 ± 700	17 ± 8	208 ± 15	0.5 ± 0.2
Z+hl	100700 ± 800	490 ± 28	724 ± 21	4.9 ± 0.3
Z+hf	23030 ± 300	17300 ± 110	225 ± 8	106 ± 4
Wl	0.8 ± 0.1	–	0.3 ± 0.0	–
W+hl	13 ± 1.8	0.2 ± 0.1	1.2 ± 0.2	–
W+hf	1.6 ± 0.5	1.0 ± 0.1	0.2 ± 0.0	0.1 ± 0.0
SM Vh	308 ± 14	367 ± 16	5.3 ± 0.3	2.7 ± 0.2
Total	142710 ± 260	24400 ± 100	1313 ± 16	142 ± 5
Data	142713	24379	1307	142

Figure D.1: The predicted and observed event yields in the signal regions defined in the text. The yields in the 1 and 2 b-tag regions correspond to the HVT fit for a signal of mass 700 GeV. The term Top summarizes events from $t\bar{t}$, single-top, $t\bar{t}H$and $t\bar{t}V$. The quoted uncertainties are the statistical and systematic uncertainties combined in quadrature after the fit. The uncertainties in the individual background predictions are larger than the total background uncertainty due to correlations in the normalisation parameters in the fit. Reproduced from Ref. [15].

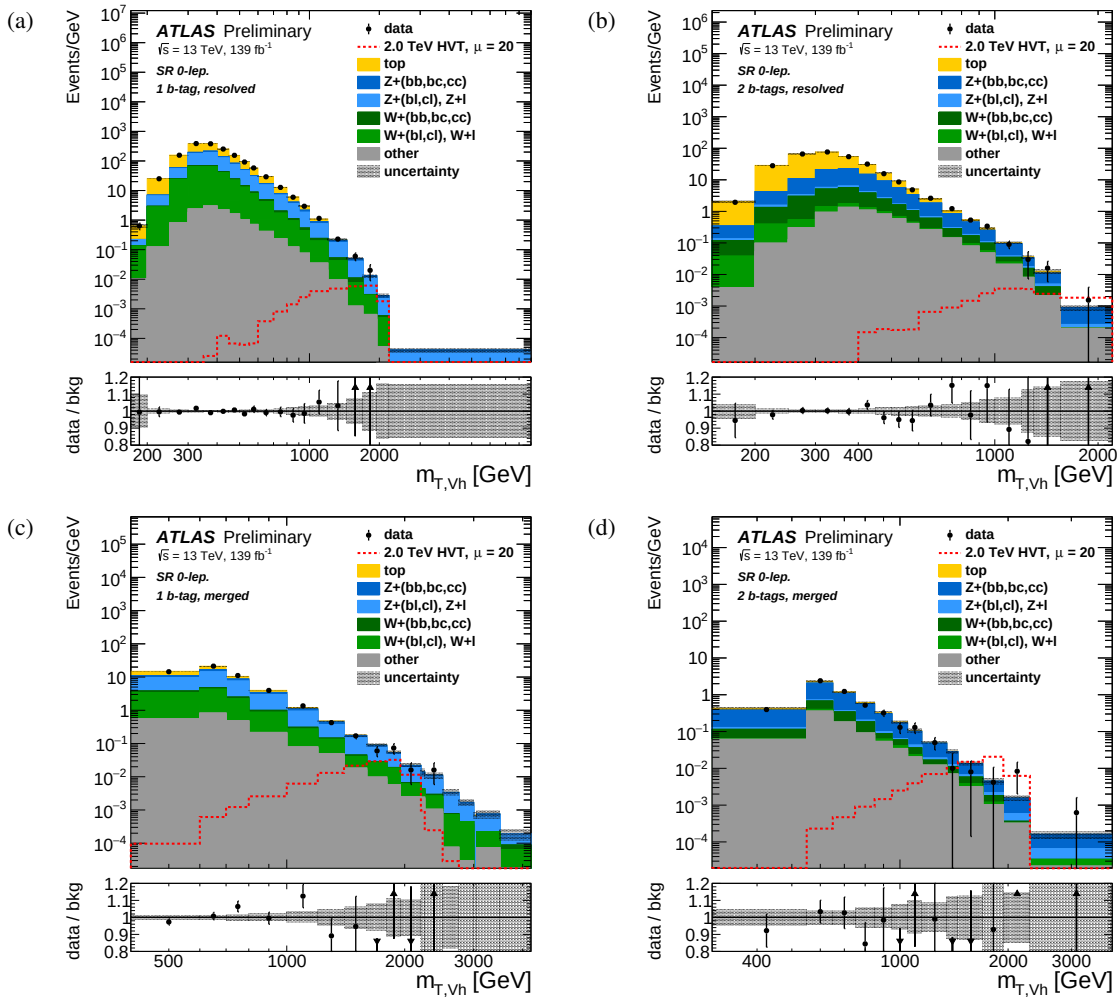

Figure D.2: Observed and expected post-fit $m_{\mathrm{T,}\,Vh}$ distributions in the $\nu\bar{\nu}b\bar{b}$ signal regions, with *(a)* 1 b-tag and *(b)* 2 b-tag events with the resolved topology and *(c)* 1 b-tag and *(d)* 2 b-tag events with the merged topology. The expected signal distribution from a HVT Z' boson with signal strength $\mu = 20$ and a mass of 2 TeV is shown as the dotted red line. The data-to-background ratio where the hatched area indicates the post-fit background uncertainty is shown in the bottom panels. Reproduced from Ref. [15].

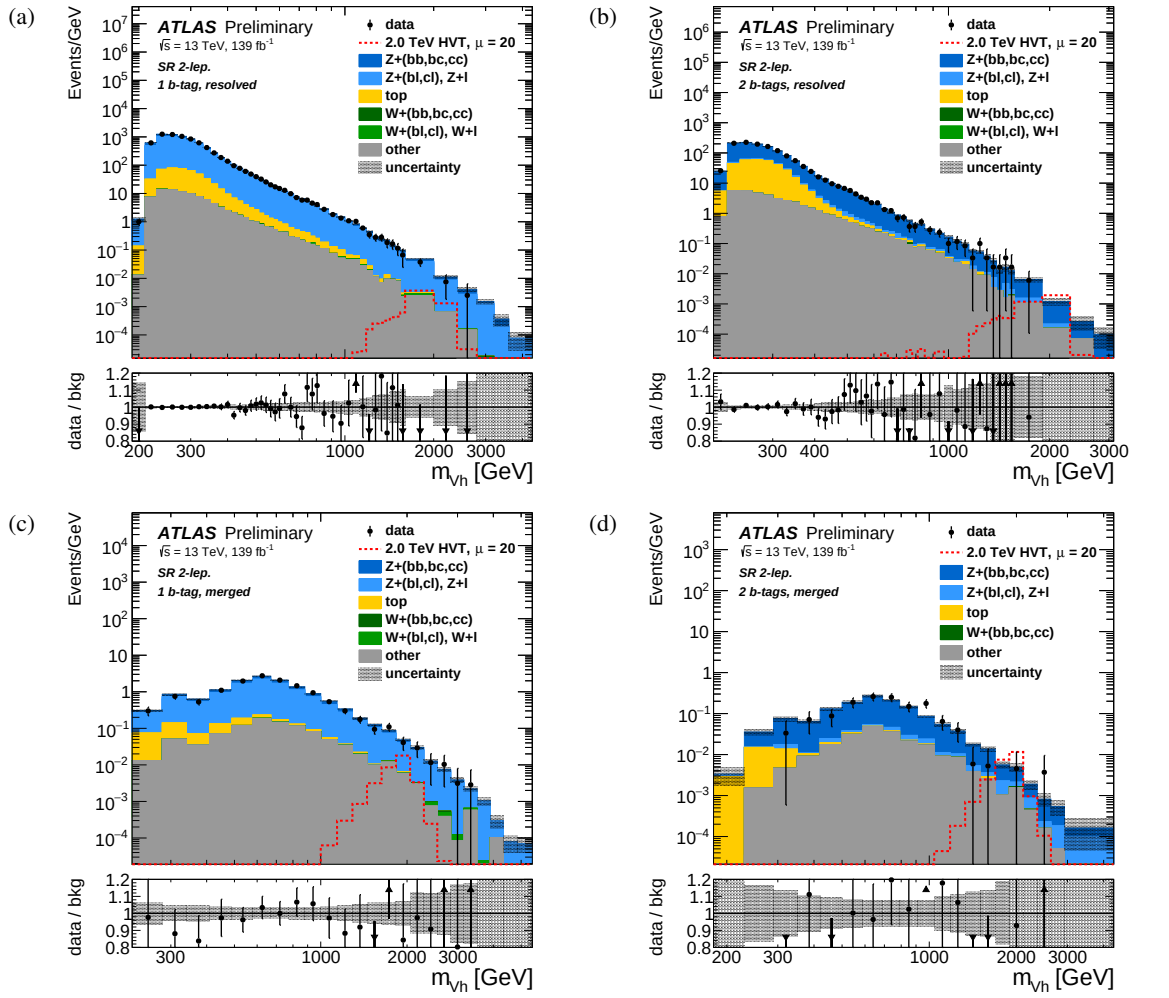

Figure D.3: Observed and expected post-fit m_{Vh} distributions in the $\ell^{\pm}\ell^{\mp}b\bar{b}$ signal regions, with *(a)* 1 b-tag and *(b)* 2 b-tag events with the resolved topology and *(c)* 1 b-tag and *(d)* 2 b-tag events with the merged topology. The expected signal distribution from a HVT Z' boson with signal strength $\mu = 20$ and a mass of 2 TeV is shown as the dotted red line. The data-to-background ratio where the hatched area indicates the post-fit background uncertainty is shown in the bottom panels. Reproduced from Ref. [15].

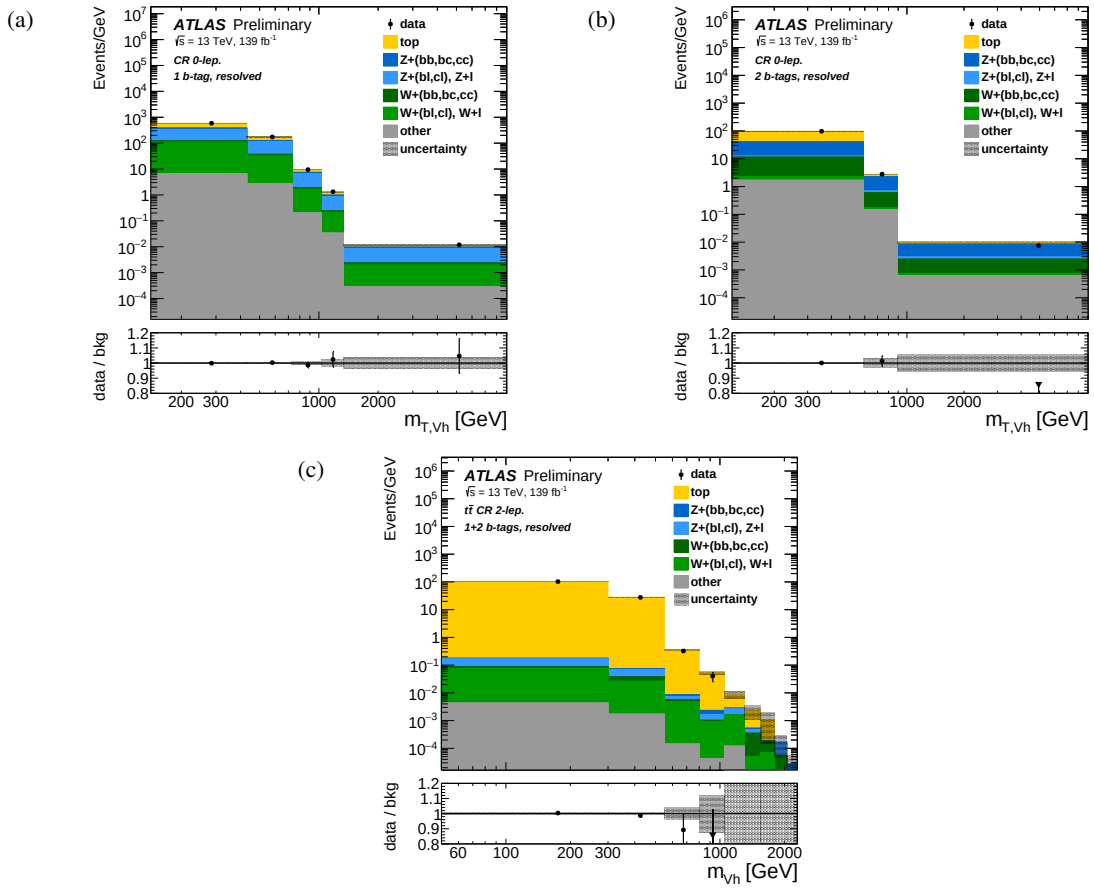

Figure D.4: Observed and expected post-fit $m_{\mathrm{T},\,Vh}$ and m_{Vh} distributions in the $\nu\bar{\nu}b\bar{b}$ and $\ell^{\pm}\ell^{\mp}b\bar{b}$ control regions, with *(a)* 1 b-tag and *(b)* 2 b-tag events in the sideband control regions with the resolved topology, and *(e)* 1 and 2 b-tag events in the opposite-flavour control region with resolved topology in the $\ell^{\pm}\ell^{\mp}b\bar{b}$ final state. The data-to-background ratio where the hatched area indicates the post-fit background uncertainty is shown in the bottom panels. Reproduced from Ref. [15].

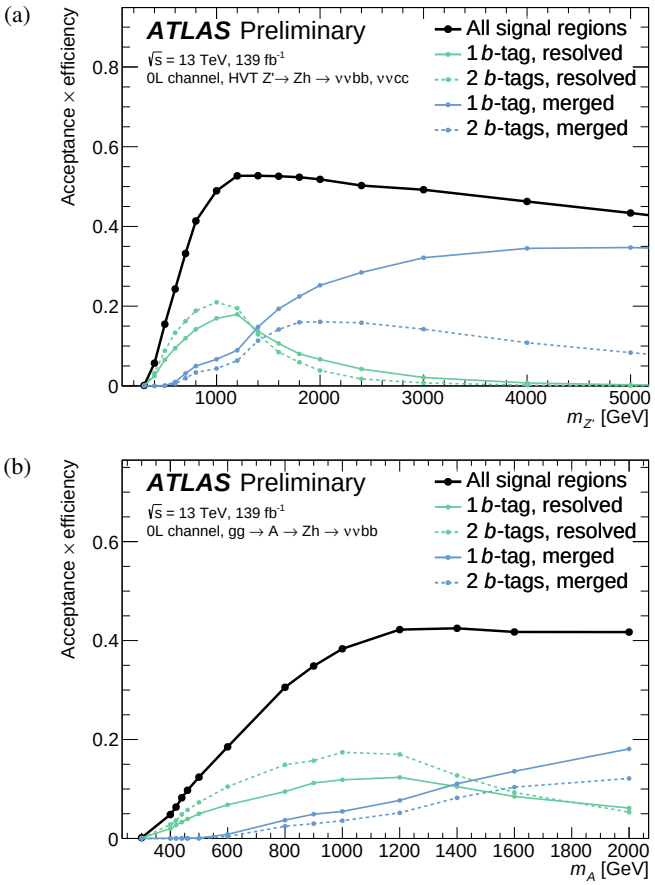

Figure D.5: Product of acceptance and efficiency for the *(a)* $Z' \to Zh \to \nu\bar{\nu}b\bar{b}$ and *(b)* $gg \to A \to Zh \to \nu\bar{\nu}b\bar{b}$ as a function of the resonance mass for the 0-lepton SR. The figures show the total product of acceptance and efficiency and the separate values for the various SR. Reproduced from Ref. [15].

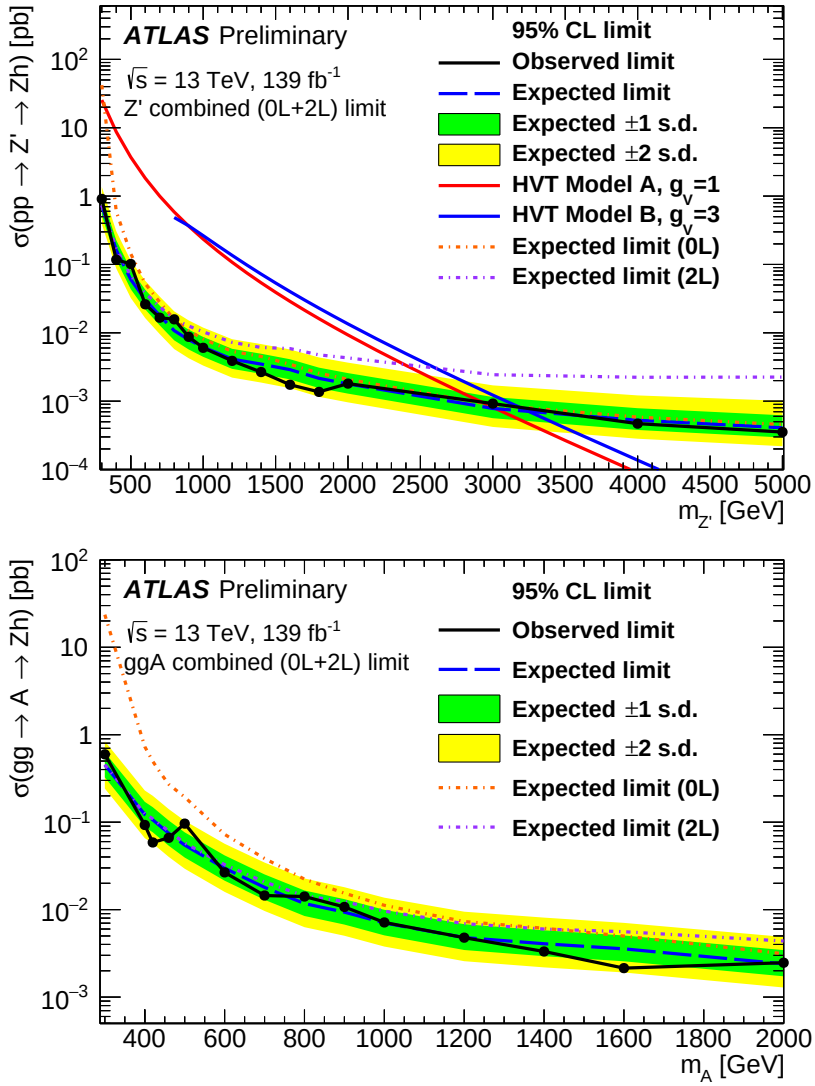

Figure D.6: Upper limits at the 95 % C.L. on the product of the cross section for *(a)* $pp \to Z'$ and *(b)* $gg \to A$ and their respective branching fraction to Zh from the combination of the 0-lepton and 2-lepton channels. For the $gg \to A$ search, the possible signal components of the data are interpreted assuming pure gluon fusion production and a branching fraction $h \to b\bar{b} = 0.569$ [261], while for the Z' search a branching fraction $h \to b\bar{b}, c\bar{c}$ of 0.598 is assumed. The limits obtained in the 0-lepton and 2-lepton channels individually are also added. Reproduced from Ref. [15].

D.2 Pull distributions

D.2.1 Pull distributions obtained from the Z'/ggA fit

The post-fit pull distributions of all nuisance parameters in the combined analysis of the $\nu\bar{\nu}b\bar{b}$ and $\ell^{\pm}\ell^{\mp}b\bar{b}$ final states for the Z'/ggA fit setup are shown in Figures D.7 and D.8.

D.2.2 Pull distributions obtained from the bbA fit

The post-fit pull distributions of all nuisance parameters in the combined analysis of the $\nu\bar{\nu}b\bar{b}$ and $\ell^{\pm}\ell^{\mp}b\bar{b}$ final states for the bbA fit setup are shown in Figures D.9 and D.10.

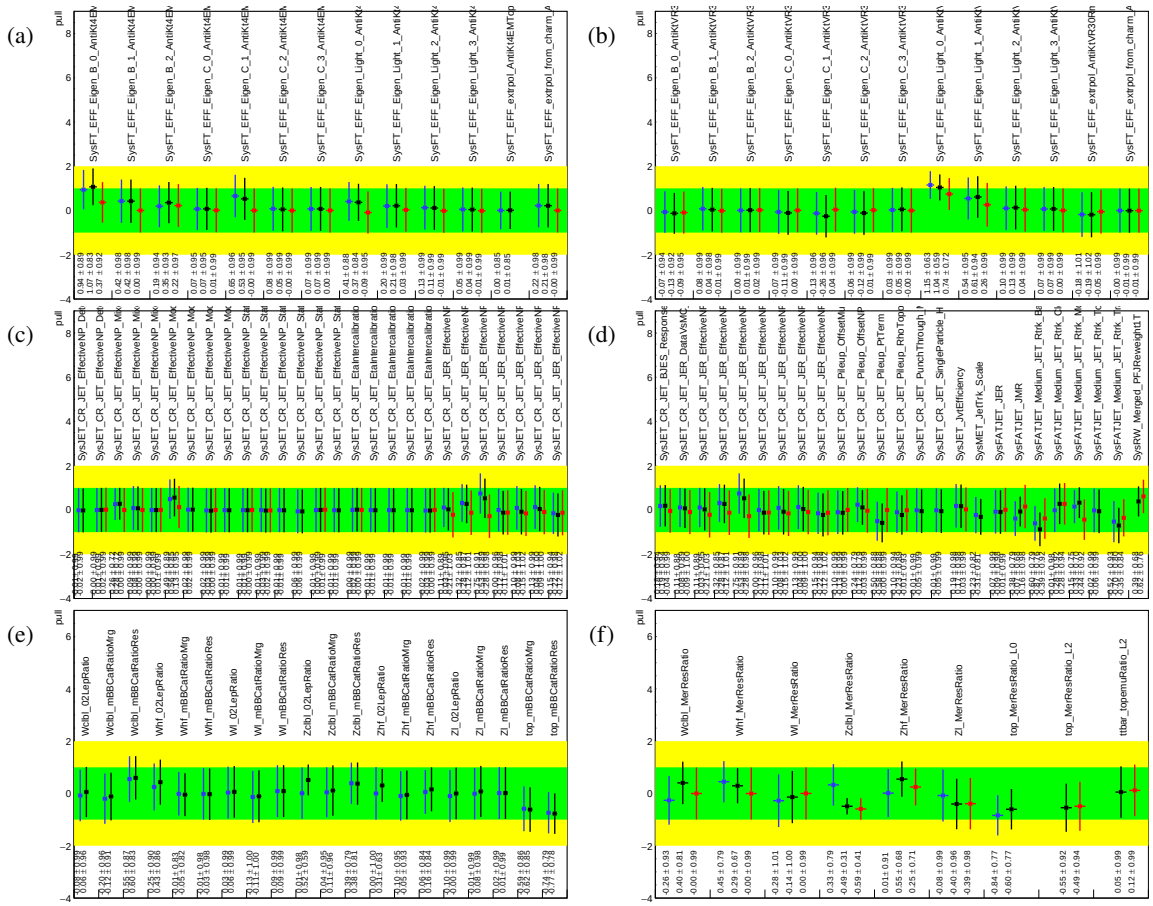

Figure D.7: The observed post-fit nuisance parameter pulls $(\hat{\theta} - \theta_0)/\Delta\theta$ for the combined fit of the $\nu\bar{\nu}b\bar{b}$ and $\ell^{\pm}\ell^{\mp}b\bar{b}$ final states using the Z'/ggA fit model. The nuisance parameters are separated into broad categories: *(a)* b-tagging related uncertainties in the resolved topology, *(b)* b-tagging related uncertainties in the merged topology, *(c)* and *(d)* jet-related uncertainties, *(e)* and *(f)* normalisation ratios between signal and control regions, resolved and merged topology, and the two final states. For every nuisance parameter, up to three markers are shown. The blue, black, and red markers indicate the post-fit pull for the corresponding parameter in the dedicated $\nu\bar{\nu}b\bar{b}$, combined, and dedicated $\ell^{\pm}\ell^{\mp}b\bar{b}$ analysis, respectively. The explicit post-fit pull values are also quoted for every nuisance parameter. The fit is performed on the LHC Run 2 dataset with an integrated luminosity of 139 fb^{-1}, recorded at $\sqrt{s} = 13$ TeV.

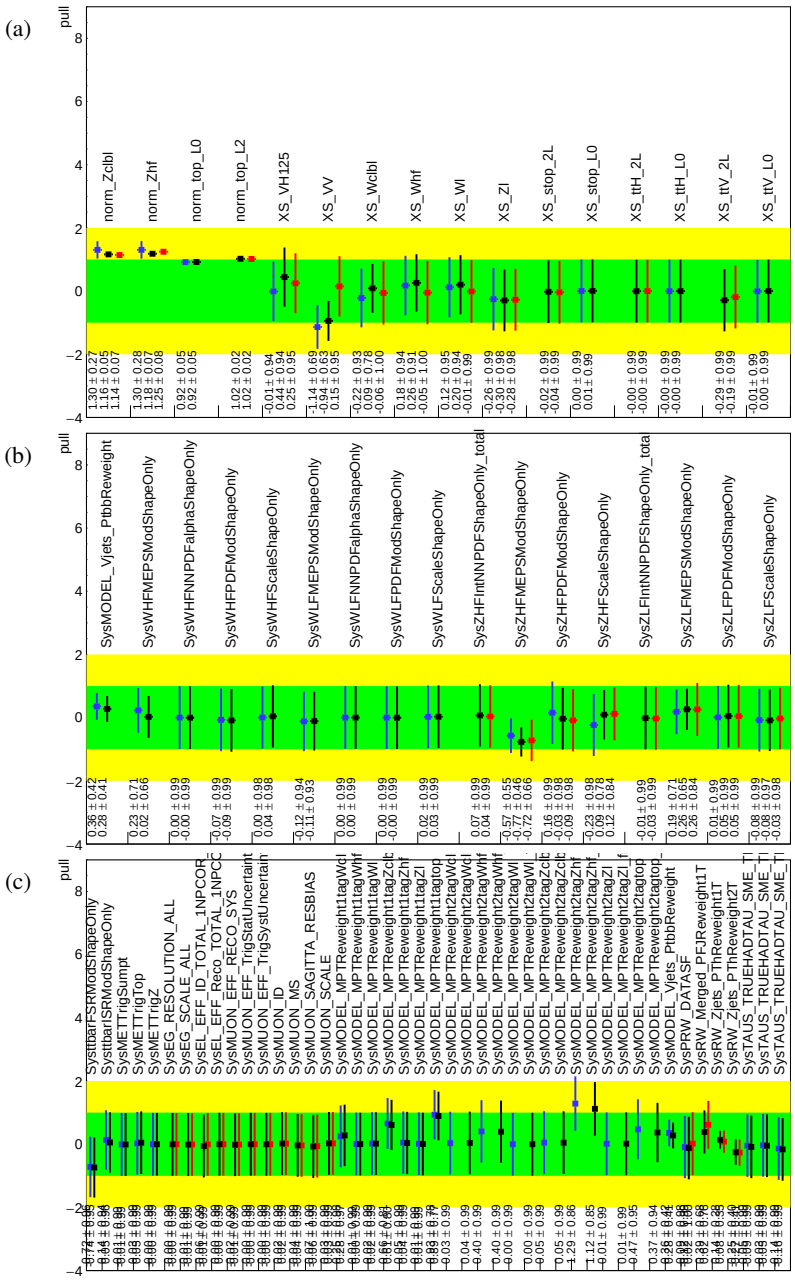

Figure D.8: The observed post-fit nuisance parameter pulls $(\hat{\theta} - \theta_0)/\Delta\theta$ for the combined fit of the $\nu\bar{\nu}b\bar{b}$ and $\ell^{\pm}\ell^{\mp}b\bar{b}$ final states using the Z'/ggA fit model. The nuisance parameters are separated into broad categories: *(a)* normalisation nuisance parameters, *(b)* theory uncertainties, and *(c)* other. For every nuisance parameter, up to three markers are shown. The blue, black, and red markers indicate the post-fit pull for the corresponding parameter in the dedicated $\nu\bar{\nu}b\bar{b}$, combined, and dedicated $\ell^{\pm}\ell^{\mp}b\bar{b}$ analysis, respectively. The explicit post-fit pull values are also quoted for every nuisance parameter. The fit is performed on the LHC Run 2 dataset with an integrated luminosity of 139 fb^{-1}, recorded at $\sqrt{s} = 13$ TeV.

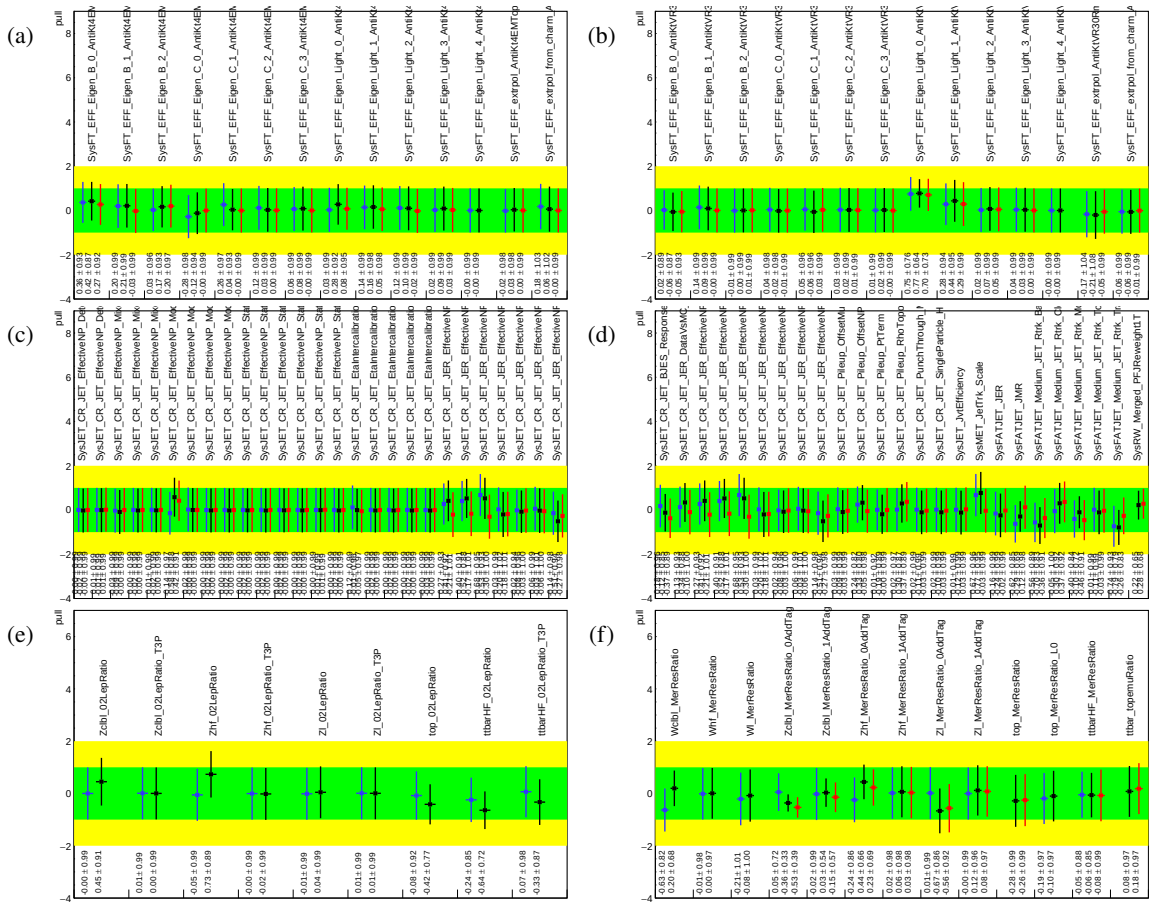

Figure D.9: The observed post-fit nuisance parameter pulls $(\hat{\theta} - \theta_0)/\Delta\theta$ for the combined fit of the $\nu\bar{\nu}b\bar{b}$ and $\ell^{\pm}\ell^{\mp}b\bar{b}$ final states using the bbA fit model. The nuisance parameters are separated into broad categories: *(a)* b-tagging related uncertainties in the resolved topology, *(b)* b-tagging related uncertainties in the merged topology, *(c)* and *(d)* jet-related uncertainties, *(e)* and *(f)* normalisation ratios between signal and control regions, resolved and merged topology, and the two final states. For every nuisance parameter, up to three markers are shown. The blue, black, and red markers indicate the post-fit pull for the corresponding parameter in the dedicated $\nu\bar{\nu}b\bar{b}$, combined, and dedicated $\ell^{\pm}\ell^{\mp}b\bar{b}$ analysis, respectively. The explicit post-fit pull values are also quoted for every nuisance parameter. The fit is performed on the LHC Run 2 dataset with an integrated luminosity of 139 fb^{-1}, recorded at $\sqrt{s} = 13$ TeV.

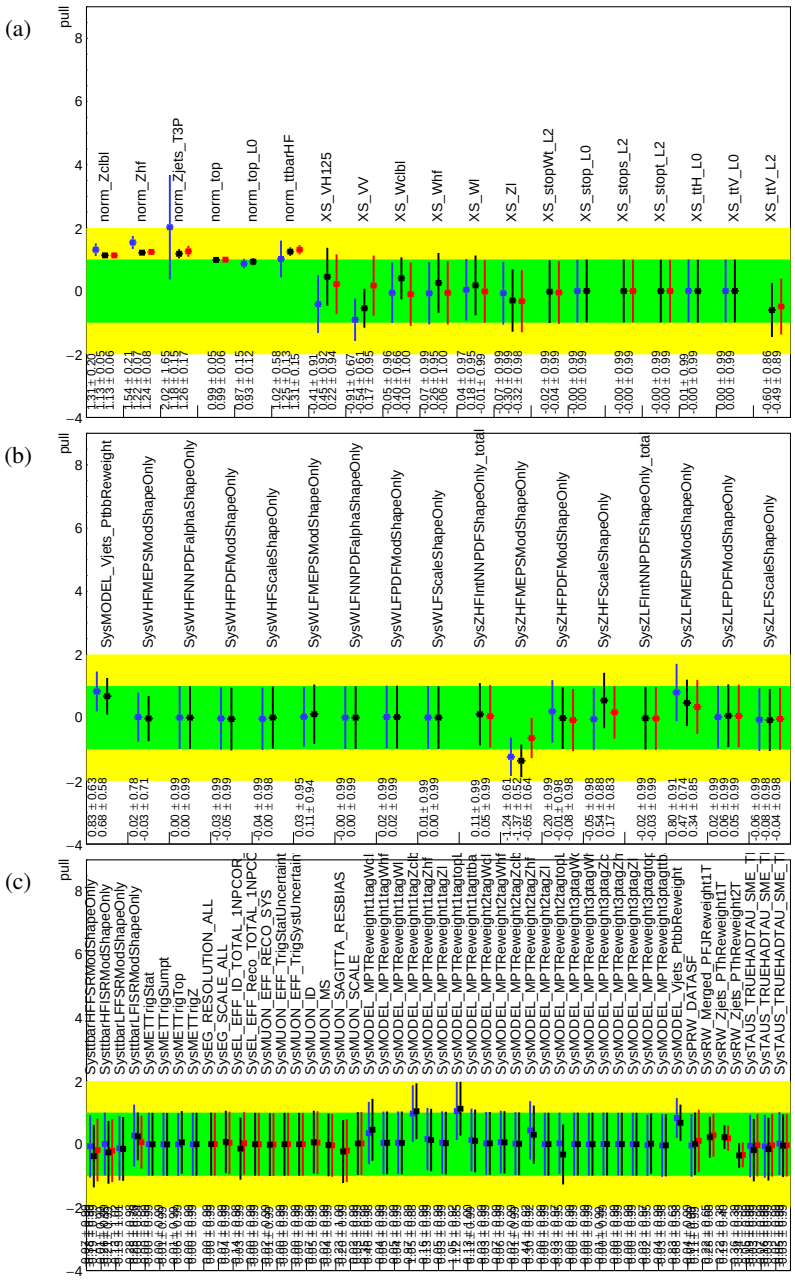

Figure D.10: The observed post-fit nuisance parameter pulls $(\hat{\theta} - \theta_0)/\Delta\theta$ for the combined fit of the $\nu\bar{\nu}b\bar{b}$ and $\ell^{\pm}\ell^{\mp}b\bar{b}$ final states using the bbA fit model. The nuisance parameters are separated into broad categories: *(a)* normalisation nuisance parameters, *(b)* theory uncertainties, and *(c)* other. For every nuisance parameter, up to three markers are shown. The blue, black, and red markers indicate the post-fit pull for the corresponding parameter in the dedicated $\nu\bar{\nu}b\bar{b}$, combined, and dedicated $\ell^{\pm}\ell^{\mp}b\bar{b}$ analysis, respectively. The explicit post-fit pull values are also quoted for every nuisance parameter. The fit is performed on the LHC Run 2 dataset with an integrated luminosity of 139 fb^{-1}, recorded at $\sqrt{s} = 13$ TeV.

BIBLIOGRAPHY

[1] J. Ballam et al., eds., *Proceedings, 6th Annual Conference on High Energy Nuclear Physics: Rochester, New York, USA, April 3-7, 1956*, Interscience, 1956.

[2] G. Arnison et al., *Experimental observation of isolated large transverse energy electrons with associated missing energy at s=540 GeV*, Physics Letters B **122** (1983) 103, ISSN: 0370-2693, URL: https://www.sciencedirect.com/science/article/pii/0370269383911772.

[3] M. Banner et al., *Observation of Single Isolated Electrons of High Transverse Momentum in Events with Missing Transverse Energy at the CERN anti-p p Collider*, Phys. Lett. B **122** (1983) 476.

[4] G. Arnison et al., *Experimental Observation of Lepton Pairs of Invariant Mass Around 95-GeV/c**2 at the CERN SPS Collider*, Phys. Lett. B **126** (1983) 398.

[5] P. Bagnaia et al., *Evidence for $Z^0 \to e^+e^-$ at the CERN $\bar{p}p$ Collider*, Phys. Lett. B **129** (1983) 130.

[6] F. Abe et al., *Observation of Top Quark Production in $\overline{p}p$ Collisions with the Collider Detector at Fermilab*, Phys. Rev. Lett. **74** (14 1995) 2626, URL: https://link.aps.org/doi/10.1103/PhysRevLett.74.2626.

[7] S. Abachi et al., *Observation of the Top Quark*, Phys. Rev. Lett. **74** (14 1995) 2632, URL: https://link.aps.org/doi/10.1103/PhysRevLett.74.2632.

[8] ATLAS Collaboration, *Observation of a new particle in the search for the Standard Model Higgs boson with the ATLAS detector at the LHC*, Phys. Lett. B **716** (2012) 1, arXiv: 1207.7214 [hep-ex].

[9] CMS Collaboration,
Observation of a new boson at a mass of 125 GeV with the CMS experiment at the LHC,
Phys. Lett. B **716** (2012) 30, arXiv: 1207.7235 [hep-ex].

[10] G. Hooft, 'Naturalness, Chiral Symmetry, and Spontaneous Chiral Symmetry Breaking',
Recent Developments in Gauge Theories, ed. by G. Hooft et al., Springer US, 1980 135,
ISBN: 978-1-4684-7571-5, URL: https://doi.org/10.1007/978-1-4684-7571-5_9.

[11] G. C. Branco et al., *Theory and phenomenology of two-Higgs-doublet models*,
Phys. Rept. **516** (2012) 1, arXiv: 1106.0034 [hep-ph].

[12] D. Pappadopulo, A. Thamm, R. Torre and A. Wulzer,
Heavy Vector Triplets: Bridging Theory and Data, JHEP **09** (2014) 060,
arXiv: 1402.4431 [hep-ph].

[13] ATLAS Collaboration, *Search for heavy resonances decaying to a W or Z boson and a Higgs boson in final states with leptons and b-jets in* 36.1 fb^{-1} *of* pp *collision data at* $\sqrt{s}$ = 13 *TeV with the ATLAS detector*, ATLAS-CONF-2017-055, 2017,
URL: https://cds.cern.ch/record/2273871.

[14] ATLAS Collaboration,
Search for heavy resonances decaying into a W or Z boson and a Higgs boson in final states with leptons and b-jets in $36 fb^{-1}$ *of* $\sqrt{s}$ = 13 *TeV* pp *collisions with the ATLAS detector*,
JHEP **03** (2018) 174, arXiv: 1712.06518 [hep-ex], Erratum: JHEP **11** (2018) 051.

[15] *Search for heavy resonances decaying into a Z boson and a Higgs boson in final states with leptons and b-jets in* 139 fb^{-1} *of* pp *collisions at* $\sqrt{s}$ = 13TeV *with the ATLAS detector*,
tech. rep. ATLAS-CONF-2020-043, CERN, 2020,
URL: https://cds.cern.ch/record/2728053.

[16] *Search for heavy resonances decaying into a W boson and a Higgs boson in final states with leptons and b-jets in* 139 fb^{-1} *of* pp *collisions at* $\sqrt{s}$ = 13 TeV *with the ATLAS detector*,
tech. rep., All figures including auxiliary figures are available at
https://atlas.web.cern.ch/Atlas/GROUPS/PHYSICS/CONFNOTES/ATLAS-CONF-2021-026:
CERN, 2021, URL: http://cds.cern.ch/record/2773302.

[17] *Standard Model Summary Plots March 2021*, tech. rep., All figures including auxiliary figures are available at https://atlas.web.cern.ch/Atlas/GROUPS/PHYSICS/PUBNOTES/ATL-PHYS-PUB-2021-005: CERN, 2021,
URL: http://cds.cern.ch/record/2758261.

[18] W. Hollik, *Quantum field theory and the Standard Model*, (2010), arXiv: 1012.3883,
URL: https://arxiv.org/abs/1012.3883.

[19] M. Maggiore, *A Modern introduction to quantum field theory*, 2005.

[20] M. E. Peskin and D. V. Schroeder, *An Introduction to quantum field theory*, Addison-Wesley, 1995, ISBN: 978-0-201-50397-5.

[21] M. D. Schwartz, *Quantum Field Theory and the Standard Model*, Cambridge University Press, 2014, ISBN: 978-1-107-03473-0, 978-1-107-03473-0.

[22] C. N. Yang and R. L. Mills, *Conservation of Isotopic Spin and Isotopic Gauge Invariance*, Phys. Rev. **96** (1 1954) 191, URL: https://link.aps.org/doi/10.1103/PhysRev.96.191.

[23] G. 't Hooft and M. J. G. Veltman, *Regularization and Renormalization of Gauge Fields*, Nucl. Phys. B **44** (1972) 189.

[24] E. Noether, *Invarianten beliebiger Differentialausdrücke*, ger, Nachrichten von der Gesellschaft der Wissenschaften zu Göttingen, Mathematisch-Physikalische Klasse **1918** (1918) 37, URL: http://eudml.org/doc/59011.

[25] D. J. Gross and F. Wilczek, *Ultraviolet Behavior of Nonabelian Gauge Theories*, Phys. Rev. Lett. **30** (1973) 1343, ed. by J. C. Taylor.

[26] D. J. Gross and F. Wilczek, *Asymptotically Free Gauge Theories - I*, Phys. Rev. D **8** (1973) 3633.

[27] H. D. Politzer, *Reliable Perturbative Results for Strong Interactions?*, Phys. Rev. Lett. **30** (1973) 1346, ed. by J. C. Taylor.

[28] H. Fritzsch, M. Gell-Mann and H. Leutwyler, *Advantages of the Color Octet Gluon Picture*, Phys. Lett. B **47** (1973) 365.

[29] S. L. Glashow, *Partial Symmetries of Weak Interactions*, Nucl. Phys. **22** (1961) 579.

[30] S. Weinberg, *A Model of Leptons*, Phys. Rev. Lett. **19** (1967) 1264.

[31] A. Salam, *Weak and Electromagnetic Interactions*, Conf. Proc. C **680519** (1968) 367.

[32] F. Englert and R. Brout, *Broken Symmetry and the Mass of Gauge Vector Mesons*, Phys. Rev. Lett. **13** (1964) 321, ed. by J. C. Taylor.

[33] P. W. Higgs, *Broken symmetries, massless particles and gauge fields*, Phys. Lett. **12** (1964) 132.

[34] P. W. Higgs, *Broken Symmetries and the Masses of Gauge Bosons*, Phys. Rev. Lett. **13** (1964) 508, ed. by J. C. Taylor.

[35] G. S. Guralnik, C. R. Hagen and T. W. B. Kibble, *Global Conservation Laws and Massless Particles*, Phys. Rev. Lett. **13** (1964) 585, ed. by J. C. Taylor.

[36] P. W. Higgs, *Spontaneous Symmetry Breakdown without Massless Bosons*, Phys. Rev. **145** (1966) 1156.

[37] T. W. B. Kibble, *Symmetry breaking in nonAbelian gauge theories*, Phys. Rev. **155** (1967) 1554, ed. by J. C. Taylor.

[38] T. Nakano and K. Nishijima, *Charge Independence for V-particles*, Prog. Theor. Phys. **10** (1953) 581.

[39] M. Gell-Mann, *The interpretation of the new particles as displaced charge multiplets*, Nuovo Cim. **4** (1956) 848.

[40] N. Cabibbo, *Unitary Symmetry and Leptonic Decays*, Phys. Rev. Lett. **10** (1963) 531.

[41] M. Kobayashi and T. Maskawa, *CP Violation in the Renormalizable Theory of Weak Interaction*, Prog. Theor. Phys. **49** (1973) 652.

[42] M. Tanabashi et al., *Review of Particle Physics*, Phys. Rev. D **98** (3 2018) 030001, URL: https://link.aps.org/doi/10.1103/PhysRevD.98.030001.

[43] D. V. Forero, M. Tortola and J. W. F. Valle, *Global status of neutrino oscillation parameters after Neutrino-2012*, Phys. Rev. D **86** (2012) 073012, arXiv: 1205.4018 [hep-ph].

[44] B. Pontecorvo, *Neutrino Experiments and the Problem of Conservation of Leptonic Charge*, Zh. Eksp. Teor. Fiz. **53** (1967) 1717.

[45] Z. Maki, M. Nakagawa and S. Sakata, *Remarks on the unified model of elementary particles*, Prog. Theor. Phys. **28** (1962) 870.

[46] M. Aker et al., *First operation of the KATRIN experiment with tritium*, Eur. Phys. J. C **80** (2020) 264, arXiv: 1909.06069 [physics.ins-det].

[47] A. D. Sakharov, *Violation of CP Invariance, C asymmetry, and baryon asymmetry of the universe*, Pisma Zh. Eksp. Teor. Fiz. **5** (1967) 32.

[48] G. W. Anderson and L. J. Hall, *The Electroweak phase transition and baryogenesis*, Phys. Rev. D **45** (1992) 2685.

[49] P. G. Harris et al., *New experimental limit on the electric dipole moment of the neutron*, Phys. Rev. Lett. **82** (1999) 904.

[50] M. Pospelov and A. Ritz, *Electric dipole moments as probes of new physics*, Annals Phys. **318** (2005) 119, arXiv: hep-ph/0504231.

[51] J. E. Kim and G. Carosi, *Axions and the Strong CP Problem*, Rev. Mod. Phys. **82** (2010) 557, [Erratum: Rev.Mod.Phys. 91, 049902 (2019)], arXiv: 0807.3125 [hep-ph].

[52] G. 't Hooft et al., eds., *Recent Developments in Gauge Theories. Proceedings, Nato Advanced Study Institute, Cargese, France, August 26 - September 8, 1979*, vol. 59, 1980 pp.1.

[53] E. Accomando, A. Belyaev, L. Fedeli, S. F. King and C. Shepherd-Themistocleous, *Z' physics with early LHC data*, Phys. Rev. **D83** (2011) 075012, arXiv: 1010.6058 [hep-ph].

[54] V. D. Barger, W.-Y. Keung and E. Ma, *A Gauge Model With Light W and Z Bosons*, Phys. Rev. **D22** (1980) 727.

[55] J. L. Hewett and T. G. Rizzo, *Low-Energy Phenomenology of Superstring Inspired E(6) Models*, Phys. Rept. **183** (1989) 193.

[56] M. Cvetic and S. Godfrey, *Discovery and identification of extra gauge bosons*, (1995) 383, arXiv: hep-ph/9504216 [hep-ph].

[57] T. G. Rizzo, 'Z' phenomenology and the LHC', *Proceedings of Theoretical Advanced Study Institute in Elementary Particle Physics : Exploring New Frontiers Using Colliders and Neutrinos (TASI 2006): Boulder, Colorado, June 4-30, 2006*, 2006 537, arXiv: hep-ph/0610104 [hep-ph], URL: http://www-public.slac.stanford.edu/sciDoc/docMeta.aspx?slacPubNumber=slac-pub-12129.

[58] P. Langacker, *The Physics of Heavy Z' Gauge Bosons*, Rev. Mod. Phys. **81** (2009) 1199, arXiv: 0801.1345 [hep-ph].

[59] E. Salvioni, G. Villadoro and F. Zwirner, *Minimal Z-prime models: Present bounds and early LHC reach*, JHEP **11** (2009) 068, arXiv: 0909.1320 [hep-ph].

[60] E. Salvioni, A. Strumia, G. Villadoro and F. Zwirner, *Non-universal minimal Z' models: present bounds and early LHC reach*, JHEP **03** (2010) 010, arXiv: 0911.1450 [hep-ph].

[61] M. S. Chanowitz, *A Heavy little Higgs and a light Z' under the radar*, Phys. Rev. **D84** (2011) 035014, arXiv: 1102.3672 [hep-ph].

[62] E. Salvioni, 'Some Z-prime and W-prime models facing current LHC searches', *Proceedings, 20th International Workshop on Deep-Inelastic Scattering and Related Subjects (DIS 2012): Bonn, Germany, March 26-30, 2012*, 2012 609.

[63] E. Accomando, D. Becciolini, A. Belyaev, S. Moretti and C. Shepherd-Themistocleous, *Z' at the LHC: Interference and Finite Width Effects in Drell-Yan*, JHEP **10** (2013) 153, arXiv: 1304.6700 [hep-ph].

[64] M. Schmaltz and C. Spethmann, *Two Simple W' Models for the Early LHC*, JHEP **07** (2011) 046, arXiv: 1011.5918 [hep-ph].

[65] C. Grojean, E. Salvioni and R. Torre, *A weakly constrained W' at the early LHC*, JHEP **07** (2011) 002, arXiv: 1103.2761 [hep-ph].

[66] R. Torre, *Limits on Leptophobic W' after 1 fb^{-1} of LHC Data: A Lesson on parton Level Simulations*, (2011), arXiv: 1109.0890 [hep-ph].

[67] R. Torre, *An isosinglet W' at the LHC: updated bounds from direct searches*, PoS **CORFU2011** (2011) 036, arXiv: 1204.4364 [hep-ph].

[68] P. Langacker and S. U. Sankar, *Bounds on the Mass of W(R) and the W(L)-W(R) Mixing Angle xi in General SU(2)-L x SU(2)-R x U(1) Models*, Phys. Rev. **D40** (1989) 1569.

[69] Z. Sullivan, *Fully Differential W' Production and Decay at Next-to-Leading Order in QCD*, Phys. Rev. **D66** (2002) 075011, arXiv: hep-ph/0207290 [hep-ph].

[70] T. G. Rizzo, *The Determination of the Helicity of W' Boson Couplings at the LHC*, JHEP **05** (2007) 037, arXiv: 0704.0235 [hep-ph].

[71] M. Frank, A. Hayreter and I. Turan, *Production and Decays of W_R bosons at the LHC*, Phys. Rev. **D83** (2011) 035001, arXiv: 1010.5809 [hep-ph].

[72] E. Accomando et al., *Interference effects in heavy W'-boson searches at the LHC*, Phys. Rev. **D85** (2012) 115017, arXiv: 1110.0713 [hep-ph].

[73] K. Agashe et al., *LHC Signals for Warped Electroweak Neutral Gauge Bosons*, Phys. Rev. **D76** (2007) 115015, arXiv: 0709.0007 [hep-ph].

[74] K. Agashe, S. Gopalakrishna, T. Han, G.-Y. Huang and A. Soni, *LHC Signals for Warped Electroweak Charged Gauge Bosons*, Phys. Rev. **D80** (2009) 075007, arXiv: 0810.1497 [hep-ph].

[75] ATLAS Collaboration, *Search for Dark Matter Produced in Association with a Higgs Boson decaying to $b\bar{b}$ at $\sqrt{s}$ = 13 TeV with the ATLAS Detector using 79.8 fb^{-1} of proton–proton collision data*, ATLAS-CONF-2018-039, 2018, URL: https://cds.cern.ch/record/2632344.

[76] R. Contino, D. Marzocca, D. Pappadopulo and R. Rattazzi, *On the effect of resonances in composite Higgs phenomenology*, JHEP **10** (2011) 081, arXiv: 1109.1570 [hep-ph].

[77] B. Bellazzini, C. Csaki, J. Hubisz, J. Serra and J. Terning, *Composite Higgs Sketch*, JHEP **11** (2012) 003, arXiv: 1205.4032 [hep-ph].

[78] E. Accomando, L. Fedeli, S. Moretti, S. De Curtis and D. Dominici, *Charged di-boson production at the LHC in a 4-site model with a composite Higgs boson*, Phys. Rev. **D86** (2012) 115006, arXiv: 1208.0268 [hep-ph].

[79] A. E. Carcamo Hernandez, C. O. Dib and A. R. Zerwekh, *The Effect of Composite Resonances on Higgs decay into two photons*, Eur. Phys. J. **C74** (2014) 2822, arXiv: 1304.0286 [hep-ph].

[80] M. S. Chanowitz and W. Kilgore, *Complementarity of resonant and nonresonant strong W W scattering at the LHC*, Phys. Lett. **B322** (1994) 147, arXiv: hep-ph/9311336 [hep-ph].

[81] R. Barbieri, G. Isidori, V. S. Rychkov and E. Trincherini, *Heavy Vectors in Higgs-less models*, Phys. Rev. **D78** (2008) 036012, arXiv: 0806.1624 [hep-ph].

[82] R. Barbieri, A. E. Carcamo Hernandez, G. Corcella, R. Torre and E. Trincherini, *Composite Vectors at the Large Hadron Collider*, JHEP **03** (2010) 068, arXiv: 0911.1942 [hep-ph].

[83] R. Barbieri, S. Rychkov and R. Torre, *Signals of composite electroweak-neutral Dark Matter: LHC/Direct Detection interplay*, Phys. Lett. **B688** (2010) 212, arXiv: 1001.3149 [hep-ph].

[84] A. E. Carcamo Hernandez and R. Torre, *A 'Composite' scalar-vector system at the LHC*, Nucl. Phys. **B841** (2010) 188, arXiv: 1005.3809 [hep-ph].

[85] A. E. Carcamo Hernandez, *Top quark effects in composite vector pair production at the LHC*, Eur. Phys. J. **C72** (2012) 2154, arXiv: 1008.1039 [hep-ph].

[86] O. Cata, G. Isidori and J. F. Kamenik, *Drell-Yan production of Heavy Vectors in Higgsless models*, Nucl. Phys. **B822** (2009) 230, arXiv: 0905.0490 [hep-ph].

[87] E. Accomando, D. Becciolini, S. De Curtis, D. Dominici and L. Fedeli, *W' production at the LHC in the 4-site Higgsless model*, Phys. Rev. **D84** (2011) 115014, arXiv: 1107.4087 [hep-ph].

[88] A. Falkowski, C. Grojean, A. Kaminska, S. Pokorski and A. Weiler, *If no Higgs then what?*, JHEP **11** (2011) 028, arXiv: 1108.1183 [hep-ph].

[89] ATLAS Collaboration, *Search for production of WW/WZ resonances decaying to a lepton, neutrino and jets in pp collisions at $\sqrt{s} = 8$ TeV with the ATLAS detector*, Eur. Phys. J. C **75** (2015) 209, arXiv: 1503.04677 [hep-ex], Erratum: Eur. Phys. J. C **75** (2015) 370.

[90] ATLAS Collaboration, Eur. Phys. J. C **75** (2015) 370.

[91] ATLAS Collaboration, *Search for resonant diboson production in the $\ell\ell q\bar{q}$ final state in pp collisions at $\sqrt{s} = 8$ TeV with the ATLAS detector*, Eur. Phys. J. C **75** (2015) 69, arXiv: 1409.6190 [hep-ex].

[92] ATLAS Collaboration, *Search for WZ resonances in the fully leptonic channel using pp collisions at $\sqrt{s} = 8$ TeV with the ATLAS detector*, Phys. Lett. B **737** (2014) 223, arXiv: 1406.4456 [hep-ex].

[93] ATLAS Collaboration, *Search for high-mass diboson resonances with boson-tagged jets in proton–proton collisions at $\sqrt{s} = 8$ TeV with the ATLAS detector*, JHEP **12** (2015) 055, arXiv: 1506.00962 [hep-ex].

[94] G. Altarelli, B. Mele and M. Ruiz-Altaba, *Searching for New Heavy Vector Bosons in $p\bar{p}$ Colliders*, Z. Phys. C **45** (1989) 109, [Erratum: Z.Phys.C 47, 676 (1990)].

[95] ATLAS Collaboration, *Combination of searches for WW, WZ, and ZZ resonances in pp collisions at $\sqrt{s} = 8$ TeV with the ATLAS detector*, Phys. Lett. B **755** (2016) 285, arXiv: 1512.05099 [hep-ex].

[96] ATLAS Collaboration, *Search for a new resonance decaying to a W or Z boson and a Higgs boson in the $\ell\ell/\ell\nu/\nu\nu + b\bar{b}$ final states with the ATLAS detector*, Eur. Phys. J. C **75** (2015) 263, arXiv: 1503.08089 [hep-ex].

[97] P. Fayet, *Supersymmetry and Weak, Electromagnetic and Strong Interactions*, Phys. Lett. **64B** (1976) 159.

[98] P. Fayet, *Spontaneously Broken Supersymmetric Theories of Weak, Electromagnetic and Strong Interactions*, Phys. Lett. **69B** (1977) 489.

[99] G. R. Farrar and P. Fayet, *Phenomenology of the Production, Decay, and Detection of New Hadronic States Associated with Supersymmetry*, Phys. Lett. **76B** (1978) 575.

[100] P. Fayet, *Relations Between the Masses of the Superpartners of Leptons and Quarks, the Goldstino Couplings and the Neutral Currents*, Phys. Lett. **84B** (1979) 416.

[101] S. Dimopoulos and H. Georgi, *Softly Broken Supersymmetry and SU(5)*, Nucl. Phys. **B193** (1981) 150.

[102] J. E. Kim, *Light Pseudoscalars, Particle Physics and Cosmology*, Phys. Rept. **150** (1987) 1.

[103] N. Turok and J. Zadrozny, *Electroweak baryogenesis in the two-doublet model*, Nucl. Physics, Sect. B (1991), ISSN: 05503213.

[104] S. L. Glashow and S. Weinberg, *Natural Conservation Laws for Neutral Currents*, Phys. Rev. **D15** (1977) 1958.

[105] E. A. Paschos, *Diagonal Neutral Currents*, Phys. Rev. **D15** (1977) 1966.

[106] D. Kominis, *The phenomenology of the CP-odd scalar in two-doublet models*, Nuclear Physics B **427** (1994) 575, ISSN: 0550-3213, URL: http://www.sciencedirect.com/science/article/pii/0550321394906416.

[107] ATLAS Collaboration, *Search for a CP-odd Higgs boson decaying to Zh in pp collisions at $\sqrt{s} = 8$ TeV with the ATLAS detector*, Phys. Lett. B **744** (2015) 163, arXiv: 1502.04478 [hep-ex].

[108] ATLAS Collaboration, *Search for neutral Higgs bosons of the minimal supersymmetric standard model in pp collisions at $\sqrt{s} = 8$ TeV with the ATLAS detector*, JHEP **11** (2014) 056, arXiv: 1409.6064 [hep-ex].

[109] O. S. Brüning et al., *LHC Design Report*, CERN Yellow Reports: Monographs, CERN, 2004, URL: http://cds.cern.ch/record/782076.

[110] O. S. Brüning et al., *LHC Design Report*, CERN Yellow Reports: Monographs, CERN, 2004, URL: http://cds.cern.ch/record/815187.

[111] M. Benedikt, P. Collier, V. Mertens, J. Poole and K. Schindl, *LHC Design Report*, CERN Yellow Reports: Monographs, CERN, 2004, URL: http://cds.cern.ch/record/823808.

[112] F. Marcastel, *CERN's Accelerator Complex. La chaîne des accélérateurs du CERN*, (2013), General Photo, URL: https://cds.cern.ch/record/1621583.

[113] *ATLAS Collaboration Luminosity Public Results*, https://twiki.cern.ch/twiki/bin/view/AtlasPublic/LuminosityPublicResultsRun2, Accessed: 30 Jan 2020.

[114] ATLAS Collaboration, *The ATLAS Experiment at the CERN Large Hadron Collider*, JINST **3** (2008) S08003.

[115] M. Capeans et al., *ATLAS Insertable B-Layer Technical Design Report*, tech. rep. CERN-LHCC-2010-013. ATLAS-TDR-19, 2010, URL: https://cds.cern.ch/record/1291633.

[116] *ATLAS Insertable B-Layer Technical Design Report Addendum*, tech. rep. CERN-LHCC-2012-009. ATLAS-TDR-19-ADD-1, Addendum to CERN-LHCC-2010-013, ATLAS-TDR-019, 2012, URL: https://cds.cern.ch/record/1451888.

[117] F. Hartmann, *Evolution of Silicon Sensor Technology in Particle Physics*, Springer Tracts Mod. Phys. **275** (2017) pp.1.

[118] M. Lozano et al., 'Comparison of radiation hardness of P-in-N, N-in-N, and N-in-P silicon pad detectors', *IEEE Trans. Nucl. Sci.* Vol. 52, 5 II, 2005 1468.

[119] Y. Unno et al., 'Evaluation of radiation damaged p-in-n and n-in-n silicon microstrip detectors', *1998 IEEE Nucl. Sci. Symp. Conf. Rec. 1998 IEEE Nucl. Sci. Symp. Med. Imaging Conf. (Cat. No.98CH36255)*, vol. 2, IEEE, 1998 846, ISBN: 0-7803-5021-9, URL: http://ieeexplore.ieee.org/document/774304/.

[120] ATLAS Collaboration, *Performance of the ATLAS trigger system in 2015*, Eur. Phys. J. C **77** (2017) 317, arXiv: 1611.09661 [hep-ex].

[121] ATLAS Collaboration, *Performance of the ATLAS Trigger System in 2010*, Eur. Phys. J. C **72** (2012) 1849, arXiv: 1110.1530 [hep-ex].

[122] Arantxa Ruiz, Martnez, *The ATLAS Run-2 Trigger Menu for Higher Luminosities: Design, Performance and Operational Aspects*, EPJ Web Conf. **182** (2018) 02083, URL: https://doi.org/10.1051/epjconf/201818202083.

[123] ATLAS Collaboration, *Trigger Menu in 2017*, ATL-DAQ-PUB-2018-002, 2018, URL: https://cds.cern.ch/record/2625986.

[124] *Trigger menu in 2018*, tech. rep. ATL-DAQ-PUB-2019-001, CERN, 2019, URL: https://cds.cern.ch/record/2693402.

[125] ATLAS Collaboration, *The ATLAS Simulation Infrastructure*, Eur. Phys. J. C **70** (2010) 823, arXiv: 1005.4568 [physics.ins-det].

[126] GEANT4 Collaboration, S. Agostinelli et al., *GEANT4 – a simulation toolkit*, Nucl. Instrum. Meth. A **506** (2003) 250.

[127] ATLAS Collaboration, *The simulation principle and performance of the ATLAS fast calorimeter simulation FastCaloSim*, ATL-PHYS-PUB-2010-013, 2010, URL: https://cds.cern.ch/record/1300517.

[128] ATLAS Collaboration, *The new Fast Calorimeter Simulation in ATLAS*, ATL-SOFT-PUB-2018-002, 2018, URL: https://cds.cern.ch/record/2630434.

[129] T. Cornelissen et al., *Concepts, Design and Implementation of the ATLAS New Tracking (NEWT)*, tech. rep. ATL-SOFT-PUB-2007-007. ATL-COM-SOFT-2007-002, CERN, 2007, URL: https://cds.cern.ch/record/1020106.

[130] ATLAS Collaboration,
Vertex Reconstruction Performance of the ATLAS Detector at $\sqrt{s}$ = 13 TeV,
ATL-PHYS-PUB-2015-026, 2015, URL: https://cds.cern.ch/record/2037717.

[131] ATLAS Collaboration, *Electron identification measurements in ATLAS using $\sqrt{s}$ = 13 TeV data with 50 ns bunch spacing*, ATL-PHYS-PUB-2015-041, 2015,
URL: https://cds.cern.ch/record/2048202.

[132] ATLAS Collaboration, *Electron reconstruction and identification in the ATLAS experiment using the 2015 and 2016 LHC proton–proton collision data at $\sqrt{s}$ = 13 TeV*,
Eur. Phys. J. C **79** (2019) 639, arXiv: 1902.04655 [hep-ex].

[133] ATLAS Collaboration, *Electron efficiency measurements with the ATLAS detector using the 2015 LHC proton–proton collision data*, ATLAS-CONF-2016-024, 2016,
URL: https://cds.cern.ch/record/2157687.

[134] M. Cacciari and G. P. Salam, *Pileup subtraction using jet areas*, Phys. Lett. B **659** (2007) 119,
URL: www.elsevier.com/locate/physletb.

[135] ATLAS collaboration, *Muon reconstruction performance of the ATLAS detector in proton–proton collision data at $\sqrt{s}$=13 TeV*, Eur. Phys. J. C **76** (2016),
URL: https://cds.cern.ch/record/2139897.

[136] J. Illingworth and J. Kittler, *A survey of the hough transform*,
Computer Vision, Graphics, and Image Processing **44** (1988) 87, ISSN: 0734-189X, URL:
http://www.sciencedirect.com/science/article/pii/S0734189X88800331.

[137] ATLAS Collaboration,
Topological cell clustering in the ATLAS calorimeters and its performance in LHC Run 1,
Eur. Phys. J. C **77** (2017) 490, arXiv: 1603.02934 [hep-ex].

[138] S. D. Ellis and D. E. Soper, *Successive Combination Jet Algorithm For Hadron Collisions*, (1993), arXiv: 9305266 [hep-ph], URL: http://arxiv.org/abs/hep-ph/9305266%20http://dx.doi.org/10.1103/PhysRevD.48.3160.

[139] Y. L. Dokshitzer, G. D. Leder, S. Moretti and B. R. Webber, *Better Jet Clustering Algorithms*, (1997), arXiv: 9707323 [hep-ph], URL: http://arxiv.org/abs/hep-ph/9707323%20http://dx.doi.org/10.1088/1126-6708/1997/08/001.

[140] M. Wobisch and T. Wengler,
Hadronization Corrections to Jet Cross Sections in Deep-Inelastic Scattering, (1999),
arXiv: 9907280 [hep-ph], URL: http://arxiv.org/abs/hep-ph/9907280.

[141] G. C. Blazey et al.,
Run II Jet Physics: Proceedings of the Run II QCD and Weak Boson Physics Workshop,
(2000), arXiv: 0005012 [hep-ex], URL: http://arxiv.org/abs/hep-ex/0005012.

[142] M. Cacciari, G. P. Salam and G. Soyez, *The anti-k_t jet clustering algorithm*, JHEP **04** (2008) 063, arXiv: 0802.1189 [hep-ph].

[143] M. Cacciari, G. P. Salam and G. Soyez, *FastJet user manual*, Eur. Phys. J. C **72** (2012) 1896, arXiv: 1111.6097 [hep-ph].

[144] D. Krohn, J. Thaler and L.-T. Wang, *Jets with variable R*, Journal of High Energy Physics **2009** (2009) 059, URL: https://doi.org/10.1088%2F1126-6708%2F2009%2F06%2F059.

[145] ATLAS Collaboration, *Boosted Object Tagging with Variable-R Jets in the ATLAS Detector*, ATL-PHYS-PUB-2016-013, 2016, URL: https://cds.cern.ch/record/2199360.

[146] ATLAS Collaboration, *Variable Radius, Exclusive-k_T, and Center-of-Mass Subjet Reconstruction for Higgs($\rightarrow b\bar{b}$) Tagging in ATLAS*, ATL-PHYS-PUB-2017-010, 2017, URL: https://cds.cern.ch/record/2268678.

[147] ATLAS Collaboration, *Tagging and suppression of pileup jets with the ATLAS detector*, ATLAS-CONF-2014-018, 2014, URL: https://cds.cern.ch/record/1700870.

[148] ATLAS Collaboration, *Reconstruction, Energy Calibration, and Identification of Hadronically Decaying Tau Leptons in the ATLAS Experiment for Run-2 of the LHC*, ATL-PHYS-PUB-2015-045, 2015, URL: https://cds.cern.ch/record/2064383.

[149] ATLAS Collaboration, *Expected performance of missing transverse momentum reconstruction for the ATLAS detector at $\sqrt{s}$ = 13 TeV*, ATL-PHYS-PUB-2015-023, 2015, URL: https://cds.cern.ch/record/2037700.

[150] ATLAS Collaboration, *Object-based missing transverse momentum significance in the ATLAS Detector*, ATLAS-CONF-2018-038, 2018, URL: https://cds.cern.ch/record/2630948.

[151] ATLAS Collaboration, *Improving jet substructure performance in ATLAS using Track-CaloClusters*, ATL-PHYS-PUB-2017-015, 2017, URL: https://cds.cern.ch/record/2275636.

[152] ATLAS Collaboration, *Performance of the ATLAS track reconstruction algorithms in dense environments in LHC Run 2*, Eur. Phys. J. C **77** (2017) 673, arXiv: 1704.07983 [hep-ex].

[153] ATLAS Collaboration, *ATLAS b-jet identification performance and efficiency measurement with $t\bar{t}$ events in pp collisions at $\sqrt{s}$ = 13 TeV*, Eur. Phys. J. C **79** (2019) 970, arXiv: 1907.05120 [hep-ex].

[154] J. Alwall et al., *The automated computation of tree-level and next-to-leading order differential cross sections, and their matching to parton shower simulations*, JHEP **07** (2014) 079, arXiv: 1405.0301 [hep-ph].

[155] R. Frederix et al., *The automation of next-to-leading order electroweak calculations*, J. High Energy Phys. **2018** (2018) 185, ISSN: 1029-8479, URL: https://doi.org/10.1007/JHEP07(2018)185.

[156] R. D. Ball et al., *Parton distributions with LHC data*, Nucl. Phys. B **867** (2013) 244, arXiv: 1207.1303 [hep-ph].

[157] T. Sjöstrand, S. Mrenna and P. Skands, *A brief introduction to PYTHIA 8.1*, Computer Physics Communications **178** (2008) 852, ISSN: 0010-4655, URL: http://www.sciencedirect.com/science/article/pii/S0010465508000441.

[158] T. Sjöstrand, S. Mrenna and P. Z. Skands, *PYTHIA 6.4 physics and manual*, JHEP **05** (2006) 026, arXiv: hep-ph/0603175.

[159] ATLAS Collaboration, *ATLAS Pythia 8 tunes to* 7 *TeV data*, ATL-PHYS-PUB-2014-021, 2014, URL: https://cds.cern.ch/record/1966419.

[160] P. Nason, *A new method for combining NLO QCD with shower Monte Carlo algorithms*, JHEP **11** (2004) 040, arXiv: hep-ph/0409146.

[161] S. Frixione, P. Nason and C. Oleari, *Matching NLO QCD computations with parton shower simulations: the POWHEG method*, JHEP **11** (2007) 070, arXiv: 0709.2092 [hep-ph].

[162] S. Alioli, P. Nason, C. Oleari and E. Re, *A general framework for implementing NLO calculations in shower Monte Carlo programs: the POWHEG BOX*, JHEP **06** (2010) 043, arXiv: 1002.2581 [hep-ph].

[163] P. Z. Skands, *Tuning Monte Carlo generators: The Perugia tunes*, Phys. Rev. D **82** (2010) 074018, arXiv: 1005.3457 [hep-ph].

[164] H.-L. Lai et al., *New parton distributions for collider physics*, Phys. Rev. D **82** (7 2010) 074024, URL: https://link.aps.org/doi/10.1103/PhysRevD.82.074024.

[165] M. Beneke, P. Falgari, S. Klein and C. Schwinn, *Hadronic top-quark pair production with NNLL threshold resummation*, Nucl. Phys. B **855** (2012) 695, arXiv: 1109.1536 [hep-ph].

[166] M. Cacciari, M. Czakon, M. Mangano, A. Mitov and P. Nason, *Top-pair production at hadron colliders with next-to-next-to-leading logarithmic soft-gluon resummation*, Phys. Lett. B **710** (2012) 612, arXiv: 1111.5869 [hep-ph].

[167] P. Bärnreuther, M. Czakon and A. Mitov, *Percent Level Precision Physics at the Tevatron: First Genuine NNLO QCD Corrections to $q\bar{q} \to t\bar{t} + X$*, Phys. Rev. Lett. **109** (2012) 132001, arXiv: 1204.5201 [hep-ph].

[168] M. Czakon and A. Mitov, *NNLO corrections to top-pair production at hadron colliders: the all-fermionic scattering channels*, JHEP **12** (2012) 054, arXiv: 1207.0236 [hep-ph].

[169] M. Czakon and A. Mitov,
NNLO corrections to top pair production at hadron colliders: the quark-gluon reaction,
JHEP **01** (2013) 080, arXiv: 1210.6832 [hep-ph].

[170] M. Czakon, P. Fiedler and A. Mitov,
Total Top-Quark Pair-Production Cross Section at Hadron Colliders Through $O(\alpha_S^4)$,
Phys. Rev. Lett. **110** (25 2013) 252004,
URL: https://link.aps.org/doi/10.1103/PhysRevLett.110.252004.

[171] M. Czakon and A. Mitov,
Top++: A program for the calculation of the top-pair cross-section at hadron colliders,
Comput. Phys. Commun. **185** (2014) 2930, arXiv: 1112.5675 [hep-ph].

[172] M. Czakon, D. Heymes and A. Mitov,
Dynamical scales for multi-TeV top-pair production at the LHC, JHEP **04** (2017) 071,
arXiv: 1606.03350 [hep-ph].

[173] M. Aliev et al., *HATHOR: HAdronic Top and Heavy quarks crOss section calculatoR*,
Comput. Phys. Commun. **182** (2011) 1034, arXiv: 1007.1327 [hep-ph].

[174] P. Kant et al., *HatHor for single top-quark production: Updated predictions and uncertainty estimates for single top-quark production in hadronic collisions*,
Comput. Phys. Commun. **191** (2015) 74, arXiv: 1406.4403 [hep-ph].

[175] N. Kidonakis, *Two-loop soft anomalous dimensions for single top quark associated production with a W- or H-*, Phys. Rev. D **82** (2010) 054018, arXiv: 1005.4451 [hep-ph].

[176] R. D. Ball et al., *Parton distributions for the LHC run II*, JHEP **04** (2015) 040,
arXiv: 1410.8849 [hep-ph].

[177] T. Sjöstrand et al., *An introduction to PYTHIA 8.2*, Comput. Phys. Commun. **191** (2015) 159,
arXiv: 1410.3012 [hep-ph].

[178] ATLAS Collaboration, *Measurement of the Z/γ^* boson transverse momentum distribution in pp collisions at $\sqrt{s} = 7$ TeV with the ATLAS detector*, JHEP **09** (2014) 145,
arXiv: 1406.3660 [hep-ex].

[179] T. Gleisberg et al., *Event generation with SHERPA 1.1*, JHEP **02** (2009) 007,
arXiv: 0811.4622 [hep-ph].

[180] T. Gleisberg and S. Höche, *Comix, a new matrix element generator*, JHEP **12** (2008) 039,
arXiv: 0808.3674 [hep-ph].

[181] F. Cascioli, P. Maierhöfer and S. Pozzorini, *Scattering Amplitudes with Open Loops*, Phys. Rev. Lett. **108** (2012) 111601, arXiv: 1111.5206 [hep-ph].

[182] S. Höche, F. Krauss, M. Schönherr and F. Siegert, *QCD matrix elements + parton showers. The NLO case*, JHEP **04** (2013) 027, arXiv: 1207.5030 [hep-ph].

[183] K. Melnikov and F. Petriello, *Electroweak gauge boson production at hadron colliders through $O(\alpha_s^2)$*, Phys. Rev. D **74** (2006) 114017, arXiv: hep-ph/0609070.

[184] D. J. Lange, *The EvtGen particle decay simulation package*, Nucl. Instrum. Meth. A **462** (2001) 152.

[185] ATLAS Collaboration, *Summary of ATLAS Pythia 8 tunes*, ATL-PHYS-PUB-2012-003, 2012, URL: https://cds.cern.ch/record/1474107.

[186] A. Martin, W. Stirling, R. Thorne and G. Watt, *Parton distributions for the LHC*, Eur. Phys. J. C **63** (2009) 189, arXiv: 0901.0002 [hep-ph].

[187] ATLAS Collaboration, *ATLAS data quality operations and performance for 20152018 data-taking*, Journal of Instrumentation **15** (2020) P04003, URL: https://doi.org/10.1088%2F1748-0221%2F15%2F04%2Fp04003.

[188] M. Cacciari, G. P. Salam and G. Soyez, *The catchment area of jets*, Journal of High Energy Physics **2008** (2008) 005, URL: https://doi.org/10.1088%2F1126-6708%2F2008%2F04%2F005.

[189] ATLAS Collaboration, *Search for WW/WZ resonance production in $\ell\nu qq$ final states in pp collisions at $\sqrt{s} = 13$ TeV with the ATLAS detector*, JHEP **03** (2018) 042, arXiv: 1710.07235 [hep-ex].

[190] ATLAS Collaboration, *Searches for heavy ZZ and ZW resonances in the $\ell\ell qq$ and $\nu\nu qq$ final states in pp collisions at $\sqrt{s} = 13$ TeV with the ATLAS detector*, JHEP **03** (2018) 009, arXiv: 1708.09638 [hep-ex].

[191] ATLAS Collaboration, *Luminosity determination in pp collisions at $\sqrt{s} = 8$ TeV using the ATLAS detector at the LHC*, Eur. Phys. J. C **76** (2016) 653, arXiv: 1608.03953 [hep-ex].

[192] ATLAS Collaboration, *Muon reconstruction performance of the ATLAS detector in proton–proton collision data at $\sqrt{s} = 13$ TeV*, Eur. Phys. J. C **76** (2016) 292, arXiv: 1603.05598 [hep-ex].

[193] ATLAS Collaboration, *Jet energy scale measurements and their systematic uncertainties in proton–proton collisions at $\sqrt{s}$ = 13 TeV with the ATLAS detector*, Phys. Rev. D **96** (2017) 072002, arXiv: 1703.09665 [hep-ex].

[194] ATLAS Collaboration, *Jet energy resolution in proton–proton collisions at $\sqrt{s}$ = 7 TeV recorded in 2010 with the ATLAS detector*, Eur. Phys. J. C **73** (2013) 2306, arXiv: 1210.6210 [hep-ex].

[195] ATLAS Collaboration, *Performance of jet substructure techniques for large-R jets in proton–proton collisions at $\sqrt{s}$ = 7 TeV using the ATLAS detector*, JHEP **09** (2013) 076, arXiv: 1306.4945 [hep-ex].

[196] ATLAS Collaboration, *Performance of b-jet identification in the ATLAS experiment*, JINST **11** (2016) P04008, arXiv: 1512.01094 [hep-ex].

[197] J. Butterworth et al., *PDF4LHC recommendations for LHC Run II*, J. Phys. G **43** (2016) 023001, arXiv: 1510.03865 [hep-ph].

[198] I. W. Stewart and F. J. Tackmann, *Theory Uncertainties for Higgs and Other Searches Using Jet Bins*, Phys. Rev. D **85** (2012) 034011, arXiv: 1107.2117 [hep-ph].

[199] S. Jiggins, 'Search for new resonances decaying to a Standard Model Vector boson (W/Z) and Higgs boson in the $\ell\ell b\bar{b}$, $\ell\nu b\bar{b}$ & $\nu\nu b\bar{b}$ channels in pp collisions at $\sqrt{s}$ = 13 TeV with the ATLAS detector', Thesis (Doctoral): University College London, 2018, URL: https://discovery.ucl.ac.uk/id/eprint/10044750/.

[200] L. Moneta, K. Cranmer, G. Schott and W. Verkerke, 'The RooStats project', *Proc. 13th Int. Work. Adv. Comput. Anal. Tech. Phys. Res. PoS(ACAT2010)*, vol. 93, Sissa Medialab, 2011 057, URL: https://pos.sissa.it/093/057.

[201] G. Cowan, K. Cranmer, E. Gross and O. Vitells, *Asymptotic formulae for likelihood-based tests of new physics*, Eur. Phys. J. C **71** (2011) 1554, arXiv: 1007.1727 [physics.data-an], Erratum: Eur. Phys. J. C **73** (2013) 2501.

[202] A. Wald, *Tests of Statistical Hypotheses Concerning Several Parameters When the Number of Observations is Large*, Transactions of the American Mathematical Society **54** (1943) 426, ISSN: 00029947, URL: http://www.jstor.org/stable/1990256.

[203] O. Behnke, K. Kröninger, T. Schörner-Sadenius and G. Schott, eds., *Data analysis in high energy physics: A practical guide to statistical methods*, Wiley-VCH, 2013, ISBN: 978-3-527-41058-3, 978-3-527-65344-7, 978-3-527-65343-0.

[204] ATLAS Collaboration, *Calibration of the b-tagging efficiency on charm jets using a sample of W + c events with $\sqrt{s}$ = 13 TeV ATLAS data*, ATLAS-CONF-2018-055, 2018, URL: https://cds.cern.ch/record/2652195.

[205] N. D. Christensen and C. Duhr, *FeynRules Feynman rules made easy*, Computer Physics Communications **180** (2009) 1614, ISSN: 0010-4655, URL: http://www.sciencedirect.com/science/article/pii/S0010465509000733.

[206] A. Alloul, N. D. Christensen, C. Degrande, C. Duhr and B. Fuks, *FeynRules ă2.0ă A complete toolbox for tree-level phenomenology*, Computer Physics Communications **185** (2014) 2250, ISSN: 0010-4655, URL: http://www.sciencedirect.com/science/article/pii/S0010465514001350.

[207] T. Jeo, J. M. Lindert, P. Nason, C. Oleari and S. Pozzorini, *An NLO+PS generator for $t\bar{t}$ and Wt production and decay including non-resonant and interference effects*, Eur.Phys.J.C **76** (2016) 691, arXiv: 1607.04538 [hep-ph].

[208] ATLAS Collaboration, *Study of heavy flavor quarks produced in association with top quark pairs at $\sqrt{s}$ = 7 TeV using the ATLAS detector*, Phys. Rev. D **89** (2014) 072012, arXiv: 1304.6386 [hep-ex].

[209] A. Bredenstein, A. Denner, S. Dittmaier and S. Pozzorini, *NLO QCD corrections to pp —> t anti-t b anti-b + X at the LHC*, Phys. Rev. Lett. **103** (2009) 012002, arXiv: 0905.0110 [hep-ph].

[210] ATLAS Collaboration, *Search for the standard model Higgs boson produced in association with top quarks and decaying into a $b\bar{b}$ pair in pp collisions at $\sqrt{s}$ = 13 TeV with the ATLAS detector*, Phys. Rev. D **97** (2018) 072016, arXiv: 1712.08895 [hep-ex].

[211] ATLAS Collaboration, *Observation of Higgs boson production in association with a top quark pair at the LHC with the ATLAS detector*, Phys. Lett. B **784** (2018) 173, arXiv: 1806.00425 [hep-ex].

[212] S. Frixione, E. Laenen, P. Motylinski, C. White and B. R. Webber, *Single-top hadroproduction in association with a W boson*, JHEP **07** (2008) 029, arXiv: 0805.3067 [hep-ph].

[213] F. Buccioni et al., *OpenLoops 2*, Eur. Phys. J. C **79** (2019) 866, ISSN: 1434-6052, URL: https://doi.org/10.1140/epjc/s10052-019-7306-2.

[214] G. Cullen et al., *Automated one-loop calculations with GoSam*, Eur. Phys. J. C **72** (2012) 1889, ISSN: 1434-6052, URL: https://doi.org/10.1140/epjc/s10052-012-1889-1.

[215] K. Hamilton, P. Nason and G. Zanderighi, *MINLO: multi-scale improved NLO*, J. High Energy Phys. **2012** (2012) 155, ISSN: 1029-8479, URL: https://doi.org/10.1007/JHEP10(2012)155.

[216] A. Denner, S. Dittmaier, S. Kallweit and A. Muck, *Electroweak corrections to Higgs-strahlung off W/Z bosons at the Tevatron and the LHC with HAWK*, JHEP **03** (2012) 075, arXiv: 1112.5142 [hep-ph].

[217] A. Denner, S. Dittmaier, S. Kallweit and A. Mück, *HAWK 2.0: A Monte Carlo program for Higgs production in vector-boson fusion and Higgs strahlung at hadron colliders*, Comput. Phys. Commun. **195** (2015) 161, arXiv: 1412.5390 [hep-ph].

[218] G. Avoni et al., *The new LUCID-2 detector for luminosity measurement and monitoring in ATLAS*, JINST **13** (2018) P07017.

[219] ATLAS Collaboration, *Luminosity determination in pp collisions at $\sqrt{s} = 13$ TeV using the ATLAS detector at the LHC*, ATLAS-CONF-2019-021, 2019, URL: https://cds.cern.ch/record/2677054.

[220] G. Aad et al., *Performance of the missing transverse momentum triggers for the ATLAS detector during Run-2 data taking*, Journal of High Energy Physics **2020** (2020) 80, ISSN: 1029-8479, URL: https://doi.org/10.1007/JHEP08(2020)080.

[221] G. Aad et al., $E_{\mathrm{T}}^{\mathrm{miss}}$ *trigger public results website*, https://twiki.cern.ch/twiki/bin/view/AtlasPublic/MissingEtTriggerPublicResults, 2021 (accessed 18 May 2021).

[222] A. M. Sirunyan et al., *Observation of Higgs Boson Decay to Bottom Quarks*, Phys. Rev. Lett. **121** (12 2018) 121801, URL: https://link.aps.org/doi/10.1103/PhysRevLett.121.121801.

[223] G. Aad et al., *Jet energy scale and resolution measured in proton-proton collisions at $\sqrt{s} = 13$ TeV with the ATLAS detector*, (2020), arXiv: 2007.02645 [hep-ex].

[224] ATLAS Collaboration, *In situ calibration of large-radius jet energy and mass in 13 TeV proton–proton collisions with the ATLAS detector*, Eur. Phys. J. C **79** (2019) 135, arXiv: 1807.09477 [hep-ex].

[225] ATLAS Collaboration, *Optimisation and performance studies of the ATLAS b-tagging algorithms for the 2017-18 LHC run*, ATL-PHYS-PUB-2017-013, 2017, URL: https://cds.cern.ch/record/2273281.

[226] ATLAS Collaboration, *Measurement of b-tagging efficiency of c-jets in $t\bar{t}$ events using a likelihood approach with the ATLAS detector*, ATLAS-CONF-2018-001, 2018, URL: https://cds.cern.ch/record/2306649.

[227] L. Lonnblad, *Correcting the color dipole cascade model with fixed order matrix elements*, JHEP **05** (2002) 046, arXiv: hep-ph/0112284.

[228] L. Lonnblad and S. Prestel, *Matching Tree-Level Matrix Elements with Interleaved Showers*, JHEP **03** (2012) 019, arXiv: 1109.4829 [hep-ph].

[229] M. Bähr et al., *Herwig++ physics and manual*, Eur. Phys. J. C **58** (2008) 639, arXiv: 0803.0883 [hep-ph].

[230] ATLAS Collaboration, *Search for heavy resonances decaying to a Z boson and a photon in pp collisions at $\sqrt{s}$ = 13 TeV with the ATLAS detector*, ATLAS-CONF-2016-010, 2016, URL: https://cds.cern.ch/record/2139795.

[231] G. Aad et al., 'Formulae for Estimating Significance', Manuscript in preparation.

[232] M. Baak, S. Gadatsch, R. Harrington and W. Verkerke, *Interpolation between multi-dimensional histograms using a new non-linear moment morphing method*, Nucl. Instrum. Meth. A **771** (2015) 39, arXiv: 1410.7388 [physics.data-an].

[233] B. D. Yabsley, *Neyman \& Feldman-Cousins intervals for a simple problem with an unphysical region, and an analytic solution*, (2006), arXiv: hep-ex/0604055.

[234] ATLAS Collaboration, *Search for resonances decaying into a weak vector boson and a Higgs boson in the fully hadronic final state produced in proton–proton collisions at $\sqrt{s}$ = 13 TeV with the ATLAS detector*, Phys. Rev. D **102** (2020) 112008, arXiv: 2007.05293 [hep-ex].

[235] ATLAS Collaboration, *Search for heavy diboson resonances in semileptonic final states in pp collisions at $\sqrt{s}$ = 13 TeV with the ATLAS detector*, Eur. Phys. J. C **80** (2020) 1165, arXiv: 2004.14636 [hep-ex].

[236] ATLAS Collaboration, *Combination of searches for heavy resonances decaying into bosonic and leptonic final states using 36 fb^{-1} of proton–proton collision data at $\sqrt{s}$ = 13 TeV with the ATLAS detector*, Phys. Rev. D **98** (2018) 052008, arXiv: 1808.02380 [hep-ex].

[237] B. Mellado Garcia, P. Musella, M. Grazzini and R. Harlander, *CERN Report 4: Part I Standard Model Predictions*, (2016), URL: https://cds.cern.ch/record/2150771.

[238] P. P. Gadow, 'Search for Dark Matter Produced in Association with Hadronically Decaying Bosons at $\sqrt{s}$ = 13 TeV with the ATLAS Detector at the LHC', Presented 03 Nov 2020, 2020, URL: http://cds.cern.ch/record/2744557.

[239] ATLAS Collaboration, *Search for dark matter produced in association with a dark Higgs boson decaying into $W^{\pm}W^{\mp}$ or ZZ in fully hadronic final states from $\sqrt{s}$ = 13 TeV pp collisions recorded with the ATLAS detector*, Phys. Rev. Lett. **126** (2021) 121802, arXiv: 2010.06548 [hep-ex].

[240] ATLAS Collaboration, *Track assisted techniques for jet substructure*, ATL-PHYS-PUB-2018-012, 2018, URL: https://cds.cern.ch/record/2630864.

[241] D. Eriksson, J. Rathsman and O. Stal, *2HDMC: Two-Higgs-Doublet Model Calculator Physics and Manual*, Comput. Phys. Commun. **181** (2010) 189, arXiv: 0902.0851 [hep-ph].

[242] R. V. Harlander, S. Liebler and H. Mantler, *SusHi: A program for the calculation of Higgs production in gluon fusion and bottom-quark annihilation in the Standard Model and the MSSM*, Comput. Phys. Commun. **184** (2013) 1605, arXiv: 1212.3249 [hep-ph].

[243] R. V. Harlander and W. B. Kilgore, *Next-to-next-to-leading order Higgs production at hadron colliders*, Phys. Rev. Lett. **88** (2002) 201801, arXiv: hep-ph/0201206.

[244] R. V. Harlander and W. B. Kilgore, *Higgs boson production in bottom quark fusion at next-to-next-to leading order*, Phys. Rev. D **68** (2003) 013001, arXiv: hep-ph/0304035.

[245] R. Harlander and P. Kant, *Higgs production and decay: Analytic results at next-to-leading order QCD*, JHEP **12** (2005) 015, arXiv: hep-ph/0509189.

[246] ATLAS Collaboration, *Measurement of the Inelastic Proton–Proton Cross Section at $\sqrt{s} = 13$ TeV with the ATLAS Detector at the LHC*, Phys. Rev. Lett. **117** (2016) 182002, arXiv: 1606.02625 [hep-ex].

[247] ATLAS Collaboration, *Electron and photon energy calibration with the ATLAS detector using LHC Run 1 data*, Eur. Phys. J. C **74** (2014) 3071, arXiv: 1407.5063 [hep-ex].

[248] ATLAS Collaboration, *Electron and photon energy calibration with the ATLAS detector using data collected in 2015 at $\sqrt{s} = 13$ TeV*, ATL-PHYS-PUB-2016-015, 2016, URL: https://cds.cern.ch/record/2203514.

[249] ATLAS Collaboration, *Early Inner Detector Tracking Performance in the 2015 Data at $\sqrt{s} = 13$ TeV*, ATL-PHYS-PUB-2015-051, 2015, URL: https://cds.cern.ch/record/2110140.

[250] ATLAS Collaboration, *Pile-up subtraction and suppression for jets in ATLAS*, ATLAS-CONF-2013-083, 2013, URL: https://cds.cern.ch/record/1570994.

[251] ATLAS Collaboration, *Monte Carlo Calibration and Combination of In-situ Measurements of Jet Energy Scale, Jet Energy Resolution and Jet Mass in ATLAS*, ATLAS-CONF-2015-037, 2015, URL: https://cds.cern.ch/record/2044941.

[252] ATLAS Collaboration, *Data-driven determination of the energy scale and resolution of jets reconstructed in the ATLAS calorimeters using dijet and multijet events at* $\sqrt{s} = 8$ *TeV*, ATLAS-CONF-2015-017, 2015, URL: https://cds.cern.ch/record/2008678.

[253] ATLAS Collaboration, *Jet Calibration and Systematic Uncertainties for Jets Reconstructed in the ATLAS Detector at* $\sqrt{s} = 13$ *TeV*, ATL-PHYS-PUB-2015-015, 2015, URL: https://cds.cern.ch/record/2037613.

[254] ATLAS Collaboration, *Optimisation of the ATLAS b-tagging performance for the 2016 LHC Run*, ATL-PHYS-PUB-2016-012, 2016, URL: https://cds.cern.ch/record/2160731.

[255] ATLAS Collaboration, *Calibration of b-tagging using dileptonic top pair events in a combinatorial likelihood approach with the ATLAS experiment*, ATLAS-CONF-2014-004, 2014, URL: https://cds.cern.ch/record/1664335.

[256] ATLAS Collaboration, *Calibration of the performance of b-tagging for c and light-flavour jets in the 2012 ATLAS data*, ATLAS-CONF-2014-046, 2014, URL: https://cds.cern.ch/record/1741020.

[257] ATLAS Collaboration, *Identification of Boosted, Hadronically-Decaying W and Z Bosons in* $\sqrt{s} = 13$ *TeV Monte Carlo Simulations for ATLAS*, ATL-PHYS-PUB-2015-033, 2015, URL: https://cds.cern.ch/record/2041461.

[258] ATLAS Collaboration, *Jet mass reconstruction with the ATLAS Detector in early Run 2 data*, ATLAS-CONF-2016-035, 2016, URL: https://cds.cern.ch/record/2200211.

[259] ATLAS Collaboration, *Performance of large-R jets and substructure reconstruction with the ATLAS detector*, ATLAS-CONF-2012-065, 2012, URL: https://cds.cern.ch/record/1459530.

[260] A. Collaboration, *Athena*, version 21.0.127, 2021, URL: https://doi.org/10.5281/zenodo.4772550.

[261] ATLAS Collaboration, *Search for new resonances decaying to a W or Z boson and a Higgs boson in the* $\ell\ell b\bar{b}$, $\ell\nu b\bar{b}$, *and* $\nu\nu b\bar{b}$ *channels in* pp *collisions at* $\sqrt{s} = 13$ *TeV with the ATLAS Detector*, ATLAS-CONF-2015-074, 2015, URL: https://cds.cern.ch/record/2114846.

List of Figures

List of Tables

ACRONYMS

2HDM	Two-Higgs Doublet Model
ATLAS	A Toroidal LHC ApparatuS
BSM	beyond the Standard Model
CERN	European Organization for Nuclear Research
CKM	Cabibbo-Kobayashi-Maskawa
CSC	Cathode Strip Chamber
DY	Drell-Yan
EGM	extended gauge model
EM	electromagnetic
EW	electroweak
FCal	forward calorimeter
FCNC	flavour changing neutral current
HEC	hadronic end-cap calorimeter
HLT	high-level trigger
HVT	Heavy Vector Triplet
IBL	Insertable B-Layer
ID	inner detector
JVT	Jet Vertex Tagger
L1	level-1
L1Calo	L1 calorimeter trigger
L1Muon	L1 muon trigger
L1Topo	L1 topological trigger
LAr	liquid Argon
LHC	Large Hadron Collider
LINAC	linear accelerator
LO	leading-order

MC	Monte Carlo
MDT	Monitored Drift Tube
ME	matrix element
MS	muon spectrometer
MSSM	Minimal Supersymmetric extension of the standard model
NLL	next-to-leading-logarithm
NLO	next-to-leading-order
NNLL	next-to-next-to-leading-logarithm
NNLO	next-to-next-to-leading-order
NP	nuisance parameter
NWA	narrow width approximation
PDF	parton distribution function
p.d.f.	probability density function
PS	Proton Synchrotron
PSB	Proton Synchrotron Booster
PV	primary vertex
QCD	quantum chromodynamics
SCT	Semi-Conductor Tracker
SM	Standard Model
TCC	Track-CaloCluster
TDAQ	Trigger and Data Acquisition
TRT	Transition Radiation Tracker
VBF	vector boson fusion
VEV	vacuum expectation value
VR	variable radius